Joint supervision between:

Universidade de Brasília

Instituto de Geociências

Programa de Pós-Graduação em Geologia

Université de Bretagne-Occidentale

École Doctorale des Sciences de la Mer et du Littoral

Laboratoire Géosciences Océan – GEO OCEAN

Henrique Serratt

Sistemas de Hidrogênio Natural em Margens Passivas Vulcânicas

(Natural Hydrogen Systems in Volcanic Passive Margins)

Thesis advisors:

Dr. Adalene Moreira Silva

Dr. Laurent Geoffroy

Co-advisor

Dr. Farid Chemale Jr.

Thesis N°226 (UnB)

Brasília

December 19, 2025

Joint supervision between:

Universidade de Brasília

Instituto de Geociências

Programa de Pós-Graduação em Geologia

Doutorado em Geologia

Université de Bretagne Occidentale

Université de Bretagne-Occidentale

École Doctorale des Sciences de la Mer et du Littoral

Laboratoire Géosciences Océan – GEO OCEAN

Doctorat in géosciences marines

Henrique Serratt

Thesis N°226 (UnB)

Natural Hydrogen Systems in Volcanic Passive Margins

Thesis advisors:

Dr. Adalene Moreira Silva (UnB)

Dr. Laurent Geoffroy (UBO)

Co-advisor

Dr. Farid Chemale Jr. (UNISINOS-UERJ)

This thesis is part of the requirements to obtain the title of “Doutor em Geologia” from Universidade de Brasília and “Doctorate in Géosciences Marines” from Université de Bretagne-Occidentale.

CIP - Catalogação na Publicação

Serratt, Henrique
S226n Natural Hydrogen Systems in Volcanic Passive Margins / Henrique Serratt; orientador Adalene Moreira Silva; Laurent Geoffroy; co-orientador ; Farid Chemale Junior. Brasília, 2025.
302 p. Ilustrado.

Orientadora: Adalene Moreira Silva; Laurent Geoffroy;co-orientador: Farid Chemale Junior.
Tese (doutorado) - Universidade de Brasília, Instituto de Geociências, Programa de Pós-Graduação em Geologia, 2025.

1. Bacia de Pelotas. 2. Margem passiva vulcânica. 3. Hidrogênio natural. 4. América do Sul. 5. Atlântico Sul. I. Moreira Silva, Adalene, orient. Geoffroy, Laurent, orient II. Farid Chemale Junior, Co-orient. III Título.

Doctoral Defense Committee:

1- Dr.Elton Luiz Dantas

Universidade de Brasília

2- Dr. Humberto Reis

HR Consulting Energy and Geosciences/UFMG

3- Dr. Isabelle Moretti

E2S-UPPA, Sorbonne Université - France

4- Dr. Geoffroy Mohn

University of Cergy-Pontoise, France

5- Dr. Jean-Luc Le Pennec

Université de Bretagne Occidentale

6- Dr. Francisco Hilario Rego Bezerra

Universidade Federal do Rio Grande do Norte

Doctoral Defense Substitutes Committee:

1- Dr. Lucieth Cruz Vieira

Universidade de Brasília

2- Dr. Omar Maiga

Hydrogen naturel

Thesis structure

This thesis is presented as a collection of articles, in accordance with the Jointly Supervised PhD (Cotutelle) agreement between UnB and UBO (attached). The structure consists of an introduction, two papers, and a conclusion chapter, which serve to integrate the articles and ensure the overall coherence of the research. The entire thesis and its articles are written in English. As stipulated by the agreement, abstracts are also provided in Portuguese and French. Finally, additional papers authored or co-authored by the PhD candidate are attached to this document.

Acknowledgments

I would first and foremost like to thank my wife, Monique Bordignon Chiele, for her unwavering support in all aspects of my life, both academic and personal. This research would not have been possible without the support of Dr. Farid Chemale Jr. I am deeply grateful for all the resources, opportunities, and contacts he provided, which made this work a reality. I also extend my sincere gratitude to my advisors, Dr. Adalene Moreira Silva and Dr. Laurent Geoffroy, for their support and guidance. I am grateful to the entire NGA team for their support, especially Tiago Girelli, Matheus Fernandes da Cruz, and Claudia Teixeira.

I thank CNPC Brasil (China National Petroleum Corporation) and CAPES (grant #88887.886595/2023-00) for their essential financial support. My gratitude is also extended to ANP (Brazilian National Agency for Petroleum, Natural Gas and Biofuels) and ANCAP (Administración Nacional de Combustibles, Alcoholes y Portland - Uruguay) for granting access to data. Finally, I am grateful to Schlumberger and Eliis for providing academic licenses for Petrel™ and PaleoScan™.

Summary

Figures index

Tables index

Resumo da Tese

Utilizando a região da Bacia de Pelotas como estudo de caso, esta tese de doutorado visa investigar a possibilidade de geração, acumulação e preservação de hidrogênio natural (H_2) em bacias desenvolvidas sobre margens passivas vulcânicas (VPMs). Demonstra-se que o H_2 pode ser produzido a partir de rochas vulcânicas em VPMs e que minerais de enxofre em sedimentos marinhos siliciclásticos sobrejacentes podem atuar como sumidouro para uma quantidade significativa de H_2 produzido por essas rochas. Para criar um modelo em escala de bacia que oriente a prospecção de H_2 na região, este estudo combina dados sísmicos e de poços com análises petrográficas e geoquímicas. O estudo identifica um potencial significativo para a geração de H_2, principalmente a partir da oxidação de minerais ferrosos presentes em rochas vulcânicas. O período mais favorável à geração de H_2 situa-se entre cerca de 128 Ma e 76 Ma, quando ocorreram os principais eventos magmáticos, período em que os reservatórios apresentam o menor teor de enxofre. No entanto, fatores de risco significativos para a acumulação de H_2 incluem o consumo biológico, sedimentos ricos em enxofre, vazamentos para a atmosfera e a retenção de H_2 nos basaltos. Muitos desses riscos não são quantificáveis, como, por exemplo, a quantidade de vazamento de H_2 ou o consumo biológico. Esta pesquisa propõe uma mudança de paradigma na exploração de H_2, sugerindo que a prioridade deve ser dada às condições de preservação, em vez do potencial da rocha geradora, ressaltando a importância de cap rocks e reservatórios eficazes com baixo teor de enxofre e baixa atividade microbiana.

Palavras-chave: Bacia de Pelotas; Margem passiva vulcânica; Hidrogênio natural; América do Sul; Atlântico Sul.

Abstract

Using the Pelotas Basin as a case study, this doctoral thesis aims to investigate the possibility of generating, accumulating, and preserving natural hydrogen (H_2) in basins developed on volcanic passive margins (VPMs). It demonstrates that H_2 can be produced from volcanic rocks in VPMs and that sulfur minerals in overlying siliciclastic marine sediments can act as a sink for a significant amount of H_2 produced by these rocks. To create a basin-scale model to guide H_2 prospecting in the region, this study combines seismic and well data with petrographic and geochemical analyses. The study identifies significant potential for H_2 generation, primarily from the oxidation of ferrous minerals in volcanic rocks. The most favorable period for H_2 generation is between approximately 128 Ma and 76 Ma, when the main magmatic events occurred, a period in which the reservoirs have the lowest sulfur mineral content. However, significant risk factors for H_2 accumulation include biological consumption, sulfur-rich sediments, atmospheric leakage, and H_2 retention in basalts. Many of these risks are not quantifiable, such as the amount of H_2 leakage or biological consumption. This research proposes a paradigm shift in H_2 exploration, prioritizing preservation conditions over the potential of the source rock and highlighting the importance of cap rocks and effective reservoirs with low sulfur content and low microbial activity.

Keywords: Pelotas Basin; Volcanic passive margin; Natural hydrogen; South America; South Atlantic.

.

Résumé de la Thèse

En prenant le bassin de Pelotas comme cas d'étude, cette thèse de doctorat vise à étudier la possibilité de générer, d'accumuler et de préserver l'hydrogène naturel (H_2) dans les bassins développés sur les marges passives volcaniques (VPM). Elle démontre que l'H_2 peut être produit à partir des roches volcaniques des VPM et que les minéraux soufrés présents dans les sédiments marins siliciclastiques sus-jacents peuvent agir comme un puits pour une quantité importante d'H_2 produit par ces roches. Afin de créer un modèle à l'échelle du bassin pour guider la prospection d'H_2 dans la région, cette étude combine des données sismiques et de puits avec des analyses pétrographiques et géochimiques. L'étude identifie un potentiel important pour la production d'H2, principalement à partir de l'oxydation des minéraux ferreux dans les roches volcaniques. La période la plus favorable à la production d'H_2 se situe entre environ 128 Ma et 76 Ma, lorsque les principaux événements magmatiques se sont produits, période pendant laquelle les réservoirs ont la plus faible teneur en minéraux soufrés. Cependant, les facteurs de risque importants pour l'accumulation d'H_2 comprennent la consommation biologique, les sédiments riches en soufre, les fuites atmosphériques et la rétention d'H_2 dans les basaltes. Bon nombre de ces risques ne sont pas quantifiables, comme les fuites d'hydrogène ou la consommation biologique. Cette recherche propose un changement de paradigme dans l'exploration de l'hydrogène, en donnant la priorité aux conditions de préservation plutôt qu'au potentiel de la roche mère, et en soulignant l'importance des roches de couverture et des réservoirs efficaces à faible teneur en soufre et à faible activité microbienne.

Mots-clés : Bassin de Pelotas; marge passive volcanique; hydrogène naturel; Amérique du Sud; Atlantique Sud.

Resumo expandido

Esta tese de doutorado investiga o potencial de geração, acumulação e preservação de hidrogênio natural (H_2) em margens passivas vulcânicas (VPMs), utilizando a Bacia de Pelotas (Sul do Brasil e Uruguai) como estudo de caso. O objetivo central é caracterizar o sistema de hidrogênio em escala de bacia, avaliando se os volumes massivos de rochas vulcânicas (Seaward Dipping Reflectors - SDRs) podem sustentar sistemas econômicos de H_2. Especificamente, busca-se quantificar as fontes de geração, definir o arcabouço geométrico e térmico da bacia e identificar os principais mecanismos de perda (sinks). A tese foi estruturada em dois artigos: o primeiro, publicado no periódico *Tectonophysics* sob o título *Unraveling the geological history of the South Atlantic margin: Records of West Gondwana Breakup from South Brazil and Uruguay margin*, foca na caracterização geoquímica e isotópica do magmatismo pré, sin e pós-rift. O segundo artigo, intitulado *Natural H_2 potential in mature Volcanic Passive Margins* e submetido ao periódico *Journal of South American Earth Sciences*, provê, além da caracterização geométrica, geocronológica e térmica da Bacia de Pelotas, uma avaliação detalhada dos elementos do sistema hidrogênio, incluindo fontes, reservatórios e selos.

O estudo integrou a interpretação de 448 linhas sísmicas 2D e dados de 21 poços exploratórios para reconstruir a arquitetura da margem. Foram realizadas análises petrográficas, geoquímicas (XRF, ICP-OES, ICP-MS) e isotópicas (Sr e Nd) para investigar a evolução das fontes magmáticas e a interação fluido-rocha. A geocronologia foi refinada por meio de datações U-Pb em zircões de encontrados nas rochas vulcânicas (basaltos e peperitos) e $^{40}Ar/^{39}Ar$ em basaltos. Modelos geométricos e térmicos regionais permitiram quantificar o potencial de geração via oxidação de minerais ferrosos (Fe^{2+}) nos SDRs, termogênese de matéria orgânica e radiólise da água intersticial em sedimentos e embasamento.

Os resultados demonstram um potencial de geração massivo, estimado em patamares superiores a 10^{12} toneladas métricas, processo dominado pela oxidação de minerais ferrosos nas sequências vulcânicas. Novas idades de $^{40}Ar/^{39}Ar$ situam os principais eventos magmáticos e hidrotérmicos entre aproximadamente 128 Ma e 76 Ma, indicando uma janela de geração prolongada. A pesquisa confirmou a extensão offshore da Bacia do Paraná (Grupo Itararé) sob o setor meridional da margem, fornecendo evidências diretas de sedimentos permo-carboníferos abaixo da seção de rift, o que amplia as possibilidades de geração termogênica.

Entretanto, identificaram-se sumidouros (sinks) significativos que limitam a acumulação econômica, entre eles temos: 1) Sinks Geoquímicos: sedimentos marinhos ricos em enxofre propiciam a Redução Termoquímica de Sulfatos (TSR) e outras reações envolvendo enxofre, que consomem o H_2; 2) Sinks Biológicos: a presença de uma zona de hidratos de gás de origem biológica abrangendo 45.000 km^2 sugere uma biosfera profunda ativa, onde comunidades microbianas utilizam o H_2 para metanogênese; 3) Retenção e Vazamento: a porosidade vesicular dos basaltos e a reativação de falhas no cap rock representam riscos à estanqueidade do sistema.

A viabilidade econômica em VPMs depende, portanto, mais das condições de preservação do que do potencial bruto da rocha geradora. Na Bacia de Pelotas, rochas cretáceas são os alvos mais prospectivos por coincidirem com o timing de geração e apresentarem menor exposição a contaminantes. Além das estimativas de H_2, o estudo detalhou a evolução tectono-estratigráfica da margem. A espessura sedimentar total da Bacia de Pelotas foi calculada em 11,37 km, o que evidencia uma subsidência massiva e contínua. A análise sísmica permitiu identificar a migração de três depocentros principais ao longo da história da bacia, refletindo variações na dinâmica de carga sedimentar e ajustes tectônicos regionais durante o drift. Adicionalmente, estabeleceu-se um gradiente geotérmico médio de 30,2 °C/km para as bacias de Pelotas e Punta del Este. Este gradiente não apenas serviu de parâmetro para a calibração dos modelos de geração termogênica e radiolítica desta tese, mas também constitui um dado de referência para futuras explorações de recursos energéticos, incluindo hidrocarbonetos.

Palavras-chave: Bacia de Pelotas; Margem passiva vulcânica; Hidrogênio natural; América do Sul; Atlântico Sul.

1 Introduction

This doctoral thesis aims to investigate the potential for hydrogen gas generation, accumulation, and preservation in volcanic passive margins (VPMs). For this purpose, the Pelotas Basin is used as an example of a VPM. The guiding hypothesis of this research is that the massive volumes of volcanic rocks observed in the Pelotas Basin could serve as a favorable source of a natural H_2 system. However, uncertainty remains regarding the capacity of marine siliciclastic sedimentary rocks to host an H_2 reservoir.

The chemical interaction between rocks and water is recognized as the main driver of natural H_2 formation (e.g., Smith et al., 2005; Worman et al., 2020; Zgonnik, 2020). Among these processes, serpentinization is the most well-documented mechanism, involving the alteration of olivine and pyroxene, and is identified as the primary global source of natural H_2 (Zgonnik, 2020, and references therein). Nevertheless, several other inorganic reactions between rocks and water can also produce H_2 as a byproduct, such as magmatic crystallization (Worman et al., 2020), siderite dissolution (Milési et al., 2016), biotite hydration (Murray et al., 2020), or, more generally, the oxidation of Fe^{2+}-bearing minerals in contact with water (e.g., Osselin et al., 2022).

This thesis is structured as a collection of papers, in accordance with the joint supervision agreement signed by UnB and UBO (Annex 1). It includes one published article (Chapter 3 and Annex 2) that redefines the understanding of the margin extending from the Brazilian state of Santa Catarina to the Uruguayan department of Treinta y Tres. This paper also serves as the geological setting chapter of the thesis, presenting the current state of knowledge on the margin's geology and expanding the understanding of the regional geological framework.

The second paper, currently under review (Chapter 4), focuses on the natural hydrogen system of the Pelotas Basin. During the investigation of potential H_2 systems, unexpected findings also contributed to refining the geological knowledge of the study area. Additional research not directly related to the PhD is provided in Annex 3 (other articles where I am the first author) and Annex 4 (other articles where I am a co-author).

1.1 Objectives

The main objective of this thesis is to investigate and characterize the Pelotas Basin as a representative example of a volcanic passive margin (VPM) and to assess its potential for the generation, accumulation, and preservation of economic hydrogen gas resources.

1.1.1 Specific objectives

- Perform a petrological characterization of the margin through petrographic and geochemical analyses (whole-rock and isotopic composition) of rocks composing the seaward dipping reflectors (SDRs) and associated volcanic sequences (Pre-rift and Late-rift stages).
- Constrain the ages and magmatic sources of the SDRs and related volcanic rocks in the study area.
- Develop a geometrical model of the Pelotas Basin based on seismic interpretation.
- Construct a regional-scale thermal model for the Pelotas Basin.
- Identify potential H_2 source rocks, reservoirs, and cap rocks within the Pelotas Basin and propose an integrated model for assessing its hydrogen potential, including implications for other Volcanic Passive Margins.

1.2 Theoretical background

The universe, in terms of matter, is composed essentially of hydrogen (~70.6 %), helium (27.5 %), and a pinch of everything else (Lodders, 2019). On the other hand, in the Earth's crust, where this study was carried out, hydrogen is not the most abundant element, but rather the 10th (Haynes, 2016). Even though it is highly abundant, its existence as an element was not recognized until the last three centuries by Henry Cavendish. The hydrogen gas (H_2) was discovered along with the element. Although natural H_2 is found at lower concentrations in the atmosphere (0.00005 %; Haynes, 2016), it can be much higher in some places, for instance, at the Eternal Flames in Turkey, believed to be the first Olympic Flames. It has been leaking and burning H_2 together with natural gas, which has a 7.5-11.3% H_2 concentration, for at least 2,000 years (Zgonnick, 2020). Hydrogen gas has been used as a source of energy at least since the 19th century (Figure 1-1). As Smith et al. (2005) reported: "*Before discovery of North Sea gas, the UK's domestic gas was generated from bituminous coal at gasworks and known as "towngas", a mixture of producer gas and coal gas which had a composition of about 51% hydrogen, 15% carbon monoxide, 21% methane, 10% carbon dioxide and nitrogen and 3% other alkanes.*".

Figure 1-1 : Commemorative plaque of the Gas Light & Coke Company, in Great Peter Street. Photo from Andrew Davidson under CC BY-SA 3.0 available in Wikipedia. This is likely the first industrial plant for H2 production (although this is not its primary objective).

The issue with H_2 produced from fossil fuels (informally categorized as black, brown, or gray) is its carbon footprint. For instance, black and brown hydrogen, the most CO_2-intensive, is produced by gasifying bituminous coal and lignite, emitting between 22 and 26 kilograms of carbon dioxide equivalent per kilogram of hydrogen (kg CO_2e/kg H_2; IEA, 2024). The most common method, gray hydrogen, is produced via steam methane reforming of natural gas and has a carbon footprint of approximately 10-12 kg CO_2e/kg H_2 (IEA, 2024). In both cases, greenhouse gas emissions are a byproduct of the process, making it incompatible with the decarbonization needed to reduce climate change.

On the other hand, green hydrogen is basically CO_2-free. Green hydrogen is hydrogen produced by the electrolysis of water. When analyzed from an energetic perspective, green hydrogen is a way to store energy produced from solar or wind. However, it is an inefficient way to do it. For instance, if we consider water electrolysis efficiency(~86%), the energy required to compress hydrogen to 700 bar and deliver it to a vehicle (5 to 20% of the H_2 total energy), and fuel cell efficiency (60%), the combined efficiency of these processes may vary between 41% and 49% (Rivard et al., 2019; Figure 1-2).

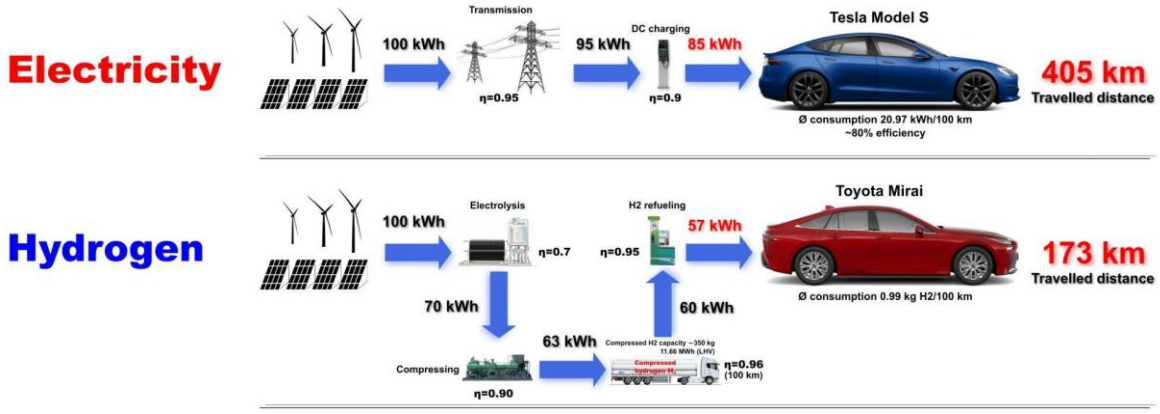

Figure 1-2 : Figure from Michael Sura (consultant) illustrating the efficiency of green hydrogen systems compared to a traditional electric car. The values differ from those in Rivard et al. (2019). However, it illustrates the chain of energy loss in the green hydrogen systems.

Natural hydrogen, unlike the traditional black, grey, or brown hydrogen, does not produce CO_2 as a byproduct (Figure 1-3), and unlike green hydrogen, it is an energy source (Prinzhofer et al., 2018; Maiga et al., 2023; Maiga et al., 2024), not just an energy storage product. The main issue is that, as of December 2025, only one naturally occurring H_2 field is

known to be economically viable (Prinzhofer et al., 2018; Maiga et al., 2023). Research on natural hydrogen has been conducted in several countries, including Brazil (e.g., Serratt et al., 2024; Freitas et al., 2024; Prinzhofer et al., 2024; Flude 2025), France (e.g., Murray et al., 2020), Australia (e.g., Boreham et al., 2021), and the United States (e.g., Guélard et al., 2017). However, there is still no evidence that these occurrences are economically viable. Zgonnik (2020, Figure 1-4) compiled an exhaustive list of known natural H_2 anomalies (>10%) worldwide. These global occurrences can be grouped into five main mechanisms of natural H_2 production that guide this research: organic matter overmaturation, inorganic mineral alteration, radiolysis, biological hydrogen generation, and mantle degassing.

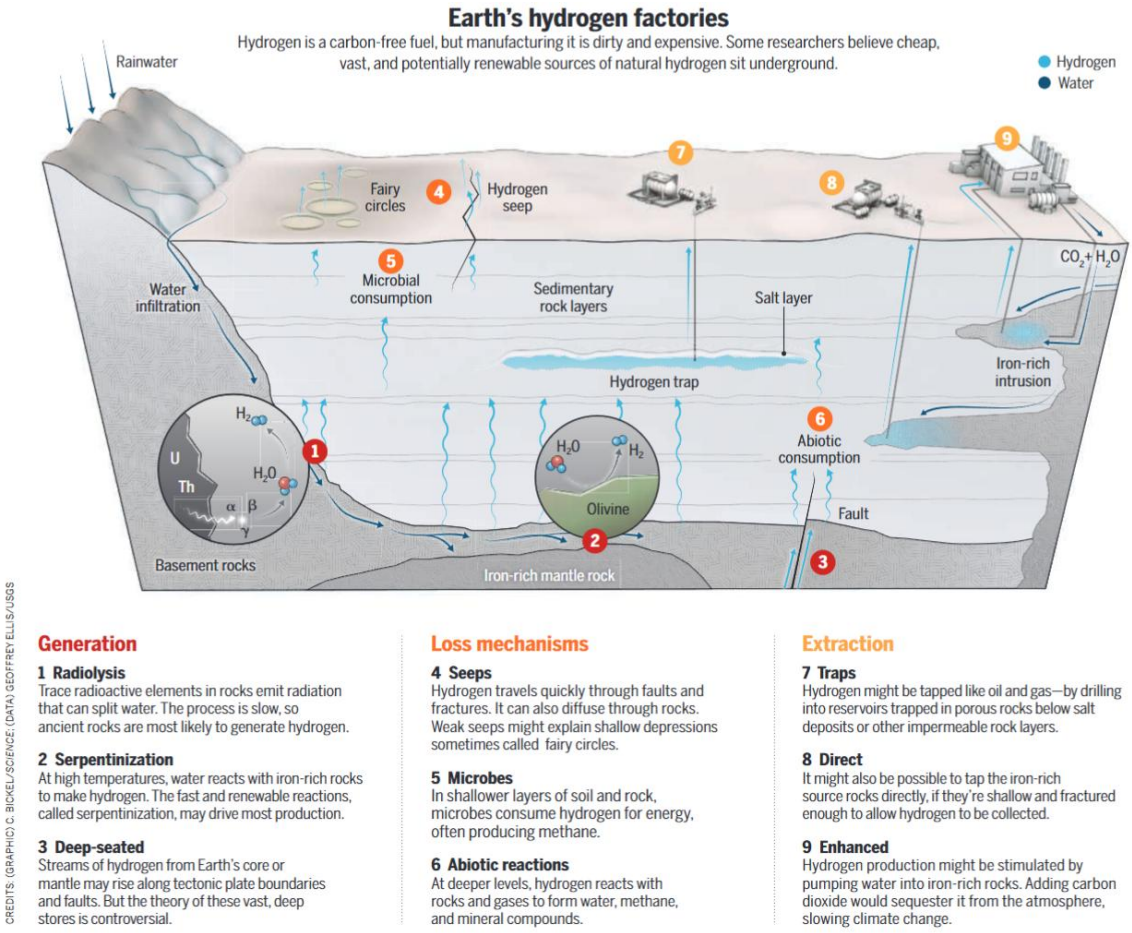

Figure 1-3. Image compiling some mechanisms of generation and loss of natural hydrogen. Figure from Hand, 2023.

As previously discussed, H_2 can be produced through thermogenic processes. Early investigations into natural hydrogen systems indicated that carbon-related reactions, such as

graphitization at approximately 600 °C, generate hydrogen gas, as observed by Apps and van de Kamp (1993) and expressed in the following reaction:

$$CH_4 = C + 2H_2$$

Previous research has demonstrated that thermogenic H_2 can form with yields of up to 20 mg H_2 per gram of total organic carbon (TOC) within an optimal temperature range of 220 °C to 330 °C (Mahlstedt et al., 2024). However, this temperature interval overlaps the typical range of hydrocarbon generation (Hunt, 1996; Mahlstedt et al., 2024). During hydrocarbon formation, H_2 may be consumed (Apps and van de Kamp, 1993; He et al., 2024; Mahlstedt et al., 2024). Mahlstedt et al. (2024) also noted that petroleum can serve as a potential sink for H_2, with hydrogenation processes enhancing hydrocarbon quality. Therefore, the thermogenic "window" for hydrogen gas formation is likely to occur between the end of CH_4 generation (around 250 °C) and the upper thermal limit of approximately 350 °C, as demonstrated by Mahlstedt et al. (2024).

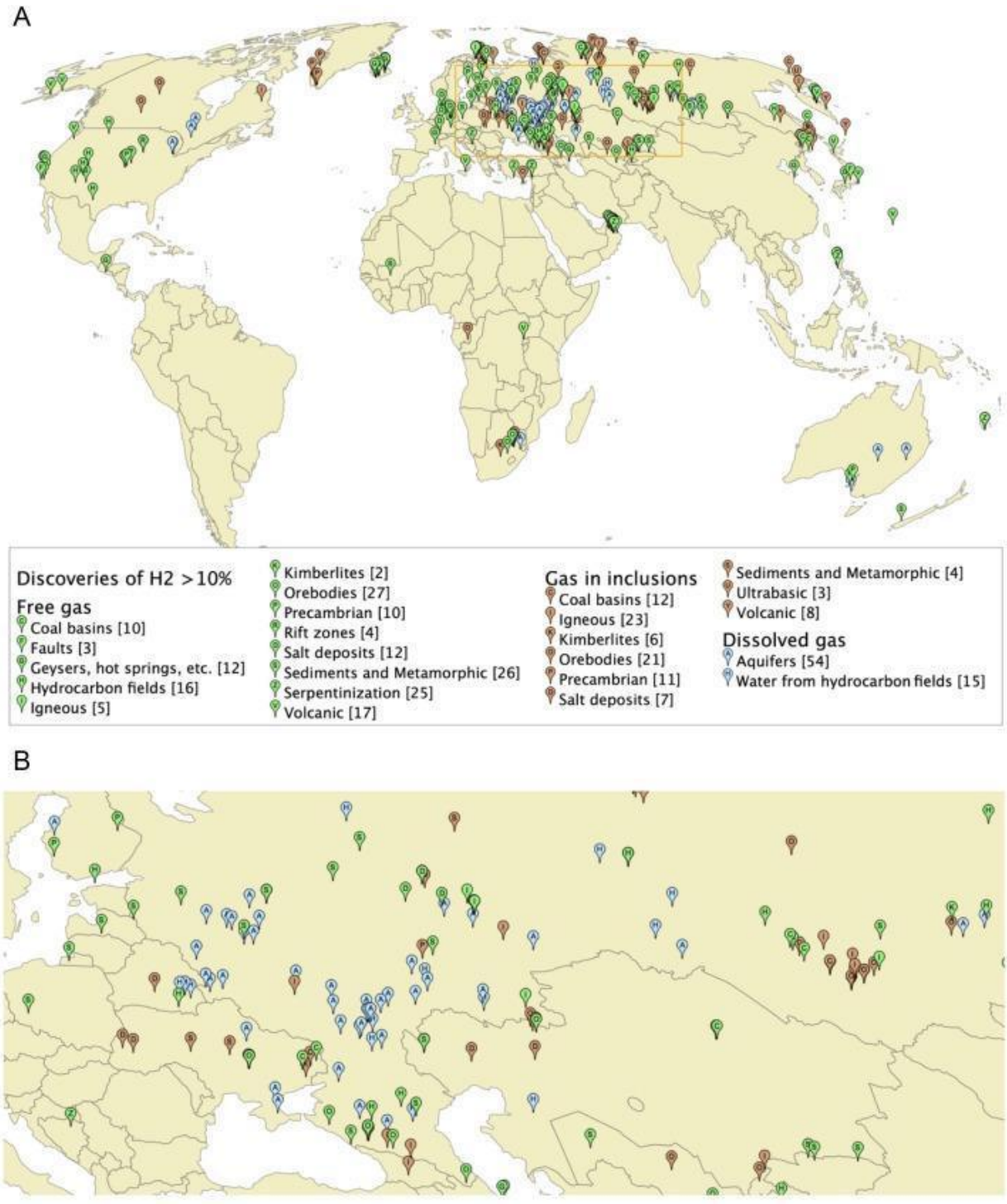

Figure 1-4. Map of known natural H_2 anomalies (compiled until 2020) from Zgonnik (2020). (a) Locations of hydrogen detections in natural environments at concentrations >10% volume. The higher concentration of markers in Eastern Europe and Northern Asia reflects more frequent targeted research in these areas, not necessarily a greater abundance of hydrogen. The orange rectangle highlights the area shown in (b). (b) Detailed map of the area outlined by the orange rectangle in (a).

The natural production of H_2 through the alteration of inorganic minerals is a widespread geochemical process (Smith et al., 2005; Murray et al., 2020; Worman et al., 2020; Zgonnik,

2020; Osselin et al., 2022; He et al., 2024), primarily driven by the oxidation of ferrous iron-bearing minerals (Fe^{2+}). Most of the known natural H_2 anomalies worldwide are attributed to these reactions, with serpentinization being the most common process (Zgonnik, 2020). Serpentinization refers to the hydration of olivine into serpentine and its associated by-products (Smith et al., 2005; Zgonnik, 2020):

$$6(Mg,Fe)_2SiO_4\ (\text{Olivine}) + 7H_2O \rightarrow 3Mg_3Si_2O_5(OH)_4\ (\text{Serpentine}) + Fe_3O_4\ (\text{Magnetite}) + H_2$$

Other reactions may also play a role (He et al., 2024), such as the transformation of pyrrhotite (FeS) into pyrite (FeS_2):

$$1.5FeS\ (\text{Pyrrhotite}) + H_2O \rightarrow 0.75FeS_2\ (\text{Pyrite}) + 0.25Fe_3O_4\ (\text{Magnetite}) + H_2$$

The crystallization of basic magmas in contact with seawater could work as an H_2 source, as pointed out by Worman et al. (2020):

$$2(FeO)_{magma} + (H_2O)_{seawater} \rightarrow (Fe_2O_3)_{rock} + H_2$$

Biotite hydration can also act as a potential source of H_2 (Murray et al., 2020):

$$KFe_3(AlSi_3)O_{10}(OH)_2\ (\text{Biotite}) + 4H^+ + 4H_2O\ (\text{water}) \rightarrow Fe_3O_4\ (\text{Magnetite}) + H_2 + K^+ + Al_3^+ + 3H_4SiO_4\ (\text{Silicic acid})$$

In general, H_2 production through the alteration of inorganic minerals can be simplified as the oxidation of Fe^{2+} in minerals to Fe^{3+}. The free electrons react with water to form molecular hydrogen (H_2), while oxygen is incorporated into the mineral structure (Figure 1-5; Mayhew et al., 2013; Worman et al., 2016; Worman et al., 2020).

While the generation of H2 during high-temperature serpentinization (≥200 °C) is well established, Mayhew et al. (2013) demonstrated that these reactions can also occur at much lower temperatures. In laboratory experiments, fluids reacted with minerals such as olivine, pyroxene, and magnetite at 55 °C and 100 °C, resulting in measurable H2 production. The fundamental mechanism involves the oxidation of Fe(II) in primary minerals to Fe(III) in secondary phases, which in turn reduces water to form H_2 gas. However, the authors observed that the total amount of H_2 produced did not correlate directly with the rock's bulk Fe(II) content, reaction temperature, or mineral surface area. Instead, they found a strong correlation between H_2 generation and the presence of spinel-group minerals (e.g., magnetite, chromite; Figure 1-5) in the starting materials, suggesting that these mineral surfaces act as catalysts by promoting electron transfer to adsorbed water molecules. Oxidizing conditions are essential for H_2 production (Worman et al., 2020; Zgonnik, 2020; Boreham et al., 2021). Additionally, pH may play a crucial role, as experimental studies have demonstrated that H_2 production increases with increasing pH (McCollom et al., 2020).

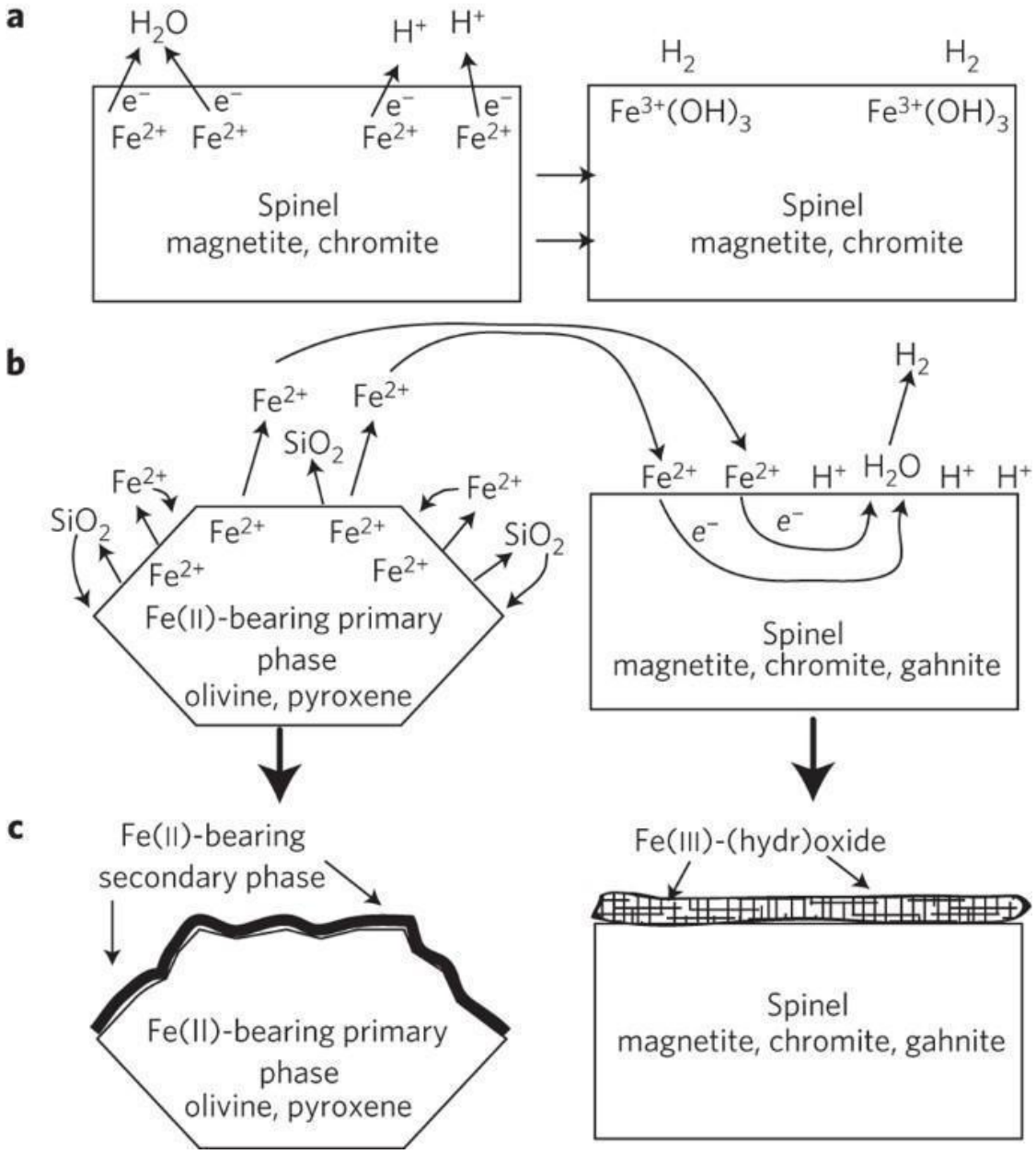

Figure 1-5. Schematics of mineral/water interaction producing H2 image from Mayhew et al. (2013). Production and Inhibition of H2 from Fe(II)-Bearing Minerals (a–c).(a) H2 is generated initially by electron transfer from structural Fe(II) in spinel to adsorbed water/protons. (b) The reaction is sustained by the continuous release of Fe(II) from dissolving silicates, which then participates in the interfacial electron transfer on the spinel surface. (c) H2 production stops when secondary surface layers precipitate, either inhibiting Fe(II) release from silicates or forming an oxidized, passivating layer on the spinel.

Radiolysis of water is considered a minor source of H_2 (Zgonnik, 2020). The decay of radionuclides such as ^{235}U, ^{238}U, ^{232}Th, and ^{40}K, naturally present in rocks, produces alpha and beta particles as well as gamma rays. When this radiation interacts with water molecules within rock pores, it generates new combinations of hydrogen and oxygen species (Bouquet et al.,

2017; Figure 1-6). The rate of H_2 production can be quantified using equations defined by Aitken (1985; see Section 2.3, Methods).

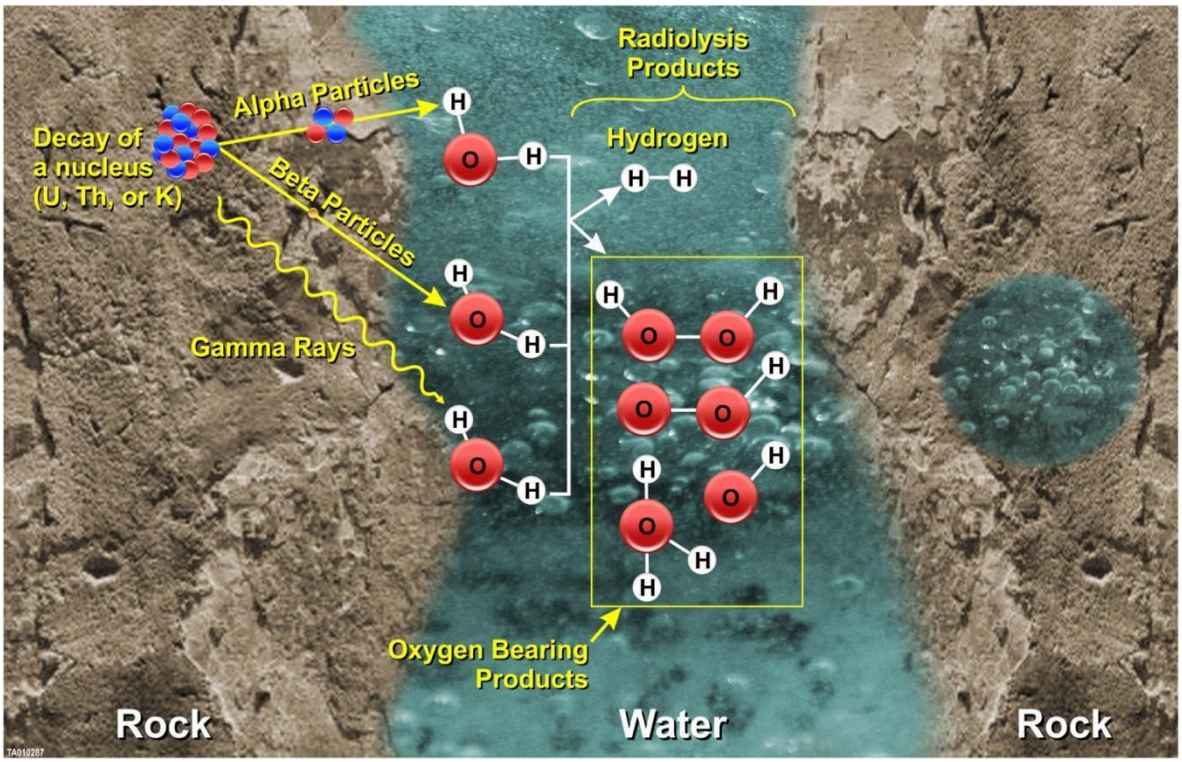

Figure 1-6. Figure from Bouquet et al. (2017), summarizing the radiolysis process. This figure illustrates the process of water decomposition caused by ionizing radiation from radionuclides. The resulting products are formed through a sequence of physicochemical steps that begin with the excitation and ionization of the water molecule. A comprehensive list of products and the full chain of reactions can be found in Le Caër (2011).

Microorganisms can produce H_2 through fermentation, nitrogen fixation, and the anaerobic degradation of organic matter (Zgonnik, 2020; Dowaidar, 2025). However, because microorganisms that consume H_2 as an energy source always coexist with those that produce it, these processes do not lead to significant accumulations in nature. Consequently, hydrogen generated by biological activity is rapidly consumed and converted into other compounds, such as methane (Zgonnik, 2020). Soils primarily act as a sink, removing hydrogen from the atmosphere rather than serving as a substantial net source, since the rate of H_2 production in soil environments is minimal compared with its consumption (Zgonnik, 2020).

The Earth's mantle may also represent an important source of H_2. The presence of hydrogen gas in the mantle is evidenced by H_2 found in diamond inclusions (Zgonnik, 2020,

and references therein). Several H_2 anomalies across Eurasia show a positive correlation with helium anomalies, suggesting a possible mantle origin (Zgonnik, 2020, and references therein).

The only proven economic case for the natural extraction of H_2 on a commercial scale is in Bourakebougou, Mali (Prinzhofer et al., 2018; Maiga et al., 2023; Maiga et al., 2024). This case shows low ^3He concentrations, interpreted as evidence of the absence of mantle contributions. (Prinzhofer et al., 2018). The CH_4 occurrence in the Bourakebougou H_2 field is associated with CO_2 hydrogenation, not thermogenesis (Prinzhofer et al., 2018). Maiga et al. (2023) assume that the primary H_2 source should be related to the oxidation of Fe^{2+} rich minerals. The reservoir pressure increased during the first 11 years of production, interpreted as continuous gas recharge (Maiga et al., 2023). The only known reservoir shows an active source, which could be a critical aspect for prospection. The reservoir rocks are carbonates (porosity range: 0.21-14.32%) and sandstones (porosity range: 4.52-6.37% - Maiga et al., 2023). Dolerite sills serve as effective cap rocks in the region (Figure 1-7; Maiga et al., 2024). Additionally, Maiga et al. (2024) point out that aquifers could also contribute to H_2 retention. H_2 storage studies also point to evaporitic rocks as potential seals (Gelman et al., 2025), but also fine-grained siliciclastic rocks (Iyare et al., 2025).

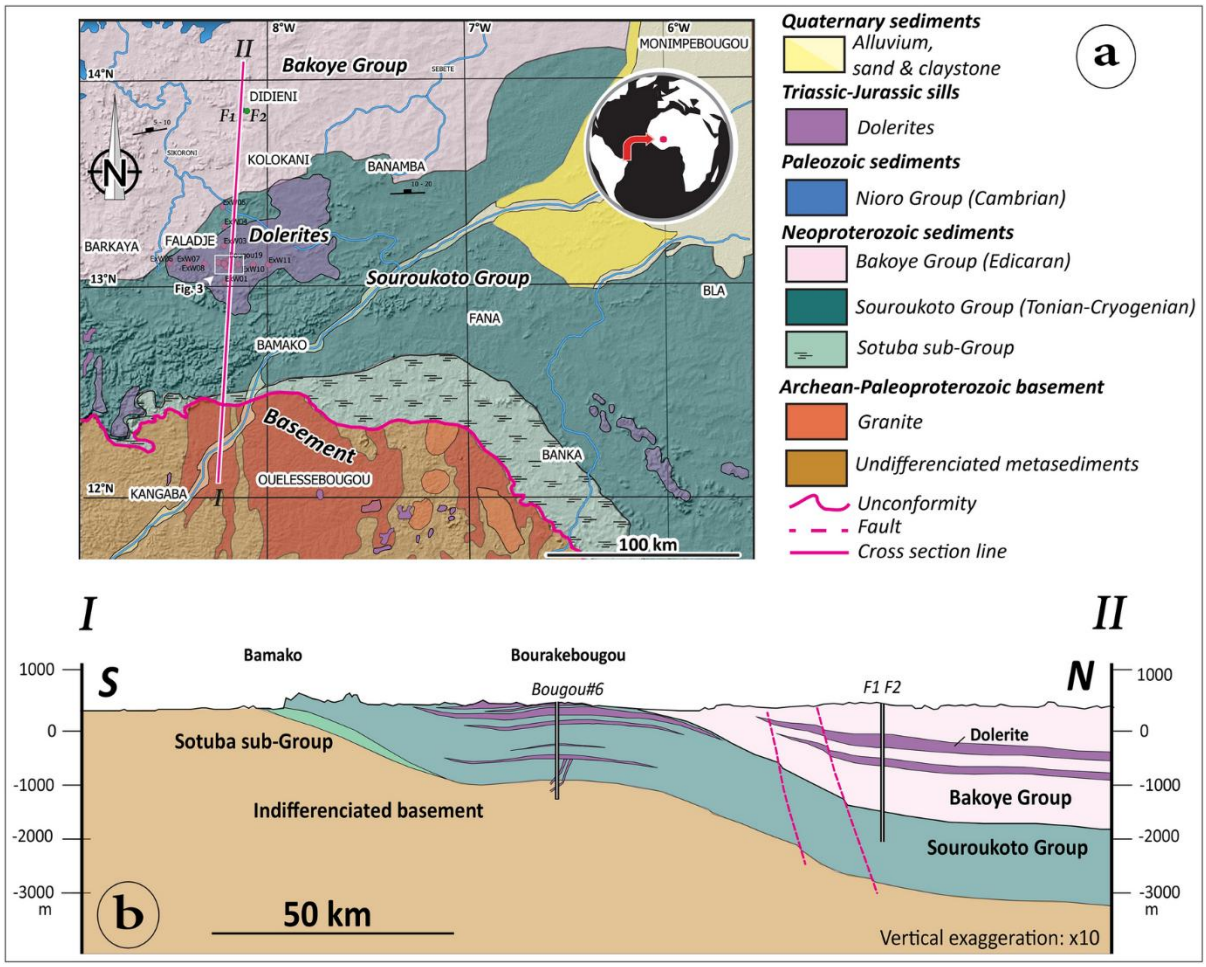

Figure 1-7. Image from Maiga et al. (2023) showing the presence of sills in the only proven economic natural H2 system. Maiga et al. (2024) point out that sills work as an effective seal for H2 systems(a) Geological map of the study area, adapted from the Global Geological Map of Mali (1/1,500,000; DNGM29). (b) Simplified structural cross-section corresponding to the line indicated in Figure 1(a).

For economic concentrations of natural H_2, it is necessary not just to produce H_2, but also to accumulate it. The H_2 accumulation issues are primarily due to its small size (2.89 Å) and gaseous nature (Ismaili, 2015). The caprocks should be highly efficient, and even the smallest fracture can allow H_2 loss. Secondly, the H_2 is reactive. In that way, it could sink due to biological activity or due to hydrocarbon formation. However, inorganic reactions could be a main sink factor with the formation of H_2S by thermochemical sulfate reduction (TSR; Figure 1-8.; Ahmadpour & Gholami, 2025):

$$4H_2 + SO_4^{2-} + 2H^+ \rightarrow H_2S + 4H_2O$$

The H_2 dissociation $H_2 \leftrightarrow 2H^+ + 2e^-$ leads to the acidification of rock fluids and the consequent availability of SO_4^{2-} due to the ionic dissociation of sulfates in the rocks. That makes sulfur concentrations in reservoirs prohibitive for economic H_2 reservoirs. Other possible reaction products related to pyrite are also expected, since the coexistence of pyrite and hydrogen is not thermodynamically stable and leads to the following reaction with the generation of pyrrhotite, mackinawite, and troilite (Truche et al., 2010; Ahmadpour & Gholami, 2025):

$$FeS_2 + (1-X)H_2 \rightarrow FeS_{1+X} + (1-X)H_2S \qquad \text{for } (0 \leq X < 0.125)$$

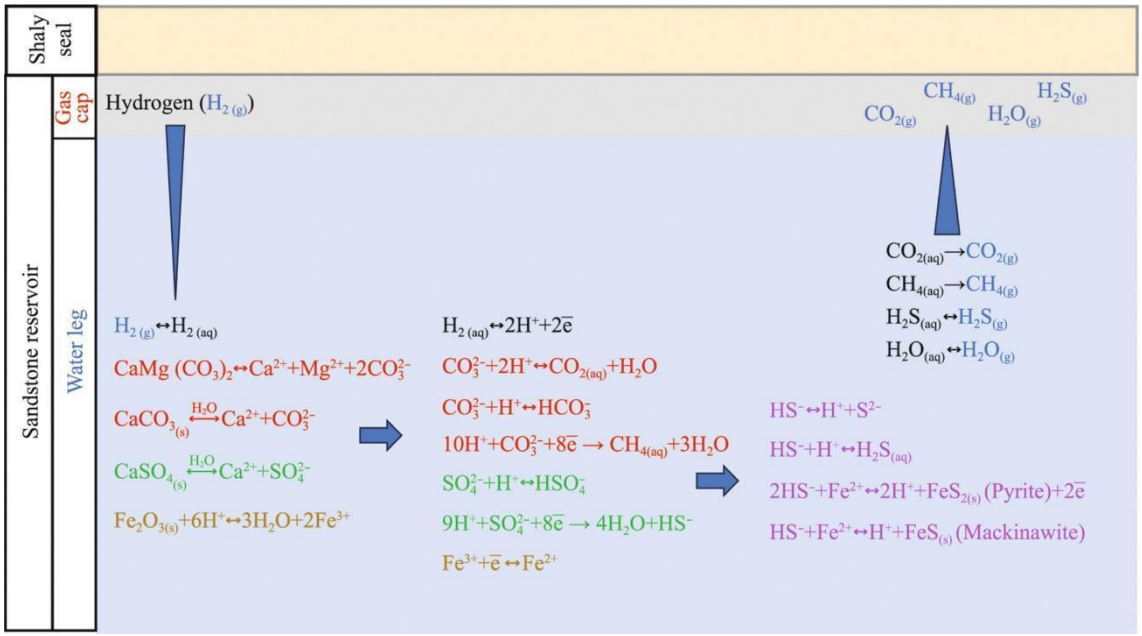

Figure 1-8. Image from the research by Ahmadpour and Gholami (2025), which focused on hydrogen storage. However, it can be applied to natural H2 prospection by understanding the H2 sink zones. The figure show an interconnected network of reactions involved in the thermochemical sulphate reduction (TSR) process.

1.3 Study Area

The Pelotas Basin (study area) developed above a volcanic passive margin (VPM) characterized by thick seaward dipping reflectors (SDRs) that can reach up to 17 km in thickness (Stica et al., 2014; Geoffroy et al., 2015; Harkin, 2020; Chauvet et al., 2021; Serratt et al., 2022; Serratt et al., 2024). As previously discussed, this thesis hypothesizes that the massive volume of volcanic rocks in the Pelotas Basin could serve as a favorable source of a

natural H_2 system, driven by the oxidation of Fe-bearing minerals within these rocks (Figure 1-9).

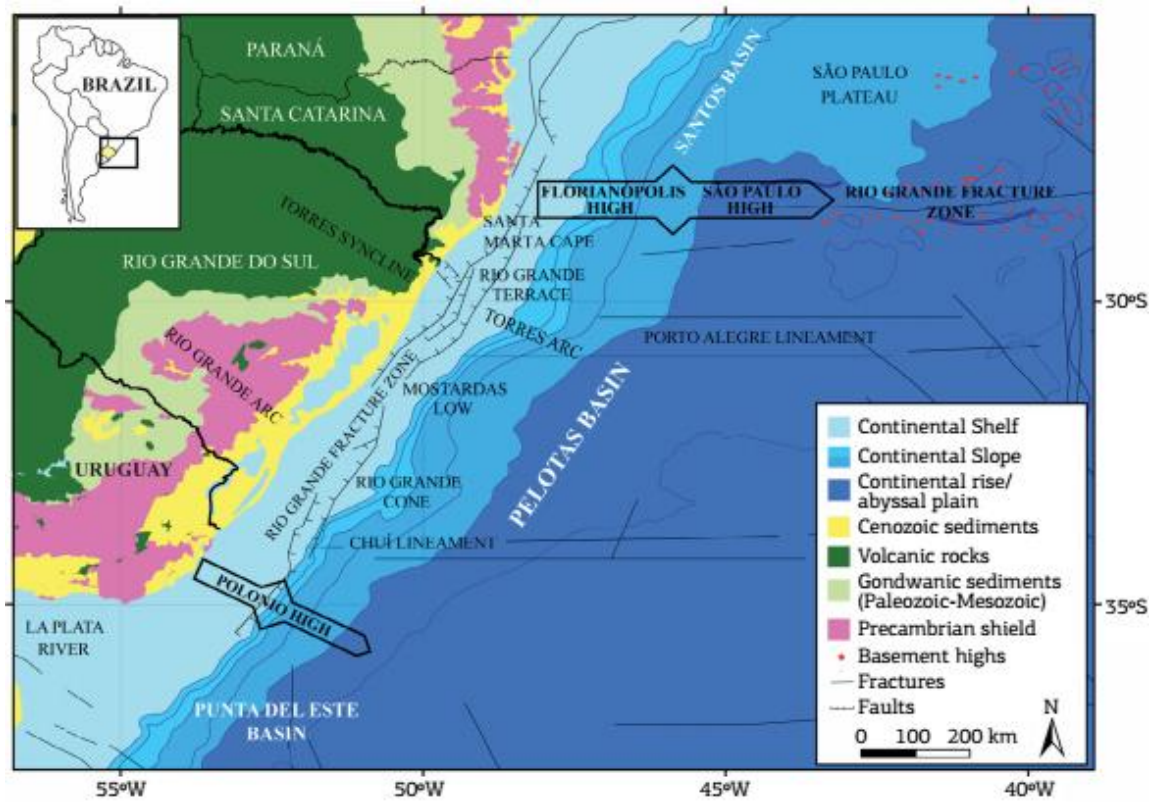

Figure 1-9. This study was carried out in the Pelotas Basin, located in the Atlantic margin of South America between Punta del Este and Santos basins. Figure originally from Rosa et al. (2017). Location map of the Pelotas Basin showing the principal structural features. The map synthesizes data from multiple works on the basin's structure, including Miranda (1970); Urien & Martins (1978); Alves (1977, 1981); Gamboa & Rabinowitz (1981); Dias et al. (1994); Fontana (1996); and CPRM (2008).

VPMs are the most common form of passive margins (Eldholm et al., 1994; Geoffroy, 2005). Following Geoffroy (2005 - Figure 1-10), the overall features that discriminate VPM and sedimentary passive margins are: I) Narrow (necked) margins; II) Significant igneous crust; III) Seaward crustal flexure and continentward-dipping Faults. IV) Seaward Dipping Reflectors (SDRs). SDR is a seismic facies, Mutter et al. (1982) formalized the concept of it, describing them with five criteria: (1) the reflectors dip seaward; (2) individual reflectors have an arcuate shape formed by a gentle upward convexity; (3) there is a down-section and down-dip increase in the dip; (4) these characteristics combine to create an overall wedge-shaped appearance, with

reflectors diverging seaward; and (5) there is no clear basal termination to the wedge and no evidence of a bottom-set aspect to the reflectors.

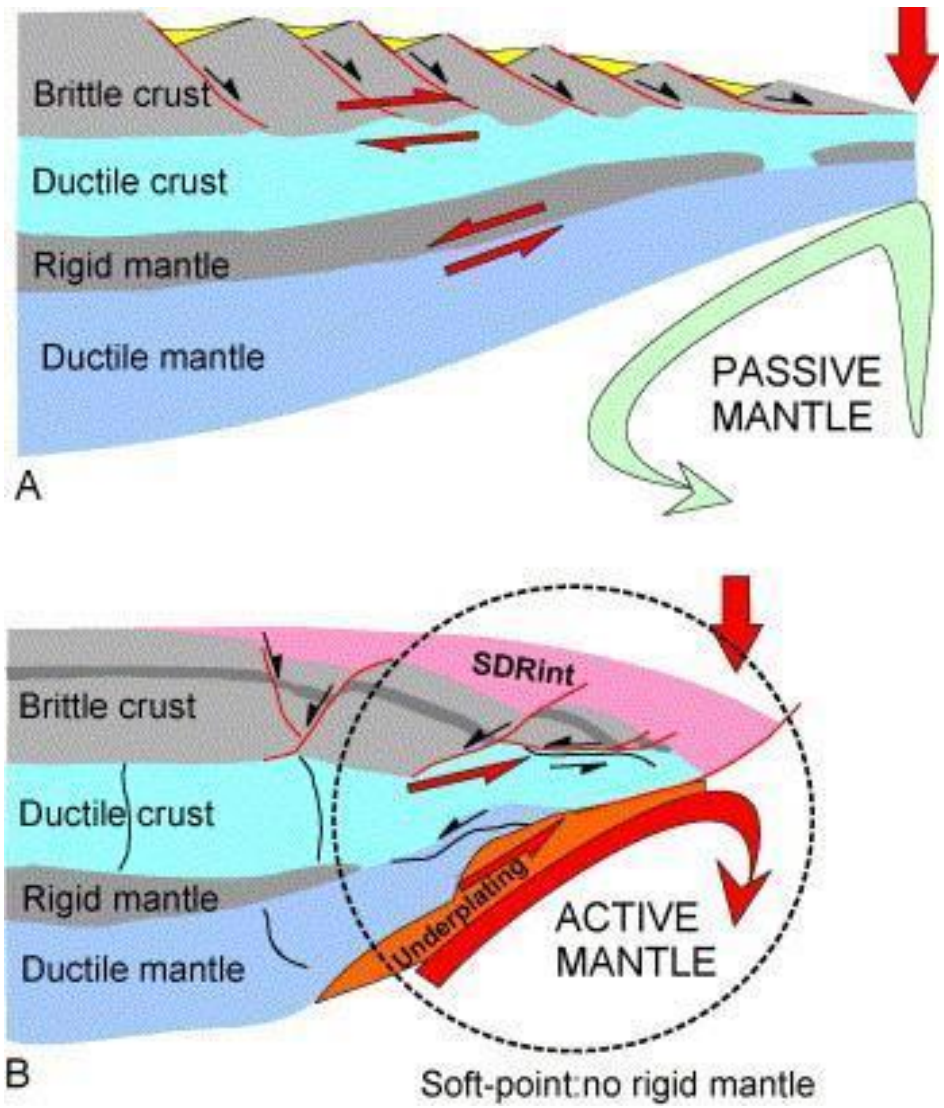

Figure 1-10. Original figure from Geoffroy (2005). The figure illustrates two models: (A) Sedimentary Passive Margin (SPM), associated with passive mantle dynamics, and (B) Volcanic Passive Margin (VPM), associated with active mantle dynamics. The models are based on published works (Brun and Beslier 1996; Callot 2002; Callot et al. 2002; Gac and Geoffroy 2004) and analogical and numerical experiments. The vertical red arrow marks the break-up area and the location of the first oceanic crust. (See text for further explanation.)

1.4 Rationale

Natural hydrogen is emerging as a carbon-free energy resource with the potential to transform the global energy sector, driven by the urgent need for a sustainable energy transition worldwide. The Bourakebougou field in Mali represents the world's most emblematic example of a successfully exploited natural hydrogen accumulation. Since 2012, a well in this field has been continuously used to generate clean electricity for the local community, demonstrating the viability of this energy source (Prinzhofer et al., 2018; Maiga, 2023; Maiga, 2024).

Despite volcanic passive margins (VPMs) being the most abundant type of passive margin (Geoffroy, 2005), they remain a frontier in natural hydrogen exploration. To date, research in divergent settings has primarily focused on the hydrogen-generating potential of magma-poor rifted margins (Liu et al., 2023) and active rifts (Deville et al., 2023; Pasquet et al., 2023), which represent the incipient stages of VPM development. However, the USGS (United States Geological Survey - Gelman et al., 2025) has identified the East Coast Magnetic Anomaly (ECMA), i.e., the North American SDRs, as a potential hydrogen source. Consequently, the hydrogen systems of mature VPMs have never been systematically investigated, representing a significant scientific gap that this doctoral research seeks to address.

Historically, South America has been the least-studied continent for natural hydrogen, as reflected in maps of known H_2 anomalies up to 2020 (Zgonnik, 2020; Figure 1-4). This scarcity is not due to unfavorable geological conditions but rather to a historical lack of research. However, exploration efforts have recently begun in Brazil (Serratt et al., 2024; Prinzhofer et al., 2024; Freitas et al., 2025), while the country's passive margins remain unexplored for hydrogen.

In summary, hydrogen geology is an emerging scientific field with numerous knowledge gaps. This thesis investigates the H_2 system within the continent that has been least studied in this context, focusing on offshore regions of a Volcanic Passive Margin (VPM). This geological setting has not been previously explored for its hydrogen potential.

2 Materials and Methods

This section provides a detailed description of the materials and methods employed in this study, including their sources and theoretical background. The selected approaches were designed to meet the research's general and specific objectives, establishing a direct link between the scientific questions and the analytical procedures used.

2.1 Materials

The materials employed in this study were obtained from three primary institutions: the Brazilian National Agency of Petroleum, Natural Gas and Biofuels (ANP), the National Administration of Fuels, Alcohol and Portland (ANCAP) of Uruguay, and the Ocean Drilling Program (ODP). Access to these datasets was granted through formal cooperation agreements established between these institutions and the Geology and Geophysics Research Group (NGA) at Universidade do Vale do Rio dos Sinos, where I was affiliated during the development of this doctoral research. The post-stack, time-domain SEG-Y reflection seismic data were from 15 surveys totaling 448 seismic lines (Figure 2-1).

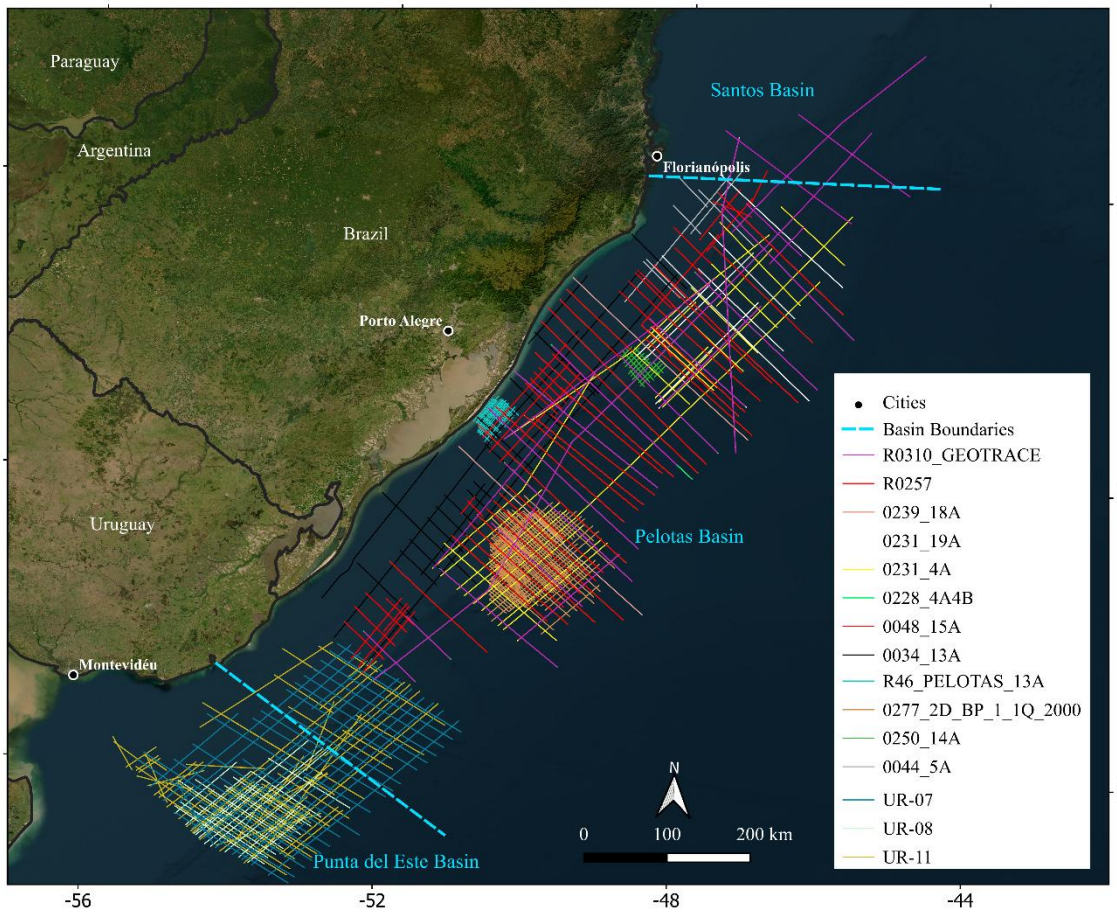

Figure 2-1. Seismic lines location map.

The well cores, well cuttings, BHTs, lithological logs, petrophysical logs, and reports from 21 wells are presented in Figure 2-2 and summarized in Table 2-1. One additional well from ODP (516) was used to compare basalts from the margin with those from the Rio Grande Rise. Drill core samples from the Pelotas Basin margin were obtained to characterize the volcanic and sedimentary sequences that compose the Seaward Dipping Reflectors (SDRs) and associated volcanic units (Pre-rift and Late-rift). These cores provided the material used for petrographic, geochemical, and isotopic analyses (Table 2-2). The samples were selected based on lithological diversity, preservation quality, and stratigraphic representativeness. BHTs served as the basis for the thermal model.

Table 2-1. List of well materials and their sources

Well	Source	Material
1-BPS-7-BP	ANP	Logs (GR, RHOB, NPHI, Caliper), Cuttings, BHTs
1-BPS-8-BP	ANP	Logs (GR, RHOB, NPHI, Caliper), Cuttings, BHTs
1-BRSA-61-RSS	ANP	BHTs
1-RSS-2-RS	ANP	Logs, BHTs
1-RSS-3-RS	ANP	Cores, Logs, BHTs
1-SCS-1-SC	ANP	Cores, Logs
1-SCS-2-SC	ANP	Logs, BHTs
1-SCS-3B-SC	ANP	Cores, Logs, BHTs
2-BPS-6A-BP	ANP	Cores, Cuttings, Logs (GR, RHOB, NPHI, DT, Caliper), BHTs
2-RSS-1-RS	ANP	Logs, BHTs
2-TO-1-RS	ANP	Cores
Gaviotin-1	ANCAP	Cores, Logs, BHTs
Lobo-1	ANCAP	Cores, Logs
Raya-X-1	ANCAP	Logs, BHTs
U516	ODP	Cores
2-PN-1-RS	ANP	Logs
2-PJ-1-RS	ANP	Logs
2-CA-1-RS	ANP	Logs
2-CL-1-RS	ANP	Logs
2-MO-1-RS	ANP	Logs
2-PS-1-RS	ANP	Logs
2-GA-1-RS	ANP	Logs
2-GA-2-RS	ANP	Logs

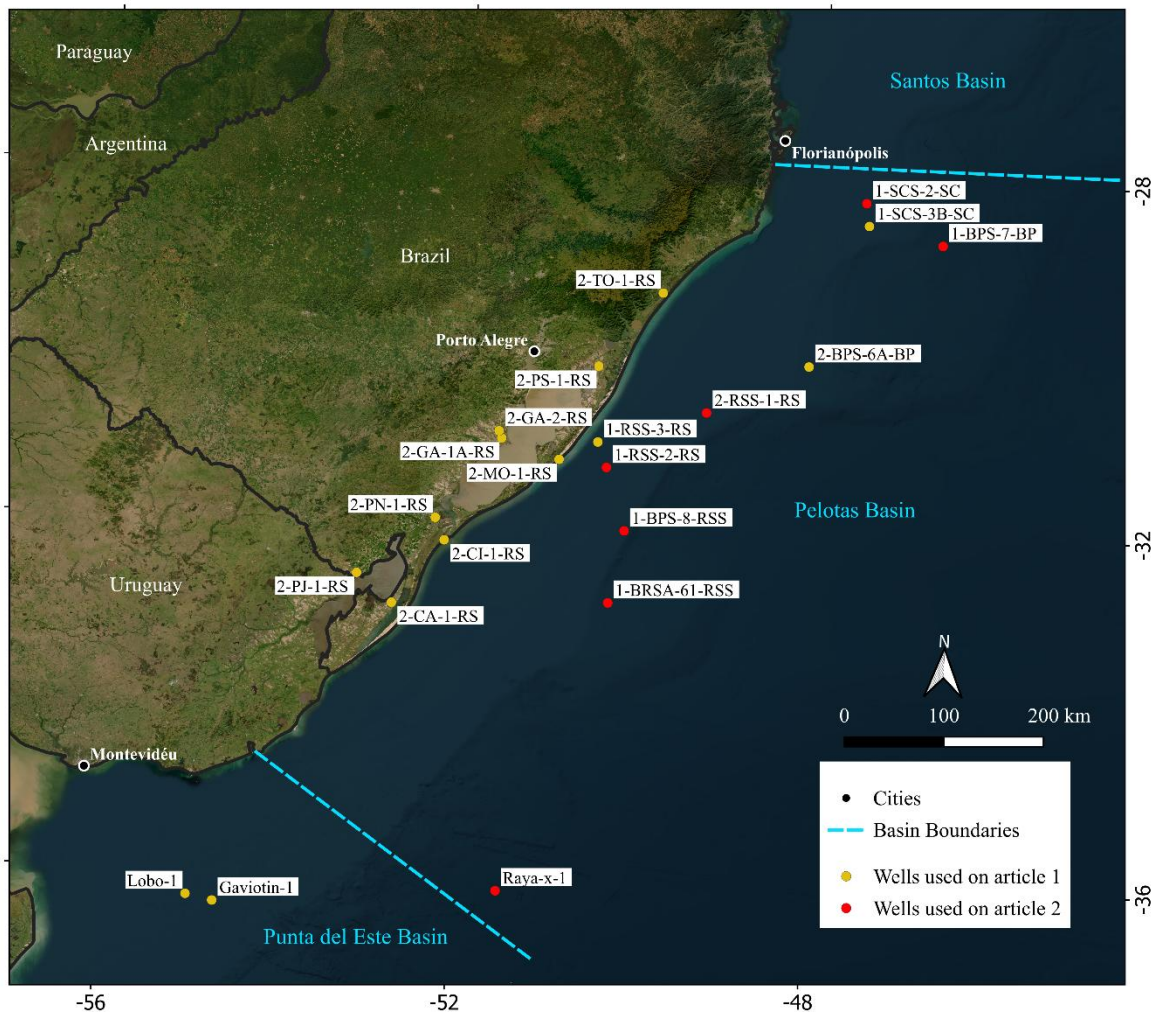

Figure 2-2. Wells' location map. Wells used in Article 1 were also used in Article 2, but not vice versa.

In parallel, efforts were made to obtain complementary data from the conjugated margin. In 2022, I traveled to Namibia to present the poster titled 'The Economic Potential of South Atlantic Volcanic Passive Margins: The New Frontier' at the Hydrocarbon Potential in Namibia conference (AAPG). During this visit, I initiated preliminary negotiations to establish a collaboration between NGA and Namibian governmental entities. As part of this initiative, I formally invited representatives from the Ministry of Mines and Energy of Namibia to visit Brazil to advance discussions concerning a potential data-sharing agreement. Although the visit took place, the agreement was not formalized at that time (the first semester of 2023), and negotiations continue to be ongoing. Consequently, no Namibian data were incorporated into

the present research. This data could have played an important role in validating models, since Namibia is the conjugate margin of South Brazil.

Table 2-2. Well cores analyzed and techniques performed.

Well ID	Depth (m)	Rock Type	Tectonic Setting	Analyses Performed
Gaviotin-1	3629	Sandstone	Pre-Rift (Paraná Basin)	Petrography, U-Pb
Lobo-1	2622, 2627, 2629	Basalt	Pre-Rift (Paraná LIP)	Petrography, XRD, Geochemistry, Sr-Nd
1-RSS-3-RS	3555, 3904, 3905	Basalt	Pre-Rift (Paraná LIP)	Petrography, XRD, Geochemistry, U-Pb, Sr-Nd, $^{40}Ar/^{39}Ar$
1-SCS-3B-SC	4732, 4735	Basalt	Rift (SDR)	Petrography, XRD, Geochemistry, Sr-Nd, $^{40}Ar/^{39}Ar$
2-BPS-6A-BP	5377, 5378	Peperite	Late-Rift	Petrography, XRD, Geochemistry, U-Pb, $^{40}Ar/^{39}Ar$
2-BPS-6A-BP	6153, 6154, 6155	Basalt	Late-Rift	Petrography, XRD, Geochemistry, Sr-Nd, $^{40}Ar/^{39}Ar$
2-BPS-6A-BP	4721	Sandstone	Sedimentary	Geochemistry
2-BPS-6A-BP	5071	Calcarenite	Sedimentary	Geochemistry
2-TO-1-RS	-	Granitoid	Basement	Geochemistry
U516	1260.6, 1269.6	Basalt	Oceanic Plateau	Geochemistry, Sr-Nd

2.2 Methods

This chapter outlines the analytical procedures employed to investigate the potential natural H_2 system in the Pelotas Basin. The methods used include petrophysics, seismic reflection, petrography supported by X-ray diffraction, geochemical, and geochronological data. Those data were used to characterize the study area and assess the potential for hydrogen generation and preservation.

2.2.1 Petrophysics

Petrophysical methods were employed for three objectives: correlating well data with seismic profiles (seismic-well tie), identifying potential H_2 reservoirs, and identifying possible zones of high H_2 production through radiolysis. The seismic-well tie was achieved by generating synthetic seismograms, which required a combination of check shots (when available), the sonic (DT) log, and the density (RHOB) log. The gamma-ray log (GR) was used to identify regions favorable for radiolysis. For quality control, the caliper log was used to identify intervals of borehole collapse or mud cakes where log readings are unreliable.

Caliper

The caliper log (Figure 2-3) measures the borehole diameter using extendable arms with sensors that record diameter variations along the wellbore, allowing the identification of collapse zones and mud cake buildup on the walls. The caliper measurements provide information about lithological conditions, including the degree of consolidation and the presence of weak zones. It can also identify permeable-porous intervals, calculate mud cake thickness, determine borehole volume, and assess wall integrity. Additionally, the caliper can serve as a quality control parameter for other logs, as variations in borehole diameter may compromise the accuracy of their records (Serra, 2004). The caliper itself is not a petrophysical method in the *strict sensu,* since it does not measure any rock property, but it serves as a reference for data quality.

Figure 2-3. Six-arm Caliper Logging Tool (HCAL) from the Landsea company. The “arms” measures the diameter of the hole. (http://www.lsea.com.sg/oilandgas/accessorial-logging-tool/six-arm-caliper-logging-tool-hcal/).

Check Shoots

Check Shoots is a method that measures the seismic travel time from the surface to a specific depth (Figure 2-4). The P-wave velocities of formations along the wellbore are obtained by placing a geophone at the depth of interest, generating an energy source at the surface, and recording the resulting signal (Asquith et al., 2004). This data, again, is not a petrophysical measurement, but it was used (when available) to calibrate the sonic log, ensuring an accurate seismic-well tie.

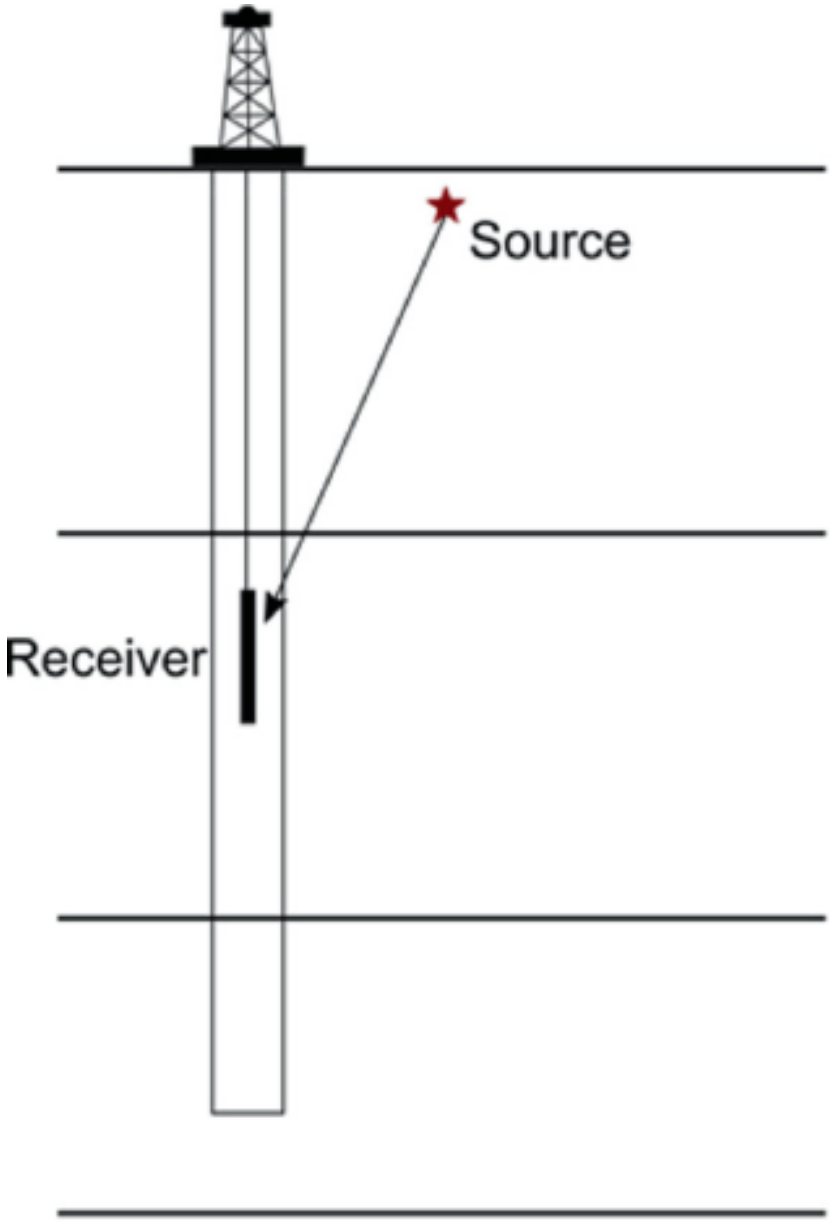

Figure 2-4. Basic schematic of a check shot method, where a source near the surface produces a mechanical wave that is recorded in the receiver; the travel time is used for the seismic-well tie process (figure adapted from Jones and Azevedo, 2023).

Sonic (DT)

Sonic log records travel time of P-waves by depth. It is recorded in microseconds per foot or meter. The tool consists of one or more sources that emit mechanical waves and a receiver that records the arrival times of the wave traveling through the rocks around the borehole (Asquith et al., 2004 – Figure 2-5). The application of this log in the present study, in conjunction with the density log, was to calculate the acoustic impedance needed to generate synthetic seismograms.

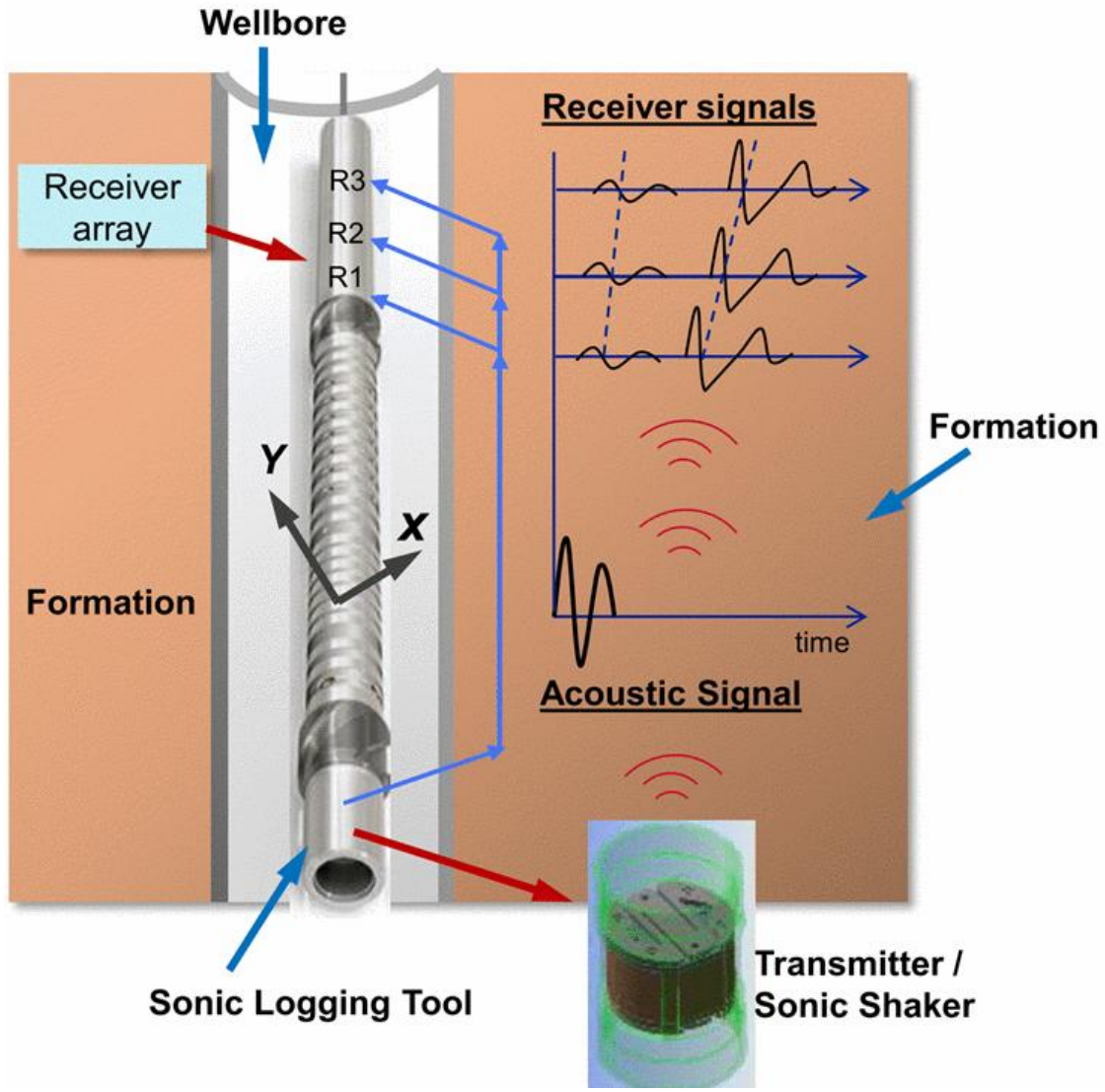

Figure 2-5. Basic elements of a Sonic logging tool, where an acoustic signal from a source travels, figure from Song et al. (2016).

Density (RHOB)

The density log measures the rock's bulk density and its fluid content. The tool emits gamma rays into the formation that interact with electrons in the formation via Compton scattering, and the energy of scattered gamma rays returning to detectors in the tool is inversely proportional to the formation's electron density, which is then converted to bulk density (Baker et al., 2015; Figure 2-6). In this thesis, the density log was used for two purposes: to calculate acoustic impedance for the seismic-well tie and, in combination with the neutron log, to identify potential H_2 reservoirs (Maiga et al., 2023).

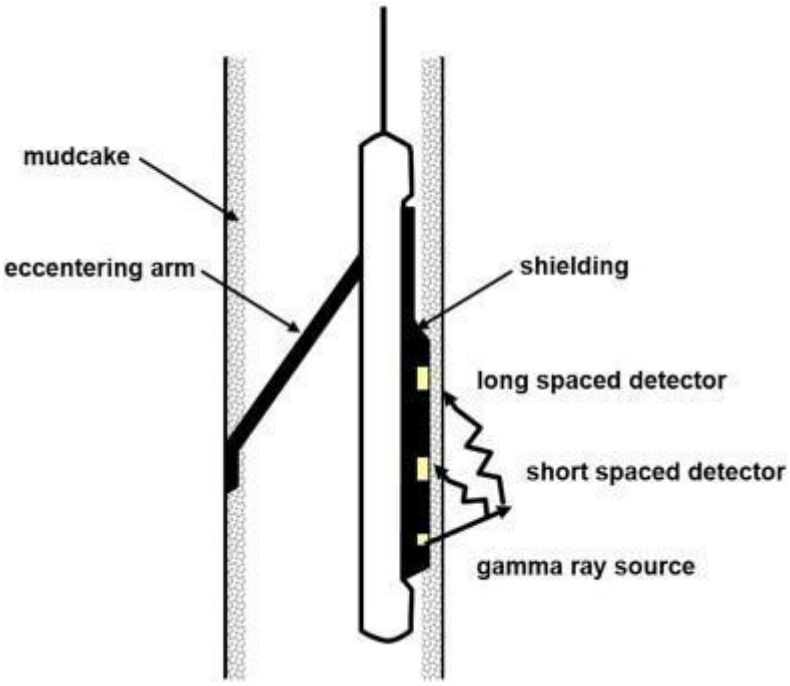

Figure 2-6. Figure from Baker et al., (2015) showing the basic work of an density logging tool. Figure from Schematic of a compensated density logging tool. The GRs from the source are scattered back toward the detectors. Modern tools may have more than two detectors.

Neutron porosity (NPHI)

The neutron porosity log measures the hydrogen in the formation, given as volume of hydrogen per rock volume (Labani, 2014). The tool emits high-energy neutrons that are slowed down mainly through collisions with hydrogen nuclei. Once hydrogen is concentrated in pore fluids (water or hydrocarbons), the tool response indicates porosity (Asquith et al., 2004). The neutron log shows a good response for H_2 anomalies detection in the Bourakebougou H_2 field in Mali, where known hydrogen accumulations correspond to a specific petrophysical signature: anomalously high neutron porosity (NPHI) readings are combined with anomalously low density (RHOB) readings (Maiga et al., 2023). While this crossover is a key indicator for potential H_2 reservoirs, it is not restricted to H_2 anomalies and must be interpreted within the geological context (Figure 2-7).

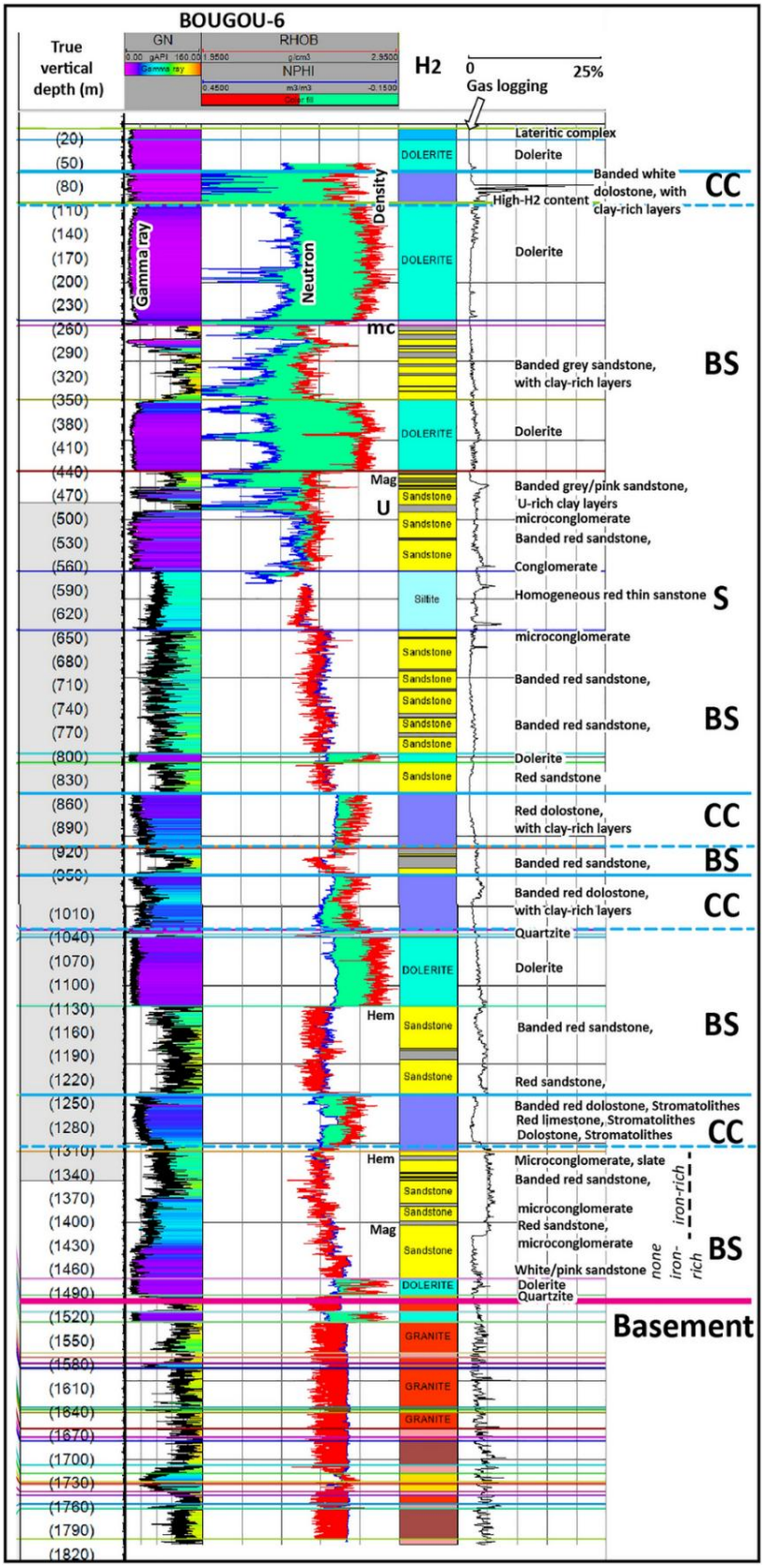

Figure 2-7. Figure from Maiga et al., 2023 showing the aforementioned anomaly: original captions: “Synthetic stratigraphic log and electric logging of the Bougou#6 borehole, which is the most characteristic of the area studied in the Bourakebougou sector, from the surface to the basement. CC cap carbonate, BS banded sandstone, S massive sandstone, mc zone of intense

contact metamorphism, Mag presence of magnetite, U uranium-rich level, Hem presence of hematite. The colored lines correspond to the well tops.”.

Gamma Ray (GR)

The gamma-ray log is a passive measurement of the natural radioactivity of the formation, primarily resulting from the decay of potassium (^{40}K) and from the radiogenic series of uranium (eU) and thorium (eTh). Conventionally, it is used to differentiate lithologies, particularly shales, which tend to concentrate these radioactive elements, from cleaner sandstones and carbonates (Asquith et al., 2004). In this study, however, the GR log was used to identify intervals with anomalously high radioactivity that may serve as potential sources for H_2 generation through the radiolysis of pore water (Blair et al., 2007; Boreham et al., 2020; Zgonnik, 2020).

2.2.2 Seismic data

Seismic reflection data were utilized to interpret the geological framework and constrain the geometry of rock units throughout the basin. The dataset comprises 2D post-stack time-migrated (PSTM) seismic lines, which were acquired and processed by industry contractors. This data was made available through institutional repositories, provided by ANP (Brazil) and ANCAP (Uruguay).

Seismic acquisition and processing.

he seismic reflection method relies on three fundamental components. First, a controlled source with a known position generates a mechanical wave that propagates into the subsurface. Second, subsurface geological interfaces reflect or refract the wave. A reflection occurs at boundaries where there is a contrast in acoustic impedance, defined as the product of seismic velocity and bulk density. Such contrasts typically arise from variations in lithology, compaction, porosity, and fluid content. The third component consists of an array of receivers, also with known positions, that record the reflected waves. The depth to a reflector is expressed in the time domain as two-way travel time (TWT). Modern seismic acquisition employs

multiple receivers, introducing redundancy in the dataset. The level of this redundancy, known as the fold, is a key indicator of data quality.

This research analysed 15 seismic surveys, provided by different companies and using different processing workflows. However, here is a list of common basic elements of seismic processing (Yimaz, 2001). Seismic processing is a multi-stage, iterative computational process that aims to transform raw field data into a geologically interpretable profile. The process includes steps as:

Geometry settings, to position all aforementioned reflection seismic elements into a profile.

Signal filtering, which improves the signal-to-noise ratio by attenuating random and coherent noise.

Spherical divergence compensation, which applies a gain to correct for the natural decay of wave energy as it spreads.

Deconvolution, which is applied to enhance temporal resolution by removing the blurring effect of the seismic wavelet, thereby compressing it to reveal sharper details of the analyzed area. Subsequently, the NMO stack utilizes a velocity model (Figure 2-8) to align reflection events across redundant data gathers (NMO correction) and then "stacks" these aligned traces to boost the coherent signal and cancel out random noise.

Migration corrects geometric distortions by repositioning dipping reflectors and collapsing diffractions to their origin locations, resulting in a seismic section that accurately represents the local geology.

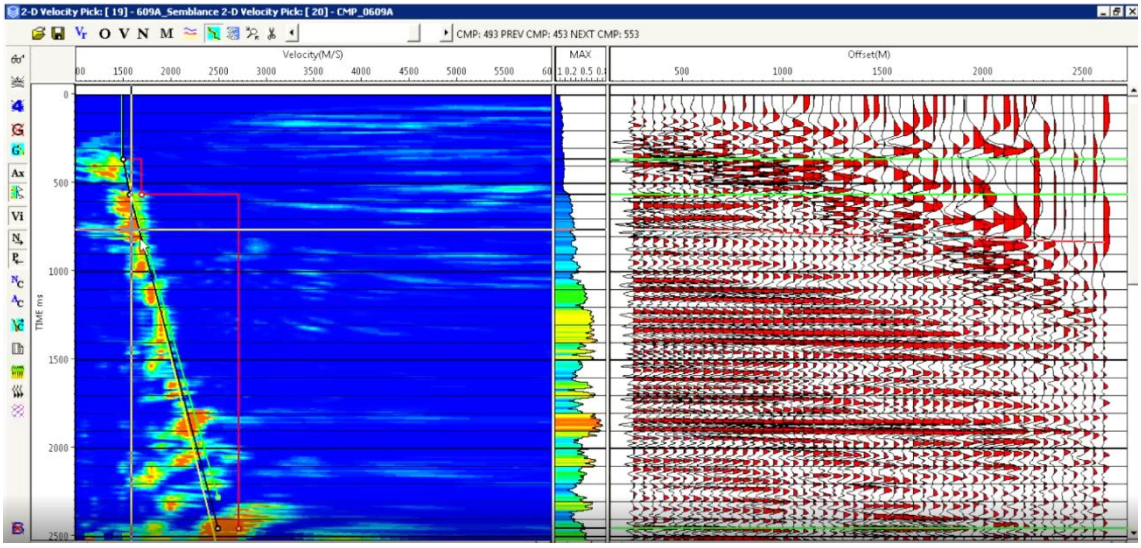

Figure 2-8. Example of interactive seismic velocity analysis using Schlumberger Vista 2016 software. The panel on the left displays the velocity spectrum, commonly known as a semblance plot. On this plot, coherence is measured as a function of velocity (horizontal axis) and two-

way time (vertical axis), with hot colors (yellow and red) indicating the optimal stacking velocities that will best align the reflection events for stacking. The panel on the right shows all redundant data from a single Common Midpoint (CMP) gather, where seismic traces are organized horizontally by their source-receiver distance (offset). This panel provides a real-time visualization of the Normal Moveout (NMO) correction being applied. As the velocity function (black line on left panel) is picked on the semblance plot, the hyperbolic reflection events on the CMP gather are flattened, confirming the accuracy of the velocity selection before the final stacking process. Image from personal archive.

Seismic well tie

The seismic-well tie is a process that precedes the seismic interpretation (Annex 3 - Supplementary Material - Article 1). That consists of correlating well data, measured initially in depth, with seismic data, which is recorded in time. To achieve this, a synthetic seismogram is generated from the well's sonic and density logs. When available, check shots are used to calibrate the sonic profile. These logs are used to calculate the rock's acoustic impedance. Next, the contrast between the different impedance layers is used to generate a series of reflection coefficients. This series of reflectors is then convolved with a wavelet. The result is the synthetic seismogram, which is adjusted and correlated with the real seismic traces near the well to ensure the best possible match. Once the correlation is validated, the geological markers from the well can be precisely positioned on the seismic section, allowing the interpretation of the layers to be confidently extended throughout the basin.

Seismic Interpretation.

Seismic interpretations in this research were primarily based on the well data. We based our interpretations on lithologies and ages (from this research or previous). However, the surfaces were not evaluated in terms of sequence stratigraphy. For sedimentary rocks, the reflectors were interpreted as surfaces of the same age (Vail, 1997). However, for hard rocks, this is not true. For instance, at the Victory Gold Mine (Stolz et al., 2004), geological models derived from well cores and mining data indicate that the continuity of some reflectors is meaningless (Figure 2-9). However, the use of seismic facies could be helpful to identify different bodies in the context of hard rocks. In that way, we use seismic facies as the main tool to segregate non-sedimentary geological units. Assuming seismic facies as a setting of reflectors that share geometry, continuity of reflectors, and amplitude.

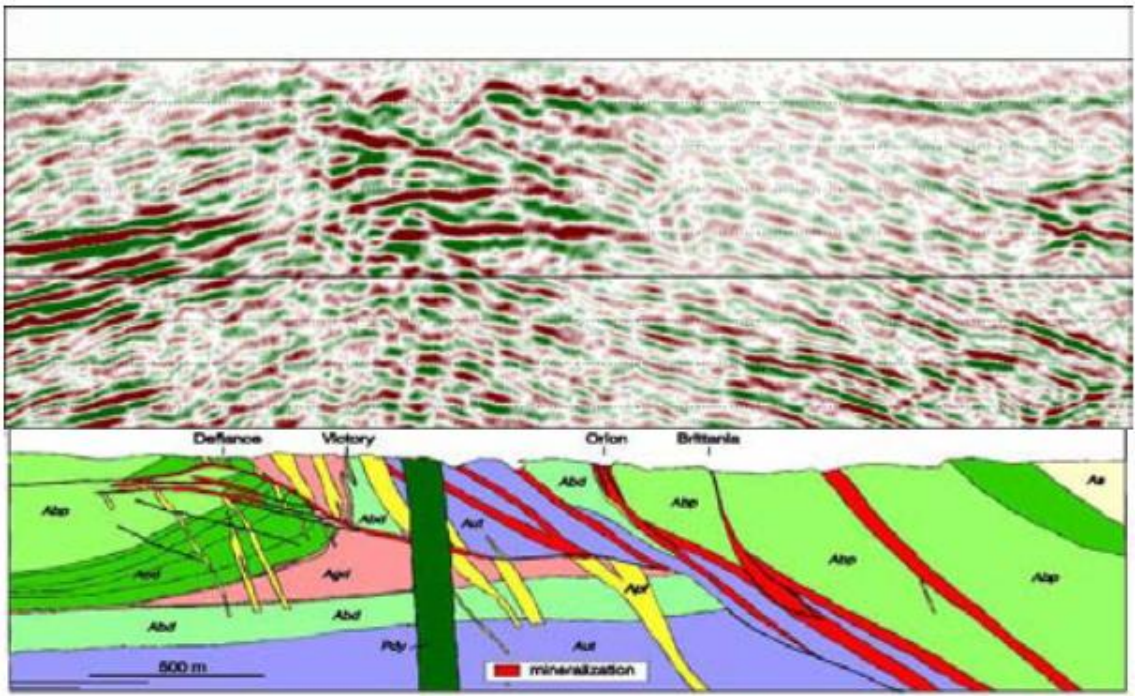

Figure 2-9. Image from Stolz et al. (2004) comparing seismic reflection data with a geological model beneath the Victory Gold Mine. (a) Detail of the reprocessed seismic section; (b) Geological cross section derived from drilling and mining data. Light green represents basalts, purple represents ultramafic rocks, dark green represents dolerites, pink and yellow represent porphyries, and red indicates gold lodes.

Velocity Model

The construction of a velocity model is a key stage in the seismic workflow, as it enables the migration of seismic data and interpretations from the time domain to the depth domain. To develop a regional model, it is essential to account for factors such as geological complexity, lateral and vertical heterogeneities, data quality and availability, and computational constraints (Bulhões et al., 2014). The velocity model for the Pelotas Basin was developed using Petrel software (SLB) and incorporates the interpreted horizons (Seafloor, Chattian Top, Thanetian Top, Cretaceous Top, Turonian Top, and Base of model), together with average velocity data derived from wells. Covering the entire basin, the model supports the conversion of seismic data and its interpretations to the depth domain. Figure 2-10 illustrates an example of the time-to-depth conversion applied to a seismic line from the northern sector of the Pelotas Basin.

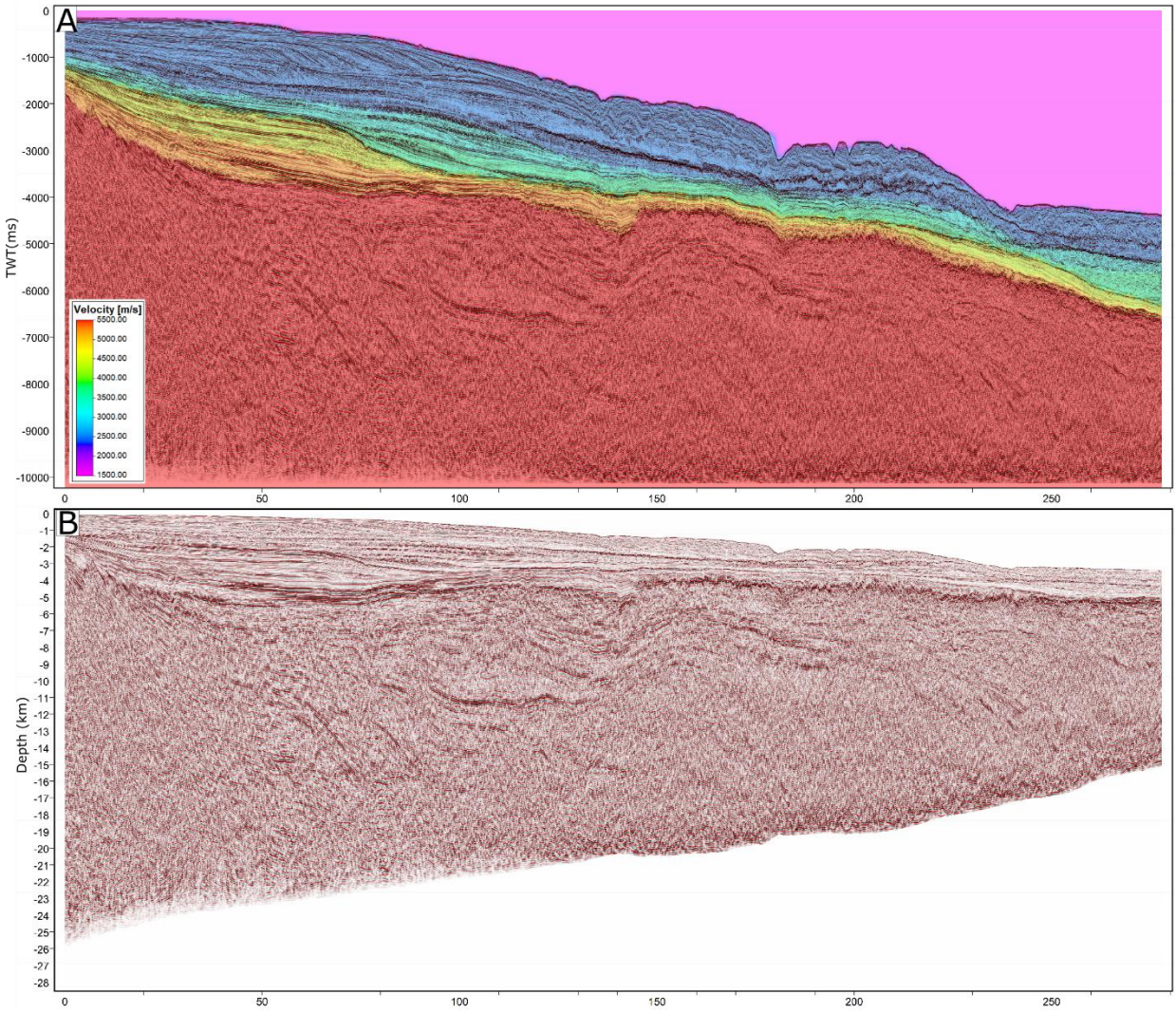

Figure 2-3. Dip-oriented seismic section from the northern region of the Pelotas Basin. In A), a time-domain seismic section overlaid with the velocity model. In B), the seismic section is converted to the depth domain.

2.2.3 Petrography

Petrographic analysis was performed following traditional methods (Gill, 2010), using standard thin sections (~30 µm thick) examined under a petrographic microscope. The observations were conducted in two main stages. In plane-polarized light (PPL), the properties of phenocrysts, such as crystal shape, color, pleochroism, and relief, were described. In cross-polarized light (XPL), a second polarizer (the analyzer) was inserted to reveal additional optical features, including birefringence (observed as interference colors), extinction angles, and twinning. The identification of the groundmass, clay minerals, and highly altered mineral phases was supported by X-ray diffraction (XRD) analyses.

2.2.4 X-ray diffraction

X-ray diffraction (XRD) analyses were performed by staff at the Universidade de Brasília (UnB) to identify the mineral constituents of the samples (Figure 2-11). The XRD method is based on the principle that crystalline materials diffract X-rays at characteristic angles (2θ), according to Bragg's Law. For whole-rock analysis, samples were powdered, and a portion was mounted as a randomly oriented powder to identify the bulk mineral assemblage.

The clay-sized fraction (<2 μm) was separated from the coarser material by double centrifugation and subjected to three standard treatments to enable accurate clay mineral identification: (i) air-dried oriented mounts to enhance basal reflections, (ii) ethylene glycol solvation to expand swelling clays such as smectite, and (iii) heating to 490°C to collapse swelling clays and test for thermally sensitive phases such as kaolinite. The unambiguous identification of clay species was achieved by comparing peak shifts or peak disappearances across diffractograms obtained from these treatments. All analyses were carried out on a Rigaku Ultima IV diffractometer, and diffraction patterns were interpreted using MDI Jade® 9 software.

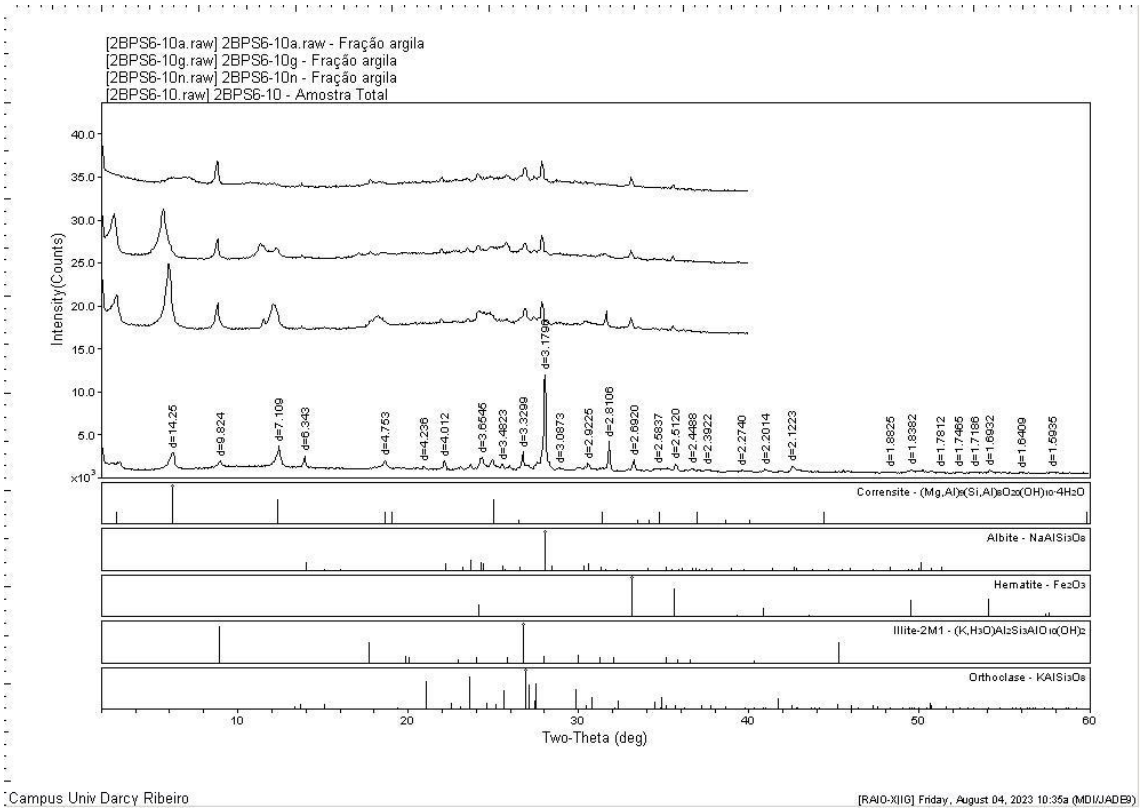

Figure 2-11. Representative X-ray diffraction (XRD) patterns for the sample at depth of 5378.8 m at well 2-BPS-6A The upper rectangle shows the plotting intensity versus diffraction angle (2θ). The bottom pattern shows the whole-rock analysis. The upper three patterns show the oriented clay fraction (<2 μm) subjected to standard diagnostic treatments: air-dried (natural state), solvated with ethylene glycol (glycolated), and heated to 490°C. The rectangles below are the minerals identified with the assistance of the software. All the XRD results are in the Annex 3- Supplementary materials from the first article.

2.2.5 Whole rock geochemistry

Whole-rock geochemical characterization was made through a multi-technique approach. Three primary methods were employed: X-ray Fluorescence (XRF), Inductively Coupled Plasma - Optical Emission Spectrometry (ICP-OES), and Inductively Coupled Plasma - Mass Spectrometry (ICP-MS). XRF is a technique that analyzes rock samples prepared as either fused glass beads or pressed powder pellets; it operates by bombarding the sample with a primary X-ray beam, which excites atoms to emit secondary, characteristic fluorescent X-rays, whose energies and intensities are measured to quantify major-element concentrations. For major and minor elements, solution-based plasma spectrometry techniques were used, which require complete sample digestion. This critical step was accomplished via lithium borate fusion, a process that dissolves rock powder in a flux at high temperature to form a

homogeneous glass bead, which is subsequently dissolved in acid to ensure that all mineral phases, including refractory ones, are in solution. The resulting solution was then analyzed by ICP-OES, a technique in which atoms are excited in a high-temperature argon plasma (~10,000 K), and the intensity of the light they emit at specific, characteristic wavelengths is measured. For the determination of trace and rare earth elements at very low concentrations, ICP-MS was utilized; this method uses the plasma to ionize the atoms, which are then separated by a mass spectrometer based on their mass-to-charge ratio, providing sensitivity down to the parts-per-billion level.

2.2.6 Isotopic Methods

U-Pb Geochronology

The U–Pb geochronological method in zircon is based on the mineral's ability to behave as a nearly closed system for uranium and lead under a wide range of geological conditions. The zircon crystallization process incorporates significant amounts of U and Th into its crystal while excluding common Pb at the time of formation (Gehrels, 2014; Wang et al., 2023). Its high closure temperature (~900 °C) and resistance to chemical and physical alteration allow the U–Pb system to remain intact even after metamorphic overprinting or diagenetic processes. Two independent decay schemes ($^{238}U \rightarrow ^{206}Pb$ and $^{235}U \rightarrow ^{207}Pb$) run simultaneously, with well-determined decay constants. The concordance between the two systems, first formalized by Wetherill (1956), provides an intrinsic test for closed-system behavior, making zircon one of the most robust geochronometers available.

Advances in instrumentation have produced multiple analytical approaches for U–Pb zircon dating, each with distinct strengths and limitations. Isotope dilution–thermal ionization mass spectrometry (ID-TIMS) is regarded as the more precise method for achieving analytical uncertainties as low as 0.02% (2σ), but it requires complete dissolution of grains, which is time- and labor-intensive (Schmitz and Kuiper, 2013). Secondary ion mass spectrometry (SIMS) and its specialized implementation, SHRIMP (Sensitive High-Resolution Ion MicroProbe), enable in situ analyses with high spatial resolution (down to ~20 μm), making them well suited for dating inherited cores, metamorphic overgrowths, or complex zoning, with typical uncertainties of 1–3% (Cocherie and Robert, 2008; Chemale et al., 2011). Laser ablation–inductively coupled plasma mass spectrometry (LA-ICP-MS), especially in multi-collector configuration (LA-MC-

ICP-MS), offers rapid data acquisition and high resolution and is widely used for detrital zircon provenance studies, although it typically provides lower precision than SIMS or ID-TIMS.

In igneous systems, U–Pb zircon dating is a primary tool for determining crystallization ages, constraining the timing of magmatic emplacement. Integration of cathodoluminescence (CL) or backscattered electron (BSE) imaging within situ geochronology enables targeted analysis of pristine magmatic zones while avoiding inherited components or domains affected by Pb loss. In plutonic and volcanic contexts, U–Pb ages provide key constraints for reconstructing magmatic histories, residence times, and differentiation, and for correlating magmatism with tectonic and climatic events. In volcanic packages, zircon crystals were formed shortly before the magmatic event and can anchor stratigraphic frameworks and calibrate paleoenvironmental records with high temporal resolution (Bowring and Schmitz, 2003).

In sedimentary contexts, U–Pb zircon geochronology is applied mainly in two ways: (i) dating interbedded volcaniclastics, such as tuffs, to directly constrain depositional ages, and (ii) determining the provenance of sedimentary deposits via detrital zircon age spectra. For the first application, chemical abrasion–ID-TIMS (CA-ID-TIMS) is preferred when ultra-high precision is needed, achieving uncertainties on the order of 0.2% enabling detailed modeling of sedimentary and fossil events durations (Gehrels, 2014). For provenance studies, LA-ICP-MS (quicker) and SIMS (better resolution) allow rapid generation of large detrital zircon datasets, revealing source terranes, sediment routing pathways, and basin evolution. Determining maximum depositional ages requires careful selection of the youngest zircon grains and discrimination between magmatic, inherited, and recycled populations, often in combination with stratigraphic, geochemical, and tectonic constraints.

Sm-Nd system

The samarium–neodymium (Sm–Nd) system is based on the α-decay of 147Sm to ^{143}Nd, with a long half-life of approximately 106 Ga ($\lambda = 6.54 \times 10–12\ yr^{-1}$). Both Sm and Nd are rare earth elements (REE) with similar geochemical behavior during igneous processes, being predominantly trivalent, incompatible, and immobile (DePaolo, 1981; Dickin, 2005). This geochemical coherence reduces fractionation during partial melting and crystallization, allowing the Sm–Nd system to preserve primary isotopic signatures even in rocks affected by metamorphism. The system is particularly valuable because it is less susceptible to post-

formational alteration than Rb–Sr, and Nd is generally immobile in most geological fluids. These characteristics make Sm–Nd isotope geochemistry a powerful tool for dating mantle-derived rocks, tracking crust–mantle evolution, and determining model ages (TDM) relative to a chondritic uniform reservoir (CHUR).

Sm–Nd isotopic analysis requires high-precision mass spectrometry, typically using thermal ionization mass spectrometry (TIMS) or, recently, multi-collector inductively coupled plasma mass spectrometry (MC-ICP-MS). The method involves chemical separation of Sm and Nd using ion-exchange chromatography, followed by isotope ratio measurement. TIMS has long been the reference technique, offering precision on the order of ±0.000005 for $^{143}Nd/^{144}Nd$ ratios, while MC-ICP-MS provides comparable precision with faster throughput and the ability to measure multiple isotopes simultaneously (Dickin, 2005). Age determinations rely on constructing isochrons, either from whole-rock suites or mineral separates, where the slope corresponds to the age and the intercept gives the initial $^{143}Nd/^{144}Nd$ ratio. Precise quantification of the Sm/Nd ratio is essential, as small analytical errors can propagate into significant uncertainties in calculated ages and εNd values.

In igneous petrology, Sm–Nd isotopes are widely used to constrain the timing of magmatic crystallization, the degree of mantle depletion, and crustal contamination processes (Allegre and Othman, 1980). In mafic and ultramafic rocks, due to their high REE contents and relatively simple isotopic histories, they often yield precise Sm–Nd ages that closely approximate their formation ages. The εNd constraint, expressed on 143Nd/144Nd from CHUR in parts per 10,000, is particularly informative, where positive εNd values generally indicate derivation from a depleted mantle source, whereas negative values reflect contributions from older, enriched continental crust. Sm–Nd provides robust constraints on magma genesis, crust–mantle interaction, and large igneous province evolution. In sedimentary provenance studies, Sm–Nd isotopes are primarily used to provide constraints on the crustal residence period of detrital material and to distinguish between juvenile and recycled crustal sources.

Ar/Ar

The $^{40}Ar/^{39}Ar$ dating technique is an improvement from the K–Ar method, designed to overcome some of its analytical limitations by allowing both potassium and argon to be measured from the same aliquot through neutron irradiation (McDougall & Harrison, 1999; Dickin, 2005). The naturally occurring ^{39}K is converted to ^{39}Ar by fast-neutron bombardment

in a nuclear reactor, enabling the determination of the ^{40}K content indirectly from the measured ^{39}Ar. The analytical procedure involves sample irradiation with a neutron flux monitor of known age, commonly sanidine from the Fish Canyon Tuff, to determine the neutron fluence parameter. Step-heating using resistance or laser furnaces allows argon isotopes to be released from different domains within the crystal, producing age spectra that can reveal diffusion profiles, partial resetting, or heterogeneous excess argon distributions (Phillips & Matchan, 2013). Precision can reach 0.1–0.2% for high-quality samples and well-characterized standards, but it depends on accurate corrections for interfering isotopes produced during irradiation (e.g., from Ca, K, and Cl). In igneous petrology, Ar-Ar dating is widely used for constraining volcanic ages, cooling ages of plutonic systems, and the interval of magmatic activity. Sanidine and plagioclase from volcanic units can yield eruption ages with temporal resolution of tens of thousands of years, allowing calibration of stratigraphic sequences and correlation with paleoclimatic and paleomagnetic records (McDougall & Harrison, 1999).

2.2.7 H_2 system evaluation

In this study, the H_2 system was investigated in parallel with a conventional petroleum system (Prinzhofer et al., 2018; Serratt et al., 2024). Accordingly, it was necessary to define the potential source rocks, reservoirs, seals, and sinks within the study area. The sources were classified according to their contribution to H_2 generation: some were quantitatively estimated in terms of order of magnitude (e.g., thermogenic, radiolytic, and inorganic mineral alteration processes), while others were qualitatively assessed (e.g., biological activity). Reservoirs were quantitatively evaluated through petrophysical data, whereas seal and caprock effectiveness were examined qualitatively. Among the sinks, only pyrite dissolution was quantified in terms of order of magnitude, while hydrocarbon consumption, biological oxidation, and mechanical leakage were also discussed qualitatively.

Quantified Sources

Thermogenic

Experimental studies with kerogen types 2 and 3 point out that rocks with organic matter could produce H_2 with a potential of 20 mg H_2/g TOC (Total Organic Carbon; Mahlstedt et al., 2024) for each gram of TOC between the temperatures that mark the end of CH_4 generation

(250°C) and 330°C (Mahlstedt et al., 2024). We use the CH_4 upper limit for generation once hydrocarbon (oil and gas) generation could consume H_2 (Mahlstedt et al., 2024). The volume of sedimentary rocks under these thermal conditions was constrained using a geometrical model derived from seismic analysis and a basin thermal model developed using BHTs. The TOC was taken from previous Brazilian governmental studies (ANP). Assuming the rock's density and average TOC, a bulk TOC mass was inferred and using the 20 mg H_2/g TOC ratio (Mahlstedt et al., 2024), a total potential of H_2 by thermogenesis was inferred.

Rock Water Interaction

In this work, for a basin-scale estimate, the H_2 production by Fe^{2+} oxidation was simplified by the FeO oxidation by water reaction, following Worman et al. (2016 and 2020) simplifications. That implies a maximum potential of production given by the proportion of $2Fe^{2+}$ to $1H_2$ or 55.402g Fe^{+2} to 1g H_2.

$$2FeO\ (\text{in minerals}) + H_2O \rightarrow Fe_2O_3\ (\text{in minerals}) + H_2$$

This simplification was used to calculate H_2 in the basalts, assuming a primary magmatic $Fe^{3+}/\Sigma Fe$ ratio of 0.143 (Zhang et al.,2018). In this way, all Fe^{3+} values higher than this observed in geochemical values imply that the aforementioned proportion generated H_2. However, part of this H_2 could be trapped in the basalts itself (Worman et al., 2016). The geometry of basalts was constrained from the bibliography (Chauvet et al., 2021) and using new geochemical data to constrain the bulk Fe^{2+} and Fe^{total} in the volcanic rocks.

Radiolysis

The H_2 produced in a volume of rock water saturated per unit of time was estimated following Atike 1985 equations with parameters compiled by Bouquet et al., (2017):

$$P_{H^2} = \sum_{i} \quad (G_{H_2,I} \sum_{s} \quad D_{s,i})$$

Where P_{H2} is the number of particles produced per unit of time

i is the radiation type (α,β,γ)

s is the radiogenic nuclide (^{40}K, ^{232}Th, ^{235}U, ^{238}U)

$G_{H2,i}$ is the radiation chemical yield of $H2$ in water for radiation type; we used the values compiled by Bouquet et al. (2017), presented in Table 2-1:

Table 2-3. Values of radiation chemical yield ($G_{H2,i}$) by each Radiation (i) type (Harris & Pimblott 2002; Lin et al. 2005; Bouquet et al., 2017).

Radiation (i)	Radiation chemical yield ($G_{H2,i}$) (Molecules/Joule)
α	6E+16
β	3.7E+16
γ	2.5E+16

$D_{s,i}$ is the radiation dose absorbed by water due to radiation type "i" emitted by

radionuclide "s"; given by:

$$D_{s,i} = \frac{V p_r A_s \sum E_{i,s}}{\frac{1}{1-\phi} + \frac{p_r}{S_i p_w \phi}}$$

where, V is the volume of the analyzed body.

p_r is the rock density.

p_w is water density.

Φ is the porosity.

S_i is the mass stopping powers of water to rock, given by Hofmann (1992) in Table 2-2

Table 2-4. Data of mass stopping powers of water to rock (Hofmann, 1992).

Radiation (i)	Mass stopping powers of water to rock (S_i)
α	1.5
β	1.25
γ	1.14

$\sum E_{i,s}$ is the sum of the decay energy of the radionuclide "s" by emission of the radiation "i", defined by Blair et al. (2007), presented in Table 2-3

Table 2-5. values of $\sum E_{i,s}$ decay energy by each radiation type by radionuclide (Blair et al., 2007).

Radionuclide (s)	Radiation (i)	Decay energy sum (∑Ei,s) (J/decay)
40K	α	0
	β	$1.88E^{-13}$
	γ	$2.51E^{-14}$
232Th	α	$5.76E^{-12}$
	β	$4.55E^{-13}$
	γ	$3.6E^{-13}$
235U	α	$5.45E^{-12}$
	β	$1.67E^{-12}$
	γ	$8.81E^{-14}$
238U	α	$6.88E^{-12}$
	β	$9.76E^{-13}$
	γ	$2.73E^{-13}$

A_s is the activity of the radionuclide "s" given by:

$$A_s = \lambda \cdot N$$

Where λ is the radionuclide decay constant, in this research, it was assumed as derived from the half-life values compiled by Bouquet et al. (2017) presented in Table 4.

Table 2-6- Radionuclides (s) half-lifes, Bouquet et al. (2017).

Radionuclide (s)	Half-life, years (λ)
^{40}K	$1{,}25 \times 10^{9}$
^{232}Th	$1{,}4 \times 10^{10}$
^{235}U	$7{,}04 \times 10^{8}$
^{238}U	$4{,}46 \times 10^{9}$

And N is the Number of radionuclides “s” per kg of rock.

The abundance of each radionuclide was estimated from (Haynes, 2016). In that way, we assume ^{238}U as 99.274% of the mass of U in the rocks and ^{235}U as 0.720%; ^{232}Th was assumed as 100% of Th; and ^{40}K was assumed as 0.012% of the mass of K in the rocks.

Biological

Microorganisms are pointed out as a potential H_2 source (Dowaidar, 2025), although they are more probably a sink factor (Zgonick, 2020; Thaysen et al., 2023). There is no known way to quantify it at the Pelotas Basin, and this work did not address any approach to deal with this issue.

Reservoirs

To evaluate reservoirs, a petrophysical analysis was conducted on key intervals using well log data. Effective porosity, which represents the interconnected pore space available for gas accumulation, was calculated from density logs after correcting for the volume of clay derived from gamma-ray logs. Additionally, the neutron log was utilized as a tool for direct hydrogen detection, as its characteristically high reading provides a key geophysical signature for the presence of free H2 gas within the reservoir pore space (Maiga et al., 2023).

Seal/cap rock

The evaluation of potential cap rocks targeted sills (Maiga et al., 2024) and evaporites (Gelman et al., 2025), which are known to be highly effective seals for natural hydrogen systems. While fine-grained siliciclastic rocks are present, it is not known if they could be an effective cap rock (Maiga et al., 2024). A potential seal is a thick igneous sill, as interpreted from seismic lines. Although this feature has not yet been drilled, its confirmation would be significant, as dolerite intrusions are proven to be the primary trapping mechanism in analogous productive fields (Section 4. Article 2).

Sinks

Almost all sinks are not possible to quantify. For instance, carbon dioxide is hydrogenated into CH_4 (Prinzhofer et al., 2018). However, since the CO_2 content in the basin is unknown, this sink cannot be quantified. Similarly, the total amount of H_2 leakage is unknown, and it depends on whether siltstone and claystones can serve as a caprock for H_2 systems. There is ample evidence of microbial activity at the Pelotas Basin, as observed in the biological CH_4 found as BSRs (Bottom Simulating Reflector; Sad et al., 1998; Miller et al., 2015). However, quantifying microbial H2 consumption is not viable.

Sulfur-related sinks were quantified; the sulfur in marine sediments was assumed to be mostly pyrite. In that way, since the coexistence of pyrite and hydrogen is not thermodynamically stable, it was assumed the following equation as a potential sink for the bulk basin sulfur content (Truche et al., 2010; Ahmadpour & Gholami, 2025)

$$FeS_2+(1-X)H_2 \rightarrow FeS1+X+(1-X)H_2S \qquad \text{for } (0 \leq X < 0.125)$$

It was tested with values of X=0.

3 Article 1

This chapter is an adapted version of an article published in the scientific journal Tectonophysics. It is called "**Unraveling the geological history of the South Atlantic margin: Records of West Gondwana Breakup from South Brazil and Uruguay margin".** It provides a comprehensive synthesis of the majority of existing knowledge regarding the genesis of the Pelotas Basin and the margin configuration. Furthermore, the chapter aims to expand upon this established understanding by introducing new data and interpretations, contributing to a more complete picture of the region's geological evolution.

This chapter addressed the specific objective I) • Perform a petrological characterization of the margin through petrographic and geochemical analyses (whole-rock and isotopic composition) of rocks composing the seaward dipping reflectors (SDRs) and associated volcanic sequences (Pre-rift and Late-rift stages). And partially addressed the specific objective II)• Constrain the ages and magmatic sources of the SDRs and related volcanic rocks in the study area.

The first article presents efforts to characterize the margin of southern Brazil and Uruguay. This is an authorial research article; however, it was developed collaboratively. I hereby specify the contributions of each participant to enable the PhD committee to evaluate my individual work accurately.

Henrique Serratt (Ph.D. Candidate): Responsible for the interpretation of seismic data, petrographic analyses supported by X-ray diffraction, and the interpretation of geochemical and isotopic data, including Sr and Nd isotopic results. Integrated datasets prepared the figures, and wrote the manuscript, ensuring coherence between data, methods, and interpretations.

Adalene Moreira Silva (UnB), Laurent Geoffroy(UBO), and Farid Chemale Jr.(UNISINOS): PhD supervisors. Provided conceptual guidance, supervised the research process, and conducted the final manuscript revision. They also secured the necessary resources and institutional support.

Bruno Conti (ANCAP): Representative of the Uruguayan government in the UNISINOS cooperation agreement. Facilitated access to data and samples from Uruguay and validated geological descriptions related to the Uruguayan margin.

Marly Babinski (USP) and **Peng Peng (UCAS)**: External collaborators who made the analytical procedures in the lab related to isotopes. Marly Babinski conducted Sr and Nd isotope analyses; Peng Peng performed part of the U-Pb geochronological analyses.

Catarina Laboure Bemfica Toledo (UnB) and Ilana Lehn (UNISINOS): Provided support in petrography.

Monique Aparecida Marchese Rizzi (UNISINOS): Contributed expertise on the Pelotas Basin, validating the related text.

Claudia Domingues Teixeira (UNISINOS): Assisted in gravimetric modeling (not included in the final manuscript). Assisted with discussions on basement interpretations and rift evolution.

Matheus Fernandes da Cruz (UNISINOS): Conducted seismic well-tie correlations.

Tiago Jonatan Girelli (UNISINOS): Carried out U-Pb analytical work and confirmed the presence of Paraná Basin sedimentary rocks beneath the Punta del Este Basin.

Unraveling the geological history of the South Atlantic margin: Records of West Gondwana Breakup from South Brazil and Uruguay margin

Henrique Serratt [a,b,c], Tiago Jonatan Girelli [c], Matheus Fernandes da Cruz [c], Claudia Domingues Teixeira [c], Ilana Lehn [c], Monique Aparecida Marchese Rizzi [c], Marly Babinski [d], Catarina Laboure Bemfica Toledo [a], Peng Peng [e,f], Bruno Conti [g], Adalene Moreira Silva [a], Laurent Geoffroy [b], Farid Chemale Junior [c,h]

[a] Instituto de Geociências, Universidade de Brasília, 70910-900 Brasília, DF, Brazil

[b] UMR CNRS-IFREMER-CNRS-UBS 6538 Geo-Ocean, IUEM, Universit´e de Bretagne Occidentale, France

[c] Geology and Geophysics Research Group – NGA, Universidade do Vale do Rio do Sinos, São Leopoldo, RS, Brazil

[d] Universidade de São Paulo, Instituto de Geociências, Rua do Lago, 562, São Paulo, Brazil

[e] China-Brazil Joint Geoscience Research Center, State Key Laboratory of Lithospheric Evolution, Institute of Geology and Geophysics, Chinese Academy of Sciences, Beijing 100029, China

[f] College of Earth and Planetary Sciences, University of Chinese Academy of Sciences, Beijing 100049, China

[g] Exploration & Production, ANCAP, Montevideo, Uruguay

[h] Postgraduate Program in Geosciences, Universidade Estadual do Rio do Janeiro, Rio de Janeiro, RJ, Brazil

Highlights

- Integration of rock analysis from offshore Uruguay, Brazil, and the Rio Grande Rise.
- South Atlantic Magmatic Evolution from Lower to Upper Cretaceous.
- Direct evidence of the Paraná Basin towards the offshore South America platform.
- SDRs and related magmatic rocks were developed over the continental crust.
- Rio Grande Rise and Walvis Ridge share similar isotopic signatures.

Keywords

Pelotas Basin, Punta del Este Basin, Seaward dipping reflectors, Geochemistry, Volcanic passive margin, Paraná Basin

Abstract

Continental Flood Basalts, Seaward Dipping Reflectors (SDRs), and oceanic plateaus or seamounts often occur in close geographic proximity. In South America, the Paraná-Etendeka Continental Flood Basalts are followed by SDR-related magmatism, and even after the formation of oceanic crust, anomalous magmatism persists in the region, as seen in the Walvis Ridge and Rio Grande Rise. This study investigates volcanic and sedimentary rocks from offshore wells in the Pelotas and Punta del Este basin margins, revealing the offshore extension of the Paraná Basin. Our data demonstrate geochemical and isotopic affinities between margin volcanic rocks and the Paraná-Etendeka Large Igneous Province. The basalts from the margin display OIB- and E-MORB-like geochemical and isotopic compositions consistent with EMI and EMII mantle sources. However, these isotopic signatures may have been modified by assimilation of continental crust or subcontinental lithospheric mantle. The presence of zircon xenocrysts supports this interpretation and suggests that volcanic rocks from the margin were emplaced above the continental crust with magmatic assimilation of rocks from the Dom Feliciano Belt. The Rio Grande Rise also exhibits an EMI-like isotopic fingerprint similar to the Walvis Ridge, indicating a possible shared origin during the Cretaceous. However, this isotopic content may also result from magmatic assimilation of continental crust slivers or subcontinental lithospheric mantle. These findings highlight the role of a persistent thermal anomaly throughout the magmatic evolution of the South Atlantic.

3.1 Introduction

Gondwana breakup was a major tectonic event that shaped the modern configuration of continents and oceans. This process occurred in multiple stages over an extended period from the Late Triassic to the Early Cretaceous. Although the cause of rifting remains debated (e.g., Nance et al., 2014; Frizon de Lamotte et al., 2015), fragmentation of this supercontinent led to the opening of the South Atlantic, Indian, and Southern oceans, separating South America, Africa, Antarctica, India, and Australia (Veevers, 2012). The breakup had a profound impact on the global climate, ocean circulation patterns, and the evolution and distribution of flora and fauna across the newly separated landmasses (Torsvik and Cocks, 2013). Specifically regarding the West Gondwana breakup, evidence suggests that the process likely began during the Berriasian–Valanginian (145–132.6 Ma; Lovecchio et al., 2024).

The magmatism related to the West Gondwana breakup and the South Atlantic Formation can be divided into four main types: (I) The Continental Flood Basalts (CFB), represented by the Paraná-Etendeka Large Igneous Province (LIP) which occurred mainly during 135.0 ± 0.6 and 133.2 ± 0.3 Ma (Gomes and Vasconcelos, 2021); (II) The volcanic wedges observed along the margin as Seaward Dipping Reflectors (SDR), which formed between 134 to 113 Ma (Chauvet et al., 2021); (III) The Mid Ocean Ridge Basalts (MORB) that constitute the oceanic crust. (IV); The volcanic plateaus, islands, and seamounts developed throughout the history of the South Atlantic Ocean (From 114 ma to today - Hoyer et al., 2022; Homrighausen et al., 2019). Among these magmatisms, the SDR remains the least directly studied, often being analyzed primarily through geophysical methods in the region (e.g., Harkin et al., 2020; Chauvet et al., 2021; Serratt et al., 2022; Teixeira et al., 2025a).

In order to directly investigate the SDRs, we analyzed samples from five offshore well cores in the Pelotas and Punta del Este basins' margins and one from the Rio Grande Rise. These five wells are all exploratory boreholes that drilled through the Cenozoic and Early Cretaceous drift sections, recovering rocks beneath the drift sequences. This study aims to assess the age, magmatic sources, and relations between CFB, SDR, and oceanic features (islands, seamounts, and oceanic plateaus) in the region. To accomplish this objective, we conducted a detailed investigation incorporating petrography, X-ray diffraction (XRD), geochemical analysis, U-Pb geochronology, and Nd and Sr isotopic studies of rock samples from beneath the drift section of the Pelotas and Punta del Este basins.

3.2 Geological setting

The study area lies along the South Atlantic margin, specifically within the southern Brazil and Uruguay regions (encompassing the Pelotas and Punta del Este basins, Fig. 3-1) and the Rio Grande Rise. During most of the Phanerozoic, this area remained connected to Namibia as part of the Gondwana supercontinent (Teixeira et al., 2025a and references therein). During the Early Paleozoic, assembly of Gondwana in this region produced its most extensive geological feature, the Dom Feliciano Belt (DFB). This belt formed through subduction of the Adamastor Ocean during the convergence of Rio de la Plata, Congo, and Kalahari paleoplates from the Neoproterozoic to the Early Paleozoic (e.g., Gresse et al., 1996; Chemale Jr et al., 2012; Caxito et al., 2022; Teixeira et al., 2025b). The crystalline basement of southernmost

Brazil and Uruguay consists of rocks from the DFB and the Rio de la Plata Craton, overlain by sedimentary units of the Paraná and Pelotas basins (Stica et al., 2014; Gordon and Mohriak, 2015; Teixeira et al., 2025b).

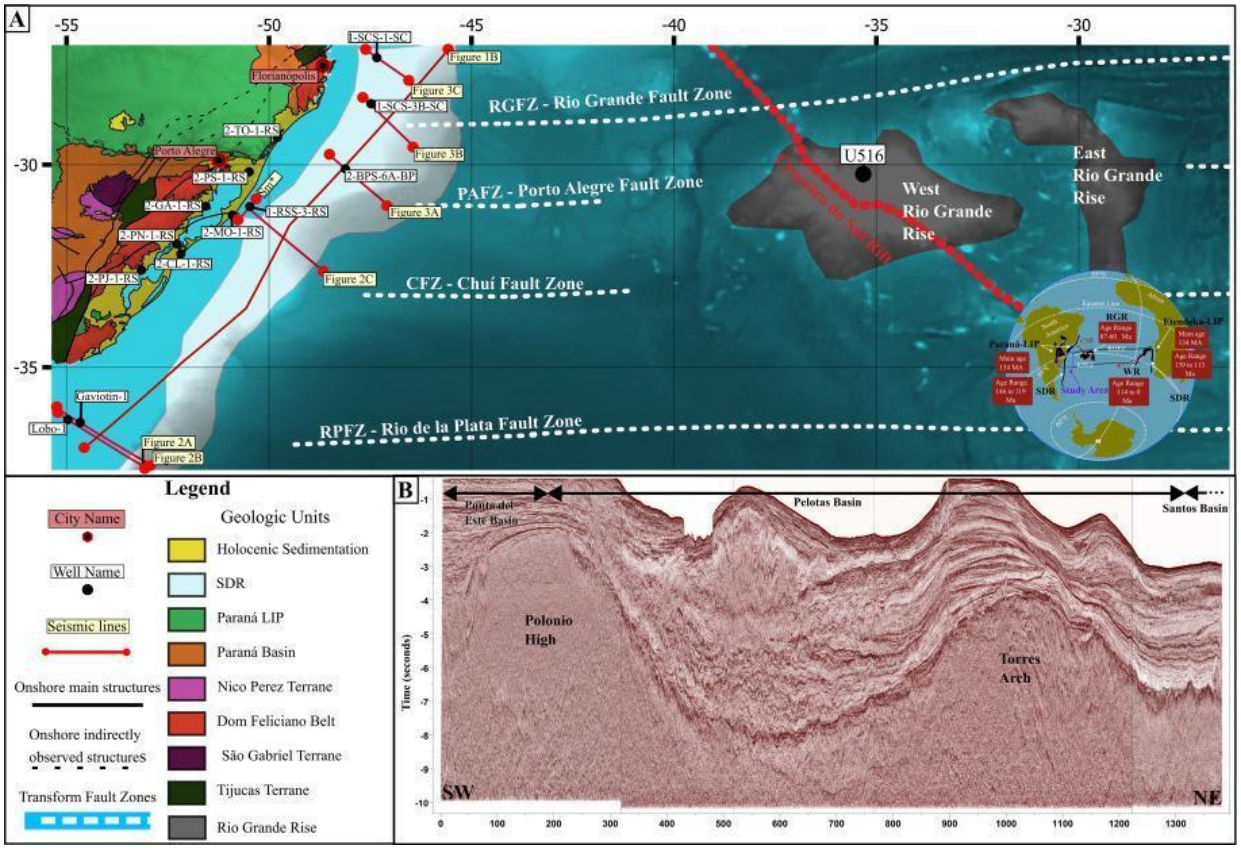

Figure 3-1.A) Location map showing the position of the seismic lines and the wells used in this study. The LIPs and Rio Grande Rise boundaries are adapted from Whittaker et al. (2015), while the SDRs are based on Chauvet et al. (2021), Sm* seismic line in supplementary material 2; in the mini-globe: The Paraná-Etendeka magmatism ages are compiled by Gomes and Vasconcelos (2021); The WR- Walvis Ridge ages are compiled by Homrighausen et al. (2019), the red arrow shows the age of the elder to youngest seamounts. The Rio Grande Rise ages were from Hoyer et al. (2022), CSR – Cruzeiro do Sul Rift. Onshore geological units and structures from Teixeira et al. (2025b). B) A composition of five strike-direction seismic lines showing the regional tectonic framework. We highlighted two structures: the Polonio High, interpreted as a Proterozoic basement high (Conti et al., 2017), and the Torres Arch, characterized by an exceptionally thick SDR package compared to other areas of the margin (Stica et al., 2014; Gordon and Mohriak, 2015; Harkin et al., 2020; Chauvet et al., 2021). (For interpretation of the references to colour in this figure legend, the reader is referred to the web version of this article.)

The Paraná Basin is the largest intracratonic basin in South America, predominantly located in Brazil and extending into Paraguay, Argentina, and Uruguay (Milani et al., 2007). Its offshore extension below the Pelotas Basin has been hypothesized based on seismic data,

though direct confirmation remains limited. Seismic surveys have suggested its presence beneath the Pelotas Basin in Uruguay and the northernmost portion of the Pelotas Basin in Brazil (Holz et al., 2010; Conti et al., 2017). The only well that recovered Paraná Basin rocks beneath the Pelotas Basin is the onshore well 2-TO-1-RS (Fig. 3-1; Bueno et al., 2007; Holz et al., 2010) located in the northern portion of the Pelotas Basin. In this area, the Paraná Basin is limited to a structural depression known as the Torres Syncline, which constitutes the easternmost onshore exposure of the Paraná–Etendeka flood basalts in South America (Waichel et al., 2012). The Paraná Basin developed primarily before the breakup of Gondwana and contains six supersequences: Rio Ivaí, Paraná, Gondwana I, Gondwana II, Gondwana III, and Bauru. Within our study area (southern Brazil and Uruguay), three of these supersequences are present (Milani et al., 2007): Gondwana I (comprising the Itararé and Passa Dois groups); Gondwana II (comprising the Piramboia and Santa Maria formations), and Gondwana III (comprising the Botucatu Formation and Serra Geral Group). The Serra Geral Group is also recognized as part of the Paraná-Etendeka Large Igneous Province (LIP), which covers an extensive area of approximately 1,000,000 km2.

The Paraná-Etendeka LIP (PEL) was commonly interpreted as the result of magmatic activity driven by a plume (sometimes called Tristan da Cunha Plume) during the breakup of the Gondwana supercontinent (Ewart et al., 1998; Marsh et al., 2001; Ewart et al., 2004; Gibson et al., 2006; Zhou et al., 2020; Beccaluva et al., 2020). However, alternative models suggest that its formation should be attributed to regional thermal anomalies without plume involvement, such as small-scale convection (Mutter et al., 1988; King and Anderson, 1995; Ernesto et al., 2002; Bologna et al., 2022). Some authors argue that plume influence was primarily limited to heat transfer with minimal mass contribution (Peate, 1997; Peate et al., 1999; Marques et al., 1999). The main magmatic event of Paraná-Etendeka LIP occurred between 135.0 ± 0.6 and 133.2 ± 0.3 Ma (Gomes and Vasconcelos, 2021, and the references therein), with continued minor magmatism lasting until at least 119 Ma in South America and 113 Ma in Africa, as recorded in dyke swarms (Will et al., 2016; Hartmann et al., 2019).

The Paraná LIP constitutes the South American part of the PEL. These rocks usually are referred to as the Serra Geral Group (Rossetti et al., 2018). The Serra Geral Group can be divided into two sub-provinces: the low-Ti sub-province, mainly in the south, and the high-Ti, mostly distributed from the center to the north (Rossetti et al., 2018). Further classification identifies at least seven formations within The Serra Geral Group: Paranapanema, Pitanga, Ribeira, Esmeralda, Palmas, Urubici, and Gramado (Rossetti et al., 2018). In southern Brazil

and Uruguay, the low-Ti formations predominate, including Gramado (characterized by pahoehoe fields of basalts and basaltic andesites, occur above the Botucatu Formation sandstones), Palmas (composed of dacites and rhyolites), and the Esmeralda (consisting of basaltic pahoehoe flow field), The High Ti (Ti/Y > 310) Urubicy formation is also present in this region (Rossetti et al., 2018).

Breakup of West Gondwana was marked by magmatic activity along the rifted margin of the South Atlantic Austral Segment, forming a volcanic passive margin characterized by the presence of Seaward Dipping Reflectors (SDRs; Stica et al., 2014; Geoffroy et al., 2015; Chauvet et al., 2021; Serratt et al., 2022; Lovecchio et al., 2024). The West Gondwana breakup began near the latitude of the Falkland/Malvinas Islands and moved northward in a zipper style (Rabinowitz and LaBrecque, 1979; Moulin et al., 2010; Collier et al., 2017; Hall et al., 2018; Chauvet et al., 2021; Serratt et al., 2022; Lovecchio et al., 2024). The rifting process likely started during Berriasian–Valanginian (145–132.6 Ma.; Lovecchio et al., 2024). In the area of this study, Pelotas and Punta del Este basins, SDR was formed between 131 and 113 Ma (Chauvet et al., 2021), making these features at least 2 million years younger than the main Paraná LIP event in the region. However, the elder ages are from magnetostratigraphy and could be meaningless in the region (Serratt et al., 2022). This volcanic passive margin extends over the entire Austral Segment of the South Atlantic Ocean and exhibits characteristic architecture dominated by SDRs (Gladczenko et al., 1997; Franke et al., 2007; Stica et al., 2014; Geoffroy et al., 2015; Gordon and Mohriak, 2015; Harkin et al., 2020; Chauvet et al., 2021; Serratt et al., 2022; Lovecchio et al., 2024).

SDRs are seismic facies characterized by sigmoidal wedges that prograde oceanward. Mutter et al. (1982) formalized the concept of a volcanic extrusion associated with the early stages of oceanic crust development by defining five criteria: (1) the reflectors consistently dip seaward; (2) individual reflectors have an arcuate shape formed by a gentle upward convexity; (3) both down-section and down-dip progression show increasing dip angle; (4) these characteristics combine to create overall wedge-shaped geometry with reflectors diverging seaward; and (5) the wedge lack clear basal termination and evidence of a bottom-set structure in the reflectors. Analysis of SDR composition from Ocean Drilling Program (ODP) drilling reveals that volcanic material predominates, though thin layers of sedimentary rocks are also present (e.g., Larsen et al., 1994; Philipp et al., 2001). Inner SDR outcrops have been identified in West Greenland (Geoffroy et al., 1998), where Agranier et al. (2019) identified four distinct units corresponding to magmatic activity around 61–54 Ma. The first unit records a partial

melting from a plume-like source deeper than 75 km and formed in a lacustrine environment, evidenced by hyaloclastites and pillow lavas. Units two and three show progressively shallower lithospheric melting with mixed contribution from the Iceland hotspot and the local crust material. The fourth unit again reflects a deeper source. In contrast, units two to four were formed in subaerial environments, hosting pahoehoe structures and lacking pillow lavas. These volcanic rocks are intercalated with thin tuff horizons (less than 50 cm), basaltic pebble conglomerates (less than 10 m), and occasionally claystones (less than 1 m). However, the overall SDR package remains predominantly volcanic in composition.

SDRs in the study area exhibit diverse compositional characteristics, including basalts, andesites, and trachyandesites (Bueno et al., 2007). The thickness of the SDR package increases as it extends northward in the Pelotas Basin, reaching up to 17 km (Gordon and Mohriak, 2015; Gordon et al., 2017; Harkin et al., 2020). Researchers have interpreted volcanic rocks in the region as part of pre-syn- and late-rift, categorizing them within the Imbituba and Curumin formations of the Pelotas Basin (Dias et al., 1994; Bueno et al., 2007; Stica et al., 2014; Gordon and Mohriak, 2015; Serratt et al., 2022). Historically, the SDRs are classified as part of the Pelotas Basin (Bueno et al., 2007; Stica et al., 2014; Gordon and Mohriak, 2015; Serratt et al., 2022) as they infill depressions created by half-grabens structures. These authors follow the definition of the basin of Ingersoll (2011), which considers any depression-filling accumulation of volcanic or sedimentary material as constituting a sedimentary basin. Previous geochemical analysis of Pelotas Basin basalts indicates a mixed source involving subcontinental lithospheric mantle and Normal Mid-Ocean Ridge Basalts sources (N-MORB; Lobo et al., 2006). This study suggests that magmatism originated from small-scale convection cells, arguing that the heterogeneity in the samples indicates a lack of a large-scale plume, which would produce a more homogeneous composition (Lobo et al., 2006). In the northern region of the study area, particularly around the Torres Arch (situated between the Porto Alegre Fault Zone and Rio Grande Fault Zone; Fig. 3-1), Harkin et al. (2020) identified that the most distal SDR regions display a density inconsistent with purely basalt composition, implying the presence of volcanoclastic or sedimentary rocks. Similarly, Serratt et al. (2022) reported some peperites in well 2-BPS-6A-BP (Fig. 3-1), further supporting the presence of sedimentary components within the predominantly volcanic SDR package.

The South Atlantic conjugate margins display significant asymmetry in their crustal architecture, particularly in the SDRs volume and distribution, a common feature of volcanic passive margins (Becker et al., 2014; Reuber et al., 2019; Chauvet et al., 2021; Abdelmalak et

al., 2025). This SDR sequence challenges the identification of the precise Continental-Ocean Boundary (COB), especially in areas influenced by intense magmatism, such as the Pelotas and Punta del Este basins. Discrepancies of over 100 km in COB interpretations have been noted for the South Atlantic (e.g., Rabinowitz and LaBrecque, 1979; versus Cainelli and Mohriak, 1999), leading to the proposal of a continent-ocean transition zone (COTZ; Eagles et al., 2015). Additionally, seismic and potential field data indicate the presence of hyperextended continental crust beneath these margins, extending up to 450 km in some areas. This hyperextension plays a crucial role in shaping the tectonic framework of the region (Teixeira et al., 2025a).

Even after the SDR magmatism ceased, the region continued to experience magmatic activity. This magmatic activity led to the formation of the Rio Grande Rise and Walvis Ridge, both genetically linked (Hoyer et al., 2022). Its genesis is often pointed to be related to the Tristan da Cunha plume (Homrighausen et al., 2019; Hoyer et al., 2022), the same plume related to Paraná-Etendeka LIP (Gibson et al., 2006; Zhou et al., 2020; Beccaluva et al., 2020). On the other hand, some authors point to alternative formation mechanisms. These include: (1) a volcanic edifice or plateau rooted in the mantle; (2) an intraplate shear zone affecting continental and oceanic crust; (3) an oceanic area of igneous over-productivity caused by a hotspot or a thermal anomaly in the mantle; (5) a palaeo-spreading center in the Cretaceous Atlantic Ocean; an area of excessive volcanic activity resulting from mantle differentiation due to adiabatic decompression; (6) an isolated remnant of continental crust left outboard of the Brazilian continental margin during the drifting process (Mohriak et al., 2010, and the references within).

3.3 Samples and methods

An integrated geophysical and geochemical study was conducted across six wells. In five wells (Gaviotin-1; Lobo-1; 1-RSS-3-RS; 2-BPS-6A-BP; 1-SCS-3B-SC – Fig. 3-1), we analyzed samples from beneath the drift section of the Pelotas and Punta del Este basins, and one well was from the Rio Grande Rise (U516 – Fig. 3-1). One of the analyzed samples is a sedimentary rock that comes from a depth of 3629 m in the Gaviotin-1 well in the Punta del Este Basin. All the others samples from the margin are volcanic rocks from Lobo-1 (depths: 2622, 2627, and 2629 m; Fig. 3-1, Fig. 3-2), 1-RSS-3-RS (depths: 3555.1, 3555.8, 3904.9, and 3905.8 m; Fig. 3-1, Fig. 3-2), 2-BPS-6A-BP (depths: 5075.45, 5350.9, 5378.5, 5378.8,

5379.25, 6154.6, and 6155 m; Fig. 1, Fig. 2), and 1-SCS-3B-SC (depths: 4732, 4732.8 m; Fig. 3-1, Fig. 3-2). The Rio Grande Rise samples are obtained from the U516 well core at 1260.60 and 1269.60 m (Fig. 3-1). The lithological profiles for all Pelotas and Punta del Este basins wells are provided in Supplementary material 1; while all data from well U516 is available by DSDP legacy data (leg 72, site 516; Barker et al., 1983).

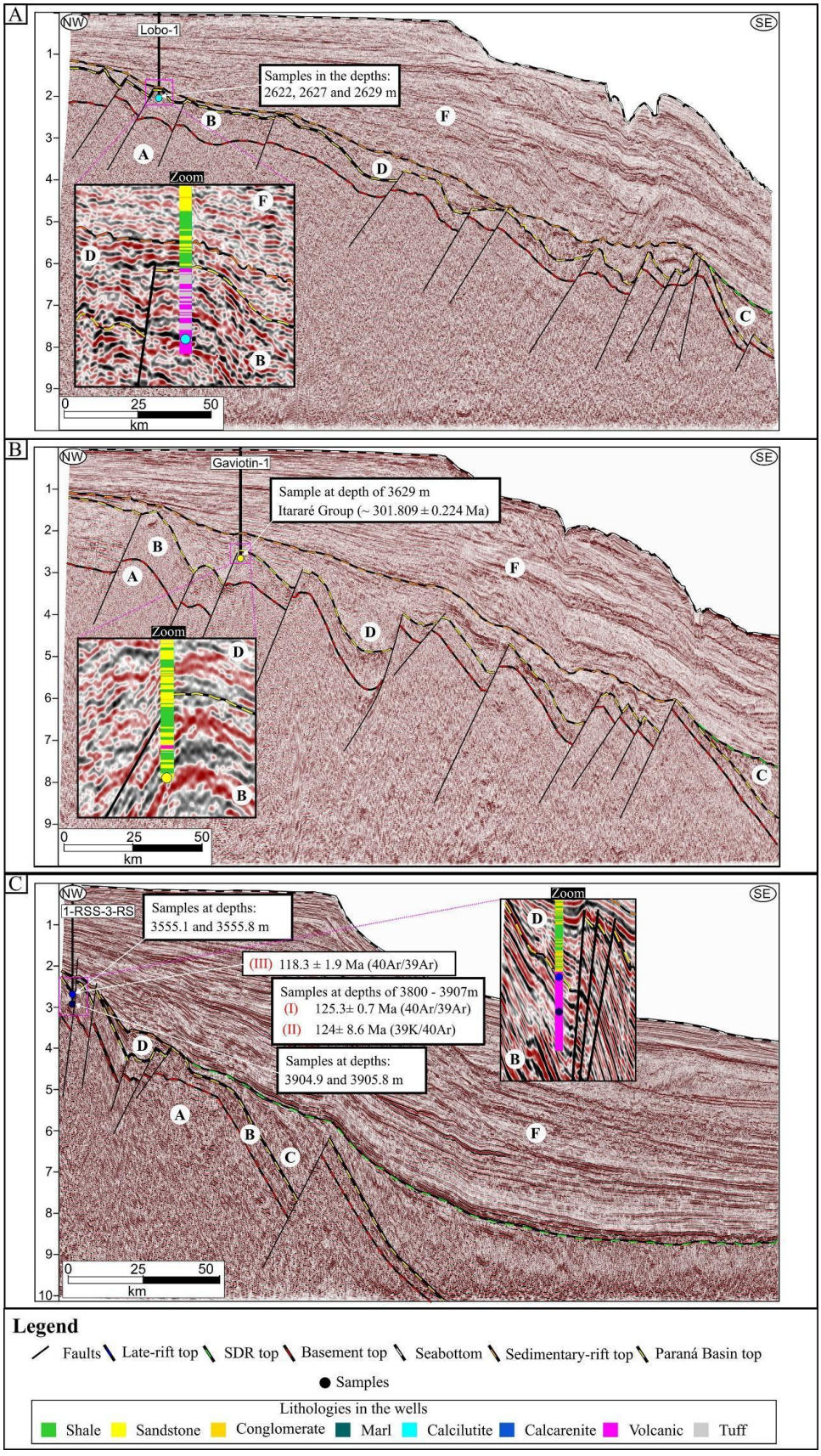

Figure 3-2. Seismic lines from the Pelotas and Punta del Este basins, their respective positions are indicated in Fig. 1. The colorful circles are the position from the samples, and white circles with letters are the interpreted tectonic units (A) Neoproterozoic Basement, (B) Paraná Basin,

(C) SDR, (D) Late-Rift, (E) Late-Rift, (F) Drift. (I) data from Misuzaki and Saracchine, 1990b (II) data from Lobo, 2000 (III) data from Lobo (2007). A) Seismic line near the well Lobo-1 shows samples analyzed from the bottom of the well classified as Paraná LIP (Serra Geral Group in Paraná Basin stratigraphy (B). Observe the SDRs (C) in the distal section, they are stratigraphically above these traps; (B) Seismic line near the Gaviotin-1 well also presents analyzed samples classified as Paraná-Basin (Itararé Group), with distinguishable SDRs in the distal section above the Paraná Basin. C) Seismic line near the 1-RSS-3-RS well, in a region called Mostardas Low (Cassel et al., 2022). The samples from the bottom of the well were classified as Paraná-Basin (Serra Geral Group, also known as Paraná LIP), despite the previous classification of these samples being Imbituba Formation (see the discussion).

3.3.1 Seismic analysis

The tectonic architecture interpretation of this region was based on six dip-direction seismic lines closest to the wells (uninterpreted seismic lines are available in Supplementary material 2). We conducted the interpretation using Paleoscan™ 2023 software, relying upon previous regional interpretations (Stica et al., 2014; Gordon and Mohriak, 2015; Conti et al., 2017; Harkin et al., 2020; Chauvet et al., 2021; Serratt et al., 2022; Teixeira et al., 2025a). Well data were integrated with seismic data to enhance seismic interpretation using Petrel 2023™. Our primary goal focused on interpreting the basalt samples by integrating the sonic and density logs (DT and RHOB) from the wells to generate synthetic seismograms, allowing for precise correlation between well data and seismic reflectors (detailed in Supplementary material 3). Following this well-seismic tie, we constrained several geological units along these seismic lines based on their seismic facies and groups of seismic facies.

3.3.2 Petrography XRD supported

Thin sections were prepared from 13 representative margin samples and analyzed using conventional petrography. The samples included one sedimentary rock and 12 basalt samples. We used X-ray diffraction (XRD) to support mineral identification for the volcanic rocks. For XRD analysis, samples were pulverized using an agate mortar and pestle, and the clay fraction was separated by double centrifugation. First, the samples were centrifuged in distilled water at 750 rpm for 7 min, followed by a second centrifugation at 3000 rpm for 30 min, using the supernatants from the first stage. Precipitates from the second centrifugation were used to prepare oriented clay, which was air-dried before analysis. Glycolated samples were prepared by exposing them to an ethylene glycol atmosphere for 12 h. The samples were dehydrated by heating to 490 °C for 4 h before analysis. X-ray diffraction was done using a Rigaku Ultima IV

diffractometer at Brasilia University, with 35 kV and 15 mA parameters. Whole samples were scanned from 2 to 60° and clay fractions from 2 to 40° (2θ), with a 0.05° step and 5°/min speed. The diffractograms were analyzed using MDI/Jade® 9 software, with the full results provided in Supplementary material 4.

3.3.3 Whole-rock Geochemistry

Whole-rock geochemical analyses were performed on all volcanic samples. Fresh samples were selected, avoiding the sedimentary inputs from the peperites or the amygdales. We crushed the samples to <0.5 cm and ground them into powders (<200 mesh) using an agate mortar and pestle. After fusing the samples with lithium metaborate/tetraborate, major- and trace-element content were determined by dissolving the resulting molten bead in a weak nitric acid solution. Major elements were determined by ICP-OES and trace elements by ICP-MS at Actlabs in Ontario, Canada, and Geosol in Minas Gerais, Brazil. Blank achieved was <0.01 % for major elements and < 0.1 ppm in REE. Additionally, we analyzed two samples from Rio Grande Rise, from well U516 at depths of 1263 and 1268 m. ALS Labs, United Kingdom, carried out these analyses. Data and standards for major and minor elements are available in Supplementary material 5.

The percentages of major element oxides were recalculated to 100 wt% on an anhydrous basis. We applied diagrams (LeBas et al., 1986; Pearce and Wyman, 1996; Pearce, 2008) based on mobile and immobile elements to determine the rock types and tectonic setting. We also plotted our data with legacy data from Paraná Etendeka LIP (Gibson et al., 2006; Zhou et al., 2020; Mansur et al., 2021) and South Atlantic OIB (Ocean Island Basalts; Walvis Ridge - Homrighausen et al., 2019; Rio Grande - Rise Hoyer et al., 2022) for classification and tectonic setting comparison. Normalized spidergrams were made using NMORB (Normal Mid Ocean Ridge Basalts) values (Sun and McDonough, 1989). REE values were also normalized by chondrite using Boynton (1984) values. Europium and cerium anomalies (Eu/Eu* and Ce/Ce*, respectively) were determined with neighboring elements (La – Pr and Sm – Gd) using the methodology of Taylor and McLennan (1985).

3.3.4 U-Pb zircon dating

U-Pb geochronology was carried out on four basalt samples (those with zircon fertility). Isotope U-Pb data were obtained at the Institute of Geology and Geophysics of the Chinese Academy of Science (IGGCAS - Beijing) and the University of Ouro Preto (UFOP) in Brazil. Sample preparation was conducted at Vale do Rio dos Sinos University (UNISINOS). The process included crushing the samples with a jaw crusher and disc mill, followed by heavy mineral concentration using dense liquids (bromoform and diiodomethane). Zircon grains were hand-picked under a binocular microscope and polished in 1-in. round epoxy mounts. Before analysis, the samples were characterized using plane-polarized light and backscattered electron (BSE) imaging.

At the University of Ouro Preto, we analyzed one sample (Gaviotin-1) using a Laser Ablation system (Photon-machines Excimer Laser λ = 193 nm) coupled with a sector field inductively coupled plasma mass spectrometer (ThermoFisher Element II). U-Pb zircon data were obtained using peak jumping mode with 20 s background measurement, followed by 20 s sample ablation with a 20 μm spot size, 15 % laser energy, 10 Hz shot frequency, and 15 s shutter delay. Laser spots were placed on zircon rims to certify that the last tectonic event was analyzed. The common Pb correction was based on 204Pb composition, following Stacey and Kramers (1975). The decay constant of Jaffey et al. (1971) was applied, and uncertainty propagation was followed by Horstwood et al. (2016). Data reduction was made using the Silva et al. (2023) Saturn software. We used the reference zircon (GJ-1) for laser-induced elemental fractionation and instrumental mass discrimination corrections. To ensure precision and accuracy, we analyzed reference zircons: Plešovice (337 ± 3.8 Ma; Sláma et al., 2008) and BB-1 (562.58 ± 0.26 Ma; Santos et al., 2017). The results were concordant with experimental errors: 557.7 ± 3.9 Ma (2σ, n = 18) for BB-1 and 338.4 ± 2.3 Ma (2σ, n = 23) for Plešovice.

At IGGCAS - Beijing, three samples were analyzed: 1) Well 1-RSS-3-RS at depth 3904.9 m; 2) Well 2-BPS-6A-BP at depth 5378.8 m; and 3) Well 2-BPS-6A-BP at depth 5379.25 m. The analyses used a sector field SF-ICP-MS (Element XR, ThermoFisher Scientific) and a 193 nm ArF excimer laser (Geolas HD, Coherent). The U-Pb laser methodology is described by Wu et al. (2019). Data were reduced using an in-house Excel spreadsheet (Chemale Jr. et al., 2012). To ensure precision and accuracy, we analyzed reference zircons: SA01 (537.85 ± 2.71 Ma; Huang et al., 2020) and 91500 zircon (1065.4 ± 0.6 Ma; Wiedenbeck et al., 1995 and Wiedenbeck et al., 2004). The results were concordant with experimental errors: 535.2 ± 1.3 Ma (2σ, n = 35) for SA01 and 1063.0 ± 2.3 Ma (2σ, n = 32)

for 91,500. Following Puetz et al. (2021), data was organized, where only the best ages of groups 1 to 5 were plotted for KDE diagrams (data in Supplementary Material 6). The KDE and Concordia diagrams were plotted using IsoplotR software (Vermeesch, 2018). All data are found in Supplementary Material 6.

3.3.5 Sr and Nd isotopes

Eight basalt samples were selected for Sr and Nd isotope analysis based on their relatively low degree of modification by late-stage hydrothermal processes and limited interaction with sedimentary rocks during extrusion. Two volcanic rock samples were collected from the Rio Grande Rise at 1263 m and 1268 m depths. From the well 1-RSS-3-RS, samples were analyzed from depths of 3555.10 m and 3905.20 m. From the well 2-BPS-6 A-BP, isotope compositions were determined for samples from 6154.6 m and 6155 m depths. Additional samples were analyzed from the well 1-SCS-3B-SC (Santa Catarina State) at a 4732 m depth and from Lobo-1 (Uruguay) at a 2626 m depth.

The samples were initially crushed, milled, and sieved. Sr and Nd isotope analyses were conducted at the Geochronology Center of the University of São Paulo (CPGEO-USP). Chemical digestion was performed using HF, HNO_3, and HCl in Savillex® vials. Sr and Nd were separated chromatographically in two steps: first, Sr and rare earth elements (REE) were separated from the bulk sample using AG50W-X8 resin; second, Nd was separated using a lanthanide-specific (LN) resin. Isotope analyses were carried out using a Thermo-Ionization Mass Spectrometer (TIMS) – Triton. The 87Sr/86Sr isotope ratios were normalized to 86Sr/88Sr = 0.1194, and the 143Nd/144Nd ratios were normalized to 146Nd/144Nd = 0.7219 (DePaolo, 1981). Analytical blank concentrations for Sr and Nd were below 197 pg/g and 10 pg/g, respectively.

The average 87Sr/86Sr value for the NBS-987 standard, measured between February 2024 and January 2025, was 0.710266 ± 0.000007. The 143Nd/144Nd ratio for the JNDi standard, measured from March 2024 to February 2025, was 0.5210096 ± 0.000004. Sr and Nd isotope data for all analyzed samples are presented in Supplementary Material 7.

3.4 Results

The volcanic rocks are more homogeneous than previously reported (Bueno et al., 2007). All of these volcanic rocks are basalts or peperites with basaltic composition. We observe strong hydrothermal alteration in all these rocks. Based on the geochemical composition, the source appears to be intermediate between EMORB (Enriched Mid Ocean Ridge Basalts) and OIB (Ocean Island Basalts). The sedimentary rock from Gaviotin 1- is from the Itararé Group (Paraná Basin), as observed by its detrital zircons ages. However, we could not constrain the age of the basalts by their zircon content because their age is the same as the host rock (assimilated during magmatism – See the discussion) or they contain detrital zircons (related to the peperites). The isotopic signature shows a negative εNd value signature for most samples and an 87Sr/86Sr compatible with either a continental crust contamination or EMI and EMII mantle reservoirs.

3.4.1 Tectonic environment

We identified six distinct tectonic contexts from seismic data of the margin, classified based on seismic facies and well data (Fig. 3-2, Fig. 3-3; A-Basement, B-Paraná-Basin, C-SDR, D-Sedimentary Rift, E-Late-Rift, F-Drift). (A) Neoproterozoic Basement: The Neoproterozoic basement represents the Dom Feliciano Belt and, in seismic data, corresponds to the most chaotic seismic facies beneath all other identified geological units. (B) Paraná Basin Section: The Paraná Basin section (including the Paraná Large Igneous Province), representing the pre-rift section, is characterized by continuous reflectors that are intersected by rift faults. (C) SDR Section: We identified SDRs according to the aforementioned definition by Mutter et al. (1982). (D) Sedimentary rift section: Besides the SDRs, we also identified a sedimentary rift, observed as reflectors filling half-grabens, which display a distinct basal reflector indicative of significant lithological changes. The upper limit of this unit is the base of the drift, and it is always an irregular surface at Punta del Este Basin, which we interpreted as an erosive surface or regional unconformity. As this top surface did not produce a high amplitude reflection, it corroborates the interpretation that it and the drift section have approximately the same density, corresponding to sedimentary rocks. This section was also recovered in the well 1-RSS-3-RS (Cassino Formation – Bueno et al., 2007 – Fig.3- 2C), Gaviotin-1, and Lobo-1 (Fig. 3-2A-B). (E) Late-Rift Section: We interpreted this based on the post-rift basalts interpretations from Serratt et al. (2022), which consist of volcanic rocks (including peperites) observed in the well

2-BPS-6 A-BP and visualized in one seismic line above the SDRs (Fig. 3-3A). This section corresponds to a “sag geometry” as described by Stica et al. (2014) or unit “H” as described by Gordon and Mohriak (2015). (F) Drift Section: This section is characterized by a group of seismic facies exhibiting the most continuous reflectors of all units, situated just below the sea bottom, that is, the first reflector (Fig. 3-2, Fig. 3-3). The base of the Drift stage is marked by high-amplitude reflections when they occur above SDRs, marking a drastic change in lithology. The interpretation of this unit was calibrated using well data tied to the seismic lines.

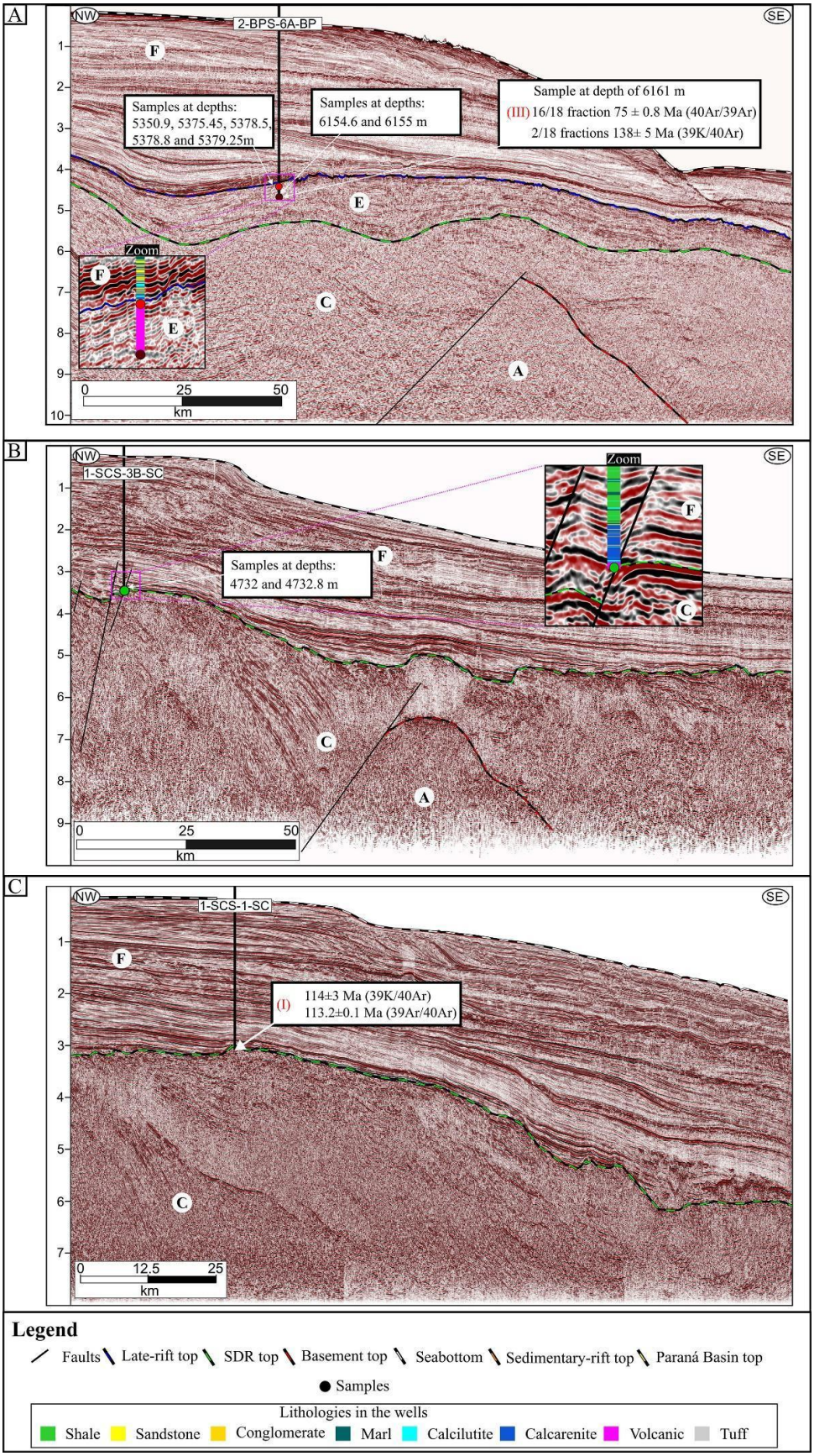

Figure 3-3. Seismic lines from the Pelotas and Santos basins, their respective positions are indicated in Fig. 1. The colorful circles are the position from the samples, and white circles with

letters are the interpreted tectonic units (A) Neoproterozoic Basement, (B) Paraná Basin, (C) SDR,(D) Late-Rift, (E) Late-Rift, (F) Drift. (I) data from Misuzaki and Saracchine, 1990b (II) data from Lobo, 2000 (III) data from Lobo, 2007. A) Seismic line near the well 2-BPS-6 A-BP. These rocks were classified as Curumin Formation (Pelotas Basin; Bueno et al., 2007); usually, these rocks are classified as SDR (Stica et al., 2014; Harkin et al., 2020; Chauvet et al., 2021). However, these rocks above the SDR do not fit the five SDR criteria (Mutter et al., 1982), so we classified them as a late-rift section. B) Seismic line near the well 1-SCS-3B-SC. The samples from the bottom of the well are the Curumin Formation (Bueno et al., 2007), and these rocks were observed in seismic as an SDR in Santos Basin. C) Seismic line near the well 1-SCS-1-SC. The bottom of this well-recovered SDR with age is constrained by Misuzaki (Misuzaki and Saracchine, 1990a, apud Gordon and Mohriak, 2015).

3.4.2 Petrographic interpretation

Here, we present and describe the samples thin sections in groups based on their tectonic context from Section 4.1. Additionally, the observed mineral assemblages and textures are summarized in Table 1. All volcanic samples have some degree of alteration that can cause atypical diffractometric measurements due to mineral replacement and intermediate phases. Some primary minerals, such as olivine, are absent, as the original olivine has been entirely replaced by iddingsite or serpentine. Therefore, the XRD results (Supplementary Material 4) do not reflect the original mineral assemblage but rather the current altered state.

Table 3-1. Summary of the observed minerals, textures, and structures.

Empty Cell	**Group**	**Rock**	**Primary mineralogy**	**Secondary mineralogy**	**Structures**	**Textures**
Pre rift	Gaviotin-1	Sandstone	Quartz			
	Lobo-1	Basalt	Plagioclase, Augite, K-feldspar	Ceruenite, Hematite Calcite, Basaluminite, Scolecite	Amygdales, Fractures	Porphyritic
	Lower 1-RSS-3-RS	Basalt	Plagioclase, Augite	Ceruenite, Laumonite, Heulandite, Saponite, Stilpnomelane, Hematite		Porphyritic
	Upper 1-RSS-3-RS	Basalt	Plagioclase, Augite, Olivine (replaced), Apatite	Ceruenite, Analcime, Muscovite, Biotite, Hematite	Amygdales	Porphyritic
Rift	1-SCS-3B-SC	Basalt	Plagioclase, olivine (replaced)	Iddingsite, Ilite, Calcite, Kaolinite, Dolomite, Hematite	Amygdales	Porphyritic
Late rift	Lower 2-BPS-6A-BP	Basalt	Plagioclase, Augite, Olivine (replaced)	Clinochlore, Hematite	Amygdales	Porphyritic
	Upper 2-BPS-6A-BP	Peperite	Plagioclase, Augite, Olivine (replaced), Quartz	Ceruenite, Clinochlore, Clinochloriside, Hematite		Porphyritic

Pre-Rift (Paraná Basin)

The rocks interpreted in the seismic section as pre-rift are from the wells Gaviotin-1 (depth: 3629 m), Lobo-1 (depths: 2622, 2627, and 2629 m) in Punta del Este Basin, and Lower

1-RSS-3-RS (depths from 3904 to 3905 m), and Upper 1-RSS-3-RS (depth: 3555 m) in Pelotas Basin.

The analyzed sample from the Gaviotin-1 well at 3629 m consists of medium to coarse-grained sandstone composed primarily of siliciclastic grains. These grains range from medium to coarse sand-sized and are predominantly monocrystalline quartz. The grains exhibit moderate sphericity, with some displaying elongation, varying from subrounded to angular shapes. Diagenetic features include point, planar, and slightly sutured grain contacts, with no visible porosity observed in the thin section.

The analyzed sample from the Lobo-1 well consists of basalts with a porphyritic texture. At a depth of 2622 m, we found euhedral augite phenocrysts up to 2 mm undergoing alteration process (Fig. 4B). These minerals show some chemical alteration but much less than those in the sample from 2627 m. The groundmass hosts fine-grained acicular plagioclase (albite), pyroxene (augite), feldspar (microcline; detected in the XRD only), hematite, and secondary minerals including corrensite and calcite. The interpretation of this thin section and the others was supported by XRD analysis (Supplementary Material 4). At a depth of 2627 m, amygdales filled with corrensite, scolecite, and basaluminite up to 1 mm were identified. The rock is fractured, and the secondary porosity is filled with minerals from late fluid percolation; these fractures cut through the amygdales (Fig. 4A). The groundmass hosts fine-grained acicular plagioclase (albite), pyroxene (augite), feldspar (microcline; detected in the XRD only), opaque minerals (hematite), and secondary minerals (corrensite). At a depth of 2629 m, the rocks consist of basalts with a porphyritic texture. However, observing phenocryst borders is challenging due to the high degree of mineral substitution. Some of these were originally plagioclase crystals. Nonetheless, some parts of the phenocrysts remain unaltered and are identified as pyroxenes (Fig. 4C). The matrix hosts fine-grained plagioclase (albite), pyroxene (augite), opaque minerals (hematite), and secondary minerals (corrensite, basaluminite, scolecite). The mineral assemblage, along with the observed processes of mineral replacement and the late-filled fractures, provides evidence of a hydrothermal process.

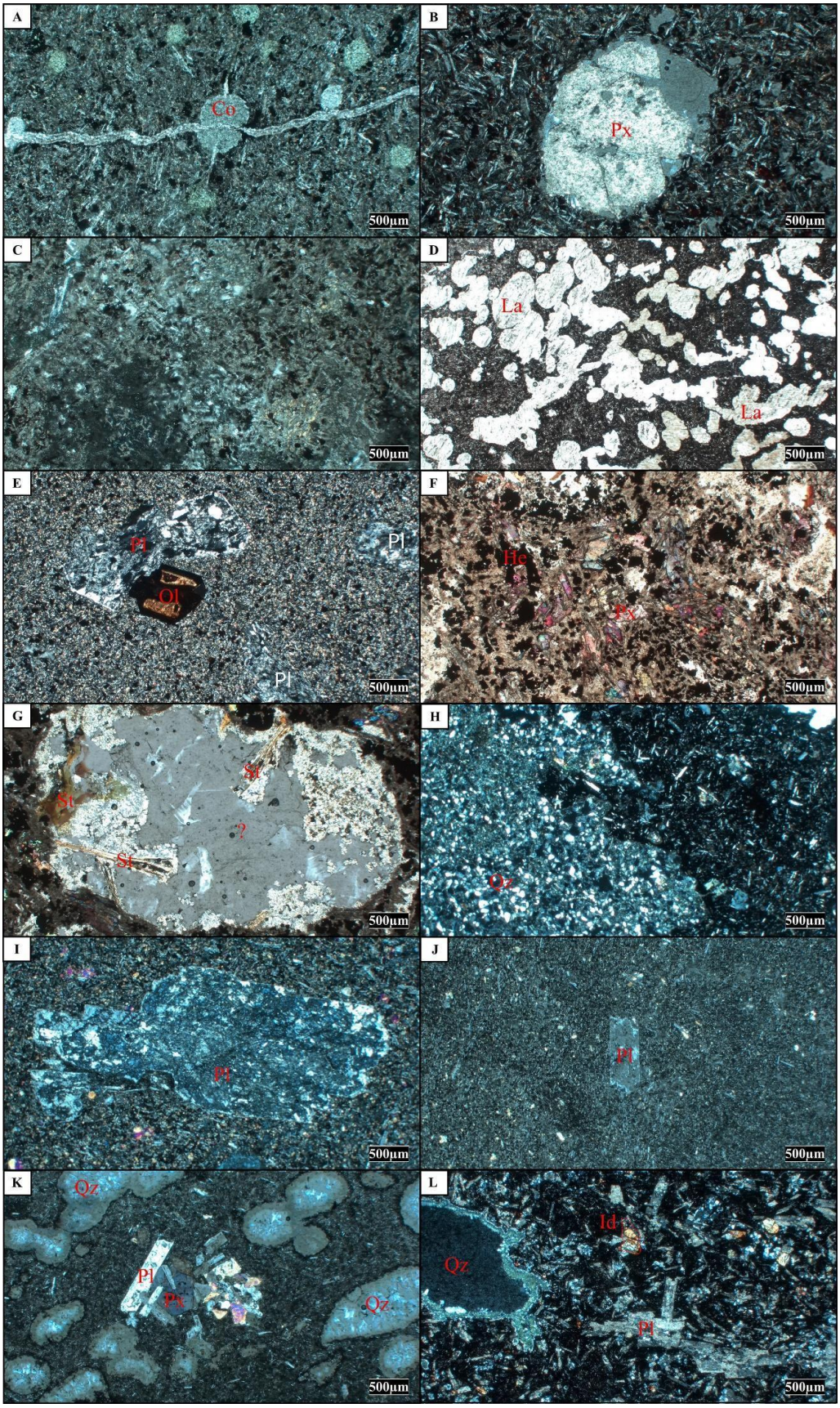

Figure 3-4. Petrographic photos from: A) Well Lobo-1, the sample from a depth of 2627 m, showing a microscale fracture filled by minerals from late fluid percolation, this fracture cuts a rounded corrensite (Co) mass surrounded by a groundmass of acicular plagioclase, secondary,

and opaque minerals; B) Well Lobo-1, sample from a depth of 2622 m, the image is centralized in an augite (Px) phenocryst undergoing an intense alteration process, surrounded by a groundmass of acicular plagioclase, secondary, and opaque minerals; C) Well Lobo-1, sample from a depth of 2629 m showing the extreme mineral alteration of this rock; D) Well 1-RSS-3-RS, sample from a depth of 3555 m, showing amygdaloidal basalt filled with laumontite (La); E) Well 1-RSS-3-RS, sample from a depth of 3555 m, showing phenocrysts of olivine (Ol) replaced by hematite and unidentified mineral, with anorthite (Pl) phenocrysts surrounded by a very thin groundmass; F) Well 1-RSS-3-RS, sample from a depth of 3905 m showing altered augite (Px) with not clear borders, large hematite (He) mass, and a few small amygdales surrounded by an strongly altered groundmass; G) Well 1-RSS-3-RS, sample from a depth of 3904 m, the image is centralized on an amygdale filled with an unidentified mineral hosting stilpnomelane (St) growing inside it; H) Well 2-BPS-6 A-BP, sample from a depth of 5378 m, showing the contact of basalt with the sedimentary quartz (Qz) in a peperite; I) Well 2-BPS-6 A-BP, sample from a depth of 5378 m, similar to image 4H but far from the sedimentary/basalt contact zone, showing a porphiritic texture with a 5 mm plagioclase (Pl) at the center of the image; J) Well 2-BPS-6 A-BP, sample from a depth of 6154 m, the image is centralized on a plagioclase (Pl) phenocryst with 1 mm surrounded by a fine matrix; K) Well 2-BPS-6 A-BP, sample from a depth of 6155 m the image is centralized on a phenocryst cluster, where the plagioclase (Pl) limits the pyroxene growth (Px), The sample also contains amygdales filled with quartz (Qz); L) Well 1-SCS-3B-SC from at a depth at 4732 m, showing plagioclase (Pl) and iddingsite (Id) phenocrysts up to 1 mm, surrounded by a groundmass with fine-grained plagioclase, secondary minerals, and opaque minerals, with a few amygdales filled mostly with quartz (Qz).

The analyzed sample from the 1-RSS-3-RS well at a depth of 3555 m is an amygdaloidal basalt with a very fine texture near the amygdales (Fig. 3-4D). In regions distant from the amygdales, the rock exhibits a porphyritic texture with altered plagioclase (anorthite) and pyroxene (augite) phenocrysts that reach up to 3 mm (Fig. 3-4E). The groundmass hosts fine-grained plagioclase (anorthite), pyroxene (augite), opaque minerals (hematite), and secondary minerals (corrensite, laumontite, heulandite, saponite). Additionally, samples obtained from the same well at 3904 m and 3905 m are basalts with few amygdales (Fig. 3-4G). These samples display a porphyritic texture with highly altered pyroxene (augite) phenocrysts without clear borders due to extensive alteration (Fig. 3-4F). The groundmass hosts fine-grained feldspar (orthoclase), pyroxene (augite), acicular apatites, opaque minerals (hematite), and secondary minerals (corrensite, analcime, muscovite, and stilpnomelane).

Rift

The samples interpreted in seismic as rift rocks are from the 1-SCS-3B-SC well at a depth of 4732 m. It is a basalt with amygdales filled mostly with quartz, calcite, and dolomite (Fig. 3-4L). This rock shows a porphyritic texture with plagioclase (anorthite) and iddingsite

phenocrysts measuring up to 1 mm (Fig. 4L). The groundmass hosts fine-grained plagioclase (anorthite), secondary minerals (illite, calcite, kaolinite, and dolomite), and opaque minerals (hematite).

Late-rift

The samples interpreted in seismic as late-rift rocks are from the 2-BPS-6A-BP well. At a depth of 5378 m, these samples are peperites with a very fine texture near the sedimentary rock interface (Fig. 4H). However, a few centimeters from the sedimentary contact, the texture changes to porphyritic with highly altered plagioclase (anorthite) phenocrysts measuring up to 5 mm (Fig. 4I). The matrix hosts fine-grained plagioclase (anorthite), pyroxene (augite), opaque minerals (hematite), and secondary minerals (corrensite, clinochrysotile). The sediments are mostly quartz sands with some clay minerals.

The analyzed sample from the lower 2-BPS-6A-BP well at a depth of 6154 m is a basalt. The rock shows a porphyritic texture with plagioclase (anorthite) phenocrysts up to 1 mm (Fig. 4J). The groundmass hosts fine-grained plagioclase (anorthite) and pyroxene (augite), opaque minerals (hematite), and secondary minerals (clinochlore). At a depth of 6155 m, the sample is a basalt with few amygdales (Fig. 4K). The rock exhibits a porphyritic texture with plagioclase (anorthite) and pyroxene (augite) phenocrysts measuring up to 1.5 mm. The matrix hosts fine-grained plagioclase (anorthite) and pyroxene (augite). Secondary and opaque minerals were not identified. The presence of amygdales is limited, suggesting a relatively homogenous alteration process that affected the overall mineral assemblage. The consistent texture and mineralogy across these depths indicate a uniform volcanic origin, likely influenced by similar magmatic processes during its formation.

3.4.3 Geochemical data

This section presents a synthesis of the geochemical results (Fig. 3-5). The full results can be found in Supplementary Material 5. The samples are divided as follows: 1) Lobo-1 (depths: 2622, 2627, and 2629 m); 2) Lower 1-RSS-3-RS (depths: 3904.9 and 3905.8 m); 3) Upper 1-RSS-3-RS (depths: 3555.1 and 3555.8 m); 4) Lower 2-BPS-6 A-BP (depths: 6154.6, and 6155 m); 5) Upper 2-BPS-6A-BP (depth: 5378.5 m); 6) 1-SCS-3B-SC (depths: 4732 and 4732.8 m); 7) U516 (depths: 1263 and 1268 m). The geochemical analysis of the samples

indicates a distinct REE pattern and a geotectonic classification of basalts that align with Enriched Mid Ocean Ridge Basalts (EMORB) to Ocean Island Basalts (OIB) composition.

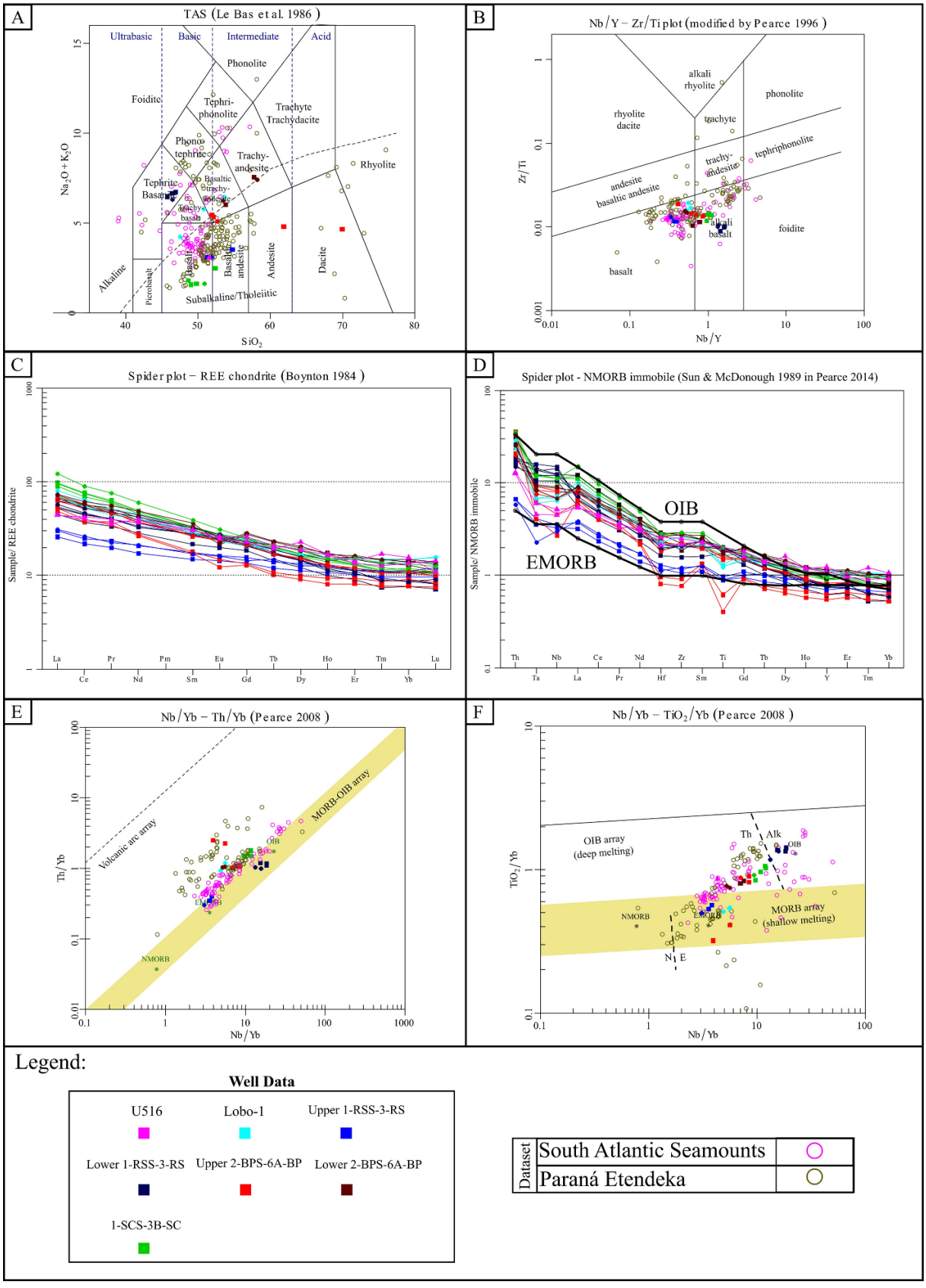

Figure 3-5. Geochemical diagrams: A) Rock classification diagram using mobile elements, total alkalis vs silica (TAS- LeBas et al., 1986); B) Rock classification diagram using immobile elements, Nb/Y vs. Zr/TiO2 (Pearce and Wyman, 1996); C) REE spidergram, data normalized by chondrite (Boynton, 1984); D) Spider plot based on immobile elements normalized by

NMORB (Sun and McDonough, 1989 in Pearce, 2014); OIB and EMORB data from McDonough and Sun (1995); E) Tectonic environment diagram using immobile elements Nb/Yb vs. Th/Yb (Pearce, 2008); F) Tectonic environment diagram using immobile elements Nb/Yb vs. TIO2/Yb (Pearce, 2008). Datasets: (1): Paraná Etendeka LIP; Paraná LIP - Gibson et al., 2006; Mansur et al., 2021; Etendeka LIP -Zhou et al., 2020; (2): South Atlantic seamounts: Walvis Ridge - Homrighausen et al., 2019; Rio Grande – Rise - Hoyer et al., 2022. Samples represented in filled circles are data from Activation Lab, Triangles are from ALS, and squares from Geosol.

Data Reliability

The presence of chemical alteration processes identified in the petrographic analysis raises questions about the representativeness of the rock compositions concerning the original magmatism. The loss on ignition (LOI) values, ranging from 1.79 to 19.24 % with an average of 7.08 ± 5.97 %, further indicate potential inconsistencies. When using a rock classification diagram based on mobile elements, such as SiO_2 vs. total alkalis (LeBas et al., 1986; Fig. 3-5A), the basalts from the studied wells exhibit a wide compositional range, from sub-alkaline basalts to trachyandesite. In contrast, when plotted in an immobile elements diagram (Pearce and Wyman, 1996), all samples are classified as basalts (sub-alkaline to alkaline), consistent with petrographic observations. Consequently, we avoid using diagrams based on mobile elements (e.g., Cs, Rb, K, Ba, Sr, Pb). The Ce anomaly varies from 0.04 to 6.67 %, with an average of 3.05 ± 2.46 %, suggesting the reliability of the relative concentrations of immobile elements. Four samples exhibit negative cerium anomalies greater than 5 %, indicating potential trace element alterations due to seawater influences. However, the geochemical fingerprints of these rocks remain sufficiently similar to those of nearby samples to warrant their inclusion in our study, given the challenges associated with accessing these rock samples. Since these rocks are from regions with difficult access, it is important to explore all available data.

Pre-rift magmatism

The composition of pre-rift stage rocks shows a range of compositions from sub-alkaline basalts found in the upper 1-RSS-3-RS and in the well Lobo-1 to alkaline basalts in the lower 1-RSS-3-RS (based on Pearce and Wyman, 1996; Fig. 3-5B). The upper 1-RSS-3-RS and the Lobo-1 well compositions resemble an enriched mid-ocean ridge basalt (EMORB). Nb/Yb vs. TiO_2/Yb plots (Pearce, 2008; Fig. 3-5F) indicate a shallow melting process. In contrast, the

rocks from lower 1-RSS-3-RS exhibit characteristics akin to (OIB) in the same plot, suggesting a deeper melting origin. The REE patterns from these rocks do not exhibit any Eu anomaly (Fig. 3-5C). In a spider plot of immobile elements, these rocks are plotted between EMORB and OIB, with Lobo-1 samples and Lower 1-RSS-3-RS closer to OIB and those from Upper 1-RSS-3-RS nearer to EMORB (Fig. 3-5D). Significant differences between the volcanic layers of 1-RSS-3-RS and the rocks from Lobo-1 emerge when comparing Nb/Yb vs. Th/Yb plots (Fig. 3-5E). This plot (Fig. 3-5E) distinguishes the rocks from the Paraná-Etendeka Large Igneous Province (PEL) and the Walvis Ridge/Rio Grande Rise very well. The samples from Lobo-1 display remarkable similarity to the Paraná-Etendeka LIP, whereas the 1-RSS-3-RS samples align more closely with Walvis Ridge/Rio Grande Rise (data from Walvis Ridge - Homrighausen et al., 2019; Rio Grande Rise - Hoyer et al., 2022; Paraná-Etendeka LIP - Gibson et al., 2006; Mansur et al., 2021; Zhou et al., 2020).

Rift magmatism

The rift stage rocks from well 1-SCS-3B-SC are characterized as alkali basalts (Pearce and Wyman, 1996; Fig. 3-5B) with a source akin to Ocean Island Basalts (OIB) in both Pearce (2008) diagrams (Fig. 3-5E-F). These rocks exhibit enrichment in Th/Yb relative to Nb/Yb, similar to Paraná-Etendeka LIP rocks (Fig. 3-5E). Additionally, the REE patterns do not show an Eu anomaly (Fig. 3-5C), and their composition closely resembles OIB in spider plots (Fig. 3-5D).

Late-rift magmatism

The late-rift stage rocks from well 2-BPS-6 A-BP are characterized as sub-alkaline to alkali basalts (Pearce and Wyman, 1996; Fig. 3-5B). It is important to remember that the Upper 2-BPS-6 A-BP are peperites, which can cause some unusual patterns in spiderplots in some samples (Fig. 3-5D) or produce very heterogeneous results in tectonic plots (Fig. 3-5E-F). Most of these rocks generally exhibit a compositional fingerprint similar to an OIB, and the samples from the rift magmatism (1-SCS-3B-SC - Fig. 3-5 C-F).

Rio Grande rise

The rocks from Rio Grande Rise are sub-alkaline basalts (Fig. 3-5B), with REE and spider plot patterns similar to those of the margin (Fig. 3-5C-D). These rocks have a composition that resembles an EMORB composition (Fig. 3-5E-F).

U-Pb analysis in zircons

U-Pb studies were conducted on four samples. One sedimentary sample corresponds to the Gaviotion-1 well; three are from the basalts of 1-RSS-3-RS and 2-BPS-6A-BP wells. In the sample from well Gaviotin-1 at 3629 m, which consists of sedimentary rocks from the Pre-rift, 110 zircon grains were analyzed. Zircons dominantly present magmatic growth zoning, and a few grains show high-grade metamorphic rims and recrystallization textures. Zircons are predominantly prismatic and secondarily rounded with 150 to 500 μm size. The sample shows a mean U-Pb peak related to Neoproterozoic (550–650 Ma) (Fig. 3-6A), with a secondary zircon population with Tonian, Stenian, and Rhyacian ages.

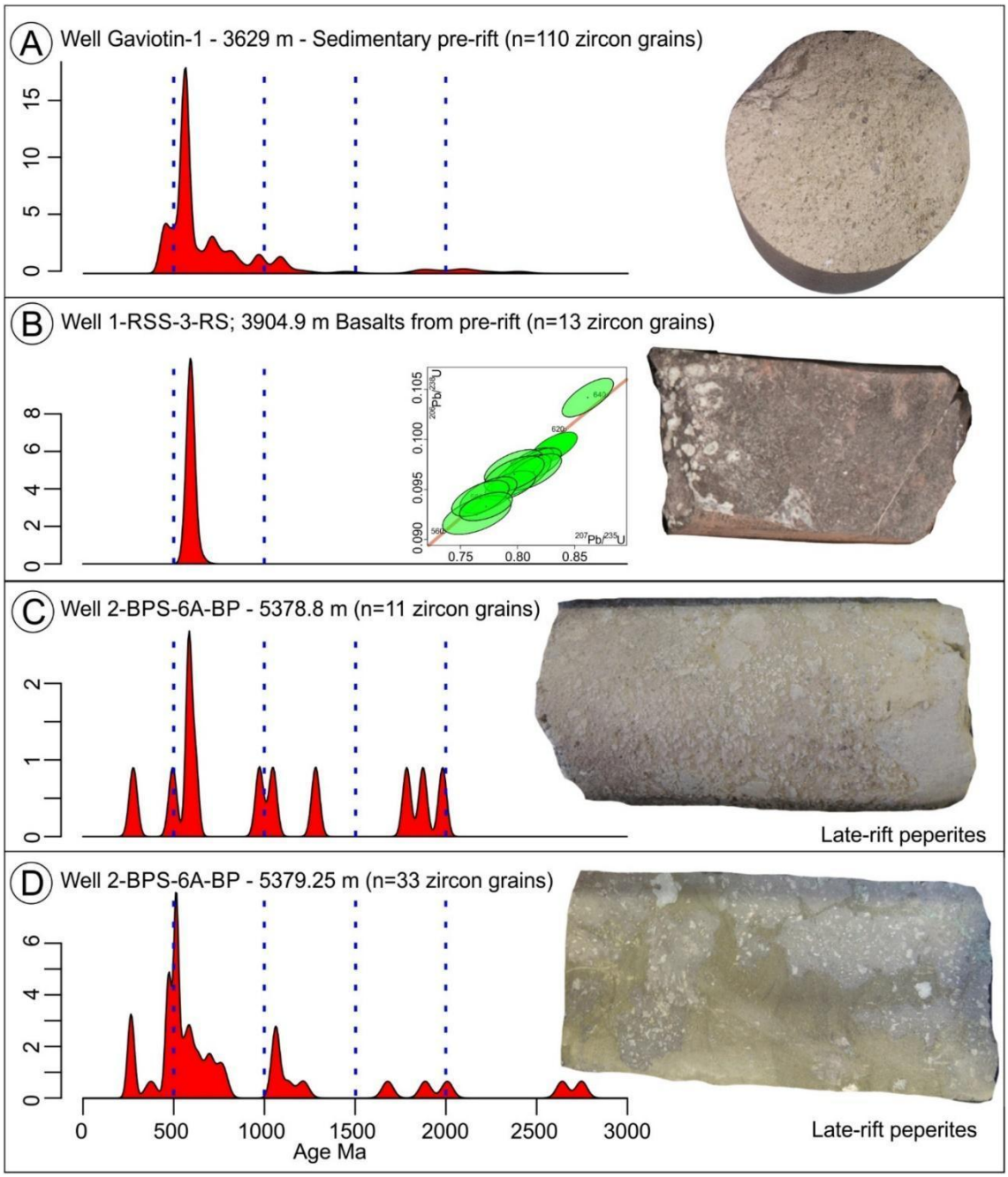

Figure 3-6. U-Pb data and analyzed samples. A) Sample Gaviotin-1 - 3629 m, from the pre-rift sedimentary section of the Punta del Este Basin. B) Sample 1-RSS-3-RS, 3904.9 m from basalts of the pre-rift section in the Pelotas Basin. C and D) Samples from well 2-BPS-6A-BP from peperites of the Pelotas Basin late-rift section. KDE and Concordia diagrams were plotted using IsoplotR software (Vermeesch, 2018).

In the sample from well 1-RSS-3-RS at a depth of 3904 m, which consists of basalts from the Pre-rift section, 13 zircon grains were analyzed to constrain their age. The grains are dominantly prismatic morphology with rounded corners, alternating between magmatic growth texture in the core and recrystallization textures in the rim. A high-grade metamorphic texture

is also identified in the zircon rims. The zircon size varies from 80 to 250 μm. The zircon population was related to the Neoproterozoic with a concordia age of 588.24 ± 5 Ma.

In two samples in the well, 2-BPS-6A-BP zircons were found, consisting of peperites of the late-rift section at 5378,8 (n = 11 zircon grains) and the other at 5379,25 (n = 33 zircon grains). The grains are both prismatic with rounded corners and rounded in morphology. Magmatic growth texture and recrystallization textures were identified. Few grains were prismatic with only magmatic texture. The age spectrum comprises different peaks, similar in both samples, comprehending a main peak in the Neoproterozoic and secondary peaks of Permian, Mesoproterozoic, and Paleoproterozoic ages.

3.4.4 Geochemical data

We analyzed the Nd and Sr isotopic composition of at least one sample from each well that contains volcanic rocks. This dataset was plotted with published data from the Walvis Ridge (Homrighausen et al., 2019) and the Paraná Large Igneous Province (Bologna et al., 2022; Fig. 3-7). The samples from the Rio Grande Rise display negative εNd(i) values and low 87Sr/86Sr(i) ratios, similar to those observed in the Walvis Ridge (Homrighausen et al., 2019). The samples from the lower section of well 2-BPS-6A-BP and well 1-SCS-3B-SC exhibit nearly identical isotopic signatures, close to the Gramado magmatic type of the Paraná LIP (Bologna et al., 2022), but with more negative εNd(i) and lower $^{87}Sr/^{86}Sr(i)$ ratios. The sample from well Lobo-1 also shows an isotopic signature similar to the Gramado type, with 87Sr/86Sr(i) values consistent with this magmatism but with εNd(i) values even more negative than those of the aforementioned samples, representing the most negative εNd(i) and the highest $^{87}Sr/^{86}Sr(i)$ values in the dataset. The lower sample from well 1-RSS-3-RS is compatible with the Gramado magmatic type; in contrast, the upper sample from the same well is the only one with a positive εNd(i) value and exhibits an $^{87}Sr/^{86}Sr(i)$ ratio similar to that of the Walvis Ridge. This sample (from the well upper 1-RSS-3-RS) plots near the Esmeralda magmatic type and the isotopic compositions of the lower and upper samples from well 1-RSS-3-RS differ significantly.

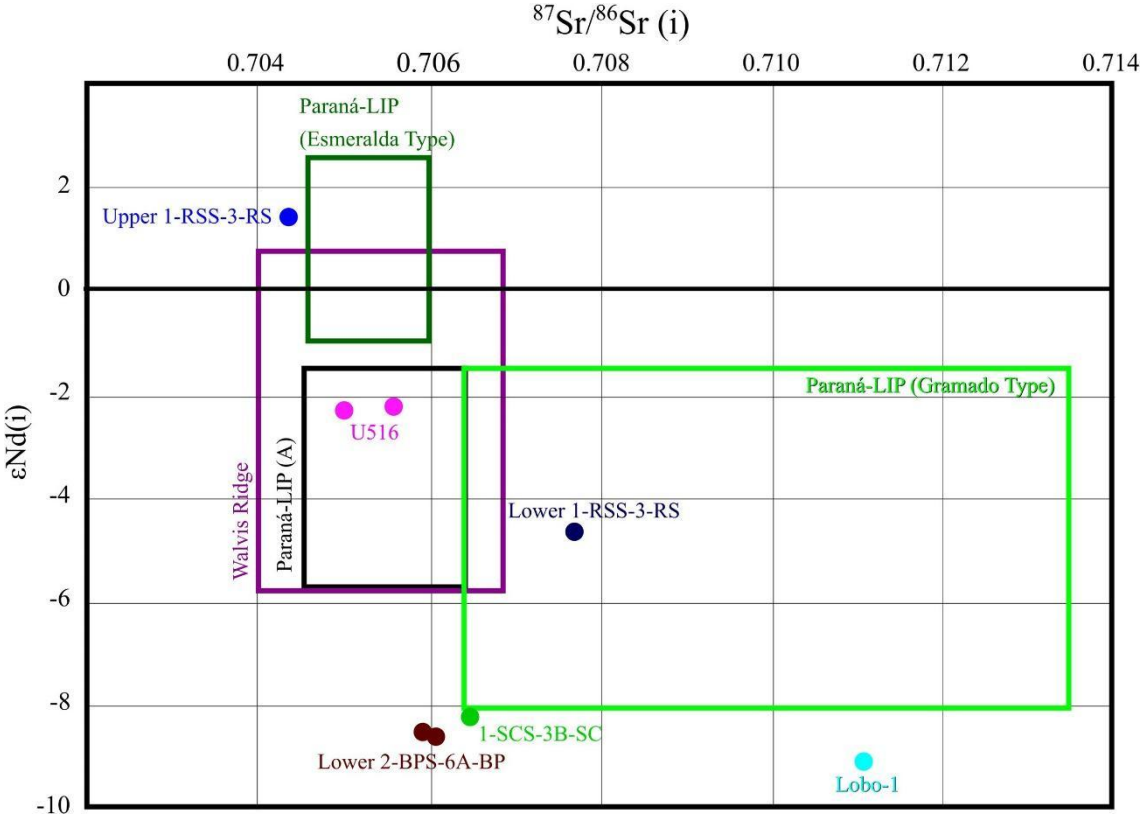

Figure 3-7. Plot of data of εNd(i) and 87Sr/86Sr. The fields are the limits of these isotopic ratios observed in the Walvis Ridge (in purple, Homrighausen et al., 2019) and the Paraná-LIP, subdivided into Esmeralda magmatic type, in dark green; Gramado type, in green; and the black field (Paraná LIP (A)) is the superposition of data from the Pitanga, Paranapanema, Urubici, and Ribeira formations, data compiled by Bologna et al. (2022). (For interpretation of the references to colour in this figure legend, the reader is referred to the web version of this article).

3.4.5 Discussion

3.4.6 Pre-rift section: The offshore extension of Paraná Basin

The Gaviotin-1 well (Fig. 1), drilled at a depth of 3629 m (Fig. 3-2B) below the drift section of offshore Punta del Este Basin, was identified in seismic lines as part of the pre-rift section, which we interpret as Paraná Basin. Detrital zircon U-Pb analysis presents evidence of Permo-Carboniferous Paraná Basin deposits beneath the Punta del Este Basin. The detrital spectra distribution is consistent with the detrital material found in Itararé Group deposits of the Paraná Basin in southernmost Brazil, as documented by Tedesco et al. (2019). The sample from the Gaviotin-1 well represents the southernmost evidence of the offshore extension of Paraná Basin and the most robust evidence of its offshore extension.

As the pre-rift section from Gaviotin-1 corresponds to the Paraná Basin (Itararé Group), we further hypothesize that the volcanic rocks from the pre-rift section in the nearby Lobo-1 well (30 km away) are part of the Paraná LIP (Serra Geral Group in Paraná Basin stratigraphy), based on both their proximity and similar seismic facies (Fig. 3-2A-B). The recovered rocks are basalts with many amygdales (Fig. 3-4A), indicating that we recovered samples from the top of the lava flow. We found no evidence of subaqueous volcanism, pointing to these rocks representing subaerial volcanism. In terms of geochemical composition, the basalts from Lobo-1 are subalkaline (Fig. 3-5B) and indicate a shallow magmatic source (Fig. 3-5F), with a composition similar to that observed in the PEL (Fig. 3-5E-F). We observed high 87Sr/86Sr(i) and low εNd(i) values(Fig. 3-7), which could be interpreted as continental crust melt (including sediment) or a plume related to an EMII reservoir (Zindler and Hart, 1986). The εNd(i) is even lower than the values observed in Paraná LIP. However, the 87Sr/86Sr(i) is compatible with the Gramado magma type, widespread in the southern part of the Paraná-LIP, and the largest e member of the Low-Ti lava field (Ti/Y < 310, Rossetti et al., 2018). The Lobo-1 samples have Ti/Y ranging from 323 to 348, which is over 310, yet very close to this value. In general, the composition is similar to the Gramado magmatic type from Paraná-LIP, and considering the tectonic context observed in seismic lines, probably these rocks are part of Paraná-LIP.

The pre-rift section drilled in well 1-RSS-3-RS (Fig. 3-1, Fig. 3-2C), previously classified as the Imbituba Formation (Pelotas Basin – Bueno et al., 2007), contains Gramado and Esmeralda-type lavas from the Paraná LIP. Samples from this well range from alkali basalts in the lower unit to sub-alkaline basalts in the upper unit (Fig. 3-5B). The Th/Yb vs. Nb/Yb plot (Fig. 3-5E) indicates minimal crustal contamination. However, 11 Neoproterozoic zircons dated at 588.24 ± 5 Ma (Fig. 3-6B) suggest assimilation from the Dom Feliciano Belt, which is the basement of Pelotas, Punta del Este and Paraná basins in this region (Stica et al., 2014; Gordon and Mohriak, 2015; Teixeira et al., 2025a; Teixeira et al., 2025b). The zircon morphology is also compatible with a granitic/gneiss source (with clear zonation). The isotopic signatures ($^{87}Sr/^{86}Sr$(i) and εNd(i); Fig. 7) also suggest continental crust assimilation or an EMI source (Zindler and Hart, 1986) for the lower 1-RSS-3-RS. The abundance of amygdales in the upper unit (Fig. 3-4D) points to subaerial lava emplacement. Subparallel seismic reflectors (Fig. 3-2C) support a pre-rift setting, though slight divergence in the upper reflectors may indicate a transition to an early rifting phase (Gordon and Mohriak, 2015). Radiometric ages from 3800 to 3907 m depths range from 125.3 ± 0.7 Ma to 118.3 ± 1.9 Ma ($^{40}Ar/^{39}Ar$ and $^{39}K/^{40}Ar$; compiled by Gordon and Mohriak, 2015), compatible with the late Paraná magmatism phase

(Hartmann et al., 2019). However, due to altered plagioclases (Fig. 3-4), concern is required when interpreting these ages, since plagioclases are no longer a closed system, and most isotopic age data is classified. Isotopic signatures from the lower unit match the Gramado type (part of Paraná LIP), while the upper unit aligns with the Esmeralda type (part of Paraná LIP; Bologna et al., 2022; Fig. 3-7), consistent with the onshore stratigraphy where Esmeralda basalts overlie Gramado basalts or Palmas rhyolites (Rossetti et al., 2018). The existence of the Paraná-LIP at the base of Santos (Camboriú Formation - Moreira et al., 2007) and Campos basins (Cambiúnas Formation - Winter et al., 2007) is additional evidence of the offshore extension of the Paraná LIP beneath Pelotas and Punta del Este basins.

The Paraná-Etendeka LIP (PEL) genesis was sometimes suggested to be related to the Tristan da Cunha plume (Ewart et al., 1998; Marsh et al., 2001; Ewart et al., 2004; Gibson et al., 2006; Zhou et al., 2020; Beccaluva et al., 2020). However, the $^{87}Sr/^{86}Sr(i)$ and εNd(i) signatures associated with the Neoproterozoic basement zircon xenocrysts are clear evidence of the continental crust and/or continental lithospheric mantle assimilation. Our isotopic analysis supports multiple interpretations of the magmatic source, as the observed in the isotopic ($^{87}Sr/^{86}Sr(i)$ and εNd(i)) and chemical signatures could equally be attributed to either mantle plumes from EMI or EMII reservoirs (Zindler and Hart, 1986) or the melting of continental crust or subcontinental lithospheric mantle (Marques et al., 2018). However, we observe an isotopic signature overlap of PEL (Pitanga, Paranapanema, Urubici, and Ribeira formations) and Walvis Ridge/Rio Grande Rise data, which suggests that they could share the same source.

3.4.7 Rift and late Rift in Pelotas, Punta del Este, and south of Santos basins

The rifting stage in the Pelotas and Punta del Este basins is characterized by antithetical half-grabens filled by sedimentary rocks at the proximal portion and SDRs at distal regions. SDR rocks were sampled exclusively in the northern Pelotas Basin at well 1-SCS-3B-SC and southernmost of Santos Basin, in well 1-SCS-1-SC (by Misuzaki and Saracchine, 1990b) on the north flank of Torres Arch. These rocks from 1-SCS-3B-SC are alkali basalts exhibiting an Ocean Island Basalts affinity (OIB; Fig. 5). Bueno et al. (2007) previously pointed to significant lithological heterogeneity in volcanic rocks from the margin, ranging from basalts to trachyandesites. However, their findings were based on major element classifications (Fig. 3-5A), which may not accurately represent the original compositions due to chemical alteration

processes. Our analysis of trace elements (Fig. 3-5B) indicates that all volcanic rocks from the margin are more homogeneous than previously reported, ranging from sub-alkaline basalts to alkaline basalts.

In the late-rift section of the 2-BPS-6 A-BP well, we encountered basalts and peperites. These peperites likely formed when hot lava interacted with wet sediments. The basalts and peperites are overlain by a marine sedimentary section Aptian in age (Arai, 2009), which further supports an interpretation of a near-shore magmatic event (Fig. 8). The detrital ages of these sediments provide evidence of erosion of Paraná Basin in the rift shoulders, now the Uruguayan and Brazilian coasts. The volcanic rocks chemical composition (Fig. 3-5) and isotopic signature (Fig. 3-7) from the lower 2-BPS-6 A-BP are almost the same as those observed in the 1-SCS-3B-SC well. Generally, we assume that all these rocks of the Torres Arch (2-BPS-6A-BP, 1-SCS-3B-SC, and 1-SCS-1-SC) represent the same magmatism within different tectonic contexts. As the rift propagated from South to North, while the Pelotas Basin became tectonically quiet (in the well 2-BPS-6 A-BP – Fig. 3-3A), the rocks were still faulting towards Santos Basin (wells 1-SCS-3B-SC and 1-SCS-1-SC, Fig. 3B-C). Due to the proximity and isotopic similarities of these wells, we assume the ages of 114 ± 3 Ma (K-Ar) and 113.2 ± 0.1 Ma (^{40}Ar-^{39}Ar) from Misuzaki (Misuzaki and Saracchine, 1990a; in Gordon and Mohriak, 2015) to the top of Torres Arch. This ages supports the hypothesis of sedimentary assimilation in the edges of this volcanic structure (Torres Arch), once the sedimentary deposition of Santos Basin started at Barremian (125.77 to 121.4 ± 0.6 - Moreira et al., 2007). This could explain the low-density SDRs observed by Harkin et al. (2020).

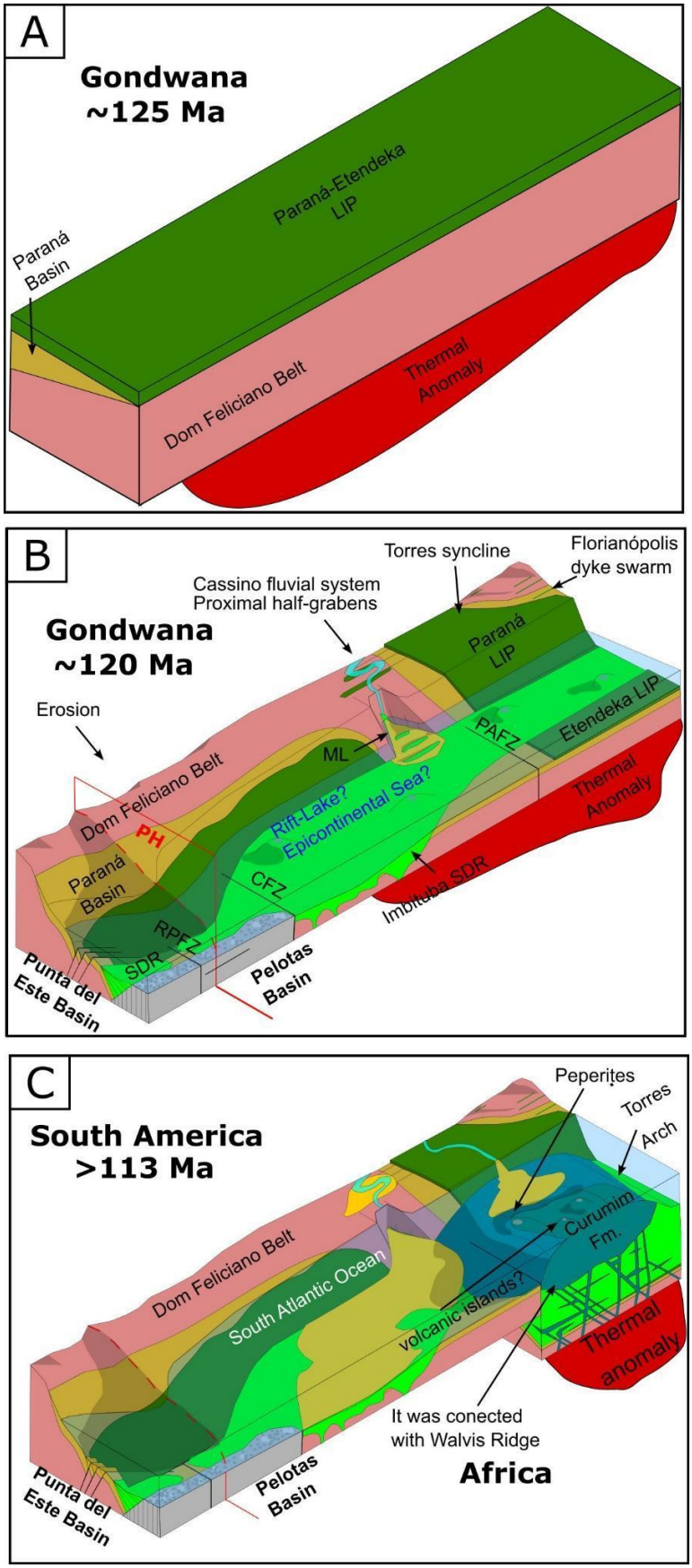

Figure 3-8. Overview of Margin Evolution. A) Pre-Rift Stage: At this stage, the Paraná-Etendeka Large Igneous Province (LIP) was extensive across the region, covering sedimentary

deposits of the Botucatu Formation, with the majority of this magmatic activity occurring around ~135 Ma. By 125 Ma, magmatic activity was minimal (Gomes and Vasconcelos, 2021, and references therein). During this stage, magmatism assimilated parts of the host rock, primarily those of the Dom Feliciano Belt at the continental margin. At this moment the thermal anomaly covers a wide area. B) Rift Stage: The rift stage is marked predominantly by Seaward Dipping Reflectors (SDRs) attributed to the Imbituba and Curumin Formations (Pelotas Basin – sensu Bueno et al., 2007). Sedimentary rocks from the rift Cassino Formation, fulfilling proximal half-grabens are reported in the well 1-RSS-3-RS (Bueno et al., 2007). We also observed some halfgrabens that are fulfilled by sedimentary rocks within the Punta del Este Basin south of Polonio High (PH). Erosion of the rift shoulders during this phase likely prevented the preservation of Paraná Basin rocks at the margin. With exception of the position of the well 2-TO-1-RS, this region records an depression of Paraná Basin know as Torres Syncline. ML- Mostardas Low; RPFZ- Rio de La Plata Fracture Zone; CFZ - Chuì Fracture Zone; PAFZ – Porto Alegre Fracture Zone C) Late-rift Stage: This stage was characterized by volcanic activity without significant new accommodation space creation. The magmatism was synchronous to sedimentary deposition. Based on its age, and position this magmatism is related to the Walvis Ridge, and represent the shrinkage of the thermal anomaly. Peperites samples in this section indicate volcanic activity in a wet depositional environment. Regional studies of the Torres Arch (Misuzaki and Saracchine, 1990a apud Gordon and Mohriak, 2015) and the Walvis Ridge (Rohde et al., 2013) suggest this magmatic phase lasted until ~113 Ma.

Paleogeographic reconstructions correlate the Torres Arch region with the early position of the Walvis Ridge (Homrighausen et al., 2019; Chauvet et al., 2021). This corroborates the Torres Arch volcanic activity occurring at approximately 114 ± 3 Ma (K-Ar) and 113.2 ± 0.1 Ma (^{40}Ar-^{39}Ar; Misuzaki and Saracchine, 1990a; apud Gordon and Mohriak, 2015) since the ages of 114.1 ± 0.4 Ma are found in the oldest rocks of the Walvis Ridge (Rohde et al., 2013). These radiometric ages are compatible with the micropaleontology age observed in the sedimentary section above the volcanic layers of Torres Arch, which are Aptian in age (Arai, 2009). However, there is no evidence that late magmatism (Until 113 Ma) was widespread; we assume that it was restricted to the Torres Arch region (Fig. 3-1, Fig. 3-8) while it was connected to Walvis Ridge (Chauvet et al., 2021).

These findings suggest a volcanic stack in the margin, spanning from approximately 125.3 ± 0.7 Ma to 113.2 ± 0.1 Ma (Misuzaki and Saracchine, 1990a apud Gordon and Mohriak, 2015). This supports the hypothesis by Serratt et al. (2022) that the region contains multiple volcanic layers of different ages. Additionally, it highlights the limitations of magnetostratigraphy in the area, as at least six magnetic field reversals are stacked within these volcanic units (Gee and Kent, 2007), complicating the interpretation of the magnetic record.

The magmatism source from the Torres arch looks similar to the Gramado magmatic type source, as observed by its isotopic content (Paraná-LIP – Fig. 3-7). However, the data

could be interpreted in two ways, the source could be an EMI reservoir plume or the magmatic assimilation of the crust/sub continental lithospheric mantle, for the same reasons mentioned in the pre-rift section. Some previous research points that there is not necessary a plume to cause this magmatism (Lobo et al., 2006; Sauter et al., 2023). The isotopic signature of SDRs and related rocks does not reflect the εNd and 87Sr/86SR values observed in Walvis Ridge and Rio Grande Rise (Fig. 7). However, on the African side, we can observe that Walvis Ridge is a direct continuation of the SDRs near the Rio Grande Fracture Zone (Chauvet et al., 2021). We interpret this as the Torres Arch and Walvis Ridge having the same source but with more continental contamination in the rocks of the margin.

3.4.8 Rio Grande Rise

The Rio Grande Rise shows an isotopic signature compatible with Walvis Ridge (Fig. 3-7). This reinforces the paleogeographic models from Hoyer et al. (2022), where these two structures are genetically linked. The isotopic content of these samples points to an EMI reservoir (Zindler and Hart, 1986). However, we cannot confirm the plume model suggested by Hoyer et al. (2022). Notably, εNd values can even indicate some degree of continental contamination. The South Atlantic Ocean has the largest record of zircon xenocrysts in its Mid-Ocean Ridge, which Bea et al. (2020) interpreted as evidence of continental slivers preserved in the Mid Ocean Ridge. The possible presence of these slivers could cause negative values of εNd and lead to misinterpretation of the isotopic data.

We updated the Courtillot et al. (1999) observations of the close spatial and temporal relationship between Continental Flood Basalts (CFBs), SDR, and seamounts worldwide. Notable examples include the juxtaposition of the Etendeka Traps with African SDRs (Chauvet et al., 2021), as well as the Central Atlantic Magmatic Province (CAMP) and the United States of America East Coast SDRs, associated with the East Coast Magnetic Anomaly (ECMA; Davis et al., 2018). Other significant examples include the Deccan Traps and associated SDRs and Chagos-Laccadive Plateau in India (Verma and Khosla, 2019; Geoffroy et al., 2020), the North Atlantic Igneous Province (NAIP) encompassing the United Kingdom and Greenland onshore plateaus with adjacent SDRs (Meyer et al., 2007). The Afro-Arabian LIP (Hofmann et al., 1997) and the active SDR formation observed in Djibouti (Chauvet et al., 2023) support this relation. Nearby, these volcanic successions include volcanic islands, seamounts, and volcanic plateaus such as the Rio Grande Rise and Walvis Ridge. The Iceland island near West Greenland SDR

(Agranier et al., 2019) suggests that these features are genetically linked. Although the SDRs and Rio Grande Rise did not show the same isotopic signature, all these magmatic units (CFB, SDR, oceanic plateaus) appear to be related to the same persistent thermal anomaly in the region (Foulger, 2018).

3.5 Conclusion

Geological and geochemical evidence supports the offshore continuation of the Paraná Basin beneath the Pelotas and Punta del Este basins. This is particularly exemplified by findings from the Gaviotin-1 well, which recovered Permo-Carboniferous deposits of the Itararé Group (Paraná Basin), confirmed by its distinctive detrital zircon content. The geochemical signatures from volcanic rocks in the Lobo-1 and 1-RSS-3-RS wells, combined with seismic interpretations, suggest that these units belong to the Paraná-Etendeka Large Igneous Province (LIP), known as the Serra Geral Group in the Paraná Basin stratigraphy. These findings suggest that sedimentary and volcanic rocks of the Paraná Basin likely extend across significant segments of the offshore continental margin.

All volcanic samples from the margin are basalts, ranging from sub-alkaline to alkaline compositions, and display varying degrees of continental crust contamination. This contamination is evidenced by their geochemical and isotopic signatures and the presence of zircon xenocrysts. We conclude that all analyzed volcanic rocks from the margin are formed above the continental crust. However, the precise location of the continent-ocean boundary (COB) remains unclear, especially considering that features such as the Rio Grande Rise may involve fragments of continental crust.

The rift stage in the Pelotas and Punta del Este basins is characterized predominantly by volcanic seaward-dipping reflectors (SDRs), though sedimentary rocks also appear in proximal sectors, indicating contemporaneous deposition during rifting. This observation supports the hypothesis that sedimentation occurs within SDR formation. Notable, the well 2-BPS-6A-BP contains peperites, indicating that late-stage rift magmatism interacted with coastal sedimentary environments, containing sediments derived from Paraná Basin erosion.

The volcanic rocks from the margin exhibit geochemical compositions similar to OIB and E-MORB, with isotopic signatures compatible with EMI and EMII plume reservoirs. However, these characteristics may reflect significant assimilation of continental crust or

subcontinental lithospheric mantle, an interpretation reinforced by the occurrence of zircon xenocrysts in well 1-RSS-3-RS. As a result, the primary mantle source remains uncertain.

The Rio Grande Rise shares the same isotopic fingerprint as the Walvis Ridge, providing further support for their conjugate origin during the Late Cretaceous. This fingerprint is suggestive of an EMI source (possibly plume-related). However, this fingerprint can have been modified by the assimilation of slivers of continental crust, which are widespread throughout the South Atlantic, making the source unclear.

Although the mantle source remains unconstrained, our observations reflect a sequence of magmatic events extending from the Gondwanan continental flood basalts (CFBs) through rift-related SDRs to oceanic plateaus and volcanic islands of the South Atlantic. This sequence appears to be a common feature of volcanic passive margins and points to long-lived thermal anomalies acting throughout their evolution.

3.6 Declaration of competing interest

We declare that we have no economic interest on this research.

3.7 Acknowledgments

This article is part of HS Ph.D. thesis. The authors thank the CNPC Brasil (China National Petroleum Corporation) for the financial support. We also thanks ANP (Brazilian National Agency for Petroleum, Natural Gas and Biofuels) and ANCAP (Uruguayan Administración Nacional de Combustibles, Alcoholes y Portland) for providing access to data. We are grateful to Schlumberger and Eliis for granting academic licenses for the PetrelTm and PaleoScan™ software, respectively. FCJ thanks CNPq for grant #4081942021-9 and INCT-Atlantico (grant #406898/2022-7). HS thanks CAPES for grant #88887.886595/2023-00.

3.8 CRediT authorship contribution statement

Henrique Serratt: Writing – review & editing, Writing – original draft, Visualization, Methodology, Investigation, Formal analysis, Data curation, Conceptualization. Tiago Jonatan Girelli: Writing – original draft, Methodology, Investigation, Formal analysis. Matheus Fernandes da Cruz: Visualization, Software, Methodology, Data curation. Claudia Domingues

Teixeira: Writing – review & editing, Investigation, Formal analysis. Ilana Lehn: Writing – review & editing, Writing – original draft, Validation, Formal analysis. Monique Aparecida Marchese Rizzi: Writing – review & editing, Writing – original draft, Data curation. Marly Babinski: Formal analysis, Methodology, Validation. Catarina Laboure Bemfica Toledo: Writing – review & editing, Validation, Supervision, Methodology, Investigation. Peng Peng: Methodology, Formal analysis. Bruno Conti: Validation, Resources, Data curation. Adalene Moreira Silva: Writing – review & editing, Validation, Supervision, Data curation, Conceptualization. Laurent Geoffroy: Writing – review & editing, Supervision. Farid Chemale Junior: Writing – review & editing, Validation, Supervision, Resources, Project administration, Funding acquisition, Data curation, Conceptualization.

3.9 References

Abdelmalak, M.M., Rossetti, L.M., Millett, J.M., Planke, S., Jerram, D.A., Faleide, J.I., Polteau, S., 2025. Breakup Magmatism in the South Atlantic: Mechanisms and Implications.

Agranier, A., Maury, R.C., Geoffroy, L., Chauvet, F., Le Gall, B., Viana, A.R., 2019. Volcanic record of continental thinning in Baffin Bay margins: insights from Svartenhuk Halvø Peninsula basalts, West Greenland. Lithos 334, 117–140.

AGU, Geophysical Monograph Series, pp. 217–245. https://doi.org/10.1029/ GM100p0217.

Arai, M., 2009. South Atlantic Aptian paleogeography: a new model based on recent Brazilian micropaleontological data. Boletim de Geocieˆncias da Petrobras 17 (2), 331–351.

Barker, P.F., Johnson, D.A., Carlson, R.L., Cepek, P., Coulbourn, W.T., Gamboa, L.A.,Hamilton, N., de Melo, U., Pujol, C., Shor, A.N., Suzyumov, A.E., Tjalsma, L.R.C., Walton, W.H. (Eds.), 1983. Initial reports of the Deep Sea Drilling Project, Volume 72: Leg 72, Santos, Brazil to Santos, Brazil, February–April 1980. U.S. Government Printing Office. In: https://doi.org/10.2973/dsdp.proc.72.1983.

Bea, F., Bortnikov, N., Montero, P., Zinger, T., Sharkov, E., Silantyev, S., Molina- Palma, J.F., 2020. Zircon xenocryst evidence for crustal recycling at the Mid-Atlantic Ridge. Lithos 354, 105361.

Beccaluva, L., Bianchini, G., Natali, C., Siena, F., 2020. Plume-related Parana`-Etendeka igneous province: an evolution from plateau to continental rifting and breakup. Lithos 362, 105484.

Becker, K., Franke, D., Trumbull, R., Schnabel, M., Heyde, I., Schreckenberger, B., Krawczyk, C.M., 2014. Asymmetry of high-velocity lower crust on the South Atlantic rifted margins and implications for the interplay of magmatism and tectonics in continental breakup. Solid Earth 5 (2), 1011–1026.

Bologna, M.S., Júnior, E.R.V.R., Ernesto, M., Marques, L.S., 2022. The Paran´a Magmatic Province: state-of-the-art in the geophysical and geochemical investigations. Brazil. J. Geophys. 40 (6), 43–66.

Boynton, W.V., 1984. Cosmochemistry of the rare earth elements: Meteorite studies. In: Developments in geochemistry, vol. 2. Elsevier, pp. 63–114.

Bueno, G.V., Zacharias, A.A., Oreiro, S.G., Cupertino, J.A., Falkenhein, F.U.H., Martins Neto, M.A., 2007. Bacia de Pelotas. Boletim de Geociencias da Petrobras 15, 551–559.

Cainelli, C., Mohriak, W.U., 1999. Some remarks on the evolution of sedimentary basins along the Eastern Brazilian continental margin. Episodes J. Int. Geosci. 22 (3), 206–216.

Cassel, M.C., Chemale Jr., F., Vargas, M.R., de Souza, M.K., Girelli, T.J., de Oliveira, G.S., 2022. From the Andes and the Drake Passage to the Rio Grande Submarine Fan: paleoclimatic and paleogeographic evidence in the Cenozoic Era from the South Atlantic–Austral Segment, Pelotas Basin. Glob. Planet. Chang. 213, 103838.

Caxito, F.A., Hartmann, L.A., Heilbron, M., Pedrosa-Soares, A.C., Bruno, H., Basei, M.A., Chemale, F., 2022. Multi-proxy evidence for subduction of the Neoproterozoic Adamastor Ocean and Wilson cycle tectonics in the South Atlantic Brasiliano Orogenic System of Western Gondwana. Precambrian Res. 376, 106678.

Chauvet, F., Geoffroy, L., Le Gall, B., Jaud, M., 2023. Volcanic passive margins and breakup processes in the southern Red Sea. Gondwana Res. 117, 169–193.

Chauvet, F., Sapin, F., Geoffroy, L., Ringenbach, J.C., Ferry, J.N., 2021. Conjugate volcanic passive margins in the austral segment of the South Atlantic–architecture and development. Earth Sci. Rev. 212, 103461. https://doi.org/10.1016/j. earscirev.2020.103461.

Chemale Jr., F., Kawashita, K., Dossin, I.A., A´vila, J.N., Justino, D., Bertotti, A.L., 2012. U–Pb zircon in situ dating with LA–MC–ICP–MS using a mixed detector configuration. An. Acad. Bras. Cienc. 84, 275–295.

Chemale Jr., F., Mallmann, G., de F´atima Bitencourt, M., Kawashita, K., 2012. Time constraints on magmatism along the Major Gercino Shear Zone, southern Brazil: implications for West Gondwana reconstruction. Gondwana Res. 22 (1), 184–199.

Collier, J.S., McDermott, C., Warner, G., Gyori, N., Schnabel, M., McDermott, K., Horn, B. W., 2017. New constraints on the age and style of continental breakup in the South Atlantic from magnetic anomaly data. Earth Planet. Sci. Lett. 477, 27–40. https:// doi.org/10.1016/j.epsl.2017.08.007.

Conti, B., de Jesus Perinotto, J.A., Veroslavsky, G., Castillo, M.G., de Santa Ana, H., Soto, M., Morales, E., 2017. Speculative petroleum systems of the southern Pelotas Basin, offshore Uruguay. Mar. Pet. Geol. 83, 1–25.

Courtillot, V., Jaupart, C., Manighetti, I., Tapponnier, P., Besse, J., 1999. On causal links between flood basalts and continental breakup. Earth Planet. Sci. Lett. 166 (3–4), 177–195.

Davis, J.K., Be´cel, A., Buck, W.R., 2018. Estimating emplacement rates for seaward- dipping reflectors associated with the US East Coast magnetic Anomaly. Geophys. J. Int. 215 (3), 1594–1603. https://doi.org/10.1093/gji/ggy360.

DePaolo, D.J., 1981. Nd isotopic studies: some new perspectives on Earth structure and evolution. Eos Trans. Am. Geophys. Union 62 (14). https://doi.org/10.1029/ EO062i014p00137-01, 137-137.

Dias, J.L., Sad, A.R., Fontana, R.L., Feijo´, F.J., 1994. Bacia de Pelotas. Boletim de Geociências da Petrobras 8 (1), 235–245.

Eagles, G., P´erez-Díaz, L., Scarselli, N., 2015. Getting over continent-ocean boundaries. Earth Sci. Rev. 151, 244–265. https://doi.org/10.1016/j.earscirev.2015.10.009.

Ernesto, M., Marques, L.S., Piccirillo, E.M., Molina, E.C., Ussami, N., Comin- Chiaramonti, P.I.E.R.O., Bellieni, G., 2002. Paran´a Magmatic Province–Tristan da Cunha plume system: fixed versus mobile plume, petrogenetic considerations and alternative heat sources. J. Volcanol. Geotherm. Res. 118 (1–2), 15–36.

Ewart, A., Marsh, J.S., Milner, S.C., Duncan, A.R., Kamber, B.S., Armstrong, R.A., 2004. Petrology and geochemistry of early cretaceous bimodal continental flood volcanism of the NW Etendeka,

Namibia. Part 1: introduction, mafic lavas and re-evaluation of mantle source components. J. Petrol. 45 (1), 59–105.

Ewart, A., Milner, S.C., Armstrong, R.A., Dungan, A.R., 1998. Etendeka volcanism of the Goboboseb Mountains and Messum Igneous Complex, Namibia. Part I: Geochemical evidence of early Cretaceous Tristan plume melts and the role of crustal contamination in the Parana´–Etendeka CFB. J. Petrol. 39 (2), 191–225.

Foulger, G.R., 2018. Origin of the South Atlantic igneous province. J. Volcanol.

Franke, D., Neben, S., Ladage, S., Schreckenberger, B., Hinz, K., 2007. Margin segmentation and volcano-tectonic architecture along the volcanic margin off Argentina/Uruguay, South Atlantic. Mar. Geol. 244 (1–4), 46–67.

Frizon de Lamotte, D., Fourdan, B., Leleu, S., Leparmentier, F., de Clarens, P., 2015. Style of rifting and the stages of Pangea breakup. Tectonics 34 (5), 1009–1029.

Gee, J.S., Kent, D.V., 2007. Source of oceanic magnetic anomalies and the geomagnetic polarity timescale. Geomagnetism 5, 455–507.

Geoffroy, L., Burov, E.B., Werner, P., 2015. Volcanic passive margins: another way to break up continents. Sci. Rep. 5 (1), 1–12. https://doi.org/10.1038/srep14828.

Geoffroy, L., Gelard, J.P., Lepvrier, C., Olivier, P., 1998. The coastal flexure of Disko (West Greenland), onshore expression of the ‘oblique reflectors’. J. Geol. Soc. Lond. 155 (3), 463–473.

Geoffroy, L., Guan, H., Gernigon, L., Foulger, G.R., Werner, P., 2020. The extent of continental material in oceans: C-Blocks and the Laxmi Basin example. Geophys. J. Int. 222 (3), 1471–1479.Geotherm. Res. 355, 2–20.

Gibson, S.A., Thompson, R.N., Day, J.A., 2006. Timescales and mechanisms of plume–lithosphere interactions: 40Ar/39Ar geochronology and geochemistry of alkaline igneous rocks from the Paran´a–Etendeka large igneous province. Earth Planet. Sci. Lett. 251 (1–2), 1–17.

Gladczenko, T.P., Hinz, K., Eldholm, O., Meyer, H., Neben, S., Skogseid, J., 1997. South Atlantic volcanic margins. J. Geol. Soc. Lond. 154 (3), 465–470.

Gomes, A.S., Vasconcelos, P.M., 2021. Geochronology of the Parana´-Etendeka large igneous province. Earth Sci. Rev. 220, 103716.

Gordon, A.C., Mohriak, W.U., 2015. Seismic Volcano-Stratigraphy in the Basaltic Complexes on the Rifted Margin of Pelotas Basin, Southeast Brazil.

Gordon, A.C., Mohriak, W.U., Heilbron, M., 2017. From SE Parana´ to Pelotas Basin, a geophysical-geological transect traversing two of the world's largest igneous provinces in South America. In: 15th International Congress of the Brazilian Geophysical Society, Rio de Janeiro, Brazil, 31 July to 3 August, 2017, Abstracts, 1–6.

Gresse, P.G., Chemale, F., Da Silva, L.C., Walraven, F., Hartmann, L.A., 1996. Late-to post-orogenic basins of the Pan-African–Brasiliano collision orogen in southern Africa and southern Brazil. Basin Res. 8 (2), 157–171.

Hall, S.A., Bird, D.E., McLean, D.J., Towle, P.J., Grant, J.V., Danque, H.A., 2018. New constraints on the age of the opening of the South Atlantic Basin. Mar. Pet. Geol. 95, 50–66.

Harkin, C., Kusznir, N., Roberts, A., Manatschal, G., Horn, B., 2020. Origin, composition, and relative timing of seaward dipping reflectors on the Pelotas rifted margin. Mar. Pet. Geol. 114, 104235. https://doi.org/10.1016/j.marpetgeo.2020.104235.

Hartmann, L.A., Baggio, S.B., Brückmann, M.P., Knijnik, D.B., Lana, C., Massonne, H.J., Arena, K.R., 2019. U-Pb geochronology of Paran´a volcanics combined with trace element geochemistry of the zircon crystals and zircon Hf isotope data. J. S. Am. Earth Sci. 89, 219–226.

Hofmann, C., Courtillot, V., Feraud, G., Rochette, P., Yirgu, G., Ketefo, E., Pik, R., 1997. Timing of the Ethiopian flood basalt event and implications for plume birth and global change. Nature 389 (6653), 838. https://doi.org/10.1038/39853.

Holz, M., Kalkreuth, W., Rolim, S.B.A., 2010. Extension of the Parana´ Basin to offshore Brazil: implications for coalbed methane evaluation. Mar. Pet. Geol. 27 (5), 1119–1132.

Homrighausen, S., Hoernle, K., Hauff, F., Wartho, J.A., van den Bogaard, P., Garbe- Scho¨nberg, D., 2019. New age and geochemical data from the Walvis Ridge: the temporal and spatial diversity of South Atlantic intraplate volcanism and its possible origin. Geochim. Cosmochim. Acta 245, 16–34.

Horstwood, M.S., Koˇsler, J., Gehrels, G., Jackson, S.E., McLean, N.M., Paton, C., Schoene, B., 2016. Community-derived standards for LA-ICP-MS U-(Th-) Pb geochronology–uncertainty propagation, age interpretation and data reporting. Geostand. Geoanal. Res. 40 (3), 311–332.

Hoyer, P.A., Haase, K.M., Regelous, M., O'Connor, J.M., Homrighausen, S., Geissler, W. H., Jokat, W., 2022. Mantle plume and rift-related volcanism during the evolution of the Rio Grande Rise. Commun. Earth Environ. 3 (1), 18.

Huang, C., Wang, H., Yang, J.H., Ramezani, J., Yang, C., Zhang, S.B., Wu, S.T., 2020. SA01–a proposed zircon reference material for microbeam U-Pb age and Hf-O isotopic determination. Geostand. Geoanal. Res. 44 (1), 103–123.

Ingersoll, R.V., 2011. Tectonics of sedimentary basins, with revised nomenclature. In: Tectonics of Sedimentary Basins: Recent Advances, pp. 1–43.

Jaffey, A.H., Flynn, K.F., Glendenin, L.E., Bentley, W.T., Essling, A.M., 1971. Precision measurement of half-lives and specific activities of U 235 and U 238. Phys. Rev. C 4 (5), 1889.

King, S.D., Anderson, D.L., 1995. An alternative mechanism of flood basalt formation. Earth Planet. Sci. Lett. 136 (3–4), 269–279.

Larsen, H.C., Saunders, A.D., Clift, P.D., 1994. Introduction: Breakup of the Southeast Greenland margin and the formation of the Irminger Basin: Background and scientific objectives. In: Proceedings of the Ocean Drilling Program. Part A, Initial Report, Vol. 152, pp. 5–16.

LeBas, M., Maitre, R.L., Streckeisen, A., Zanettin, B., IUGS Subcommission on the Systematics of Igneous Rocks, 1986. A chemical classification of volcanic rocks based on the total alkali-silica diagram. J. Petrol. 27 (3), 745–750.

Lobo, J.T., 2000. Petrogeˆnese dos basaltos do Eocreta´ceo Inferior das bacias de Campos e Pelotas, SE do Brasil. Universidade do Estado de Rio de Janeiro, Faculdade de Geología, p. 97. Msc dissertation.

Lobo, J.T., 2007. Petrogenese das rochas bas´alticas do Eocret´aceo das bacias de Campos e Pelotas, e implicaço˜es na geodinˆamica de rifteamento do Gondwana ocidental.Universidade do Estado do Rio De Janeiro, Faculdade de Geologia, p. 171. PhD dissertation.

Lobo, J.T., Szatmari, P., Duarte, B.P., 2006. Tipos de fontes associadas as suítes basálticas de Campos e de Pelotas (Sul-Sudeste) e modelos geodinˆamicos de ruptura do Gondwana ocidental. Boletim de Geociencias da Petrobras 14 (2), 269–285.

Lovecchio, J.P., Abdelmalak, M.M., Planke, S., Silio, O., Rohais, S., Arismendi, S., Ramos, V.A., 2024. Mesozoic rifting in SW Gondwana and breakup of the Southern South Atlantic Ocean. Geol. Soc. Lond. Spec. Publ. 547 (1). SP547-2023.

Mansur, E., Barnes, S.J., Janasi, V., Henrique-Pinto, R., Alves, A., Marteleto, N.S., 2021. The distribution of platinum-group elements and Te, As, Bi, Sb and Se (TABS+) in the Parana´ Magmatic Province: effects of crystal fractionation, sulfide segregation and magma degassing. Lithos 400, 106374.

Marques, L.S., De Min, A., Rocha, E.R.V., Babinski, M., Bellieni, G., Figueiredo, A.M.G., 2018. Elemental and Sr-Nd-Pb isotope geochemistry of the Floriano´polis Dyke Swarm (Paran´a Magmatic Province): crustal contamination and mantle source constraints. J. Volcanol. Geotherm. Res. 355, 149–164. https://doi.org/10.1016/j. jvolgeores.2017.07.005.

Marques, L.S., Dupre, B., Piccirillo, E.M., 1999. Mantle source compositions of the Parana´ Magmatic Province (southern Brazil): evidence from trace element and Sr-Nd-Pb isotope geochemistry. J. Geodyn. 28, 439–458. https://doi.org/10.1016/s0264- 3707(99)00020-4.

Marsh, J.S., Ewart, A., Milner, S.C., Duncan, A.R., Miller, R.M., 2001. The Etendeka Igneous Province: magma types and their stratigraphic distribution with implications for the evolution of the Paran´a-Etendeka flood basalt province. Bull. Volcanol. 62, 464–486.

McDonough, W.F., Sun, S.S., 1995. The composition of the Earth. Chem. Geol. 120 (3–4), 223–253.

Meyer, R., van Wijk, J., Gernigon, L., 2007. The North Atlantic Igneous Province: A Review of Models for its Formation.

Milani, E.J., Melo, J.H.G., Souza, P.A., Fernandes, L.A., França, A.B., 2007. Bacia do Parana´. Boletim de Geociˆencias— Petrobras 15, 265–287.

Misuzaki, A.M.P., Saracchine, F.E., 1990. Cata´logo geral de dados geocronolo´gicos da Petrobra´s: Relato´rio Interno. Petrobra´s/Cenpes/Divex/Setec, Rio de Janeiro, Brasil, pp. 1–30.

Mohriak, W.U., No´brega, M., Odegard, M.E., Gomes, B.S., Dickson, W.G., 2010. Geological and Geophysical Interpretation of the Rio Grande Rise, South-Eastern Brazilian Margin: Extensional Tectonics and Rifting of Continental and Oceanic Crusts.

Moreira, J.L.P., Madeira, C.V., Gil, J.A., Machado, M.A.P., 2007. Bacia de Santos. Boletim de Geociencias da PETROBRAS 15 (2), 531–549.

Moulin, M., Aslanian, D., Unternehr, P., 2010. A new starting point for the South and Equatorial Atlantic Ocean. Earth Sci. Rev. 98 (1–2), 1–37. https://doi.org/10.1016/ j.earscirev.2009.08.001.

Mutter, J.C., Buck, W.R., Zehnder, C.M., 1988. Convective partial melting: 1. A model for the formation of thick basaltic sequences during the initiation of spreading. J. Geophys. Res. Solid Earth 93 (B2), 1031–1048.

Mutter, J.C., Talwani, M., Stoffa, P.L., 1982. Origin of seaward-dipping reflectors in oceanic crust off the Norwegian margin by “subaerial sea-floor spreading”. Geology 10 (7), 353–357.

Nance, R.D., Murphy, J.B., Santosh, M., 2014. The supercontinent cycle: a retrospective essay. Gondwana Res. 25 (1), 4–29.

Pearce, J.A., 2008. Geochemical fingerprinting of oceanic basalts with applications to ophiolite classification and the search for Archean oceanic crust. Lithos 100, 14–48. https://doi.org/10.1016/j.lithos.2007.06.016.

Pearce, J.A., 2014. Immobile element fingerprinting of ophiolites. Elements 10 (2), 101–108.

Pearce, J.A., Wyman, D.A., 1996. A user’s guide to basalt discrimination diagrams. Trace element geochemistry of volcanic rocks: applications for massive sulphide exploration. Geol. Assoc. Canada Short Course Notes 12, 79–113.

Peate, D.W., 1997. The Parana´-Etendeka Province. In: Mahoney, J.J., Coffin, M.F. (Eds.), Large Igneous Provinces: Continental, Oceanic, and Planetary Flood Volcanism.

Peate, D.W., Hawkesworth, C.J., Mantovani, M.M.S., Rogers, N.W., Turner, S.P., 1999. Petrogenesis and stratigraphy of the high-Ti/Y Urubici magma type in the Paran´a flood basalt province and implications for the nature of ‘Dupal’-type mantle in the South Atlantic region. J. Petrol. 40 (3), 451–473. https://doi.org/10.1093/ petrology/40.3.451.

Philipp, H., Eckhardt, J.D., Puchelt, H., 2001. Platinum-group elements (PGE) in basalts of the seaward-dipping reflector sequence, SE Greenland coast. J. Petrol. 42 (2), 407–432.

Puetz, S.J., Spencer, C.J., Ganade, C.E., 2021. Analyses from a validated global UPb detrital zircon database: enhanced methods for filtering discordant UPb zircon analyses and optimizing crystallization age estimates. Earth Sci. Rev. 220, 103745.

Rabinowitz, P.D., LaBrecque, J., 1979. The mesozoic South Atlantic Ocean and evolution of its continental margins. J. Geophys. Res. 84 (B11), 5973–6002. https://doi.org/ 10.1029/jb084ib11p05973.

Reuber, K., Mann, P., Pindell, J., 2019. Hotspot origin for asymmetrical conjugate volcanic margins of the austral South Atlantic Ocean as imaged on deeply penetrating seismic reflection lines. Interpretation 7 (4), SH71-SH97.

Rohde, J.K., van den Bogaard, P., Hoernle, K., Hauff, F., Werner, R., 2013. Evidence for an age progression along the Tristan-Gough volcanic track from new 40Ar/39Ar ages on phenocryst phases. Tectonophysics 604, 60–71.

Rossetti, L., Lima, E.F., Waichel, B.L., Hole, M.J., Simo˜es, M.S., Scherer, C.M., 2018. Lithostratigraphy and volcanology of the Serra Geral Group, Parana´-Etendeka Igneous Province in southern Brazil: Towards a formal stratigraphical framework. J. Volcanol. Geotherm. Res. 355, 98–114.

Santos, M.M., Lana, C., Scholz, R., Buick, I., Schmitz, M.D., Kamo, S.L., Gerdes, A.,Corfu, F., Tapster, S., Lancaster, P., Storey, C.D., Basei, M.A.S., Tohver, E., Alkmim, A., 2017. A new appraisal of Sri Lankan BB zircon as a reference material for LA-ICP-MS U-Pb geochronology and Lu-Hf isotope tracing. Geostand. Geoanal. Res. 41 (3), 335–358.

Sauter, D., Manatschal, G., Kusznir, N., Masquelet, C., Werner, P., Ulrich, M., Autin, J., 2023. Ignition of the southern Atlantic seafloor spreading machine without hot- mantle booster. Sci. Rep. 13 (1), 1195.

Serratt, H., Domingues Teixeira, C., Girelli, T.J., de Souza, M.K., Rodrigues Vargas, M., Moreira Silva, A., Chemale Jr., F., 2022. Seaward-dipping reflector influence on seafloor magnetostratigraphy - a Pelotas Basin view. Geophys. Res. Lett. 49 (23), e2022GL100382.

Silva, J.P., Lana, C., Mazoz, A., Buick, I., Scholz, R., 2023. U-Pb Saturn: new U-Pb/Pb-Pb Data Reduction Software for LA-ICP-MS. Geostand. Geoanal. Res. 47 (1), 49–66.

Slama, J., Kosler, J., Condon, D.J., Crowley, J.L., Gerdes, A., Hanchar, J.M.,Whitehouse, M.J., 2008. Plesovice zircon—a new natural reference material for U–Pb and Hf isotopic microanalysis. Chem. Geol. 249 (1–2), 1–35.

Stacey, J.T., Kramers, I., 1975. Approximation of terrestrial lead isotope evolution by a two-stage model. Earth Planet. Sci. Lett. 26 (2), 207–221.

Stica, J.M., Zal´an, P.V., Ferrari, A.L., 2014. The evolution of rifting on the volcanic margin of the Pelotas Basin and the contextualization of the Paran´a–Etendeka LIP in the separation of Gondwana in the South Atlantic. Mar. Pet. Geol. 50, 1–21. https:// doi.org/10.1016/j.marpetgeo.2013.10.015.

Sun, S.S., McDonough, W.F., 1989. Chemical and isotopic systematics of oceanic basalts: implications for mantle composition and processes. Geol. Soc. Lond. Spec. Publ. 42 (1), 313–345.

Taylor, S.R., McLennan, S.M., 1985. The Continental Crust: Its Composition and Evolution, 312. Blackwell, Oxford. https://doi.org/10.1002/gj.3350210116.

Tedesco, J., Cagliari, J., Júnior, F.C., Girelli, T.J., Lana, C., 2019. Provenance and paleogeography of the Southern Parana´ Basin: Geochemistry and UPb zircon geochronology of the Carboniferous-Permian transition. Sediment. Geol. 393, 105539.

Teixeira, C.D., Girelli, T.J., Serratt, H., Chemale Jr., F., 2025b. Revisiting the Dom Feliciano Belt and surrounding areas–An integrated geophysical and isotope geology approach. Earth Sci. Rev., 105135 https://doi.org/10.1016/j. earscirev.2025.105135.

Teixeira, C.D., Girelli, T.J., Serratt, H., Oliveira, H.O.S., Cruz, M.F., Conti, B.,Chemale Jr., F., 2025a. Paleogeographic significance of unknown hyperextended continental crust in South Atlantic conjugated margin. Geosci. Front. 16 (1), 101934. https://doi.org/10.1016/j.gsf.2024.101934.

Torsvik, T.H., Cocks, L.R.M., 2013. Gondwana from top to base in space and time. Gondwana Res. 24 (3–4), 999–1030. https://doi.org/10.1016/j.gr.2013.06.012.

Veevers, J.J., 2012. Reconstructions before rifting and drifting reveal the geological connections between Antarctica and its conjugates in Gondwanaland. Earth Sci. Rev. 111 (3–4), 249–318. https://doi.org/10.1016/j.earscirev.2011.11.009.

Verma, O., Khosla, A., 2019. Developments in the stratigraphy of the Deccan Volcanic Province, peninsular India. Compt. Rendus Geosci. 351 (7), 461–476.

Vermeesch, P., 2018. IsoplotR: a free and open toolbox for geochronology. Geosci. Front.9 (5), 1479–1493.

Waichel, B.L., de Lima, E.F., Viana, A.R., Scherer, C.M., Bueno, G.V., Dutra, G., 2012. Stratigraphy and volcanic facies architecture of the Torres Syncline, Southern Brazil, and its role in understanding the Parana–Etendeka Continental Flood Basalt Province. J. Volcanol. Geotherm. Res. 215, 74–82.

Whittaker, Joanne, Afonso, C., Masterton, J., Müller, Sheona, Wessel, Dietmar, Williams, Paul, Maria, Simon Seton, 2015. Long-term interaction between mid-ocean ridges and mantle plumes. Nat. Geosci. 8, 25–2015. https://doi.org/10.1038/ NGEO2437.

Wiedenbeck, M., Hanchar, J.M., Peck, W.H., Sylvester, P., Valley, J., Whitehouse, M., Zheng, Y.F., 2004. Further characterisation of the 91500 zircon crystal. Geostand. Geoanal. Res. 28 (1), 9–39.

Wiedenbeck, M.A.P.C., Alle, P., Corfu, F.Y., Griffin, W.L., Meier, M., Oberli, F.V., Spiegel, W., 1995. Three natural zircon standards for U-Th-Pb, Lu-Hf, trace element and REE analyses. Geostand. Newslett. 19 (1), 1–23.

Will, T.M., Frimmel, H.E., Pfaender, J.A., 2016. Mo¨we Bay Dykes, Northwestern Namibia: Geochemical and geochronological evidence for different mantle source regions during the cretaceous opening of the South Atlantic. Chem. Geol. 444, 141–157.

Winter, W.R., Jahnert, R.J., França, A.B., 2007. Bacia de campos. Boletim de Geociências da PETROBRAS 15 (2), 511–529.

Wu, G., Wo¨rner, K.P., Jochum, B., Stoll, K. Simon, Kronz, A., 2019. Geostand. Geoanal. Res.

Zhou, H., Hoernle, K., Geldmacher, J., Hauff, F., Homrighausen, S., Garbe-Scho¨nberg, D., Jung, S., 2020. Geochemistry of Etendeka magmatism: Spatial heterogeneity in the Tristan-Gough plume head. Earth Planet. Sci. Lett. 535, 116123.

Zindler, A., Hart, S., 1986. Chemical geodynamics. In: IN: Annual Review of Earth and Planetary Sciences, 14. Annual Reviews, Inc, Palo Alto, CA, pp. 493–571. Volume 14 (A87–13190 03–46).

4 Article 2

The article presented in this chapter is a continuation of the first, which set the geological context of this research and makes a characterization of the basalts (that is, the main H_2 source in the region); it addresses the hydrogen geology of this environment. However, once the U-Pb failed to constrain the basalts' age in the first article, a new attempt was made to age the rocks again using the Ar/Ar system, which allowed for the completion of objective II) Constrain the ages and magmatic sources of the SDRs and related volcanic rocks in the study area. This research also addressed the specific objectives III) Develop a geometrical model of the Pelotas Basin based on seismic interpretation. IV) Construct a regional-scale thermal model for the Pelotas Basin. And V) Identify potential H_2 source rocks, reservoirs, and cap rocks within the Pelotas Basin and propose an integrated model for assessing its hydrogen potential, including implications for other Volcanic Passive Margins. As it was developed collaboratively, I hereby specify the contributions of each participant to enable the PhD committee to evaluate my individual work accurately.

Henrique Serratt (PhD Candidate): Developed the geological concept for the region, supported by the interpretation of seismic and geochemical data. Also constructed a thermal model for the study area and performed calculations to quantify both hydrogen sources (including thermogenesis, radiolysis, Fe^{2+} oxidation, etc.) and potential sinks. They were also responsible for writing the manuscript and creating figures.

Adalene Moreira Silva (UnB), Laurent Geoffroy(UBO), and Farid Chemale Jr.(UNISINOS): PhD supervisors. Provided conceptual guidance, supervised the research process, and conducted the final manuscript revision. They also secured the necessary resources and institutional support.

Matheus Fernandes da Cruz (UNISINOS): Conducted seismic well-tie correlations and petrophysics calculations, assisted with the figures.

Tiago Jonatan Girelli (UNISINOS),Wenbei Shi (UCAS), and **Peng Peng (UCAS)**: performed the Ar/Ar analysis.

Marcos Klunk (UNISINOS), Chemical models validation.

Bruno Conti (ANCAP): Representative of the Uruguayan government in the UNISINOS cooperation agreement. Facilitated access to data and samples from Uruguay and validated geological descriptions related to the Uruguayan margin.

Natural H_2 potential in mature Volcanic Passive Margins

Abstract

Natural H_2 potential in Volcanic Passive Margins: The Pelotas Basin case

Abstract

Volcanic passive margins are the most common type of passive margin. However, this environment was never studied in terms of hydrogen geology. This research evaluates the potential of the natural hydrogen (H_2) system in the Pelotas Basin, which is developed above a volcanic passive margin in the South Atlantic. It evaluates how prospective these areas are. For that purpose, we integrated an extensive dataset, including 448 2D seismic lines, well logs, and provided new geochemical and $^{40}Ar/^{39}Ar$ geochronological data to model the H_2 sources and sinks in the region. The results indicate immense H_2 generation potential, with Fe^{2+}-bearing mineral oxidation being the most significant source (>10^{12} t - metric tonne), followed by magmatic degassing (>10^{10} t), thermogenic production from organic matter (>10^{10} t), radiolysis (>10^{10} t), and fractures (>10^{9} t). However, new $^{40}Ar/^{39}Ar$ ages (~128–76 Ma) suggest that the main H_2-generating hydrothermal events occurred early in the basin's history (128-76 Ma), which makes the Cretaceous reservoirs rocks the most likely to host economic H_2 occurrences. Petrophysical analysis found no evidence of current H_2 accumulations, although it could be a methodological issue. The basin also contains massive H_2 sinks, including sulfur-rich marine sediments (>10^{11} t) and extensive microbial communities, as indicated by a 45,000 km² biological origin gas hydrate zone. We conclude that, despite its vast source potential, the timing and the geological and biological sinks limit the Pelotas Basin economic H_2 potential to Cretaceous rocks.

3.5 Introduction

Hydrogen gas has been identified as a key element in the energy transition (Kovač et al., 2021). There are two primary methods of producing low-CO_2 hydrogen gas. The first method is called Green Hydrogen, which is hydrogen gas produced by hydrolysis using low-carbon energy sources (Kourougianni et al., 2024). The energy sources could be wind, solar, or hydro. Regardless of the source, green hydrogen is always a way to store energy. On the other hand, natural hydrogen (also known as white hydrogen) can be a source of energy, similar to oil and gas. Natural hydrogen can be directly pumped from underground rocks (e.g., in the case of Mali - Prinzhofer et al., 2018). In this way, green hydrogen and natural hydrogen are distinct paradigms; one is a means of storing energy, while the other is a means of producing energy. Of course, both have more applications than their energetic use, such as in fertilizers and the chemical industry.

The occurrence of natural hydrogen is recorded in almost all geological settings, although it is mainly found in low volumes (Zgonnik, 2020). Nevertheless, most of these occurrences are related to five natural phenomena that can produce H_2 as a direct product or byproduct. These are: I) mineral alteration resulting from rock-water interactions (Berndt et al., 1996; Smith et al., 2005; Worman et al., 2016; Murray et al., 2020; Truche et al.,2020; Worman et al.,2020; Zgonnik, 2020; Boreham et al., 2021). II) Overmaturation of organic matter (Smith et al., 2005; Zgonnik, 2020; Boreham et al., 2021; Mahlstedt et al., 2022; Horsfield et al.,2022; Serratt et al., 2024); III) Hydrogen gas degassing from the mantle (Zgonnik, 2020); IV) Radiolysis (Bouquet et al., 2017; Boreham et al., 2021; Zgonnik, 2020); V) H_2 produced by microorganisms (Dowaidar, 2025). If we consider all these kinds of possibilities of hydrogen production, it is difficult to think of a geological environment that cannot produce H_2. However, economically viable hydrogen gas reservoirs such as the Mali case are rare (Prinzhofer et al., 2018). This observation suggests that preserving hydrogen could be more relevant than producing it.

The USGS (Gelman et al., 2025) notes that rocks from the East Coast Magnetic Anomaly (ECMA) have the potential to be a source rock for a hydrogen system. That raises questions about whether all mature volcanic passive margins could host potential hydrogen reservoirs. To evaluate this, we investigated the Pelotas Basin region in the South of Brazil and Uruguay. Previous research in this region, focusing on H_2 prospection in southern Brazil (Serratt et al., 2024) and Uruguay (Sequeira et al., 2025), was limited to onshore regions. To understand the potential of the offshore Pelotas Basin as a host for a hydrogen system, we analyzed seismic lines to provide the first integrated isopach maps (south Brazil and Uruguay) and calculated the volume of sedimentary rocks. We estimated the volume of Seaward Dipping Reflectors (SDRs) and associated volcanic rocks using previously published data. We provided new geochemical data for the basalts and sediments, analyzing them in conjunction with previously published data. We provide new $^{40}Ar/^{39}Ar$ ages for the basalts. We reviewed three wells with recorded neutron logs to evaluate the presence of H_2 in the region. We did not find any direct evidence of H_2 accumulation, although we observed both massive H_2 production and massive H_2 sinks potential. The main issues related to basins in VPM are the timing of the H_2 production and the sulfur related sinks, (potential) hydrocarbons, cap rock fractures, and microbial content on the sedimentary section, which could be the main challenge for H_2 accumulations.

3.5.1 Geological settings

The Pelotas Basin (PB) developed along a volcanic passive margin (VPM) situated between the Santos and Punta del Este basins (Figure 4-1). The sedimentation occurred over a heterogeneous basement comprising the Phanerozoic Paraná Basin and the Neoproterozoic Dom Feliciano Belt (Dias et al., 1994; Bueno et al., 2007; Holz et al., 2010; Conti et al., 2017; Teixeira et al., 2025a; Teixeira, 2025b; Serratt et al., 2025). The exact age of breakup at this location is an ongoing debate; magnetostratigraphy has been employed to constrain the age of breakup basalts (e.g., Rabinowitz and LaBrecque, 1979; Moulin et al., 2010; Chauvet et al., 2021), Serratt et al. (2022) questioned the accuracy of this method, as the regional volcanic sequences represent a prolonged stacking period. Furthermore, previous U-Pb zircon ages from these basalts failed to constrain the magmatic age; the recovered grains were not primary volcanic crystals but were instead inherited from the Dom Feliciano Belt or detrital zircons associated with peperites (Serratt et al., 2025). Although compiled K-Ar and $^{40}Ar/^{39}Ar$ data indicate volcanic ages ranging from 125.3 ± 0.7 to 75 ± 0.8 Ma, these results exhibit significant stratigraphic inconsistencies (Gordon & Mohriak, 2015). Consequently, Serratt et al. (2025) proposed that magmatism ceased at 113.2 ±0.1 Ma by integrating the Gordon and Mohriak (2015) dataset with paleogeographic correlations from Chauvet et al. (2021).

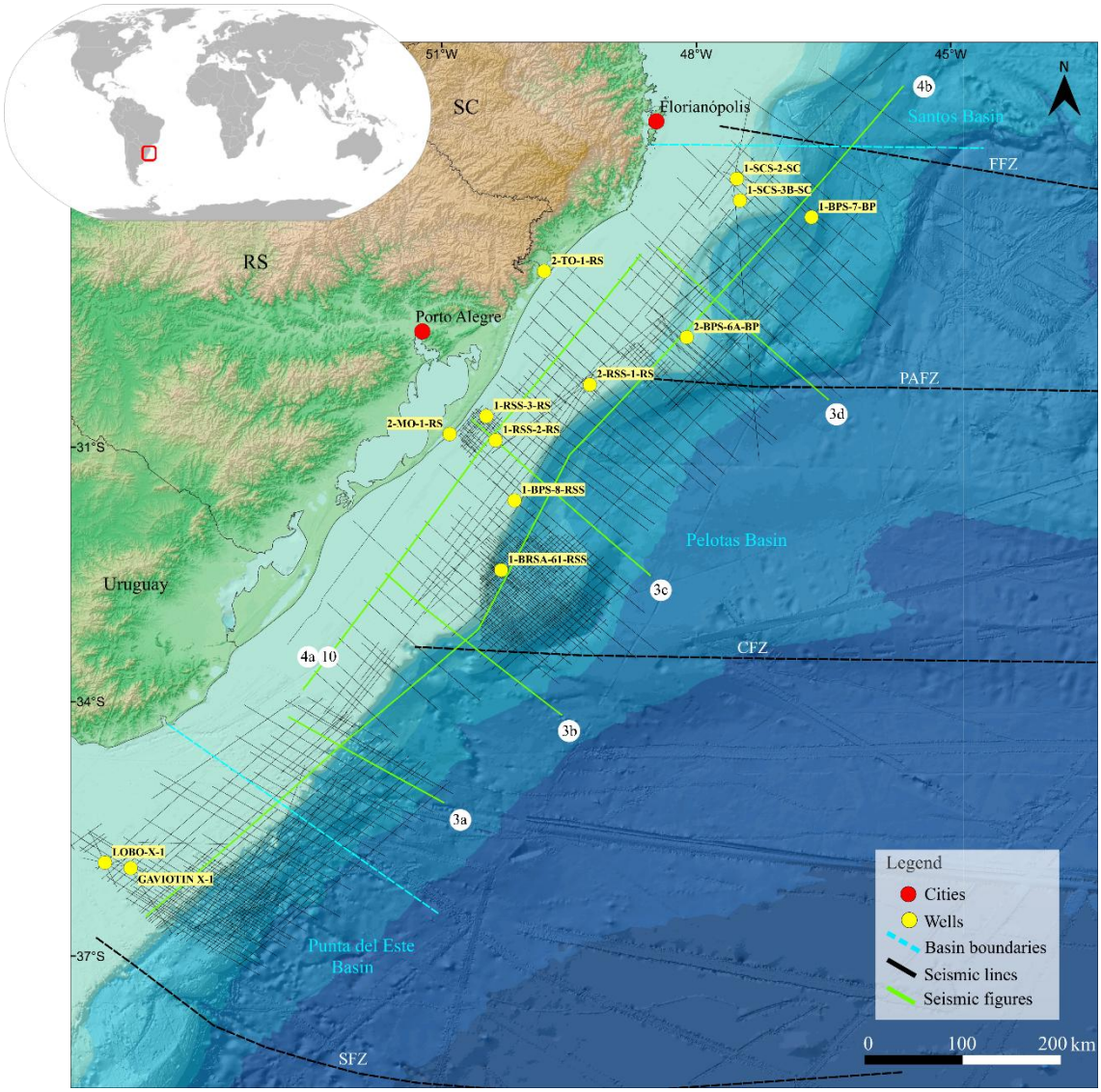

Figure 4-1. Study area location map, showing the position of wells and seismic lines

The sedimentation of the rift stage of the PB is recorded by the Cassino Formation (Figure 4-2), as identified in well 1-RSS-3 (Dias et al., 1994; Bueno et al., 2007). This unit comprises conglomerates and siltstones deposited within half-grabens in the basin's proximal section, interpreted as progradational alluvial fans extending from the flexural border toward lacustrine depocenters (Bueno et al., 2007). These sedimentary rocks overlie the basalts of the Imbituba Formation, the oldest strata within the basin (Bueno et al., 2007; Serratt et al., 2022). Alternatively, some authors (Gordon & Mohriak, 2015; Serratt et al., 2025) suggest these volcanic rocks may belong to the Serra Geral Group of the Paraná Basin. Stratigraphically

above both the Imbituba and Cassino formations are the Curumim Formation volcanics (Figure 2), which are restricted to the Torres Arch region between the Florianópolis and Porto Alegre fracture zones (Bueno et al., 2007; Serratt et al., 2025). This magmatic event constitutes a sequence up to 17 km thick (Harkin et al., 2020). Once the thickness of the PB volcanic pile is inversely proportional to the drift-stage accommodation space (Cassel et al., 2024), the northern sector of the basin contains the thinnest sedimentary package. Furthermore, the Torres Arch acted as a structural barrier that delimited the Ariri Formation evaporites (equivalent to the Santos Basin salt) to the northern flank of the structure.

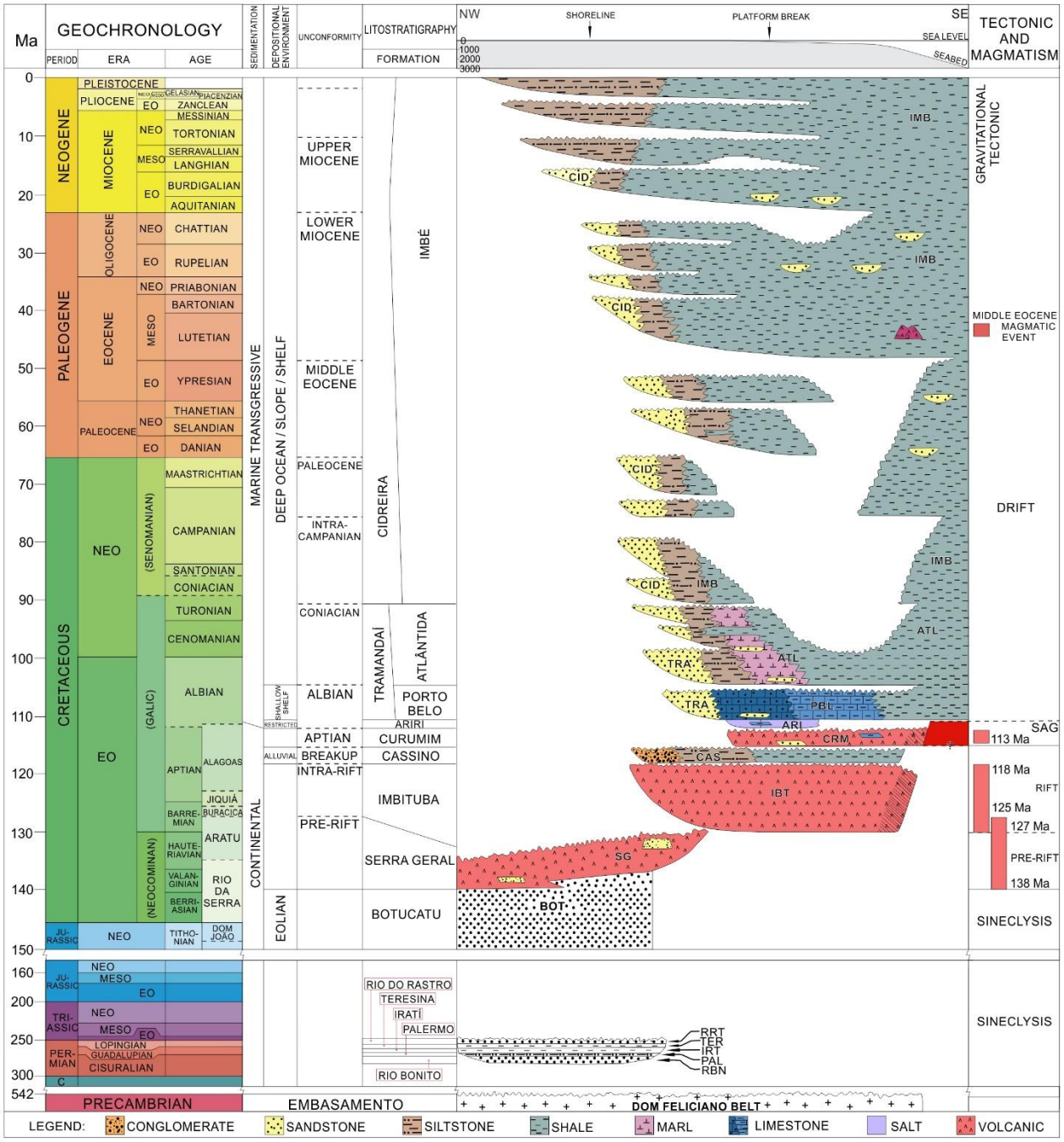

Figure 4-1. Pelotas Basin stratigraphic chart (modified from Bueno et al., 2007).

Five distinct formations represent drift-stage sedimentation in the Pelotas Basin (Bueno et al., 2007). The sequence initiates with the Albian Porto Belo Formation (Figure 4-2), which is interpreted as a mixed shallow-shelf environment deposited atop the Torres Arch. Within the Albian, an unconformity delimits the top of the Porto Belo strata, signaling the onset of marl and mudstone deposition of the Atlântida Formation (Figure 4-2). During this interval, proximal

sedimentation is recorded by the siliciclastic rocks of the Tramandaí Formation (Figure 4-2). On the southern flank of the Torres Arch, the Porto Belo units overlie the Curumim Formation volcanics. By the end of the Turonian, the proximal Tramandaí deposits were succeeded by those of the Cidreira Formation (Figure 4-2). Concurrently, in distal settings, the Atlântida Formation was overlain by the interbedded shales and siltstones of the Imbé Formation (Figure 2), a depositional regime that continues to the present day.

Previous research (Cassel et al., 2022) identified significant shifts in the basin's depocenters. The initial depocenter was located within the Mostardas Low graben; however, it migrated southward during the Chattian, a move linked to the uplift of the Eastern Cordillera along the western margin of South America. This subsequent depocenter consists of a thick, shale-dominated succession known as the Rio Grande Submarine Fan or Rio Grande Cone Megaslide Complex (Tagliaro et al., 2024), formerly referred to as the Rio Grande Cone (Martins et al., 1984). The deposition of the Rio Grande Cone Megaslide Complex initiated during the Miocene (Zerfass et al., 2014; Tagliaro et al., 2024) and primarily comprises mudstones and siltstones, with subordinate sandstones (Chemale et al., 2021; Maraschin et al., 2024).

Sediments within the Rio Grande Cone Megaslide Complex were primarily derived from the La Plata River system and central and southern Argentine rivers. This material was transported northward over approximately 1000 km via longshore drift and ocean currents (Chemale et al., 2021; Rizzi et al., 2022; Cassel et al., 2022). Subordinate sediment input was also provided by the Camaquã and Jacuí river systems, which drain the Uruguayan–Rio Grande do Sul Shield and the Paraná Basin (Martins et al., 1984; Urien & Martins, 1978; Zouain, 1986; Castillo-Lopez, 2009; Chemale et al., 2021; Rizzi et al., 2022).

The Rio Grande Cone Megaslide Complex hosts a gas hydrate stability zone covering approximately 45,000 km², delimited at its base by a prominent Bottom-Simulating Reflector

(BSR) (Sad et al., 1998; Miller et al., 2015; Tagliaro et al., 2024). Although this BSR indicates widespread gas in the system, all samples analyzed to date have been identified as biogenic in origin (Miller et al., 2015).

3.5.2 Materials and methods

To investigate potential natural hydrogen (H_2) systems in the Pelotas Basin, the methodology was structured into two primary phases. The first phase focuses on regional characterization, which involves constructing a geometric basin model using seismic reflection data, analyzing petrophysical logs, and generating new geochemical data. This stage also includes compiling existing datasets to develop a regional thermal model. The subsequent phase, H_2 system evaluation, consists of an integrated analysis of these results to assess the fundamental components of the H_2 system, including potential source rocks, migration pathways, reservoirs, seals, and sinks.

3.5.2.1 Regional characterization

Geometrical modeling

This section details the procedures employed to model the geometric framework, thermal regime, lithological composition, and petrophysical data of the Pelotas Basin. The workflow integrates standard geophysical and geochemical analyses with legacy and regional datasets.

Geometric modeling of the Pelotas Basin utilized a comprehensive regional dataset comprising 112 2D Post-Stack Time Migrated (PSTM) seismic lines from Uruguay, provided by the Administración Nacional de Combustibles, Alcoholes y Portland (ANCAP), and 336 2D PSTM lines from Brazil, provided by the Agência Nacional do Petróleo, Gás Natural e Biocombustíveis (ANP). The survey area encompasses the Pelotas Basin, with a buffer zone

extending southward into the Punta del Este Basin and northward toward the southern Santos Basin. Additionally, data from 12 wells in the Pelotas Basin and two in the Punta del Este Basin were integrated (Figure 4-1). This study builds upon the seismic-to-well tie established by Serratt et al. (2025), expanding the interpretative framework with five additional wells: 1-BPS7-BP, 2-RSS-1-RS, 1-RSS2-RS, 1-BPS-8-RSS, and 1-BRSA-61-RSS. Detailed well-tie procedures for these new data points are provided in Supplementary Material 1.

Seismic analysis of the sedimentary succession (Figures 4-3 and 4-4) was performed by mapping six key stratigraphic surfaces: (I) the seafloor; (II) the top of the Paleogene (Chattian); (III) the top of the Thanetian; (IV) the top of the Cretaceous (Maastrichtian); (V) the top of the Turonian; and (VI) the model base—a diachronous surface encompassing volcanic rocks, Paleozoic strata of the Paraná Basin, and the granitic basement of the Dom Feliciano Belt. The seafloor was identified as the first prominent positive-amplitude reflector on the seismic profiles. Chronostratigraphic control for these surfaces was established using biostratigraphic markers documented in the literature, which guided the identification of horizons in the following wells: 1-SCS-3-SC (T at 3720 m, Gomide, 1989; C at 2921 m, Guerra et al., 2012; TH at 2669 m, Koutsoukos, 1982; P at 1694 m, Koutsoukos, 1982); 1-SCS-2-SC (T at 3490 m, C at 2633 m, TH at 2610 m, and P at 1450 m; all from Gomide, 1989); 1-BPS-7-BP (T at 5820 m, C at 4675 m, TH at 4428 m, Zerfass, 2009; P at 3266 m); 2-BPS-6A-BP (T at 4077 m, C at 3897 m, TH at 2619 m, Zerfass, 2009; P at 1674 m, Zerfass et al., 2014); 1-RSS-2-RS (T at 4304 m, Guerra et al., 2012; C at 4026 m, Guerra et al., 2012; TH at 2763 m; P at 1450 m); 2-RSS-1-RS (C at 3899 m, Guerra et al., 2012; TH at 3131 m, Gomide, 1989; P at 1806 m, Gomide, 1989); 1-RSS-3-RS (T at 1740 m, Fontana, 1996; C at 1930 m, Fontana, 1996; P at 1015 m, Gomide, 1989); 1-BPS-8-BP (P at 2497 m); Raya-X-1 (P at 5600 m, based on in-house biostratigraphy of the nannofossil *Reticulofenestra filewiczii*); and Gaviotin X-1 (C at 1829 m, Daners and Guerstein, 2004; TH at 1695 m, Novo, 2023; P at 1219 m, Novo, 2023). The model

base comprises the top of the basalts, the Paraná Basin sedimentary section, and the underlying plutonic and metamorphic rocks of the Dom Feliciano Belt. Volcanic units were delineated based on lithological logs from wells 1-RSS-3-RS (3500 m), 2-BPS-6A-BP (5368 m), 1-SCS-2-SC (4447 m), 1-SCS-3-SC (4670 m), and Lobo-1 (2200 m). Additionally, a marker at 3629 m was used to track the Paraná Basin section in the Gaviotin X-1 well (Serratt et al., 2025), while the top of the crystalline basement was interpreted based on the identification of chaotic seismic facies.

Seismic interpretation was initiated at well locations and subsequently propagated across the entire study area. Surface interpolation was performed using the Petrel™ (SLB) convergent interpolation algorithm (2 x 2 km grid increment; pre-processed via smooth cubic spline refinement of polygons), yielding time-structure maps for all interpreted horizons (Supplementary Material 2). A regional velocity model was then constructed by integrating the time-surfaces with average velocity data derived from the wells (Supplementary Material 3). Using the Petrel™ Domain Conversion Module, this velocity model enabled depth conversion of these surfaces (Supplementary Material 4), allowing the generation of isopach maps for the target intervals.

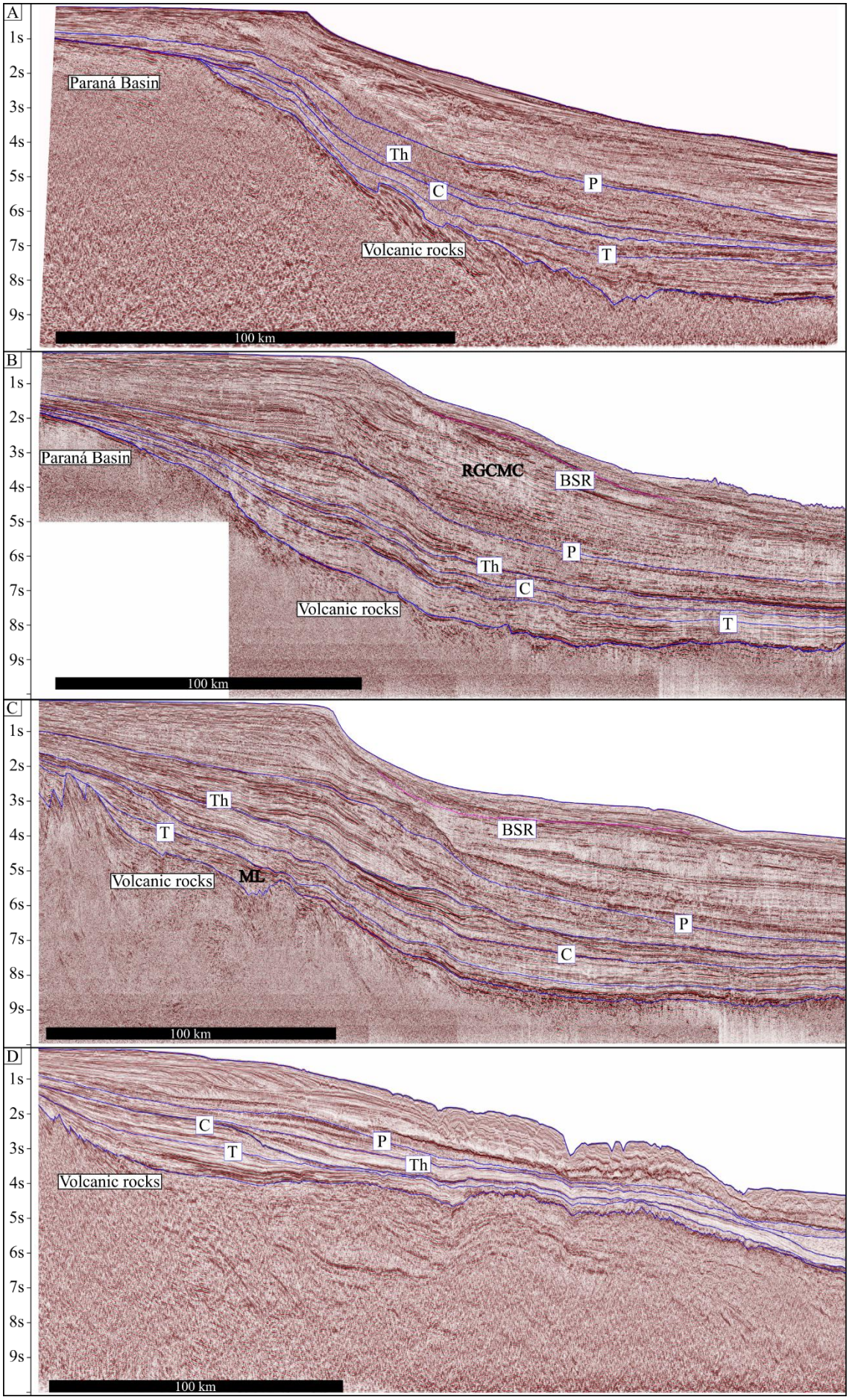
A
1s
2s
3s
4s
5s
6s
7s
8s
9s
Paraná Basin
Th
C
P
Volcanic rocks
T
100 km
B
Paraná Basin
RGCMC
BSR
P
Th
C
Volcanic rocks
T
100 km
C
Th
T
BSR
Volcanic rocks
ML
P
C
100 km
D
C
T
P
Th
Volcanic rocks
100 km

Figure 4-3. Dip-oriented seismic lines in the time domain, with NW-SE orientation showing the analyzed surfaces, the top of Turonian (T), top of Cretaceous (C - or Maastrichtian), top of Thanetian (Th), and the top of Paleogene (P - or Chattian). The BSR-Bottom Simulating Reflector (pink line) is a gas hydrate zone of biological origin (Miller et al., 2015). Could H_2 feed part of the extensive bacterial community of the Pelotas Basin? RGCMC - Rio Grande Cone Megaslide Complex, ML - Mostardas Low. A) Southmost of PB (Uruguay); B) South region of PB, south of RGCMC; C) Central region of PB, cutting the ML; D) North region of PB (Torres Arch).

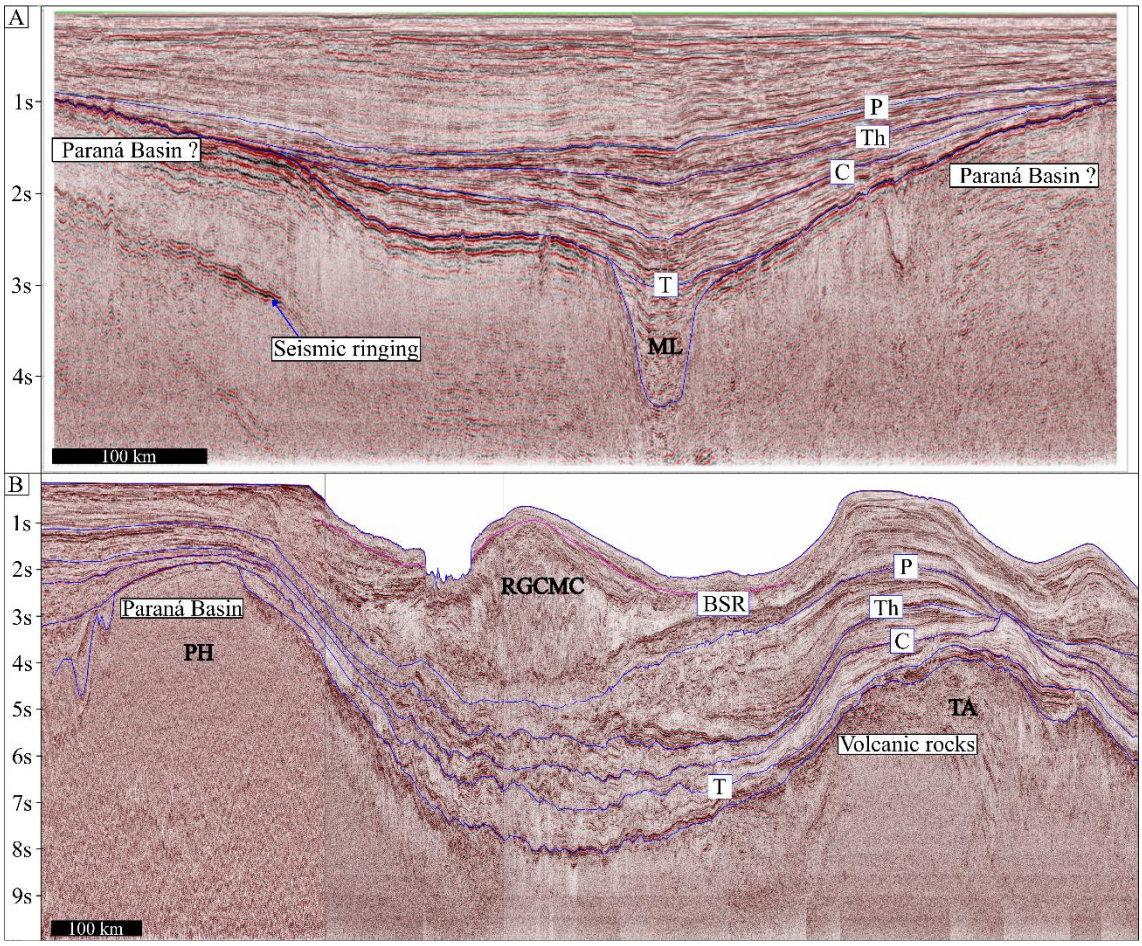

Figure 4-2. Along strike seismic lines composition, in the time domain, with SW-NE orientation showing the analyzed surfaces, the top of Turonian (T), top of Cretaceous (C - or Maastrichtian), top of Thanetian (Th), the top of Paleogene (P - or Chattian), and the BSR-Bottom Simulating Reflector (pink line). A) The proximal section shows the ML - Mostardas Low; B) The distal section from Punta del Este to Santos basins shows all the PB extension and the three depocenter changes. We can observe PH-Polonio High, a granitic basement feature, and TA-Torres Arch, a volcanic structure formed during the early development of the Pelotas Basin, which is directly linked to the Walvis Ridge at the conjugate Margin (Serratt et al., 2025).

A first-order estimate of the volcanic rock volume was performed for this study. Due to velocity constraints in the deeper sections of the model, specifically regarding the SDRs and

the crystalline basement. Volcanic volumes were estimated by extracting data from seismic profiles published by Chauvet et al. (2021). The total volume was calculated by multiplying the mean cross-sectional area (derived from thickness and length measurements) by the basin's lateral along-strike extent. These thickness measurements were sampled at 10-km equally spaced intervals across seismic sections IV, V, and VI from Chauvet et al. (2021) (see Supplementary Material 5).

Petrophysical Analysis

A petrophysical investigation was conducted on all wells containing neutron porosity (NPHI) logs, which are considered the primary diagnostic tool for H_2 identification when direct gas analysis is unavailable (Maiga et al., 2023). This dataset includes wells 2-BPS-6-BP, 1-BPS-7-BP, and 1-BPS-8-BP (Figures 4 and 5). The petrophysical workflow followed a two-fold approach: the first stage involved evaluating porosity within data-bearing intervals, followed by a systematic assessment to identify the potential presence of H2 based on neutron log response.

Average porosity values for the intervals of interest were determined through a sequential petrophysical analysis of well log data, primarily utilizing Gamma Ray (GR) and Formation Density (RHOB) logs. The workflow consisted of three main stages. First, the shale volume (Vshale) was estimated for each depth interval. This process involved normalizing the raw GR log response to a dimensionless Gamma Ray Index (GR) using clean-sand and pure-shale baselines identified within the logged sections (Equation 1). A linear model was then applied, assuming a direct proportionality between the GR and shale content (Equation 2; Asquith & Gibson, 1983). Second, total porosity (ϕT) was derived from the RHOB log using the standard density-derived porosity equation, which accounts for the bulk density measured by the log relative to the assumed matrix and fluid densities (Equation 3; Serra, 1984, 1986). Finally, the effective porosity (ϕE), representing the interconnected pore volume, was

calculated by correcting the total porosity for the interpreted shale volume (Equation 4). All petrophysical modeling was performed using Techlog™ 2024 (SLB), and detailed porosity calculation records are available in the supplementary material 6.

$$I_{GR} = \frac{GR_{log} - GR_{min}}{GR_{max} - GR_{min}} \quad (1)$$

$$V_{shale} = I_{GR} \quad (2)$$

$$\phi_T = \frac{\rho_{ma} - \rho_{pb}}{\rho_{ma} - \rho_f} \quad (3)$$

$$\phi_E = \phi_T \times (1 - V_{shale}) \quad (4)$$

Where:

I_{GR} = Gamma Ray Index

GR_{log} = Gamma ray log

GR_{min} = Gamma ray log

GR_{max} = Gamma ray log

V_{shale}= Shale volume

ϕ_t= Total Porosity

ρ_{ma}= matrix density

ρ_b= formation density

ρ_f= fluid density

ϕ_E= Effective porosity

The identification of potential H_2 occurrences followed the petrophysical methodology proposed by Maiga et al. (2023). This approach relies on detecting a decrease in bulk density (ρ_b or RHOB) indicative of porosity filled with a low-density fluid, coupled with an anomalously high reading in the neutron porosity (ϕ_N or NPHI) log. This dual response results in a significant divergence on the NPHI-RHOB cross-plot, which is distinct from the conventional "gas crossover" typically observed in hydrocarbon-bearing reservoirs, where ϕ_N readings are characteristically low. The high apparent neutron porosity in H_2 systems is attributed to the high hydrogen atom concentration per unit volume (the Hydrogen Index, I_H) of molecular hydrogen under specific reservoir conditions. Given the absence of direct gas sampling, this log-based signature served as the primary proxy for H_2 detection (Figure 4-5).

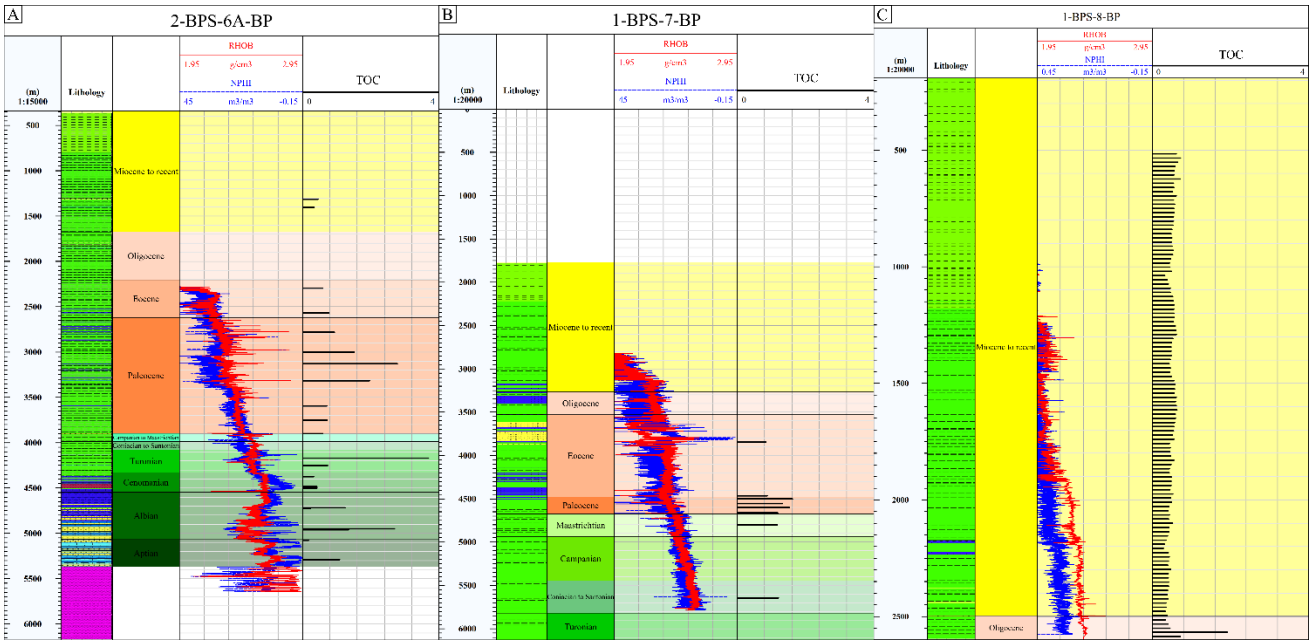

Figure 4-5. Well logs recording gamma ray (GR), caliper, density (RHOB), neutron porosity (NPHI), and total organic Carbon (TOC) recorded in the ANP wells: A)2-BPS-6A-BP; B)1-BPS-7-BP; C)1-BPS-8-BP.

Geochemical data

Total Organic Carbon (TOC) data were retrieved from the ANP public database (Figure 5). The wells previously selected for petrophysical analysis (2-BPS-6-BP, 1-BPS-7-BP, and 1-

BPS-8-BP) were utilized to investigate the distribution and quality of potential source rocks for natural hydrogen by over maturation of organic matter.

To evaluate the potential for H_2 generation via water-rock interaction, new geochemical data were acquired from five basalt core samples. This dataset, analyzed in conjunction with previously published data from Serratt et al. (2025), includes samples from the following offshore wells: 1-RSS-3 (3902 m); 2-BPS-6A-BP (5377 m and 6153 m); and 1-SCS-3B (4735 m and 5071 m). Major elements were analyzed by Inductively Coupled Plasma Optical Emission Spectrometry (ICP-OES), while trace elements were determined via inductively coupled plasma mass spectrometry (ICP-MS). The oxidation state of the basaltic rocks was characterized by measuring ferrous iron (FeO) content through volumetric titration, with ferric iron (Fe_2O_3) subsequently calculated by determining the difference from the total iron content (Fe_{total}).

A similar analytical procedure, excluding FeO quantification, was applied to 286 sedimentary drill cutting samples. These samples were obtained from three wells: 2-BPS-6A-BP (159 samples), 1-BPS-7-BP (90 samples), and 1-BPS-8-BP (37 samples). The geochemical characterization of these sedimentary units aimed to investigate H_2 production via water radiolysis and to identify potential H_2 sinks, particularly those related to sulfur minerals. The complete geochemical dataset generated for this study is provided in Supplementary Material 7.

Ages

$^{40}Ar/^{39}Ar$ geochronology was performed on basalts from the basin floor to constrain the timing of initial magmatism. The analyzed samples correspond to those previously characterized for Nd and Sr isotopes by Serratt et al. (2025), retrieved from the following locations: Well 1-RSS-3-RS (3555.10 m and 3905.20 m); Well 2-BPS-6A-BP (6154.6 m and 6155 m); and Well 1-SCS-3B-SC (4732 m). For sample preparation, aliquots were wrapped in

aluminum foil to form wafers and stacked in quartz vials alongside the international YBCs sanidine standard (29.286 ± 0.045 Ma; Wang et al., 2014). Neutron irradiation was conducted for 75.6 hours at the Min Jiang Testing Reactor (MJTR), Nuclear Power Institute of China (NPIC), Sichuan. $^{40}Ar/^{39}Ar$ analyses were performed using a CO_2 laser (Teledyne Photon Machines Fusion 10.6) coupled with a Noblesse mass spectrometer at the Institute of Geology and Geophysics of the Chinese Academy of Sciences (IGGCAS). The applied Ca and K correction factors were: $[^{36}Ar/^{37}Ar]Ca = 0.000230 \pm 0.0000008$; $[^{39}Ar/^{37}Ar]$ Ca = 0.00066 ± 0.0000010; and $[^{40}Ar/^{39}Ar]\_K = 0.00788 \pm 0.000258$. Ages were calculated using the decay constant of 5.543 X 10^{-10} yr^{-1} (Steiger and Jäger, 1977), with all uncertainties quoted at the 2σ level. Plateau ages were defined by three or more contiguous steps, accounting for more than 50% of the total ^{39}Ar released and yielding concordant ages at a 95% confidence level. Reported age uncertainties are internal, incorporating analytical errors and uncertainties related to blanks, interference factors, mass discrimination, and J-values; the error on the total decay constant was not propagated. Data processing was conducted using ArArCALC (Koppers, 2002). The complete geochronological dataset is presented in Supplementary Material 8.

Thermal Model

A regional geothermal gradient was established using modeled seafloor temperatures and Bottom-Hole Temperatures (BHT) from exploratory wells. For the Brazilian sector, BHT data were retrieved from the ANP (wells 1-BRSA-61, 1-SCS-2-SC, 2-BPS-6A-BP, 1-SCS-3B, and 1-RSS-3-RS - Figure 1). These BHTs were corrected using the Bullard (1947) or Lachenbruch and Brewer (1959) methods, with specific procedures for each well detailed in Supplementary Material 9. Additionally, data for the Raya and Gaviotin wells in Uruguay (Figure 1) were sourced from Novo et al. (2023). The seafloor temperature (Tsb) was modeled using an empirical equation derived from a logarithmic regression ($R^2 = 0.9263$) between deep-water temperature measurements from the World Ocean Atlas (WOA 2018) and their

corresponding depths. This model considered all data points within the Pelotas Basin regional extent (26.5° to 37.5°S; 43.5° to 52.5° W; see Supplementary Material 10). Accordingly, T_{sb} is expressed as a function of depth (D) in equation (5):

$$T_{sb} = -4.071 \ln(D) + 34.556 \quad (5)$$

The regional geothermal gradient was then calculated via linear regression of the integrated temperature dataset (corrected BHTs and modeled Tsb) against depth. Using the seafloor as the zero-depth datum, the slope of this linear fit defines the constant geothermal gradient applied throughout this study.

3.5.2.2 H_2 system evaluation

The integrated datasets and models described in the previous sections served as the foundation for characterizing the potential natural hydrogen system of the Pelotas Basin. Following an exploratory framework analogous to conventional petroleum systems, the H2 play elements, including source rocks, migration pathways, reservoirs, seals, and sinks, were systematically evaluated. Given the limited existence of data and methods to evaluate natural hydrogen on volcanic passive margins, specific components were assessed qualitatively to establish a conceptual model for the region.

Sources

Potential sources for natural hydrogen systems are multifaceted and include mechanisms such as Fe(II) oxidation (Mayhew et al., 2013; Worman et al., 2016, 2020; Zgonnik, 2020; Boreham et al., 2021; Osselin et al., 2022), magmatic degassing (Hekinian et al., 1973; Worman et al., 2020), pyrite formation (Drobner et al., 1990; Rickard et al., 1997; Deville et al., 2023; Pasquet et al., 2023), tectonically induced H_2 generation (Worman et al., 2020), and radiolysis (Bouquet et al., 2017). Furthermore, H_2 may originate from organic matter

overmaturation (Mahlstedt et al., 2022; Boreham et al., 2023; Moretti et al., 2024) and biological processes (Dowaidar, 2025).

Experimental studies on kerogen types II and III indicate that organic-rich rocks can produce H_2 with a potential of 20mg H_2 / 1g TOC at temperatures between 220°C and 330°C (Mahlstedt et al., 2022). The total thermogenic H_2 potential was estimated using the following workflow:

1. TOC Averaging: Average TOC values were calculated for three stratigraphic intervals: Cretaceous, Paleocene, and Recent (Neogene to Quaternary).
2. Volume Calculation: The volume of sedimentary rocks within each unit was delineated within the 220°C to 330°C temperature range, based on the established regional thermal model.
3. Mass Estimation: Assuming a bulk sedimentary rock density of 2.4 g/cm³ (following Jones, 2007, for Mesozoic sandstones) and the average TOC for each period, the total TOC mass was estimated for these volumes.
4. Potential Inference: Finally, the 20mg H_2 / 1g TOC ratio (Mahlstedt et al., 2022) was applied to the estimated TOC mass to infer the total thermogenic H_2 potential.

The H_2 produced per unit of time by radiolysis in the whole volume of the basin, determined by seismic analysis, and assumed water saturated, was estimated following Atike 1985 equations (6 and 7) with parameters compiled by Bouquet et al. (2017):

$$P_{H2} = \sum_i (G_{H2,i} \sum_S D_{s,i}) \quad (6)$$

Where P_{H2} is the number of particles produced per unit of time per unit of volume

i is the radiation type (α,β,γ)

s is the radiogenic nuclide (^{40}K, ^{232}Th, ^{235}U, ^{238}U)

$G_{H2,i}$ is the radiation chemical yield of $H2$ in water for radiation type; we used the values compiled by Bouquet et al. (2017), presented in Table 4-1:

Table 4-1. values of radiation chemical yield ($G_{H2,i}$) by each Radiation (i) type (Harris & Pimblott, 2002; Lin et al., 2005; compiled by Bouquet et al., 2017).

Radiation (i)	Radiation chemical yield ($G_{H2,i}$) (Molecules/Joule)
α	6×10^{16}
β	3.7×10^{16}
γ	2.5×10^{16}

Ds,i is the radiation dose absorbed by water due to radiation type "i" emitted by radionuclide "s"; given by equation (8):

$$D_{s,i} = \frac{V \rho_r A_s \sum E_{i,s}}{\frac{1}{1-\phi} + \frac{\rho_r}{S_i + \rho_w + \phi}} \quad (7)$$

Where V is the volume of the analyzed body.

p_r is the rock density.

p_w is water density.

ϕ is the porosity.

S_i is the mass stopping powers of water to rock, given by Hofmann (1992) in Table 4-2.

Table 4-2. Data of mass stopping powers of water to rock (Hofmann, 1992).

Radiation (i)	Mass stopping powers of water to rock (S_i)
α	1.5
β	1.25

γ	1.14

$\sum E_{i,s}$ is the sum of the decay energy of the radionuclide "s" by emission of the radiation "i", defined by Blair et al. (2007), presented in Table 4-3.

Table 4-3. Values of E i,s, decay energy by each radiation type (i) by radionuclide (s) (Blair et al., 2007).

Radionuclide (s)	Radiation (i)	Decay energy (J/decay)
40K	α	0
	β	1.88×10^{-13}
	γ	2.51×10^{-14}
232Th	α	5.76×10^{-12}
	β	4.55×10^{-13}
	γ	3.6×10^{-13}
235U	α	5.45×10^{-12}
	β	1.67×10^{-12}
	γ	8.81×10^{-14}
238U	α	6.88×10^{-12}
	β	9.76×10^{-13}
	γ	2.73×10^{-13}

A_s is the activity of the radionuclide "s" given by equation (8).

$$A_s = \lambda \cdot N \qquad (8)$$

Where λ is the decay constant, which is related to half-life by the following equation (9).

$$\lambda = \frac{ln\,(2)}{t_{1/2}} \qquad (9)$$

Where $t_{(1/2)}$ was assumed as the values compiled by Bouquet et al. (2017) presented in Table 4.

Table 4. Radionuclides (s) half-life, Bouquet et al. (2017).

Radionuclide (s)	Half-life in years ($t_{(1/2)}$)
^{40}K	$1{,}25 \times 10^{9}$
^{232}Th	$1{,}4 \times 10^{10}$
^{235}U	$7{,}04 \times 10^{8}$
^{238}U	$4{,}46 \times 10^{9}$

Moreover, N is the Number of radionuclides “s” per kg of rock.

For this calculation, the average basin porosity from petrophysics was used. The amount of radionuclides was based on the whole-basin mass, determined by multiplying the volume of the basin, as measured by seismic data, by the sedimentary density (2.4g/cm³, Jones, 2007). The bulk content of K, U, and Th was determined by averaging the concentration of each element in the analyzed well cuttings. The abundance of each radionuclide was estimated by Haynes (2016). In that way, we assume 238U as 99.274% of the mass of U in the rocks and ^{235}U as 0.720%; ^{232}Th was assumed as 100% of Th; and ^{40}K was assumed as 0.012% of the mass of K in the rocks.

For a cumulative H_2 curve, we calculated an incremental production for every million years. The change in basin volume was determined by a volumetric sedimentation rate, as determined through seismic analyses and the stratigraphic ages analyzed.

The oxidation of Fe^{2+} bearing minerals is the most well-studied hydrogen-generation phenomenon. However, the most famous process is serpentinization; there is a range of processes related to Fe^{2+} oxidation to Fe^{3+} where H_2 is a byproduct (Smith et al., 2005; Marcaillou et al., 2011; Milesi et al., 2016; Worman et al., 2016; Worman et al.,2020; Zgonnik, 2020; Osselin et al., 2022). In this work, for a basin-scale estimate, we used the bulk Fe Total and Fe^{2+} content in volcanic rocks to determine a theoretical H2 production by this way. we

simplified H_2 production through Fe^{2+} oxidation using the FeO oxidation by water reaction, following the simplifications by Worman et al. (2016 and 2020). That implies a maximum potential of production given by the proportion of $2Fe^{2+}$ to $1H_2$ or 110.804g Fe^{+2} to 1g H_2 taken from the stoichiometry of the reaction (10).

$$2FeO\ (\text{in minerals}) + H_2O \rightarrow Fe_2O_3\ (\text{in minerals}) + H_2 \qquad (10)$$

This simplification was used to calculate H_2 in the basalts, assuming a primary magmatic $Fe^{3+}/\Sigma Fe$ ratio of 0.143 (Zhang et al.,2018). In that way, all Fe^{3+} values higher than those observed in geochemistry imply that the aforementioned proportion generated H_2.

H_2 yields from magmatic degassing and H_2 related to faults and fracturing were estimated using the constants compiled by Worman et al. (2020). For magmatic degassing, a value of 3.1×10^{10} mol H_2/km^3 of basalt was adopted, while generation via rock fracturing was calculated assuming a yield of 1×10^9 mol H_2/km^3 of basalt. Other potential mechanisms, such as anaerobic microbial fermentation (Dowaidar, 2025) and radiolysis within igneous units, were qualitatively recognized as potential contributors to the system. However, these processes were not quantified in the current study as the available dataset precluded a robust numerical evaluation of their specific yields. There is no disseminated pyrite on the basalts (serratt et al., 2025); its occurrence should be limited in the stokworks region (irrelevant if compared with the size of the magmatism). In that way, we did not calculate the H_2 related to volcanic pyrite (Worman et al., 2020). In the same way, the sedimentary pyrite is shallow and bacteria-related (Sekerci et al., 2025), and the whole H_2 produced by it should leak into the atmosphere or be consumed by other microorganisms. In that way, we considered it net-zero H_2.

Reservoirs

Lithologies characterized by high porosity and permeability are essential for the potential economic exploitation of natural hydrogen, following an exploratory logic analogous to conventional petroleum systems. Accordingly, this study identified regions with high

effective porosity through the aforementioned petrophysical evaluation. To complement these results, a stratigraphic framework was established by integrating geochronological data and lithological descriptions from the literature, enabling the delineation of potential reservoir units across the basin.

Seals

Sills (Maiga et al., 2023, 2024), evaporites (Ahmadpour and Gholami, 2024; Gelman et al., 2025), and shales (Iyare et al., 2025) have been identified as the primary sealing lithologies within H_2 systems. In the Bourakébougou field (Mali), a dolerite sill acts as the main seal (Maiga et al., 2024); consequently, similar igneous units constitute a critical focus of this investigation. Additionally, evaporites and fine-grained siliciclastics are expected to function as effective stratigraphic barriers (Ahmadpour and Gholami, 2024; Gelman et al., 2025; Iyare et al., 2025). The presence and integrity of these units in the Pelotas Basin were evaluated through an integrated review of the basin's lithostratigraphy (Serratt et al., 2022, 2025) and detailed seismic attribute analysis to confirm their lateral continuity and structural geometry.

Sinks

The analysis of H_2 sinks in this study focuses on the primary mechanisms identified in the literature, accounting for the inherent uncertainties in basin-wide quantification. The H_2 sink associated with hydrocarbon formation, or contact with existing accumulations, was considered a potential sink (Mahlstedt et al., 2022). This evaluation requires the assumption that the Pelotas Basin hosts, or has produced, hydrocarbons in significant volumes. While the precise distribution (if it exists) of hydrocarbons in the basin remains a subject of ongoing exploration, it is recognized that petroleum systems could act as major H_2 consumers, particularly during upward migration of the H_2. Other potential sinks, such as CO_2 hydrogenation (Prinzhofer et al., 2018), diffusive leakage, and microbial consumption, also remain difficult to quantify without data and were thus treated as qualitative uncertainty factors.

On the other hand, the retention capacity of basalts was quantified based on the framework by Worman et al. (2020), estimated at 1.7×10^{10} mol H_2/km^3 (3.40 × 10^4 t H2/km3). Furthermore, sulfur minerals were identified as a potential sink through thermochemical or biological sulfate reduction (Ahmadpour & Gholami, 2024). Given the predominantly marine nature of the Pelotas Basin sediments, it is assumed that sulfur is primarily hosted in pyrite (Fes2), which becomes unstable and reacts with hydrogen within the 90-180°C temperature range (Truche et al., 2010; Ahmadpour & Gholami, 2024). Accordingly, bulk sulfur content from sedimentary well-cutting samples was used to estimate pyrite sink capacity via the stoichiometric relation (11):

$$FeS_2 + (1\text{-}X)H_2 \rightarrow FeS_{1+X} + (1\text{-}X)\ H_2S \text{ for } (0 \leq X < 0.125) \quad (11)$$

For these calculations, the value of X was assumed to be 0 representing a consumption ratio of 1g of H_2 for each 32.065 g of sulfur. This evaluation was applied strictly to lithologies currently within the 90-180° C thermal window, as well as those that historically passed through this temperature interval.

3.5.3 Results

The results of this study are structured according to the aforementioned methods. The results are organized into two: 1) Regional Characterization: This section provides the geological baseline required for the study.2) H_2 system evaluation: Building upon the regional data, this part provides an assessment of the natural hydrogen system, presenting the analysis of sources, reservoirs, cap rocks, and sinks individually.

3.5.3.1 Regional Characterization

This section is dedicated to more concrete results using well-established methods. These methods include seismic analysis, thermal modeling, whole-rock geochemistry, TOC data compilation, and new $^{40}Ar/^{39}Ar$ data.

Seismic analysis

Our seismic analysis reveals a more complex depositional history for the Pelotas Basin than previously reported (Figure 4-6). Through seismic analyses, we observed two depocenter shifts in the Pelotas Basin, more than previously reported by Cassel et al. (2022). We estimated the total deposition as 11.37 km (Figure 4-6a). The deposition between the base of the model and the Turonian (89.8 Ma) was concentrated in the southern part of the basin. This early phase accumulated up to 4.64 km of sediment, foreshadowing the location of the future Rio Grande Cone Megaslide Complex (Figure 4-6f). This interval records a volume of 3.41×10^5 km^3 of sediment (ignoring the Punta del Este Basin). The basin maintains its depocenter during the Turonian (89.8 Ma)- Maastrichtian (66 Ma) interval, with a maximum thickness of 2.28 km during this period (Figure 6e). This interval records a volume of 1.58×10^5 km^3 of sediment. The first major shift occurred during the Maastrichtian(66 Ma)-Thanetian (59.24 Ma) interval. During this time, the primary depocenter migrated northwestward to a position offshore of the Mostardas Low, where a maximum of 2.63 km of sediment was deposited (Figure 6d). This interval records a volume of 1.22×10^5 km^3 of sediment. The depocenter continues to migrate northwestward at a significantly reduced rate during the Thanetian (59.24 Ma)- Chatian (23.03 Ma) interval, attaining a maximum thickness of 3.53 km. This interval records a volume of 2.56 $\times 10^5$ km^3 of sediment. The second and final shift happened after the Chattian (23.04 Ma), when the depocenter migrated back southward to its modern-day position. This migration initiated the formation of the Rio Grande Cone Megaslide Complex, which reaches a thickness of 4.64 km, confirming the observations of Cassel et al. (2022) for this final stage. This interval records a volume of 5.15×10^5 km^3 of sediments.

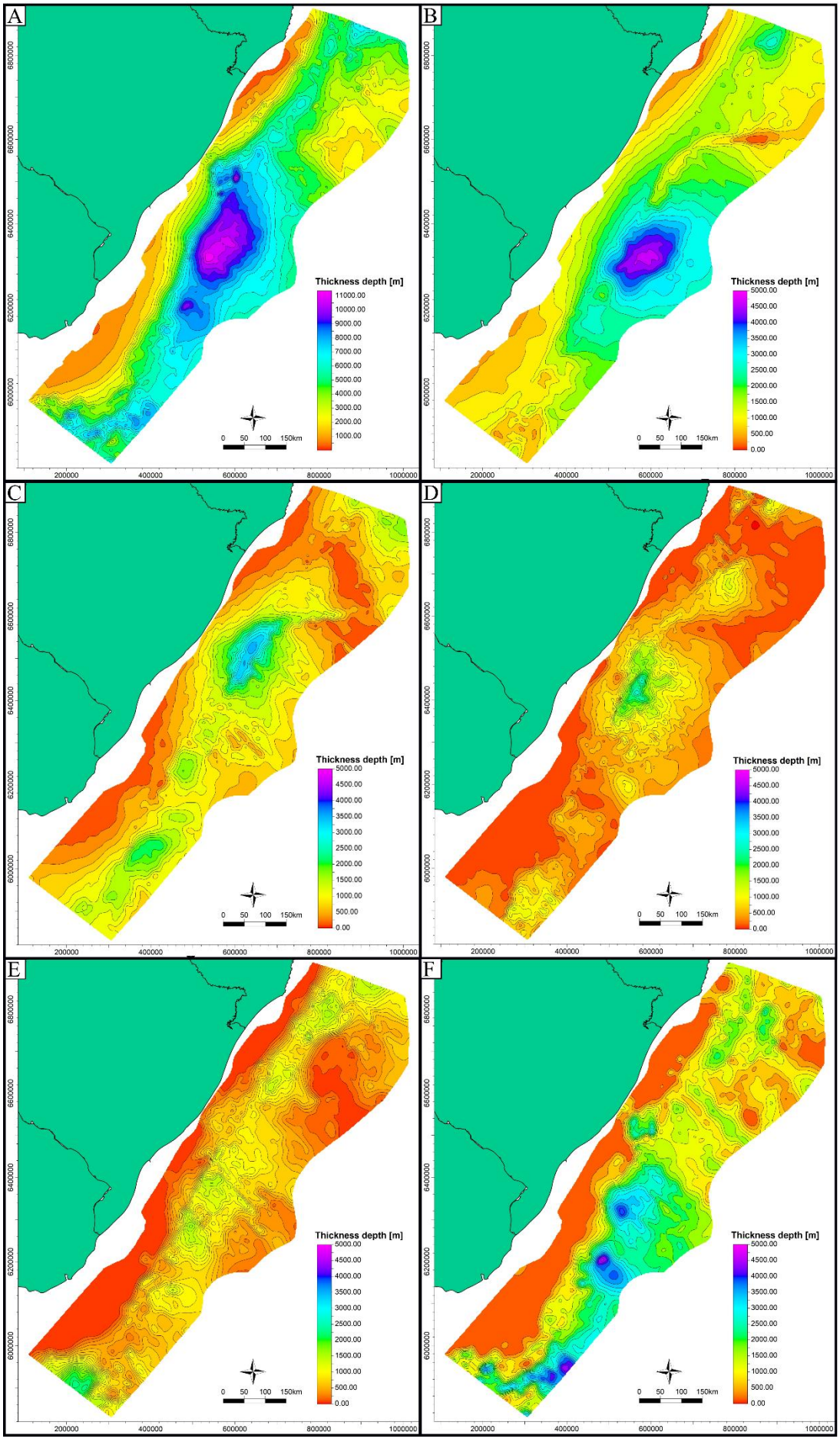
A
B
C
D
E
F
Thickness depth [m]
11000.00
10000.00
9000.00
8000.00
7000.00
6000.00
5000.00
4000.00
3000.00
2000.00
1000.00
4500.00
3500.00
2500.00
1500.00
500.00
0.00
0 50 100 150km
200000
400000
600000
800000
1000000
6000000
6200000
6400000
6600000
6800000

Figure 4-3. Isopach maps of the Pelotas Basin (and Punta del Este) intervals. A) Seafloor - Base of model; B) Seafloor - Chattian: C) Chattian - Thanetian; D) Thanetian - Maastrichtian; E) Maastrichtian - Turonian; F) Turonian - Base of Model.

Petrophysics

The petrophysical logs (Figure 4-5) show a predictable background trend but reveal several specific features. The gamma-ray logs show no anomalous radioactive zones that could produce a higher H_2 volume by radiolysis. In sections with reliable caliper readings, the neutron and density logs generally show a normal compaction trend, with porosity decreasing and density increasing with depth. However, the following key features were identified in the three analyzed wells. Well 1-BPS-8-BP clearly marks the transition from unconsolidated to consolidated sediments at approximately 1900 m, identified by an abrupt decrease in neutron porosity and a corresponding sharp increase in density logs. In well 1-BPS-7-BP, the data is unreliable above 3130 m due to significant borehole collapse, as indicated by the caliper log. Below this depth, three distinct zones (3613-3675 m, 3723–3835 m, and 3861-3873 m) show a combination of low neutron porosity and low bulk density. This response suggests the presence of possible reservoir rock with natural gas, but it did not host high H_2 content (low NPHI). Well 2-BPS-6A-BP exhibits two potential reservoir zones, marked by a crossover between the neutron and density logs, a typical indicator of light hydrocarbons. These crossovers occur in sandstones between 3898 m and 3904 m and in limestones between 5103 m and 5150 m. There is no evidence of any H_2 concentrations.

It was possible to evaluate the porosity of the well 2-BPS-6A in the interval 2572 – 5368 m, 2-BPS-7 in the interval 3150 to 5787m, and 2-BPS-8 at the interval 1900 - 2568 m. In well 2-BPS-6A, the average porosity is 5.6% ± 5.9%. The aforementioned natural gas evidence was observed in rocks with porosity of 10-11% at depths of 3898m and 3904m. Some sections of the well show porosity exceeding 20%, although this may be an artifact of well collapse (as

recorded in the caliper). A potential reservoir was observed in the 5034-5036 m interval within sandstones that host an average porosity of 9.8%. Well 2-BPS-7 shows an average porosity of 6.7% ± 7.7% in the analyzed section. Very high porosity (>20%) was found in the intervals 3614.1-3679.2 m and 3723.45-3837.9m, which are Eocene sandstones. In well 2-BPS-8, we found an average porosity of 1.4% ± 3.4%. Some spots with very high porosity were found in the 1901-1913 m range; however, these are associated with hole enlargement (high caliper). In that way, we assume a bulk basin porosity of 5.6%, which is the weighted average porosity of the wells.

Geochemical Data

The Total Organic Carbon (TOC) data compilation of 150 samples reveals variations with age, indicating that the Cretaceous section contains the most promising source rocks. While the overall mean TOC is 0.7 wt.%, the Cretaceous samples (n = 18) exhibit the highest average TOC of 1.57 ± 1.27%, with a maximum value of 3.68%. The source potential decreases in younger rocks, with the Paleogene (17 samples) averaging 1.16 ± 0.66 wt.% and the Neogene (115 samples) showing the poorest potential with an average of 0.49 ± 0.09 wt.%. If we examine the mean TOC, the 2-BPS-6A-BP shows the highest value at 1.41%, the 1-BPS-7 has a mean of 1.21%, and the 1-BPS-8 has an average TOC of 0.5%. However, this well-based comparison should be interpreted with caution, as the distribution and number of samples from each age are not consistent (see Figure 4-5).

The full dataset of geochemical data is presented in Supplementary Material 7. The relevant elements for hydrogen systems in the sedimentary well cuttings are presented in Figure 4-7. The sedimentary well cuttings show a moderate to low concentration of radioactive elements for the bulk basin (average K = 1.82 %, U = 1.79 ppm, Th = 7.14 ppm). Sulfur, which can act as a sink for H_2 (Ahmadpour & Gholami, 2024), was analyzed in the 286 sedimentary well cutting samples. The mean sulfur concentration is 0.7 ± 0.4 %, with a general trend of

increasing concentration towards the top of the sedimentary section (Figure 4-7). Sporadic peaks of high concentration were observed, such as a value of 2.77% at a depth of 4140 m in well 2-BPS-6A. The basaltic rocks (this research's new data + Serratt et al., 2025) show an average Fe_2O3 (total) of 10.08%, with FeO (five samples from well cores) ranging from 1.38 to 7.62% and an average of 4.88% ± 2.33%. Sulfur and radioactive elements in basalts are at their lowest levels in all analyzed geological units, with average values of S < 0.01%, K = 1.38%, U = 0.74 ppm, and Th = 3.96 ppm.

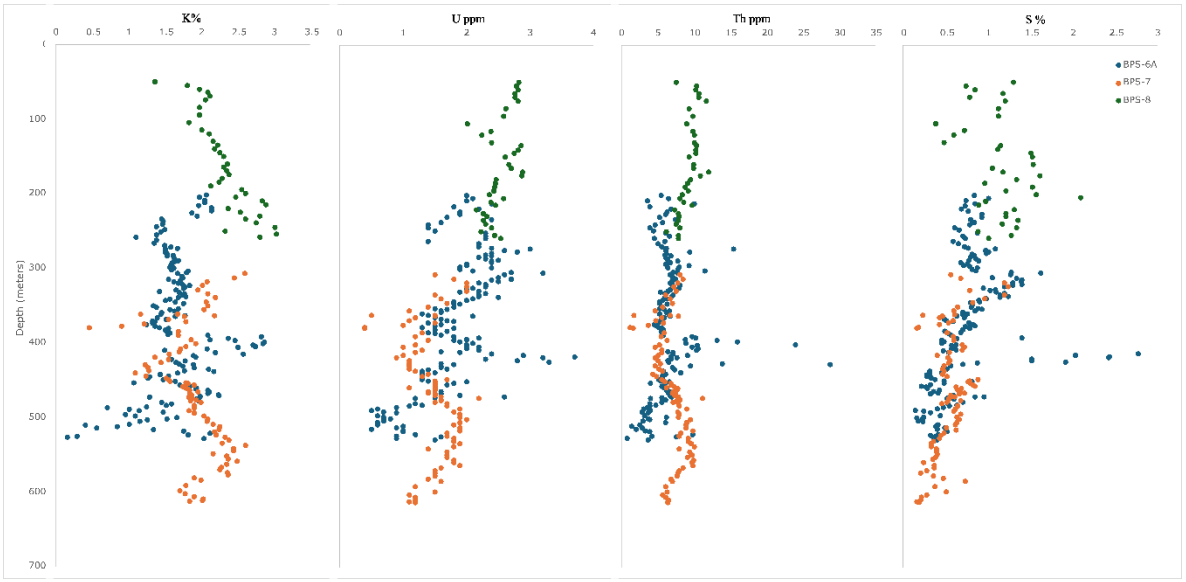

Figure 4-4. Elemental profiles of K, U, Th, and S versus the depth in meters. Data from wells 2-BPS-6A, 1-BPS-7-BP, and 1-BPS-8-BP.

$^{40}Ar/^{39}Ar$ ages

The $^{40}Ar/^{39}Ar$ ages (Figure 4-8) show a complex volcanic system. For instance, in the well 1-RSS-3, the deepest sample (3904-3905 m) shows a plateau age of 100.11 ± 1.95 Ma and a total fusion age of 103.54 ± 1.26 Ma. On the other hand, the sample at 3555 m depth shows an age plateau of 128.14 ± 3.10 Ma, with total fusion at 122.64 ± 2.46 Ma. In well 2-BPS6A-BP, three ages are approximately similar at a depth of 5378.5m, showing plateaus of 76.45 ± 1.24 Ma, 78.90 ± 1.79 Ma, and 79.19 ± 3.14 Ma. With total fusion 76.59 ± 1.10, 83.44 ± 1.12 Ma, and

74.95 ± 1.06 Ma. The sample from well 1-SCS-3b shows a plateau age of 121.08 ± 3.09 Ma and a total fusion age of 141.06 ± 2.48 Ma.

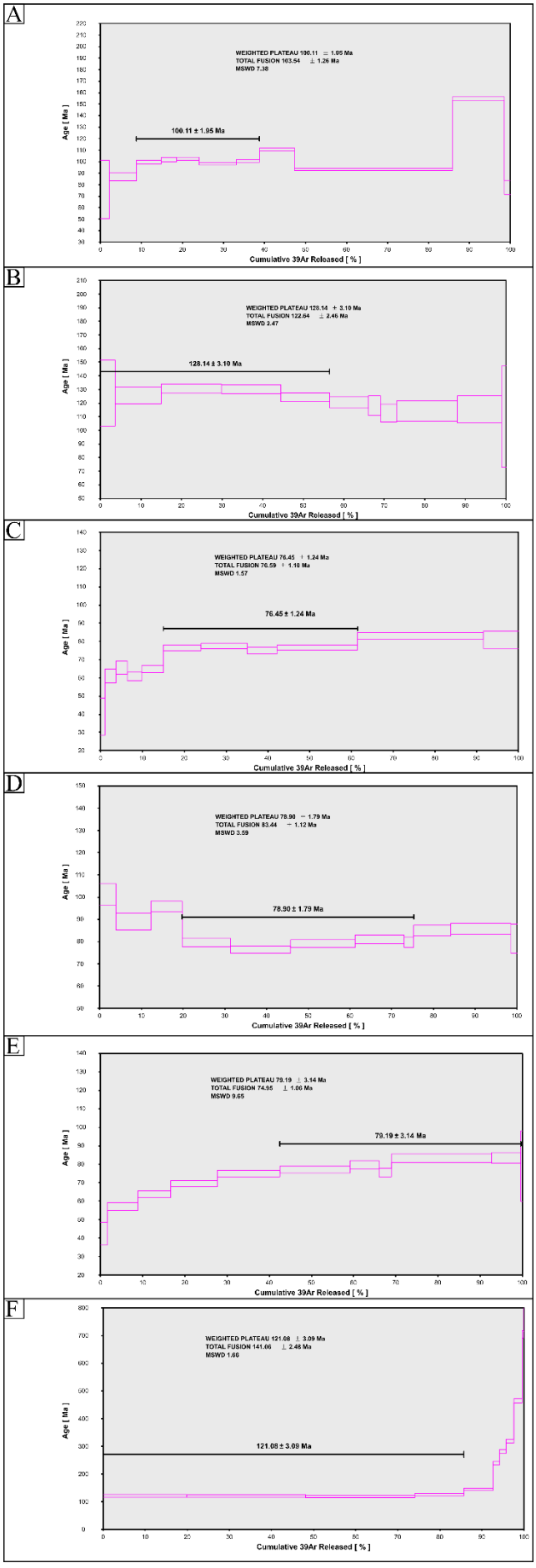
A
WEIGHTED PLATEAU 100.11 ± 1.95 Ma
TOTAL FUSION 103.54 ± 1.26 Ma
MSWD 7.38
100.11 ± 1.95 Ma
Age [Ma]
Cumulative 39Ar Released [%]
B
WEIGHTED PLATEAU 128.14 ± 3.10 Ma
TOTAL FUSION 122.64 ± 2.46 Ma
MSWD 2.47
128.14 ± 3.10 Ma
Age [Ma]
Cumulative 39Ar Released [%]
C
WEIGHTED PLATEAU 76.45 ± 1.24 Ma
TOTAL FUSION 76.59 ± 1.16 Ma
MSWD 1.57
76.45 ± 1.24 Ma
Age [Ma]
Cumulative 39Ar Released [%]
D
WEIGHTED PLATEAU 78.90 ± 1.79 Ma
TOTAL FUSION 83.44 ± 1.12 Ma
MSWD 3.59
78.90 ± 1.79 Ma
Age [Ma]
Cumulative 39Ar Released [%]
E
WEIGHTED PLATEAU 79.19 ± 3.14 Ma
TOTAL FUSION 74.95 ± 1.06 Ma
MSWD 9.65
79.19 ± 3.14 Ma
Age [Ma]
Cumulative 39Ar Released [%]
F
WEIGHTED PLATEAU 121.08 ± 3.09 Ma
TOTAL FUSION 141.06 ± 2.48 Ma
MSWD 1.66
121.08 ± 3.09 Ma
Age [Ma]
Cumulative 39Ar Released [%]

Figure 5. 40Ar/39Ar plateaus ages from the Samples: A) Well 1-RSS-3 (3905 m); B) Well 1-RSS-3 (3555 m); C) Well 2-BPS6A-BP (5378.5 m – sample A); D) Well 2-BPS6A-BP (5378.5 m – sample B); E) Well 2-BPS6A-BP (5378.5 m – sample C); F) Well 1-SCS-3b (4732 m).

Thermal modeling

A strong linear correlation ($R^2 = 0.9755$) was observed between temperature and depth (relative to the seabed) using the combined dataset of corrected BHTs and modeled seabed temperatures (Figure 4-9). The empirical equation (12) describes this relationship:

$$T=0.0302 \cdot D+13.383 \quad (12)$$

Where T is the temperature in °C and D is the depth from the seafloor in meters. To validate this model, we tested alternative models, such as those that excluded the seabed temperature data or used sea level as the datum; however, the chosen model consistently yielded the highest correlation coefficient. Furthermore, data for each well were analyzed individually to ensure the Simpson Paradox did not skew the overall trend. Based on this correlation, we assume a regional thermal gradient of 30.2 °C/km, a value similar to that observed in the Santos Basin post-salt section (29.9 °C/km; Zuo et al., 2023).

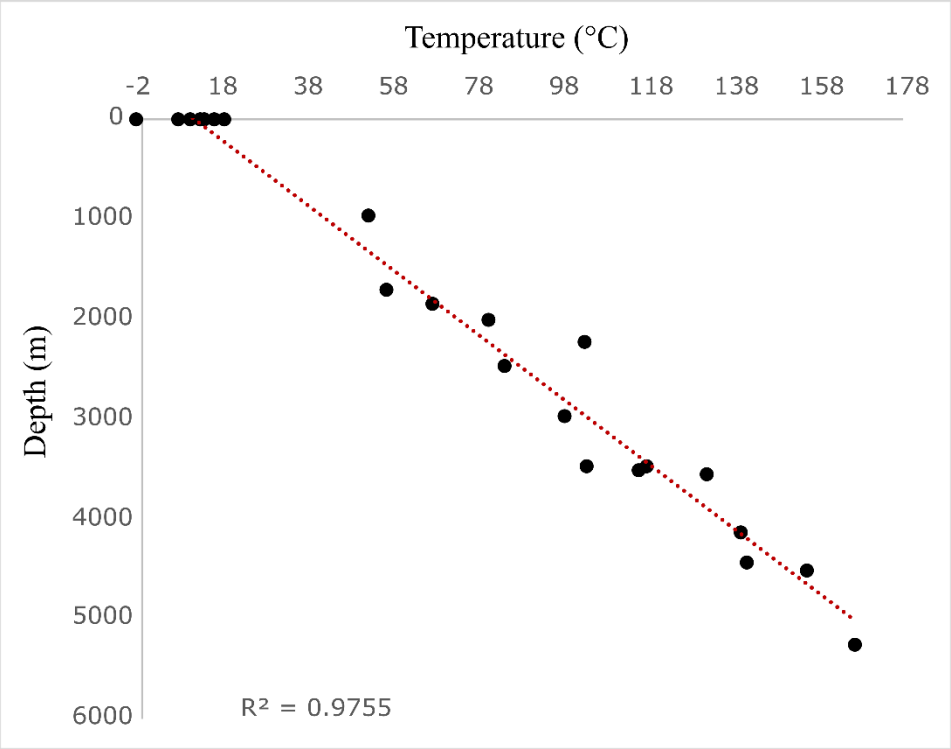

Figure 4-6. Plot using Bottom Holes Temperatures (BHTs) and modeled sea floor temperatures vs depth with seafloor as datum.

4.2. H_2 system evaluation

The H_2 system was evaluated using a method similar to that used for oil system evaluation. That is in terms of source, reservoir, cap rocks, and sink.

Sources

Our thermal model indicates that rocks within the thermogenic H_2 generation interval (220-330 °C; Mahlstedt et al., 2022) are primarily located in the Cretaceous section (Figure 10), encompassing 9.71×10^4 km^3 of rocks within this interval. Considering a bulk sedimentary density of 2.4g/cm3, this implies that the Paleogene package in the 220-330 °C interval has a bulk mass of 3.85×10^{10} t, and the Cretaceous has a bulk mass of 2.33×10^{14} t. Considering the average TOC of each interval as 1.16% for Paleogene and 1.57% for Cretaceous, that implies a bulk organic carbon mass of 4.47×10^8 t in Paleogene and 3.66×10^{12} t in Cretaceous in the

220-330 °C interval. Taking the H_2 potential proportion found by Mahlstedt et al. (2022) of 20 mg H_2/g TOC, it implies a total H_2 potential of 7.32×10^{10} t.

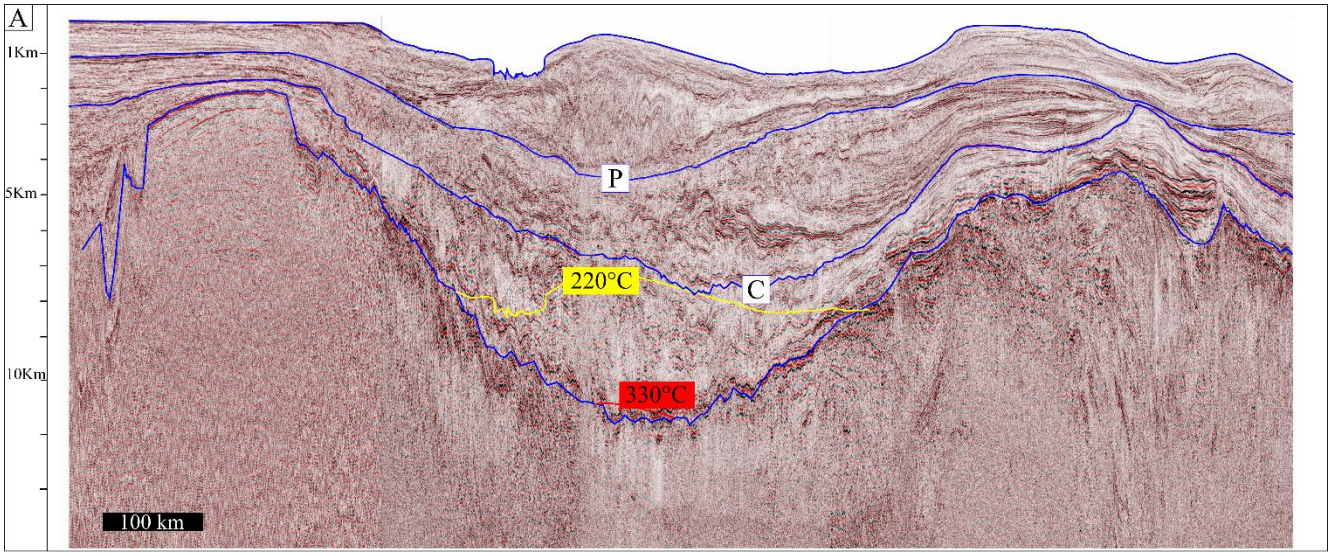

Figure 4-7. Along strike seismic lines composition, in the depth domain, with a SW-NE orientation. Colorful lines represent isotherms of 220 °C (yellow) and 330 °C (red). The composition represents the distal section from Punta del Este to Santos basins, showing all the PB extension and the three depocenter changes. Observe that almost all thermogenic H_2 potential is in Cretaceous (C) rocks.

Fe^{2+} Bearing minerals oxidation produces H_2 through a series of reactions, ranging from low temperatures (e.g., weathering, Geymond et al., 2022) to high temperatures (e.g., Serpentinization – Zgonnik, 2020), that can produce H^2 as a byproduct. It is noted that the main process related to natural H_2 production is related to Fe^{+2} oxidation (Smith et al., 2005; Worman et al., 2016, 2020; Zgonnik, 2020; Geymond et al., 2022; Liu et al., 2023). In that way, large-scale research simplifies the problem as reaction (10)

In that way, each 55.402g of Fe^{2+} oxidizes to Fe^{3+} has the potential to produce 1g H_2. However, Mayhew et al. (2013) observed that the total mass of Fe^{2+} or even the surface area of Fe^{2+} bearing minerals was not directly related to final H_2 production. Instead, it was related to the spinel's content (such as magnetite) that acts as a catalyst. Additionally, there is no evidence

that all the volcanic rocks (even those that are highly fractured and faulted) are in contact with water.

Based on the volume of volcanic rocks in 1.39×10^6 km^3, considering the basalt density as 2.9g/cm^3 ($2.90x10^9$ t/Km^3; Philpotts & Ague, 2009), that implies a bulk mass of $4.03x10^{15}$ t of volcanic rocks with an average 10.08% of Fe2O3(total) that is a 7.05% of Fe(total), which means 2.84×10^{14} t of Fe(total). The average FeO in these rocks is 4.88%, which is 3.79% of Fe^{2+}, implying a current bulk mass of 1.53×10^{14} t of Fe^{2+}, and considering that the initial $Fe^{3+}/\Sigma Fe$ ratio of 0.143 (Zhang et al.,2018). The original Fe2+ content was 2.44×10^{14} t. In this way, the difference between the original and current Fe^{2+} content is equal to the bulk oxidized Fe, that is, 9.06×10^{13} t. That implies a maximum theoretical production of 1.64×10^{12} t of H_2 by the basalts.

Radiolysis has been identified as a potential source of H_2 (Bouquet et al., 2017). We evaluated the basin H_2 production using the average concentration of radioactive elements from the sedimentary rock well cuttings (K=1.82%; Th=7.14 ppm; U=1.79 ppm). We use it to calculate the radionuclide activity of the isotopes ^{40}K, ^{232}Th, ^{235}U, and ^{238}U using equation (8), where N is the number of radionuclides for each kilogram of rock. In that way, the observed concentrations imply a mass of 18.2g of K/kg of rock, 7.14×10^{-3}g of Th/kg rock, and 1.79×10^{-3}g of U/kg rock. Based on the aforementioned isotopic abundance (Haynes, 2016), we determined the N values, and consequently, the values of As (Activity of radionuclide "s"), as presented in Table 5.

Table 5. Calculated radionuclide activity (As).

	N	λ (Decay/s)	As (Bq/kg)
^{40}K	3.29×10^{19}	1.76×10^{-17}	5.79×10^{02}
^{235}U	3.30×10^{16}	3.12×10^{-17}	1.03
^{238}U	4.50×10^{18}	4.93×10^{-18}	22.2
^{232}Th	1.85×10^{19}	1.57×10^{-18}	29.1

Applying these values to equation (3) and considering ϕ=5.6%, and rock density as 2.4g/cm^3. It implied a total H_2 molecule production of 2.00x10^{09} molecules per second per m^3. That is 211.07 H_2 t/Ma/km^3. By dividing the volume of rocks for each previously analyzed stratigraphic interval by its duration, we calculated a volumetric depositional rate. We created a curve of volumetric evolution, excluding sediment compaction (Figure 4-11). We calculated the H_2 radiogenic production for every million years and a cumulative H_2 production of 1.54 × 10^{10} tons for the whole basin history.

Applying these values to equation (7) and considering ϕ=5.6%, and rock density as 2.4g/cm^3. It implied a total H_2 production rate of 2.00×10^9 molecules per second per m^3. That is 211.07 H_2 t/Ma/km^3. By dividing the volume of rocks for each previously analyzed stratigraphic interval of the basin by its duration, we calculated a volumetric depositional rate. We created a curve of volumetric evolution, excluding sediment compaction (Figure 4-11). We calculated the H_2 radiogenic production per million years and a cumulative H_2 production of 1.54 × 10^{10} t over the whole basin history.

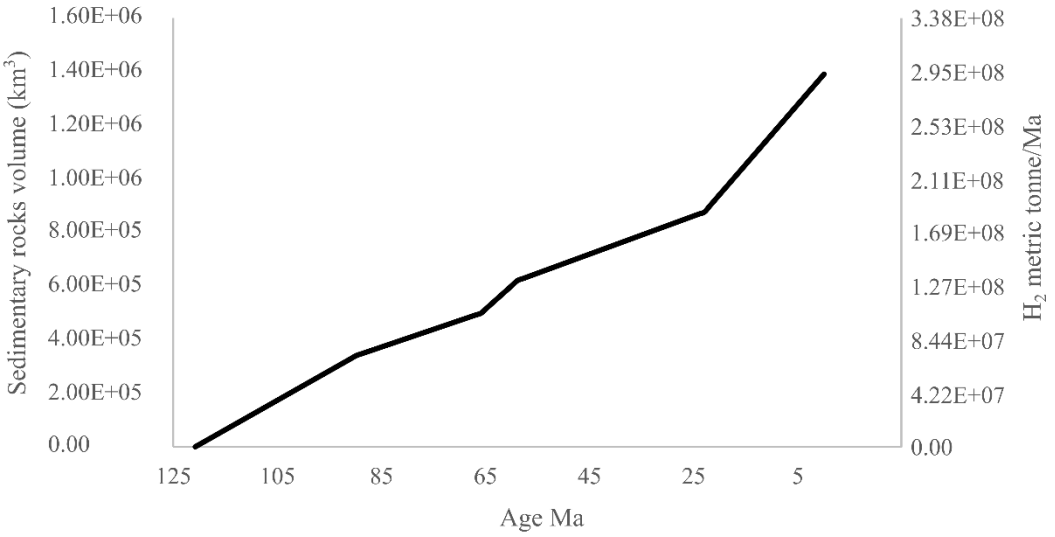

Figure 4-11. Volumetric evolution of the Pelotas Basin throughout time, disregarding the sedimentary compaction. Based on the basin interpretation carried out in this study. A volumetric sedimentation rate was determined for each analyzed interval, assuming a base of 121 Ma for the sedimentary section. The volume of rocks was assumed to be proportional to their radionuclide production.

We estimated the H_2 production through magmatic degassing and rock fracturing. The magmatic degassing was estimated in 8.62 x 10^{10} t of H_2, while H_2 produced in basalt fractures was estimated in 2.78 x 10^9 t, both based on Worman et al. (2020) productivity coefficients.

H_2 occurrences and reservoir rocks

No obvious H_2 concentration was observed in the Pelotas Basin through our petrophysics analyses. However, some segments could be a good reservoir, in classical petroleum system terms. For instance, the Eocene hosts sandstones that could act as good reservoirs in well 2-BPS-7, and some Cretaceous segments at 2-BPS-6A host rocks with porosity even higher than reservoirs in Mali (Maiga et al., 2023,2024). However, the availability of reservoirs in the Pelotas Basin appears very limited based on the current dataset.

Any sills were recorded on wells in the sedimentary section. However, we found evidence of drift-stage magmatism in $^{40}Ar/^{39}Ar$ ages, ranging from 100.11 to 76.45 Ma, which could have produced some sills within the sedimentary section. However, there is a lack of direct evidence of its existence within the sedimentary pile. The evaporites are restricted to the northern sector of the basin and are only a few meters thick (Bueno et al., 2007). On the other hand, if fine-grained siliciclastic rocks serve as an effective cap rock, as pointed out by Iyare et al. (2025), the Pelotas Basin has considerable capacity to retain H_2 in the sedimentary pile. Mainly, cap rocks occur from the Neogene to the recent section.

Cap rock

Any sills were recorded on wells in the sedimentary section. However, we found evidence of drift-stage magmatism in $^{40}Ar/^{39}Ar$ ages, ranging from 100.11 to 76.45 Ma, which could have produced some sills within the sedimentary section. However, there is a lack of direct evidence of its existence within the sedimentary pile. The evaporites are restricted to the northern sector of the basin and are only a few meters thick (Bueno et al., 2007). On the other hand, if fine-grained siliciclastic rocks serve as an effective cap rock, as pointed out by Iyare et

al. (2025), the Pelotas Basin has considerable capacity to retain H2 in the sedimentary pile. Mainly, cap rocks occur from the Neogene to the recent section.

Sinks

We made an order-of-magnitude estimate of the H_2 sink via inorganic reactions, using a model of H_2 consumption by pyrite (Truche et al., 2010). We estimated the volume of sedimentary rocks within the thermal range of 90-180°C at 5.08×10^5 km^3. Although if we consider a sedimentation temperature of 20°C, all sedimentary rocks that were at temperatures above 180°C at some point were in the 90-180°C interval. In that way, we estimate the volume of rocks at temperatures above 90° to be 7.24×10^5 km^3. Taking the aforementioned density of sedimentary rocks in 2.4g/cm3, which implies a bulk density for the rocks in the 90-180°C interval of 1.22×10^{15} Tons of rocks, and for all rocks with temperatures above 90°C, a mass of 1.74×10^{15} t. Taking the average sulfur content of the rocks (0.7%) implies a bulk sulfur mass of 8.53×10^{12} t of sulfur in the 90-180°C interval and 1.22×10^{13} t of sulfur in the sedimentary rocks beneath the isotherm of 90°C. Considering equation (11) and the sedimentary section average S bulk sulfur mass, with a 100% efficiency of reaction (11), it implies a maximum potential sink of 2.66×10^{11} t of H_2. In the 90-180°C interval, and 3.80×10^{11} t of H_2 potentially sink in the sedimentary rocks that is higher than the intrabasin production (radiolysis and thermogenic). The H_2 retained in basalts was assumed as 3.40 t H_2/km^3 (Worman et al., 2016), which is a bulk mass of 4.73×10^{10} t.

Most sinks are not quantifiable using our dataset. For instance, the total hydrogenation of CO_2 (Prinzhofer et al., 2018) will depend on the availability of CO_2. Additionally, biological consumption and leakage cannot be quantified. However, the presence of 45,000 km^2 of biogenic gas hydrates, observed as BSRs (Miller et al., 2015), provides evidence of extensive microbial communities at shallow levels in the Pelotas Basin. These communities could consume H_2 that reaches shallow levels, which is an important H_2 sink (Worman et al., 2020;

Zgonnik, 2020). The hydrocarbons should also act as an important sink (Mahlstedt et al., 2022), although the thermal and COT data suggest the presence of hydrocarbons in the basin; more robust investigations should be carried out on this topic.

3.5.4 Discussion

3.5.4.1 Methodological limitations

Despite significant uncertainties, our analytical framework enables us to synthesize a vast dataset from a hydrogen geology perspective. This research takes a regional approach, making generalizations (temperature, composition, porosity, Fe^{2+} oxidation) for a region approximately the size of Germany. Its objective is to estimate the order of magnitude of some processes. Even for well-consolidated geological systems, such as oil systems, in basins with much more robust datasets, there remains significant uncertainty. Hydrogen geology is an incipient science, and the results should be carefully evaluated using a regional approach.

We did not find direct evidence of H_2 in the petrophysics analyses; however, we should consider several points. Free gases with a high hydrogen (H_2) concentration exhibit distinct behavior, producing abnormally high NPHI readings and resulting in an asymmetric crossover. This effect was observed in the Bourakebougou field in Mali (Maiga et al., 2023). In contrast, in deeper reservoirs where hydrogen is dissolved in water, this anomaly disappears. Therefore, interpreting RHOB and NPHI profiles in H_2-rich systems requires caution, as the NPHI response strongly depends on the gas's physical state and the formation saturation conditions. In that way, if the H_2 is dissolved in water, which should be expected at regions deeper than 800 m (Maiga et al., 2023), it could not produce a reading compatible with the H_2 in the formation. In that way, we advise future researchers to be careful when using NPHI logs in offshore settings.

3.5.4.2 Stratigraphic observations

The distribution of the sedimentary packages was used to develop thermogenic models. However, we observed a not-reported depocenter change. Pelotas Basin Cretaceous sedimentation is recorded exclusively in offshore wells (2-BPS-6A-BP; 1-RSS-2-RS; 2-RSS-1-RS; 1-RSS-3-RS; 1-SCS-3-SC; 1-SCS-2-SC; 1-BPS-7-BP) and analyzed wells from surrounding basins, such as Gaviotin X-1 and Lobo-1 (Punta del Este Basin). In PB, these wells record conglomerated rocks in the proximal half-grabens (well 1-RSS-3-RS) and limestones and siliciclastic rocks from the Tramandaí and Porto Belo formations in the Torres Arch region (Wells 2-BPS-6A-BP; 1-SCS-3-SC; 1-SCS-2-SC). During the Cretaceous, the depocenter was located near the current basin depocenter, the RGCMC region. The previous study on the Pelotas Basin depocenters by Cassel et al. (2022) could not identify this depocenter because it relied on only four seismic lines, which were incorrectly assumed to represent the entire basin. This study uses 448 seismic lines to ensure we can visualize the entire basin.

Cassel et al. (2024) noted an inverse relationship between post-breakup (drift stage) accommodation space and SDR thickness, supported by an isostatic model of continental lithosphere thinning and decompression melting during break-up. The first depocenter of the basin, observed in this research, should have been influenced by interactions between magmatism and isostatic compensation, as suggested by the theoretical models of Cassel et al. (2024). Most of the Cretaceous deposition occurs in regions with thinner volcanic rocks/continental crust. Additionally, the Proterozoic basement, currently exposed as the Polonio High, serves as an important southern boundary of the depocenter. In contrast, the northern boundary is delimited by volcanic rocks of the Torres Arch (Figure 4-4). To the west, the depocenter is constrained by the slope marking the crustal thinning zone, often called the necking domain (Geoffroy, 2005; Stica et al., 2014; Chauvet et al., 2021; Teixeira et al., 2025a). This necking zone coincides with the western limit of the volcanic rocks observed as SDRs

(Figure 3). The observations of this study reinforce the deep connection between volcanic emplacement and accommodation space in the region, as supported by Cassel et al. (2024).

The Cretaceous packages are absent in onshore wells (Serratt et al., 2025). The erosive nature of the Cretaceous surface (Cassel et al., 2022) likely explains this absence in the basin's proximal sections. Similarly, the Paraná Basin is absent in all wells of the Pelotas Basin except for 2-TO-1-RS. This erosion is attributed to the 50 Ma uplift event, associated with the rise of the Domeyko Cordillera and Puna Plateau (Cassel et al., 2022). However, the Parana Basin erosion could be old and related to the pre-breakup uplift.

Following this erosive event, the depocenter shifted to a new position (Figure 4-6). We hypothesized that change is related to the occurrence of the geographically restricted northernmost Curumin Formation volcanic rocks (Dias et al., 1994; Bueno et al., 2007; Gordon & Mohriak, 2015; Serratt et al., 2025). The late magmatism in this region, as indicated by our $^{40}Ar/^{39}Ar$ ages, caused localized late thermal subsidence after the Cretaceous, leading to a northward migration of the depocenter (similar to that proposed by Pindell and Heyn, 2022, for the Gulf of Mexico).

The second depocenter, previously identified as the first PB depocenter (Cassel et al., 2022), was deposited in front of the Mostardas Low (Figures 4-4 and 4-6). This structure may have influenced sedimentary input, particularly if it extends into onshore regions, as suggested by magnetotelluric surveys (Menezes et al., 2021). Provenance studies also support this catchment of sedimentary input from onshore. Girelli et al. (2023), studying Paleocene samples from well 1-RSS-2-RS in the Mostardas Low region, found a detrital zircon provenance signature restricted to sources along the coast near the Mostardas Low. This provenance indicates that sedimentary influx into the second depocenter should be driven by rivers such as the paleo-Camaquã and Jacuí, which flowed into this depression, supplying sediments and

shaping the second PB depocenter. As the first one, the top of this depocenter corresponds to an erosive surface (Cassel et al., 2022).

The third depocenter is located south of the second (Figure 6) and corresponds to the RGCMC (Zerfass et al., 2014; Cassel et al., 2022; Tagliaro et al., 2024). This depocenter migration was studied by Cassel et al. (2022), who attributed it to the rise of the Eastern Cordillera in western South America.

3.5.4.3 Early H_2 systems

The first step to understanding the H_2 production basalt-related is to obtain reliable ages for these rocks. In well 1-RSS-3, the new $^{40}Ar/^{39}Ar$ ages reveal a complex evolution for the region. A sample from the upper part of the volcanic section at 3555 m, previously interpreted as an early-rift SDR of the Imbituba Formation (Bueno et al., 2007), yielded a plateau age of 128.14 ± 3.10 Ma, compatible with late Paraná-Etendeka continental flood basalts late magmatism (pre-rift; Gomes & Vasconcelos, 2021). On the other hand, a deeper sample at 3905 m, previously interpreted as pre-rift Paraná-Etendeka (Serratt et al., 2025), yielded a younger plateau age of 100.11 ± 1.95 Ma. The younger sample shows fewer amygdales and a higher degree of hydrothermal alteration compared to the shallower, older sample, which is full of amygdales and resembles the top of a lava flow (Serratt et al., 2025). This leads to the interpretation that deeper, younger basalt represents a later intrusive magmatic event that cross-cuts the older lava flows from the Paraná-Etendeka continental flood basalts (Pre-rift; Gomes & Vasconcelos, 2021).

The $^{40}Ar/^{39}Ar$ results from well 2-BPS-6A-BP reveal a hydrothermal event during the Late Cretaceous, younger than the main rift phase. Three of our analyses from a single depth (5378.5 m) yielded a consistent cluster of plateau ages: 76.45 ± 1.24 Ma, 78.90 ± 1.79 Ma, and 79.19 ± 3.14 Ma. These ages are remarkably similar to a 75+-0.8 Ma age reported from a 6161 m interval in the same well (Gordon and Mohriak, 2015 and references within) and are

synchronous with Late Cretaceous magmatism documented on the Rio Grande Rise (Davidson et al., 2025) and the conjugate African margin magmatism (Homrighausen et al.,2019 and references within). This young age creates a geological contradiction. The dated basalts are from the same core interval where peperites have been reported, implying extrusion in wet sediments (Serratt et al., 2025).

Furthermore, these basalts are overlain by Aptian-aged sediments (~125–113 Ma; Arai, 2009). While this stratigraphic relationship argues against an intrusive origin, the consistent repetition of the ~76–79 Ma age in our data, its independent confirmation in previous work (Gordon and Mohriak, 2015 and references within), and its regional significance (Homrighausen et al.,2019; Davidson et al., 2025) suggest the age is geologically meaningful. Therefore, we interpret these results as evidence of a previously unidentified Late Cretaceous (Campanian) hydrothermal event in this part of the basin. A hydrothermal activity so intense that it could open the mineral system should be related to magmatic activity; the ages recorded in this well did not reflect the age of the rocks but rather a magmatic/hydrothermal event at that time.

The sample from well 1-SCS-3B, identified as an SDR by Serratt et al. (2025), yielded a plateau age of 121.08 ± 3.09 Ma. We assume this age to be the rock's age, and it was also assumed to be the maximum depositional age for the basin.

Magmatic events, such as those identified at ~76 to 128 Ma, are likely responsible for most of the H_2 production. Therefore, most H_2 production should occur between 128 and 76 Ma due to hydrothermal circulation and magma degassing (Figure 4-12), as currently observed in the VPM under development in Djibouti (Pasquetet al., 2021; Deville et al., 2023). Early-stage rock hydrothermal alteration could have produced most of the region's H_2 potential (Volcanic related H_2 1.64×10^{12} t vs basin related H_2 8.86×10^{10} t Figure 4-12). There are some

potential reservoir rocks in this Cretaceous interval that could host an H_2 system, but a play-scale-focused research program should be conducted once the risks are very high (Figure 12).

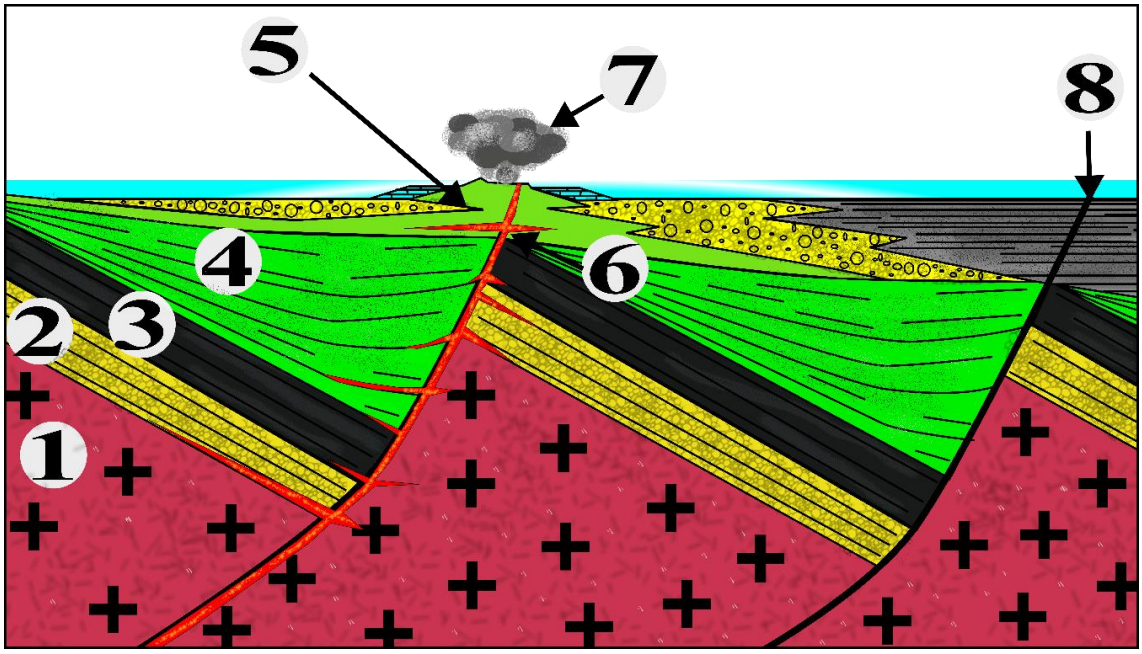

Figure 4-8. Schematic, out of scale, of early-stage (~120 Ma) north of Pelotas Basin development showing: 1) Dom Feliciano granitic rocks; 2) Parana Basin sedimentary section. 3) Paraná-Etendeka- LIP, or Serra Geral group; 4) SDR; 5) Late magmatism interdigitated with sediments (as evidenced by the peperites), the lava/water interaction could be an important H_2 source (Worman et al., 2020); 6) Late intrusions related to hydrothermal alterations and consequently H_2 production (Worman et al., 2020); 7) Magma degassing an H_2 source unlike to be preserved; 8)Faults and fracturing of rock ruptures chemical bonds, producing radicals that can react with water to produce H2 (Worman et al.,2020).

3.5.4.4 H_2 system balance: sources vs sinks

We compared five possible sources: intra-basin radiolysis, magmatic degassing, basalt fractures, thermogenic, and Fe^{+2} mineral-bearing oxidation. These sources are orders of magnitude different, in the following crescent order of H_2 production: basalt fractures (2.78×10^9 t), intra-basin radiolysis (1.54×10^{10} t), thermogenic (7.32×10^{10} t), magmatic degassing (8.62×10^{10} t), and Fe+2 mineral-bearing oxidations in volcanic rocks (1.64×10^{12} t).

The production by degassing (8.62×10^{10} t) was probably restricted to early basin stages, although it is unlikely to have been preserved. In the same way, the H_2 is associated with

fractures (2.78×10^9 t), the least effective process, and one that depends on tectonic activity. The radiolysis shows a production of 1.54×10^{10} t. However, it is also the most underestimated in our calculations, as it was not considered for the basalts and the granitic basement (which could produce a significant amount). We did not do it due to a lack of geometrical constraints. However, its low production radiolysis makes it a constant H_2 producer, which is its most notable quality.

Thermogenic processes involving organic matter are indeed a potent source of H_2. However, the primary risk associated with this source is its spatial proximity with hydrocarbon generation. During the thermal cracking of organic matter, highly reactive hydrocarbon radicals and unsaturated molecules are formed alongside H_2. Due to its high reactivity, the generated hydrogen is readily consumed in reactions that saturate these hydrocarbon compounds(Mahlstedt et al., 2022). This process effectively turns the organic-rich rock into an "impenetrable H_2 sink," preventing the preservation and accumulation of free hydrogen, thereby masking its true generation potential (Mahlstedt et al., 2022).

Fe^{+2} mineral-bearing oxidation shows the best potential. However, it should have occurred in higher volume while the magmatic system was active (~128-76 Ma; Figure 12). This late thermal activity (76 Ma) was probably restricted to the Torres Arch region. There are some sandstones in the Cretaceous that could work as reservoirs, such as the 5034-5036 m depth interval in the well 2-BPS-6A. The fine-grained siliciclastic or hybrid fabric (carbonatic + siliciclastic) with very low porosity could act as cap rock in this system. However, the integrity of these cap rocks should be investigated to ensure they are not fractured. The Cretaceous also has the lowest sulfur content (Figure 4-5). This interval is the most promising for H_2 accumulation.

A way to evaluate the potential for H_2 accumulation in sedimentary basins is to examine the balance between its sources and sinks. This was the study's primary goal. However, it

remains challenging to quantify each source and sink. We identify as possible sources such Biological production (unknown production), basalt fractures (2.78 x 10^9 t), magmatic degassing (8.26 x 10^{10} t), thermogenic production (7.32x10^{10} t;), radiolysis intra-basin (1.54x10^{10} t), radiolysis external sources (unknow production); Fe oxidation intra-basin (unknow production); Fe Oxidation external sources (Max 1.64 x 1012). In addition, possible sinks: Biological consumption (unknown loss); H_2 leakage (unknown loss); CO_2 hydrogenation (unknown loss); Hydrocarbon-related loss (unknown loss); retained H_2 (4.73 x 10^{10} t); sulfur-related sink (3.80 x 10^{11} t). Taking all maximum values, the final balance is 1.39 × 10^{12} t of hydrogen potential (ignoring all the sinks that we could not evaluate quantitatively). However, many of these processes are diachronous, and much of the potential production should have occurred before 76 Ma. This interval is the most prospective. However, the uncertainty about sinks makes it extremely risky.

3.5.5 Conclusion

Through analyses of the seismic data, we observed a previously unreported change in the basin's depocenter during the Cretaceous. Our velocity models suggest that the Pelotas Basin depocenter could reach a depth of 11.37 km. We also dated the basalts by $^{40}Ar/^{39}Ar$ in the well 2-BPS-6 at depth of 5378.5m we found the ages 76.45 ± 1.24 Ma, 78.90 ± 1.79 Ma, and 79.19 ± 3.14 Ma; in well 1-RSS-3 at a depth of 3555 m, we obtained an age of 128.14 ± 3.10 Ma, and an intrusive rock at 3904-3905 m with age of 100.11 ± 1.95 Ma. In well 1-SCS-3B at 4732 m, we obtained an age of 121.08 ± 3.09 Ma for the SDRs; we assume this is the maximum depositional age for sediments above it.

We quantitatively evaluated multiple sources of H_2 in the Pelotas Basin. These include intra-basin radiolysis, magmatic degassing, fracture-related H_2, thermogenic, and Fe2+ mineral-bearing oxidation. The Fe+2 mineral-bearing oxidation shows the highest potential; however, its timing is just favorable for accumulation before 76 Ma (the latest recorded

hydrothermal pulse). However, some Cretaceous rocks with good porosity may host this early H_2 production. The thermogenic H_2 is a good source, but its nature, associated with hydrocarbon formation, makes it potentially "stillborn". Radiolysis produces H_2 continuously, but it is widespread throughout the basin. The shallow levels of the basin did not record reservoir rocks, and its high sulfur content and microbial activity make it unlikely for H_2 concentrations.

In oil and gas systems, the exploration paradigm is typically source rock first; in hydrogen systems, almost any rock can serve as a source due to an abundance of processes (e.g., thermogenesis, radiolysis, iron oxidation). The real challenge is finding the right conditions to accumulate and preserve H_2. Therefore, the paradigm for H_2 prospection should be focused on preservation and accumulation conditions. In that way, in addition to sealing quality, rock reservoirs with low sulfur and no microorganisms are indispensable for H_2 systems. The sulfur content in the Pelotas Basin is sufficient to sink all H_2 production related to the sedimentary rocks (radiolysis and thermogenesis); only the H_2 from the basalts' alteration could form an economical concentration. In that way, marine siliciclastic rocks should be avoided as the main target for reservoirs because of their high sulfur content, which could act as a potent sink.

Declaration of Competing Interest

We declare that we have no economic interest in this research.

Acknowledgments

This article is part of the HS Ph.D. thesis. The authors thank the CNPC Brasil (China National Petroleum Corporation) for the financial support. We also thank ANP (Brazilian National Agency for Petroleum, Natural Gas and Biofuels) and ANCAP (Uruguayan Administración Nacional de Combustibles, Alcoholes y Portland) for providing access to data. We thank the institute of geology and geophysics from the chinese academy of sciences and to China-Brazil joint research center for the technical support. We are grateful to Schlumberger for granting academic licenses for the PetrelTM software, respectively. FCJ thanks CNPq for grant #4081942021-9 and INCT-Atlantico (grant #406898/2022-7). H.S. acknowledges CAPES for grant #88887.886595/2023-00 and finance code 001 (Portal de Periódicos). A.M. Silva also acknowledges CNPq for her research grant (#309946/2023-4).

Declaration of generative AI and AI-assisted technologies in the manuscript preparation process

During the preparation of this work, the authors used Google Gemini in order to improve text fluency. After using this tool/service, the authors reviewed and edited the content as needed and take full responsibility for the content of the published article.

3.5.6 References

Anjos-Zerfass, G.S., 2009. Estudos paleoambientais com base em isótopos de carbono, oxigênio e estrôncio em foraminíferos do Terciário da Bacia de Pelotas. [Palaeoenvironmental study based on carbon, oxygen and strontium isotopes in foraminifers from the Tertiary of the Pelotas Basin]. Ph.D. Thesis, Universidade Federal do Rio Grande do Sul.

ASQUITH, G; GIBSON, C. Basic Well Logs Analysis for Geologists: AAPG Methods in Exploration Series. 3.ed. Tulsa, Oklahoma: American Association of Petroleum Geologists, 1983.

Berndt, M. E., Allen, D. E. & Seyfried, W. E. 1996. Reduction of CO2 during serpentinization of olivine at 300 C and 500 bar. Geology, 24, 351–354.

Boreham, C. J., Edwards, D. S., Czado, K., Rollet, N., Wang, L., van der Wielen, S., ... & Henson, P. A. (2021). Hydrogen in Australian natural gas: occurrences, sources and resources. The APPEA Journal, 61(1), 163-191.

Bouquet, A., Glein, C. R., Wyrick, D., & Waite, J. H. (2017). Alternative energy: production of H2 by radiolysis of water in the rocky cores of icy bodies. The Astrophysical Journal Letters, 840(1), L8

Bueno, G. V., Zacharias, A. A., Oreiro, S. G., Cupertino, J. A., Falkenhein, F. U., & Neto, M. A. M. (2007). Bacia de Pelotas. Boletim de Geociências da Petrobras, 15(2), 551-559.

Cassata, W. S., Renne, P. R., & Shuster, D. L. (2009). Argon diffusion in plagioclase and implications for thermochronometry: A case study from the Bushveld Complex, South Africa. Geochimica et Cosmochimica Acta, 73(21), 6600-6612.

Cassel, M. C., Chemale Jr., F., Vargas, M. R., Souza, M. K., Girelli, T. J., and Oliveira, G. S.: From the Andes and the Drake Passage to the Rio Grande Submarine Fan: paleoclimatic and paleogeographic evidence in the Cenozoic Era from the South Atlantic – Austral Segment, Pelotas Basin, Global Planet. Change, 213, 103838, https://doi.org/10.1016/j.gloplacha.2022.103838, 2022.

Cassel, M. C., Kusznir, N., Manatschal, G., & Sauter, D. (2024). Along-strike variation in volcanic addition controlling post-breakup sedimentary infill: Pelotas margin, austral South Atlantic. Solid Earth, 15(10), 1265-1279.

Castillo López, L. A. (2009). Interpretação sismoestratigráfica e geonorfologia sísmica do Cone de Rio Grande, Bacia de Pelotas.

Chauvet, F., Sapin, F., Geoffroy, L., Ringenbach, J. C., & Ferry, J. N. (2021). Conjugate volcanic passive margins in the austral segment of the South Atlantic–Architecture and development. Earth-Science Reviews, 212, 103461.

Chemale Junior, F. , Lavina, E. L. C., Carassai, J. J., Girelli, T. J., & Lana, C. (2021). Andean orogenic signature in the Quaternary sandy barriers of Southernmost Brazilian Passive Margin–Paradigm as a source area. Geoscience Frontiers, 12(4), 101119.

Conti, B., de Jesus Perinotto, J. A., Veroslavsky, G., Castillo, M. G., de Santa Ana, H., Soto, M., & Morales, E. (2017). Speculative petroleum systems of the southern Pelotas Basin, offshore Uruguay. Marine and Petroleum Geology, 83, 1-25.

Daners, G., & Guerstein, G. R. (2004). Dinoflagelados del Maastrichtiense-Paleógeno en la Formación Gaviotín, cuenca Punta del Este. Cuencas sedimentarias de Uruguay, 2, 37-62.

Dias, J. L., Sad, A. R., Fontana, R. L., & Feijó, F. J. (1994). Bacia de Pelotas. Boletim de Geociências da PETROBRAS, 8(1), 235-245.

do Monte Guerra, R., Tokutake, L. R., & Fauth, G. (2012). Cretaceous calcareous nannofossils from Pelotas Basin, Brazil: Biostratigraphic and paleoecological inferences. Journal of South American Earth Sciences, 36, 55-71.

Drobner, H. Huber, H. G. Wächtershäuser, D. Rose, K. O. Stetter, Pyrite formation linked with hydrogen evolution under anaerobic conditions. Nature 346, 742–744 (1990).

Finlay, A. J., Wray, D. S., Comfort, G., & Moore, J. K. (2023). Radioactive heat production variations in the Faroe–Shetland Basin: key new heat production, geological and geochronological data for regional and local basin modelling. Petroleum Geoscience, 29(4), petgeo2022-039.

Fontana, R. L. (1996). Geotectônica e sismoestratigrafia da Bacia de Pelotas e Plataforma de Florianópolis. Universidade Federal do Rio Grande do Sul. Tese de Doutorado em Geociências. Porto Alegre, RS, 2.

Gelman, S. E., Hearon, J. S., & Ellis, G. S. (2025). Prospectivity mapping for geologic hydrogen (No. 1900). US Geological Survey.

Geymond, U., Ramanaidou, E., Lévy, D., Ouaya, A., & Moretti, I. (2022). Can weathering of banded iron formations generate natural hydrogen? Evidence from Australia, Brazil and South Africa. Minerals, 12(2), 163.

Girelli, T., Rizzi, M., Lehn, I., Serratt, H., Chieli, M., Teixeira, C., ... & Chemale, F. (2023, September). The Geochemical Fingerprint of the Pelotas and Punta del Este Basins. In First EAGE Conference on South Atlantic Offshore Energy Resources (Vol. 2023, No. 1, pp. 1-6). European Association of Geoscientists & Engineers.

Gomide, J. (1989). Bacia de Pelotas–Biocronoestratigrafia baseada em nanofósseis calcários. In Congresso brasileiro de Paleontologia (Vol. 11, No. 1989, pp. 338-351).

Gordon, A. C., & Mohriak, W. U. (2015). Seismic volcano-stratigraphy in the basaltic complexes on the rifted margin of Pelotas Basin, Southeast Brazil.

Harkin, C., Kusznir, N., Roberts, A., Manatschal, G., & Horn, B. (2020). Origin, composition and relative timing of seaward dipping reflectors on the Pelotas rifted margin. Marine and Petroleum Geology, 114, 104235.

Harkin, C., Kusznir, N., Roberts, A., Manatschal, G., & Horn, B. (2020). Origin, composition and relative timing of seaward dipping reflectors on the Pelotas rifted margin. Marine and Petroleum Geology, 114, 104235.

Hedley, R., Intawong, A., Winter, F., & Sibeya, V. (2022). Hydrocarbon play concepts in the Orange Basin in light of the Venus and Graff oil discoveries. First Break, 40(5), 91-95.

Hekinian, M. Chaigneau, J. L. Cheminee, Popping rocks and lava tubes from the Mid-Atlantic Rift Valley at 36°N. Nature 245, 371–373 (1973).

Holz, M., Kalkreuth, W., & Rolim, S. B. A. (2010). Extension of the Paraná Basin to offshore Brazil: Implications for coalbed methane evaluation. Marine and Petroleum Geology, 27(5), 1119-1132.

Horsfield, B., Mahlstedt, N., Weniger, P., Misch, D., Vranjes-Wessely, S., Han, S., & Wang, C. (2022). Molecular hydrogen from organic sources in the deep Songliao Basin, PR China. International Journal of Hydrogen Energy, 47(38), 16750-16774.

Iyare, U. C., Zandanel, A., Neil, C. W., KC, B., Rock, M., Li, W., ... & Gross, M. R. (2025). Impact of hydrogen exposure on the integrity of shale caprock for underground hydrogen storage. International Journal of Hydrogen Energy, 161, 150706.

Jones, F. (2007). Geophysics foundations: Physical properties: density.

Koppers, A.A.P., 2002. ArArCALC--software for 40Ar/39Ar age calculations. Computers & Geosciences 28, 605-619.

Kourougianni, F., Arsalis, A., Olympios, A. V., Yiasoumas, G., Konstantinou, C., Papanastasiou, P., & Georghiou, G. E. (2024). A comprehensive review of green hydrogen energy systems. Renewable Energy, 231, 120911.

Koutsoukos, E. A. M. (1982). Geohistória e paleoecologia das bacias marginais de Florianópolis e Santos. In Congresso brasileiro de Geologia, XXXII, Salvador, Anais (Vol. 5, pp. 2369-2382).

Kovač, A., Paranos, M., & Marciuš, D. (2021). Hydrogen in energy transition: A review. International Journal of Hydrogen Energy, 46(16), 10016-10035.

Mahlstedt, N., Horsfield, B., Weniger, P., Misch, D., Shi, X., Noah, M., & Boreham, C. (2022). Molecular hydrogen from organic sources in geological systems. Journal of Natural Gas Science and Engineering, 105, 104704.

Maiga, O., Deville, E., Laval, J., Prinzhofer, A., & Diallo, A. B. (2023). Characterization of the spontaneously recharging natural hydrogen reservoirs of Bourakebougou in Mali. Scientific Reports, 13(1), 11876.

Maiga, O., Deville, E., Laval, J., Prinzhofer, A., & Diallo, A. B. (2024). Trapping processes of large volumes of natural hydrogen in the subsurface: The emblematic case of the Bourakebougou H2 field in Mali. International Journal of Hydrogen Energy, 50, 640-647.

Maraschin, A. J., Luvizotto, G. L., Ketzer, J. M. M., Mizusaki, A. M., & de Menezes, M. R. F. (2024). On the radiometric significance of glauconies in studies of provenance: An example of the quaternary marine sequences of the Rio Grande Cone (Pelotas basin, southern Brazil). Journal of South American Earth Sciences, 141, 104936.

Martins, I. D. R. (1984). Modelo Sedimentar do Cone de Rio Grande. Pesquisas em Geociências, 16, 91.

Miller, D. J., Ketzer, J. M., Viana, A. R., Kowsmann, R. O., Freire, A. F. M., Oreiro, S. G., ... & Sbrissa, G. F. (2015). Natural gas hydrates in the Rio Grande Cone (Brazil): A new province in the western South Atlantic. Marine and Petroleum Geology, 67, 187-196. https://doi.org/10.1016/j.marpetgeo.2015.05.012.

Moulin, M., Aslanian, D., & Unternehr, P. (2010). A new starting point for the South and Equatorial Atlantic Ocean. Earth-Science Reviews, 98(1-2), 1-37.

Murray, J., Clément, A., Fritz, B., Schmittbuhl, J., Bordmann, V., & Fleury, J. M. (2020). Abiotic hydrogen generation from biotite-rich granite: A case study of the Soultz-sous-Forêts geothermal site, France. Applied Geochemistry, 119, 104631.

Novo, R., de Jesus Perinotto, J. A., Castillo, M. G., & Conti, B. (2023). Heat flow modelling of the Punta del Este Basin (offshore Uruguay) and its correlation with structural crustal domains. Tectonophysics, 854, 229812.

O'Reilly, S. Y., & Griffin, W. L. (2010). The continental lithosphere–asthenosphere boundary: can we sample it?. Lithos, 120(1-2), 1-13.

Prinzhofer, A., Cissé, C. S. T., & Diallo, A. B. (2018). Discovery of a large accumulation of natural hydrogen in Bourakebougou (Mali). International Journal of Hydrogen Energy, 43(42), 19315-19326.

Rabinowitz, P. D., & LaBrecque, J. (1979). The Mesozoic South Atlantic Ocean and evolution of its continental margins. Journal of Geophysical Research: Solid Earth, 84(B11), 5973-6002.

Ramires, M. L., Nieto de Castro, C. A., Nagasaka, Y., Nagashima, A., Assael, M. J., & Wakeham, W. A. (1995). Standard reference data for the thermal conductivity of water. Journal of Physical and Chemical Reference Data, 24(3), 1377-1382.

Rickard, G. W. Luther, Kinetics of pyrite formation by the H2S oxidation of iron (II) monosulfide in aqueous solutions between 25 and 125°C: The mechanism. Geochim. Cosmochim. Acta 61, 135–147 (1997)

Rizzi, M. A. M., Dillenburg, S. R., Takehara, L., Girelli, T. J., Wust, C. F., de Carvalho Lana, C., & Junior, F. C. (2022). Andean fingerprint on placer sands from the southern Brazilian coast. Sedimentary Geology, 428, 106061.

Sad, A. R. E., Silveira, D. P., Machado, D. A. P., Silva, S. R. P., & Maciel, R. R. (1998). Marine gas hydrates evidence along the Brazilian coast. In Proc. AAPG international conference and exhibition. Rio de Janeiro, Brazil. Nov (pp. 8-11).

Sekerci, F., Fischer, S., Joshi, P., Peiffer, S., Kappler, A., & Mansor, M. (2025). Sulfur microenvironments as hotspots for biogenic pyrite formation. Scientific Reports, 15(1), 20148.

Sequeira, M., Morales, E., Moretti, I., Veroslavsky, G., Plenc, F., d'Avila, R., & de Santa Ana, H. (2025). Natural Hydrogen in Uruguay: Catalog of H2-Generating Rocks, Prospective Exploration Areas, and Potential Systems. Geosciences, 15(2), 54.

Serra, O. (1984). Fundamentals of well-log interpretation: Vol. 1. The acquisition of logging data. Elsevier.

Serra, O. (1986). Fundamentals of well-log interpretation: Vol. 2. The interpretation of logging data. Elsevier.

Serratt, H., Cupertino, J. A., Cruz, M. F., Girelli, T. J., Lehn, I., Teixeira, C. D., ... & Chemale Jr, F. (2024). Southern Brazil hydrogen systems review. International Journal of Hydrogen Energy, 69, 347-357.

Serratt, H., Domingues Teixeira, C., Girelli, T. J., de Souza, M. K., Rodrigues Vargas, M., Moreira Silva, A., & Chemale Jr., F. (2022). Seaward-dipping reflector influence on seafloor magnetostratigraphy—A Pelotas Basin view. Geophysical Research Letters, 49(23), e2022GL100382.

Serratt, H., Girelli, T. J., Da Cruz, M. F., Teixeira, C. D., Lehn, I., Rizzi, M., ... & Junior, F. C. (2025). Unraveling the geological history of the South Atlantic margin: Records of West Gondwana Breakup from South Brazil and Uruguay margin. Tectonophysics, 230790.

Smith, N. J. P., Shepherd, T. J., Styles, M. T., & Williams, G. M. (2005). Hydrogen exploration: a review of global hydrogen accumulations and implications for prospective areas in NW Europe.

Steiger, R. H., Jäger, E. 1977. Subcommission on geochronology: convention on the use of decay constants in geo-and cosmochronology. Earth and Planetary Science Letters 36, 359-362.

Stica, J. M., Zalán, P. V., & Ferrari, A. L. (2014). The evolution of rifting on the volcanic margin of the Pelotas Basin and the contextualization of the Paraná–Etendeka LIP in the separation of Gondwana in the South Atlantic. Marine and Petroleum Geology, 50, 1-21.

Tagliaro, G., Britzke, A., Gama, M. A., Bauli, P., Negrão, A. P., & Jovane, L. (2024). Neogene evolution of the margin adjacent to the La Plata River Delta (Pelotas Basin): Sedimentary pathways and the origins of the Rio Grande Cone. Basin Research, 36(1), e12848.

Teixeira, C. D., Girelli, T. J., Serratt, H., & Chemale, F. (2025b). Revisiting the Dom Feliciano Belt and surrounding areas–An integrated geophysical and isotope geology approach. Earth-Science Reviews, 105135.

Teixeira, C. D., Girelli, T. J., Serratt, H., Oliveira, H. O. S., Cruz, M. F., Conti, B., ... & Chemale Jr, F. (2025a). Paleogeographic significance of unknown hyperextended continental crust in South Atlantic conjugated margin. Geoscience Frontiers, 16(1), 101934.

Truche, L., Berger, G., Destrigneville, C., Guillaume, D., & Giffaut, E. (2010). Kinetics of pyrite to pyrrhotite reduction by hydrogen in calcite buffered solutions between 90 and 180 C: Implications for nuclear waste disposal. Geochimica et Cosmochimica Acta, 74(10), 2894-2914.

Urien C.M. & Martins L.R.S. 1978. Structural & physiographic map of eastern South America & western South Africa. Porto Alegre, Centro de Estudos de Geologia Costeira e Oceânica (CECO/UFRGS), Série Mapas, 03.

Wang, F., F. Jourdan, C.-H. Lo, S. Nomade, H. Guillou, R.X. Zhu, L. Yang, W. Shi, H. Feng, L. Wu, H. Sang, 2014.YBCs: A new standard for 40Ar/39Ar dating. Chemical Geology, 388: 87-98. doi:10.1016/j.chemgeo.2014.09.003

Worman, S. L., Pratson, L. F., Karson, J. A., & Klein, E. M. (2016). Global rate and distribution of H2 gas produced by serpentinization within oceanic lithosphere. Geophysical Research Letters, 43(12), 6435-6443.

Worman, S. L., Pratson, L. F., Karson, J. A., & Schlesinger, W. H. (2020). Abiotic hydrogen (H2) sources and sinks near the Mid-Ocean Ridge (MOR) with implications for the subseafloor biosphere. Proceedings of the National Academy of Sciences, 117(24), 13283-13293.

York, D., (1969), Least squares fitting of a straight line with correlated errors. Earth Planet. Sci. Lett. 5, 320-324.

Zalán, P.; Etherington,R; Cvetkovic, M. (2022). Pelotas Basin in Brazil – A Fantastic Analogue to the Orange Basin in Namibia. GEO ExPro 5-2022.

Zerfass, G. D. S. D. A., Chemale, F., Jr., Moura, C. A. V., Costa, K. B., & Kawashita, K. (2014). Strontium isotope stratigraphy of the Pelotas Basin. Brazilian Journal of Geology, 44, 23–38.

Zgonnik, V. (2020). The occurrence and geoscience of natural hydrogen: A comprehensive review. Earth-Science Reviews, 203, 103140.

Zhang, W. F., Li, J. J., Zheng, D. W., Sun, S. H., Guo, Y. F., Zhang, J., Xiao, M., Wang, J. J., Zhang, Y. L., Jiang, Y. D., Xu, Y. G. 2023. Sample neutron irradiation with the Min Jiang Testing Reactor (MJTR): implications for high-precision 40Ar/39Ar dating. Journal of Analytical Atomic Spectrometry 38, 1540-1548.

Zouain, R. N. A. (1986). Aspectos da dinâmica sedimentar no Rio de la Plata exterior e plataforma interna adjacente. Instituto de Geociências, Universidade Federal do Rio Grande do Sul, Porto Alegre, Dissertação de Mestrado.

Zuo, G., Wang, H., Lan, L., Zhang, Y., Zuo, Y., Yang, L., ... & Yang, M. (2023). Present geothermal field of the Santos Basin, Brazil. Scientific Reports, 13(1), 12369.

5 Conclusion

Using geological, geochemical, and geophysical data, this study enhanced the understanding of the Pelotas Basin margin's evolution and constrained its H_2 potential at the basin scale. This research addressed the data and analyses required for basin characterization within the play-based exploration framework. Overall, the results highlight the need for a follow-up study focusing on the sequence stratigraphy of the Cretaceous to define a potential play in this interval (Figure 5-1).

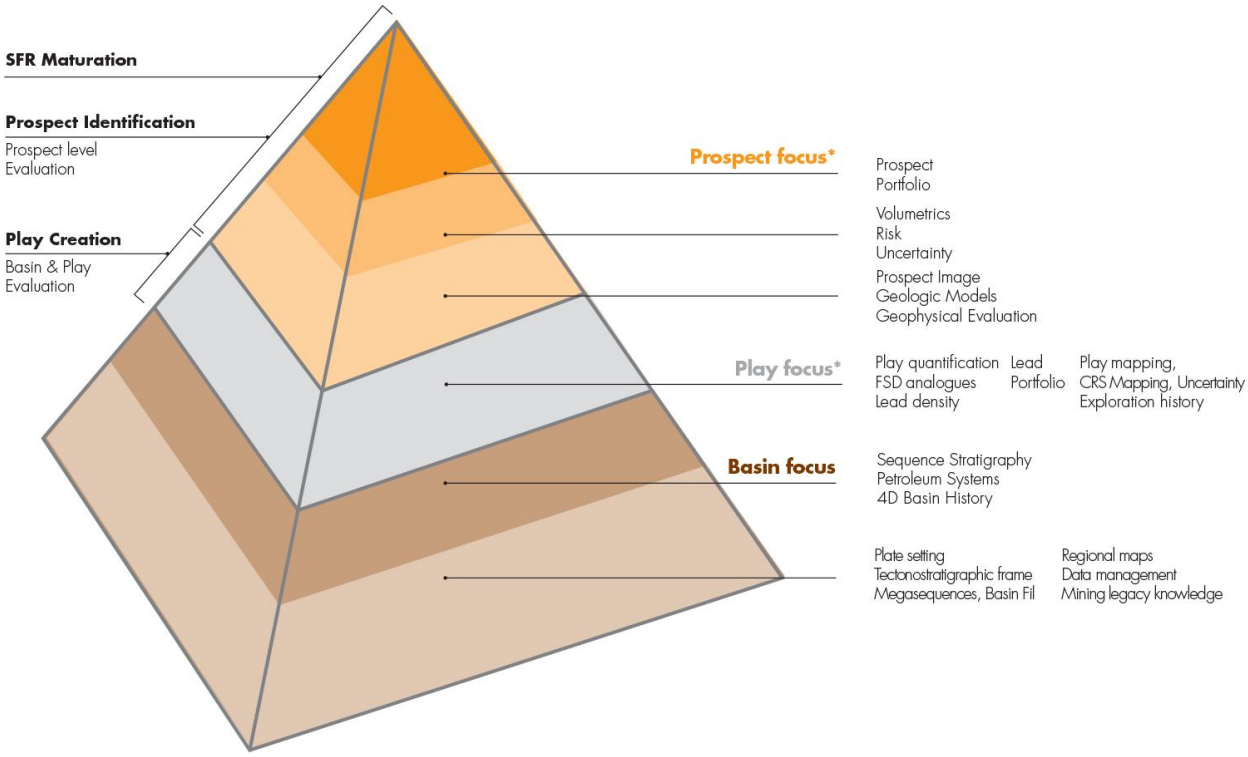

Figure 5-1. The play-based exploration pyramid (figure from Royal Dutch Shell, 2014). Originally developed for the oil industry, the framework can be readily adapted to H_2 exploration by considering the specific characteristics of hydrogen systems. This study adopts a basin-scale perspective, addressing large-scale aspects such as plate tectonic setting, tectonostratigraphic framework, basin fill, regional mapping, data management, and H_2 systems. The framework remains incomplete pending sequence stratigraphic interpretation and the development of a detailed 4D basin evolution model.

This research contributed to improving the understanding of regional geology. For instance, the Gaviotín-1 well recovered Permo-Carboniferous deposits of the Itararé Group (Paraná Basin). Furthermore, geochemical signatures from volcanic rocks in the Lobo-1 and 1-RSS-3-RS wells, combined with seismic interpretations, suggest that these units belong to the Paraná–Etendeka Large Igneous Province (LIP), known as the Serra Geral Group in the Paraná Basin stratigraphic framework. These findings indicate that the sedimentary and volcanic

sequences of the Paraná Basin likely extend across the offshore continental margin, with an extent comparable to that of the continental crust.

Previous research has identified a wide range of volcanic compositions in rocks from the Pelotas Basin. All volcanic samples analyzed from the margin are basalts, ranging from sub-alkaline to alkaline compositions, and display varying degrees of continental crust contamination, as indicated by their geochemical and isotopic signatures, and the presence of zircon xenocrysts. We conclude that all analyzed volcanic rocks from the margin were basalts formed above the continental crust.

New $^{40}Ar/^{39}Ar$ dating of these basalts constrains the timing of these magmatic events. In well 1-RSS-3 (at 3555 m), it was obtained an age of 128.14 ± 3.10 Ma, and an intrusive sample at 3904-3905 m with an age of 100.11 ± 1.95 Ma. In well 1-SCS-3B (at 4732 m), it was obtained an age of 121.08 ± 3.09 Ma. A later hydrothermal pulse was recorded in well 2-BPS-6 (at 5378.5m), with ages of 76.45 ± 1.24 Ma, 78.90 ± 1.79 Ma, and 79.19 ± 3.14 Ma. Despite these results, the nature of the mantle source for volcanism remains uncertain. The rocks exhibit geochemical compositions like OIB and E-MORB, with isotopic signatures compatible with EMI and EMII reservoirs. However, these characteristics may reflect significant assimilation of continental crust or subcontinental lithospheric mantle, an interpretation reinforced by the zircon xenocrysts in well 1-RSS-3-RS. The precise location of the continent-ocean boundary (COB) also remains unclear, mainly as features like the Rio Grande Rise may involve continental crust fragments. Although the mantle source is unconstrained, our observations reveal a sequence of magmatic events from 134 Ma continental flood basalts (CFBs) through rift-related SDRs to oceanic plateaus and late magmatism in the margin at 76 Ma.

Concerning hydrogen geology, this magmatism could have released approximately 8.26 × 10^{10} metric tonnes (t) of H_2 through degassing. The faults movement during early South Atlantic Ocean development could have produced 2.78 x 10^9 t of H_2 locally in the Pelotas Basin region. Moreover, the Oxidation of Fe^{2+} bearing minerals in these rocks could have produced about 8.2 x 10^{11} t, although mostly of it should be produced during the 128.14 ± 3.10 Ma to 76.45 ± 1.24 Ma interval. Being the sedimentary rocks of this interval, the most prospective. A shift in the basin depocenter was observed during the Cretaceous. The earliest depocenter is located beneath the Rio Grande Cone Mega-slide Complex, which represents the interval with the highest potential for H_2 accumulation. Beyond this magmatic framework, it was also possible to quantitatively assess other potential sources of natural hydrogen (H_2) in the Pelotas Basin, including intra-basin radiolysis (1.54 × 10^{10} t) and thermogenic generation (7.32 × 10^{10}

t). Thermogenic H_2 represents a potentially significant source; however, its potential association with hydrocarbon formation makes it likely to be "stillborn." The thermogenic H_2 volume was estimated using a regional thermal gradient of 30.2 °C/km, derived from bottom-hole temperature data. Radiolytic H_2, in contrast, is continuously produced but is widely distributed throughout the basin. Radiolysis remains an interesting and persistent source as long as radioactive decay continues, although its production rate is relatively low. Among the sinks, sulfur was identified as a major one, with a maximum theoretical capacity of 3.80×10^{11} t of H_2. Another sink is the H_2 retained in the basalts, which was estimated at 4.73×10^{10} t of H_2. In general, siliciclastic rocks from marine environments are unfavorable for H_2 preservation. However, the number of sinks that could not be quantified with the dataset used in this thesis is considerable and includes H_2 leakage to the atmosphere, CO_2 hydrogenation, and biological consumption. In the Pelotas Basin, the latter may represent a significant sink, as more than 45,000 km² of biogenic gas hydrates occur within the basin's shallow sediments, making it a high-risk prospect. In general, basins developed in VPM environments have all the elements required for intra-basin H_2 generation, including radiolytic and thermogenic sources, with an additional contribution from magmatism during the early stages of their evolution. Therefore, the magmatic stages represent the most prospective intervals, and young VPMs such as the Red Sea could be the most favorable settings for H_2 systems.

We observed that rocks formed from deep siliciclastic marine sediments have high sulfur contents, which could act as an important sink, making them less favorable for H_2 reservoirs. Consequently, even onshore basins that record old siliciclastic deep marine strata could be less favorable for H_2 accumulation.

The data in this research suggest a shift in exploration paradigms. In oil and gas systems, the focus is on source rock. However, in hydrogen systems the primary challenge lies in identifying the geological conditions that allow hydrogen to accumulate and be preserved. Therefore, the paradigm for H_2 prospection should focus on preservation and accumulation conditions, meaning that seal quality and reservoirs rocks with low sulfur and low microbial activity are favorable.

6 References

References from chapters 1, 2, and 5:

Ahmadpour, S., & Gholami, R. (2025). Hydrogen sulfide in underground hydrogen storage sites: Implication of thermochemical sulfate reduction. *Deep Underground Science and Engineering*.

Aitken M. J. 1985 *Thermoluminescence Dating* (New York: Academic)

Allegre, C. J., & Othman, D. B. (1980). Nd-Sr isotopic relationship in granitoid rocks and continental crust development: a chemical approach to orogeny. Nature, 286(5771), 335-342. (Note: This seems to be the commonly cited 1980 paper by Allegre & Othman on this topic, though the journal differs from your text citation "Eos").

Allègre, C. J., & Othman, D. B. (1980). Nd–Sr isotopic relationship in granitoid rocks and continental crust development: a chemical approach to orogenesis. *Nature*, *286*(5771), 335-342.

Apps, J. A., & van de Kamp, P. C. (1984). Energy gases of abiogenic origin in the Earth's crust. *US Geological Survey Professional Paper*, (1570), 81.

ASQUITH, G; GIBSON, C. Basic Well Logs Analysis for Geologists: AAPG Methods in Exploration Series. 3.ed. Tulsa, Oklahoma: American Association of Petroleum Geologists, 1983.

Baker, R. O., Yarranton, H. W., & Jensen, J. L. (2015). Openhole Well LogsLog Interpretation Basics. *Practical Reservoir Engineering and Characterization, Elsevier*, *534*, 297-343.

Baker, R. O., Yarranton, H. W., & Jensen, J. L. (2015). Openhole Well LogsLog Interpretation Basics. *Practical Reservoir Engineering and Characterization, Elsevier*, *534*, 297-343.

Blair, P., Chadwick, K., D'Hondt, S., Spivack, A., & Pockalny, R. (2007). Radiolytic hydrogen and microbial respiration in subsurface sediments. Astrobiology, 7(2), 335-344.

Boreham CJ, Davies JB. Carbon and hydrogen isotopes of the wet gases produced by gamma-ray-induced polymerisation of methane: insights into radiogenic mechanism and natural gas formation. Radiat Phys Chem 2020;168:108546.

Boreham CJ, Edwards DS, Feitz AJ, Murray AP, Mahlstedt N, Horsfield B. Modelling of hydrogen gas generation from overmature organic matter in the Cooper Basin, Australia. The APPEA J 2023;63(2):S351–6.

Boreham, C. J., Edwards, D. S., Czado, K., Rollet, N., Wang, L., van der Wielen, S., ... & Henson, P. A. (2021). Hydrogen in Australian natural gas: occurrences, sources and resources. The APPEA Journal, 61(1), 163-191.

Bouquet, A., Glein, C. R., Wyrick, D., & Waite, J. H. (2017). Alternative energy: Production of H2 by radiolysis of water in the rocky cores of icy bodies. The Astrophysical Journal Letters, 840(1), L8.

Bowring, S. A., & Schmitz, M. D. (2003). High-precision U–Pb zircon geochronology and the stratigraphic record. Reviews in mineralogy and geochemistry, 53(1), 305-326.

Bulhões, E. M., Guerra, F. P., Johann, P. R., & Machado, A. S. (2014, August). Geostatistical 3D Density Modeling: Integrating Seismic Velocity and Well Logs. In 14th International Congress of the Brazilian Geophysical Society & EXPOGEF, Rio de Janeiro, Brazil, 18-21 August 2014 (pp. 411-416). Society of Exploration Geophysicists and Brazilian Geophysical Society.

Bullard, E. C. (1947). The time necessary for a bore hole to attain temperature equilibrium. Monthly Notices of the Royal Astronomical Society, Geophysical Supplement, 5(5), 127-130.

Chauvet, F., Sapin, F., Geoffroy, L., Ringenbach, J. C., & Ferry, J. N. (2021). Conjugate volcanic passive margins in the austral segment of the South Atlantic–Architecture and development. Earth-Science Reviews, 212, 103461.

Chemale Jr, F., Kawashita, K., Dussin, I. A., Ávila, J. N., Justino, D., & Bertotti, A. L. (2012). U–Pb zircon in situ dating with LA–MC–ICP–MS using a mixed detector configuration. Anais da Academia Brasileira de Ciências, 84, 275-295. (Note: This matches the 2012 reference in your text, not 2011).

de Freitas, V. A., Prinzhofer, A., Françolin, J. B., Ferreira, F. J. F., & Moretti, I. (2024). Natural hydrogen system evaluation in the São Francisco Basin (Brazil). *Science and Technology for Energy Transition*, *79*, 95.

DePaolo, D. J. (1981). Nd isotopic studies: Some new perspectives on earth structure and evolution. Eos, Transactions American Geophysical Union, 62(14), 137-141.

Deville, E., Prinzhofer, A., Pillot, D., Bats, J., Goulaouic, H., & Calassou, S. (2023). Natural hydrogen potential and basaltic alteration in the Asal–Ghoubbet rift, Republic of Djibouti. BSGF-Earth Sciences Bulletin, 194, 10.

Dickin, A. P. (2005). Radiogenic isotope geology. Cambridge University Press.

Dowaidar, M. (2025). Microbial pathways for sustainable hydrogen production. *International Journal of Hydrogen Energy*, *142*, 825–841. https://doi.org/10.1016/j.ijhydene.2024.12.446

Flude, S., Warr, O., Magalhães, N., Bordmann, V., Fleury, J. M., Reis, H., ... & Ballentine, C. J. (2025). Generation, migration and accumulation of natural hydrogen and helium in the intracratonic São Francisco Basin, eastern Brazil: implications for the understanding and exploration of natural H2 systems. Geoenergy, 3(1), geoenergy2024-042.

Gao, Q., Piotrowski, A. M., Li, Z., Loh, P. S., Han, C., Wang, Z., ... & Chen, Y. (2024). Geochemical behavior of C, N, and S in sediments of Hangzhou Bay, Southeastern China: implications for the study of paleoclimate and sea-level changes. *Frontiers in Marine Science*, *11*, 1308739.

Gehrels, G. E. (2014). Detrital zircon U-Pb geochronology applied to tectonics. Annual Review of Earth and Planetary Sciences, 42, 127-149.

Gelman, S. E., Hearon, J. S., & Ellis, G. S. (2025). *Prospectivity mapping for geologic hydrogen* (No. 1900). US Geological Survey.

Geoffroy, L. (2005). Volcanic passive margins. Comptes Rendus Geoscience, 337(16), 1395-1408.

Geoffroy, L., Burov, E. B., & Werner, P. (2015). Volcanic passive margins: another way to break up continents. Scientific reports, 5(1), 14828.

Gill, B. C., Lyons, T. W., & Saltzman, M. R. (2007). Parallel, high-resolution carbon and sulfur isotope records of the evolving Paleozoic marine sulfur reservoir. *Palaeogeography, Palaeoclimatology, Palaeoecology*, *256*(3-4), 156-173.

Gill, R. (2010). Igneous rocks and processes: a practical guide. John Wiley & Sons.

Guélard, J., Beaumont, V., Rouchon, V., Guyot, F., Pillot, D., Jezequel, D., ... & Deville, E. (2017). Natural H2 in Kansas: Deep or shallow origin?. Geochemistry, Geophysics, Geosystems, 18(5), 1841-1865.

Hand, E. (2023). Hidden hydrogen. Science (New York, NY), 379(6633), 630-636.

Harkin, C., Kusznir, N., Roberts, A., Manatschal, G., & Horn, B. (2020). Origin, composition and relative timing of seaward dipping reflectors on the Pelotas rifted margin. Marine and Petroleum Geology, 114, 104235.

Harris, R. E., & Pimblott, S. M. (2002). On 3H β-particle and 60Co γ irradiation of aqueous systems. *Radiation research*, *158*(4), 493-504.

Haynes, W. M. (2016). *CRC handbook of chemistry and physics*. CRC press.

He, K., Wang, X., Yang, C., & Zhang, S. (2024). Hydrocarbon gas generation from direct and indirect hydrogenation of organic matter: Implications from hydrothermal experiments. *Processes*, *12*(3), 458.

Horsfield B, Mahlstedt N, Weniger P, Misch D, Vranjes-Wessely S, Han S, Wang C. Molecular hydrogen from organic sources in the deep Songliao Basin, PR China. Int J Hydrogen Energy 2022;47(38):16750–74.

Hunt, J. M. (1996). *Petroleum geochemistry and geology*. WH Freeman.

IEA (2024), *Global Hydrogen Review 2024*, IEA, Paris https://www.iea.org/reports/global-hydrogen-review-2024, Licence: CC BY 4.0

Ismail, Ahmad Fauzi; Khulbe, Kailash; Matsuura, Takeshi, *Gas Separation Membranes: Polymeric and Inorganic*, Springer, 2015 ISBN 3319010956.

Iyare, U. C., Zandanel, A., Neil, C. W., KC, B., Rock, M., Li, W., ... & Gross, M. R. (2025). Impact of hydrogen exposure on the integrity of shale caprock for underground hydrogen storage. *International Journal of Hydrogen Energy*, *161*, 150706.

Kovač, A., Paranos, M., & Marciuš, D. (2021). Hydrogen in energy transition: A review. *International Journal of Hydrogen Energy*, *46*(16), 10016-10035.

Lachenbruch, A. H., & Brewer, M. C. (1959). *Dissipation of the temperature effect of drilling a well in Arctic Alaska* (Vol. 1083, No. C). US Government Printing Office.

Le Caër S. 2011 *Water* **3** 235

Lodders, K. (2019). Solar elemental abundances. *arXiv preprint arXiv:1912.00844*.

Mahlstedt, N., Horsfield, B., Weniger, P., Misch, D., Shi, X., Noah, M., & Boreham, C. (2022). Molecular hydrogen from organic sources in geological systems. *Journal of Natural Gas Science and Engineering*, *105*, 104704.

Maiga, O., Deville, E., Laval, J., Prinzhofer, A., & Diallo, A. B. (2023). Characterization of the spontaneously recharging natural hydrogen reservoirs of Bourakebougou in Mali. *Scientific Reports*, *13*(1), 11876.

Maiga, O., Deville, E., Laval, J., Prinzhofer, A., & Diallo, A. B. (2024). Trapping processes of large volumes of natural hydrogen in the subsurface: The emblematic case of the Bourakebougou H2 field in Mali. *International Journal of Hydrogen Energy*, *50*, 640-647.

Mayhew, L. E., Ellison, E. T., McCollom, T. M., Trainor, T. P., & Templeton, A. S. (2013). Hydrogen generation from low-temperature water–rock reactions. *Nature Geoscience*, *6*(6), 478-484.

McCollom, T. M., Klein, F., Solheid, P., & Moskowitz, B. (2020). The effect of pH on rates of reaction and hydrogen generation during serpentinization. *Philosophical Transactions of the Royal Society A*, *378*(2165), 20180428.

Micheal, D. (2024, November). *Comparing carbon emissions of different hydrogen production methods and exploring future innovations*. New York University.

Milesi, V., Prinzhofer, A., Guyot, F., Benedetti, M., & Rodrigues, R. (2016). Contribution of siderite–water interaction for the unconventional generation of hydrocarbon gases in the Solimões basin, north-west Brazil. *Marine and Petroleum Geology*, *71*, 168-182.

Miller, D. J., Ketzer, J. M., Viana, A. R., Kowsmann, R. O., Freire, A. F. M., Oreiro, S. G., ... & Sbrissa, G. F. (2015). Natural gas hydrates in the Rio Grande Cone (Brazil): A new province in the western South Atlantic. *Marine and Petroleum Geology*, *67*, 187-196.

Murray, J., Clément, A., Fritz, B., Schmittbuhl, J., Bordmann, V., & Fleury, J. M. (2020). Abiotic hydrogen generation from biotite-rich granite: A case study of the Soultz-sous-Forêts geothermal site, France. *Applied Geochemistry*, *119*, 104631.

Mutter, J. C., Talwani, M., & Stoffa, P. L. (1982). Origin of seaward-dipping reflectors in oceanic crust off the Norwegian margin by "subaerial sea-floor spreading". *Geology*, *10*(7), 353-357.

Osselin, F., Soulaine, C., Fauguerolles, C., Gaucher, E. C., Scaillet, B., & Pichavant, M. (2022). Orange hydrogen is the new green. *Nature Geoscience*, *15*(10), 765-769.

Pasquet, G., Idriss, A. M., Ronjon-Magand, L., Ranchou-Peyruse, M., Guignard, M., Duttine, M., ... & Moretti, I. (2023). Natural hydrogen potential and basaltic alteration in the Asal–Ghoubbet rift, Republic of Djibouti. *BSGF-Earth Sciences Bulletin*, *194*(1), 9.

Philpotts, Anthony R.; Ague, Jay J. (2009). *Principles of igneous and metamorphic petrology* (2nd ed.). Cambridge, UK: Cambridge University Press.

Prinzhofer, A., Cissé, C. S. T., & Diallo, A. B. (2018). Discovery of a large accumulation of natural hydrogen in Bourakebougou (Mali). International Journal of Hydrogen Energy, 43(42), 19315-19326.

Rivard, E., Trudeau, M., & Zaghib, K. (2019). Hydrogen storage for mobility: a review. *Materials*, *12*(12), 1973.

Rivard, E., Trudeau, M., & Zaghib, K. (2019). Hydrogen storage for mobility: a review. *Materials*, *12*(12), 1973.

Rosa, A. L., Borba, A. W. D., Hillebrand, G., Tedesco, J., & Lopes, R. D. C. P. (2017). Pelotas Basin. Brazilian Geological Sites, 281-294.

Royal Dutch Shell, 2014: Play Based Exploration, A Guide for AAPG's Imperial Barrel Award Participation

Sad, A. R. E., Silveira, D. P., Machado, D. A. P., Silva, S. R. P., & Maciel, R. R. (1998, November). Marine gas hydrates evidence along the Brazilian coast. In AAPG International Conference and Exhibition.

Serra, Oberto; Serra, Lorenzo (2004). *Well logging : data acquisition and applications*. Méry Corbon, France. ISBN 978-1-62198-787-1. OCLC 860900113.

Serratt, H., Cupertino, J. A., Cruz, M. F., Girelli, T. J., Lehn, I., Teixeira, C. D., ... & Chemale Jr, F. (2024). Southern Brazil hydrogen systems review. International Journal of Hydrogen Energy, 69, 347-357.

Serratt, H., Domingues Teixeira, C., Girelli, T. J., de Souza, M. K., Rodrigues Vargas, M., Moreira Silva, A., & Chemale Jr., F. (2022). Seaward-dipping reflector influence on seafloor magnetostratigraphy—A Pelotas Basin view. Geophysical Research Letters, 49(23), e2022GL100382.

Smith NJP, Shepherd TJ, Styles MT, Williams GM. Hydrogen exploration: a review of global hydrogen accumulations and implications for prospective areas in NW Europe. Geol Soc Lond Petrol Geol Conf Series 2005;6(1):349–58. The Geological Society of London.

Song, X., Zhao, Y., & Dykstra, J. (2016, July). Acoustic ringing effect mitigation for oil well sonic logging. In *2016 American Control Conference (ACC)* (pp. 436-441). IEEE.

Stica, J. M., Zalán, P. V., & Ferrari, A. L. (2014). The evolution of rifting on the volcanic margin of the Pelotas Basin and the contextualization of the Paraná–Etendeka LIP in the separation of Gondwana in the South Atlantic. Marine and Petroleum Geology, 50, 1-21.

Truche L, McCollom TM, Martinez I. Hydrogen and abiotic hydrocarbons: molecules that change the world. Elements: An Int Mag Mineral Geochem Petrol 2020;16(1):13–8.

Truche, L., Berger, G., Destrigneville, C., Guillaume, D., & Giffaut, E. (2010). Kinetics of pyrite to pyrrhotite reduction by hydrogen in calcite buffered solutions between 90 and 180 C: Implications for nuclear waste disposal. *Geochimica et Cosmochimica Acta*, *74*(10), 2894-2914.

Tylor-Jones, T., & Azevedo, L. (2023). Seismic Well Ties and Wavelets. In *A Practical Guide to Seismic Reservoir Characterization* (pp. 107-122). Cham: Springer International Publishing.

Worman, S. L., Pratson, L. F., Karson, J. A., & Klein, E. M. (2016). Global rate and distribution of H2 gas produced by serpentinization within oceanic lithosphere. *Geophysical Research Letters*, *43*(12), 6435-6443.

Worman, S. L., Pratson, L. F., Karson, J. A., & Schlesinger, W. H. (2020). Abiotic hydrogen (H2) sources and sinks near the Mid-Ocean Ridge (MOR) with implications for the subseafloor biosphere. *Proceedings of the National Academy of Sciences*, *117*(24), 13283-13293.

Yilmaz, Ö. (2001). *Seismic data analysis: Processing, inversion, and interpretation of seismic data*. Society of exploration geophysicists.

Zgonnik, V. (2020). The occurrence and geoscience of natural hydrogen: A comprehensive review. *Earth-Science Reviews*, *203*, 103140.

Zhang, W. F., Li, J. J., Zheng, D. W., Sun, S. H., Guo, Y. F., Zhang, J., Xiao, M., Wang, J. J., Zhang, Y. L., Jiang, Y. D., Xu, Y. G. 2023. Sample neutron irradiation with the Min Jiang Testing Reactor (MJTR): implications for high-precision $^{40}Ar/^{39}Ar$ dating. Journal of Analytical Atomic Spectrometry 38, 1540-1548.

Attachments

Joint supervision contract

UnB

UBO
Université de Bretagne Occidentale

JOINTLY SUPERVISED PhD (COTUTELLE) AGREEMENT

- Having regard to the amended Act no. 84-52 of 26 January 1984 on higher education
- Having regard to the Decree of 25 May 2016 on doctoral training;
- Having regard to the favourable opinion of the competent authorities for each institution;
- Having regard to the Brazilian Legislation and the regulation of the graduate program in Geology of the Institute of Geosciences of UnB (IG-UnB)

Between:

Université de Bretagne Occidentale (UBO)

with its registered office at 3, rue des Archives - CS 93837
29238 BREST Cedex 3 (France)
represented by its **President, Prof. Pascal OLIVARD**

on the one hand

and,

Universidade de Brasilia (UnB)

with its registered office at: Campus Darcy Ribeiro, UnB – Brasília, DF, 70910-900

represented by **its Secretary for International Affairs, Prof. Dr. Virgílio Pereira de Almeida**

on the other hand,

hereinafter referred to individually as "the Party" and collectively as "the Parties"

It has been agreed that Mr Henrique SERRATT hereinafter referred to as "the Student", shall carry out a jointly supervised (cotutelle) PhD.

The effectiveness of this Agreement relies on the application of the laws on doctoral training in force at Université de Bretagne Occidentale and at Universidade de Brasilia.

Article 1 - Registration / Acceptance as a PhD student

Name: SERRATT
First name: HENRIQUE
Address (France): Laboratoire GEO-OCEAN - Plouzané - France
Address (country of origin): 175 Pio XII Street, apartment 104; São Leopoldo
Rio Grande Do Sul - Brasil
Date and place of birth: 07/Setembro/1994 - Brasil
Who holds a Master degree: Sedimentary Geology

On: Vale do Rio dos Sinos university (UNISINOS)
Date of registration at UBO: March 2023
Doctoral School: Ecole Doctorale des Sciences de la Mer et du Littoral
Date of pre-registration at UnB: August 2021
Faculty/Department/School: Graduate Geology Program, Institute of Geosciences
Funding: CAPES-PRINT-UNB

Subject: "The impact of seaward dipping reflectors on thermal development of volcanic passive margin basins"

Article 2

The scheduled duration of the research is four years. Where necessary, this duration may be extended, in accordance with applicable laws in both countries and with thesis regulations in both institutions.

Article 3

The duration of the PhD training shall be divided between the two institutions involved in the joint supervision (cotutelle) by alternating periods in the two countries. Time spent in the two countries shall be balanced and is scheduled as follows*:

Time spent in France	Months
From: September 2023 To: August 2024	12
Total	**12**

Time spent in Brazil	Months
From: August 2021 To: August 2023	25
From: September 2024 To: July 2025	11
Total	**36**

* The periods of time spent abroad are not definitive and may be changed according to the progress of the research. No less than 1/3 of the time allotted for preparing the thesis should be spent in either of the partner institutions.

Article 4

Each year, the PhD student shall be enrolled at both institutions but registration fees will be waived in one of them:

2021/2022	Registration fees will be paid at UnB
2022/2023	Registration fees will be paid at UnB
2023/2024	Registration fees will be paid at UBO
2024/2025	Registration fees will be paid at UnB

The Student is responsible for finding accommodation. However, the host University will, wherever possible, help the Student in this endeavour. All living and accommodation expenses are the Student's responsibility.

Article 5

The Student shall have social security and health coverage (in agreement with legal requirements in each country) for the entire duration of the doctoral training. The Student must also make sure he is guaranteed in terms of civil liability.

Article 6

Acceptance of the co-tutelle agreement does not entail any additional financial obligation for any for the signing Universities.

TITLE II: EDUCATIONAL ARRANGEMENTS

Article 7

The two thesis directors jointly supervise the research and training activities of the Student. They undertake to fully perform the role of thesis supervisor for the candidate and to make any necessary arrangements in this context.

Article 8

The doctoral project is supervised by :

- Scientific Supervisor at UBO: Pr. Laurent GEOFFROY, Laboratory GEO-OCEAN
- Scientific Supervisor at UnB: Pr. Adalene Moreira SILVA, Institute of Geosciences
- Co supervisor UnB: Farid CHEMALE Jr, Institute of Geosciences

Article 9

The provisional subject of the thesis submitted by the PhD student is: "The impact of seaward dipping reflectors on thermal development of volcanic passive margin basins"

The thesis shall give rise to a single defense, which will take place at **UnB - Brasilia** and will be recognized by both parties. The defense can be organized in the framework of a video conference.

Two referees, having no link with the two institutions or with the PhD project and nominated jointly by both institutions, will examine the PhD thesis work in advance and provide the authorization for defense.

The composition of the jury shall be in accordance with laws in both countries. Either way, the jury must include both PhD supervisors as well as external examiners who are not affiliated to the universities in which the Student is enrolled. The jury shall not exceed eight (8) members. Representation of women and men should be balanced. The chairman of the jury signs a defense report that is countersigned by the members of the jury.

The defense shall comply with regulations in force in both countries.

Article 10

The PhD dissertation shall be submitted in the form of a monograph or a collection of scientific papers.

The thesis shall be written in the following language: English
The thesis shall be defended in the following language: English
The languages of the oral and written summary are: Portuguese and French

The thesis shall include the imprint of the logo of the 2 (two) universities involved in this agreement together with the Pelotas Basin project logo. The *cotutelle* relationship shall be clear from the cover/title page.

Article 11

The degrees: both Universities agree, based on the report of a single defense, to confer the grade of

- "Doctor in Géosciences marines" for Université de Bretagne Occidentale"

And

- "Doctor in Geology" for Universidade de Brasília

The institution in which the defense takes place agrees to transmit one copy of the complete defense file to the partner institution.

Article 12

Publication, exploitation and protection of the thesis and of the results of the PhD research work are under the responsibility of the signing Universities and should be carried out in accordance with the current specific regulations in both countries and in both institutions.

The Student commits himself to abiding by the rules in force in both countries to for filing, reporting and reproducing the thesis.

Article 13

Both partner universities, concerned about the interest of doctoral students and with the will to the develop cooperation and between their respective countries, undertake to respect the above provisions and take the necessary measures to ensure the present agreement is applied under the best possible conditions.

In case of any dispute, the Parties undertake to attempt to resolve the dispute amicably.

Article 14

The present agreement may be modified or terminated by mutual agreement reflecting in a written amendment signed by the president of the Universidade de Brasilia (UnB) and by the President of the Université de Bretagne Occidentale.

Should the co-tutelle be terminated by one of the Parties, it shall submit a written notice to the other Party, indicating the reasons for its decision.

All concerned Party including any host institution should be notified of this decision within one month period.

Done in 4 copies, in English and Portuguese.

Brasília, on (insert date) _____

Universidade de Brasília
Secretary for International Affairs

Assinado de forma digital por Virgilio Pereira de Almeida:65939875653
Dados: 2023.03.29 09:25:36 -03'00'

Mr. Virgílio Pereira de Almeida
Secretary for International Affairs,

Brasília, on (insert date) _____

gov.br
Documento assinado digitalmente
ROBERTA MARY VIDOTTI
Data: 30/03/2023 15:21:34-0300
Verifique em https://validar.iti.gov.br

Mrs Roberta Mary VIDOTTI
Coordinator of the Graduate Geology Program

Brasília, on (insert date) _____

gov.br
Documento assinado digitalmente
ADALENE MOREIRA SILVA
Data: 30/03/2023 18:03:46-0300
Verifique em https://validar.iti.gov.br

Mrs Adalene MOREIRA SILVA
Thesis Supervisor

Brest, on (insert date) _____ 23 MAI 2023

M. Pascal OLIVARD
President of Université de Bretagne Occidentale

Brest, on (insert date) _____ 5/05/2023

Mrs Catherine MEUR-FEREC
Director of the Doctoral School

Brest, on (insert date) _____

Marc-André GUTSCHER
Directeur
Geo-Ocean UMR6538
Plouzané le 02/05/23

Mr Marc-André GUTSCHER
Director of the Laboratory

Brest, on (insert date) _____

Plouzané, le
02/05/2023

Mr Laurent GEOFFROY
Thesis Supervisor

Brasília, on (insert date)

gov.br
Documento assinado digitalmente
HENRIQUE SERRATT
Data: 31/03/2023 09:56:33-0300
Verifique em https://validar.iti.gov.br

Mr Henrique SERRATT
PhD student

Article 1

Tectonophysics 910 (2025) 230790

Contents lists available at ScienceDirect

Tectonophysics

journal homepage: www.elsevier.com/locate/tecto

Unraveling the geological history of the South Atlantic margin: Records of West Gondwana Breakup from South Brazil and Uruguay margin

Henrique Serratt [a,b,c,*], Tiago Jonatan Girelli [c], Matheus Fernandes da Cruz [c], Claudia Domingues Teixeira [c], Ilana Lehn [c], Monique Aparecida Marchese Rizzi [c], Marly Babinski [d], Catarina Laboure Bemfica Toledo [a], Peng Peng [e,f], Bruno Conti [g], Adalene Moreira Silva [a], Laurent Geoffroy [b], Farid Chemale Junior [c,h]

[a] Instituto de Geociências, Universidade de Brasília, 70910-900 Brasília, DF, Brazil
[b] UMR CNRS-IFREMER-CNRS-UBS 6538 Geo-Ocean, IUEM, Université de Bretagne Occidentale, France
[c] Geology and Geophysics Research Group – NGA, Universidade do Vale do Rio do Sinos, São Leopoldo, RS, Brazil
[d] Universidade de São Paulo, Instituto de Geociências, Rua do Lago, 562, São Paulo, Brazil
[e] China-Brazil Joint Geoscience Research Center, State Key Laboratory of Lithospheric Evolution, Institute of Geology and Geophysics, Chinese Academy of Sciences, Beijing 100029, China
[f] College of Earth and Planetary Sciences, University of Chinese Academy of Sciences, Beijing 100049, China
[g] Exploration & Production, ANCAP, Montevideo, Uruguay
[h] Postgraduate Program in Geosciences, Universidade Estadual do Rio do Janeiro, Rio de Janeiro, RJ, Brazil

ARTICLE INFO

Keywords:
Pelotas Basin
Punta del Este Basin
Seaward dipping reflectors
Geochemistry
Volcanic passive margin
Paraná Basin

ABSTRACT

Continental Flood Basalts, Seaward Dipping Reflectors (SDRs), and oceanic plateaus or seamounts often occur in close geographic proximity. In South America, the Paraná-Etendeka Continental Flood Basalts are followed by SDR-related magmatism, and even after the formation of oceanic crust, anomalous magmatism persists in the region, as seen in the Walvis Ridge and Rio Grande Rise. This study investigates volcanic and sedimentary rocks from offshore wells in the Pelotas and Punta del Este basin margins, revealing the offshore extension of the Paraná Basin. Our data demonstrate geochemical and isotopic affinities between margin volcanic rocks and the Paraná-Etendeka Large Igneous Province. The basalts from the margin display OIB- and E-MORB-like geochemical and isotopic compositions consistent with EMI and EMII mantle sources. However, these isotopic signatures may have been modified by assimilation of continental crust or subcontinental lithospheric mantle. The presence of zircon xenocrysts support this interpretation, and suggests that volcanic rocks from the margin were emplaced above the continental crust with magmatic assimilation of rocks from Dom Feliciano Belt. The Rio Grande Rise also exhibits an EMI-like isotopic fingerprint similar to the Walvis Ridge, indicating a possible shared origin during the Cretaceous. However, this isotopic content may also result from magmatic assimilation of continental crust slivers or subcontinentallithospheric mantle. These findings highlight the role of a persistent thermal anomaly throughout the magmatic evolution of the South Atlantic.

1. Introduction

Gondwana breakup was a major tectonic event that shaped the modern configuration of continents and oceans. This process occurred in multiple stages over an extended period from the Late Triassic to the Early Cretaceous. Although the cause of rifting remains debated (e.g., Nance et al., 2014; Frizon de Lamotte et al., 2015), fragmentation of this supercontinent led to the opening of the South Atlantic, Indian, and Southern oceans, separating South America, Africa, Antarctica, India, and Australia (Veevers, 2012). The breakup profoundly impacted global climate, ocean circulation patterns, and the evolution and distribution of flora and fauna across the newly separated landmasses (Torsvik and Cocks, 2013). Specifically regarding the West Gondwana breakup, evidence suggests the process likely started during the Berriasian–Valanginian (145–132.6 Ma.; Lovecchio et al., 2024).

The magmatism related to the West Gondwana breakup and the

* Corresponding author at: Instituto de Geociências, Universidade de Brasília, 70910-900 Brasília, DF, Brazil.
E-mail address: hserratt@unisinos.br (H. Serratt).

https://doi.org/10.1016/j.tecto.2025.230790
Received 30 December 2024; Received in revised form 17 April 2025; Accepted 16 May 2025
Available online 22 May 2025

South Atlantic Formation can be divided into four main types: (I) The Continental Flood Basalts (CFB), represented by the Paraná-Etendeka Large Igneous Province (LIP) which occurred mainly during 135.0 ± 0.6 and 133.2 ± 0.3 Ma (Gomes and Vasconcelos, 2021); (II) The volcanic wedges observed along the margin as Seaward Dipping Reflectors (SDR), which formed between 134 to 113 Ma (Chauvet et al., 2021); (III) The Mid Ocean Ridge Basalts (MORB) that constitute the oceanic crust. (IV); The volcanic plateaus, islands, and seamounts developed throughout the history of the South Atlantic Ocean (From 114 ma to today - Hoyer et al., 2022; Homrighausen et al., 2019). Among these magmatisms, the SDR remains the least directly studied, often being analyzed primarily through geophysical methods in the region (e.g., Harkin et al., 2020; Chauvet et al., 2021; Serratt et al., 2022; Teixeira et al., 2025a).

In order to directly investigate the SDRs, we analyzed samples from five offshore well cores in the Pelotas and Punta del Este basins margins and one from the Rio Grande Rise. These five wells are all exploratory boreholes that drilled through the Cenozoic and Early Cretaceous drift sections, recovering rocks beneath the drift sequences. This study aims to assess the age, magmatic sources, and relations between CFB, SDR, and oceanic features (islands, seamounts, and oceanic plateaus) in the region. To accomplish this objective, we conducted a detailed investigation incorporating petrography, X-ray diffraction (XRD), geochemical analysis, U-Pb geochronology, and Nd and Sr isotopic studies of rocks samples from beneath the drift section of the Pelotas and Punta del Este basins.

2. Geological setting

The study area lies along the South Atlantic margin, specifically within the southern Brazil and Uruguay regions (encompassing the Pelotas and Punta del Este basins, Fig. 1) and the Rio Grande Rise. During most of the Phanerozoic, this area remained connected to Namibia as part of the Gondwana supercontinent (Teixeira et al., 2025a and references therein). During the Early Paleozoic, assembly of Gondwana in this region produced its most extensive geological feature, the Dom Feliciano Belt (DFB). This belt formed through subduction of the Adamastor Ocean during the convergence of Rio de la Plata, Congo, and Kalahari paleoplates from the Neoproterozoic to the Early Paleozoic (e.g., Gresse et al., 1996; Chemale Jr et al., 2012; Caxito et al., 2022; Teixeira et al., 2025b). The crystalline basement of southernmost Brazil and Uruguay consists of rocks from the DFB and the Rio de la Plata Craton, overlain by sedimentary units of the Paraná and Pelotas basins (Stica et al., 2014; Gordon and Mohriak, 2015; Teixeira et al., 2025b).

The Paraná Basin is the largest intracratonic basin in South America, predominantly located in Brazil and extending into Paraguay, Argentina, and Uruguay (Milani et al., 2007). Its offshore extension below the Pelotas Basin has been hypothesized based on seismic data, though direct confirmation remains limited. Seismic surveys have suggested its presence beneath the Pelotas Basin in Uruguay and the northernmost portion of the Pelotas Basin in Brazil (Holz et al., 2010; Conti et al., 2017). The only well that recovered Paraná Basin rocks beneath the Pelotas Basin is the onshore well 2-TO-1-RS (Fig. 1; Bueno et al., 2007; Holz et al., 2010) located in the northern portion of the Pelotas Basin. In this area, the Paraná Basin is limited to a structural depression known as the Torres Syncline, which constitutes the easternmost onshore exposure of the Paraná–Etendeka flood basalts in South America (Waichel et al., 2012). The Paraná Basin developed primarily before the breakup of Gondwana and contains six supersequences: Rio Ivaí, Paraná, Gondwana I, Gondwana II, Gondwana III, and Bauru. Within our study area (southern Brazil and Uruguay), three of these supersequences are present (Milani et al., 2007): Gondwana I (comprising the Itararé and Passa Dois groups); Gondwana II (comprising the Piramboia and Santa Maria formations), and Gondwana III (comprising the Botucatu Formation and Serra Geral Group). The Serra Geral Group is also recognized as part of the Paraná-Etendeka Large Igneous Province (LIP), which covers an extensive area of approximately 1,000,000 km^2.

The Paraná-Etendeka LIP (PEL) was commonly interpreted as the result of magmatic activity driven by a plume (sometimes called Tristan da Cunha Plume) during the breakup of the Gondwana supercontinent (Ewart et al., 1998; Marsh et al., 2001; Ewart et al., 2004; Gibson et al., 2006; Zhou et al., 2020; Beccaluva et al., 2020). However, alternative models suggest that its formation should be attributed to regional thermal anomalies without plume involvement, such as small-scale convection (Mutter et al., 1988; King and Anderson, 1995; Ernesto et al., 2002; Bologna et al., 2022). Some authors argue that plume influence was primarily limited to heat transfer with minimal mass contribution (Peate, 1997; Peate et al., 1999; Marques et al., 1999). The main magmatic event of Paraná-Etendeka LIP occurred between 135.0 ± 0.6 and 133.2 ± 0.3 Ma (Gomes and Vasconcelos, 2021, and the references therein), with continued minor magmatism lasting until at least 119 Ma in South America and 113 Ma in Africa, as recorded in dyke swarms (Will et al., 2016; Hartmann et al., 2019).

The Paraná LIP constitutes the South American part of the PEL. These rocks usually are referred to as the Serra Geral Group (Rossetti et al., 2018). The Serra Geral Group can be divided into two sub-provinces: the low-Ti sub-province, mainly in the south, and the high-Ti, mostly distributed from the center to the north (Rossetti et al., 2018). Further classification identifies at least seven formations within The Serra Geral Group: Paranapanema, Pitanga, Ribeira, Esmeralda, Palmas, Urubici, and Gramado (Rossetti et al., 2018). In southern Brazil and Uruguay, the low-Ti formations predominate, including Gramado (characterized by pahoehoe fields of basalts and basaltic andesites, occur above the Botucatu Formation sandstones), Palmas (composed of dacites and rhyolites), and the Esmeralda (consisting of basaltic pahoehoe flow field), The High Ti (Ti/Y > 310) Urubicy formation is also present in this region (Rossetti et al., 2018).

Breakup of West Gondwana was marked by magmatic activity along the rifted margin of the South Atlantic Austral Segment, forming a volcanic passive margin characterized by the presence of Seaward Dipping Reflectors (SDRs; Stica et al., 2014; Geoffroy et al., 2015; Chauvet et al., 2021; Serratt et al., 2022; Lovecchio et al., 2024). The West Gondwana breakup began near the latitude of the Falkland/Malvinas Islands and moved northward in a zipper style (Rabinowitz and LaBrecque, 1979; Moulin et al., 2010; Collier et al., 2017; Hall et al., 2018; Chauvet et al., 2021; Serratt et al., 2022; Lovecchio et al., 2024). The rifting process likely started during Berriasian–Valanginian (145–132.6 Ma.; Lovecchio et al., 2024). In the area of this study, Pelotas and Punta del Este basins, SDR was formed between 131 and 113 Ma (Chauvet et al., 2021), making these features at least 2 million years younger than the main Paraná LIP event in the region. However, the elder ages are from magnetostratigraphy and could be meaningless in the region (Serratt et al., 2022). This volcanic passive margin extends over the entire Austral Segment of the South Atlantic Ocean and exhibits characteristic architecture dominated by SDRs (Gladczenko et al., 1997; Franke et al., 2007; Stica et al., 2014; Geoffroy et al., 2015; Gordon and Mohriak, 2015; Harkin et al., 2020; Chauvet et al., 2021; Serratt et al., 2022; Lovecchio et al., 2024).

SDRs are seismic facies characterized by sigmoidal wedges that prograde oceanward. Mutter et al. (1982) formalized the concept of a volcanic extrusion associated with the early stages of oceanic crust development by defining five criteria: (1) the reflectors consistently dip seaward; (2) individual reflectors have an arcuate shape formed by a gentle upward convexity; (3) both down-section and down-dip progression show increasing dip angle; (4) these characteristics combine to create overall wedge-shaped geometry with reflectors diverging seaward; and (5) the wedge lack clear basal termination and evidence of a bottom-set structure in the reflectors. Analysis of SDR composition from Ocean Drilling Program (ODP) drilling reveals that volcanic material predominates, though thin layers of sedimentary rocks are also present (e.g., Larsen et al., 1994; Philipp et al., 2001). Inner SDR outcrops have been identified in West Greenland (Geoffroy et al., 1998),

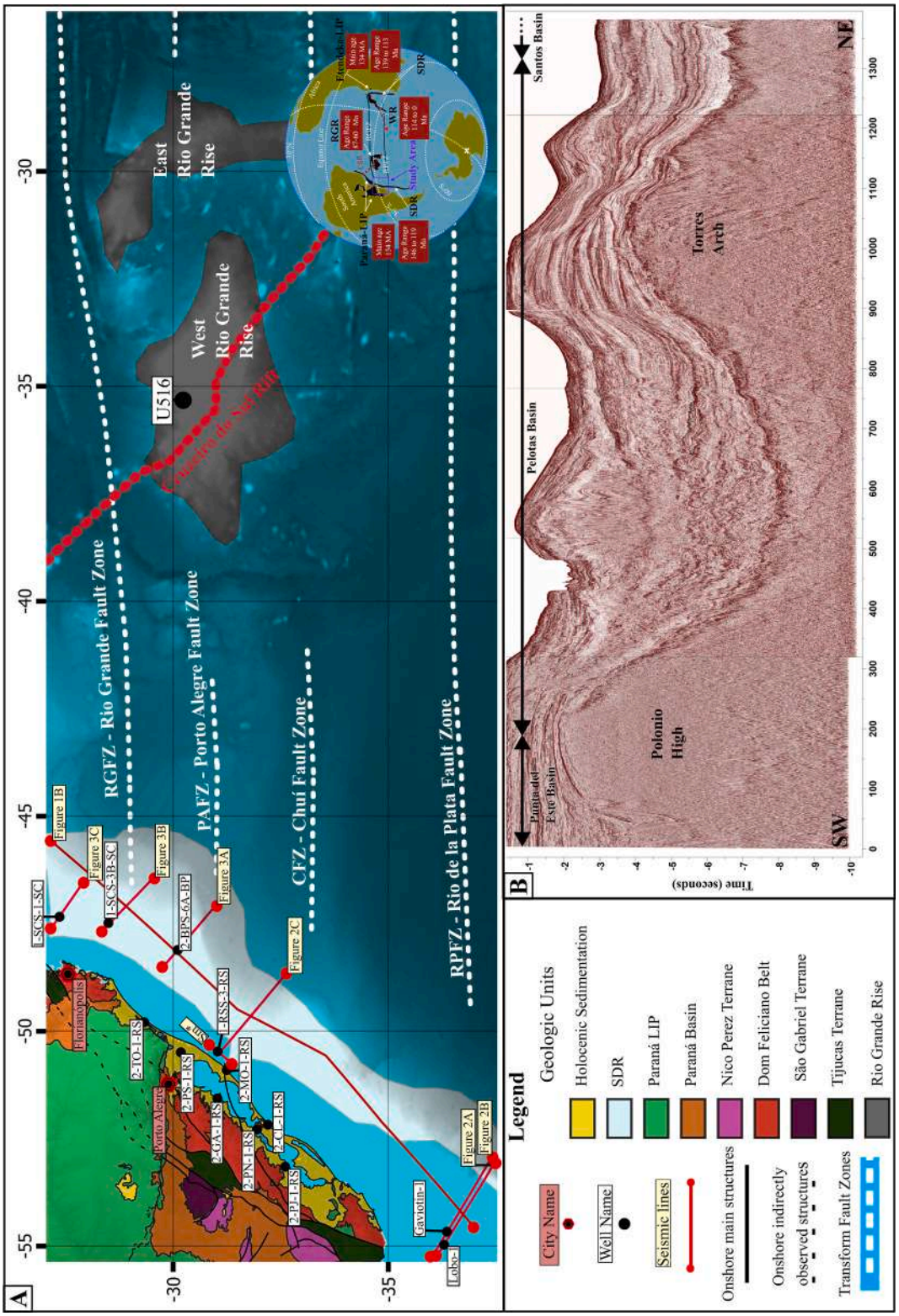

Fig. 1. A) Location map showing the position of the seismic lines and the wells used in this study. The LIPs and Rio Grande Rise boundaries are adapted from Whittaker et al. (2015), while the SDRs are based on Chauvet et al. (2021), Sm* seismic line in supplementary material 2; in the mini-globe: The Paraná-Etendeka magmatism ages are compiled by Gomes and Vasconcelos (2021); The WR- Walvis Ridge ages are compiled by Homrighausen et al. (2019), the red arrow shows the age of the elder to youngest seamounts. The Rio Grande Rise ages were from Hoyer et al. (2022), CSR – Cruzeiro do Sul Rift. Onshore geological units and structures from Teixeira et al. (2025b). B) A composition of five strike-direction seismic lines showing the regional tectonic framework. We highlighted two structures: the Polonio High, interpreted as a Proterozoic basement high (Conti et al., 2017), and the Torres Arch, characterized by an exceptionally thick SDR package compared to other areas of the margin (Stica et al., 2014; Gordon and Mohriak, 2015; Harkin et al., 2020; Chauvet et al., 2021). (For interpretation of the references to colour in this figure legend, the reader is referred to the web version of this article.)

where Agranier et al. (2019) identified four distinct units corresponding to magmatic activity around 61–54 Ma. The first unit records a partial melting from a plume-like source deeper than 75 km and formed in a lacustrine environment, evidenced by hyaloclastites and pillow lavas. Units two and three show progressively shallower lithospheric melting with mixed contribution from the Iceland hotspot and the local crust material. The fourth unit again reflects a deeper source. In contrast, units two to four were formed in subaerial environments, hosting pahoehoe structures and lacking pillow lavas. These volcanic rocks are intercalated with thin tuff horizons (less than 50 cm), basaltic pebble conglomerates (less than 10 m), and occasionally claystones (less than 1 m). However, the overall SDR package remains predominantly volcanic in composition.

SDRs in the study area exhibit diverse compositional characteristics, including basalts, andesites, and trachyandesites (Bueno et al., 2007). The thickness of the SDR package increases as it extends northward in the Pelotas Basin, reaching up to 17 km (Gordon and Mohriak, 2015; Gordon et al., 2017; Harkin et al., 2020). Researchers have interpreted volcanic rocks in the region as part of pre-syn- and late-rift, categorizing them within the Imbituba and Curumin formations of the Pelotas Basin (Dias et al., 1994; Bueno et al., 2007; Stica et al., 2014; Gordon and Mohriak, 2015; Serratt et al., 2022). Historically, the SDRs are classified as part of the Pelotas Basin (Bueno et al., 2007; Stica et al., 2014; Gordon and Mohriak, 2015; Serratt et al., 2022) as they infill depressions created by half-grabens structures. These authors follow the definition of the basin of Ingersoll (2011), which considers any depression-filling accumulation of volcanic or sedimentary material as constituting a sedimentary basin. Previous geochemical analysis of Pelotas Basin basalts indicates a mixed source involving subcontinental lithospheric mantle and Normal Mid-Ocean Ridge Basalts sources (N-MORB; Lobo et al., 2006). This study suggests that magmatism originated from small-scale convection cells, arguing that the heterogeneity in the samples indicates a lack of a large-scale plume, which would produce a more homogeneous composition (Lobo et al., 2006). In the northern region of the study area, particularly around the Torres Arch (situated between the Porto Alegre Fault Zone and Rio Grande Fault Zone; Fig. 1), Harkin et al. (2020) identified that the most distal SDR regions display a density inconsistent with purely basalt composition, implying the presence of volcanoclastic or sedimentary rocks. Similarly, Serratt et al. (2022) reported some peperites in well 2-BPS-6A-BP (Fig. 1), further supporting the presence of sedimentary components within the predominantly volcanic SDR package.

The South Atlantic conjugate margins display significant asymmetry in their crustal architecture, particularly in the SDRs volume and distribution, a common feature of volcanic passive margins (Becker et al., 2014; Reuber et al., 2019; Chauvet et al., 2021; Abdelmalak et al., 2025). This SDR sequence challenges the identification of the precise Continental-Ocean Boundary (COB), especially in areas influenced by intense magmatism, such as the Pelotas and Punta del Este basins. Discrepancies of over 100 km in COB interpretations have been noted for the South Atlantic (e.g., Rabinowitz and LaBrecque, 1979; versus Cainelli and Mohriak, 1999), leading to the proposal of a continent-ocean transition zone (COTZ; Eagles et al., 2015). Additionally, seismic and potential field data indicate the presence of hyperextended continental crust beneath these margins, extending up to 450 km in some areas. This hyperextension plays a crucial role in shaping the tectonic framework of the region (Teixeira et al., 2025a).

Even after the SDR magmatism ceased, the region continued to experience magmatic activity. This magmatic activity led to the formation of the Rio Grande Rise and Walvis Ridge, both genetically linked (Hoyer et al., 2022). Its genesis is often pointed to be related to the Tristan da Cunha plume (Homrighausen et al., 2019; Hoyer et al., 2022), the same plume related to Paraná-Etendeka LIP (Gibson et al., 2006; Zhou et al., 2020; Beccaluva et al., 2020). On the other hand, some authors point to alternative formation mechanisms. These include: (1) a volcanic edifice or plateau rooted in the mantle; (2) an intraplate shear zone affecting continental and oceanic crust; (3) an oceanic area of igneous over-productivity caused by a hotspot or a thermal anomaly in the mantle; (5) a palaeo-spreading center in the Cretaceous Atlantic Ocean; an area of excessive volcanic activity resulting from mantle differentiation due to adiabatic decompression; (6) an isolated remnant of continental crust left outboard of the Brazilian continental margin during the drifting process (Mohriak et al., 2010, and the references within).

3. Samples and methods

An integrated geophysical and geochemical study was conducted across six wells. In five wells (Gaviotin-1; Lobo-1; 1-RSS-3-RS; 2-BPS-6A-BP; 1-SCS-3B-SC – Fig. 1), we analyzed samples from beneath the drift section of the Pelotas and Punta del Este basins, and one well was from the Rio Grande Rise (U516 – Fig. 1). One of the analyzed samples is a sedimentary rock that comes from a depth of 3629 m in the Gaviotin-1 well in the Punta del Este Basin. All the others samples from the margin are volcanic rocks from Lobo-1 (depths: 2622, 2627, and 2629 m; Figs. 1 and 2), 1-RSS-3-RS (depths: 3555.1, 3555.8, 3904.9, and 3905.8 m; Figs. 1 and 2), 2-BPS-6A-BP (depths: 5075.45, 5350.9, 5378.5, 5378.8, 5379.25, 6154.6, and 6155 m; Figs. 1 and 2), and 1-SCS-3B-SC (depths: 4732, 4732.8 m; Figs. 1 and 2). The Rio Grande Rise samples are obtained from the U516 well core at 1260.60 and 1269.60 m (Fig. 1). The lithological profiles for all Pelotas and Punta del Este basins wells are provided in Supplementary material 1; while all data from well U516 is available by DSDP legacy data (leg 72, site 516; Barker et al., 1983).

3.1. Seismic analysis

The tectonic architecture interpretation of this region was based on six dip-direction seismic lines closest to the wells (uninterpreted seismic lines are available in Supplementary material 2). We conducted the interpretation using Paleoscan™ 2023 software, relying upon previous regional interpretations (Stica et al., 2014; Gordon and Mohriak, 2015; Conti et al., 2017; Harkin et al., 2020; Chauvet et al., 2021; Serratt et al., 2022; Teixeira et al., 2025a). Well data were integrated with seismic data to enhance seismic interpretation using Petrel 2023™. Our primary goal focused on interpreting the basalt samples by integrating the sonic and density logs (DT and RHOB) from the wells to generate synthetic seismograms, allowing for precise correlation between well data and seismic reflectors (detailed in Supplementary material 3). Following this well-seismic tie, we constrained several geological units along these seismic lines based on their seismic facies and groups of seismic facies.

3.2. Petrography XRD supported

Thin sections were prepared from 13 representative margin samples and analyzed using conventional petrography. The samples included one sedimentary rock and 12 basalt samples. We used X-ray diffraction (XRD) to support mineral identification for the volcanic rocks. For XRD analysis, samples were pulverized using an agate mortar and pestle, and the clay fraction was separated by double centrifugation. First, the samples were centrifuged in distilled water at 750 rpm for 7 min, followed by a second centrifugation at 3000 rpm for 30 min, using the supernatants from the first stage. Precipitates from the second centrifugation were used to prepare oriented clay, which was air-dried before analysis. Glycolated samples were prepared by exposing them to an ethylene glycol atmosphere for 12 h. The samples were dehydrated by heating to 490 °C for 4 h before analysis. X-ray diffraction was done using a Rigaku Ultima IV diffractometer at Brasilia University, with 35 kV and 15 mA parameters. Whole samples were scanned from 2 to 60° and clay fractions from 2 to 40° (2θ), with a 0.05° step and 5°/min speed. The diffractograms were analyzed using MDI/Jade® 9 software, with the full results provided in Supplementary material 4.

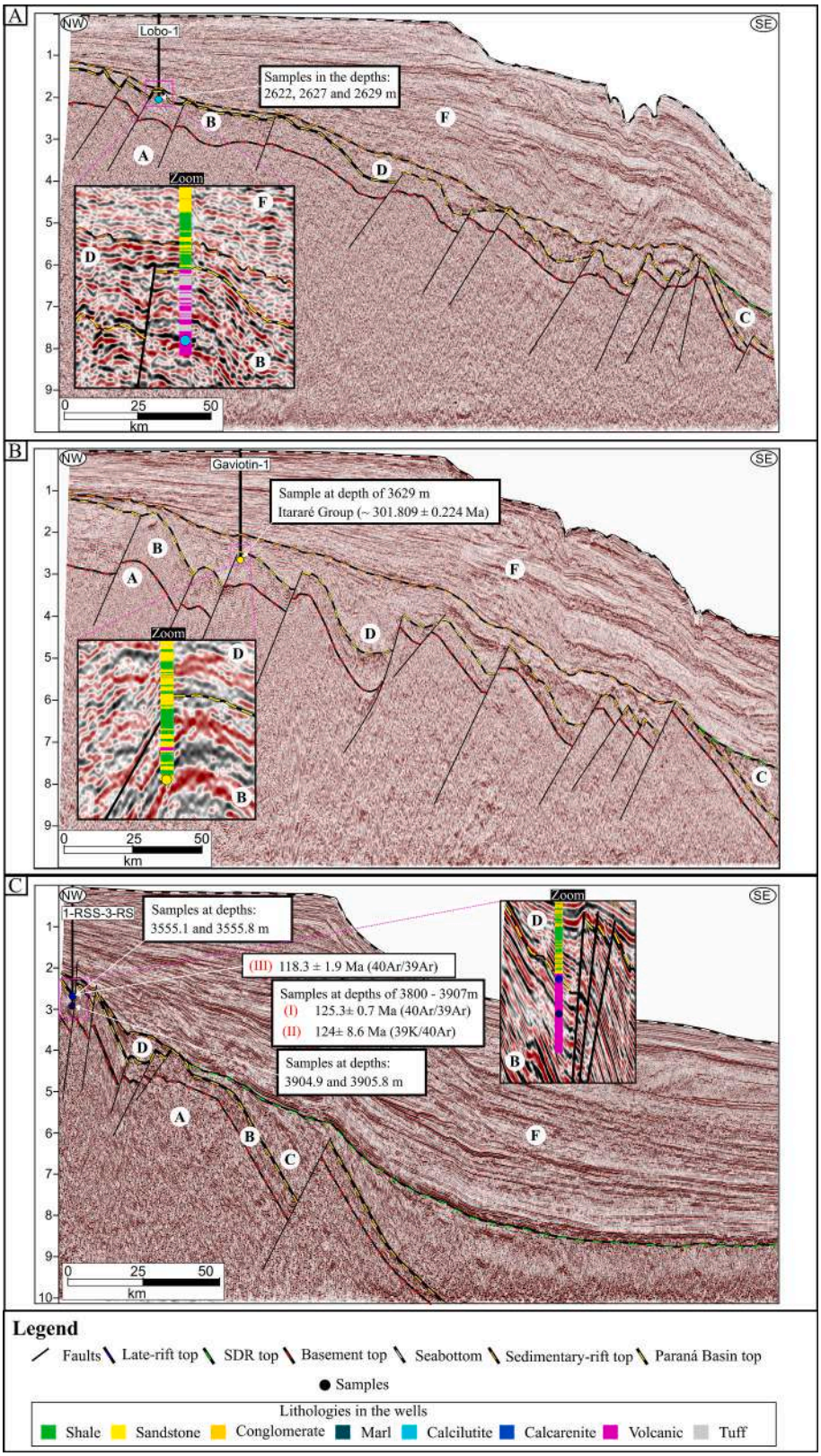

Fig. 2. Seismic lines from the Pelotas and Punta del Este basins, their respective positions are indicated in Fig. 1. The colorful circles are the position from the samples, and white circles with letters are the interpreted tectonic units (A) Neoproterozoic Basement, (B) Paraná Basin, (C) SDR, (D) Late-Rift, (E) Late-Rift, (F) Drift. (I) data from Misuzaki and Saracchine, 1990b (II) data from Lobo, 2000 (III) data from Lobo (2007). A) Seismic line near the well Lobo-1 shows samples analyzed from the bottom of the well classified as Paraná LIP (Serra Geral Group in Paraná Basin stratigraphy (B). Observe the SDRs (C) in the distal section, they are stratigraphically above these traps; (B) Seismic line near the Gaviotin-1 well also presents analyzed samples classified as Paraná-Basin (Itararé Group), with distinguishable SDRs in the distal section above the Paraná Basin. C) Seismic line near the 1-RSS-3-RS well, in a region called Mostardas Low (Cassel et al., 2022). The

samples from the bottom of the well were classified as Paraná-Basin (Serra Geral Group, also known as Paraná LIP), despite the previous classification of these samples being Imbituba Formation (see the discussion).

3.3. Whole-rock Geochemistry

Whole-rock geochemical analyses were performed on all volcanic samples. Fresh samples were selected, avoiding the sedimentary inputs from the peperites or the amygdales. We crushed the samples to <0.5 cm and ground them into powders (<200 mesh) using an agate mortar and pestle. After fusing the samples with lithium metaborate/tetraborate, major- and trace-element content were determined by dissolving the resulting molten bead in a weak nitric acid solution. Major elements were determined by ICP-OES and trace elements by ICP-MS at Actlabs in Ontario, Canada, and Geosol in Minas Gerais, Brazil. Blank achieved was <0.01 % for major elements and < 0.1 ppm in REE. Additionally, we analyzed two samples from Rio Grande Rise, from well U516 at depths of 1263 and 1268 m. ALS Labs, United Kingdom, carried out these analyses. Data and standards for major and minor elements are available in Supplementary material 5.

The percentages of major element oxides were recalculated to 100 wt % on an anhydrous basis. We applied diagrams (LeBas et al., 1986; Pearce and Wyman, 1996; Pearce, 2008) based on mobile and immobile elements to determine the rock types and tectonic setting. We also plotted our data with legacy data from Paraná Etendeka LIP (Gibson et al., 2006; Zhou et al., 2020; Mansur et al., 2021) and South Atlantic OIB (Ocean Island Basalts; Walvis Ridge - Homrighausen et al., 2019; Rio Grande - Rise Hoyer et al., 2022) for classification and tectonic setting comparison. Normalized spidergrams were made using NMORB (Normal Mid Ocean Ridge Basalts) values (Sun and McDonough, 1989). REE values were also normalized by chondrite using Boynton (1984) values. Europium and cerium anomalies (Eu/Eu* and Ce/Ce*, respectively) were determined with neighboring elements (La – Pr and Sm – Gd) using the methodology of Taylor and McLennan (1985).

3.4. U-Pb zircon dating

U-Pb geochronology was carried out on four basalt samples (those with zircon fertility). Isotope U-Pb data were obtained at the Institute of Geology and Geophysics of the Chinese Academy of Science (IGGCAS - Beijing) and the University of Ouro Preto (UFOP) in Brazil. Sample preparation was conducted at Vale do Rio dos Sinos University (UNISINOS). The process included crushing the samples with a jaw crusher and disc mill, followed by heavy mineral concentration using dense liquids (bromoform and diiodomethane). Zircon grains were hand-picked under a binocular microscope and polished in 1-in. round epoxy mounts. Before analysis, the samples were characterized using plane-polarized light and backscattered electron (BSE) imaging.

At the University of Ouro Preto, we analyzed one sample (Gaviotin-1) using a Laser Ablation system (Photon-machines Excimer Laser λ = 193 nm) coupled with a sector field inductively coupled plasma mass spectrometer (ThermoFisher Element II). U-Pb zircon data were obtained using peak jumping mode with 20 s background measurement, followed by 20 s sample ablation with a 20 μm spot size, 15 % laser energy, 10 Hz shot frequency, and 15 s shutter delay. Laser spots were placed on zircon rims to certify that the last tectonic event was analyzed. The common Pb correction was based on ^{204}Pb composition, following Stacey and Kramers (1975). The decay constant of Jaffey et al. (1971) was applied, and uncertainty propagation was followed by Horstwood et al. (2016). Data reduction was made using the Silva et al. (2023) Saturn software. We used the reference zircon (GJ-1) for laser-induced elemental fractionation and instrumental mass discrimination corrections. To ensure precision and accuracy, we analyzed reference zircons: Plešovice (337 ± 3.8 Ma; Sláma et al., 2008) and BB-1 (562.58 ± 0.26 Ma; Santos et al., 2017). The results were concordant with experimental errors: 557.7 ± 3.9 Ma (2σ, n = 18) for BB-1 and 338.4 ± 2.3 Ma (2σ, n = 23) for Plešovice.

At IGGCAS - Beijing, three samples were analyzed: 1) Well 1-RSS-3-RS at depth 3904.9 m; 2) Well 2-BPS-6A-BP at depth 5378.8 m; and 3) Well 2-BPS-6A-BP at depth 5379.25 m. The analyses used a sector field SF-ICP-MS (Element XR, ThermoFisher Scientific) and a 193 nm ArF excimer laser (Geolas HD, Coherent). The U-Pb laser methodology is described by Wu et al. (2019). Data were reduced using an in-house Excel spreadsheet (Chemale Jr. et al., 2012). To ensure precision and accuracy, we analyzed reference zircons: SA01 (537.85 ± 2.71 Ma; Huang et al., 2020) and 91500 zircon (1065.4 ± 0.6 Ma; Wiedenbeck et al., 1995 and Wiedenbeck et al., 2004). The results were concordant with experimental errors: 535.2 ± 1.3 Ma (2σ, n = 35) for SA01 and 1063.0 ± 2.3 Ma (2σ, n = 32) for 91,500. Following Puetz et al. (2021), data was organized, where only the best ages of groups 1 to 5 were plotted for KDE diagrams (data in Supplementary Material 6). The KDE and Concordia diagrams were plotted using IsoplotR software (Vermeesch, 2018). All data are found in Supplementary Material 6.

3.5. Sr and Nd isotopes

Eight basalt samples were selected for Sr and Nd isotope analysis based on their relatively low degree of modification by late-stage hydrothermal processes and limited interaction with sedimentary rocks during extrusion. Two volcanic rock samples were collected from the Rio Grande Rise at 1263 m and 1268 m depths. From the well 1-RSS-3-RS, samples were analyzed from depths of 3555.10 m and 3905.20 m. From the well 2-BPS-6 A-BP, isotope compositions were determined for samples from 6154.6 m and 6155 m depths. Additional samples were analyzed from the well 1-SCS-3B-SC (Santa Catarina State) at a 4732 m depth and from Lobo-1 (Uruguay) at a 2626 m depth.

The samples were initially crushed, milled, and sieved. Sr and Nd isotope analyses were conducted at the Geochronology Center of the University of São Paulo (CPGEO-USP). Chemical digestion was performed using HF, HNO_3, and HCl in Savillex® vials. Sr and Nd were separated chromatographically in two steps: first, Sr and rare earth elements (REE) were separated from the bulk sample using AG50W-X8 resin; second, Nd was separated using a lanthanide-specific (LN) resin. Isotope analyses were carried out using a Thermo-Ionization Mass Spectrometer (TIMS) – Triton. The $^{87}Sr/^{86}Sr$ isotope ratios were normalized to $^{86}Sr/^{88}Sr = 0.1194$, and the $^{143}Nd/^{144}Nd$ ratios were normalized to $^{146}Nd/^{144}Nd = 0.7219$ (DePaolo, 1981). Analytical blank concentrations for Sr and Nd were below 197 pg/g and 10 pg/g, respectively.

The average $^{87}Sr/^{86}Sr$ value for the NBS-987 standard, measured between February 2024 and January 2025, was 0.710266 ± 0.000007. The $^{143}Nd/^{144}Nd$ ratio for the JNDi standard, measured from March 2024 to February 2025, was 0.5210096 ± 0.000004. Sr and Nd isotope data for all analyzed samples are presented in Supplementary Material 7.

4. Results

The volcanic rocks are more homogeneous than previously reported (Bueno et al., 2007). All of these volcanic rocks are basalts or peperites with basaltic composition. We observe strong hydrothermal alteration in all these rocks. Based on the geochemical composition, the source appears to be intermediate between EMORB (Enriched Mid Ocean Ridge Basalts) and OIB (Ocean Island Basalts). The sedimentary rock from Gaviotin 1- is from the Itararé Group (Paraná Basin), as observed by its detrital zircons ages. However, we could not constrain the age of the basalts by their zircon content because their age is the same as the host rock (assimilated during magmatism – See the discussion) or they contain detrital zircons (related to the peperites). The isotopic signature

shows a negative εNd value signature for most samples and an $^{87}Sr/^{86}Sr$ compatible with either a continental crust contamination or EMI and EMII mantle reservoirs.

4.1. Tectonic environment

We identified six distinct tectonic contexts from seismic data of the margin, classified based on seismic facies and well data (Figs. 2 and 3; A-Basement, B-Paraná-Basin, C-SDR, D-Sedimentary Rift, E-Late-Rift, F-Drift). (A) Neoproterozoic Basement: The Neoproterozoic basement represents the Dom Feliciano Belt and, in seismic data, corresponds to the most chaotic seismic facies beneath all other identified geological units. (B) Paraná Basin Section: The Paraná Basin section (including the Paraná Large Igneous Province), representing the pre-rift section, is characterized by continuous reflectors that are intersected by rift faults. (C) SDR Section: We identified SDRs according to the aforementioned definition by Mutter et al. (1982). (D) Sedimentary rift section: Besides the SDRs, we also identified a sedimentary rift, observed as reflectors filling half-grabens, which display a distinct basal reflector indicative of significant lithological changes. The upper limit of this unit is the base of the drift, and it is always an irregular surface at Punta del Este Basin, which we interpreted as an erosive surface or regional unconformity. As this top surface did not produce a high amplitude reflection, it corroborates the interpretation that it and the drift section have approximately the same density, corresponding to sedimentary rocks. This section was also recovered in the well 1-RSS-3-RS (Cassino Formation – Bueno et al., 2007 – Fig. 2C), Gaviotin-1, and Lobo-1 (Fig. 2A-B). (E) Late-Rift Section: We interpreted this based on the post-rift basalts interpretations from Serratt et al. (2022), which consist of volcanic rocks (including peperites) observed in the well 2-BPS-6 A-BP and visualized in one seismic line above the SDRs (Fig. 3A). This section corresponds to a "sag geometry" as described by Stica et al. (2014) or unit "H" as described by Gordon and Mohriak (2015). (F) Drift Section: This section is characterized by a group of seismic facies exhibiting the most continuous reflectors of all units, situated just below the sea bottom, that is, the first reflector (Figs. 2 and 3). The base of the Drift stage is marked by high-amplitude reflections when they occur above SDRs, marking a drastic change in lithology. The interpretation of this unit was calibrated using well data tied to the seismic lines.

We classified our samples based on their geologic context of it. In our seismic interpretation, the samples from Uruguay (well Lobo-1 at depths 2622, 2627, and 2629 m, and Gaviotin-1 at 3629 m) are evidently older than the rifting, with parallel reflectors cut by antithetical faults (Fig. 2A and B). Similarly, the samples from the bottom of well 1-RSS-3-RS in Brazil (depths: 3555.1, 3555.8, 3904.9, and 3905.8 m; Fig. 2C) align with the pre-rift interpretation (i.e., Paraná Basin). However, Gordon and Mohriak (2015) also interpreted a late-rift layer at the top of this volcanic section in the well 1-RSS-3-RS (Unit "H" in Gordon and Mohriak, 2015; the same unit as recovered in 2-BPS-6A-BP). In our interpretation, these samples from 1-RSS-3-RS well are also classified as part of the pre-rift section (Paraná Basin including Paraná LIP, that is, Serra Geral Group). However, the upper volcanic rocks from well 1-RSS-3-RS represent a transition from pre-rift to rift as the top reflectors diverge. The 2-BPS-6A-BP samples (depths: 5378.5, 6154.6, and 6155 m), usually classified as SDR (Stica et al., 2014; Harkin et al., 2020; Chauvet et al., 2021), are volcanic rocks that cover the SDRs (Fig. 3A; Gordon and Mohriak, 2015; Serratt et al., 2022). We adopt the classification of a late-rift section for these rocks (Fig. 3A). The only actual SDR samples that achieve all five criteria outlined by Mutter et al. (Mutter et al., 1982; Fig. 3B-C) are found in the well 1-SCS-3B-SC (depths: 4732 and 4732.8 m) and the bottom of the well 1-SCS-1-SC from Santos Basin. We did not analyze the samples from 1-SCS-1-SC, but Misuzaki (Misuzaki and Saracchine, 1990a, apud Gordon and Mohriak, 2015) constrained the ages of the Santos Basin SDR in this well.

4.2. Petrographic interpretation

Here, we present and describe the samples thin sections in groups based on their tectonic context from Section 4.1. Additionally, the observed mineral assemblages and textures are summarized in Table 1. All volcanic samples have some degree of alteration that can cause atypical diffractometric measurements due to mineral replacement and intermediate phases. Some primary minerals, such as olivine, are absent, as the original olivine has been entirely replaced by iddingsite or serpentine. Therefore, the XRD results (Supplementary Material 4) do not reflect the original mineral assemblage but rather the current altered state.

4.2.1. Pre-Rift (Paraná Basin)

The rocks interpreted in the seismic section as pre-rift are from the wells Gaviotin-1 (depth: 3629 m), Lobo-1 (depths: 2622, 2627, and 2629 m) in Punta del Este Basin, and Lower 1-RSS-3-RS (depths from 3904 to 3905 m), and Upper 1-RSS-3-RS (depth: 3555 m) in Pelotas Basin.

The analyzed sample from the Gaviotin-1 well at 3629 m consists of medium to coarse-grained sandstone composed primarily of siliciclastic grains. These grains range from medium to coarse sand-sized and are predominantly monocrystalline quartz. The grains exhibit moderate sphericity, with some displaying elongation, varying from subrounded to angular shapes. Diagenetic features include point, planar, and slightly sutured grain contacts, with no visible porosity observed in the thin section.

The analyzed sample from the Lobo-1 well consists of basalts with a porphyritic texture. At a depth of 2622 m, we found euhedral augite phenocrysts up to 2 mm undergoing alteration process (Fig. 4B). These minerals show some chemical alteration but much less than those in the sample from 2627 m. The groundmass hosts fine-grained acicular plagioclase (albite), pyroxene (augite), feldspar (microcline; detected in the XRD only), hematite, and secondary minerals including corrensite and calcite. The interpretation of this thin section and the others was supported by XRD analysis (Supplementary Material 4). At a depth of 2627 m, amygdales filled with corrensite, scolecite, and basaluminite up to 1 mm were identified. The rock is fractured, and the secondary porosity is filled with minerals from late fluid percolation; these fractures cut through the amygdales (Fig. 4A). The groundmass hosts fine-grained acicular plagioclase (albite), pyroxene (augite), feldspar (microcline; detected in the XRD only), opaque minerals (hematite), and secondary minerals (corrensite). At a depth of 2629 m, the rocks consist of basalts with a porphyritic texture. However, observing phenocryst borders is challenging due to the high degree of mineral substitution. Some of these were originally plagioclase crystals. Nonetheless, some parts of the phenocrysts remain unaltered and are identified as pyroxenes (Fig. 4C). The matrix hosts fine-grained plagioclase (albite), pyroxene (augite), opaque minerals (hematite), and secondary minerals (corrensite, basaluminite, scolecite). The mineral assemblage, along with the observed processes of mineral replacement and the late-filled fractures, provides evidence of a hydrothermal process.

The analyzed sample from the 1-RSS-3-RS well at a depth of 3555 m is an amygdaloidal basalt with a very fine texture near the amygdales (Fig. 4D). In regions distant from the amygdales, the rock exhibits a porphyritic texture with altered plagioclase (anorthite) and pyroxene (augite) phenocrysts that reach up to 3 mm (Fig. 4E). The groundmass hosts fine-grained plagioclase (anorthite), pyroxene (augite), opaque minerals (hematite), and secondary minerals (corrensite, laumontite, heulandite, saponite). Additionally, samples obtained from the same well at 3904 m and 3905 m are basalts with few amygdales (Fig. 4G). These samples display a porphyritic texture with highly altered pyroxene (augite) phenocrysts without clear borders due to extensive alteration (Fig. 4F). The groundmass hosts fine-grained feldspar (orthoclase), pyroxene (augite), acicular apatites, opaque minerals (hematite), and secondary minerals (corrensite, analcime, muscovite, and

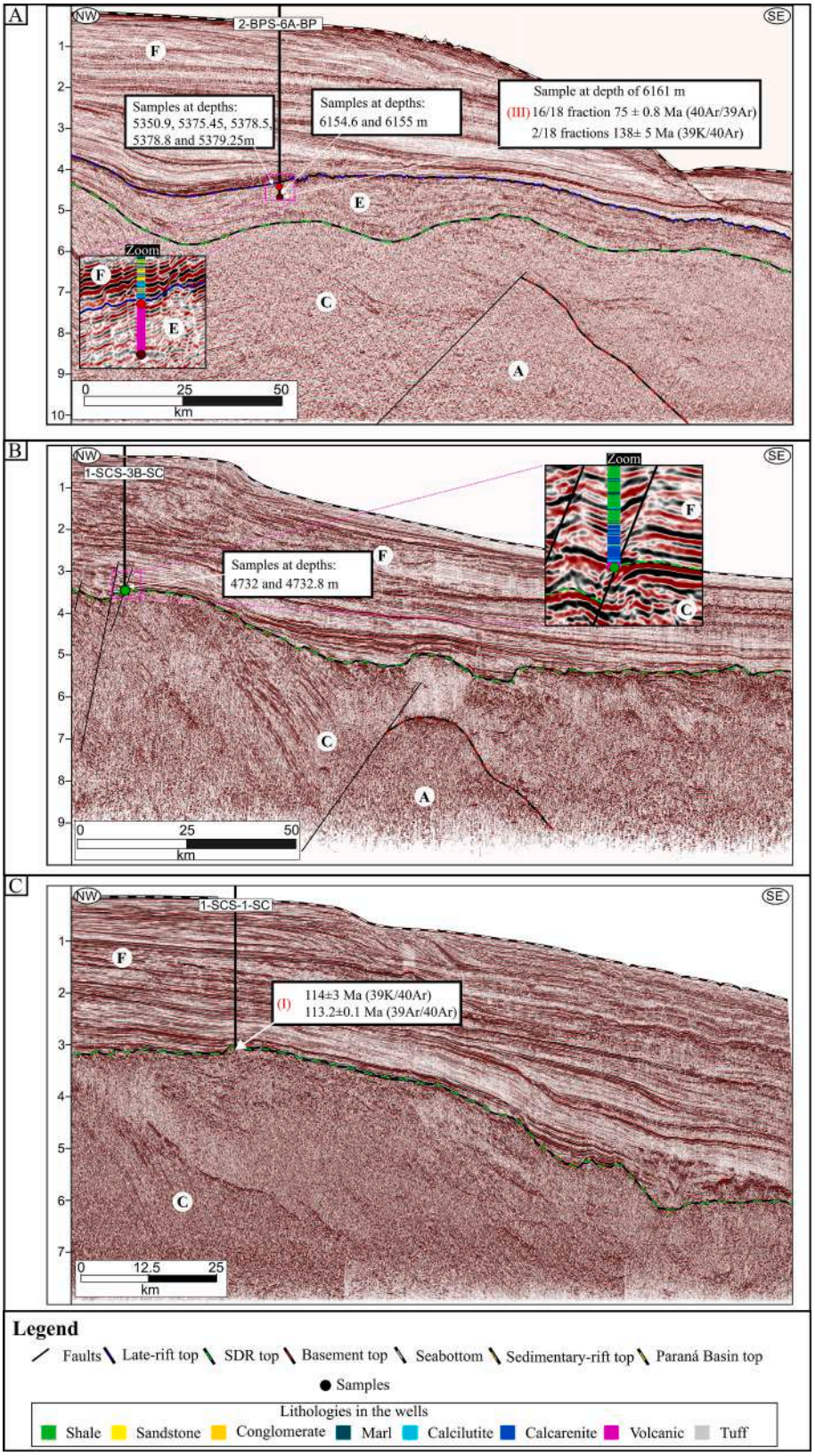

(caption on next page)

Fig. 3. Seismic lines from the Pelotas and Santos basins, their respective positions are indicated in Fig. 1. The colorful circles are the position from the samples, and white circles with letters are the interpreted tectonic units (A) Neoproterozoic Basement, (B) Paraná Basin, (C) SDR,(D) Late-Rift, (E) Late-Rift, (F) Drift. (I) data from Misuzaki and Saracchine, 1990b (II) data from Lobo, 2000 (III) data from Lobo, 2007. A) Seismic line near the well 2-BPS-6 A-BP. These rocks were classified as Curumin Formation (Pelotas Basin; Bueno et al., 2007); usually, these rocks are classified as SDR (Stica et al., 2014; Harkin et al., 2020; Chauvet et al., 2021). However, these rocks above the SDR do not fit the five SDR criteria (Mutter et al., 1982), so we classified them as a late-rift section. B) Seismic line near the well 1-SCS-3B-SC. The samples from the bottom of the well are the Curumin Formation (Bueno et al., 2007), and these rocks were observed in seismic as an SDR in Santos Basin. C) Seismic line near the well 1-SCS-1-SC. The bottom of this well-recovered SDR with age is constrained by Misuzaki (Misuzaki and Saracchine, 1990a, apud Gordon and Mohriak, 2015).

Table 1
Summary of the observed minerals, textures, and structures.

	Group	Rock	Primary mineralogy	Secondary mineralogy	Structures	Textures
	Gaviotin-1	Sandstone	Quartz			
	Lobo-1	Basalt	Plagioclase, Augite, K-feldspar	Ceruenite, Hematite Calcite, Basaluminite, Scolecite	Amygdales, Fractures	Porphyritic
Pre rift	Lower 1-RSS-3-RS	Basalt	Plagioclase, Augite	Ceruenite, Laumonite, Heulandite, Saponite, Stilpnomelane, Hematite		Porphyritic
	Upper 1-RSS-3-RS	Basalt	Plagioclase, Augite, Olivine (replaced), Apatite	Ceruenite, Analcime, Muscovite, Biotite, Hematite	Amygdales	Porphyritic
Rift	1-SCS-3B-SC	Basalt	Plagioclase, olivine (replaced)	Iddingsite, Ilite, Calcite, Kaolinite, Dolomite, Hematite	Amygdales	Porphyritic
Late rift	Lower 2-BPS-6A-BP	Basalt	Plagioclase, Augite, Olivine (replaced)	Clinochlore, Hematite	Amygdales	Porphyritic
	Upper 2-BPS-6A-BP	Peperite	Plagioclase, Augite, Olivine (replaced), Quartz	Ceruenite, Clinochlore, Clinochloriside, Hematite		Porphyritic

stilpnomelane).

4.2.2. Rift

The samples interpreted in seismic as rift rocks are from the 1-SCS-3B-SC well at a depth of 4732 m. It is a basalt with amygdales filled mostly with quartz, calcite, and dolomite (Fig. 4L). This rock shows a porphyritic texture with plagioclase (anorthite) and iddingsite phenocrysts measuring up to 1 mm (Fig. 4L). The groundmass hosts fine-grained plagioclase (anorthite), secondary minerals (illite, calcite, kaolinite, and dolomite), and opaque minerals (hematite).

4.2.3. Late-rift

The samples interpreted in seismic as late-rift rocks are from the 2-BPS-6A-BP well. At a depth of 5378 m, these samples are peperites with a very fine texture near the sedimentary rock interface (Fig. 4H). However, a few centimeters from the sedimentary contact, the texture changes to porphyritic with highly altered plagioclase (anorthite) phenocrysts measuring up to 5 mm (Fig. 4I). The matrix hosts fine-grained plagioclase (anorthite), pyroxene (augite), opaque minerals (hematite), and secondary minerals (corrensite, clinochrysotile). The sediments are mostly quartz sands with some clay minerals.

The analyzed sample from the lower 2-BPS-6A-BP well at a depth of 6154 m is a basalt. The rock shows a porphyritic texture with plagioclase (anorthite) phenocrysts up to 1 mm (Fig. 4J). The groundmass hosts fine-grained plagioclase (anorthite) and pyroxene (augite), opaque minerals (hematite), and secondary minerals (clinochlore). At a depth of 6155 m, the sample is a basalt with few amygdales (Fig. 4K). The rock exhibits a porphyritic texture with plagioclase (anorthite) and pyroxene (augite) phenocrysts measuring up to 1.5 mm. The matrix hosts fine-grained plagioclase (anorthite) and pyroxene (augite). Secondary and opaque minerals were not identified. The presence of amygdales is limited, suggesting a relatively homogenous alteration process that affected the overall mineral assemblage. The consistent texture and mineralogy across these depths indicate a uniform volcanic origin, likely influenced by similar magmatic processes during its formation.

4.3. Geochemical data

This section presents a synthesis of the geochemical results (Fig. 5). The full results can be found in Supplementary Material 5. The samples are divided as follows: 1) Lobo-1 (depths: 2622, 2627, and 2629 m); 2) Lower 1-RSS-3-RS (depths: 3904.9 and 3905.8 m); 3) Upper 1-RSS-3-RS (depths: 3555.1 and 3555.8 m); 4) Lower 2-BPS-6 A-BP (depths: 6154.6, and 6155 m); 5) Upper 2-BPS-6A-BP (depth: 5378.5 m); 6) 1-SCS-3B-SC (depths: 4732 and 4732.8 m); 7) U516 (depths: 1263 and 1268 m). The geochemical analysis of the samples indicates a distinct REE pattern and a geotectonic classification of basalts that align with Enriched Mid Ocean Ridge Basalts (EMORB) to Ocean Island Basalts (OIB) composition.

4.3.1. Data Reliability

The presence of chemical alteration processes identified in the petrographic analysis raises questions about the representativeness of the rock compositions concerning the original magmatism. The loss on ignition (LOI) values, ranging from 1.79 to 19.24 % with an average of 7.08 ± 5.97 %, further indicate potential inconsistencies. When using a rock classification diagram based on mobile elements, such as SiO_2 vs. total alkalis (LeBas et al., 1986; Fig. 5A), the basalts from the studied wells exhibit a wide compositional range, from sub-alkaline basalts to trachyandesite. In contrast, when plotted in an immobile elements diagram (Pearce and Wyman, 1996), all samples are classified as basalts (sub-alkaline to alkaline), consistent with petrographic observations. Consequently, we avoid using diagrams based on mobile elements (e.g., Cs, Rb, K, Ba, Sr, Pb). The Ce anomaly varies from 0.04 to 6.67 %, with an average of 3.05 ± 2.46 %, suggesting the reliability of the relative concentrations of immobile elements. Four samples exhibit negative cerium anomalies greater than 5 %, indicating potential trace element alterations due to seawater influences. However, the geochemical fingerprints of these rocks remain sufficiently similar to those of nearby samples to warrant their inclusion in our study, given the challenges associated with accessing these rock samples. Since these rocks are from regions with difficult access, it is important to explore all available data.

4.3.2. Pre-rift magmatism

The composition of pre-rift stage rocks shows a range of compositions from sub-alkaline basalts found in the upper 1-RSS-3-RS and in the well Lobo-1 to alkaline basalts in the lower 1-RSS-3-RS (based on Pearce and Wyman, 1996; Fig. 5B). The upper 1-RSS-3-RS and the Lobo-1 well compositions resemble an enriched mid-ocean ridge basalt (EMORB). Nb/Yb vs. TiO_2/Yb plots (Pearce, 2008; Fig. 5F) indicate a shallow melting process. In contrast, the rocks from lower 1-RSS-3-RS exhibit characteristics akin to (OIB) in the same plot, suggesting a deeper

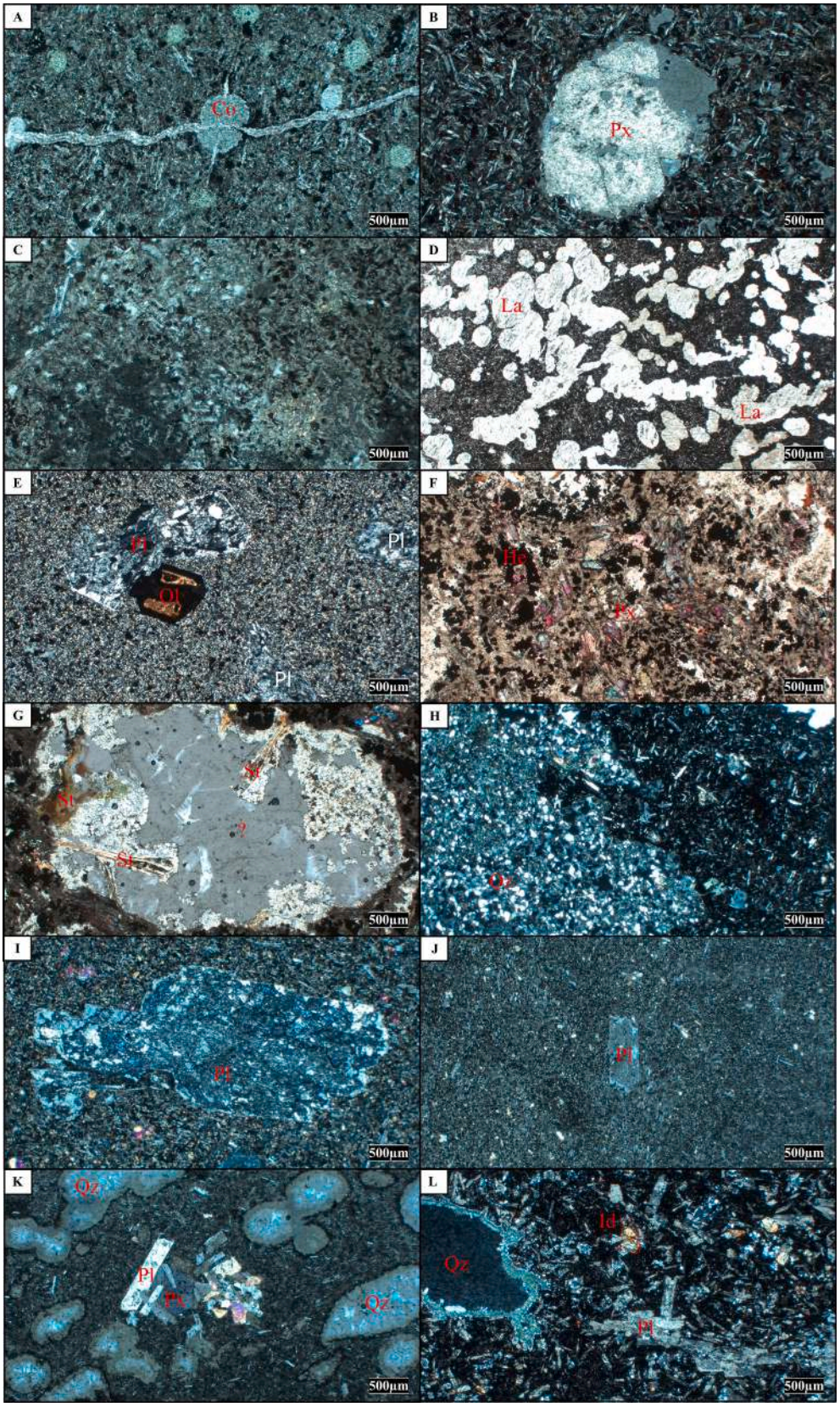

(caption on next page)

Fig. 4. Petrographic photos from: A) Well Lobo-1, the sample from a depth of 2627 m, showing a microscale fracture filled by minerals from late fluid percolation, this fracture cuts a rounded corrensite (Co) mass surrounded by a groundmass of acicular plagioclase, secondary, and opaque minerals; B) Well Lobo-1, sample from a depth of 2622 m, the image is centralized in an augite (Px) phenocryst undergoing an intense alteration process, surrounded by a groundmass of acicular plagioclase, secondary, and opaque minerals; C) Well Lobo-1, sample from a depth of 2629 m showing the extreme mineral alteration of this rock; D) Well 1-RSS-3-RS, sample from a depth of 3555 m, showing amygdaloidal basalt filled with laumontite (La); E) Well 1-RSS-3-RS, sample from a depth of 3555 m, showing phenocrysts of olivine (Ol) replaced by hematite and unidentified mineral, with anorthite (Pl) phenocrysts surrounded by a very thin groundmass; F) Well 1-RSS-3-RS, sample from a depth of 3905 m showing altered augite (Px) with not clear borders, large hematite (He) mass, and a few small amygdales surrounded by an strongly altered groundmass; G) Well 1-RSS-3-RS, sample from a depth of 3904 m, the image is centralized on an amygdale filled with an unidentified mineral hosting stilpnomelane (St) growing inside it; H) Well 2-BPS-6 A-BP, sample from a depth of 5378 m, showing the contact of basalt with the sedimentary quartz (Qz) in a peperite; I) Well 2-BPS-6 A-BP, sample from a depth of 5378 m, similar to image 4H but far from the sedimentary/basalt contact zone, showing a porphiritic texture with a 5 mm plagioclase (Pl) at the center of the image; J) Well 2-BPS-6 A-BP, sample from a depth of 6154 m, the image is centralized on a plagioclase (Pl) phenocryst with 1 mm surrounded by a fine matrix; K) Well 2-BPS-6 A-BP, sample from a depth of 6155 m the image is centralized on a phenocryst cluster, where the plagioclase (Pl) limits the pyroxene growth (Px), The sample also contains amygdales filled with quartz (Qz); L) Well 1-SCS-3B-SC from at a depth at 4732 m, showing plagioclase (Pl) and iddingsite (Id) phenocrysts up to 1 mm, surrounded by a groundmass with fine-grained plagioclase, secondary minerals, and opaque minerals, with a few amygdales filled mostly with quartz (Qz).

melting origin. The REE patterns from these rocks do not exhibit any Eu anomaly (Fig. 5C). In a spider plot of immobile elements, these rocks are plotted between EMORB and OIB, with Lobo-1 samples and Lower 1-RSS-3-RS closer to OIB and those from Upper 1-RSS-3-RS nearer to EMORB (Fig. 5D). Significant differences between the volcanic layers of 1-RSS-3-RS and the rocks from Lobo-1 emerge when comparing Nb/Yb vs. Th/Yb plots (Fig. 5E). This plot (Fig. 5E) distinguishes the rocks from the Paraná-Etendeka Large Igneous Province (PEL) and the Walvis Ridge/Rio Grande Rise very well. The samples from Lobo-1 display remarkable similarity to the Paraná-Etendeka LIP, whereas the 1-RSS-3-RS samples align more closely with Walvis Ridge/Rio Grande Rise (data from Walvis Ridge - Homrighausen et al., 2019; Rio Grande Rise - Hoyer et al., 2022; Paraná-Etendeka LIP - Gibson et al., 2006; Mansur et al., 2021; Zhou et al., 2020).

4.3.3. Rift magmatism

The rift stage rocks from well 1-SCS-3B-SC are characterized as alkali basalts (Pearce and Wyman, 1996; Fig. 5B) with a source akin to Ocean Island Basalts (OIB) in both Pearce (2008) diagrams (Fig. 5E-F). These rocks exhibit enrichment in Th/Yb relative to Nb/Yb, similar to Paraná-Etendeka LIP rocks (Fig. 5E). Additionally, the REE patterns do not show an Eu anomaly (Fig. 5C), and their composition closely resembles OIB in spider plots (Fig. 5D).

4.3.4. Late-rift magmatism

The late-rift stage rocks from well 2-BPS-6 A-BP are characterized as sub-alkaline to alkali basalts (Pearce and Wyman, 1996; Fig. 5B). It is important to remember that the Upper 2-BPS-6 A-BP are peperites, which can cause some unusual patterns in spiderplots in some samples (Fig. 5D) or produce very heterogeneous results in tectonic plots (Fig. 5E-F). Most of these rocks generally exhibit a compositional fingerprint similar to an OIB, and the samples from the rift magmatism (1-SCS-3B-SC - Fig. 5 C-F).

4.3.5. Rio Grande rise

The rocks from Rio Grande Rise are sub-alkaline basalts (Fig. 5B), with REE and spider plot patterns similar to those of the margin (Fig. 5C-D). These rocks have a composition that resembles an EMORB composition (Fig. 5E-F).

4.4. U-Pb analysis in zircons

U-Pb studies were conducted on four samples. One sedimentary sample corresponds to the Gaviotion-1 well; three are from the basalts of 1-RSS-3-RS and 2-BPS-6A-BP wells. In the sample from well Gaviotin-1 at 3629 m, which consists of sedimentary rocks from the Pre-rift, 110 zircon grains were analyzed. Zircons dominantly present magmatic growth zoning, and a few grains show high-grade metamorphic rims and recrystallization textures. Zircons are predominantly prismatic and secondarily rounded with 150 to 500 μm size. The sample shows a mean U-Pb peak related to Neoproterozoic (550–650 Ma) (Fig. 6A), with a secondary zircon population with Tonian, Stenian, and Rhyacian ages.

In the sample from well 1-RSS-3-RS at a depth of 3904 m, which consists of basalts from the Pre-rift section, 13 zircon grains were analyzed to constrain their age. The grains are dominantly prismatic morphology with rounded corners, alternating between magmatic growth texture in the core and recrystallization textures in the rim. A high-grade metamorphic texture is also identified in the zircon rims. The zircon size varies from 80 to 250 μm. The zircon population was related to the Neoproterozoic with a concordia age of 588.24 ± 5 Ma.

In two samples in the well, 2-BPS-6A-BP zircons were found, consisting of peperites of the late-rift section at 5378,8 (n = 11 zircon grains) and the other at 5379,25 (n = 33 zircon grains). The grains are both prismatic with rounded corners and rounded in morphology. Magmatic growth texture and recrystallization textures were identified. Few grains were prismatic with only magmatic texture. The age spectrum comprises different peaks, similar in both samples, comprehending a main peak in the Neoproterozoic and secondary peaks of Permian, Mesoproterozoic, and Paleoproterozoic ages.

4.5. Isotopic fingerprint

We analyzed the Nd and Sr isotopic composition of at least one sample from each well that contains volcanic rocks. This dataset was plotted with published data from the Walvis Ridge (Homrighausen et al., 2019) and the Paraná Large Igneous Province (Bologna et al., 2022; Fig. 7). The samples from the Rio Grande Rise display negative εNd(i) values and low $^{87}Sr/^{86}Sr(i)$ ratios, similar to those observed in the Walvis Ridge (Homrighausen et al., 2019). The samples from the lower section of well 2-BPS-6A-BP and well 1-SCS-3B-SC exhibit nearly identical isotopic signatures, close to the Gramado magmatic type of the Paraná LIP (Bologna et al., 2022), but with more negative εNd(i) and lower $^{87}Sr/^{86}Sr(i)$ ratios. The sample from well Lobo-1 also shows an isotopic signature similar to the Gramado type, with $^{87}Sr/^{86}Sr(i)$ values consistent with this magmatism but with εNd(i) values even more negative than those of the aforementioned samples, representing the most negative εNd(i) and the highest $^{87}Sr/^{86}Sr(i)$ values in the dataset. The lower sample from well 1-RSS-3-RS is compatible with the Gramado magmatic type; in contrast, the upper sample from the same well is the only one with a positive εNd(i) value and exhibits an $^{87}Sr/^{86}Sr(i)$ ratio similar to that of the Walvis Ridge. This sample (from the well upper 1-RSS-3-RS) plots near the Esmeralda magmatic type and the isotopic compositions of the lower and upper samples from well 1-RSS-3-RS differ significantly.

5. Discussion

5.1. Pre-rift section: The offshore extension of Paraná Basin

The Gaviotin-1 well (Fig. 1), drilled at a depth of 3629 m (Fig. 2B)

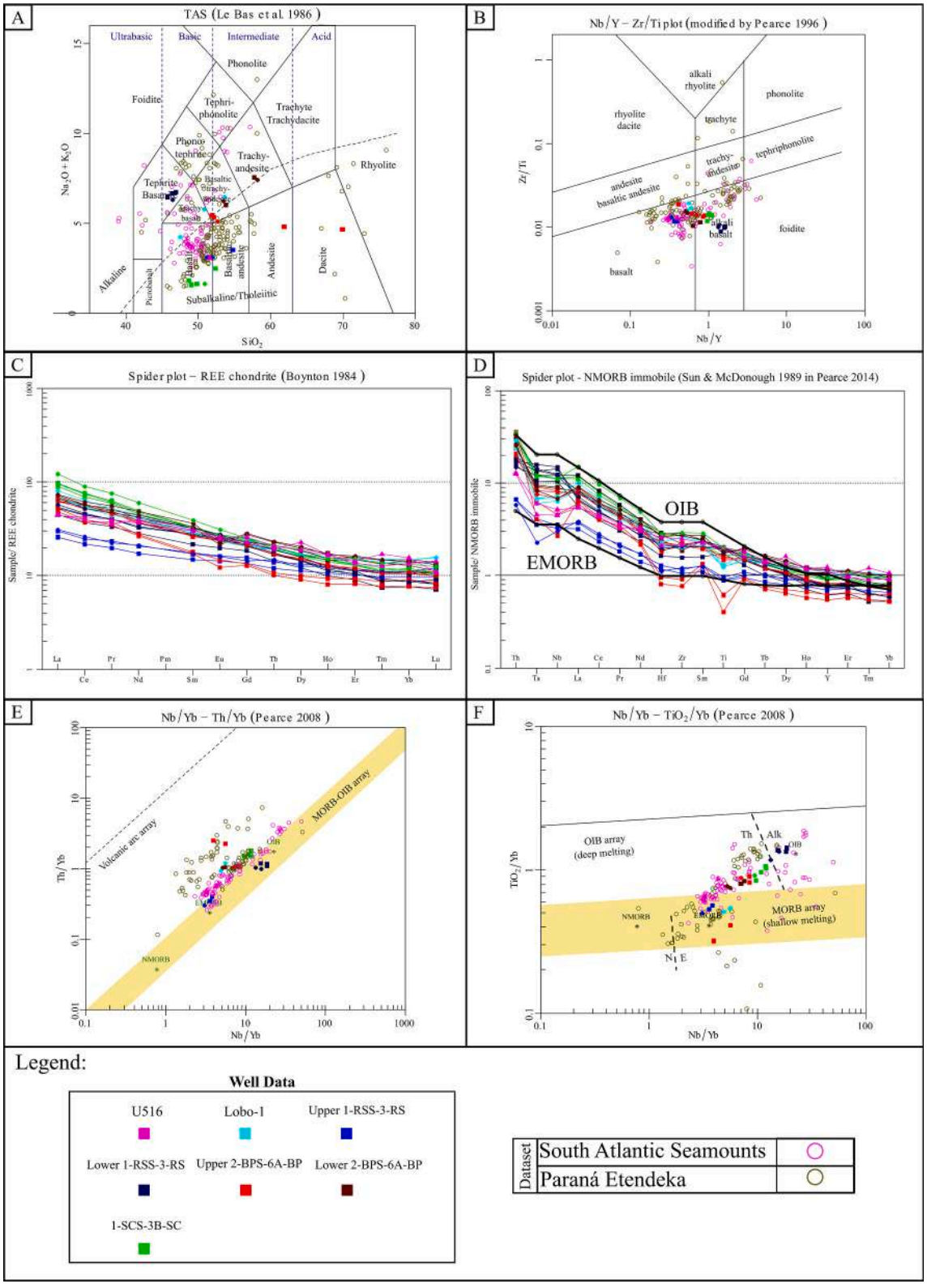

Fig. 5. Geochemical diagrams: A) Rock classification diagram using mobile elements, total alkalis vs silica (TAS- LeBas et al., 1986); B) Rock classification diagram using immobile elements, Nb/Y vs. Zr/TiO2 (Pearce and Wyman, 1996); C) REE spidergram, data normalized by chondrite (Boynton, 1984); D) Spider plot based on immobile elements normalized by NMORB (Sun and McDonough, 1989 in Pearce, 2014); OIB and EMORB data from McDonough and Sun (1995); E) Tectonic environment diagram using immobile elements Nb/Yb vs. Th/Yb (Pearce, 2008); F) Tectonic environment diagram using immobile elements Nb/Yb vs. TIO_2/Yb (Pearce, 2008). Datasets: (1): Paraná Etendeka LIP; Paraná LIP - Gibson et al., 2006; Mansur et al., 2021; Etendeka LIP -Zhou et al., 2020; (2): South Atlantic seamounts: Walvis Ridge - Homrighausen et al., 2019; Rio Grande – Rise - Hoyer et al., 2022. Samples represented in filled circles are data from Activation Lab, Triangles are from ALS, and squares from Geosol.

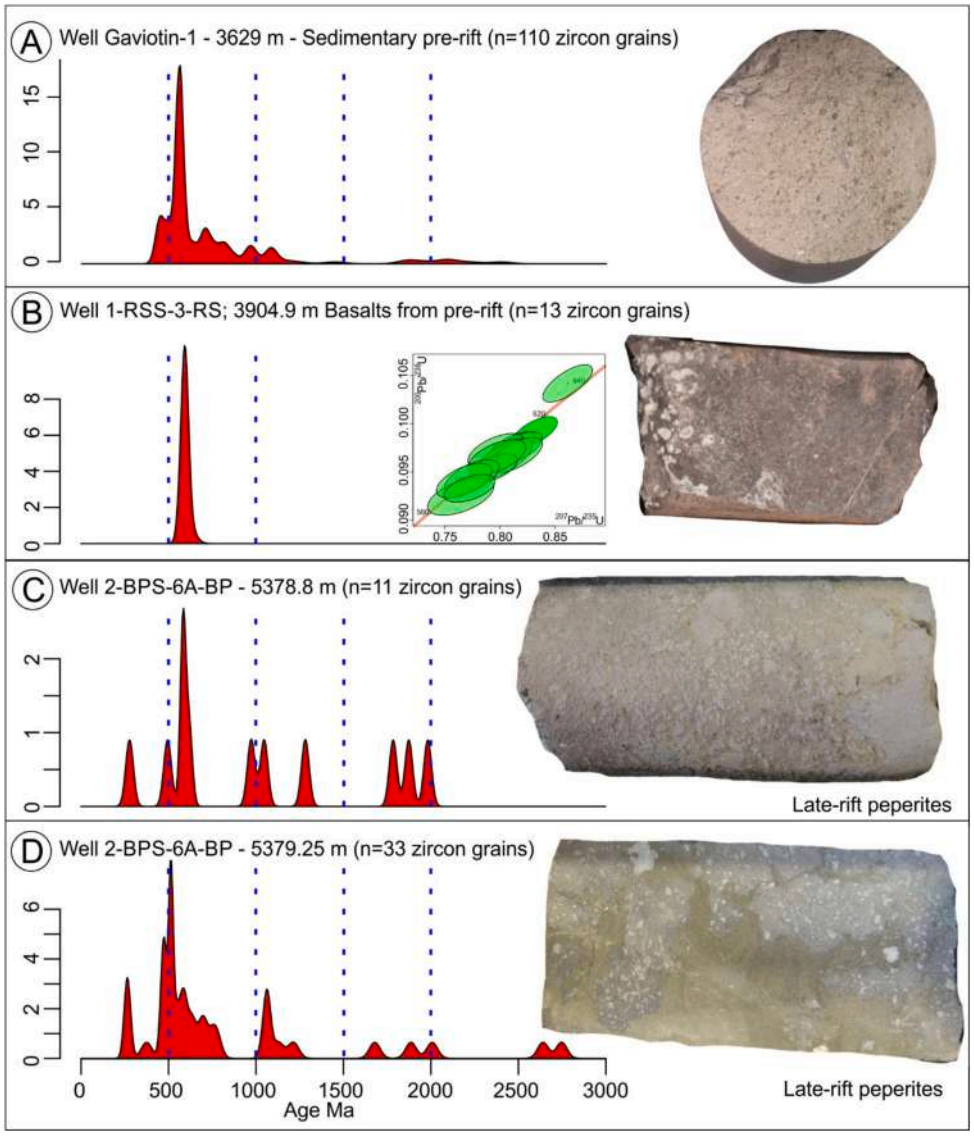

Fig. 6. U-Pb data and analyzed samples. A) Sample Gaviotin-1 - 3629 m, from the pre-rift sedimentary section of the Punta del Este Basin. B) Sample 1-RSS-3-RS, 3904.9 m from basalts of the pre-rift section in the Pelotas Basin. C and D) Samples from well 2-BPS-6A-BP from peperites of the Pelotas Basin late-rift section. KDE and Concordia diagrams were plotted using IsoplotR software (Vermeesch, 2018).

below the drift section of offshore Punta del Este Basin, was identified in seismic lines as part of the pre-rift section, which we interpret as Paraná Basin. Detrital zircon U-Pb analysis presents evidence of Permo-Carboniferous Paraná Basin deposits beneath the Punta del Este Basin. The detrital spectra distribution is consistent with the detrital material found in Itararé Group deposits of the Paraná Basin in southernmost Brazil, as documented by Tedesco et al. (2019). The sample from the Gaviotin-1 well represents the southernmost evidence of the offshore extension of Paraná Basin and the most robust evidence of its offshore extension.

As the pre-rift section from Gaviotin-1 corresponds to the Paraná Basin (Itararé Group), we further hypothesize that the volcanic rocks from the pre-rift section in the nearby Lobo-1 well (30 km away) are part of the Paraná LIP (Serra Geral Group in Paraná Basin stratigraphy), based on both their proximity and similar seismic facies (Fig. 2A-B). The recovered rocks are basalts with many amygdales (Fig. 4A), indicating that we recovered samples from the top of the lava flow. We found no evidence of subaqueous volcanism, pointing to these rocks representing subaerial volcanism. In terms of geochemical composition, the basalts from Lobo-1 are subalkaline (Fig. 5B) and indicate a shallow magmatic source (Fig. 5F), with a composition similar to that observed in the PEL (Fig. 5E-F). We observed high $^{87}Sr/^{86}Sr(i)$ and low εNd(i) values(Fig. 7), which could be interpreted as continental crust melt (including sediment) or a plume related to an EMII reservoir (Zindler and Hart, 1986). The εNd(i) is even lower than the values observed in Paraná LIP. However, the $^{87}Sr/^{86}Sr(i)$ is compatible with the Gramado magma type, widespread in the southern part of the Paraná-LIP, and the largest e member of the Low-Ti lava field (Ti/Y < 310, Rossetti et al., 2018). The Lobo-1 samples have Ti/Y ranging from 323 to 348, which is over 310, yet very close to this value. In general, the composition is similar to the Gramado magmatic type from Paraná-LIP, and considering the tectonic context observed in seismic lines, probably these rocks are part of Paraná-LIP.

The pre-rift section drilled in well 1-RSS-3-RS (Figs. 1 and 2C), previously classified as the Imbituba Formation (Pelotas Basin – Bueno et al., 2007), contains Gramado and Esmeralda-type lavas from the Paraná LIP. Samples from this well range from alkali basalts in the lower unit to sub-alkaline basalts in the upper unit (Fig. 5B). The Th/Yb vs. Nb/Yb plot (Fig. 5E) indicates minimal crustal contamination. However, 11 Neoproterozoic zircons dated at 588.24 ± 5 Ma (Fig. 6B) suggest

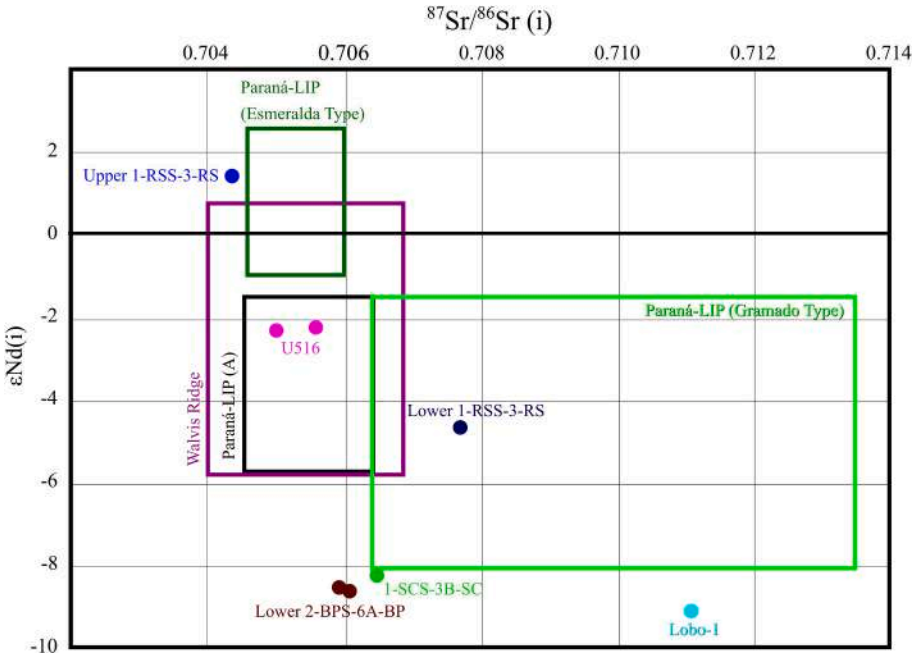

Fig. 7. Plot of data of εNd(i) and $^{87}Sr/^{86}Sr$. The fields are the limits of these isotopic ratios observed in the Walvis Ridge (in purple, Homrighausen et al., 2019) and the Paraná-LIP, subdivided into Esmeralda magmatic type, in dark green; Gramado type, in green; and the black field (Paraná LIP (A)) is the superposition of data from the Pitanga, Paranapanema, Urubici, and Ribeira formations, data compiled by Bologna et al. (2022). (For interpretation of the references to colour in this figure legend, the reader is referred to the web version of this article.)

assimilation from the Dom Feliciano Belt, which is the basement of Pelotas, Punta del Este and Paraná basins in this region (Stica et al., 2014; Gordon and Mohriak, 2015; Teixeira et al., 2025a; Teixeira et al., 2025b). The zircon morphology is also compatible with a granitic/gneiss source (with clear zonation). The isotopic signatures ($^{87}Sr/^{86}Sr$(i) and εNd(i); Fig. 7) also suggest continental crust assimilation or an EMI source (Zindler and Hart, 1986) for the lower 1-RSS-3-RS. The abundance of amygdales in the upper unit (Fig. 4D) points to subaerial lava emplacement. Subparallel seismic reflectors (Fig. 2C) support a pre-rift setting, though slight divergence in the upper reflectors may indicate a transition to an early rifting phase (Gordon and Mohriak, 2015). Radiometric ages from 3800 to 3907 m depths range from 125.3 ± 0.7 Ma to 118.3 ± 1.9 Ma ($^{40}Ar/^{39}Ar$ and $^{39}K/^{40}Ar$; compiled by Gordon and Mohriak, 2015), compatible with the late Paraná magmatism phase (Hartmann et al., 2019). However, due to altered plagioclases (Fig. 4), concern is required when interpreting these ages, since plagioclases are no longer a closed system, and most isotopic age data is classified. Isotopic signatures from the lower unit match the Gramado type (part of Paraná LIP), while the upper unit aligns with the Esmeralda type (part of Paraná LIP; Bologna et al., 2022; Fig. 7), consistent with the onshore stratigraphy where Esmeralda basalts overlie Gramado basalts or Palmas rhyolites (Rossetti et al., 2018). The existence of the Paraná-LIP at the base of Santos (Camboriú Formation - Moreira et al., 2007) and Campos basins (Cambiúnas Formation - Winter et al., 2007) is additional evidence of the offshore extension of the Paraná LIP beneath Pelotas and Punta del Este basins.

The Paraná-Etendeka LIP (PEL) genesis was sometimes suggested to be related to the Tristan da Cunha plume (Ewart et al., 1998; Marsh et al., 2001; Ewart et al., 2004; Gibson et al., 2006; Zhou et al., 2020; Beccaluva et al., 2020). However, the $^{87}Sr/^{86}Sr$(i) and εNd(i) signatures associated with the Neoproterozoic basement zircon xenocrysts are clear evidence of the continental crust and/or continental lithospheric mantle assimilation. Our isotopic analysis supports multiple interpretations of the magmatic source, as the observed in the isotopic ($^{87}Sr/^{86}Sr$(i) and εNd(i)) and chemical signatures could equally be attributed to either mantle plumes from EMI or EMII reservoirs (Zindler and Hart, 1986) or the melting of continental crust or subcontinental lithospheric mantle (Marques et al., 2018). However, we observe an isotopic signature overlap of PEL (Pitanga, Paranapanema, Urubici, and Ribeira formations) and Walvis Ridge/Rio Grande Rise data, which suggests that they could share the same source.

5.2. *Rift and late Rift in Pelotas, Punta del Este, and south of Santos basins*

The rifting stage in the Pelotas and Punta del Este basins is characterized by antithetical half-grabens filled by sedimentary rocks at the proximal portion and SDRs at distal regions. SDR rocks were sampled exclusively in the northern Pelotas Basin at well 1-SCS-3B-SC and southernmost of Santos Basin, in well 1-SCS-1-SC (by Misuzaki and Saracchine, 1990b) on the north flank of Torres Arch. These rocks from 1-SCS-3B-SC are alkali basalts exhibiting an Ocean Island Basalts affinity (OIB; Fig. 5). Bueno et al. (2007) previously pointed to significant lithological heterogeneity in volcanic rocks from the margin, ranging from basalts to trachyandesites. However, their findings were based on major element classifications (Fig. 5A), which may not accurately represent the original compositions due to chemical alteration processes. Our analysis of trace elements (Fig. 5B) indicates that all volcanic rocks from the margin are more homogeneous than previously reported, ranging from sub-alkaline basalts to alkaline basalts.

In the late-rift section of the 2-BPS-6 A-BP well, we encountered basalts and peperites. These peperites likely formed when hot lava interacted with wet sediments. The basalts and peperites are overlain by a marine sedimentary section Aptian in age (Arai, 2009), which further supports an interpretation of a near-shore magmatic event (Fig. 8). The detrital ages of these sediments provide evidence of erosion of Paraná Basin in the rift shoulders, now the Uruguayan and Brazilian coasts. The volcanic rocks chemical composition (Fig. 5) and isotopic signature (Fig. 7) from the lower 2-BPS-6 A-BP are almost the same as those observed in the 1-SCS-3B-SC well. Generally, we assume that all these rocks of the Torres Arch (2-BPS-6A-BP, 1-SCS-3B-SC, and 1-SCS-1-SC) represent the same magmatism within different tectonic contexts. As the rift propagated from South to North, while the Pelotas Basin became tectonically quiet (in the well 2-BPS-6 A-BP – Fig. 3A), the rocks were

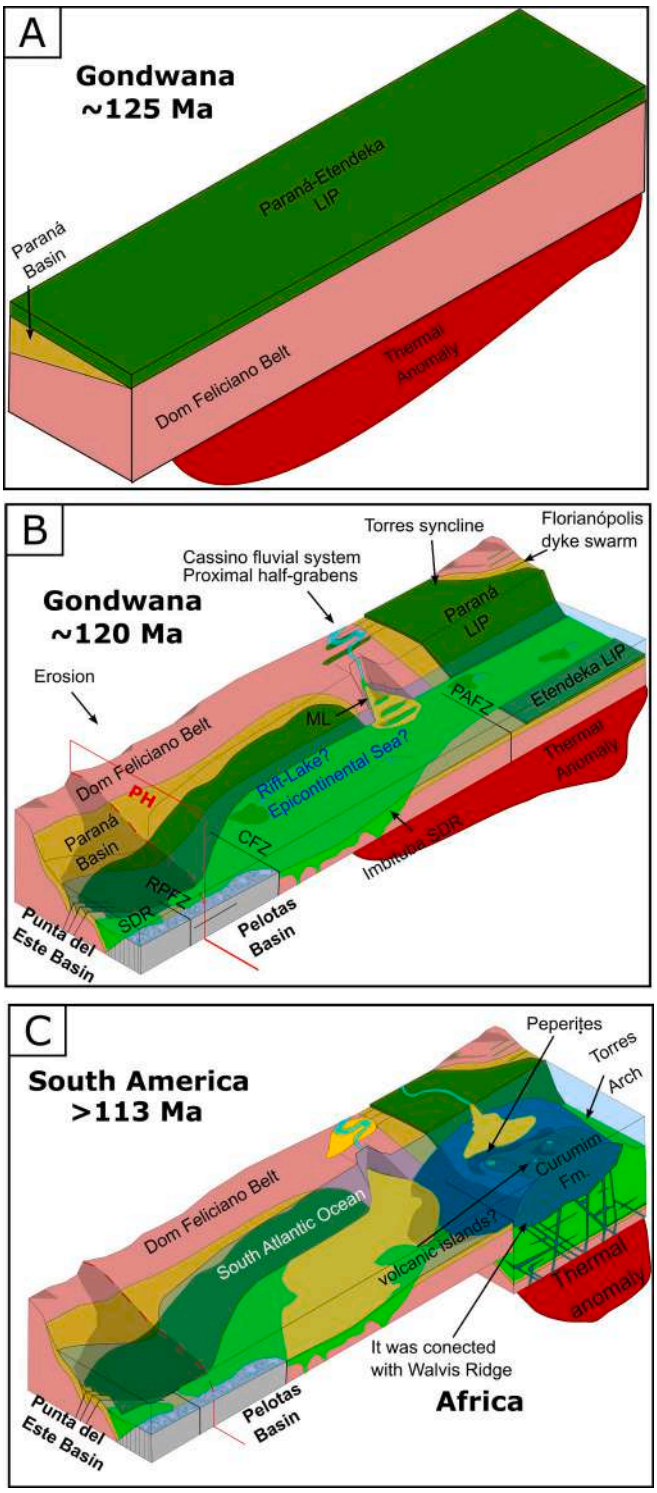

Fig. 8. Overview of Margin Evolution. A) Pre-Rift Stage: At this stage, the Paraná-Etendeka Large Igneous Province (LIP) was extensive across the region, covering sedimentary deposits of the Botucatu Formation, with the majority of this magmatic activity occurring around ~135 Ma. By 125 Ma, magmatic activity was minimal (Gomes and Vasconcelos, 2021, and references therein). During this stage, magmatism assimilated parts of the host rock, primarily those of the Dom Feliciano Belt at the continental margin. At this moment the thermal anomaly covers a wide area. B) Rift Stage: The rift stage is marked predominantly by Seaward Dipping Reflectors (SDRs) attributed to the Imbituba and Curumin Formations (Pelotas Basin – sensu Bueno et al., 2007). Sedimentary rocks from the rift Cassino Formation, fulfilling proximal half-grabens are reported in the well 1-RSS-3-RS (Bueno et al., 2007). We also observed some halfgrabens that are fulfilled by sedimentary rocks within the Punta del Este Basin south of Polonio High (PH). Erosion of the rift shoulders during this phase likely prevented the preservation of Paraná Basin rocks at the margin. With exception of the position of the well 2-TO-1-RS, this region records an depression of Paraná Basin know as Torres Syncline. ML- Mostardas Low; RPFZ- Rio de La Plata Fracture Zone; CFZ - Chuì Fracture Zone; PAFZ – Porto Alegre Fracture Zone C) Late-rift Stage: This stage was characterized by volcanic activity without significant new accommodation space creation. The magmatism was synchronous to sedimentary deposition. Based on its age, and position this magmatism is related to the Walvis Ridge, and represent the shrinkage of the thermal anomaly. Peperites samples in this section indicate volcanic activity in a wet depositional environment. Regional studies of the Torres Arch (Misuzaki and Saracchine, 1990a apud Gordon and Mohriak, 2015) and the Walvis Ridge (Rohde et al., 2013) suggest this magmatic phase lasted until ~113 Ma.

still faulting towards Santos Basin (wells 1-SCS-3B-SC and 1-SCS-1-SC, Fig. 3B-C). Due to the proximity and isotopic similarities of these wells, we assume the ages of 114 ± 3 Ma (K-Ar) and 113.2 ± 0.1 Ma (^{40}Ar-^{39}Ar) from Misuzaki (Misuzaki and Saracchine, 1990a; in Gordon and Mohriak, 2015) to the top of Torres Arch. This ages supports the hypothesis of sedimentary assimilation in the edges of this volcanic structure (Torres Arch), once the sedimentary deposition of Santos Basin started at Barremian (125.77 to 121.4 ± 0.6 - Moreira et al., 2007). This could explain the low-density SDRs observed by Harkin et al. (2020).

Paleogeographic reconstructions correlate the Torres Arch region with the early position of the Walvis Ridge (Homrighausen et al., 2019; Chauvet et al., 2021). This corroborates the Torres Arch volcanic activity occurring at approximately 114 ± 3 Ma (K-Ar) and 113.2 ± 0.1 Ma (^{40}Ar-^{39}Ar; Misuzaki and Saracchine, 1990a; apud Gordon and Mohriak, 2015) since the ages of 114.1 ± 0.4 Ma are found in the oldest rocks of the Walvis Ridge (Rohde et al., 2013). These radiometric ages are compatible with the micropaleontology age observed in the sedimentary section above the volcanic layers of Torres Arch, which are Aptian in age (Arai, 2009). However, there is no evidence that late magmatism (Until 113 Ma) was widespread; we assume that it was restricted to the Torres Arch region (Figs. 1 and 8) while it was connected to Walvis Ridge (Chauvet et al., 2021).

These findings suggest a volcanic stack in the margin, spanning from approximately 125.3 ± 0.7 Ma to 113.2 ± 0.1 Ma (Misuzaki and Saracchine, 1990a apud Gordon and Mohriak, 2015). This supports the hypothesis by Serratt et al. (2022) that the region contains multiple volcanic layers of different ages. Additionally, it highlights the limitations of magnetostratigraphy in the area, as at least six magnetic field reversals are stacked within these volcanic units(Gee and Kent, 2007), complicating the interpretation of the magnetic record.

The magmatism source from the Torres arch looks similar to the Gramado magmatic type source, as observed by its isotopic content (Paraná-LIP – Fig. 7). However, the data could be interpreted in two ways, the source could be an EMI reservoir plume or the magmatic assimilation of the crust/sub continental lithospheric mantle, for the same reasons mentioned in the pre-rift section. Some previous research points that there is not necessary a plume to cause this magmatism (Lobo et al., 2006; Sauter et al., 2023). The isotopic signature of SDRs and related rocks does not reflect the εNd and ^{87}Sr/^{86}SR values observed in Walvis Ridge and Rio Grande Rise (Fig. 7). However, on the African side, we can observe that Walvis Ridge is a direct continuation of the SDRs near the Rio Grande Fracture Zone (Chauvet et al., 2021). We interpret this as the Torres Arch and Walvis Ridge having the same source but with more continental contamination in the rocks of the margin.

5.3. Rio Grande Rise

The Rio Grande Rise shows an isotopic signature compatible with Walvis Ridge (Fig. 7). This reinforces the paleogeographic models from Hoyer et al. (2022), where these two structures are genetically linked. The isotopic content of these samples points to an EMI reservoir (Zindler and Hart, 1986). However, we cannot confirm the plume model suggested by Hoyer et al. (2022). Notably, εNd values can even indicate some degree of continental contamination. The South Atlantic Ocean has the largest record of zircon xenocrysts in its Mid-Ocean Ridge, which Bea et al. (2020) interpreted as evidence of continental slivers preserved in the Mid Ocean Ridge. The possible presence of these slivers could cause negative values of εNd and lead to misinterpretation of the isotopic data.

We updated the Courtillot et al. (1999) observations of the close spatial and temporal relationship between Continental Flood Basalts (CFBs), SDR, and seamounts worldwide. Notable examples include the juxtaposition of the Etendeka Traps with African SDRs (Chauvet et al., 2021), as well as the Central Atlantic Magmatic Province (CAMP) and the United States of America East Coast SDRs, associated with the East Coast Magnetic Anomaly (ECMA; Davis et al., 2018). Other significant examples include the Deccan Traps and associated SDRs and Chagos-Laccadive Plateau in India (Verma and Khosla, 2019; Geoffroy et al., 2020), the North Atlantic Igneous Province (NAIP) encompassing the United Kingdom and Greenland onshore plateaus with adjacent SDRs (Meyer et al., 2007). The Afro-Arabian LIP (Hofmann et al., 1997) and the active SDR formation observed in Djibouti (Chauvet et al., 2023) support this relation. Nearby, these volcanic successions include volcanic islands, seamounts, and volcanic plateaus such as the Rio Grande Rise and Walvis Ridge. The Iceland island near West Greenland SDR (Agranier et al., 2019) suggests that these features are genetically linked. Although the SDRs and Rio Grande Rise did not show the same isotopic signature, all these magmatic units (CFB, SDR, oceanic plateaus) appear to be related to the same persistent thermal anomaly in the region (Foulger, 2018).

6. Conclusion

Geological and geochemical evidence supports the offshore continuation of the Paraná Basin beneath the Pelotas and Punta del Este basins. This is particularly exemplified by findings from the Gaviotin-1 well, which recovered Permo-Carboniferous deposits of the Itararé Group (Paraná Basin), confirmed by its distinctive detrital zircon content. The geochemical signatures from volcanic rocks in the Lobo-1 and 1-RSS-3-RS wells, combined with seismic interpretations, suggest that these units belong to the Paraná-Etendeka Large Igneous Province (LIP), known as the Serra Geral Group in the Paraná Basin stratigraphy. These findings suggest that sedimentary and volcanic rocks of the Paraná Basin likely extend across significant segments of the offshore continental margin.

All volcanic samples from the margin are basalts, ranging from subalkaline to alkaline compositions, and display varying degrees of continental crust contamination. This contamination is evidenced by their geochemical and isotopic signatures and the presence of zircon xenocrysts. We conclude that all analyzed volcanic rocks from the margin are formed above the continental crust. However, the precise location of the continent-ocean boundary (COB) remain unclear, especially considering that features such as the Rio Grande Rise may involve fragments of continental crust.

The rift stage in the Pelotas and Punta del Este basins is characterized predominantly by volcanic seaward-dipping reflectors (SDRs), though sedimentary rocks also appear in proximal sectors, indicating contemporaneous deposition during rifting. This observation supports the hypothesis that sedimentation occurs within SDR formation. Notable, the well 2-BPS-6A-BP contains peperites, indicating that late-stage rift magmatism interacted with coastal sedimentary environments, containing sediments derived from Paraná Basin erosion.

The volcanic rocks from the margin exhibit geochemical compositions similar to OIB and E-MORB, with isotopic signatures compatible with EMI and EMII plume reservoirs. However, these characteristics may reflect significant assimilation of continental crust or subcontinental lithospheric mantle, an interpretation reinforced by the occurrence of zircon xenocrysts in well 1-RSS-3-RS. As a result, the primary mantle source remains uncertain.

The Rio Grande Rise shares the same isotopic fingerprint as the Walvis Ridge, providing further support for their conjugate origin during the Late Cretaceous. This fingerprint is suggestive of an EMI source (possibly plume-related). However, this fingerprint can have been modified by the assimilation of slivers of continental crust, which are widespread throughout the South Atlantic, making the source unclear.

Although the mantle source remains unconstrained, our observations reflect a sequence of magmatic events extending from the Gondwanan continental flood basalts (CFBs) through rift-related SDRs to oceanic plateaus and volcanic islands of the South Atlantic. This sequence appears to be a common feature of volcanic passive margins and points to long-lived thermal anomalies acting throughout their evolution.

CRediT authorship contribution statement

Henrique Serratt: Writing – review & editing, Writing – original draft, Visualization, Methodology, Investigation, Formal analysis, Data curation, Conceptualization. **Tiago Jonatan Girelli:** Writing – original draft, Methodology, Investigation, Formal analysis. **Matheus Fernandes da Cruz:** Visualization, Software, Methodology, Data curation. **Claudia Domingues Teixeira:** Writing – review & editing, Investigation, Formal analysis. **Ilana Lehn:** Writing – review & editing, Writing – original draft, Validation, Formal analysis. **Monique Aparecida Marchese Rizzi:** Writing – review & editing, Writing – original draft, Data curation. **Marly Babinski:** Formal analysis, Methodology, Validation. **Catarina Laboure Bemfica Toledo:** Writing – review & editing, Validation, Supervision, Methodology, Investigation. **Peng Peng:** Methodology, Formal analysis. **Bruno Conti:** Validation, Resources, Data curation. **Adalene Moreira Silva:** Writing – review & editing, Validation, Supervision, Data curation, Conceptualization. **Laurent Geoffroy:** Writing – review & editing, Supervision. **Farid Chemale Junior:** Writing – review & editing, Validation, Supervision, Resources, Project administration, Funding acquisition, Data curation, Conceptualization.

Declaration of competing interest

We declare that we have no economic interest on this research.

Acknowledgments

This article is part of HS Ph.D. thesis. The authors thank the CNPC Brasil (China National Petroleum Corporation) for the financial support. We also thanks ANP (Brazilian National Agency for Petroleum, Natural Gas and Biofuels) and ANCAP (Uruguayan Administración Nacional de Combustibles, Alcoholes y Portland) for providing access to data. We are grateful to Schlumberger and Eliis for granting academic licenses for the Petrel™ and PaleoScan™ software, respectively. FCJ thanks CNPq for grant #4081942021-9 and INCT-Atlantico (grant #406898/2022-7). HS thanks CAPES for grant #88887.886595/2023-00.

Appendix A. Supplementary data

Supplementary data to this article can be found online at https://doi.org/10.1016/j.tecto.2025.230790.

Data availability

The data that has been used is confidential.

References

Abdelmalak, M.M., Rossetti, L.M., Millett, J.M., Planke, S., Jerram, D.A., Faleide, J.I., Polteau, S., 2025. Breakup Magmatism in the South Atlantic: Mechanisms and Implications.

Agranier, A., Maury, R.C., Geoffroy, L., Chauvet, F., Le Gall, B., Viana, A.R., 2019. Volcanic record of continental thinning in Baffin Bay margins: insights from Svartenhuk Halvø Peninsula basalts, West Greenland. Lithos 334, 117–140.

Arai, M., 2009. South Atlantic Aptian paleogeography: a new model based on recent Brazilian micropaleontological data. Boletim de Geociências da Petrobras 17 (2), 331–351.

Barker, P.F., Johnson, D.A., Carlson, R.L., Cepek, P., Coulbourn, W.T., Gamboa, L.A., Hamilton, N., de Melo, U., Pujol, C., Shor, A.N., Suzyumov, A.E., Tjalsma, L.R.C., Walton, W.H. (Eds.), 1983. Initial reports of the Deep Sea Drilling Project, Volume 72: Leg 72, Santos, Brazil to Santos, Brazil, February–April 1980. U.S. Government Printing Office. In: https://doi.org/10.2973/dsdp.proc.72.1983.

Bea, F., Bortnikov, N., Montero, P., Zinger, T., Sharkov, E., Silantyev, S., Molina-Palma, J.F., 2020. Zircon xenocryst evidence for crustal recycling at the Mid-Atlantic Ridge. Lithos 354, 105361.

Beccaluva, L., Bianchini, G., Natali, C., Siena, F., 2020. Plume-related Paranà-Etendeka igneous province: an evolution from plateau to continental rifting and breakup. Lithos 362, 105484.

Becker, K., Franke, D., Trumbull, R., Schnabel, M., Heyde, I., Schreckenberger, B., Krawczyk, C.M., 2014. Asymmetry of high-velocity lower crust on the South Atlantic rifted margins and implications for the interplay of magmatism and tectonics in continental breakup. Solid Earth 5 (2), 1011–1026.

Bologna, M.S., Júnior, E.R.V.R., Ernesto, M., Marques, L.S., 2022. The Paraná Magmatic Province: state-of-the-art in the geophysical and geochemical investigations. Brazil. J. Geophys. 40 (6), 43–66.

Boynton, W.V., 1984. Cosmochemistry of the rare earth elements: Meteorite studies. In: Developments in geochemistry, vol. 2. Elsevier, pp. 63–114.

Bueno, G.V., Zacharias, A.A., Oreiro, S.G., Cupertino, J.A., Falkenhein, F.U.H., Martins Neto, M.A., 2007. Bacia de Pelotas. Boletim de Geociencias da Petrobras 15, 551–559.

Cainelli, C., Mohriak, W.U., 1999. Some remarks on the evolution of sedimentary basins along the Eastern Brazilian continental margin. Episodes J. Int. Geosci. 22 (3), 206–216.

Cassel, M.C., Chemale Jr., F., Vargas, M.R., de Souza, M.K., Girelli, T.J., de Oliveira, G.S., 2022. From the Andes and the Drake Passage to the Rio Grande Submarine Fan: paleoclimatic and paleogeographic evidence in the Cenozoic Era from the South Atlantic–Austral Segment, Pelotas Basin. Glob. Planet. Chang. 213, 103838.

Caxito, F.A., Hartmann, L.A., Heilbron, M., Pedrosa-Soares, A.C., Bruno, H., Basei, M.A., Chemale, F., 2022. Multi-proxy evidence for subduction of the Neoproterozoic Adamastor Ocean and Wilson cycle tectonics in the South Atlantic Brasiliano Orogenic System of Western Gondwana. Precambrian Res. 376, 106678.

Chauvet, F., Sapin, F., Geoffroy, L., Ringenbach, J.C., Ferry, J.N., 2021. Conjugate volcanic passive margins in the austral segment of the South Atlantic–architecture and development. Earth Sci. Rev. 212, 103461. https://doi.org/10.1016/j.earscirev.2020.103461.

Chauvet, F., Geoffroy, L., Le Gall, B., Jaud, M., 2023. Volcanic passive margins and breakup processes in the southern Red Sea. Gondwana Res. 117, 169–193.

Chemale Jr., F., Mallmann, G., de Fátima Bitencourt, M., Kawashita, K., 2012. Time constraints on magmatism along the Major Gercino Shear Zone, southern Brazil: implications for West Gondwana reconstruction. Gondwana Res. 22 (1), 184–199.

Chemale Jr., F., Kawashita, K., Dossin, I.A., Ávila, J.N., Justino, D., Bertotti, A.L., 2012. U–Pb zircon in situ dating with LA–MC–ICP–MS using a mixed detector configuration. An. Acad. Bras. Cienc. 84, 275–295.

Collier, J.S., McDermott, C., Warner, G., Gyori, N., Schnabel, M., McDermott, K., Horn, B. W., 2017. New constraints on the age and style of continental breakup in the South Atlantic from magnetic anomaly data. Earth Planet. Sci. Lett. 477, 27–40. https://doi.org/10.1016/j.epsl.2017.08.007.

Conti, B., de Jesus Perinotto, J.A., Veroslavsky, G., Castillo, M.G., de Santa Ana, H., Soto, M., Morales, E., 2017. Speculative petroleum systems of the southern Pelotas Basin, offshore Uruguay. Mar. Pet. Geol. 83, 1–25.

Courtillot, V., Jaupart, C., Manighetti, I., Tapponnier, P., Besse, J., 1999. On causal links between flood basalts and continental breakup. Earth Planet. Sci. Lett. 166 (3–4), 177–195.

Davis, J.K., Bécel, A., Buck, W.R., 2018. Estimating emplacement rates for seaward-dipping reflectors associated with the US East Coast magnetic Anomaly. Geophys. J. Int. 215 (3), 1594–1603. https://doi.org/10.1093/gji/ggy360.

DePaolo, D.J., 1981. Nd isotopic studies: some new perspectives on Earth structure and evolution. Eos Trans. Am. Geophys. Union 62 (14). https://doi.org/10.1029/EO062i014p00137-01, 137-137.

Dias, J.L., Sad, A.R., Fontana, R.L., Feijó, F.J., 1994. Bacia de Pelotas. Boletim de Geociências da Petrobras 8 (1), 235–245.

Eagles, G., Pérez-Díaz, L., Scarselli, N., 2015. Getting over continent-ocean boundaries. Earth Sci. Rev. 151, 244–265. https://doi.org/10.1016/j.earscirev.2015.10.009.

Ernesto, M., Marques, L.S., Piccirillo, E.M., Molina, E.C., Ussami, N., Comin-Chiaramonti, P.I.E.R.O., Bellieni, G., 2002. Paraná Magmatic Province–Tristan da Cunha plume system: fixed versus mobile plume, petrogenetic considerations and alternative heat sources. J. Volcanol. Geotherm. Res. 118 (1–2), 15–36.

Ewart, A., Milner, S.C., Armstrong, R.A., Dungan, A.R., 1998. Etendeka volcanism of the Goboboseb Mountains and Messum Igneous Complex, Namibia. Part I: Geochemical evidence of early Cretaceous Tristan plume melts and the role of crustal contamination in the Paraná–Etendeka CFB. J. Petrol. 39 (2), 191–225.

Ewart, A., Marsh, J.S., Milner, S.C., Duncan, A.R., Kamber, B.S., Armstrong, R.A., 2004. Petrology and geochemistry of early cretaceous bimodal continental flood volcanism of the NW Etendeka, Namibia. Part 1: introduction, mafic lavas and re-evaluation of mantle source components. J. Petrol. 45 (1), 59–105.

Foulger, G.R., 2018. Origin of the South Atlantic igneous province. J. Volcanol. Geotherm. Res. 355, 2–20.

Franke, D., Neben, S., Ladage, S., Schreckenberger, B., Hinz, K., 2007. Margin segmentation and volcano-tectonic architecture along the volcanic margin off Argentina/Uruguay, South Atlantic. Mar. Geol. 244 (1–4), 46–67.

Frizon de Lamotte, D., Fourdan, B., Leleu, S., Leparmentier, F., de Clarens, P., 2015. Style of rifting and the stages of Pangea breakup. Tectonics 34 (5), 1009–1029.

Gee, J.S., Kent, D.V., 2007. Source of oceanic magnetic anomalies and the geomagnetic polarity timescale. Geomagnetism 5, 455–507.

Geoffroy, L., Gelard, J.P., Lepvrier, C., Olivier, P., 1998. The coastal flexure of Disko (West Greenland), onshore expression of the 'oblique reflectors'. J. Geol. Soc. Lond. 155 (3), 463–473.

Geoffroy, L., Burov, E.B., Werner, P., 2015. Volcanic passive margins: another way to break up continents. Sci. Rep. 5 (1), 1–12. https://doi.org/10.1038/srep14828.

Geoffroy, L., Guan, H., Gernigon, L., Foulger, G.R., Werner, P., 2020. The extent of continental material in oceans: C-Blocks and the Laxmi Basin example. Geophys. J. Int. 222 (3), 1471–1479.

Gibson, S.A., Thompson, R.N., Day, J.A., 2006. Timescales and mechanisms of plume–lithosphere interactions: 40Ar/39Ar geochronology and geochemistry of alkaline igneous rocks from the Paraná–Etendeka large igneous province. Earth Planet. Sci. Lett. 251 (1–2), 1–17.

Gladczenko, T.P., Hinz, K., Eldholm, O., Meyer, H., Neben, S., Skogseid, J., 1997. South Atlantic volcanic margins. J. Geol. Soc. Lond. 154 (3), 465–470.
Gomes, A.S., Vasconcelos, P.M., 2021. Geochronology of the Paraná-Etendeka large igneous province. Earth Sci. Rev. 220, 103716.
Gordon, A.C., Mohriak, W.U., 2015. Seismic Volcano-Stratigraphy in the Basaltic Complexes on the Rifted Margin of Pelotas Basin, Southeast Brazil.
Gordon, A.C., Mohriak, W.U., Heilbron, M., 2017. From SE Paraná to Pelotas Basin, a geophysical-geological transect traversing two of the world's largest igneous provinces in South America. In: 15th International Congress of the Brazilian Geophysical Society, Rio de Janeiro, Brazil, 31 July to 3 August, 2017, Abstracts, 1–6.
Gresse, P.G., Chemale, F., Da Silva, L.C., Walraven, F., Hartmann, L.A., 1996. Late-to post-orogenic basins of the Pan-African–Brasiliano collision orogen in southern Africa and southern Brazil. Basin Res. 8 (2), 157–171.
Hall, S.A., Bird, D.E., McLean, D.J., Towle, P.J., Grant, J.V., Danque, H.A., 2018. New constraints on the age of the opening of the South Atlantic Basin. Mar. Pet. Geol. 95, 50–66.
Harkin, C., Kusznir, N., Roberts, A., Manatschal, G., Horn, B., 2020. Origin, composition, and relative timing of seaward dipping reflectors on the Pelotas rifted margin. Mar. Pet. Geol. 114, 104235. https://doi.org/10.1016/j.marpetgeo.2020.104235.
Hartmann, L.A., Baggio, S.B., Brückmann, M.P., Knijnik, D.B., Lana, C., Massonne, H.J., Arena, K.R., 2019. U-Pb geochronology of Paraná volcanics combined with trace element geochemistry of the zircon crystals and zircon Hf isotope data. J. S. Am. Earth Sci. 89, 219–226.
Hofmann, C., Courtillot, V., Feraud, G., Rochette, P., Yirgu, G., Ketefo, E., Pik, R., 1997. Timing of the Ethiopian flood basalt event and implications for plume birth and global change. Nature 389 (6653), 838. https://doi.org/10.1038/39853.
Holz, M., Kalkreuth, W., Rolim, S.B.A., 2010. Extension of the Paraná Basin to offshore Brazil: implications for coalbed methane evaluation. Mar. Pet. Geol. 27 (5), 1119–1132.
Homrighausen, S., Hoernle, K., Hauff, F., Wartho, J.A., van den Bogaard, P., Garbe-Schönberg, D., 2019. New age and geochemical data from the Walvis Ridge: the temporal and spatial diversity of South Atlantic intraplate volcanism and its possible origin. Geochim. Cosmochim. Acta 245, 16–34.
Horstwood, M.S., Košler, J., Gehrels, G., Jackson, S.E., McLean, N.M., Paton, C., Schoene, B., 2016. Community-derived standards for LA-ICP-MS U-(Th-) Pb geochronology–uncertainty propagation, age interpretation and data reporting. Geostand. Geoanal. Res. 40 (3), 311–332.
Hoyer, P.A., Haase, K.M., Regelous, M., O'Connor, J.M., Homrighausen, S., Geissler, W. H., Jokat, W., 2022. Mantle plume and rift-related volcanism during the evolution of the Rio Grande Rise. Commun. Earth Environ. 3 (1), 18.
Huang, C., Wang, H., Yang, J.H., Ramezani, J., Yang, C., Zhang, S.B., Wu, S.T., 2020. SA01–a proposed zircon reference material for microbeam U-Pb age and Hf-O isotopic determination. Geostand. Geoanal. Res. 44 (1), 103–123.
Ingersoll, R.V., 2011. Tectonics of sedimentary basins, with revised nomenclature. In: Tectonics of Sedimentary Basins: Recent Advances, pp. 1–43.
Jaffey, A.H., Flynn, K.F., Glendenin, L.E., Bentley, W.T., Essling, A.M., 1971. Precision measurement of half-lives and specific activities of U 235 and U 238. Phys. Rev. C 4 (5), 1889.
King, S.D., Anderson, D.L., 1995. An alternative mechanism of flood basalt formation. Earth Planet. Sci. Lett. 136 (3–4), 269–279.
Larsen, H.C., Saunders, A.D., Clift, P.D., 1994. Introduction: Breakup of the Southeast Greenland margin and the formation of the Irminger Basin: Background and scientific objectives. In: Proceedings of the Ocean Drilling Program. Part A, Initial Report, Vol. 152, pp. 5–16.
LeBas, M., Maitre, R.L., Streckeisen, A., Zanettin, B., IUGS Subcommission on the Systematics of Igneous Rocks, 1986. A chemical classification of volcanic rocks based on the total alkali-silica diagram. J. Petrol. 27 (3), 745–750.
Lobo, J.T., 2000. Petrogênese dos basaltos do Eocretáceo Inferior das bacias de Campos e Pelotas, SE do Brasil. Universidade do Estado de Rio de Janeiro, Faculdade de Geología, p. 97. Msc dissertation.
Lobo, J.T., 2007. Petrogênese das rochas basálticas do Eocretáceo das bacias de Campos e Pelotas, e implicações na geodinâmica de rifteamento do Gondwana ocidental. Universidade do Estado do Rio De Janeiro, Faculdade de Geologia, p. 171. PhD dissertation.
Lobo, J.T., Szatmari, P., Duarte, B.P., 2006. Tipos de fontes associadas às suítes basálticas de Campos e de Pelotas (Sul-Sudeste) e modelos geodinâmicos de ruptura do Gondwana ocidental. Boletim de Geociencias da Petrobras 14 (2), 269–285.
Lovecchio, J.P., Abdelmalak, M.M., Planke, S., Silio, O., Rohais, S., Arismendi, S., Ramos, V.A., 2024. Mesozoic rifting in SW Gondwana and breakup of the Southern South Atlantic Ocean. Geol. Soc. Lond. Spec. Publ. 547 (1). SP547-2023.
Mansur, E., Barnes, S.J., Janasi, V., Henrique-Pinto, R., Alves, A., Marteleto, N.S., 2021. The distribution of platinum-group elements and Te, As, Bi, Sb and Se (TABS+) in the Paraná Magmatic Province: effects of crystal fractionation, sulfide segregation and magma degassing. Lithos 400, 106374.
Marques, L.S., Dupre, B., Piccirillo, E.M., 1999. Mantle source compositions of the Paraná Magmatic Province (southern Brazil): evidence from trace element and Sr-Nd-Pb isotope geochemistry. J. Geodyn. 28, 439–458. https://doi.org/10.1016/s0264-3707(99)00020-4.
Marques, L.S., De Min, A., Rocha, E.R.V., Babinski, M., Bellieni, G., Figueiredo, A.M.G., 2018. Elemental and Sr-Nd-Pb isotope geochemistry of the Florianópolis Dyke Swarm (Paraná Magmatic Province): crustal contamination and mantle source constraints. J. Volcanol. Geotherm. Res. 355, 149–164. https://doi.org/10.1016/j.jvolgeores.2017.07.005.
Marsh, J.S., Ewart, A., Milner, S.C., Duncan, A.R., Miller, R.M., 2001. The Etendeka Igneous Province: magma types and their stratigraphic distribution with implications for the evolution of the Paraná-Etendeka flood basalt province. Bull. Volcanol. 62, 464–486.
McDonough, W.F., Sun, S.S., 1995. The composition of the Earth. Chem. Geol. 120 (3–4), 223–253.
Meyer, R., van Wijk, J., Gernigon, L., 2007. The North Atlantic Igneous Province: A Review of Models for its Formation.
Milani, E.J., Melo, J.H.G., Souza, P.A., Fernandes, L.A., França, A.B., 2007. Bacia do Paraná. Boletim de Geociências— Petrobras 15, 265–287.
Misuzaki, A.M.P., Saracchine, F.E., 1990. Catálogo geral de dados geocronológicos da Petrobrás: Relatório Interno. Petrobrás/Cenpes/Divex/Setec, Rio de Janeiro, Brasil, pp. 1–30.
Mohriak, W.U., Nóbrega, M., Odegard, M.E., Gomes, B.S., Dickson, W.G., 2010. Geological and Geophysical Interpretation of the Rio Grande Rise, South-Eastern Brazilian Margin: Extensional Tectonics and Rifting of Continental and Oceanic Crusts.
Moreira, J.L.P., Madeira, C.V., Gil, J.A., Machado, M.A.P., 2007. Bacia de Santos. Boletim de Geociencias da PETROBRAS 15 (2), 531–549.
Moulin, M., Aslanian, D., Unternehr, P., 2010. A new starting point for the South and Equatorial Atlantic Ocean. Earth Sci. Rev. 98 (1–2), 1–37. https://doi.org/10.1016/j.earscirev.2009.08.001.
Mutter, J.C., Talwani, M., Stoffa, P.L., 1982. Origin of seaward-dipping reflectors in oceanic crust off the Norwegian margin by "subaerial sea-floor spreading". Geology 10 (7), 353–357. https://doi.org/10.1130/0091-7613(1982)10<353:oosrio>2.0.co;2.
Mutter, J.C., Buck, W.R., Zehnder, C.M., 1988. Convective partial melting: 1. A model for the formation of thick basaltic sequences during the initiation of spreading. J. Geophys. Res. Solid Earth 93 (B2), 1031–1048.
Nance, R.D., Murphy, J.B., Santosh, M., 2014. The supercontinent cycle: a retrospective essay. Gondwana Res. 25 (1), 4–29.
Pearce, J.A., 2008. Geochemical fingerprinting of oceanic basalts with applications to ophiolite classification and the search for Archean oceanic crust. Lithos 100, 14–48. https://doi.org/10.1016/j.lithos.2007.06.016.
Pearce, J.A., 2014. Immobile element fingerprinting of ophiolites. Elements 10 (2), 101–108.
Pearce, J.A., Wyman, D.A., 1996. A user's guide to basalt discrimination diagrams. Trace element geochemistry of volcanic rocks: applications for massive sulphide exploration. Geol. Assoc. Canada Short Course Notes 12, 79–113.
Peate, D.W., 1997. The Paraná-Etendeka Province. In: Mahoney, J.J., Coffin, M.F. (Eds.), Large Igneous Provinces: Continental, Oceanic, and Planetary Flood Volcanism. AGU, Geophysical Monograph Series, pp. 217–245. https://doi.org/10.1029/GM100p0217.
Peate, D.W., Hawkesworth, C.J., Mantovani, M.M.S., Rogers, N.W., Turner, S.P., 1999. Petrogenesis and stratigraphy of the high-Ti/Y Urubici magma type in the Paraná flood basalt province and implications for the nature of 'Dupal'-type mantle in the South Atlantic region. J. Petrol. 40 (3), 451–473. https://doi.org/10.1093/petrology/40.3.451.
Philipp, H., Eckhardt, J.D., Puchelt, H., 2001. Platinum-group elements (PGE) in basalts of the seaward-dipping reflector sequence, SE Greenland coast. J. Petrol. 42 (2), 407–432.
Puetz, S.J., Spencer, C.J., Ganade, C.E., 2021. Analyses from a validated global UPb detrital zircon database: enhanced methods for filtering discordant UPb zircon analyses and optimizing crystallization age estimates. Earth Sci. Rev. 220, 103745.
Rabinowitz, P.D., LaBrecque, J., 1979. The mesozoic South Atlantic Ocean and evolution of its continental margins. J. Geophys. Res. 84 (B11), 5973–6002. https://doi.org/10.1029/jb084ib11p05973.
Reuber, K., Mann, P., Pindell, J., 2019. Hotspot origin for asymmetrical conjugate volcanic margins of the austral South Atlantic Ocean as imaged on deeply penetrating seismic reflection lines. Interpretation 7 (4), SH71-SH97.
Rohde, J.K., van den Bogaard, P., Hoernle, K., Hauff, F., Werner, R., 2013. Evidence for an age progression along the Tristan-Gough volcanic track from new 40Ar/39Ar ages on phenocryst phases. Tectonophysics 604, 60–71.
Rossetti, L., Lima, E.F., Waichel, B.L., Hole, M.J., Simões, M.S., Scherer, C.M., 2018. Lithostratigraphy and volcanology of the Serra Geral Group, Paraná-Etendeka Igneous Province in southern Brazil: Towards a formal stratigraphical framework. J. Volcanol. Geotherm. Res. 355, 98–114.
Santos, M.M., Lana, C., Scholz, R., Buick, I., Schmitz, M.D., Kamo, S.L., Gerdes, A., Corfu, F., Tapster, S., Lancaster, P., Storey, C.D., Basei, M.A.S., Tohver, E., Alkmim, A., 2017. A new appraisal of Sri Lankan BB zircon as a reference material for LA-ICP-MS U-Pb geochronology and Lu-Hf isotope tracing. Geostand. Geoanal. Res. 41 (3), 335–358.
Sauter, D., Manatschal, G., Kusznir, N., Masquelet, C., Werner, P., Ulrich, M., Autin, J., 2023. Ignition of the southern Atlantic seafloor spreading machine without hot-mantle booster. Sci. Rep. 13 (1), 1195.
Serratt, H., Domingues Teixeira, C., Girelli, T.J., de Souza, M.K., Rodrigues Vargas, M., Moreira Silva, A., Chemale Jr., F., 2022. Seaward-dipping reflector influence on seafloor magnetostratigraphy—a Pelotas Basin view. Geophys. Res. Lett. 49 (23), e2022GL100382.
Silva, J.P., Lana, C., Mazoz, A., Buick, I., Scholz, R., 2023. U-Pb Saturn: new U-Pb/Pb-Pb Data Reduction Software for LA-ICP-MS. Geostand. Geoanal. Res. 47 (1), 49–66.
Sláma, J., Košler, J., Condon, D.J., Crowley, J.L., Gerdes, A., Hanchar, J.M., Whitehouse, M.J., 2008. Plešovice zircon—a new natural reference material for U–Pb and Hf isotopic microanalysis. Chem. Geol. 249 (1–2), 1–35.
Stacey, J.T., Kramers, I., 1975. Approximation of terrestrial lead isotope evolution by a two-stage model. Earth Planet. Sci. Lett. 26 (2), 207–221.
Stica, J.M., Zalán, P.V., Ferrari, A.L., 2014. The evolution of rifting on the volcanic margin of the Pelotas Basin and the contextualization of the Paraná–Etendeka LIP in

the separation of Gondwana in the South Atlantic. Mar. Pet. Geol. 50, 1–21. https://doi.org/10.1016/j.marpetgeo.2013.10.015.
Sun, S.S., McDonough, W.F., 1989. Chemical and isotopic systematics of oceanic basalts: implications for mantle composition and processes. Geol. Soc. Lond. Spec. Publ. 42 (1), 313–345.
Taylor, S.R., McLennan, S.M., 1985. The Continental Crust: Its Composition and Evolution, 312. Blackwell, Oxford. https://doi.org/10.1002/gj.3350210116.
Tedesco, J., Cagliari, J., Júnior, F.C., Girelli, T.J., Lana, C., 2019. Provenance and paleogeography of the Southern Paraná Basin: Geochemistry and UPb zircon geochronology of the Carboniferous-Permian transition. Sediment. Geol. 393, 105539.
Teixeira, C.D., Girelli, T.J., Serratt, H., Oliveira, H.O.S., Cruz, M.F., Conti, B., Chemale Jr., F., 2025a. Paleogeographic significance of unknown hyperextended continental crust in South Atlantic conjugated margin. Geosci. Front. 16 (1), 101934. https://doi.org/10.1016/j.gsf.2024.101934.
Teixeira, C.D., Girelli, T.J., Serratt, H., Chemale Jr., F., 2025b. Revisiting the Dom Feliciano Belt and surrounding areas–An integrated geophysical and isotope geology approach. Earth Sci. Rev., 105135 https://doi.org/10.1016/j.earscirev.2025.105135.
Torsvik, T.H., Cocks, L.R.M., 2013. Gondwana from top to base in space and time. Gondwana Res. 24 (3–4), 999–1030. https://doi.org/10.1016/j.gr.2013.06.012.
Veevers, J.J., 2012. Reconstructions before rifting and drifting reveal the geological connections between Antarctica and its conjugates in Gondwanaland. Earth Sci. Rev. 111 (3–4), 249–318. https://doi.org/10.1016/j.earscirev.2011.11.009.
Verma, O., Khosla, A., 2019. Developments in the stratigraphy of the Deccan Volcanic Province, peninsular India. Compt. Rendus Geosci. 351 (7), 461–476.
Vermeesch, P., 2018. IsoplotR: a free and open toolbox for geochronology. Geosci. Front. 9 (5), 1479–1493.
Waichel, B.L., de Lima, E.F., Viana, A.R., Scherer, C.M., Bueno, G.V., Dutra, G., 2012. Stratigraphy and volcanic facies architecture of the Torres Syncline, Southern Brazil, and its role in understanding the Paraná–Etendeka Continental Flood Basalt Province. J. Volcanol. Geotherm. Res. 215, 74–82.
Whittaker, Joanne, Afonso, C., Masterton, J., Müller, Sheona, Wessel, Dietmar, Williams, Paul, Maria, Simon Seton, 2015. Long-term interaction between mid-ocean ridges and mantle plumes. Nat. Geosci. 8, 25–2015. https://doi.org/10.1038/NGEO2437.
Wiedenbeck, M.A.P.C., Alle, P., Corfu, F.Y., Griffin, W.L., Meier, M., Oberli, F.V., Spiegel, W., 1995. Three natural zircon standards for U-Th-Pb, Lu-Hf, trace element and REE analyses. Geostand. Newslett. 19 (1), 1–23.
Wiedenbeck, M., Hanchar, J.M., Peck, W.H., Sylvester, P., Valley, J., Whitehouse, M., Zheng, Y.F., 2004. Further characterisation of the 91500 zircon crystal. Geostand. Geoanal. Res. 28 (1), 9–39.
Will, T.M., Frimmel, H.E., Pfaender, J.A., 2016. Möwe Bay Dykes, Northwestern Namibia: Geochemical and geochronological evidence for different mantle source regions during the cretaceous opening of the South Atlantic. Chem. Geol. 444, 141–157.
Winter, W.R., Jahnert, R.J., França, A.B., 2007. Bacia de campos. Boletim de Geociências da PETROBRAS 15 (2), 511–529.
Wu, G., Wörner, K.P., Jochum, B., Stoll, K. Simon, Kronz, A., 2019. Geostand. Geoanal. Res.
Zhou, H., Hoernle, K., Geldmacher, J., Hauff, F., Homrighausen, S., Garbe-Schönberg, D., Jung, S., 2020. Geochemistry of Etendeka magmatism: Spatial heterogeneity in the Tristan-Gough plume head. Earth Planet. Sci. Lett. 535, 116123.
Zindler, A., Hart, S., 1986. Chemical geodynamics. In: IN: Annual Review of Earth and Planetary Sciences, 14. Annual Reviews, Inc, Palo Alto, CA, pp. 493–571. Volume 14 (A87–13190 03–46).

Other articles written by the PhD candidate

Geophysical Research Letters

RESEARCH LETTER
10.1029/2022GL100382

Seaward-Dipping Reflector Influence on Seafloor Magnetostratigraphy—A Pelotas Basin View

Henrique Serratt[1], Claudia Domingues Teixeira[1], Tiago Jonatan Girelli[1], Marcelo Kehl de Souza[1], Mateus Rodrigues Vargas[2], Adalene Moreira Silva[3], and Farid Chemale Jr.[1]

[1]UNISINOS: Universidade do Vale do Rio dos Sinos - Brazil, São Leopoldo, Brazil, [2]Cergy Paris Université, Neuville-sur-Oise, France, [3]UnB: Universidade de Brasília, Brasilia, Brazil

Key Points:

- Some magnetic anomalies interpreted as related to vertical fabric oceanic crust are related to seaward-dipping reflectors (SDRs)
- Seaward-dipping reflectors are different from typical oceanic crust in geometry and compositional heterogeneity
- SDR-related magnetic anomalies should not be used to constrain ages

Supporting Information:

Supporting Information may be found in the online version of this article.

Correspondence to:

H. Serratt,
henrique.serratt@gmail.com

Citation:

Serratt, H., Domingues Teixeira, C., Girelli, T. J., de Souza, M. K., Rodrigues Vargas, M., Moreira Silva, A., & Chemale, F. Jr. (2022). Seaward-dipping reflector influence on seafloor magnetostratigraphy—A Pelotas Basin view. *Geophysical Research Letters*, *49*, e2022GL100382. https://doi.org/10.1029/2022GL100382

Received 15 JUL 2022
Accepted 18 NOV 2022

Author Contributions:

Conceptualization: Henrique Serratt
Data curation: Henrique Serratt, Mateus Rodrigues Vargas
Formal analysis: Henrique Serratt, Claudia Domingues Teixeira
Funding acquisition: Farid Chemale
Investigation: Henrique Serratt
Methodology: Henrique Serratt, Claudia Domingues Teixeira, Marcelo Kehl de Souza, Adalene Moreira Silva
Project Administration: Farid Chemale
Resources: Farid Chemale
Supervision: Farid Chemale

Abstract Previous works used marine magnetic survey data and interpreted magnetic anomalies related to seaward-dipping reflectors (SDRs) as oceanic crust or SDR age constraints in the South Atlantic Ocean. However, we advise against using SDR-related magnetic anomalies to constrain ages because of the mostly low-dipping geometry causing the overlapping of rocks extruded during periods of different polarities. The data are difficult to interpret correctly because of the SDR compositional heterogeneity, sedimentary intercalations, variations in package thickness with different compositions and magnetic polarities, and the absence of a link between the SDR magmatic position and age. SDR-related magnetic anomalies are mainly caused by magnetic susceptibility contrasts rather than remanent magnetism. Due to this complexity, the SDR geometry and variable composition make SDR-related magnetic anomalies challenging to use for age constraints. The Pelotas Basin SDRs age cannot be estimated by magnetostratigraphy, and this method likely cannot constrain the age of any SDR wedge.

Plain Language Summary Since the 1960s, an increased understanding of oceanic crust chronology has quickly evolved into a field of study called magnetostratigraphy. Basaltic lavas extruded in a certain time interval acquire a positive or negative magnetic polarity according to the magnetic polarity on Earth during the extrusion. From the mid-ocean ridge to the continental oceanic boundary, the continuous and progressive accretion of the oceanic crust provides age constraints for the sea bottom. However, on volcanic passive margins, the presence of volcanic rocks with wedge geometries is abundant. These volcanic rocks are called seaward-dipping reflectors (SDRs) because of their wedge-shaped geometry toward the ocean and are usually identified by seismic reflection surveys. The presence of these volcanic wedges makes the identification of the oceanic–continental crustal boundary a challenging task. Some magnetic anomalies that some researchers state as related to a regular vertical oceanic crust are SDR-related. The SDR-related magnetic anomalies are not related to that age because SDR-related magnetic anomalies are mainly caused by magnetic susceptibility contrasts rather than remanent magnetism. We used seismic lines and magnetic data from the Pelotas Basin to illustrate how these magnetic anomalies are not age-related.

1. Introduction

Identifying marine magnetic anomalies is a trusted method for developing a detailed age model of the sea floor (Dietz, 1961; Hess, 1962; Vine & Matthews, 1963). The regular geometry of the vertical magmatic emplacement of continuous (in geological time) new rocks in the oceanic crust makes this method reliable to use in this setting. However, in volcanic passive margins (VPMs), there are several differences in the crustal geometry. The most distinctive signature of VPMs is the formation of seaward-dipping reflectors (SDRs) (Buck, 2017; Geoffroy, 2005; Hinz, 1981; Mutter et al., 1982). This thick volcanic dipping package makes the continental–ocean boundary (COB) position uncertain, and several authors have tried to delimit the COB in the South Atlantic Ocean (e.g., Cainelli & Mohriak, 1999; Chang et al., 1992; Peyve, 2010; Talwani & Abreu, 2000). Eagles et al. (2015) compiled some attempts up to 2015; however, other COBs were delimited by Stica et al. (2014) and Chauvet et al. (2021). Several studies of the evolution of the South Atlantic Ocean interpreted SDR-related magnetic anomalies as a continuation of the oceanic crust by disregarding their geometry or the origin of the magnetic anomalies close to the coast (e.g., Chauvet et al., 2021; Collier et al., 2017; Granot & Dyment, 2015; Hall et al., 2018; Koopmann et al., 2016; Moulin et al., 2010; Rabinowitz & LaBrecque, 1979; Stica et al., 2014), which occur due to the magnetic susceptibility contrast rather than remanent magnetism (Davis et al., 2018).

Validation: Marcelo Kehl de Souza, Mateus Rodrigues Vargas
Visualization: Henrique Serratt
Writing – original draft: Henrique Serratt, Claudia Domingues Teixeira, Tiago Jonatan Girelli
Writing – review & editing: Henrique Serratt, Tiago Jonatan Girelli, Adalene Moreira Silva, Farid Chemale

The Austral segment of the South Atlantic Ocean, formed during the breakup of West Gondwana, is characterized by intense magmatism on both the South American and African margins, and the segment is thereby classified as a VPM (Chauvet et al., 2021; Geoffroy, 2005; Geoffroy et al., 2015.; Gordon & Mohriak, 2015; Menzies et al., 2002; Stica et al., 2014). This type of margin development occurs in mantle environments that are hotter than average. Geoffroy et al. (2005, 2015) point to distinct features that characterize a VPM: (a) thick igneous crust; (b) narrow margins; (c) flexure of the igneous crust toward the sea, and (d) the absence of subsidence during stretching. Pelotas Basin (PB) development began in these magmatic environments on the southernmost Brazilian continental margin. The thick SDR package comprises volcanic rocks interlayered by pyroclastic and/or sedimentary rocks (Harkin et al., 2020). These SDRs were critical for shaping the morphology of the PB.

Regarding the tectonic importance of the PB in the southwestern Gondwana breakup process, a lack of knowledge remains concerning the basin age. There are no peer-reviewed radiometric ages in the basin. Similarly, the magnetostratigraphic data were interpreted following a pattern that disregarded the actual SDR geometries or the origin of the magnetic anomalies close to the coast (Chauvet et al., 2021; Collier et al., 2017; Granot & Dyment, 2015; Hall et al., 2018; Koopmann et al., 2016; Moulin et al., 2010; Rabinowitz & LaBrecque, 1979; Stica et al., 2014). The current radiometric and magnetostratigraphic ages led to noncalibrated tectono-geographic reconstructions. This work aims to demonstrate that SDR-related magnetic anomalies cannot be used to constrain an age, neither for the oceanic crust nor the SDR wedges.

2. Geological Setting

The study area of this work is the PB, which is located in the South Atlantic Ocean VPM in South America (Talwani & Abreu, 2000; Cartwright et al., 2012; Mohriak & Fainstein, 2012; Gordon & Mohriak, 2015—Figure 1). The PB covers 346,873 km^2 (Bueno et al., 2007) and is mainly offshore. This NE–SW elongated basin extends from the Brazilian State of Santa Catarina to the Uruguayan department of Treinta y Tres. The northern boundary of the basin is the Florianópolis Fault (or the Rio Grande Fracture Zone), which delimits the PB with the Santos Basin. The southern boundary, on the south, is the Polônio High, which delimits the PB and the Punta Del Este Basin.

The rocks recovered in the South sub-basin basement of the PB are mainly related to the Proterozoic granitic–gneissic Pelotas Batholith (Philipp et al., 2016). The main faults crossing the basement are NE–SW-oriented, with minor W–E orientation (Chemale Jr., 2000; Hartman et al., 2016). The NE–SW trend parallels the SDRs and the magnetic anomalies (Gordon & Mohriak, 2015; Stica et al., 2014). Basement samples recovered onshore below the PB in the South subbasin are granitoids of the Vendian magmatic arc (Pelotas Batholith). However, in the PB Northern subbasin, the basement is composed of the Paraná Large Igneous Province (LIP) extrusives and Paraná Basin Paleozoic sedimentary rocks that overlie the granitoids of the Pelotas Batholith. The recovered rocks are described in technical reports of Petrobras and are currently available via the ANP—Brazilian National Agency of Petroleum, Natural Gas and Biofuels (see Text S1 and Figures S1 and S2 in Supporting Information S1).

The Paraná–Etendeka LIP comprises continental flood basalts, ranging from tholeiitic basalts to andesite rocks. These flood basalts can reach 1,724 m thick and have an estimated volume of 1.27–1.70 × 10^6 km³ (Frank et al., 2009; Peate et al., 1992). In terms of age, these rocks were extruded over a few million years, from 135 to 133 Ma (Gomes & Vasconcelos, 2021). Synchronous with the Paraná–Etendeka main magmatic event, the South Atlantic Ocean started to open at the Agulhas Falkland Fracture Zone (Chauvet et al., 2021; Chemale et al., 2018), which is approximately 1,800 km from the Paraná–Etendeka LIP; thus, the LIP was not a primary factor in the opening of the South Atlantic Ocean. The opening occurred in steps that progressed toward the north, and the main transfer faults limited those steps, characterizing a zipper style opening. The opening of the ocean in the PB latitudes occurred between 131 and 113 Ma (Chauvet et al., 2021). However, some oceanic crust and SDR ages are constrained by SDR-related magnetic anomaly interpretations (Figure 2) and are not peer-reviewed radiometric ages.

The geochemical data from volcanic rocks in well 1-RSS-3 (Figure 1; Lobo et al., 2006) point to similarities with the Paraná LIP, such as the tholeiitic basalt composition and TiO_2 values; nevertheless, the geochemical data of well 2-BPS-6 (Figure 1) range from basalts to andesites (based on Lobo et al., 2006 data). This magmatism can be visualized seismically as SDRs (Chauvet et al., 2021; Gordon & Mohriak, 2015; Harkin et al., 2020; Stica et al., 2014). The magmatic layer is thicker in the North Subbasin, with thicknesses up to 17 km (Harkin

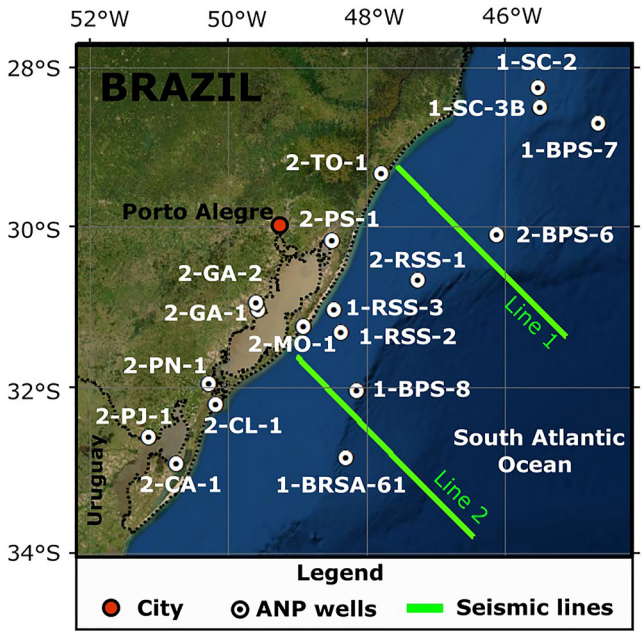

Figure 1. Study area; the green seismic lines are shown in Figure 4. The figure also shows the Brazilian National Agency of Petroleum wells in which the lithologies of the region were recorded.

et al., 2020) or less than 16 km (Chauvet et al., 2021). In the North Subbasin, a volcanic dome identified as the SDR volcanic center was mapped by Stica et al. (2014). This structure appears in previous studies as the Torres Arch (Gordon & Mohriak et al., 2015; Harkin et al., 2020; Rosa et al., 2017) or Florianópolis High (Chauvet et al., 2021). The Torres Arch has the thickest package of SDRs in the South American margin and is associated with the Walvis Ridge in the conjugate margin (Chauvet et al., 2021; Gladczenko et al., 1997; Gordon & Mohriak, 2015).

3. Materials and Methods

This study used magnetometric data and seismic surveys (Figure 1) to analyze the PB SDRs geometries and the source of the anomalous magnetic field. Two seismic lines (239–369 and 239–370) are shown, as well as the composite magnetic data derived from the Earth Magnetic Anomaly Grid (EMAG2—NOAA, National Oceanic, and Atmospheric Administration) grid and four marine surveys from ANP (P0099 B, P0108, APP040, and APP060).

Magnetic data depend on magnetic inclination, which is the main cause of distortions and changes in magnetic anomaly shapes, amplitude reduction, and map textures (Li, 2008). We observed the necessity for Reduction to Pole (RTP) in the magnetometry studies in mid-latitude anomalies (PB average inclination is ca. 40°) to eliminate this dependence. The RTP process positions the anomalous magnetic field above the magnetic anomaly source (Baranov & Naudy, 1964). We applied the reduction-to-pole transformation of total field magnetic anomalies and compared it with original data and the interpretations of Rabinowitz and LaBrecque (1979); Moulin et al. (2010); Granot and Dyment, 2015; Collier et al. (2017). We interpret the volcanic filling of the basin as three units: (a) pre-rift magmatism with reflectors limited by faults but without growth during the rift, following the general observations of Gordon and Mohriak (2015) to constrain that unit; (b) rift magmatism or the classical SDR, which is a package synchronous with the development of the fault (following the Geoffroy (2005) model); (c) post-rift magmatism, which is a magmatic package with few or no faults crossing the unit. The top of the package is delimited by a high-amplitude reflector, which occurs due to a wave velocity contrast between sedimentary and volcanic rocks, as observed in well 1-BPS-6 (see Text S2 in Supporting Information S1). We plot the magnetic data as a profile in the same position as two seismic lines with the TecVA attribute (pseudo-relief attribute, Nunes et al., 2017), which allows us to compare the observed anomalies and the source.

4. Results

The geometrical differences in the anomalous magnetic field without any data filtered and reduced to the pole are evident in the PB (Figure 3). The magnetic anomalies shift in position and intensity. The shift is not linear; generally, changes of a few hundred nT occur in the field intensity, and a few kilometers occur in the position of the magnetic anomalies. The improvement in accuracy and data visualization is significant. The absence of positive anomalies above the continental platform in the reduced pole image enhances the Pelotas Batholith and SDR west boundary. The RTP image still shows a textural change in the Torres Arch Region (TAR), where the signal shows a higher frequency and higher amplitude (Figure 3).

The seismic facies of the southern SDRs show fewer and lower-amplitude internal reflections, which are different from the northern SDRs, which have high amplitudes and numerous internal reflections (Figure 4). The northern SDRs are thicker than the southern SDRs, as previously reported (Chauvet et al., 2021; Gordon & Mohriak, 2015; Stica et al., 2014). That SDR thickness change is geographically concordant with changes in the frequency and amplitude in the RTP image in the TAR. Nevertheless, the most important observation is the low-angle dips of most of these bodies (Figure 4).

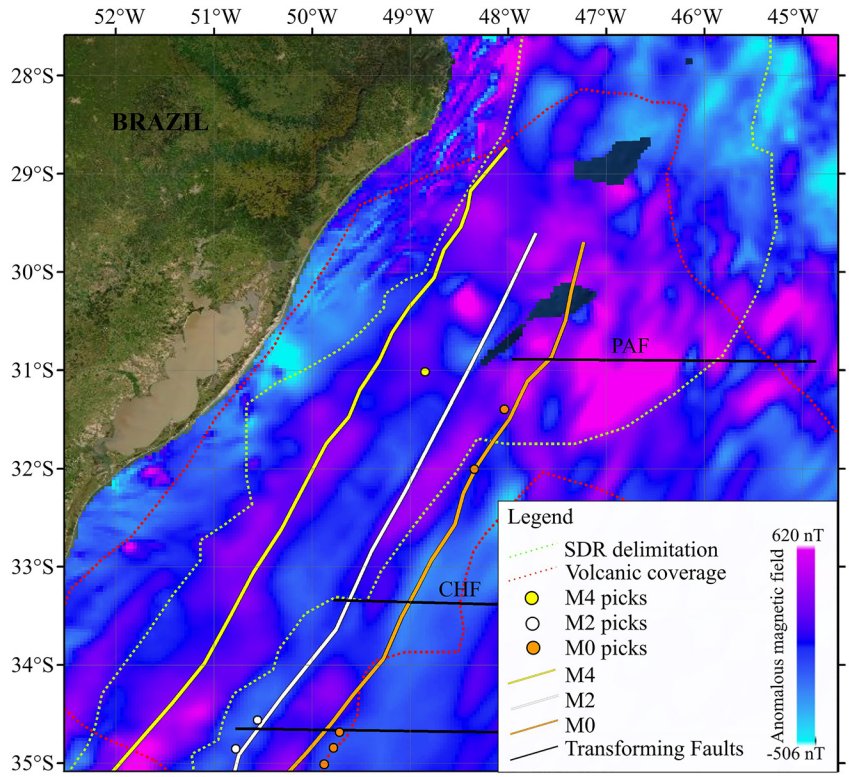

Figure 2. Combined onshore Landsat 8 image and offshore anomalous magnetic field reduced to the pole. The points represent the magnetic picks of the Seton et al. (2014) database (M4–Rabinowitz & LaBrecque, 1979; M2 and M0–Granot & Dyment, 2015). The solid lines are the interpretations of magnetic anomalies compiled by Chauvet et al. (2021), Collier et al. (2017), Moulin et al. (2010), Rabinowitz and LaBrecque (1979). The dashed green lines are the limits of the seaward-dipping reflectors (SDRs) (syn-rift magmatism) in green (Chauvet et al., 2021) and the volcanic coverage layer (post-rift magmatism) in red (Gordon & Mohriak, 2015). Magnetic anomalies are visibly related to SDRs or other volcanic rocks. In addition, the textures change northward (amplitude and frequency). Legend: PAF, Porto Alegre Fault; CHF, Chui Fault. See the methodology for the data source and processing methods.

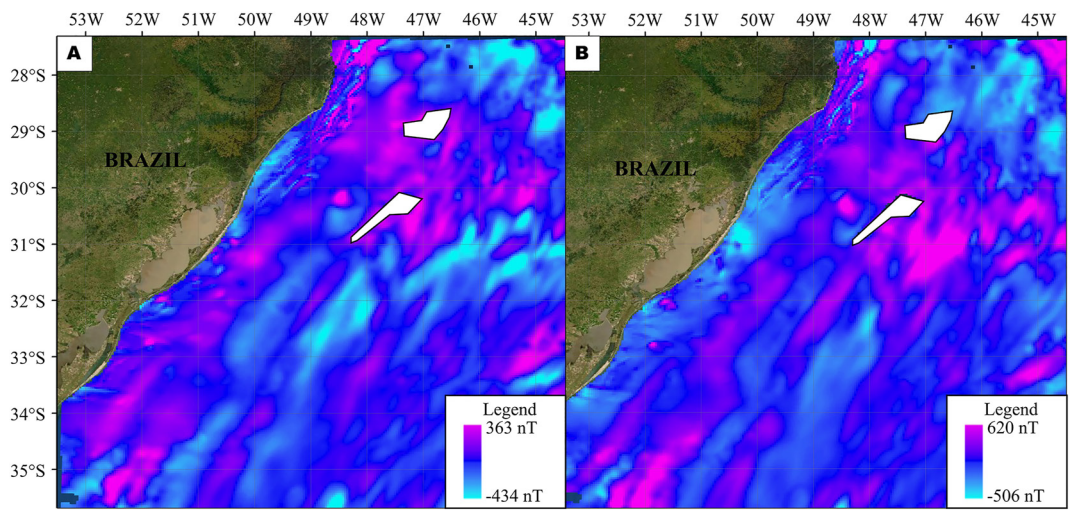

Figure 3. Anomalous magnetic field. (a) Total magnetic intensity (TMI) reduced from the International Geomagnetic Reference Field. (b) Reduction to Pole from the TMI. The magnetic directions are parallel to the main Brazilian/Pan-African structures (NE–SW). The magmatic emplacement should use these previous structures as the main conduit.

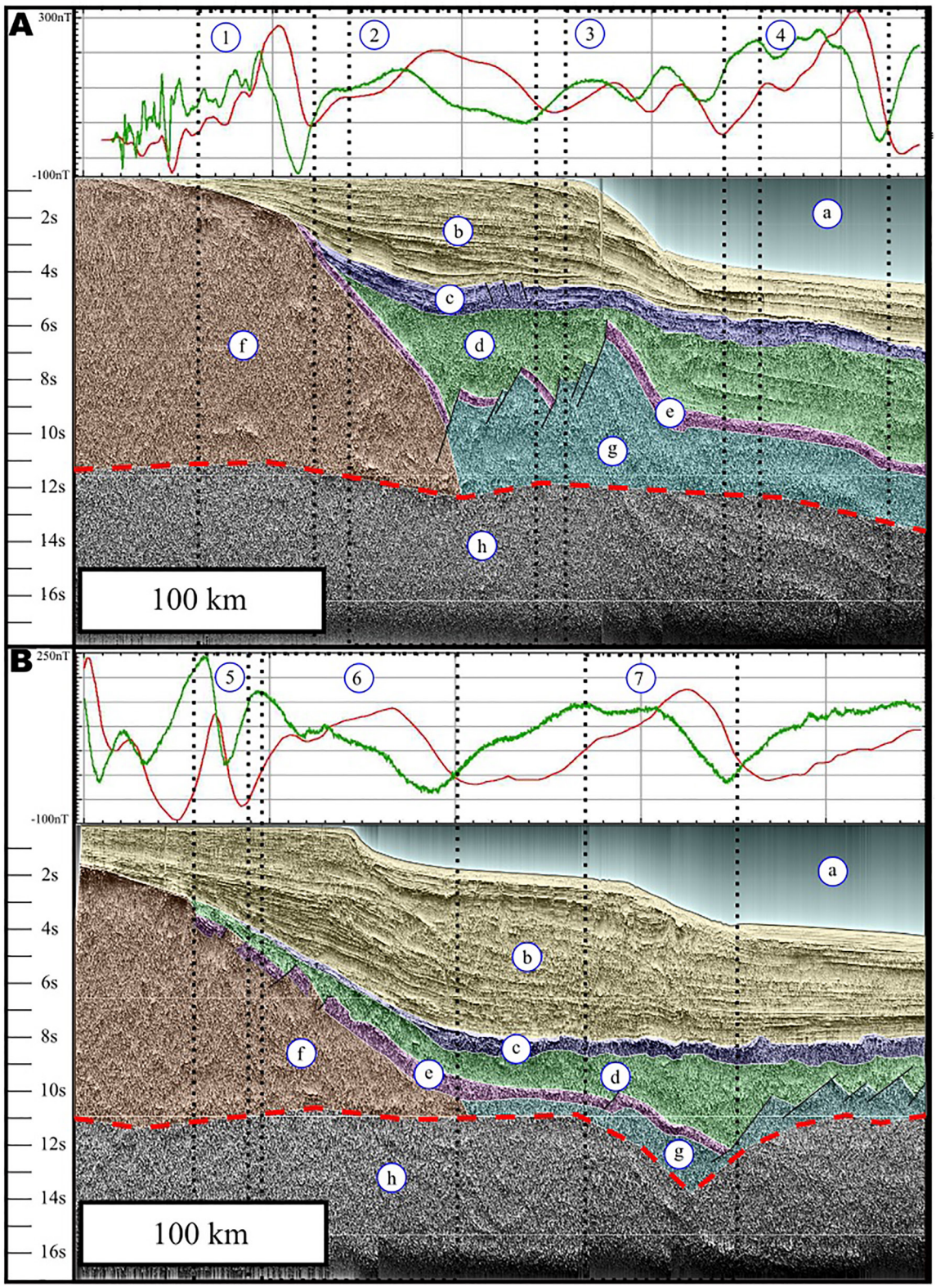

Figure 4. Composite image comparing seismic profiles (the *Y*-axis is in seconds) and magnetic anomaly profiles (green indicates raw data, and red indicates data that are reduced to pole). A-Upper composite image, northern seismic profile, line one in Figure 1. B-Bottom composite image, southern seismic profile, line two in Figure 1. We interpreted 8 seismic domains: (a) ocean; (b) sedimentary filing; (c) magmatic–sedimentary post-rift; (d) magmatic–sedimentary sin-rift; (e) magmatic–sedimentary pre-rift; (f) continental crust; (g) unidentified crust type; (h) asthenosphere. The dashed red line is the Moho discontinuity. Numbers in circles are the magnetic peaks mentioned in the text. Note that the most distal portion of the seismic line "A" shows seismic ringing.

5. Discussion

The interpretation of SDR-related magnetic anomalies as chrons is avoided worldwide. For example, the magnetic anomaly SDRs related to the east coast of the United States of America, namely, the East Coast Magnetic Anomaly (ECMA—Davis et al., 2018), are not interpreted as chrons (using Seton et al. (2014) repository of published magnetic picks), nor are the Greenland East Coast SDRs (delimited by Planke and Alvestad (1999) and compared with Seton et al. (2014) repository). However, in the South Atlantic Ocean margins, SDR-related magnetic anomalies are interpreted as ages in two ways. The first is the age of the oceanic crust (Collier et al., 2017; Hall et al., 2018; Moulin et al., 2010; Rabinowitz & LaBrecque, 1979), and the second is the age of the SDR (Chauvet et al., 2021; Koopmann et al., 2016; Stica et al., 2014). Both interpretations are misconceptions of the relations between magnetic anomalies and geology.

Remanent magnetism observed as a magnetic anomaly in an SDR environment depends on the extension rate and magmatic emplacement (Davis et al., 2018). Large SDR zones with typical extension rates (10–20 mm/yr) can destroy the original remnant magnetic signature by overlapping rocks with different polarities (Davis et al., 2018). For example, in the ECMA, an SDR-related magnetic anomaly occurs due to the magnetic susceptibility contrast between the continental crust and the SDRs (Davis et al., 2018). Based on this occurrence, many SDR-related magnetic anomalies should reflect changes in magnetic susceptibility due to lithological changes.

In the PB, the SDR geometry shows a low dip angle. On the other hand, the oceanic crust factory is sub-vertical (with the exceptions of oceanic islands and other plume-related oceanic structures, e.g., Karson, 2016), where the magnetic anomalies have been widely used to constrain the age. This finding implies that most SDR packages cross more than one magnetic anomaly (Figure 4). Even if SDR remanent magnetization is the source, the magnetic anomaly is the summation of the remanent magnetism intensity of different SDR ages (Davis et al., 2018; Gordon & Mohriak, 2015).

PB anomalies are different from ECMAs and show internal oscillations in polarity. These oscillations occur partially due to thickness variation in SDR packages, where each internal SDR package can have different magnetic polarities (as in the Davis et al. (2018) models). The thickness factor can be observed where changes in the SDR thickness are geographically coincident with changes in the amplitude and frequency of the RTP (Figure 2). In the profiles, the magnetic peaks "2" and "7" (Figure 4) are coincident with thickening of the SDR package. Peak "3" is two small peaks and is coincident with a region with a more complex geometry. Peaks "1" and "5" could be related to the magmatic feeder system. Peaks "4" and "6" occur without any geometrical change and may be due to changes in the SDR composition that can produce variations in the magnetic anomaly signals. The volcanic rocks of PB SDRs range from basalts to andesites by geochemical composition (data from Lobo et al., 2006), and distal regions have a volcanic fraction of just 45% (Harkin et al., 2020), with the other 55% being pyroclastic or siliciclastic rocks. These internal changes can produce a magnetic susceptibility contrast resulting in the anomaly. These lithological changes can be visualized in the well-cores (see Text S3 in Supporting Information S1).

A speculative interference is the old SDR remagnetization due to the younger SDR magmatism, which has not been researched in that region. The younger dike intrusions into old SDRs have been recorded in analog SDR outcrops in Greenland (Geoffroy et al., 2005). Intrusions of different ages should also contribute, causing interferences in the anomalous SDR-related magnetic field, which makes the signal questionable.

SDRs mainly develop above continental crust (Bastow & Keir, 2011; Geoffroy, 2005), and their volcanic age and position are not correlated, unlike oceanic crust. Currently, we can observe this phenomenon in a developing VPM in the Afar Rift in the Horn of Africa region. The volcanism in this region is suggested to be forming an SDR nowadays (Bastow & Keir, 2011). The oceanic crust area in the Red Sea is <200 km (Augustin et al., 2021), and most of the related SDR volcanism occurs in the continental crust (Bastow & Keir, 2011). It is essential to note the absence of a correlation between the position of continental crust volcanism and age. For instance, the positions of Dabbahu volcano and Dubbi volcano (Figure 5), which were both active during the Holocene (Field et al., 2012; Wiart & Oppenheimer, 2000), and the distance of 180 km in the dip direction, demonstrate the lack of correlation between the position and age of volcanism. In addition, the SDR-related rocks in Greenland occur above the continental crust. However, the SDRs cannot be assumed as a completely continental crust. Previous research has reported SDRs in the oceanic crust (e.g., Larsen & Jakobsdóttir, 1988). This finding implies that

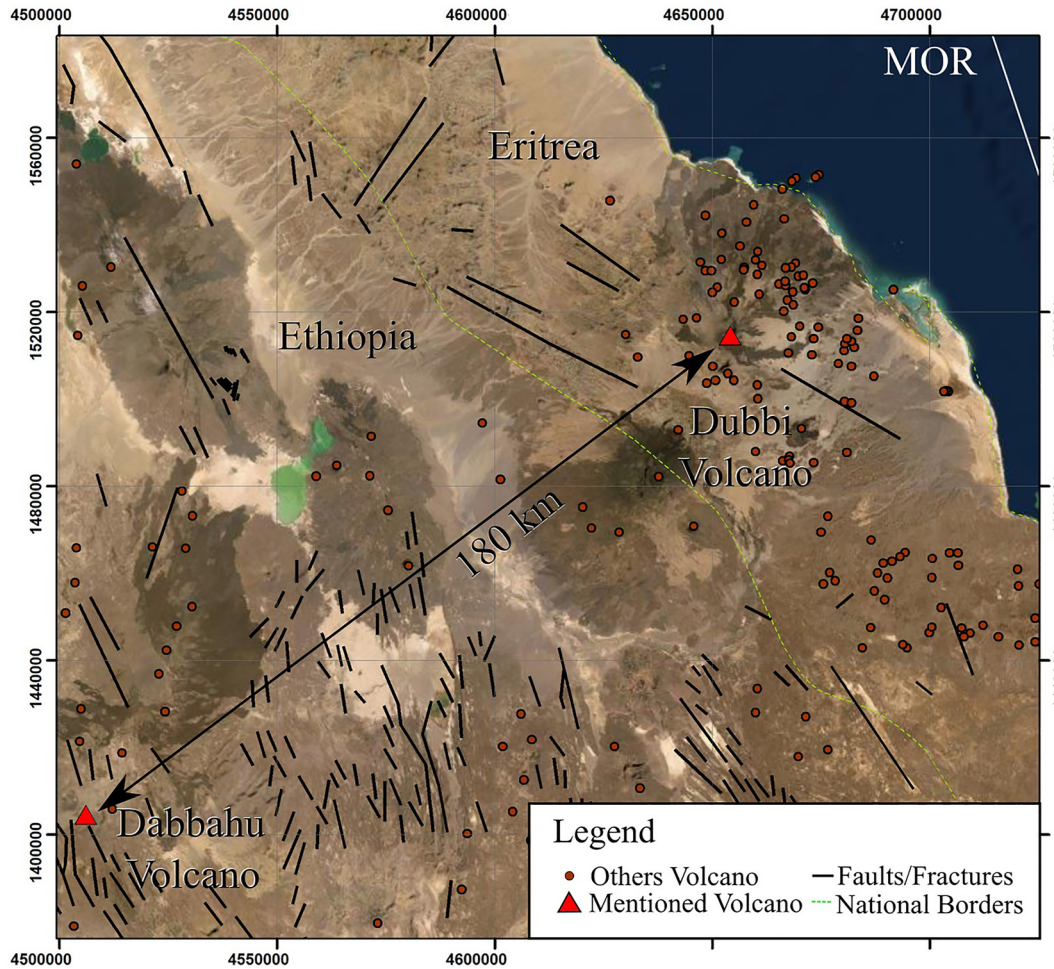

Figure 5. Landsat 8 image of the Afar Rift, highlighting volcanoes that are mentioned in the text and have erupted in the last thousand years (Field et al., 2012; Wiart & Oppenheimer, 2000). The image shows that in a continental VPM, there is no correlation between the position of magmatic extrusion and age, different from a regular oceanic crust. It is important to note that even after oceanic crust formation, this volcanism continues, and SDR packages have a pre-rift, rift, and post-rift stack.

oceanic crust can exist below some SDRs, making it even more challenging to constrain the exact age of the oceanic crust creation and COB position.

6. Conclusion

SDR-related magnetic anomalies cannot be used to constrain ages in the PB because (a) SDR dips are not vertical, which is different from regular oceanic crust fabric and causes the overlap of rocks extruded during periods of different polarities; (b) SDRs are heterogeneous (both in composition and thickness); (c) a relation between the position and age in SDR magmatism is absent, and new intrusions are located above old SDRs, and (d) the anomalous magnetic field is mainly related to the magnetic susceptibility contrast rather than remnant magnetism. The absence of published isotopic ages in the PB SDRs and the unreliability of the magnetostratigraphy in SDRs demonstrated in this study imply high uncertainty of SDRs and oceanic crust age in the region. Due to the aforementioned reasons, we do not recommend using SDR-related magnetic anomalies as age constraints in any region.

Data Availability Statement

All used ANP data (seismic survey 0239-PELOTAS-18A and magnetic surveys P0099 B, P0108, APP040, APP060) are free for research institutions and the data is available at: https://www.gov.br/anp/pt-br/assuntos/exploracao-e-producao-de-oleo-e-gas/dados-tecnicos/acesso-aos-dados-tecnicos. The NOAA Earth Magnetic Anomaly Grid (EMAG2) data is available at: https://www.ngdc.noaa.gov/geomag/emag2.html. The Seton et al. (2014) repository of "Published Magnetic Picks and Parameters for Tectonic Reconstruction" is available at: http://www.soest.hawaii.edu/PT/GSFML/HELL/index.html. The USGS satellite images are available at: https://earthexplorer.usgs.gov/.

Acknowledgments
We thank UNISINOS for the facilities used during the research. HS thanks CAPES/PROSUC for his scholarship 88887.342269/2019-00. FCJ acknowledges CNPq research fellowships Grant 301441/2019-7. We also thank W. Roger Buck and Webster Mohriak for the valuable suggestions which improve the manuscript.

References

Augustin, N., Van der Zwan, F. M., Devey, C. W., & Brandsdóttir, B. (2021). 13 million years of seafloor spreading throughout the Red Sea basin. *Nature Communications*, *12*(1), 1–10. https://doi.org/10.1038/s41467-021-22586-2

Baranov, V., & Naudy, H. (1964). Numerical calculation of the formula of reduction to the magnetic pole. *Geophysics*, *29*(1), 67–79. https://doi.org/10.1190/1.1439334

Bastow, I. D., & Keir, D. (2011). The protracted development of the continent–ocean transition in Afar. *Nature Geoscience*, *4*(4), 248–250. https://doi.org/10.1038/ngeo1095

Buck, W. R. (2017). The role of magmatic loads and rift jumps in generating seaward dipping reflectors on volcanic rifted margins. *Earth and Planetary Science Letters*, *466*, 62–69. https://doi.org/10.1016/j.epsl.2017.02.041

Bueno, G. V., Zacharias, A. A., Oreiro, S. G., Cupertino, J. A., Falkenhein, F. U. H., & Martins Neto, M. A. (2007). Bacia de Pelotas. *Boletim de Geociencias da Petrobras*, *15*, 551–559.

Cainelli, C., & Mohriak, W. U. (1999). Some remarks on the evolution of sedimentary basins along the Eastern Brazilian continental margin. *Episodes Journal of International Geoscience*, *22*(3), 206–216. https://doi.org/10.18814/epiiugs/1999/v22i3/008

Cartwright, J., Swart, R., & Corner, B. (2012). Conjugate margins of the South Atlantic: Namibia-pelotas. In *Regional geology and tectonics: Phanerozoic passive margins, cratonic basins and global tectonic maps* (pp. 202–221). Elsevier.

Chang, H. K., Kowsmann, R. O., Figueiredo, A. M. F., & Bender, A. (1992). Tectonics and stratigraphy of the East Brazil rift system: An overview. *Tectonophysics*, *213*(1–2), 97–138. https://doi.org/10.1016/0040-1951(92)90253-3

Chauvet, F., Sapin, F., Geoffroy, L., Ringenbach, J. C., & Ferry, J. N. (2021). Conjugate volcanic passive margins in the austral segment of the South Atlantic–architecture and development. *Earth-Science Reviews*, *212*, 103461. https://doi.org/10.1016/j.earscirev.2020.103461

Chemale, F., Jr. (2000). *Evolução geológica do Escudo Sul-rio-grandense* (pp. 13–52). Geologia do Rio Grande do Sul.

Chemale, F., Jr., Ramos, V. A., Naipauer, M., Girelli, T. J., & Vargas, M. (2018). Age of basement rocks from the Maurice Ewing bank and the Falkland/Malvinas plateau. *Precambrian Research*, *314*, 28–40. https://doi.org/10.1016/j.precamres.2018.05.026

Collier, J. S., McDermott, C., Warner, G., Gyori, N., Schnabel, M., McDermott, K., & Horn, B. W. (2017). New constraints on the age and style of continental breakup in the South Atlantic from magnetic anomaly data. *Earth and Planetary Science Letters*, *477*, 27–40. https://doi.org/10.1016/j.epsl.2017.08.007

Davis, J. K., Bécel, A., & Buck, W. R. (2018). Estimating emplacement rates for seaward-dipping reflectors associated with the US East Coast Magnetic Anomaly. *Geophysical Journal International*, *215*(3), 1594–1603. https://doi.org/10.1093/gji/ggy360

Dietz, R. S. (1961). Evolution by spreading of the sea floor. *Nature*, *190*(3), 854–857. https://doi.org/10.1038/190854a0

Eagles, G., Pérez-Díaz, L., & Scarselli, N. (2015). Getting over continent-ocean boundaries. *Earth-Science Reviews*, *151*, 244–265. https://doi.org/10.1016/j.earscirev.2015.10.009

Field, L., Blundy, J., Brooker, R. A., Wright, T., & Yirgu, G. (2012). Magma storage conditions beneath Dabbahu Volcano (Ethiopia) constrained by petrology, seismicity and satellite geodesy. *Bulletin of Volcanology*, *74*(5), 981–1004. https://doi.org/10.1007/s00445-012-0580-6

Frank, H. T., Gomes, M. E. B., & Formoso, M. L. L. (2009). Review of the areal extent and volume of the Serra Geral formation, Paraná Basin, South America. *Pesquisas em Geociencias*, *36*(1), 49–57. https://doi.org/10.22456/1807-9806.17874

Geoffroy, L. (2005). Volcanic passive margins. *Comptes Rendus Geoscience*, *337*(16), 1395–1408. https://doi.org/10.1016/j.crte.2005.10.006

Geoffroy, L., Burov, E. B., & Werner, P. (2015). Volcanic passive margins: Another way to break up continents. *Scientific Reports*, *5*(1), 1–12. https://doi.org/10.1038/srep14828

Gladczenko, T. P., Hinz, K., Eldholm, O., Meyer, H., Neben, S., & Skogseid, J. (1997). South Atlantic volcanic margins. *Journal of the Geological Society*, *154*(3), 465–470. https://doi.org/10.1144/gsjgs.154.3.0465

Gomes, A. S., & Vasconcelos, P. M. (2021). Geochronology of the Paraná-Etendeka large igneous province. *Earth-Science Reviews*, *220*, 103716. https://doi.org/10.1016/j.earscirev.2021.103716

Gordon, A. C., & Mohriak, W. U. (2015). Seismic volcano-stratigraphy in the basaltic complexes on the rifted margin of Pelotas Basin, Southeast Brazil. In *34th annual GCSSEPM foundation Perkins-Rosen research conference, Petroleum Systems in Rift Basins* (pp. 748–786).

Granot, R., & Dyment, J. (2015). The cretaceous opening of the South Atlantic Ocean. *Earth and Planetary Science Letters*, *414*, 156–163. https://doi.org/10.1016/j.epsl.2015.01.015

Hall, S. A., Bird, D. E., McLean, D. J., Towle, P. J., Grant, J. V., & Danque, H. A. (2018). New constraints on the age of the opening of the South Atlantic basin. *Marine and Petroleum Geology*, *95*, 50–66.

Harkin, C., Kusznir, N., Roberts, A., Manatschal, G., & Horn, B. (2020). Origin, composition, and relative timing of seaward dipping reflectors on the Pelotas rifted margin. *Marine and Petroleum Geology*, *114*, 104235. https://doi.org/10.1016/j.marpetgeo.2020.104235

Hartmann, L. A., Savian, J. F., & Lopes, W. R. (2016). Airborne geophysical characterization of geotectonic relationships in the southern Ribeira belt, Luís Alves craton, and northern Dom Feliciano belt, Brazilian Shield. *International Geology Review*, *58*(4), 471–488. https://doi.org/10.1080/00206814.2015.1089424

Hess, H. H. (1962). History of ocean basins. In A. E. J. Engel, H. L. James, & B. F. Leonard (Eds.), *Petrologic studies: A volume to honour A.F. Buddington* (pp. 559–620). Geolgical Society of America.

Hinz, K. (1981). A hypothesis on terrestrial catastrophies wedges of very thick oceanward dipping layers beneath passive continental margins. Their origin and paleoenvironmental significance. *Geologisches Jahrbuch. Reihe E, Geophysik*, (22), 3–28.

Karson, J. A. (2016). Crustal accretion of thick mafic crust in Iceland: Implications for volcanic rifted margins. *Canadian Journal of Earth Sciences*, *53*(11), 1205–1215. https://doi.org/10.1139/cjes-2016-0039

Koopmann, H., Schreckenberger, B., Franke, D., Becker, K., & Schnabel, M. (2016). The late rifting phase and continental break-up of the southern South Atlantic: The mode and timing of volcanic rifting and formation of earliest oceanic crust. *Geological Society, London, Special Publications*, *420*(1), 315–340. https://doi.org/10.1144/sp420.2

Larsen, H. C., & Jakobsdóttir, S. (1988). Distribution, crustal properties and significance of seawards-dipping sub-basement reflectors off E Greenland. *Geological Society, London, Special Publications*, *39*(1), 95–114. https://doi.org/10.1144/gsl.sp.1988.039.01.10

Li, X. (2008). Magnetic reduction-to-the-pole at low latitudes: Observations and considerations. *The Leading Edge*, *27*(8), 990–1002. https://doi.org/10.1190/1.2967550

Lobo, J. T., Szatmari, P., & Duarte, B. P. (2006). Tipos de fontes associadas às suítes basálticas de Campos e de Pelotas (Sul-Sudeste) e modelos geodinâmicos de ruptura do Gondwana ocidental. *Boletim de Geociencias da Petrobras*, *14*(2), 269–285.

Menzies, M. A., Klemperer, S. L., Ebinger, C. J., & Baker, J. (2002). Characteristics of volcanic rifted margins. *Geological Society of America Special Paper*, *362*, 1–14.

Mohriak, W. U., & Fainstein, R. (2012). Phanerozoic regional geology of the eastern Brazilian margin. In *Regional geology and tectonics: Phanerozoic passive margins, cratonic basins and global tectonic maps* (pp. 222–282). Elsevier.

Moulin, M., Aslanian, D., & Unternehr, P. (2010). A new starting point for the South and Equatorial Atlantic Ocean. *Earth-Science Reviews*, *98*(1–2), 1–37. https://doi.org/10.1016/j.earscirev.2009.08.001

Mutter, J. C., Talwani, M., & Stoffa, P. L. (1982). Origin of seaward-dipping reflectors in oceanic crust off the Norwegian margin by "subaerial sea-floor spreading". *Geology*, *10*(7), 353–357. https://doi.org/10.1130/0091-7613(1982)10<353:oosrio>2.0.co;2

Nunes, A., Glória, M., Miranda, J., Cardoso, C., Vieira Filho, C., Oliveira, J., & Borghi, L., (2017). The use of seismic attribute in 2D data: A case study. In *15th International congress of the Brazilian Geophysical Society & EXPOGEF, Rio de Janeiro, Brazil, 31 July-3 August 2017* (pp. 1268–1271). Brazilian Geophysical Societ.

Peate, D. W., Hawkesworth, C. J., & Mantovani, M. S. M. (1992). Chemical stratigraphy of the Paraná lavas (S. America): Classification of magma types and their spatial distribution. *Bulletin of Volcanology*, *55*(1–2), 119–139. https://doi.org/10.1007/bf00301125

Peyve, A. A. (2010). Tectonics and magmatism in eastern South America and the Brazil basin of the Atlantic in the Phanerozoic. *Geotectonics*, *44*(1), 60–75. https://doi.org/10.1134/s001685211001005x

Philipp, R. P., Pimentel, M. M., & Chemale, F. (2016). Tectonic evolution of the Dom Feliciano belt in Southern Brazil: Geological relationships and U-Pb geochronology. *Brazilian Journal of Genetics*, *46*(suppl 1), 83–104. https://doi.org/10.1590/2317-4889201620150016

Planke, S., & Alvestad, E. (1999). Seismic volcanostratigraphy of the extrusive breakupcomplexes in the northeast Atlantic: Implications from ODP/DSDP drilling. In *Proceedings of the Ocean Drilling Program, scientific results* (Vol. 163, pp. 3–16). Ocean Drilling Program. Retrieved from http://www-odp.tamu.edu/publications/163_SR/VOLUME/CHAPTERS/CHAP_01.PDF

Rabinowitz, P. D., & LaBrecque, J. (1979). The mesozoic South Atlantic ocean and evolution of its continental margins. *Journal of Geophysical Research*, *84*(B11), 5973–6002. https://doi.org/10.1029/jb084ib11p05973

Rosa, M. L. C. D. C., Barboza, E. G., Abreu, V. D. S., Tomazelli, L. J., & Dillenburg, S. R. (2017). High-frequency sequences in the quaternary of Pelotas Basin (coastal plain): A record of degradational stacking as a function of longer-term base-level fall. *Brazilian Journal of Genetics*, *47*(2), 183–207. https://doi.org/10.1590/2317-4889201720160138

Seton, M., Whittaker, J., Wessel, P., Müller, R. D., DeMets, C., Merkouriev, S., et al. (2014). Community infrastructure and repository for marine magnetic identifications. *Geochemistry, Geophysics, Geosystems*, *5*(4), 1629–1641. https://doi.org/10.1002/2013gc005176

Stica, J. M., Zalán, P. V., & Ferrari, A. L. (2014). The evolution of rifting on the volcanic margin of the Pelotas Basin and the contextualization of the Paraná–Etendeka LIP in the separation of Gondwana in the South Atlantic. *Marine and Petroleum Geology*, *50*, 1–21. https://doi.org/10.1016/j.marpetgeo.2013.10.015

Talwani, M., & Abreu, V. (2000). Inferences regarding initiation of oceanic crust formation from the US East Coast margin and conjugate South Atlantic margins. *Geophysical Monograph*, *115*, 211–234.

Vine, F. J., & Matthews, D. H. (1963). Magnetic anomalies over oceanic ridges. *Nature*, *4897*, 947–949. https://doi.org/10.1038/199947a0

Wiart, P., & Oppenheimer, C. (2000). Largest known historical eruption in Africa: Dubbi volcano, Eritrea, 1861. *Geology*, *28*(4), 291–294. https://doi.org/10.1130/0091-7613(2000)028<0291:lkheia>2.3.co;2

International Journal of Hydrogen Energy 69 (2024) 347–357

Contents lists available at ScienceDirect

International Journal of Hydrogen Energy

journal homepage: www.elsevier.com/locate/he

Southern Brazil hydrogen systems review

H. Serratt [a,b,c,*], J.A. Cupertino [a], M.F. Cruz [a], T.J. Girelli [a], I. Lehn [a], C.D. Teixeira [a], H.O.S. Oliveira [a], F. Chemale Jr [a]

[a] Programa de Pós-Graduação em Geologia, Universidade do Vale dos Sinos, São Leopoldo, Brazil
[b] Instituto de Geociências, Universidade de Brasília, 70910-900, Brasília, DF, Brazil
[c] UMR CNRS-IFREMER-CNRS-UBS 6538 Geo-Ocean, IUEM, Université de Bretagne Occidental, France

ARTICLE INFO

Handling Editor: Dr. E.A. Veziroglu

Keywords:
Natural hydrogen
Hydrogen system
South America platform
Renewable energy

ABSTRACT

Natural Hydrogen Gas (H_2) is producing a new golden rush worldwide due to its clean energetic features. The potential of natural hydrogen gas (H_2) in the southernmost regions of Brazil, specifically Rio Grande do Sul and Santa Catarina, remains largely unexplored. We found free H_2 occurrences identified in the intracratonic Mesozoic Paraná Basin, recognized in four formation tests performed in former exploratory wells. The data revealed H_2 concentrations ranging from 0.14% to 8.79%, albeit associated with noncommercial volumes of natural gas. These occurrences of H_2 exhibit a curious negative correlation with Helium (He), distinguishing it from many Eurasian occurrences associated with mantle sources. The Paraná Basin hosts the largest Brazilian coal reserves and organic-rich rocks. We posit that the hydrogen gas presence can be attributed to the maturation processes affecting mainly Rio Bonito, Taciba, and Ponta Grossa formations in this basin. Also, we identified hydrogen system elements in the rift-type Precambrian Camaquã Basin, which host potential source rocks, reservoirs, and seals. Until now, no H_2 measurements have been carried out in this basin. To solve this lack, it is fundamental to execute a systematic sampling survey; it will enable the identification of the potential of H_2 deposits in the Southernmost Brazilian region. This work lays the foundations for future research in the region, which is demanded to realize this economic potential.

1. Introduction

Hydrogen gas is a clean energy resource, as its combustion produces only heat and pure water. When combined with oxygen, this fuel generates electricity through hydrogen fuel cells [1]. While its primary use as an energy source is still in its infancy, it is expected to play a significant role in the future. Since 1975, the global demand for H_2 has tripled and continues to rise [2]. The issue is that hydrogen is almost entirely produced using fossil fuels, emitting 900 million tons of CO_2 per year [3], in the method denominated black, gray, or brown hydrogen. The industry considers the development of projects for green hydrogen generation to be the most favorable option, although it uses other types of energy to produce it. This process entails producing this gas from renewable energy sources like wind and solar to extract hydrogen from water by electrolysis. However, green hydrogen comes at a cost between US$ 3 to 7 per kilogram, more than double the price of gray hydrogen [3,4]. However, natural hydrogen (also called geological, white, or golden hydrogen) is expected to be cheaper and environmentally friendly than manufactured hydrogen [5,6].

Globally, more than one hundred discoveries of hydrogen gas were reported until 2020, mainly in the northern hemisphere. However, there are no discoveries of hydrogen gas higher than 10% of the free gasses in rocks in South America [7]. While initial studies on hydrogen geology in South America were conducted in the São Francisco Basin [8], these findings are confined to a relatively small region. The southernmost Brazil shows a diverse geology comprising three primary tectonic domains. These include the Precambrian to Eopaleozoic Uruguayan-Sul-Riograndense Shield, the Paleozoic to Mesozoic Intracratonic Paraná Basin, and the Mesocenozoic Passive Margin Pelotas Basin. The H_2 potential in this region is still unknown.

To defog the H_2 potential of this region, we seek to provide a comprehensive review of southernmost Brazilian geology from the perspective of hydrogen potential. This study endeavors to fill this critical knowledge gap by examining the natural hydrogen potential in the Rio Grande do Sul and southeast of Santa Catarina states, reviewing the occurrences of this gas in the wells of the region.

* Corresponding author. Programa de Pós-Graduação em Geologia, Universidade do Vale dos Sinos, São Leopoldo, Brazil.
E-mail address: hserratt@unisinos.br (H. Serratt).

https://doi.org/10.1016/j.ijhydene.2024.05.018
Received 29 November 2023; Received in revised form 8 March 2024; Accepted 2 May 2024
Available online 7 May 2024

2. The economic exploration of natural hydrogen

Periodically, diverse industries, including oil and gas, hydrogeology, and mining, confront an unusual scenario — the unexpected occurrence of a high concentration of hydrogen. For instance, consider the case of the Soviets who, while drilling a conventional clastic reservoir rich in methane in Stavropol, stumbled upon a 27.3% concentration of hydrogen gas within this reservoir [7,9–11]. A common point of contention in hydrogen geology revolves around why we seldom encounter hydrogen gas when drilling for oil (just sixteen occurrences of free H_2 higher than 10% are reported in the literature - [7]). Nevertheless, Hand [3] provides a compelling explanation for this phenomenon. In the process of hydrocarbon formation, most hydrogen gas is typically consumed. Therefore, when we discover hydrocarbons, it is reasonable to expect that the reservoir has been depleted of hydrogen gas. Consequently, it is more common to come across hydrogen discoveries made during mining activities rather than within the purview of oil companies, with a ratio of 27/16 [7]. However, the primary reason for this absence of discoveries is the infrequent measurement of hydrogen gas [3].

Economic deposits in different geological settings also showed anomalous H_2 values. A noteworthy example of discovery occurred during drilling activities at the Udachnaya kimberlite pipe. Here, an abrupt blowout resulted in a substantial blazing gas flare due to an extraordinary concentration of hydrogen gas [7], which should have led to a more accurate investigation of what happened. In 1978, during the drilling of a water well in the village of Bourakébougo, southwest of Mali, a large hydrogen gas reservoir was found [5]. In 2012, Petroma Inc. (Now rebranded to Hydroma Inc.) initiated an assessment project for the area. They identified five reservoirs interspersed with dolerite sills that facilitate the formation of the trap [5]. The mapped depths of the reservoirs range from 30 to 135 m and 1125 to 1500 m, consisting of carbonates (upper reservoir) and sandstones (lower reservoir - [5]). They used neutron logging as the primary tool for detecting the presence of natural hydrogen in evaluating these wells. The reservoir pressure has remained consistent over the past nine years, sustaining a production rate of 1500 m^3 of H_2 (Hydrogen gas) per day, with H_2 constituting 98% of the free gas [7,12]. This achievement signifies a remarkable milestone as the inaugural economic breakthrough in the natural hydrogen industry.

Regarding natural hydrogen production, the pioneer production in Mali was a significant catalyst for investor interest. In the United States of America, some companies are trying to explore H_2 in Kansas state, where previously there was reported free H_2 content of 80% [13]. New discoveries and research are being done worldwide, e.g., in Australia [14] and France [15]. In a world where hydrogen geology is rapidly becoming a more prevalent reality, such hydrogen discoveries are increasingly making their way into the spotlight.

3. Hydrogen systems

In this review, we employ the term hydrogen systems to denote a framework encompassing hydrogen gas generation, migration, and accumulation processes [14]. This conceptualization, akin to the principles governing oil systems, mirrors the quest for a dependable source rock, necessitating the identification of migration routes, reservoirs, effective traps, and sealing mechanisms. Also, we use the term hydrogen geology as a parallel to petroleum geology, which is the field of geology that investigates all elements of the hydrogen system. As we venture into the emergent field of hydrogen geology, much of the extensive knowledge acquired from the oil and gas industry forms a robust foundation upon which to build.

Even with similarities with petroleum systems, hydrogen systems have their own peculiarities. For example, detecting hydrogen gas proves more challenging than identifying oil. However, hydrogen gas (H_2) leaks induce alterations in soil and vegetation, manifesting as distinctive phenomena termed “fairy circles’’ due to their geometry [8,16]. These events clearly demonstrate the existence of a source rock and the absence of an effective seal mechanism. However, unlike oil systems, where the process of generation and accumulation unfolds over millions of years, some hydrogen systems related to rock alteration exhibit greater dynamism, with fluid residence occurring within a timescale closer to human life (ranging from decades to centuries - [17]). A significant contrast between oil and hydrogen systems lies in their source rocks. While certain rocks that serve as source rocks for oil systems might also act in the same capacity for hydrogen systems, it is pointed out that the bulk of hydrogen originates from inorganic reactions in deeper strata [7,17]. This fundamental distinction marks the main rupture of hydrogen geology from conventional hydrocarbon exploration methodologies.

The presence of free hydrogen gas with concentrations exceeding 10% has been documented in nature at least 153 times [7]. The H_2 was found in numerous geological contexts, as extensively compiled by Zgonnik [7]. His compilation reveals occurrences associated with geological environments such as orebodies, serpentinized regions, volcanic areas, hydrocarbon fields, salt deposits, coal basins, Precambrian terrains, kimberlite pipes, and fault zones. Different geological settings have reported anomalous hydrogen gas content. Four principal genetic mechanisms worldwide are recognized as hydrogen suppliers to the geological system.

Core or Mantle Origin: A crucial aspect of hydrogen gas origins is its direct release from the Earth’s lower mantle and core during geological history [7]. This primary hydrogen supply accumulates predominantly along the boundaries of tectonic plates and within deep-seated faults permeating the lithosphere. Notably, investigations conducted in Uzbekistan have linked unusual accumulations of these gasses to regions with heightened fluid conductivity, where hydrogen levels have shown a significant correlation with helium [7]. Furthermore, experimental research, as conducted by Yang et al. [18], has revealed the intriguing solubility of hydrogen in minerals under conditions analogous to those in the Earth’s mantle, implying the potential existence of substantial hydrogen reservoirs within the mantle, especially in reducing environments. Moreover, comprehensive research suggests that the upper mantle and extensive regions of the asthenosphere are notably saturated with various metals, implying that the primary fluid within these regions is likely significantly enriched in hydrogen content [7,19]. This hypothesis is further reinforced by studies examining metal inclusions within diamonds originating from the mantle [20]. A review of hydrogen concludes the existence of high amounts of it in the lower mantle or core [21]. There is a hypothesis that hydrogen plays a crucial role in addressing the Earth’s core mass deficit problem, which results from the core being approximately 10% lighter than a Fe–Ni alloy at equivalent pressure and temperature. Adding 1% by weight of hydrogen to the core has been suggested as a solution to this issue [22]. However, other solutions to the mass deficit are plausible, such as Si, S, and C [22]. Research indicates that iron hydride remains stable under the extreme conditions of the mantle and core [23], supporting Poirier’s [22] hypothesis. A recent study proposes that the Earth’s core could contain 80 ($\pm$31) times more hydrogen than the combined mass of all the hydrogen in the oceans [24], making the core a relevant hydrogen reservoir.

Rock Alteration Origin: This mechanism is predominantly exemplified by serpentinization and hydroxyl reactions [7,11,25–27]. Ultramafic rocks exposed to hydrous conditions suffer metasomatism, transforming anhydrous minerals into hydrous minerals, forming serpentine [11]. The potential for hydrogen production from ultramafic rocks hinges on several factors, including the degree of serpentinization, the timing of alteration processes, and the presence of hydrous fluids. Temperature significantly influences the rate of these reactions, with geological transformations occurring rapidly within the range of 200–300 °C and decreasing sharply below 100 °C [28]. Therefore, determining the tempo of these alterations is key to understanding the genesis of hydrogen deposits or the occurrence of gas seepage. Other

mineral alteration reactions also produce hydrogen gas as a subproduct. Reactions such as the conversion of arfvedsonite to aegirine + magnetite + quartz + H_2 [11], pyritization [29], iron minerals oxidation [13,26,30–37], and biotite hydration [15] are reported as a H_2 source.

Radiolysis Origin: Water radiolysis within the lithosphere is pointed as another mechanism for natural hydrogen generation [11,38–43]. Numerous radioactive elements in the crust, like uranium, thorium, and potassium, release sub-particles during decay. The energy released breaks down water molecules into oxygen and hydrogen [11]. Another mechanism related to radiation occurs when this process induces the polymerization of methane and the destruction of organic matter [44]. However, Zgonnik [7] indicated that radioactive decay alone probably could not produce most hydrogen gas anomalies. Usually, these anomalies should be associated with different mechanisms. Today, there is no well-established methodology to validate the total amount of hydrogen gas produced by radiolysis, and further research is

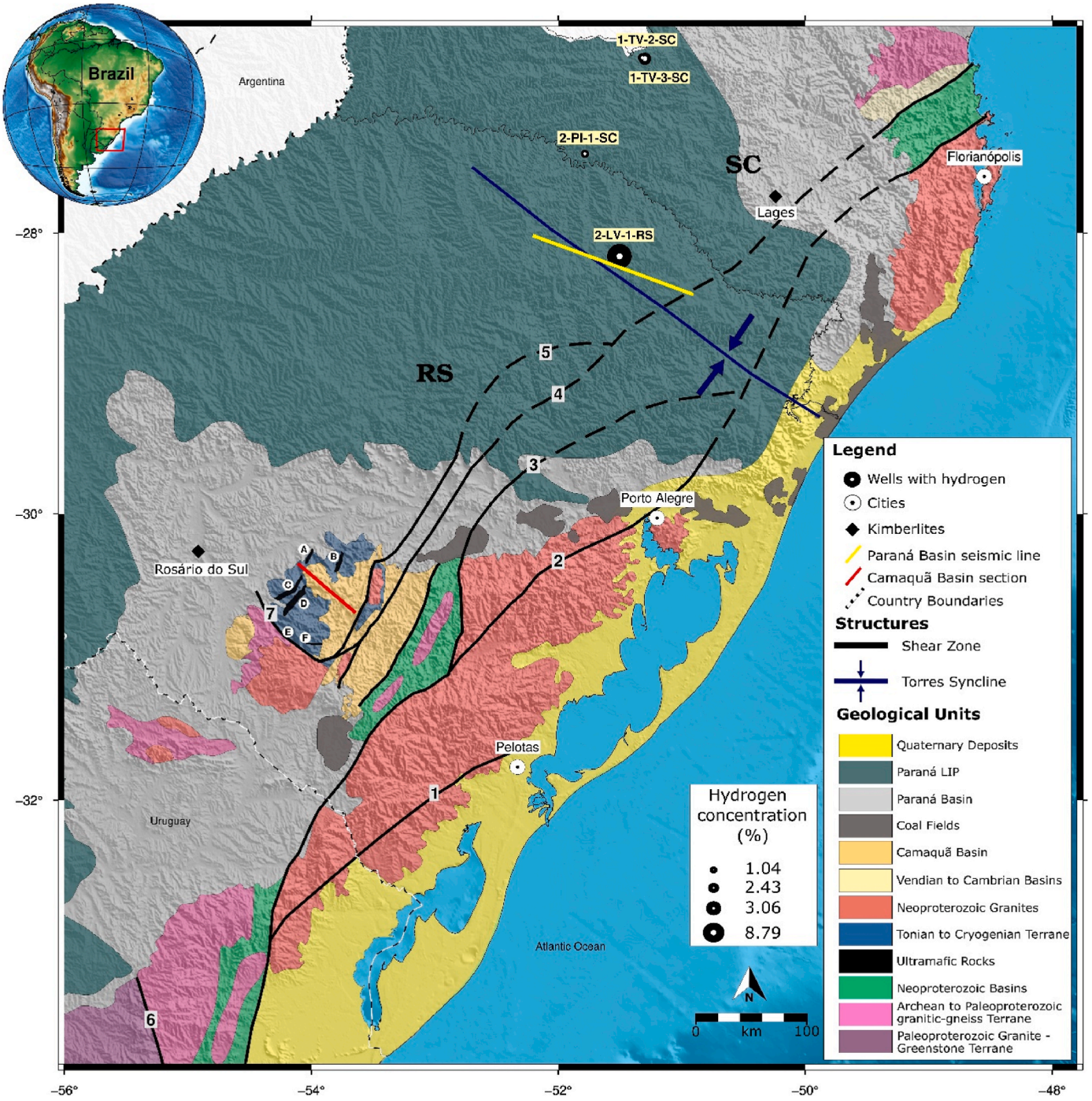

Fig. 1. A simplified regional geological map showing the potential plays of the Hidrogen Geological System in the southernmost part of Brazil. The main potential source rocks in the West Camaquã Basin are due to the presence of ultramafic rocks partially serpentinized and a possible mantle H_2 leaking in the shear zones. On the East border, the Paraná Basin has as a source rock organic-rich deposits (coals and pyrobituminous shales). The geological and structural frameworks are modified from [49]. The shear zones numbered are: 1) Cerro Amaro - Arroio Grande: 2) Major Grercino - Dorsal de Canguçu; 3) Passo do Marinheiro; 4) Perimbó - Caçapava do Sul; 5) Segredo; 6) Sarandí del Yí; 7) Ibaré. The ophiolitic bodies in the figures are A) Cambaizinho, B) Bossoroca, C) Passo do Ivo, D) Palma, E) Ibaré, F) Cerro Mantiqueiras.

needed in this field.

Organic Processes: The hydrogen generation through organic processes can be separated into two main types: biological hydrogen and thermogenic hydrogen. The biological hydrogen unfolds via multiple mechanisms, including the anaerobic decomposition of organic matter, fermentation, and nitrogen-fixing bacteria. The counterparts within geological environments often result in hydrogen generation. A complex challenge arises when these hydrogen-generating microorganisms cross paths with their hydrogen-consuming lagging behind consumption rates [7]. Consequently, the perspective presented by Hand [3] posits biological processes as more relevant for hydrogen loss than as the primary source of its genesis. However, there is a distinct trend of hydrogen production from non-biological organic processes. For instance, during the coalification process, the increase in maturity implies the H loss of the molecular structure of the coal [11,45,46]. Moreover, overmature hydrocarbon source rocks, with vitrinite reflectance (Ro) between 3 and 5%, serve as the source for molecular hydrogen generation. This H_2 generation continues even after late natural gas generation ceases [46,47]. Overmature organic-rich rocks have the potential to serve as a significant source of hydrogen, continuously generating H_2, while their hydrogen content remains unaffected by hydrocarbon formation. However, further studies are needed to investigate the interplay between H_2 consumption, generation, and temperature.

4. Rio Grande do sul and southeast Santa Catarina geology

The states of Rio Grande do Sul and Santa Catarina, situated in the southernmost region of Brazil (as shown in Fig. 1), have diverse and complex geological features. Located along the eastern margins of South America, this region encompasses three primary tectonic domains: (I) the Precambrian to Eopaleozoic Uruguayan-Sul-Riograndense Shield, (II) the Paleozoic to Mesozoic Intracratonic Paraná Basin (including the Paraná LIP - Large Igneous Intrusion), and (III) the Mesocenozoic Passive Margin Pelotas Basin. The southernmost region of Brazil and Uruguay exhibits a conjugate margin relationship with Namibia [48], which holds significance due to identified H_2 seepage sites in Namibia [16].

The Uruguayan-Sul-Riograndense Shield comprises a complex rock framework accretioned throughout several geotectonic events from Archean to Neoproterozoic [50]. The Shield is compartmented into the Rio De La Plata Craton and the Dom Feliciano Belt domains. The Rio de La Plata domain is majorly formed by Archean to Paleoprotorozoic granitic-gneiss and granite-greenstone terranes. Meanwhile, the Dom Feliciano Belt records the Neoproterozoic orogeny between Rio De La Plata Craton and Congo-Kalahari cratons [51,52]. The belt is divided into three main entities: Tonian to Cryogeniean São Gabriel Terrane, Neoproterozoic Metassedimentary Tijucas Terrane, and the Neoproterozoic Pelotas Batholith.

The São Gabriel Terrane records a Tonian juvenile arc [53–55] with a widespread presence of mafic and ultramafic rocks ([56] and references herein). In the scope of natural hydrogen potential, the most favorable geology is related to these ultramafic rocks. These rocks of the São Gabriel Terrane were partially covered by the Ediacaran - Cambrian volcano-sedimentary deposits of the Camaquã Basin [57].

The Camaquã Basin is located in the central portion of the Rio Grande do Sul State, southernmost Brazil. It rests on Neoproterozoic igneous and metamorphic rocks, as well as ophiolitic and ultramafic rocks, of the Sul-Riograndense Shield [50,58]. The basin presents a NE-SW oriented, elongated shape. It is bounded by the Tijucas Terrane (eastern margin), São Gabriel Terrane, and Rio de La Plata Craton (western and south border). Most authors [49–51,57,59–65] relate the Camaquã Basin to the late to post-collisional stages of the Brasiliano Orogeny.

According to Paim et al. [57], the Camaquã Basin represents an Ediacaran to Cambrian depositional locus of distinct basins. It records four tectonic-volcanic-sedimentary episodes evolving from compressive through transpressive and distensive tectonic regimes [66]. This progression is represented by the Maricá retroarc foreland basin, East and West Bom Jardim strike-slip basins, East and West Santa Bárbara rifts, and by the Guaritas Rift (Fig. 2). The first three units comprise organic-walled microfossils and very well-preserved microbial mats, recording the Ediacaran microorganisms living both in restrict marine, (Maricá Group) and lacustrine (Bom Jardim and Santa Barbara groups) environments [67,68]. Claystone and volcanic intervals in the basin are here recognized as possible seals for the sandstone reservoirs.

The Paraná Basin is an intracratonic basin, covering approximately 1.5 million km^2 [70,71], with an elongated main axis in the N–S direction, embracing the central-southern regions of Brazil, Paraguay, Uruguay, and northern Argentina [72]. As the largest intracratonic basin in the South American continent, Milani [71] subdivided it into six supersequences: Rio Ivaí (Ordovician-Silurian), Paraná (Devonian), Gondwana I (Carboniferous-Early Triassic), Gondwana II (Middle to Late Triassic), Gondwana III (Late Jurassic-Early Cretaceous), and Bauru (Late Cretaceous). The first three supersequences are represented by sedimentary successions defining transgressive-regressive cycles related to Paleozoic sea-level oscillations, while the others correspond to continental sediments with associated igneous rocks [71]. The accumulation of sedimentary and volcanic rocks in the basin occurred from the Ordovician to the Cretaceous, with a depocenter in the central-western portion, filling up to 8000 m in thickness [70].

In the Rio Grande do Sul and Santa Catarina states, four supersequences are recorded: Paraná, Gondwana I, II, and III. The Paraná Supersequence comprises a transgressive-regressive cycle, commencing with continental to transitional sandy sediments from the Lower Devonian Furnas Formation, overlaid by predominantly pelitic marine sediments of the Ponta Grossa Formation [71]. The Gondwana I Supersequence extends from the Upper Permian to the Lower Triassic, encompassing the largest sedimentary volume in the Paraná Basin with a maximum thickness of 2500 m [71]. This supersequence is comprised of a transgressive basal portion corresponding to the Itararé Group (Aquidauana, Lagoa Azul, Campo Mourão, Taciba Formations) and rocks from deltaic, marine, and coastal environments of the Guatá Group (Rio Bonito and Palermo formations - [73]). Subsequently, a regressive section accommodates a subsidence cycle corresponding to the Passa Dois Group (Irati, Serra Alta, Teresina, Rio do Rasto, and Pirambóia formations - [73]). The Gondwana I supersequence Guatá group holds significance in hydrogen geology due to the Sakmarian Rio Bonito Formation coals [74]. According to Milani [71], the Gondwana II supersequence is restricted to the Rio Grande do Sul state and is situated in a graben-type basin. This supersequence comprises the Rosário do Sul Group (Sanga do Cabral, Santa Maria, and Caturrita formations - [73]). The Gondwana III Supersequence is characterized as a Jurassic-Early Cretaceous supersequence and includes the stratigraphic interval in which eolian sandstones of the Botucatu Formation were deposited, overlain by the Serra Geral Formation, or Paraná-LIP (Large Igneous Province; [71,73]). This LIP consists of tholeiitic basalts to andesites, dating from 135 to 133 Ma [75]. Additionally, Cretaceous kimberlites [76,77] in the Paraná Basin are a potential geological source of hydrogen.

During the breakup of the Gondwana supercontinent, the basement structures of the Paraná Basin were intensely reactivated, resulting in the injection of a large volume of lava up to 2000 m over existing sediments, along with intrusions in the form of dikes and sills, intruding these sediments between the Paleozoic units of the basin [72,78]. This tectonic reactivation also gave rise to arches and flexures, with the Torres Syncline in the southeast of the basin being prominent. The Torres Syncline has an NW-SE orientation and a slight inclination to the NW (Fig. 1), connecting the Ponta Grossa arch to the north and the Rio Grande arch to the south [70]. Vertical movement faults are common on its surface, with the Torres-Posadas lineament being its main extension [79].

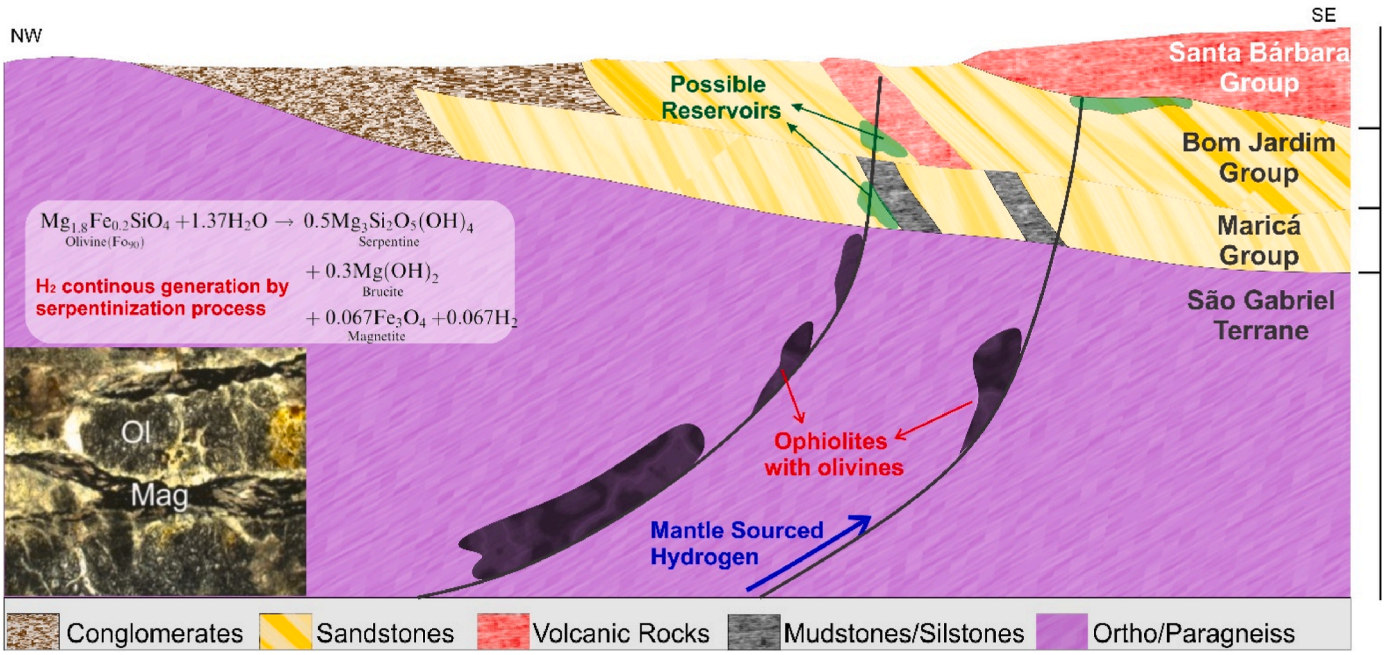

Fig. 2. Schematic model for possible H_2 sources in the Camaquã Basin region. The sources are related to core and mantle sources H_2 and by serpentinization process. Suture zones and crustal-scale faults could act as paths for continuous H_2 migration. Volcanic and thin-grained rocks of the Camaquã Basin could act as a seal for the H_2 Geological System. Left inset, thin section of Olivines in an ophiolite from São Gabriel Terrane [69].

5. Southmost Brazil hydrogen potential analyzes

This review presents the geological potential for studying hydrogen systems in the Rio Grande do Sul and Santa Catarina states. The primary objective is to elucidate prospective hydrogen resource systems characterized by their components, including source rocks, reservoirs, and seal rocks. We also reviewed all direct measurements of hydrogen carried out in wells drilled in the scope region.

5.1. Hydrogen potential in the Camaquã Basin

In the western section of the Rio Grande do Sul Shield, ophiolitic sequences from the São Gabriel Terrane lie beneath the volcano-sedimentary rocks of the Camaquã Basin (Fig. 2). These Tonian mafic-ultramafic rocks were part of the oceanic crust obducted during the closure of the Charrua Ocean ([56] and references therein). Six different ophiolitic sequences, composed of mafic-ultramafic rocks exhibiting tholeiitic signatures associated with mid-ocean ridge basalt (MORB), occur in this terrane. These sequences are characterized by the dominance of Fe–Mg minerals, particularly olivine. The metasomatic process of olivine minerals transforming in serpentine is a significant source of H_2 production [7,11].

These ophiolitic sequences, collectively named the Cerro do Ouro ophiolites [80], comprise six bodies in the region. The northwest bodies, Cambaizinho (“A" - in Fig. 1) and Cerro Mantiqueiras (“F" - in Fig. 1), represent obducted oceanic crust and mantle fragments metamorphosed in amphibolite facies, constituting the infrastructure of the Sao Gabriel Block [81]. Conversely, Bossoroca (“B" - in Fig. 1), Palma (“D" - in Fig. 1), and Ibaré (“E" - in Fig. 1), classified as the base of the superstructure, are also in amphibolite facies. All these bodies typically exhibit serpentinized regions ranging from 10 to 1000 m [81], and olivine is still frequently found [82].

The slow serpentinization process of olivines in low temperatures [28] could imply an ongoing H_2 production [11], potentially making them a continuous source of hydrogen. Additionally, another possible source of H_2 is through the oxidation of iron minerals [83], which could occur in the Banded Iron Formations (BIF) amalgamated with the mafic rocks of the Bossoroca ophiolite (“B" - in Fig. 1 [81]). These rocks lack the volume for commercial iron exploration but could serve as a minor contributor to H_2 reservoirs.

Due to the nature of ophiolitic bodies related to the Cerro do Ouro, the Ophiolitic Sequence can occur widespread as a basement of the Camaquã Basin in the São Gabriel Terrane domain. These ophiolitic bodies mark suture zones linked to lithospheric scale faults that could act as paths for fluids and gas migration to the Camaquã Basin. This framework is critical given that the olivine mineral transformation to serpentine occurs preferentially in temperatures up to 100 °C.

Besides the source rock, the Camaquã Basin also hosts deposits with reservoirs and seal rocks, characterized by a volcano-sedimentary sequence. The reservoirs occur mainly related to the fluvial-deltaic deposits composed of fine-to coarse-grained and conglomeratic sandstones of Maricá, Bom Jardim, and Santa Bárbara groups. Meanwhile, the seal occurs as the mudstone sequences of Bom Jardim and Santa Bárbara groups and the volcanic rocks of Hilário, Acampamento Velho, and RodeioVelho formations.

The Camaquã Basin fluvial-deltaic deposits present variable values of organic content. Metric layers of mudstones host microbial mats and organic-walled microfossils with the original carbonaceous matter preserved. Organic-rich layers presenting total organic carbon (TOC) values between 0.06 and 1.15% were also found [84]. Due to scarce life forms during the Precambrian period, Ediacaran rocks present low TOC values [85–87]. Besides that, the Camaquã Basin presents good values for a Precambrian basin, with better values of TOC in Bom Jardim and Santa Bárbara sequences. This organic content can be considered as a possible source of thermogenic hydrogen. Due to the lack of information regarding the maturation degree, further research is demanded to better understand this source rock concerning H_2 production by thermogenesis.

The speculative mantle-sourced hydrogen is also possible for the Camaquã Basin due to the widespread presence of lithospheric faults that mark the suture zones (ophiolitic rocks). The connection of deeper levels of the crust with the surface is expected in this region (Fig. 2). As well the serpentinization process could generated H_2 in the region, those structures can also be an important path for mantle H_2.

Regarding the radiolysis potential for H_2 generation in the Camaquã Basin region, there is no sufficient support for this. The Uranium channel

gamma-ray spectrometry map in the region reveals no significative values for the São Gabriel Terrane and even lower values for the ophiolitic associations (Fig. 3). Ediacaran potassium-rich granitoids occur in the east portion of the basin, surrounded by metamorphic rocks, and had no geological contact with the Camaquã Basin. The low permeability and porosity of these rocks also make the H_2 concentrations by radiolysis in commercial levels improbable. These granitoids also could produce H_2 through biotite hydration [15], but the same reservoir issues affect this possibility.

In the Camaquã Basin, we accessed two stratigraphic well cores (CQP-1 and CQP-2) data stored by CPRM (Brazilian Geological Survey). These dry wells had no H_2 measurement or log that could help us evaluate their potential (as neutron log). It is worth noting that the wells have been drilled on the eastern side of the basin despite the theoretical source rocks being mostly located on the western side.

As a hydrogen-possible system, the Camaquã Basin presents three possible sources. Two of these are related to the H_2 migration through deeper faults. These lithospheric faults can work as a path for mantle hydrogen gas. Also, at the lithospheric level, continued generation by olivine to serpentine transformation in the ultramafic rocks has the highest potential for this area. In addition, the presence of organic-rich levels in the middle sequences of the Camaquã Basin can be a possible thermogenic source of H_2.

5.2. Hydrogen potential in the southernmost Paraná Basin

Coal and organic-rich shales are a significant factor in the exploration of hydrogen gas. The first recorded analysis of a natural gas sample containing hydrogen gas is from a coal mine and dates to 1888 [7]. Also, Smith et al. [11] pointed out that before the discoveries of hydrocarbons in the North Sea, the United Kingdom's domestic gas was generated from bituminous coal, known as 'town gas,' which hydrogen gas corresponds to about 51%. In addition, Zgonnik [7] documented ten occurrences of H_2 in the free gasses of coal basins that were superior to 10%.

Greenwell [88] demonstrated that coalification removes hydrogen atoms from the coal structure. While wood contains approximately 12% hydrogen in its structure, anthracite has less than 2%. Naturally, we did not expect that the entirety of this hydrogen would be transformed into hydrogen gas. However, this geological environment should be one of the main targets for hydrogen geology research.

The Rio Grande do Sul and Santa Catarina states host eight known coalfields of the Rio Bonito Formation: Candiota, Iruí, Leão-Butiá, Guaíba, Faxinal, Morungava-Chico Lomã, Santa Terezinha, and Criciúma. All these are places with outcrops or a shallow occurrence of the Rio Bonito Formation (Figs. 4 and 5). However, the deep occurrence of coals occurs along a large part of the eastern border of the Paraná Basin. These coals originated through organic matter accumulation from the *Glossopteris* flora during the Sakmarian and Kungurian periods and are widespread in the region [74]. Also, in the Paraná Basin, the Irati Formation shales (TOC 8%–13% with peaks reaching 23%) and Ponta Grossa Formation shales (TOC 0.5%–2.5% [89]) could be important H_2 sources. Irati Formation shales were widely intruded by Cretaceous sills related to Paraná Lip, and their TOC maturity reaches the gas dry window [89].

The primary challenge associated with coalfields lies in their low porosity and the absence of trapping mechanisms within the shallow coal seams. However, the optimal application of coal resources for hydrogen production emerges when these coalfields are situated at significant depths and exhibit connections to potential reservoirs, enhancing their hydrogen generation and storage viability. This scenario will likely occur below the Serra Geral Formation in the Rio Grande do Sul and Santa Catarina states.

We reviewed 41 ANP legacy wells (exploratory and stratigraphic

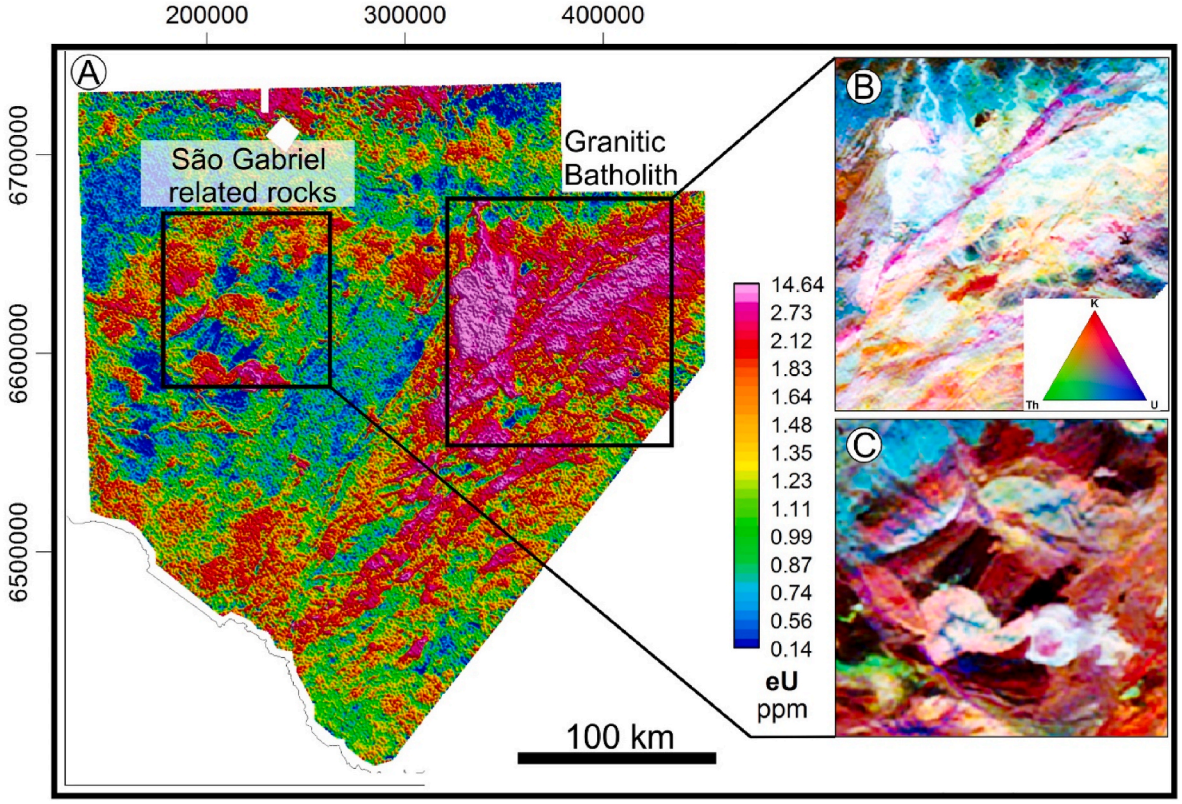

Fig. 3. Uranium channel gamma-ray spectrometry map of Sul-Riograndense Shield. The outcropping São Gabriel rocks show low U concentration, reducing the radiolysis potential in this region, given that these rocks may correspond to the Camaquã Basin basement in this sector. High U concentrations were found in the granitic batholith. Due to the northward extension of these batholiths below Paraná Basin, a major potential of radiolysis as a secondary source is plausible.

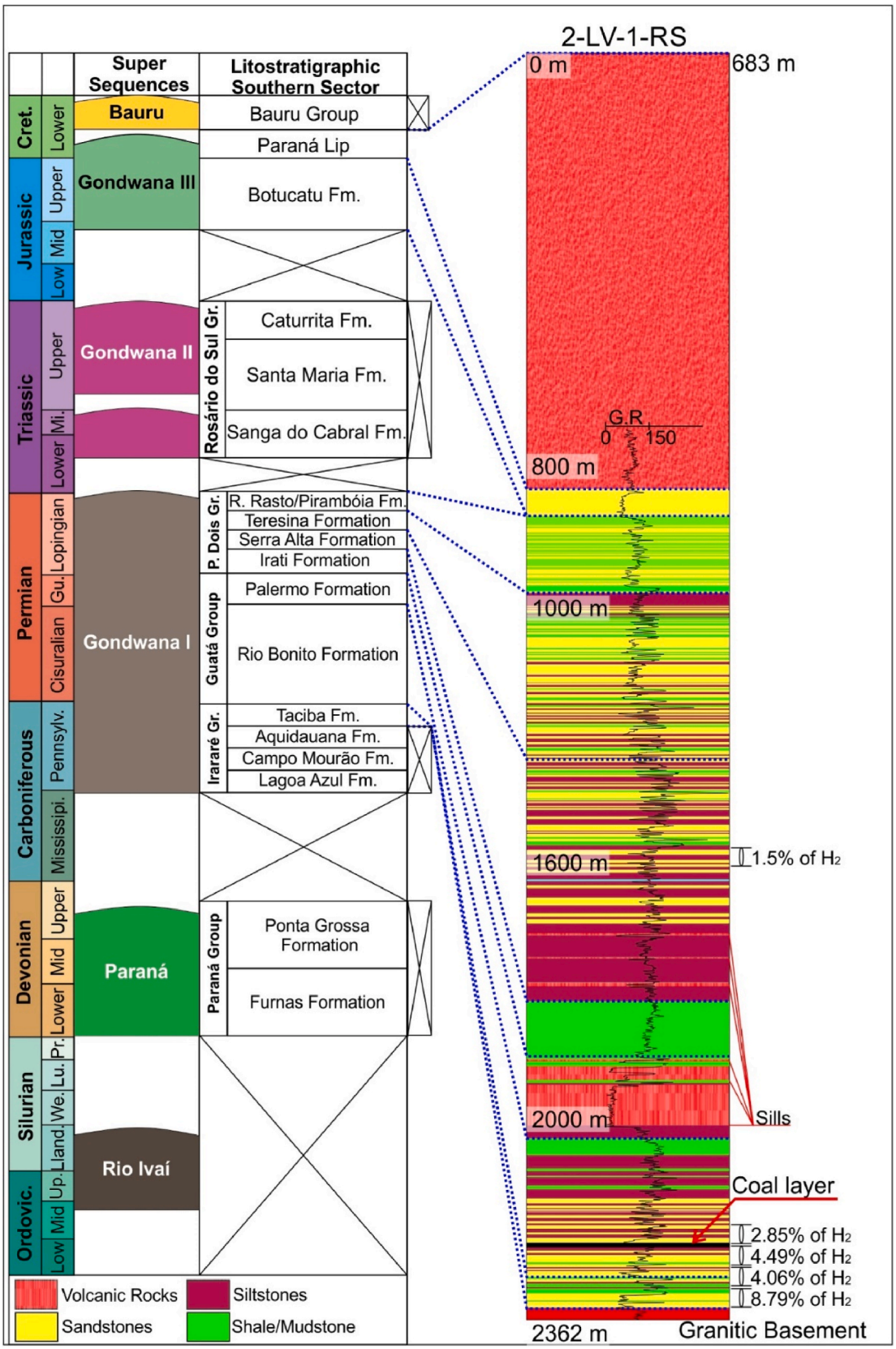

Fig. 4. Summary of Paraná Basin and well 2-LV-1-RS. On the left is the typical column for Paraná Basin in the southern sector of Paraná Basin (modified from [90]). On the right is the lithological profile of well 2-LV-1-RS. Blue dashed lines mark the top and bottom of the formation. H2 results in the formation test were identified on the right side of the well profile (data from ANP – Brazilian National Agency for Petroleum, Natural Gas and Biofuels). (For interpretation of the references to colour in this figure legend, the reader is referred to the Web version of this article.)

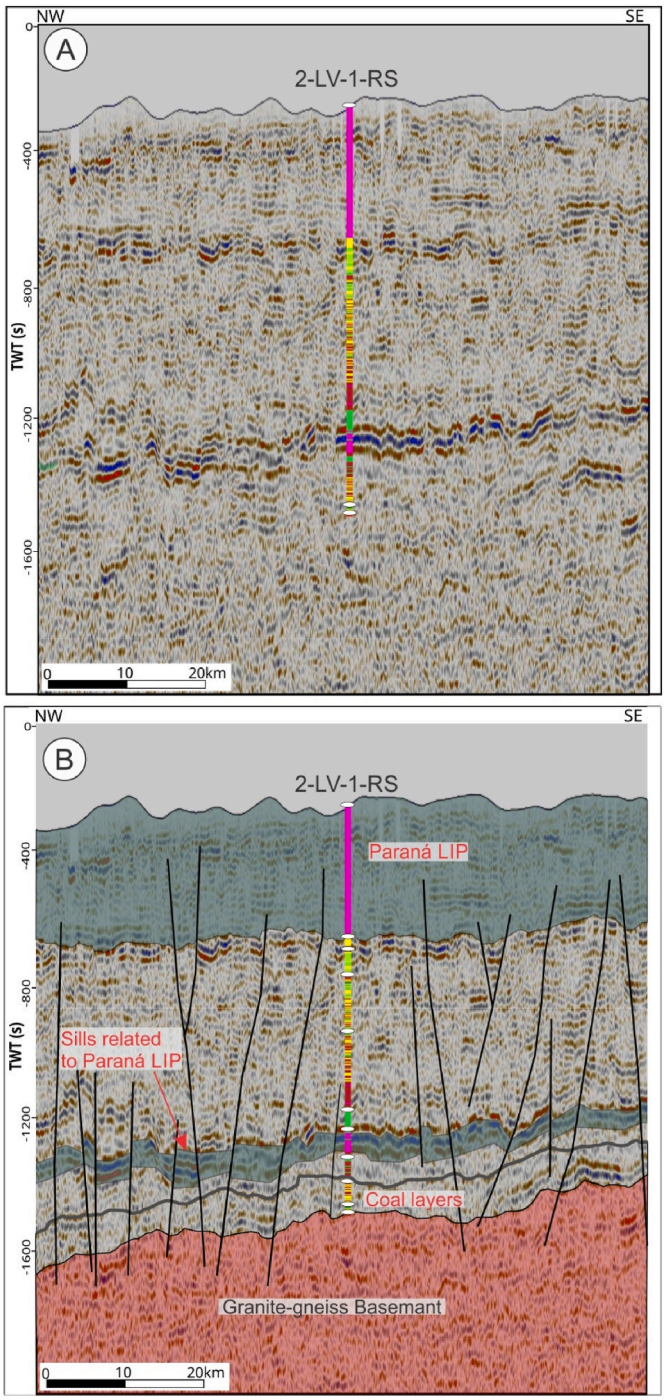

Fig. 5. The seismic line near well 2-LV-1-RS shows the geometry of layers of interest and the intrusive rocks overlying rich organic matter layers and coal deposits. The faults form an important path to leaking natural hydrogen from the deep layers to the Botucatu sandstones trapped for the Serra Geral basalts.

wells, all then dry or with noncommercial natural gas volumes) and found four wells with occurrences of free H_2 associated with natural gas. The occurrences range from 0,14% to 8,79%. In the other wells, either no analysis of the free gas present was conducted, or the levels of hydrogen detected were considered insignificant. On the well 2-LV-1-RS, in the interval 1487.13–1520 m, free hydrogen gas was detected in the Teresina Formation with free H2 content ranging from 0.86 to 3.23%. In the same well, free hydrogen gas was found in the sandstones of the Rio Bonito and Taciba formations, in the interval of 2313.08–2334.50 m, the H_2 values range from 2.85 to 8.79%. On the well, 1-TV2-SC free hydrogen was detected on the Furnas Formation sandstone depths of 2098–2917 m. The H_2 content ranges from 0.38 to 3.06%. In well 1-TV-3-SC, the hydrogen gas is hosted on the Rio Bonito Formation, at the depth interval of 2014–2018 m, and has just one measurement of H_2 content with a value of 2,43%. On the well 2-PI-01-SC, the hydrogen gas was detected in the Rio Bonito Formation at intervals 2078–2109 m (H_2 concentrations, single measurement of 0.14%). Still, in the well 2-PI-01-SC, two measurements of H_2 concentrations were made in the Itararé Group, in the intervals 2110.10–2138.90 m and free H_2 ranging from 0.71 to 1.04%. Despite the occurrence throughout the sedimentary column between the Furnas to Teresina formations, higher concentrations were found in the sandstones of the Rio Bonito Formation interval. It is important to note that this formation hosts the Paraná Basin coal deposits. Deeper concentration levels can also be related to the organic-rich matter deposits of the Ponta Grossa Formation that can supply the basin with H_2.

The well with the major free H_2 concentration is the 2-LV-1-RS (ranging from 0.86 to 8.79%; Figs. 4 and 5). This well was carried out to understand better the north flank of the Torres Syncline (Fig. 1). The geometry of the syncline could induce gas migration to the top of the flank of the structure, which can cause anomalous values of hydrogen gas. We expect an high potential of the region along the strike of the north flank of the Torres Syncline due to the direct observations.

5.2.1. *Hydrogen anomalies origin*

The origin of this hydrogen gas in the Paraná Basin is still unknown. However, we analyze the possibilities through the four mechanisms described in the Hydrogen Systems section.

Radiolysis is a controversial hydrogen formation mechanism but could still be a minor H_2 source. The eastern sector of Paraná Basin rests over the Dom Feliciano Belt granitoids (East of Dorsal de Canguçu Shear Zone - Fig. 1). High total gamma ray counts can indicate geological environments favorable for hydrogen accumulation. The radioactive decay from radioelements (especially uranium) can split water molecules to generate H_2 via radiolysis [43]. These granitoids in their outcropping area reveal high uranium, potassium, and thorium concentrations (Fig. 3a and b). For the wells where H_2 measurements were reported, just one reached the basement (Well 2-LV-1-RS), which was described as a porphyry granite with phaneritic matrix, porphyry-granular texture with quartz, biotite, hornblende, plagioclase and phenocrysts 5 cm–10 cm long of orthoclase. Gamma-ray measurements carried out in the well measured 120 cps at the basement interval (Fig. 4).

Rock alteration could occur and produce H_2 in the basin basement. The granitoids mentioned before possibly produce H_2 by rock alteration. Reactions such as biotite hydration [15] could produce an amount of H_2 superior to radiolysis. We assume that this is not the main H_2 source due to its relation with natural gas. All H_2 observed occurrences in the Paraná Basin are related to natural gas.

Core or mantle origin could be a source. According to [91], natural gas could be generated by an abiogenic mantelic source. The noncommercial volumes of natural gas found in these wells could be of abiogenic origin and, consequently, the H_2. The wells also recorded the He concentrations; unfortunately, no isotopic study was carried out in the helium, which could prove the mantle's origin or not. Regardless, in the well 2-LV-1-RS, the one with the most analyses made and with the highest values of H_2 anomalies, hydrogen gas shows an inverse proportion with He (Fig. 6). These results are the opposite of other anomalies obtained in studies carried out in Eurasia ([7] and references therein). The highest H_2 anomalies found in Parana Basin are also 52 km away from the main known large shear zone (Fig. 1), and a mantle origin is unlikable in this scenario. A possibility is the existence of kimberlite that could work as an H_2 conduit. The occurrence of kimberlite in the southwest of Parana Basin ([76,77] - Fig. 1) points to the possibility of more intrusive bodies below the Parana LIP. The proposed intrusions could fracture the region, as reported in kimberlites associated with H_2

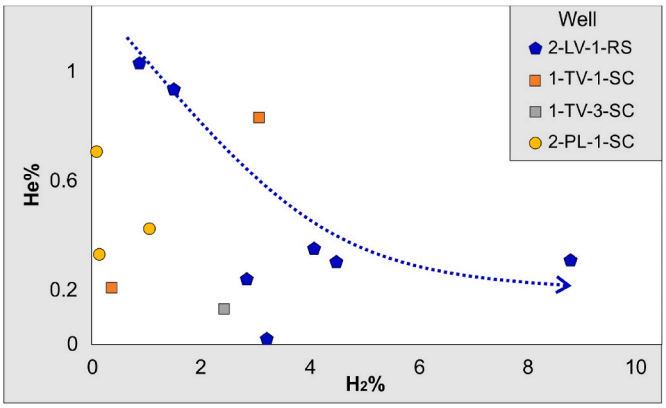

Fig. 6. H_2 versus He content plot in the Paraná Basin wells. Well, 2-LV-1-RS shows an inverse correlation between H_2 vs He.

anomalies ([7] and references therein). The intrusions and the related structures represent an important factor for the potential of H_2 in the Paraná Basin.

The highest H_2 anomalies were observed in the sandstones of the Rio Bonito and Taciba formations. The Rio Bonito Formation is renowned for its coal reserves estimated at 32 billion tons ([92] and references therein) with vitrinite reflectance (Ro) values ranging from 0.5 to 1%, [93,94]. Anomalous Ro values from 1 to 5% occur near magmatic sill intrusions [92,94]. This Ro range indicates that the maturation of organic matter is between the oil window (Ro > 0.5% [95]) and a thermally over-mature state (Ro > 1.9% [95]). The presence of over-matured organic rocks, mostly related to sill intrusions [92] in the Rio Bonito Formation holds significant potential for hydrogen prospecting, as this interval is known to produce H_2 [46,47]. Hand [3] raised concerns that H_2 consumption for hydrocarbon formation is no longer relevant for this over-matured interval due to the absence of hydrocarbon formation. However, the vitrinite reflectance and intrusions framework variations should be spatialized to better understand this H_2 system potential. Due to this, based on geological context, we assume that the up to 8% H_2 concentration is mostly related to the natural H_2 generated by the continuous maturation and evolution of the coal and shale layers.

H_2 generation related to rich organic matter shales from Ponta Grassa, Taciba, and Irati formations can also contribute as a source of H_2 in the Paraná Basin. These formations experienced similar maturation conditions, and the Irati Formation is widely intruded by magmatic sill, reaching high Ro values [89]. The anomalies observed in the gas analyses from north of Santa Catarina (1-TV-2-SC and 1-TV-3-SC) were related to the Furnas Formation stratigraphically below the coal layers. Due to the nature of the basin, stratigraphic inversions are not plausible, reinforcing the potential for H_2 generation in shales of Ponta Grossa Formation or even by fault migration. On the other hand, units such as the Teresina Formation present low TOC content (<0.3% [96]), and its potential is negligible.

6. Conclusions

Hydrogen gas related to natural gas was detected in four legacy wells in the Paraná Basin, located in the states of Rio Grande do Sul and Santa Catarina. Its values range from 0.14% to 8.79%. We assume that H_2 is mostly related to the maturation process of organic matter in Rio Bonito, Taciba and Ponta Grossa Formations due to two main reasons: I) the H_2 shows a negative correlation with He, which is different from the anomalies found in the literature related to the mantle; II) the H_2 anomaly occurs always with natural gas, due to this we propose that the process does not occur due to rock alteration (such biotite hydration) or radiolysis. However, further He isotope studies are essential to understand the H_2 nature. The regions surrounding the wells should be analyzed on the surface to identify fairy circles to understand the extension of the anomaly. However, it is essential to recognize the potential challenges posed by the prevalent agricultural activities in the region, which can significantly alter soil physically and chemically. Finally, we understand that the Camaquã Basin holds potential in the western region, mostly related to the ophiolites. To defog its potential, the dynamics and temporal aspects of serpentinization within the basement rocks of this region should be understood in further research.

Declaration of competing interest

The authors declare that they have no known competing financial interests or personal relationships that could have appeared to influence the work reported in this paper.

The authors declare the following financial interests/personal relationships which may be considered as potential competing interests.

Acknowledgments

The authors thank the ANP (Brazilian National Agency for Petroleum, Natural Gas and Biofuels) for providing access to the Paraná Basin seismic and well-log data. FCJ thanks CNPq (National Council for Scientific and Technological Development) for grant #4081942021-9. We thanks for the anonymous revisors for its constructive suggestions.

References

[1] Zhou H, Dai J, Chen X, Hu B, Wei H, Cai HH. Understanding innovation of new energy industry: observing development trend and evolution of hydrogen fuel cell based on patent mining. Int J Hydrogen Energy 2023;52:548–60.
[2] Oliveira RCD. Panorama do hidrogênio no Brasil. IPEA; 2022. https://doi.org/10.38116/td2787.
[3] Hand E. Hidden hydrogen. Science 2023;379(6633):630–6.
[4] Ball PJ, Czado K. Natural hydrogen: the new frontier. Geoscientist, March; 2022.
[5] Prinzhofer A, Cissé CST, Diallo AB. Discovery of a large accumulation of natural hydrogen in Bourakebougou (Mali). Int J Hydrogen Energy 2018;43(42):19315–26.
[6] Rigollet C, Prinzhofer A. Natural hydrogen: a new source of carbon-free and renewable energy that can compete with hydrocarbons. First Break 2022;40(10):78–84.
[7] Zgonnik V. The occurrence and geoscience of natural hydrogen: a comprehensive review. Earth Sci Rev 2020;203:103140.
[8] Prinzhofer A, Moretti I, Françolin J, Pacheco C, d'Agostino A, Werly J, Rupin F. Natural hydrogen continuous emission from sedimentary basins: the example of a Brazilian H2-emitting structure. Int J Hydrogen Energy 2019;44(12):5676–85.
[9] Angino EE, Coveney RMJ, Goebel ED, Zeller EJ, Dreschhoff GAM. Hydrogen and nitrogen - origin, distribution, and abundance, a followup. Oil Gas J 1984;82(142.146).
[10] Bohdanowicz C. Natural gas occurrences in Russia (USSR). AAPG (Am Assoc Pet Geol) Bull 1934;18(6):746–59.
[11] Smith NJP, Shepherd TJ, Styles MT, Williams GM. Hydrogen exploration: a review of global hydrogen accumulations and implications for prospective areas in NW Europe. Geol Soc Lond Petrol Geol Conf Series 2005;6(1):349–58. The Geological Society of London.
[12] Maiga O, Deville E, Laval J, Prinzhofer A, Diallo AB. Characterization of the spontaneously recharging natural hydrogen reservoirs of Bourakebougou in Mali. Sci Rep 2023;13(1):11876.
[13] Guélard J, Beaumont V, Rouchon V, Guyot F, Pillot D, Jézéquel D, Deville E. Natural H2 in K ansas: deep or shallow origin? G-cubed 2017;18(5):1841–65.
[14] Boreham CJ, Edwards DS, Czado K, Rollet N, Wang L, van der Wielen S, Henson PA. Hydrogen in Australian natural gas: occurrences, sources and resources. The APPEA J 2021;61(1):163–91.
[15] Murray J, Clément A, Fritz B, Schmittbuhl J, Bordmann V, Fleury JM. Abiotic hydrogen generation from biotite-rich granite: a case study of the Soultz-sous-Forêts geothermal site, France. Appl Geochem 2020;119:104631.
[16] Moretti I, Geymond U, Pasquet G, Aimar L, Rabaute A. Natural hydrogen emanations in Namibia: field acquisition and vegetation indexes from multispectral satellite image analysis. Int J Hydrogen Energy 2022;47(84):35588–607.
[17] Prinzhofer A, Cacas-Stentz MC. Natural hydrogen and blend gas: a dynamic model of accumulation. Int J Hydrogen Energy 2023;48(57):21610–23.
[18] Yang X, Keppler H, Li Y. Molecular hydrogen in mantle minerals. Geochem Perspect Lett 2016;2(2):160–8.
[19] Rohrbach A, Ballhaus C, Golla-Schindler U, Ulmer P, Kamenetsky VS, Kuzmin DV. Metal saturation in the upper mantle. Nature 2007;449(7161):456–8.

[20] Smith EM, Shirey SB, Nestola F, Bullock ES, Wang J, Richardson SH, Wang W. Large gem diamonds from metallic liquid in Earth's deep mantle. Science 2016;354 (6318):1403–5.
[21] Williams Q, Hemley RJ. Hydrogen in the deep Earth. Annu Rev Earth Planet Sci 2001;29(1):365–418.
[22] Poirier JP. Light elements in the Earth's outer core: a critical review. Phys Earth Planet In 1994;85(3–4):319–37.
[23] Isaev EI, Skorodumova NV, Ahuja R, Vekilov YK, Johansson B. Dynamical stability of Fe-H in the Earth's mantle and core regions. Proc Natl Acad Sci USA 2007;104 (22):9168–71.
[24] Ikuta D, Ohtani E, Sano-Furukawa A, Shibazaki Y, Terasaki H, Yuan L, Hattori T. Interstitial hydrogen atoms in face-centered cubic iron in the Earth's core. Sci Rep 2019;9(1):7108.
[25] Truche L, McCollom TM, Martinez I. Hydrogen and abiotic hydrocarbons: molecules that change the world. Elements: An Int Mag Mineral Geochem Petrol 2020;16(1):13–8.
[26] Worman SL, Pratson LF, Karson JA, Schlesinger WH. Abiotic hydrogen (H2) sources and sinks near the Mid-Ocean Ridge (MOR) with implications for the subseafloor biosphere. Proc Natl Acad Sci USA 2020;117(24):13283–93.
[27] Han S, Tang Z, Yang C, Xie L, Xiang C, Horsfield B, Wang C. Genesis and energy significance of hydrogen in natural gas. Nat Gas Geosci 2021;32(9):1270–84.
[28] Berndt ME, Allen DE, Seyfried Jr WE. Reduction of CO2 during serpentinization of olivine at 300 C and 500 bar. Geology 1996;24(4):351–4.
[29] Arrouvel C, Prinzhofer A. Genesis of natural hydrogen: new insights from thermodynamic simulations. Int J Hydrogen Energy 2021;46(36):18780–94.
[30] Neal C, Stanger G. Hydrogen generation from mantle source rocks in Oman. Earth Planet Sci Lett 1983;66:315–20.
[31] Seewald JS. Aqueous geochemistry of low molecular weight hydrocarbons at elevated temperatures and pressures: constraints from mineral buffered laboratory experiments. Geochem Cosmochim Acta 2001;65(10):1641–64.
[32] Marcaillou C, Munoz M, Vidal O, Parra T, Harfouche M. Mineralogical evidence for H2 degassing during serpentinization at 300 C/300 bar. Earth Planet Sci Lett 2011; 303(3–4):281–90.
[33] Schrenk MO, Brazelton WJ, Lang SQ. Serpentinization, carbon, and deep life. Rev Mineral Geochem 2013;75(1):575–606.
[34] Lollar BS, Onstott TC, Lacrampe-Couloume G, Ballentine CJ. The contribution of the Precambrian continental lithosphere to global H2 production. Nature 2014;516 (7531):379–82.
[35] Milesi V, Guyot F, Brunet F, Richard L, Recham N, Benedetti M, Prinzhofer A. Formation of CO2, H2 and condensed carbon from siderite dissolution in the 200–300 C range and at 50 MPa. Geochem Cosmochim Acta 2015;154:201–11.
[36] Etiope G, Whiticar MJ. Abiotic methane in continental ultramafic rock systems: towards a genetic model. Appl Geochem 2019;102:139–52.
[37] Osselin F, Soulaine C, Fauguerolles C, Gaucher EC, Scaillet B, Pichavant M. Orange hydrogen is the new green. Nat Geosci 2022;15(10):765–9.
[38] Boyd AW, Willis C, Miller OA. The radiolysis of water vapor at very high dose rates. I. Hydrogen yields from H2O, H2O–HCl, and H2O–HBr mixtures. Can J Chem 1973;51(24):4048–55.
[39] Dubessy J, Poty B, Ramboz C. Advances in COHNS fluid geochemistry based on micro-Raman spectrometric analysis of fluid inclusions. Eur J Mineral 1989;1(4): 517–34.
[40] Dzaugis ME, Spivack AJ, Dunlea AG, Murray RW, D'Hondt S. Radiolytic hydrogen production in the subseafloor basaltic aquifer. Front Microbiol 2016;7:76.
[41] Bouquet A, Glein CR, Wyrick D, Waite JH. Alternative energy: production of H2 by radiolysis of water in the rocky cores of icy bodies. Astrophys J Lett 2017;840(1): L8.
[42] Parnell J, Blamey N. Global hydrogen reservoirs in basement and basins. Geochem Trans 2017;18:1–8.
[43] Truche L, Joubert G, Dargent M, Martz P, Cathelineau M, Rigaudier T, Quirt D. Clay minerals trap hydrogen in the Earth's crust: evidence from the Cigar Lake uranium deposit, Athabasca. Earth Planet Sci Lett 2018;493:186–97.
[44] Boreham CJ, Davies JB. Carbon and hydrogen isotopes of the wet gases produced by gamma-ray-induced polymerisation of methane: insights into radiogenic mechanism and natural gas formation. Radiat Phys Chem 2020;168:108546.
[45] Horsfield B, Mahlstedt N, Weniger P, Misch D, Vranjes-Wessely S, Han S, Wang C. Molecular hydrogen from organic sources in the deep Songliao Basin, PR China. Int J Hydrogen Energy 2022;47(38):16750–74.
[46] Mahlstedt N, Horsfield B, Weniger P, Misch D, Shi X, Noah M, Boreham C. Molecular hydrogen from organic sources in geological systems. J Nat Gas Sci Eng 2022;105:104704.
[47] Boreham CJ, Edwards DS, Feitz AJ, Murray AP, Mahlstedt N, Horsfield B. Modelling of hydrogen gas generation from overmature organic matter in the Cooper Basin, Australia. The APPEA J 2023;63(2):S351–6.
[48] Chauvet F, Sapin F, Geoffroy L, Ringenbach JC, Ferry JN. Conjugate volcanic passive margins in the austral segment of the South Atlantic–Architecture and development. Earth Sci Rev 2021;212:103461.
[49] Chemale Jr F, Lavina ELC, Carassai JJ, Girelli TJ, Lana C. Andean orogenic signature in the Quaternary sandy barriers of Southernmost Brazilian Passive Margin–paradigm as a source area. Geosci Front 2021;12(4):101119.
[50] Chemale Jr, F. Evolução geológica do escudo sul-rio-grandense. Geologia do Rio Grande do Sul; 2000. p. 13–52.
[51] Hartmann LA, Chemale Jr F, Philipp RP. Evolução geotectônica do Rio Grande do Sul no pré-cambriano. Ianuzzi R. & Frantz JC.(Org.) 2007;50:97–123.
[52] Philipp RP, Pimentel MM, Chemale Jr F. Tectonic evolution of the Dom Feliciano belt in southern Brazil: geological relationships and U-Pb geochronology. Braz J Genet 2016;46:83–104.
[53] Babinski M, Chemale Jr F, Hartmann LA, Van Schmus WR, Carlos da Silva L. Juvenile accretion at 750–700 Ma in southern Brazil. Geology 1996;24(5):439–42.
[54] Leite JA, Hartman LA, Mcnaughton NJ, Chemale Jr F. SHRIMP U/Pb zircon geochronology of Neoproterozoic juvenile and crustal-reworked terranes in southernmost Brazil. Int Geol Rev 1998;40(8):688–705.
[55] Hartmann LA, Philipp RP, Santos JOS, McNaughton NJ. Time frame of 753–680 Ma juvenile accretion during the São Gabriel orogeny, southern Brazilian Shield. Gondwana Res 2011;19(1):84–99.
[56] Hartmann LA, Werle M, Michelin CR, Lana C, Queiroga GN, Castro MP, Arena KR. Proto-Adamastor ocean crust (920 Ma) described in Brasiliano Orogen from coetaneous zircon and tourmaline. Geosci Front 2019;10(4):1623–33.
[57] Paim PSG, Chemale Jr F, Lopes RDC. A bacia do Camaquã. Geologia do Rio Grande do Sul; 2000. p. 231–74.
[58] Hartmann LA, Santos JOS, McNaughton NJ. Detrital zircon U-Pb age data and precambrian provenance of the paleozoic Guaritas formation, southern Brazilian Shield. Int Geol Rev 2008;50:364–74.
[59] Almeida F. Diferenciação Tectônica da Plataforma Brasileira. Congresso Brasileiro de Geologia 1969;1:29–46. Salvador, 1969.
[60] Almeida F, Hasui Y, Brito Neves B. The upper precambrian of Southsouth America, vol. 7. Boletim IG/USP; 1976. p. 45–80. https://doi.org/10.11606/issn.2316-8978.v7i0p45-80.
[61] Almeida F, Hasui Y, Brito Neves B, Fuck R. Brazilian structural provinces: an introduction. Earth Sci Rev 1981;17(1–2):1–29. https://doi.org/10.1016/0012-8252(81)90003-9.
[62] Chemale Jr F, Hartmann LA, Silva LC. Stratigraphic and tectonism of precambrian to early paleozoic units. Acta Geol Leopoldensia 1995;42(XVIII):5–117.
[63] Fragoso-César ARS, Lavina EL, Paim PSG, Faccini UF. A antefossa molássica do cinturão Dom Feliciano no escudo do Rio Grande do Sul. Congresso Brasileiro de Geologia 1984;33:3272–83. Brasil.
[64] Fragoso-César AR, Fambrini G, Paes de Almeida R, Pelosi A, Janikian L, Riccomini C, Machado R, Nogueira A, Saes G. The Camaquã extensional basin: Neoproterozoic to early Cambrian sequences in Southernmost Brazil. Rev Bras Geociencias 2000;30:438–41.
[65] Wernick E, Hasui Y, Brito Neves BB. As regiões de dobramentos nordeste e sudeste. Congresso Brasileiro de Geologia, Brasil 1978;30(6):2493–506.
[66] Paim PSG, Junior FC, Wildner W. Estágios evolutivos da Bacia do Camaquã (RS). Ciência e Natura; 2014. p. 183–93.
[67] Lehn I, Horodyski RS, Paim PSG. Marine and non-marine strata preserving Ediacaran microfossils. Sci Rep 2019;9(1):9809.
[68] Lehn I, Paim PSG, Chemale Jr F. Integrated correlation of the Camaquã Basin (southernmost Brazil) with other ediacaran units of southwestern proto-gondwana. J South Am Earth Sci 2022;116:103812.
[69] Werle M. Evolução mineralógica e isotópica da porção sul do ofiolito Bossoroca, vol. 129. terreno São Gabriel; 2019.
[70] Zalán PV, Wolff SJCJ, Conceição JDJ, Marques A, Astolfi MAM, Vieira IS, Zanotto OA. Bacia do Paraná. Origem e evolução das bacias sedimentares. 1990. p. 135–68.
[71] Milani EJ. Evolução tectono-estratigráfica da Bacia do Paraná e seu relacionamento com a geodinâmica fanerozóica do Gondwana sul-ocidental (Doctoral dissertation. Universidade Federal do Rio Grande do Sul; 1997.
[72] Milani EJ, Melo JHG, Souza PA, Fernandes LA, França AB. Bacia do Paraná. Bol Geociencias Petrobras 2007;15:265–87.
[73] Milani EJ, França AB, Schneider RL. Bacia do Paraná. Bol Geociencias Petrobras 1994;8(1):69–82. Rio de Janeiro.
[74] Cagliari J, Lavina ELC, Philipp RP, Tognoli FMW, Basei MAS, Faccini UF. New Sakmarian ages for the Rio Bonito formation (Paraná Basin, southern Brazil) based on LA-ICP-MS U–Pb radiometric dating of zircons crystals. J S Am Earth Sci 2014; 56:265–77.
[75] Gomes AS, Vasconcelos PM. Geochronology of the Paraná-Etendeka large igneous province. Earth Sci Rev 2021;220:103716.
[76] Scheibe LF, Furtado SMA, Comin-Chiaramont P, Gomes CB. Cretaceous alkaline magmatism from Santa Catarina state, southern Brazil. In: Comin-Chiaramontim P, Gomes CB, editors. Mesozoic to cenozoic alkaline magmatism in the Brazilian platform. São Paulo: Edusp/Fapesp; 2005. p. 523–71.
[77] Conceição RV, Carniel LC, Jalowitzki T, Gervasoni F, Cedeño DG. Geochemistry and geodynamic implications on the source of paraná-etendeka large igneous province evidenced by the 128 Ma rosário-6 kimberlite, southern Brazil. Lithos 2019;328:130–45.
[78] Milani EJ, Thomaz Filho A. Sedimentary basins of south America. Tect Evol S Am 2000;31:389–449.
[79] Vitorello I, Padilha AL. Mapping of high electrical condutivity on the Torres Syncline hinge, southastern Paraná Basin. Rev Bras Geociencias 2000;30(3):535–7. São Paulo.
[80] Goñi JC. Origine des roches ultrabasiques et serpentineuses du précambrian de Rio Grande do Sul (Brèsil): mode de gisement et mineralizacions. Boletim da Escola de Geologia da URGS 1962;12:1–89. Porto Alegre.
[81] Hartmann LA, Massuda AJ, Cerva-Alves T, Lana C, Leandro CG, Savian JF. Aeromagnetometry and aerogammaspectrometry integrated with U-Pb zircon geochronology of northern Bossoroca ophiolite, Brasiliano Orogen. An Acad Bras Ciências 2021;93.
[82] Hartmann LA, Chemale Jr F. Mid amphibolite facies metamorphism of harzburgites in the Neoproterozoic Cerro Mantiqueiras Ophiolite, southernmost Brazil. An Acad Bras Ciências 2003;75:109–28.
[83] Geymond U, Ramanaidou E, Lévy D, Ouaya A, Moretti I. Can weathering of banded iron formations generate natural hydrogen? Evidence from Australia, Brazil and South Africa. Minerals 2022;12(2):163.

[84] Lehn I, Paim PSG, Chemale F. From the sea to the land: How microbial mats dominated marine and continental environments in the Ediacaran Camaquã Basin, Brazil. Geosyst Geoenviron 2024;3(3):100283. https://doi.org/10.1016/j.geogeo.2024.100283.
[85] Luening S, Kolonic S, Geiger M, Thusu B, Bell J, Craig J. Infracambrian hydrocarbon source rock potential and petroleum prospectivity of NW Africa, vol. 326. Geological Society, London, Special Publications; 2009. p. 157–80. https://doi.org/10.1144/SP326.8.
[86] Zhu G, Du D, Chen W, Sun Q, Li T, Zhang Z, Chen Z. Discovery of Precambrian thick black mudstones and its implication for hydrocarbon exploration in the southwest Tarim Basin. Petrol Res 2018;3(2):124–31. https://doi.org/10.1016/j.ptlrs.2018.06.006.
[87] Woltz CR, Porter SM, Agić H, Dehler CM, Junium CK, Riedman LA, Hodgskiss MSW, Wörndle S, Halverson GP. Total organic carbon and the preservation of organic-walled microfossils in Precambrian shale. Geology 2020;49(5):556–60. https://doi.org/10.1130/G48116.1.
[88] Greenwell A, Elsden JV, Seyler CA. Analyses of British coals and coke, and the characteristics of chief coal seams worked in the British isles. With commercial indexs and map. The Chichester: Press; 1907.
[89] Martins CMS, Cerqueira JR, Celino JJ, Ribeiro HJPS, Garcia KS, de Oliveira OMC, Queiroz AFDS. Burial history and thermal maturity of the atypical petroleum system of the Paraná Basin (Irati and Ponta Grossa formations), Brazil. J S Am Earth Sci 2022;120:104087.
[90] Philipp RP, Faccini UF, Schultz CL, Zvirtes G, Bruckmann MP, Lavina E, Basei MAS. U-Pb zircon geochronology of detrital and ash fall deposits of the southern Paraná Basin: a contribution for provenance, tectonic evolution, and the paleogeography of the SW Gondwana. Geosciences 2023;13(8):225.
[91] Liu Q, Wu X, Zhu D, Meng Q, Xu H, Peng W, Liu J. Generation and resource potential of abiogenic alkane gas under organic–inorganic interactions in petroliferous basins. J Nat Gas Geosci 2021;6(2):79–87.
[92] Kalkreuth W, Levandowski J, Weniger P, Krooss B, Prissang R, da Rosa AL. Coal characterization and coalbed methane potential of the Chico-Lomã Coalfield, Paraná Basin, Brazil–Results from exploration borehole CBM001-CL-RS. Energy Explor Exploit 2020;38(5):1589–630.
[93] Lourenzi PDS, Kalkreuth W. O potential de geração CBM (Coalbed Methane) na jazida Sul Catarinense: 1. Características petrográficas e químicas das camadas de carvão da Formação Rio Bonito, Permiano da Bacia do Paraná. Braz J Genet 2014;44:471–91.
[94] Bicca MM, Kalkreuth W, da Silva TF, de Oliveira CHE, Genezini FA. Thermal and depositional history of early-permian Rio Bonito Formation of southern Paraná Basin–Brazil. Int J Coal Geol 2020;228:103554.
[95] Mukhopadhyay PK. Vitrinite reflectance as maturity parameter: petrographic and molecular characterization and its applications to basin modeling. 1994.
[96] Rocha VDS. Análise paleoambiental da Formação Teresina, Permiano da Bacia do Paraná (Brasil), e suas implicações paleoclimáticas. 2020.

Articles published as coauthor

Gondwana Research 107 (2022) 134–145

Contents lists available at ScienceDirect

Gondwana Research

journal homepage: www.elsevier.com/locate/gr

New high-precision U-Pb zircon age of the Irati Formation (Paraná Basin) and implications for the timing of the Kungurian anoxic events recorded in southern Gondwana

Joice Cagliari [a,*], Henrique Serratt [a], Marlise C. Cassel [a], Mark D. Schmitz [b], Farid Chemale Jr. [a]

[a] Graduate Program of Geology, Universidade do Vale do Rio dos Sinos, 950 Unisinos Av., 930220-750, São Leopoldo, RS, Brazil
[b] Department of Geosciences, Boise State University, 1910 University Drive, Boise-Idaho, ID 83725, United States

ARTICLE INFO

Article history:
Received 19 May 2021
Revised 7 February 2022
Accepted 12 March 2022
Available online 16 March 2022

Keywords:
CA-IDTIMS
Black shale
Choiyoi magmatism
Kungurian
Volcanic ash
Bentonite

ABSTRACT

The early Permian Irati Formation is well known for its black shale oil and gas reserves and its widespread lateral correlation throughout the entire Paraná Basin. This unit records an effective water circulation restriction between the Whitehill-Irati Sea and the Panthalassa Ocean, which along with other factors, controlled the organic-rich shale deposition in several southern basins of Gondwana. The Permian was also a period of intense magmatism in this region due to the Terra Australis Orogen (Gondwanides Orogeny). Several volcanoclastic horizons are preserved within the sedimentary record, and in this study, a high-precision chemical abrasion isotope dilution U-Pb zircon age of 275.75 ± 0.29 Ma for a volcanic tuff in the Irati Formation of the southern Paraná Basin is presented. The Kungurian age agrees with previous published radioisitopic and relative ages for the Assistência Member (upper Irati Formation) and Mangrullo Formation, a stratigraphical correlated unit in Uruguay. In addition, zircon trace elements and whole-rock geochemistry allow the constraining of the magmatic characteristics of the volcanic source and its similarity with the lower Choiyoi magmatism (Argentina). Therefore, this study contributes to the understanding of the timing of black shale-bearing rocks of the Irati Formation and the anoxic events recorded in the southern Paraná Basin.

1. Introduction

The late Cisuralian, early Permian, is marked by widespread episodes of ocean anoxic conditions recorded in several basins across Gondwana and the North and South China paleocontinents (see review shown by Liu et al., 2017). In southern Gondwana, black shale-bearing units recording episodes of anoxic conditions are recorded in the Irati Formation (Paraná Basin, Brazil; Reis et al., 2018; Cassel et al., 2019), Mangrullo Formation (Norte Basin, in Uruguay, Santa Ana et al., 2006), Chacabuco Formation (Chaco-Paraná Basin, in Argentina, Milani and Zálan, 1999), Whitehill Formation (main Karoo Basin, in South Africa, Oelofsen and Araújo, 1983, 1987), Formation B2 (Falkland Island, Faure and Cole, 1999), and Huab Formation (Huab Basin, in Namibia, Horsthemke et al., 1990; Faure and Cole, 1999). All these units are interpreted to have been deposited in the same epicontinental sea, the Whitehill-Irati Sea (Lavina, 1992).

The Irati Formation is well known for its black shale oil and gas reserves, and for its widespread lateral correlation throughout the entire Paraná Basin (Padula, 1968; Amaral, 1971; Milani et al., 1998). Therefore, it is an excellent chronostratigraphic marker for the basin, with relevance for Gondwanan tectonics and Permian climate change as black shale facies recording the anoxic event also occur in adjacent basins and elsewhere (Liu et al., 2017; Bastos et al., 2021). Fossil content (palynomorphs, plants, mesosaurid reptiles, crustaceans, insects, fish, Cyanophyta, Chlorophyta, and microbialites, see the review of Holz et al., 2010) is a powerful correlation tool within southern Gondwanan basins. But high precision radioisotopic determinations are crucial to providing accurate and precise ages for the onset and duration of the Cisuralian anoxic events, and therefore, further global correlation studies. Several volcanoclastic horizons (bentonite) are described in this unit (Maynard et al., 1996; Rocha-Campos et al., 2006; Santos et al., 2006; Silva et al., 2017; Rocha-Campos et al., 2019). However, most of the available dates (Rocha-Campos et al., 2006; Santos et al., 2006; Rocha-Campos et al., 2019; Bastos et al., 2021) are overlapping due to their large uncertainties, constraining the Irati Formation between the Artinskian (late Cisuralian) and the Roadian (early Guadalupian) ages (Gradstein et al., 2020).

Another issue, still in discussion, is the magmatic source of the Permian volcanic ash of the Paraná Basin. Their origin has been

* Corresponding author.
E-mail address: joiceca@unisinos.br (J. Cagliari).

https://doi.org/10.1016/j.gr.2022.03.004
1342-937X/

assigned to the Choiyoi magmatism (Coutinho and Hachiro, 2005; Guerra-Sommer et al., 2008c; Rocha-Campos et al., 2011; Silva et al., 2017), the largest magmatic event in the west margin of Gondwana, recorded by felsic rocks over an area of 500,000 km^2 (from the western Andean Cordillera to the Sierra Australes) and widespread ash fall deposits in the adjacent Gondwana basins (Rocha-Campos et al., 2011; Sato et al., 2015; Strazzere et al., 2016). Although Choiyoi magmatism is widely accepted as the source of these distal volcanics, the exact location of the volcanism is still debated. According to studies performed so far, at least two possibilities are posed, the Chilean Precordillera region, north of 27°S (Sato et al., 2015), and northern Patagonia (Calarge et al., 2006; Alessandretti et al., 2013).

The aim of this contribution is thus (i) to present a new high-precision U-Pb radioisotopic age, which will contribute to constraining the time of the anoxic events recorded in the Irati Formation, southern Paraná Basin; and (ii) based on whole-rock geochemistry and zircon trace elements, to identify the source of the volcanic ash preserved within this unit.

2. Geological settings

The Paraná Basin is an intracratonic basin that spreads through central and southern Brazil, northern Argentina, Paraguay, and Uruguay, covering 1,500,000 km^2 (Milani et al., 2007) (Fig. 1A). Its Phanerozoic strata reach thicknesses up to 8 km at its depocenter, with ages spanning from the late Ordovician to the late Cretaceous. The Paraná Basin's evolution is linked to the uplift and subsidence caused by the southern Gondwana orogenies. The Gondwanan orogenic phase (Carboniferous–Triassic) consists of a second-order depositional sequence, the Gondwana I supersequence (Milani, 1997). This sequence records a transgressive–regressive trend and a gradual paleoenvironmental change, from glacially influenced at the bottom to arid conditions at the top (Milani, 1997) (see the Permian interval of the Gondwana I supersequence in Fig. 2).

The Gondwana I supersequence sedimentation begins with the glacial-influenced deposits of the Itararé Group. Overlying this unit, coastal and shallow marine facies controlled by marine transgression were deposited (Guatá Group that includes Rio Bonito and Palermo formations) (Lavina and Lopes, 1987). The succeeding unit, the Irati Formation, is composed of siliciclastic deposits with organic matter-rich intervals, carbonates, and evaporites (Lavina, 1992). The Irati Formation is overlain by the Serra Alta and Teresina formations, representing the establishment of continental environments in the basin. The top of this supersequence (Rio do Rasto and Pirambóia formations) represents non-marine sedimentation, with lacustrine, fluvial, and eolian facies indicating the establishment of arid conditions (Lavina, 1992).

The Irati Formation, the focus of this study, is composed of fine-grained siliciclastic sedimentary rocks, with organic-rich shale deposits, intercalated with carbonates and evaporites. This unit is divided into two members: Taquaral (lower) and Assistência (upper). The former is composed of claystone and siltstone, whereas the latter has siltstone and black shale, intercalated with carbonate (Mendes et al., 1966; Padula, 1968; Petri and Coimbra, 1982; Oelofsen and Araújo, 1983; Lavina, 1992; Hachiro, 1996; Milani, 1997; Araújo, 2001; Cassel et al., 2019). The Irati Formation was deposited in a restricted marine epicontinental environment, with fluctuations in salinity, substrate oxygenation, and bioproductivity (Lavina, 1992; Hachiro, 1996; Araújo, 2001; Rodrigues et al., 2010).

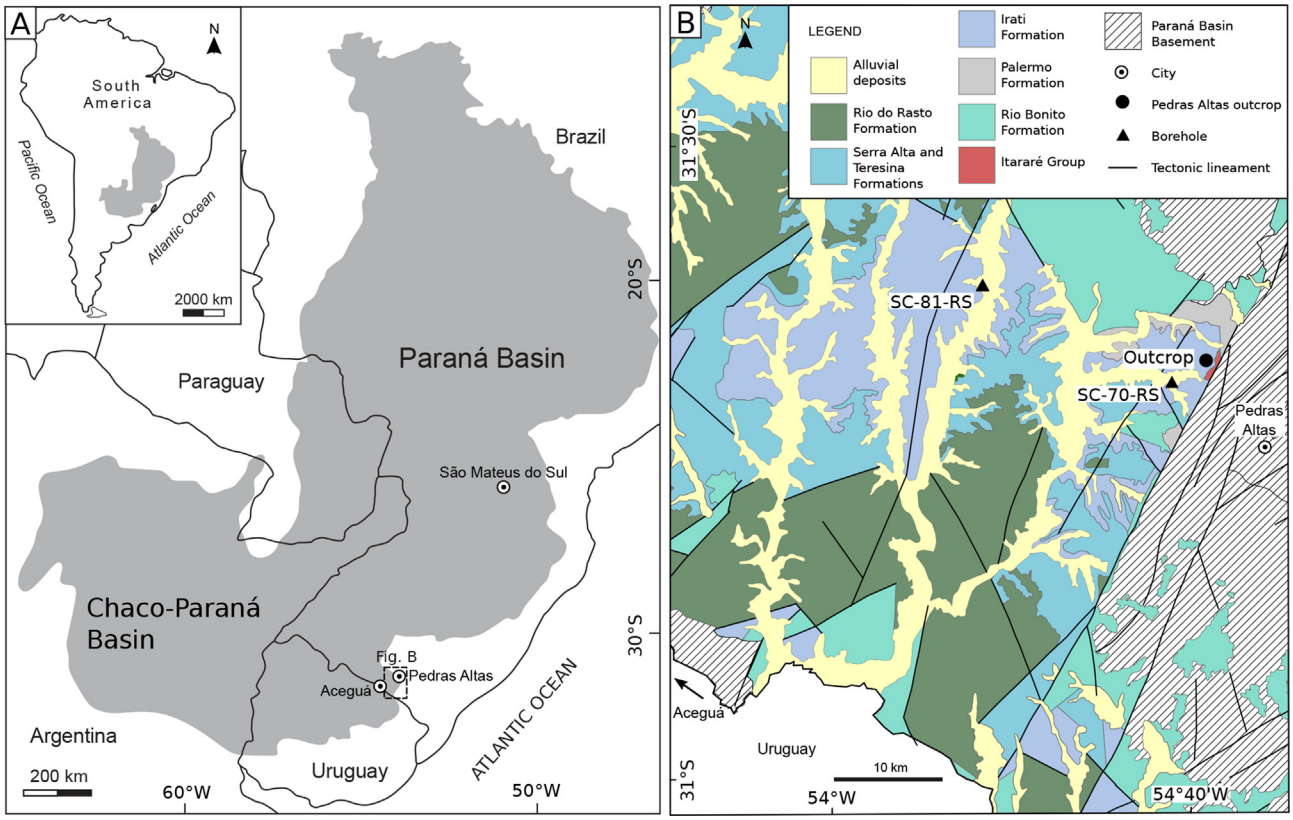

Fig. 1. (A) Paraná Basin and its extension Chaco-Paraná. Inset shows the location of Paraná Basin in the cratonic interior of South America. (B) Simplified geologic map (modified from Wildner et al., 2006) with the Pedras Altas outcrop location, from where bentonite samples were collected. Pedras Altas outcrop is located at 31° 39′ 54.899″S and 53° 38′ 8.86″W (radioisotopic age presented in this study is 275.75 ± 0.29 Ma).

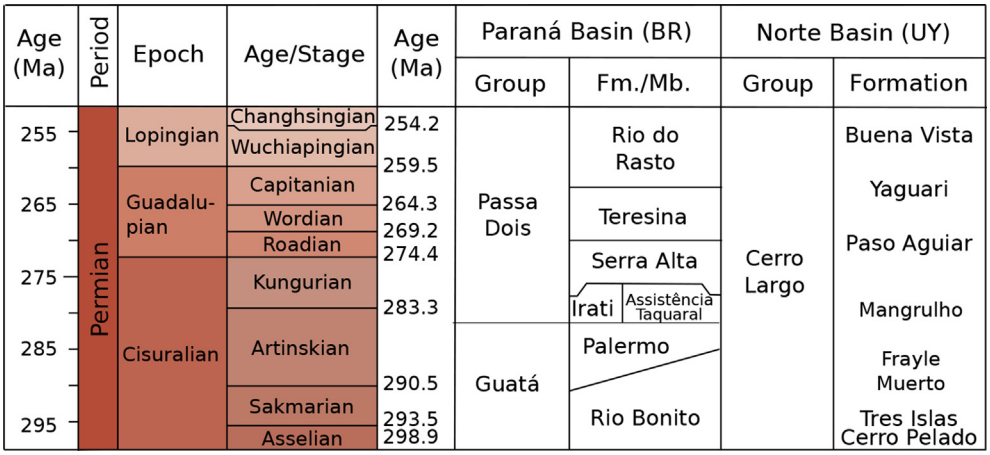

Fig. 2. Permian stratigraphy of the Paraná Basin in Brazil and Uruguay. Geological time scale is according to Gradstein et al. (2020). In Brazil, Permian Paraná Basin comprehends Guatá and Passa Dois groups, middle and upper interval of the Gondwana I Supersequence (modified from Milani et al., 2007). In Uruguay, Permian succession is represented by the Cerro Lago Group (Azcuy, 2007). The Irati Formation of the Paraná Basin is contemporaneous with the Mangrullo Formation of the Cerro Largo Group (Santa Ana et al., 2006).

It is a carbonate ramp system, divided into the external, middle, and inner ramps (Araújo, 2001), and this association represents deposition during variable restrictions in marine influx that operated in the Paraná Basin (Lavina, 1992; Milani, 1997).

Black shales and carbonates of the Assistência Member have been extensively analyzed, showing high values of total organic carbon (TOC) up to 22% in shales, and intercalated carbonates with low values of insoluble residues (Padula, 1968; Araújo, 2001; Rodrigues et al., 2010; Alferes et al., 2011). It is also characterized by the occurrence of skeletal remains of *Mesosaurus*, which can be correlated to the Whitehill Formation, in southern Africa (Oelofsen and Araújo, 1983, 1987; Lavina et al., 1991; Lavina, 1992; Soares, 2003; Cassel et al., 2019). The fossil content includes flora, insects, crustaceans, foraminifera, pollen, spores, and ichnofossils, corresponding to the *Lueckiporites virkkiae* Interval Zone in palynostratigraphy indicating an Artinskian to Roadian/Wordian age (Santos et al., 2006; Rocha et al., 2020; Souza et al., 2021).

A SHRIMP U-Pb zircon age of the Irati Formation suggests an Kungurian age (278.4 ± 2.2 Ma) for one of the bentonite horizons at the Petrobras six mine, São Mateus do Sul city (Paraná State), south of Brazil (Santos et al., 2006). Two other bentonite samples from São Mateus do Sul were dated by Rocha-Campos et al. (2019), with results corroborating the Artinskian-Kungurian age (280.0 ± 3.0 and 279.9 ± 4.8 Ma). The Mangrullo Formation, an Uruguayan correlative unit of the Irati Formation (Santa Ana et al., 2006), has a Kungurian-Roadian age (274.9 ± 2.1 and 274.9 ± 2.2 Ma), obtained from the analysis of two samples collected at the Cañada del Rodeo del Barón outcrop – located at ~ 15 km southeast of the Aceguá city (Rocha-Campos et al., 2019).

3. Methodology

Two samples of tuff (likely bentonite) were sampled (TFI-IR1 and TFI-IR2) within dark grey laminated clayey siltstone of the Irati Formation, in the southern Paraná Basin. Outcrop is located in a countryside road cut, in Pedras Altas county of the Rio Grande do Sul State, southernmost Brazil (Fig. 1). The succession is currently sub-vertical due to proximity to the Dorsal Canguçu shear zone and its reactivation systems. To place bentonite horizons in the Irati Formation stratigraphy, a geologic cross section was carried out along ~ 250 m of the countryside road. Sedimentary facies characteristics and total organic carbon (TOC, Wtd %) of the clayey siltstone located below and above the bentonite horizons (P-2 and P-4, Fig. 3) were also considered. Approximately 10 g of each sample were ground in an agate mortar and dried at 40 °C for TOC analysis. Sample aliquots were treated with 0.25 N hydrochloric acid (HCl) before measurement using a LECO SC-144DR analyzer at the Instituto Tecnológico de Paleoceanografia e Mudanças Climáticas (itt Oceaneon – Unisinos).

Zircons were separated using standard mineral separation techniques (see Cagliari et al., 2014). The handpicked grains were mounted in epoxy resin and polished to expose interior zones prior to cathodoluminescence (CL) imaging on a scanning electron microscope. Simple internal compositional zoning and the absence of inherited cores and inclusions were considered to select zircons crystals for U-Pb dating and geochemical screening by laser ablation inductively coupled plasma mass spectrometry (LA-ICP-MS). After that, young zircon crystals were selected to perform chemical abrasion isotope dilution thermal ionization mass spectrometry (CA-IDTIMS) U-Pb analyses. Both LA-ICP-MS and CA-IDTIMS analyses were performed at the Boise State University (BSU) Isotope Geology Laboratory.

LA-ICPMS analysis was performed in an X-Series II quadrupole ICPMS and New Wave Research UP-213 Nd:YAG UV (213 nm) laser ablation system. Isotope data were acquired with spot size of 25 μm and depth of ~ 25 μm, laser energy of ~ 5 J/cm^2, a repetition rate of 10 Hz and a shutter delay (gas blank) of 15 s and a total ablation signal integration of 30 s. A 1.2 L/min He gas stream carried ablated material to the nebulizer flow of the plasma. Quadrupole dwell times were 5 ms for Si and Zr, 200 ms for ^{49}Ti and ^{207}Pb, 80 ms for ^{206}Pb, 40 ms for ^{202}Hg, ^{204P}b, ^{208}Pb, ^{232}Th, and ^{238}U and 10 ms for all other high field strength elements (HFSE) and rare earth elements (REE); total sweep duration is 950 ms. For concentration calculations, each analyte's background-subtracted count rates were internally normalized to ^{29}Si and calibrated concerning NIST SRM-610 and −612 glasses as the primary standards. Analyses that appear to have intersected glass or mineral inclusions or contaminated by common Pb were discarded. For U-Pb dates, instrumental fractionation of the background-subtracted ratios was corrected, and dates were calibrated with respect to interspersed measurements of zircon standards and reference materials (Seiland, Zirconia, and Plesovice zircon). Radiogenic isotope ratio and age error propagation for all analyses include uncertainty contributions from counting statistics and background subtraction. Uncertainties from the standard calibrations are propagated into

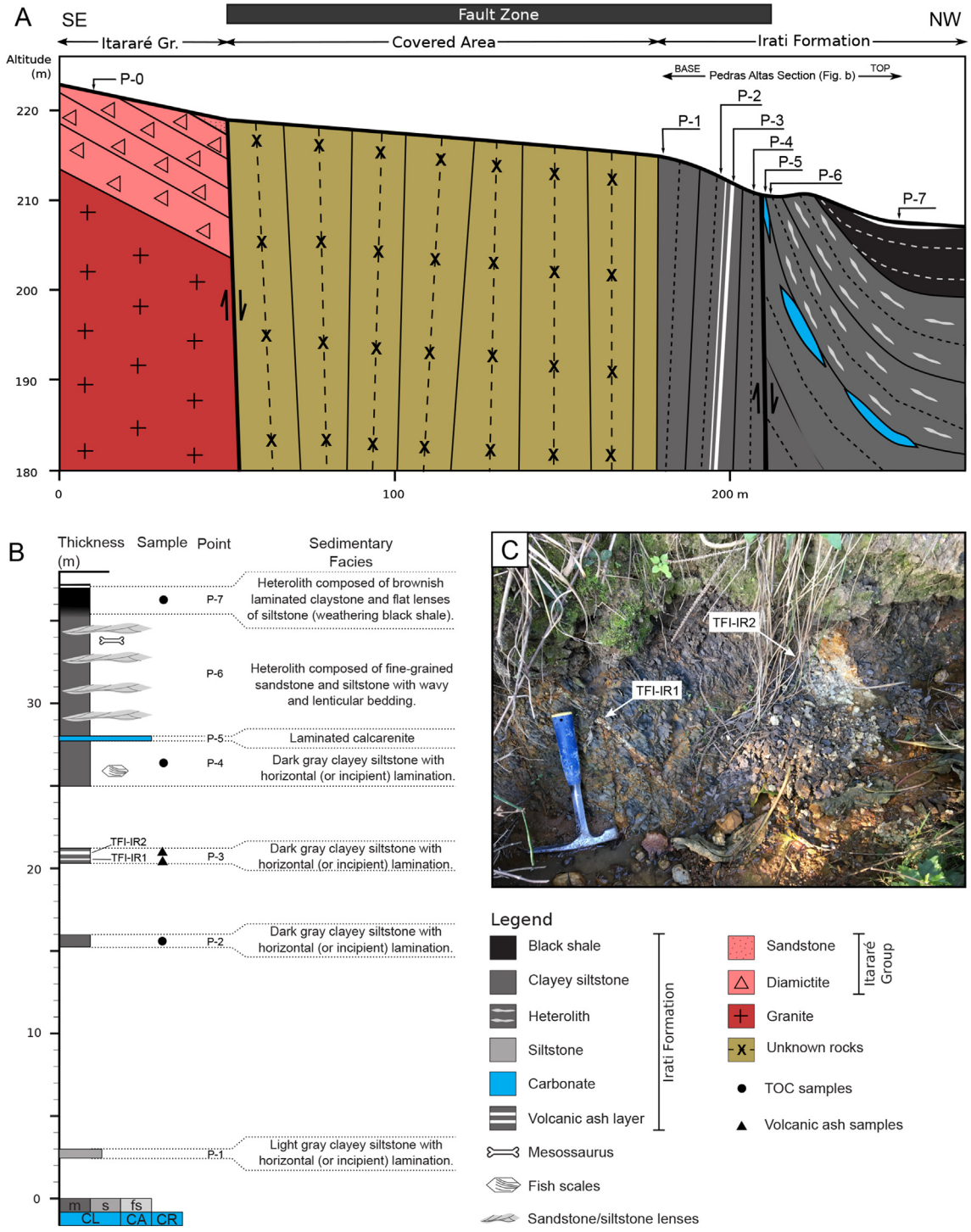

Fig. 3. (A) Pedras Altas geologic cross section along the countryside road cut. (B) Sedimentary log with facies description, TOC and volcanic ash samples location (see Table S1 for complete description and coordinates). (C) Sampled volcanic ash beds within dark gray clayey siltstone.

the errors on each date. These uncertainties are ~ 2% (2σ) for $^{206}Pb/^{238}U$ and ~ 1% (2 σ) for $^{207}Pb/^{206}Pb$. Additional details of methodology and reproducibility are reported in Rivera et al. (2013).

The analytical procedures for CA-IDTIMS include thermal annealing, chemical abrasion (modified version of Mattinson, 2005), and chemical dissolution of individual zircon crystals, followed by ion-exchange chromatography. In the annealing process, zircons were placed in a muffle furnace at 900 °C for 60 h to remove radiation damages and related leaching effects. In the chemical abrasion, the zircon crystals were subjected to a temperature of 190 °C (or 180 °C) for 12 h in a 29 M HF solution to dissolve the U-rich zones and increase concordance and precision. Before the chemical dissolution at 220 °C for 48 h in a 29 M HF solution, the samples were spiked with the EARTHTIME mixed ^{205}Pb-^{233}U-^{235}U trace solution (ET-535). After dissolution, U and Pb were separated using an HCl-based ion-exchange chromatography procedure (a modified version of Krogh, 1973) and loaded in a Re filament. U and Pb isotopic measurements were made on a Phoenix X62 multi-collector thermal ionization mass spectrometer equipped with an ion-counting Daily detector. U-Pb dates and uncertainties for each analysis were calculated using the algo-

rithms of Schmitz and Schoene (2007) and the U decay constants of Jaffey et al. (1971). Quoted errors for calculated weighted means are thus of the form ± X(Y)[Z], where X is solely analytical uncertainty, Y is the combined analytical and tracer uncertainty, and Z is the combined analytical, tracer, and ^{238}U decay constant uncertainty. Additional details of methodology are reported by Davydov et al. (2010) and Schmitz and Davydov (2012).

In addition to U-Pb LA-ICPMS and CA-IDTIMS dating, geochemical analysis was performed in the whole rock sample and selected zircon crystals to obtain information of the tectono-magmatic setting in which the magmas were formed. Major, minor, and trace elements in whole-rock were measured by acid dissolution ICP-ES/MS at AcmeLabs Inc. in Vancouver, Canada. Trace elements in zircon crystals were performed at the Boise State University (BSU) Isotope Geology Laboratory by LA-ICPMS (specifications described above).

4. Results

4.1. Pedras Altas section

The Pedras Altas section is poorly exposed in a countryside road cut, located ~ 0.5 km westward of the Dorsal Canguçu shear zone (Fig. 1B). The studied section from SE to NW consists of sandstone and diamictite of the Carboniferous Itararé Group and claystone and siltstone of the Permian Irati Formation. The Itararé units dip 15° to NW and overly the granitic rocks of the Vendian magmatic arc (Fig. 3A). These rocks are thus controlled by a set of N-S trending normal faults. Due to the main normal faulting, the Permian Irati beds are subvertical juxtaposed to the Vendian rocks and Irati sedimentary units (Fig. 3A). To the NW direction of the profile, Irati units were also deformed by a second-order normal fault. This fault juxtaposed the sub-vertical beds to SE and drag fold beds of Irati Formation to the NW (Fig. 3A). Northwestwards these beds gradually became sub-horizontal. The exposed sedimentary succession of the Irati Formation is 37 m thick considering apparent dip and true bed thickness. It is composed from base to top by, dark gray clayey siltstone with horizontal (or incipient) lamination and locally with fish scales, laminated calcarenite, heterolith composed of fine-grained sandstone (~60%) and siltstone (~40%) with wavy and lenticular bedding with bone fragments, and heterolith composed of brownish laminated claystone (~70%) and flat lenses of siltstone (~30%) (weathering black shale) (Fig. 3B, Fig. S1, and Tab. S1).

Two bentonite laminae occur within the sub-vertical dark gray clayey siltstone with incipient lamination as thin (1 and 3 cm for TFI-IR1 and TFI-IR2, respectively) whitish claystone laminae, separated by ~ 0.5 m (Fig. 3C). Average TOC (weight %) for the sub-vertical dark grey clayey siltstone sampled on both sides of the bentonite interval is 0.46 and 0.32% for P-2 and P-4, respectively, but the triplicate results show a range between 0.30 and 0.48% (Tab. S2). Triplicate results for the sub-horizontal weathering black shale (P-7) are within 0.85 and 0.86% (Tab. S2).

4.2. Radioisotopic dating

No zircon grains were recovered from the TFI-IR2 sample. From sample TFI-IR1, a total of 140 zircons crystals were handpicked and mounted in epoxy resin. Zircons are very small (<80 μm in length) with different morphologies, and some grains are elongated while others are equant.

From the analysis of cathodoluminescence, 27 zircons were selected for dating by LA-ICPMS and yielded $^{206}Pb/^{238}U$ ages ranging from 778 to 258 Ma (Fig. S2-A). The tail to older ages correlates with CL-imagery evidence of inherited cores in many zircon grains. The youngest population (n = 7, results are presented in the Tab. S1) present an LA-ICPMS $^{206}Pb/^{238}U$ weighted mean age of 271.1 ± 8.4 Ma with a mean square of weighted deviation (MSWD) of 2.4 and a probability of 0.025 (95% of confidence, Fig. S2-B). To obtain a more robust $^{206}Pb/^{238}U$ age for the TFI-IR1 sample, six zircons of this youngest population were selected to perform CA-IDTIMS analysis (Fig. 4). The selected zircons are prismatic,

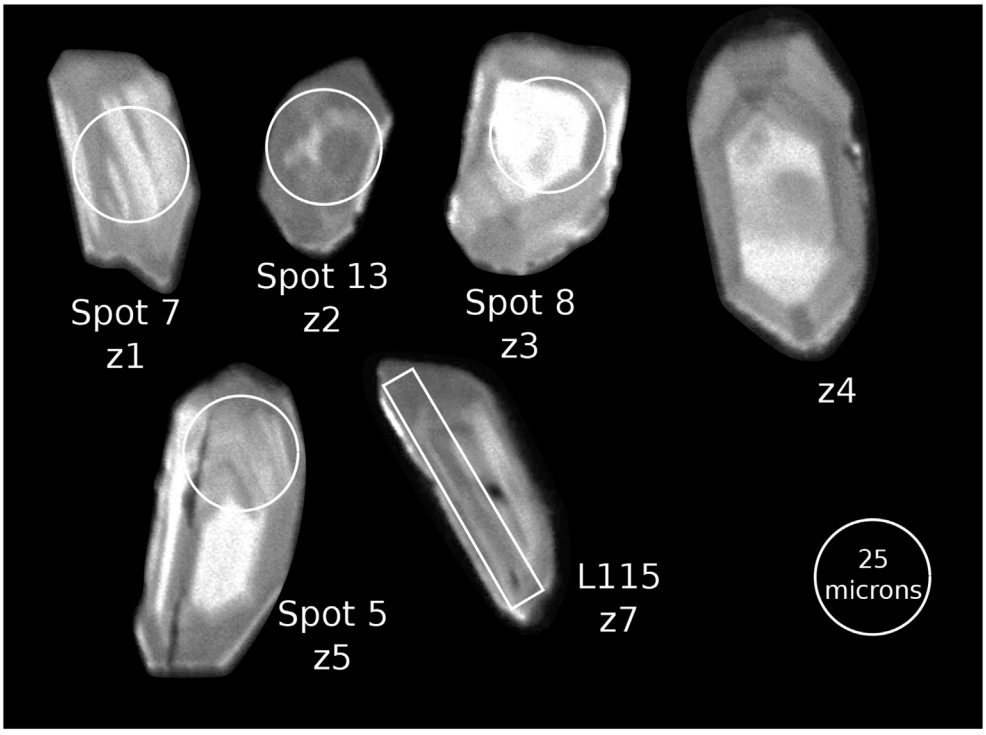

Fig. 4. Cathodoluminescence images of the selected zircons for the CA-IDTIMS radioisotopic dating. Spots and line numbers refer to the LA-ICPMS analysis (Tab. S3) and zircon numbers (z1-7) are the CA-IDTIMS identification (Tab. S4).

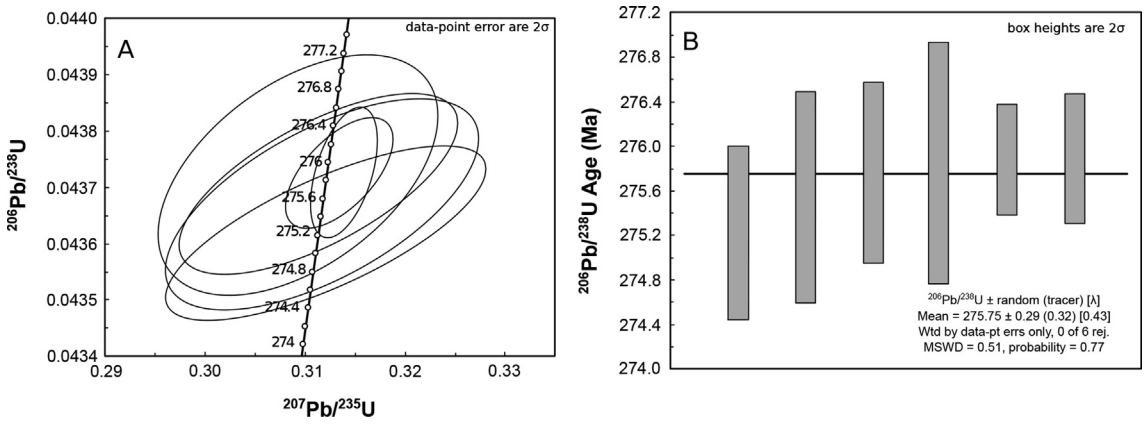

Fig. 5. U-Pb CA-IDTIMS results of the single zircon grains for the analyzed TFI-IR1 bentonite sample. (A) Concordia diagram illustrating six CA-IDTIMS dated grains; one grain was lost during the analysis perform. (B) $^{206}Pb/^{238}U$ weighted mean age of the CA-IDTIMS dated grains of Fig. A. MSWD: mean square of weighted deviates.

euhedral, ~40–65 μm long with a predominance of elongation ratios (length/width) around 2.0. Some zircons present a characteristic bright core and others are dark in the CL images (Fig. 3). The Th/U rate ranges between 0.88 and 1.20. The resulting isotope ratios and ages measured by CA-IDTIMS are concordant (Fig. 5A) with a $^{206}Pb/^{238}U$ weighted mean age of 275.75 ± 0.29 (0.32) [0.43] Ma (95% confidence interval) with MSWD of 0.51 and a probability of fit of 0.77 for all six zircon crystals (Fig. 5B). This high-precision radioisotopic dating is interpreted as the age of eruption and deposition of the bentonite layer, during the Kungurian (Gradstein et al., 2020).

4.3. Whole rock geochemistry

Based on the Winchester and Floyd (1977) diagram, bentonite samples are classified as andesite (TFI-IR1) and trachyandesite (TFI-IR2) (Fig. 6A, Tab. S5). The results reflect an affinity between the volcanic tuffs and their sources. Samples have similar Zr/TiO_2, but different Nb/Y ratios caused by a high concentration of Y in the TFI-IR1 sample (sample with the presence of zircons grains).

The geological settings determined using the Cabanis and Lecolle (1989) diagram (Fig. 6B, Tab. S5), show different contexts for bentonite samples. TFI-IR1 sample is classified as an orogenic setting in a compressive domain, represented by continental arc or island arc. A very high La concentration controls the classification of this sample. On the contrary, the tectonic affinity of the sample TFI-IR2 is related to a late- to a post-orogenic intra-continent domain, in a compressive to a distensive setting.

4.4. Zircon trace elements

Zircons of sample TFI-IR1 (Tab. S6) show, in general, a continental arc source (Cont. arc-type, Fig. 7A), based on Nb/Yb and U/Yb elemental ratios (Grimes et al., 2015). These results are in agreement with the whole rock results (item 4.2). Ti content points to a narrow range of temperature of crystallization of 747 ± 22 °C

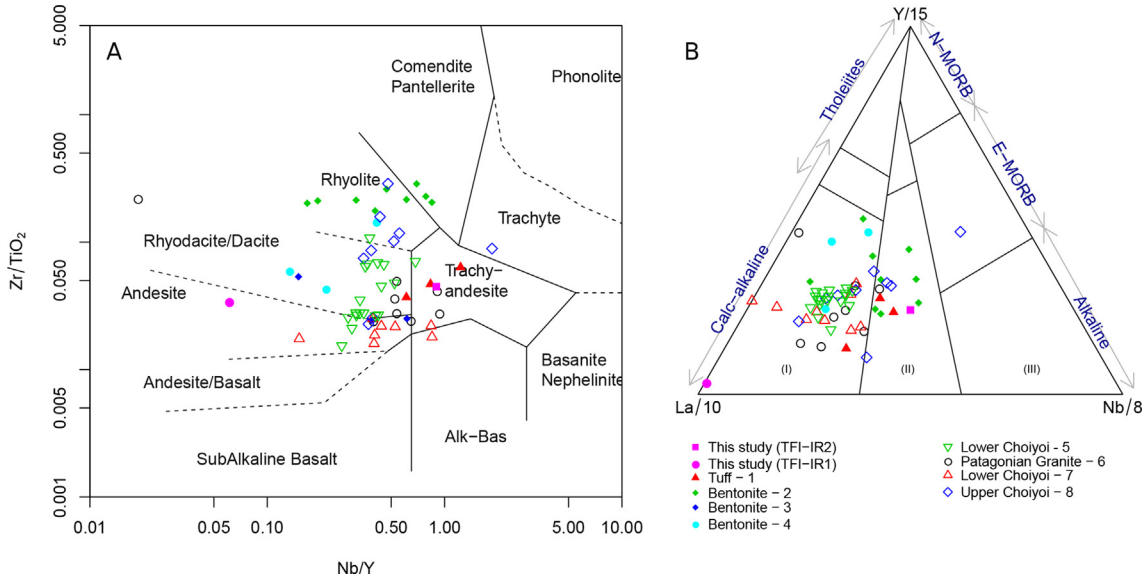

Fig. 6. (A) Winchester and Floyd (1977) rock classification diagram with immobile elements from the Irati Formation bentonite samples (this study, Maynard et al., 1996; Calarge et al., 2006; Silva et al., 2017), tuffs from San Rafael Block (Argentina, Alessandretti et al., 2013), Patagonian igneous rocks from Pankhurst et al. (2006), Lower Choiyoi volcanic rocks from Strazzere et al. (2016), Lower and Upper Choiyoi rocks from Kleiman and Japas (2009). (B) Tectonic settings discriminant diagram modified from Cabanis and LeColle (1989). Tectonic settings: I- Orogenic (compressive) domains (island arcs, active margins); II- Late- to post-orogenic (compressive to distensive) intra-continental domains; and, III- Anorogenic (distensive) domains. Samples: 1- Alessandretti et al. (2013), 2- Calarge et al. (2006), 3- Silva et al. (2017), 4- Maynard et al. (1996), 5- Strazzere et al. (2016), 6- Pankhurst et al. (2006), 7–8- Kleiman and Japas (2009).

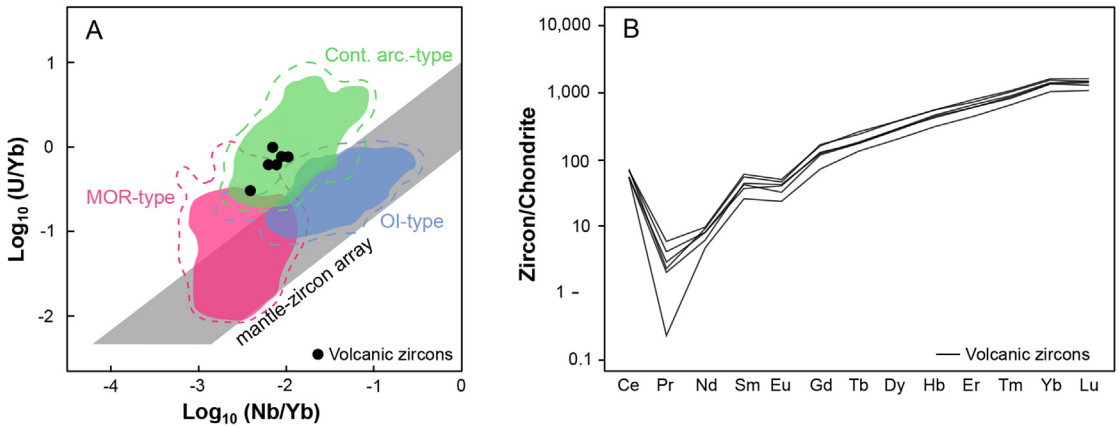

Fig. 7. (A) Tectonic settings discriminant diagram of Grimes et al. (2015) using zircons trace elements to mark the magmatic source, distinguishing the environments: Middle Ocean Ridge (MOR), Continental Arc (Cont. Arc) Ocean Islands (OI). (B) Zircons REE normalized by chondrite according to McDonough and Sun (1995) values.

(based on Watson et al., 2006). The rare earth element (REE) patterns normalized by chondrite (McDonough and Sun, 1995) for the pyroclastic zircons are similarly within a narrow range of compositions (Fig. 7B). All these geochemical criteria support an origin from a single relatively evolved intermediate magma composition.

5. Discussion

5.1. Irati Formation geochronology

Bentonite samples reported here occur within dark gray clayey siltstone, which is one of the most representative sedimentary facies of the Irati Formation in the southern basin, present in Taquaral and Assistência members (Figs. 8 and 9B). However, the succession recovered in Fig. 3B is characteristic of the Assistência Member in the southern Paraná Basin (Fig. 8 and Cassel et al., 2019). Besides that, the exposed sedimentary succession did not present diagnostic elements of the underlying and overlying units. The underlying Palermo Formation is composed of heteroliths with wavy and lenticular bedding, and intense bioturbation (Buatois et al., 2007; Milani et al., 2007; Gandini et al., 2010; Holz et al., 2010), and the overlying Serra Alta Formation has dark to light grey shale (brownish in outcrops) and siltstone but with clastic sand dykes and vertical fractures filled with calcite (Gama Jr., 1979; Milani et al., 2007; Teixeira et al., 2018).

All the Irati Formation bentonites reported so far occur within the Assistência Member or the equivalent unit in Uruguay (Santos et al., 2006; Silva et al., 2017; Craddock et al., 2019; Bastos et al., 2021). The upper portion of the Assistência Member is rich in bentonite beds; Silva (2021) identified eight bentonite beds (core HV-44-RS) and Silva et al. (2017) described seven in the southern basin.

Indeed, the position of bentonite samples identified in the Pedras Altas section was constrained by sedimentary facies description (Tab. S1), TOC content (Tab. S2) in nearby core (SC-081-RS) and the presence of bentonite in the neighboring cores (SC-081-RS and SC-070-RS, Cassel, 2017). The dark gray clayey siltstone, in which bentonite horizons were sampled, occurs in both Taquaral (between 67 and 75 m depth) and Assistência (between 47 and 56 m depth in core SC-081-RS; Fig. 7) members. In core SC-070-RS, this facies occur in two intervals of the Taquaral Member (53–57 m and 61–67 m depth) and in one interval of the Assistência Member (26–38 m depth; Fig. 7). Other siliciclastic sedimentary facies of the Irati Formation comprehends gray siltstone with sparce wavy bedding of very fine-grained sandstone, heterolithic claystone and very fine-grained sandstone, and black shale (Cassel et al., 2019). Therefore, the sedimentary facies description identify two possible stratigraphic positions, in the upper Taquaral Member and in the middle of the Assistência Member. In both intervals, the organic matter content is within the range of values obtained for P-2 and P-4 samples. Based on these criteria, the most likely position for the studied bentonite is the Assistência Member, between the black shale beds and below the upper carbonate bed (Figs. 8 and 9B).

The high-precision $^{206}Pb/^{238}U$ weighted mean age presented here (275.75 ± 0.29 Ma) indicates the analyzed bentonite was deposited in the Kungurian Stage of the Geological Time Scale (Cohen et al., 2013; Gradstein et al., 2020). Low degree of scatter in the zircon data set added to the geochemical similarities, such as REE patterns (Fig. 7B), source environment (Fig. 7A), and crystallization temperature (Ti-based) with low standard deviation (±22 °C) reinforce that the zircons dated are from the same magmatic population. Thus, this radioisotopic date is interpreted as the eruption and depositional age of the tuff and seems to be a robust geochronological contribution for the Cisuralian of the Paraná Basin. The LA-ICPMS weighted-mean age (271.1 ± 8.4 Ma) has low accuracy and low precision compared to the CA-IDTIMS result, which is ~ 1.7% older than the LA-ICP-MS. This is an expected result since zircon crystals are specifically treated to remove Pb loss domains during chemical abrasion.

Isotope dilution thermal ionization mass spectrometry (IDTIMS) is the most accurate and precise method for U and Pb isotope ratios. Two-sigma precision of individual analyses by IDTIMS is about 0.1–0.3% compared to 1–3% by laser ablation inductively coupled plasma mass spectrometers (LA-ICPMS) and secondary ion mass spectrometers (SIMS) (Bowring et al., 2006). The high precision of the IDTIMS is due to its sensitivity, ion beam stability, low magnitude of instrumental bias, and gravimetrological basis (see Schmitz et al., 2020). Besides that, chemical abrasion (CA), the standard treatment for U-Pb zircon geochronology, remove damaged mineral regions associated with Pb loss or storage of common Pb (Mattinson, 2005). For LA-ICPMS and SIMS spot analyses, the low precision prevents detecting subtle amounts of Pb loss or inheritance, producing younger or older ages, respectively (Bowring et al., 2006). For CA-IDTIMS, Pb loss and inheritance are problems solved by chemical abrasion on CL-imaged and in situ screened zircon grains, significantly reducing the degree of scattering in the zircon data set (Schmitz et al., 2020). However, for LA-ICPMS and SIMS, this represents a significant limitation for their application in high-precision geochronology. In-situ techniques are essential tools to characterize complex zircons, but their results

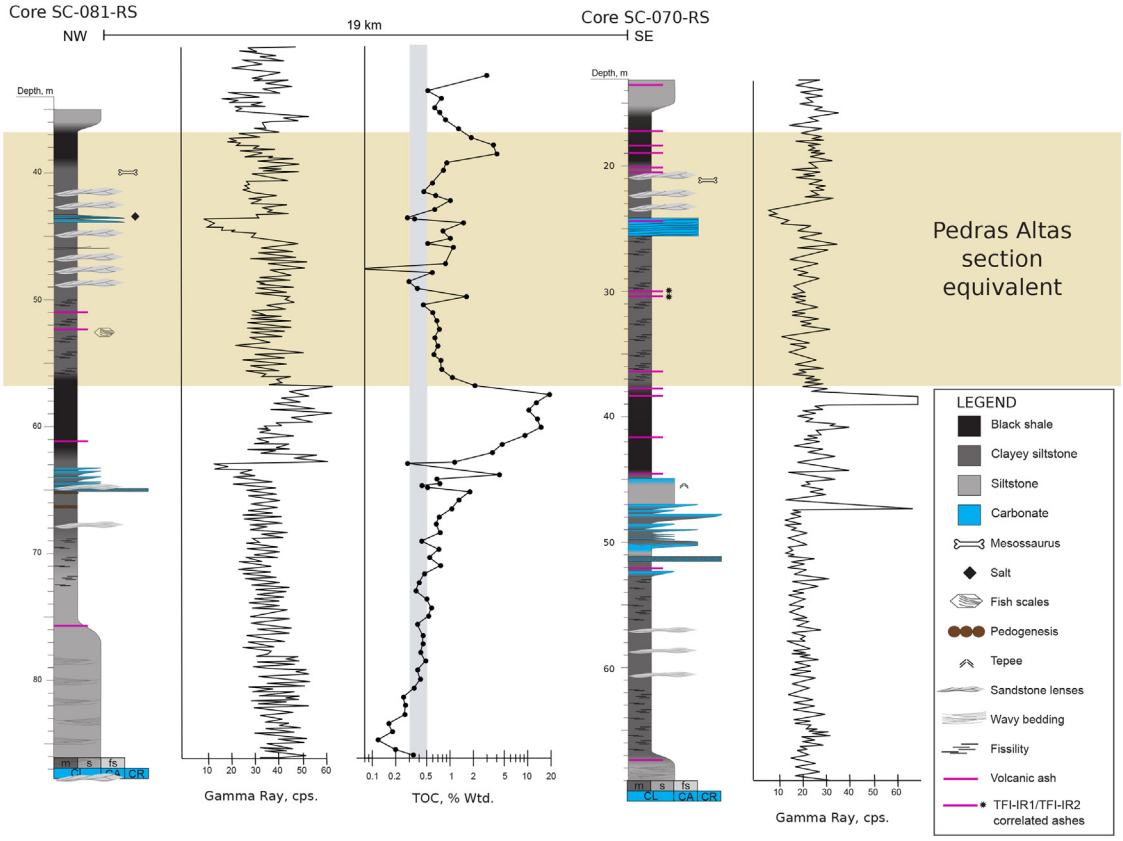

Fig. 8. Pedras Altas section located in the nearby cores (SC-081-RS and SC-070-RS) based on sedimentary facies, TOC (Total Organic Carbon) content, and the presence of bentonite. For core location, see Fig. 1. Sedimentary and TOC logs were extracted from Cassel, 2007. The grey range in the TOC log corresponds to the results obtained from P-2 and P-4 analysis (between 0.30 and 0.48%). Gamma-ray logs are from Geological Survey of Brazil. Bentonite layers were identified from core photographs.

can be inaccurate and imprecise when compared to IDTMS, as shown by Bowring et al. (2006) and seen here. Based on the obtained age in this work, we suggest that earlier SHRIMP dating of Irati Formation by Santos et al. (2006) and Rocha-Campos et al. (2019) needs to be analyzed by CA-IDTMS.

The upper black shale was the subject of the Santos et al. (2006) and Bastos et al. (2021) geochronological studies. The SHRIMP U-Pb age of 278.4 ± 2.2 Ma (Kungurian) was interpreted by Santos et al. (2006) as the crystallization age of the volcanic eruption of one bentonite layer at Petrobras-Six mine. This bentonite was sampled within the 6.4-m-thick oil shale bed in the upper section of the Assistência Member (Fig. 9A). Another bentonite sample, collected in the same mine, was analyzed by Bastos et al. (2021) by CA-IDTMS, and the $^{206}Pb/^{238}U$ age of a single zircon was 277.26 ± 0.70 Ma (Fig. 9A). Although slightly younger, this age overlaps the uncertainty of previous results obtained by Santos et al. (2006). Bastos et al. (2021) interpret the single zircon date as depositional age of the ash bed, but the low number of date zircon prevents identifying if this Permian zircon is part of the youngest population or is an inherited zircon. The lower back shale was dated by Rocha-Campos et al. (2019), from samples collected in the same area (São Mateus do Sul city). The U-Pb SHRIMP mean ages are 279.9 ± 4.8 and 280.9 ± 3.0 Ma (Fig. 9A), slightly older than the upper black shale but overlapping in the uncertainty range.

Bentonite samples of the Mangrullo Formation, the Irati Formation equivalent unit in the Norte Basin (Uruguay, Santa Ana and Gutierrez, 2000; Santa Ana et al., 2006), have SHRIMP mean ages of 274.9 ± 2.1 and 274.9 ± 2.2 Ma (Rocha-Campos et al., 2019) (Fig. 9C). They occur within black shale, at the Cañada del baron del Rodeo outcrop, in northeastern Uruguay, and are on top of a series of five bentonite layers, immediately below Passo do Aguiar Formation (Palermo Formation equivalent unit) (Rocha-Campos et al., 2019). This black shale corresponds to the upper black shale of the Irati Formation in Brazil.

Irati Formation correlation across the basin is not a complex task since black shales encompass a widespread marker across several southern Gondwanan basins. The Assistência Member (upper unit) is marked by the occurrence of two black shale beds, whereas the Taquaral Member (lower unit) by the absence of it (Fig. 9). However, radioisotopic ages from Rocha-Campos et al. (2006, 2019) for the upper Assistência Member are older than those obtained here for the middle interval of this member. The radioisotopic age of Bastos et al. (2021) reinforces these older dates, but is based on a single zircon crystal. This inconsistency cannot be explained by Pb loss, a significant issue for untreated zircons in SIMS and laser ablation analysis. This disparity is likely attributed to the heterogeneous $^{206}Pb/^{238}U$ of the zircon standard (Metcalfe et al., 2015), the absence of the youngest population of zircons in the analyzed samples, or even the criteria (which is not mentioned) used to select the coherent group of zircons.

5.2. Volcanic source

The Irati Formation records several bentonite layers preserved in the southwestern Gondwana that have been assigned to the Choiyoi magmatism (Coutinho and Hachiro, 2005; Rocha-Campos et al., 2006, 2011; Silva et al., 2017). The main arguments constraining the source to the Choiyoi magmatism are: (i) the small size of volcanic grains (Coutinho and Hachiro, 2005; Guerra-Sommer et al., 2008a,c; Santos et al., 2006; Silva et al., 2017), which

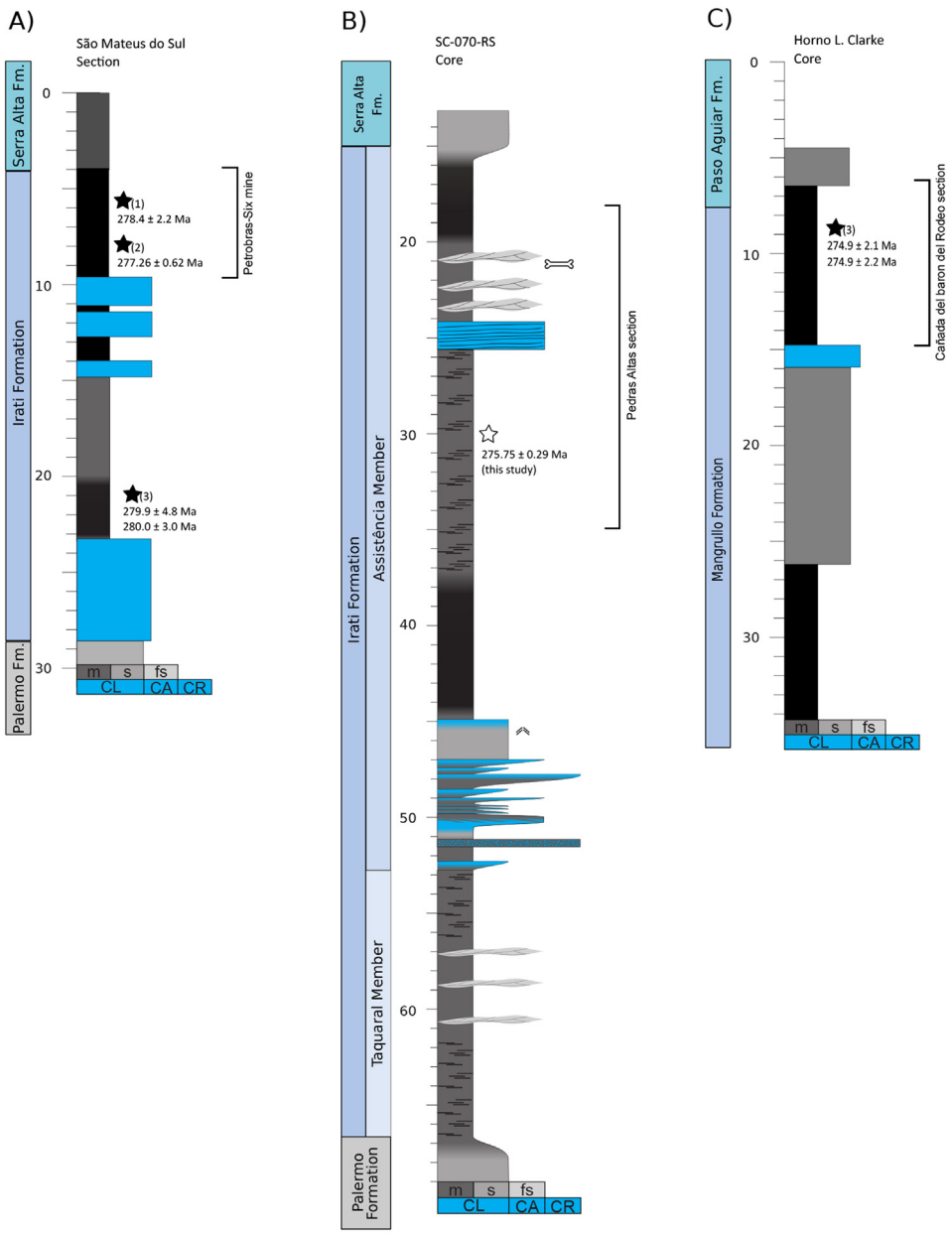

Fig. 9. Irati Formation and its correlated unit, Mangrullo Formation, in Uruguay. (A) São Mateus do Sul profile (modified from Oeslofsen and Araújo, 1983) and radioisotopic dating from: (1) Santos et al. (2006), (2) Bastos et al. (2021), and (3) Rocha-Campos et al. (2019). (B) SC-070-RS core sedimentary log (Cassel, 2007) with the position and radioisotopic age presented in this study. Pedras Altas section is located ~ 3 km northeast of the SC-070-RS well. C) Horno L. Clarke core sedimentary log (modified from Santa Ana and Gutierrez, 2000) and the radioisotopic dating from (3) Rocha-Campos et al. (2019). Bentonite samples of the Mangrullo Formation were collected at the Cañada del baron del Rodeo outcrop, which is ~ 15 km southeast of Aceguá city.

points to a remote source (the Choiyoi province is distal enough to let just the very fine-grained minerals reach the Paraná Basin, yet close enough to be the probable source); (ii) the explosivity of the Choiyoi magmatism, which can make ash clouds travel great distances (>2,500 km) (Coutinho and Hachiro, 2005; Rocha-Campos et al., 2011); (iii) the Choiyoi composition, compatible with the composition of Paraná Basin ash fall deposits (Maynard et al., 1996; Silva et al., 2017); (iv) the contemporaneity of Paraná Basin ashes (Guerra-Sommer et al., 2008a–c; Santos et al., 2006) and the Choiyoi magmatism (281.4 ± 2.5–251.9 ± 2 Ma, Rocha-Campos et al., 2011).

The TFI-IR1 whole-rock and zircon trace results show a continental arc affinity (Cabanis and Lecolle, 1989; Grimes et al., 2015), a geological setting compatible with the Choiyoi source. Besides that, the consistency in the radioisotopic dating of the volcanic zircons, the similarity in REE pattern, and the short-range of the standard deviation of temperatures (± 22 °C) point to a coherent group of zircons, which likely have the same origin.

The whole-rock geochemistry might not necessarily reflect the accurate composition of the original ash cloud, since the bentonite layer contains detrital sediment deposited at the same time as the pyroclastic material. However, geochemistry results (Fig. 6B) agree with most of the zircons trace composition results (Fig. 7) for the TIF-IR1 sample, which points to a continental arc source. In The TIF-IR2 sample show the same trachyandesite composition of the San Rafael tuff (Alessandretti et al., 2013).

Based on the Winchester and Floyd (1977) diagram (Fig. 6A), sample composition varies considerably. In this study, samples range from andesite (TIF-IR1) to trachyandesite (TIF-IR2). Samples from the same formation collected in the southern basin (Aceguá county, RS, Silva et al., 2017) have rhyodacite/dacite and andesite (the same classification of TIF-IR1, despite the difference in Nb/Y content). Bentonites from PetroSix quarry (São Mateus do Sul county, SC, Maynard et al., 1996) have rhyolite and rhyodacite/-dacite composition. Therefore, there is no strong evidence supporting that samples analyzed in this study and by Maynard et al. (1996) and Silva et al. (2017) are the same bentonite horizons.

The magmatic event generating the TIF-IR1 bentonite (275.75 ± 0.29 Ma) layer is contemporaneous with the lower Choiyoi volcanism (281.4 ± 2.5–264.7 ± 2.9 Ma, Rocha-Campos et al., 2011) whose geochemistry ranges from andesite to trachyandesite (Kleiman and Japas, 2009; Strazzere et al., 2016). The Nb/Y ratio of the Choiyoi andesite is significantly higher than the TIF-IR1 sample. The volcanic sources of Irati Formation bentonite samples (from this study and Maynard et al., 1996) are related to compressional orogenic domains (Cabanis and Lecolle, 1989). These results agree with the Lower Choiyoi (Kleiman and Japas, 2009; Strazzere et al., 2016), supporting the Choiyoi magmatism source hypothesis for TIF-IR1 sample, however, the volcanoclastic nature of TFI-IR2 could not be proved.

5.3. Kungurian anoxic events

The Irati Formation succession records a specific interval of time of the Whitehill-Irati Sea evolution. A restriction from the Panthalassa water circulation controlled the development of hypersaline conditions (Milani et al., 2007). Therefore, sediment deposition occurred in a marine restrict epicontinental environment, with fluctuations in salinity, substrate oxygenation, and bioproductivity (Lavina, 1992; Hachiro, 1996; Araújo, 2001). Different paleoenvironment conditions are reported for the Taquaral and Assistência members. The deposition of dark gray siltstones and mudstone of the Taquaral Member occurred in a low to variable salt content caused by the freshwater input from rivers (Chahud and Petri, 2013). The Assistência Member records sedimentary facies (limestones and evaporites) of shallower water to arid conditions in central and north portions of the basin. Black shale facies document water condition relatively deeper than other sedimentary facies (Oelofsen, 1981; Oelofsen and Araújo, 1983). Black shale depositional environment is marked by lower to regular salinity levels, anoxic condition, with dysoxia and even euxinia levels (Reis et al., 2018; Cassel et al., 2019), and water column stratification (Martins et al., 2020; Nascimento et al., 2021). The Assistência Member is also distinct by the occurrence of skeletal remains of *Mesosaurus*, used in the first correlation between Irati Formation and the Whitehill Formation in southern Africa (Oelofsen, 1981; Oelofsen and Araújo, 1983; Lavina, 1992).

Black shales have been associated with regional and global geologic events, such as climatic changes, oceanic anoxia, and mass extinction (Phelps et al., 2015). The black shales of the Irati Formation are an essential marker for correlations inside the basin and across the southern Gondwana since they also occurs in adjacent basins as Chaco-Paraná (Milani and Zálan, 1999), Karoo Basin (Oelofsen, 1981; Oelofsen and Araújo, 1983), Huab Basin (Horsthemke et al., 1990; Faure and Cole, 1999), and Falkland Islands (Horsthemke et al., 1990).

The high precision radioisotopic age reported here of 275.75 ± 0.29 Ma (Kungurian age) places the Irati Formation anoxic events in the global scenario. It constrains the lower and upper black shale to an older and younger age than 275.75 ± 0.29 Ma, respectively. Previously published ages are overlapping due to large uncertainty, indicating a likely interval constrained between 272.7 and 284.7 Ma for the deposition of both black shales (Santos et al., 2006; Rocha-Campos et al., 2019; Bastos et al., 2021).

Kungurian oceanic anoxic conditions were also reported in South China for the Youjiang Basin. Liu et al. (2017) described a widespread anoxic condition persisting up to the latest Kungurian in the eastern equatorial Paleo-Tethys. Its TOC (Wt. ‰) curves for the Wuzhuan section display significant peaks in the K3, K6, and K7 third-order cycles. The anoxia event recorded in the K3 cycle was explained by Liu et al. (2018) as related to warm climate conditions caused by the large production of greenhouse gas by the volcanism of the large igneous province (LIP) in northern Gondwana. This intense volcanism and tectonism caused methane scape from methane-hydrate dissociation and wildfires that produced the charcoal and inertinite preserved in the Kungurian coal beds in some basins according to Liu et al. (2018). This produced a $\delta\ ^{13}C_{org}$ negative excursion in the early Kungurian (the KIEC event), constrained by the authors between 277.9 and 277.4 Ma (K2/K3). This $\delta\ ^{13}C_{org}$ negative excursion was paired to $\delta^{13}C_{carb}$ curves from continental records in North China and Australia. These results added to the time constraint of the Irati Formation black shales point to a global control on the anoxic events recorded during the Kungurian.

6. Conclusion

The bentonite sample (TF-IR1) collected in the Assistência Member of the Irati Formation at Pedras Altas section, in southernmost Paraná Basin, has a Kungurian depositional age of 275.75 ± 0.29 Ma. This sample is slightly younger than previous ages published for the Assistência Member from bentonites collected in outcrops and cores northward of the basin. Furthermore, our result seems to be more consistent with the radioisotopic ages of the equivalent stratigraphic unit in Uruguay, the Mangrullo Formation.

This high precision radioisotopic age is important to constrain the time of both black shale anoxia events preserved in the southern Paraná Basin. They are contemporaneous to the Kungurian anoxic events recorded in the neighboring basins and in the eastern equatorial Paleo-Tethys, suggesting a global control on ocean oxygenation.

Zircon trace elements and the bulk rock composition of the dated bentonite were used to test the Choiyoi magmatism source hypothesis and obtain further information about the ash fall horizon. High variability of trace elements in the Irati Formation bentonite points to a mixture of pyroclastic and detrital zircon populations, which is also seen in the geochronology analysis. Zircon geochemistry more clearly indicates the bentonite sample's primary source in a continental arc environment, a geological setting compatible with the Choiyoi source hypothesis.

CRediT authorship contribution statement

Joice Cagliari: Conceptualization, Investigation, Formal analysis, Writing – original draft, Writing – review & editing. **Henrique Serratt:** Investigation, Formal analysis, Writing – original draft. **Marlise C. Cassel:** Formal analysis, Investigation, Validation, Writing – original draft. **Mark D. Schmitz:** Supervision, Methodology, Validation, Resources, Writing – review & editing. **Farid Chemale Jr.:** Supervision, Funding acquisition, Validation, Writing – review & editing.

Declaration of Competing Interest

The authors declare that they have no known competing financial interests or personal relationships that could have appeared to influence the work reported in this paper.

Acknowledgements

The authors thank the Sedimentology Laboratory of the Unisinos University and CSF-PVE-S Program 88887.129752/2016-00. Cagliari J. thanks CAPES scholarship – Proc. n° BEX 0097/17-9 and FAPERGS [ARD/PPP 16/2551-000274-6].

Appendix A. Supplementary data

Supplementary data to this article can be found online at https://doi.org/10.1016/j.gr.2022.03.004.

References

Alessandretti, L., Philipp, R.P., Chemale Jr., F., Brückmann, M.P., Zvirtes, G., Matté, V., Ramos, V.A., 2013. Provenance, volcanic record, and tectonic setting of the Paleozoic Ventania Fold Belt and the Claromecó Foreland Basin: Implications on sedimentation and volcanism along the southwestern Gondwana margin. J. S. Am. Earth Sci. 47, 12–31.

Alferes, C.L.F., Rodrigues, R., Pereira, E., 2011. Geoquímica orgânica aplicada à Formação Irati, na área de São Mateus do Sul (PR), Brasil. Geochimica Brasiliensis 25, 47–54.

Amaral, S.E., 1971. Geologia e petrologia da formação Irati (Permiano) no estado de São Paulo. Bol. IGA 2, 1–81.

Araújo, L.M., 2001. Análise da Expressão Estratigráfica dos Parâmetros de Geoquímica Orgânica e Inorgânica nas Sequências Deposicionais do Irati. Universidade Federal do Rio Grande do Sul, Instituto de Geociências. Ph.D. thesis.

Azcuy, C.L., 2007. Bioestratigrafía del Paleozoico Superior de América del Sur: Primera Etapa de Trabajo Hacia una Nueva Propuesta Cronoestratigráfica. Asociación Geológica Argentina, Publicación Especial 11, 9–65.

Bastos, L.P.H., Rodrigues, R., Pereira, E., Bergamaschi, S., Alferes, C.L.F., Augland, L.E., Domeier, M., Planke, S., Svensen, H.H., 2021. The birth and demise of the vast epicontinental Permian Irati-Whitehill sea: Evidence from organic geochemistry, geochronology, and paleogeography. Palaeogeog., Palaeoclimatol., Palaeoecol. 562, 110103.

Bowring, S.A., Schoene, B., Crowley, J.L., Ramezani, J., Condon, D.J., 2006. High-precision U-Pb zircon geochronology and the stratigraphic record: progress and promise. Geochronology: Emerging Opportunities, Paleontol. Soc. Pap. 12, 25–45.

Buatois, L.A., Netto, R.G., Mángano, M.G., 2007. Ichnology of Permian marginal-marine to shallow-marine coal-bearing successions: Rio Bonito and Palermo Formations, Paraná Basin, Brazil. In: MacEachern, J.A., Bann, K.L., Gringas, M.K., Pemberton, S.G. (Eds.), Applied Ichnology. Society for Sedimentary Geology Short Course Notes, 167–177.

Cabanis, B., Lecolle, M., 1989. Le diagramme La/10-Y/15-Nb/8: Un outil pour la discrimination des series volcaniques et lamise en evidence des processus demelange et/ou de contamination crustale. C. R. Acad. Sci. 309, 2023–2029.

Cagliari, J., Lavina, E.L.C., Philipp, R.P., Tognoli, F.M.W., Basei, M.A.S., Faccini, U.F., 2014. New Sakmarian ages for the Rio Bonito Formation (Paraná Basin, southern Brazil) based on LA-ICP-MS U-Pb radiometric dating of zircons crystals. J. S. Am. Earth Sci. 56, 265–277.

Calarge, L.M., Meunier, A., Lanson, B., Formoso, M.L.L., 2006. Chemical signature of two Permian volcanic ash deposits within a bentonite bed from Melo. Uruguay. An. Acad. Bras. Cienc. 78, 525–541.

Cassel, M.C., 2017. Implicações paleoambientais dos folhelhos negros na rampa carbonática da Formação Irati (Master thesis). Universidade do Vale do Rio dos Sinos.

Cassel, M.C., Lavina, E.L.C., Cagliari, J., Rodrigues, R., Pereira, E., 2019. Anoxia and salinity changes: a new Permian catastrophe record. Clim. Past Discuss. [preprint], 1–20.

Chahud, A., Petri, S., 2013. Paleontology of Taquaral Member silty shale in the State of São Paulo. Braz. J. Geol. 43, 117–123.

Cohen, K., Finney, S., Gibbard, P., Fan, J., 2013. Cohen, K.M., Finney, S.C., Gibbard, P.L., Fan, J.X. 2013 updated. The ICS International Chronostratigraphic Chart. Episodes 36, 199–204.

Coutinho, J.M.V., Hachiro, J., 2005. Distribution, mineralogy, petrography, provenance and significance of Permian ash-carrying deposits in the Paraná Basin. Geol. USP. Sér. Cient. 5, 29–39.

Craddock, J.P., Ojakangas, R.W., Malone, D.H., Konstantinou, A., Mory, A., Bauer, W., Thomas, R.J., Affinati, S.C., Pauls, K., Zimmerman, U., Botha, G., Rocha-Campos, A., Santos, P.A., Tohver, E., Riccomini, C., Martin, J., Redfern, J., Horstwood, M., Gehrels, G., 2019. Detrital zircon provenance of Permo-Carboniferous glacial diamictites across Gondwana. Earth Sci. Rev. 192, 285–316.

Davydov, V.I., Crowley, J.L., Schmitz, M.D., Poletaev, V.I., 2010. High-precision U-Pb zircon age calibration of the global Carboniferous time scale and Milankovitch band cyclicity in the Donets Basin, eastern Ukraine. Geochem. Geophys. Geosystems 11, 1–22.

Santa Ana, H., Gutierrez, L., 2000. Mangrullo Formation (North Basin, Uruguay): stratigraphy and associated mineral resources. Rev. Soc. Urug. Geol. III, 2–14.

Santa Ana, H., Goso, C., Daners, G., 2006. Cuenca Norte: estratigrafia del Carbonífero-Permico. In: Veroslavsky, G., Ubilla, M., Martínez, S. (Eds.), Cuencas sedimentarias de Uruguay: geología, paleontología y recursos naturales. DIRAC, Montevideo, pp. 147–208.

Reis, D.E.S., Rodrigues, R., Moldowan, J.M., Jones, C.M., Brito, M., Cavalcante, D.C., Portela, H.A., 2018. Biomarkers stratigraphy of Irati Formation (Lower Permian) in the southern portion of Paraná Basin (Brazil). Mar. Pet. Geol. 95, 110–138.

Faure, K., Cole, D., 1999. Geochemical evidence for lacustrine microbial blooms in the vast Permian Main Karoo, Parana, Falkland Islands and Huab basins of southwestern Gondwana. Palaeogeog. Palaeoclimatol Palaeoecol. 152, 189–213.

Gama Jr., E., 1979. A sedimentação do Grupo Passa Dois (exclusive Formação Irati): um modelo geomórfico. Rev. Bras. Geociênc. 9, 1–16.

Gandini, R., Netto, R.G., Kern, H.P., Lavina, E.L.C., 2010. Assinaturas icnológicas da sucessão sedimentar Rio Bonito no bloco central da jazida carbonífera de Iruí, Cachoeira do Sul (RS). Gaea 6, 21–43.

Gradstein, F.M., Ogg, J.G., Schmitz, M.D., Ogg, G.M., 2020. Geological Time Scale 2020. Elsevier B.V, Netherlands.

Grimes, C.B., Wooden, J.L., Cheadle, M.J., John, B.E., 2015. "Fingerprinting" tectono-magmatic provenance using trace elements in igneous zircon. Contrib. to Mineral. Petrol. 170, 1–26.

Guerra-Sommer, M., Cazzulo-Klepzig, M., Formoso, M.L.L., Menegat, R., Fo, J.G.M., 2008a. U-Pb dating of tonstein layers from a coal succession of the southern Paraná Basin (Brazil): A new geochronological approach. Gondwana Res. 14, 474–482.

Guerra-Sommer, M., Cazzulo-Klepzig, M., Menegat, R., Formoso, M.L.L., Basei, M.A.S., Barboza, E.G., Simas, M.W., 2008b. Geochronological data from the Faxinal coal succession, southern Paraná Basin, Brazil: A preliminary approach combining radiometric U-Pb dating and palynostratigraphy. J. S. Am. Earth Sci. 25, 246–256.

Guerra-Sommer, M., Cazzulo-Klepzig, M., Santos, J.O.S., Hartmann, L.A., Ketzer, J.M., Formoso, M.L.L., 2008c. Radiometric age determination of tonsteins and stratigraphic constraints for the Lower Permian coal succession in southern Paraná Basin. Brazil. Int. J. Coal Geol. 74, 13–27.

Hachiro, J., 1996. O subgrupo Irati (Neopermiano) da Bacia do Paraná. Universidade de São Paulo, Instituto de Geociências. Ph.D. thesis.

Holz, M., França, A.B., Souza, P.A., Iannuzzi, R., Rohn, R., 2010. A stratigraphic chart of the Late Carboniferous/Permian succession of the eastern border of the Paraná Basin, Brazil, South America. J. South Am. Earth Sci. 29, 381–399.

Horsthemke, E., Ledendecker, S., Porada, H., 1990. Depositional environments and stratigraphic correlation of the Karoo Sequence in northwestern Damaraland. Commun. Geological Survey Namibia 6, 63–73.

Jaffey, A.H., Flynn, K.F., Glendenin, L.E., Bentley, W.C., Essling, A.M., 1971. Precision Measurement of Half-Lives and Specific Activities of ^{235}U and ^{238}U. Phys. Rev. C 4, 1889–1906.

Kleiman, L.E., Japas, M.S., 2009. The Choiyoi volcanic province at 34°S-36°S (San Rafael, Mendoza, Argentina): Implications for the Late Palaeozoic evolution of the southwestern margin of Gondwana. Tectonophysics 473, 283–299.

Krogh, T.E., 1973. A low-contamination method for hydrothermal decomposition of zircon and extraction of U and Pb for isotopic age determinations. Geochim. Cosmochim. Acta 37, 485–494.

Lavina, E.L.C., 1992. Geologia sedimentar e paleogeografia do Neopermiano e Eotriássico (intervalo Kazaniano-Scythiano) da Bacia do Paraná (Ph.D. thesis). Universidade Federal do Rio Grande do Sul (Porto Alegre).

Lavina, E.L.C., Lopes, R.C., 1987. A transgressão marinha do Permiano Inferior e a evolução paleogeográfica do Supergrupo Tubarão no Estado do Rio Grande do Sul. Paula-Coutiana 1, 51–103.

Lavina, E.L.C., Barberena, D.C.A., Azevedo, S.A.K., 1991. Tempestades de Inverno e Altas Taxas de Mortalidade de Répteis Mesossauros. Um Exemplo a Partir do Afloramento Passo São Borja. RS. Pesqui. em Geociênc. 18, 64–70.

Liu, C., Du, Y., Jarochowska, E., Yan, J., Munnecke, A., Lu, G., 2018. A major anomaly in the carbon cycle during the late Cisuralian (Permian): Timing, underlying triggers and implications. Palaeogeogr. Palaeoclimatol Palaeoecol. 491, 112–122.

Liu, C., Jarochowska, E., Du, Y., Munnecke, A., Dai, X., 2017. Prevailing anoxia in the Kungurian (Permian) of South China: Possible response to divergent climate trends between the tropics and Gondwana. Gondwana Res. 49, 81–93.

Martins, L.L., Schulz, H., Severiano Ribeiro, H.J.P., Nascimento, C.A., Souza, E.S., Cruz, G.F., 2020. Organic geochemical signals of freshwater dynamics controlling salinity stratification in organic-rich shales in the Lower Permian Irati Formation (Paraná Basin, Brazil). Org. Geochem. 140, 103958.

Mattinson, J.M., 2005. Zircon U-Pb chemical abrasion ("CA-TIMS") method: Combined annealing and multi-step partial dissolution analysis for improved precision and accuracy of zircon ages. Chem. Geol. 220, 47–66.

Maynard, J.B., Chocyk-Jaminski, M., Gaines, R.R., Krekeler, M.P., Prokopenko, M., Summers, A.M., Huff, W.D., 1996. Bentonites in the Late Permian Tatarian Irati Formation of Brazil: geochemistry and potential of stratigraphic correlation. Proc. Ann. Meet. Geol. Soc. Am, Denver, p. 280.

McDonough, W.F., Sun, S.-S., 1995. The composition of the Earth. Chem. Geol. 120, 223–253.

Mendes, J.C., Fulfaro, V.J., Amaral, J.E., Landim, P.M.B., 1966. A Formação Irati (Permiano) e fácies associadas. Bol. Soc. Bras. Geol. 15, 23–43.
Metcalfe, I., Crowley, J.L., Nicoll, R.S., Schmitz, M., 2015. High-precision U-Pb CA-TIMS calibration of Middle Permian to Lower Triassic sequences, mass extinction and extreme climate-change in eastern Australian Gondwana. Gondwana Res. 28, 61–81.
Milani, E.J., 1997. Evolução tectono-estratigráfica da Bacia do Paraná e seu relacionamento com a geodinâmica fanerozóica do Gondwana sul-ocidental (Ph.D thesis). Universidade Federal do Rio Grande do Sul.
Milani, E.J., Faccini, U.F., Scherer, C.M., Araújo, L.M., Cupertino, J.A., 1998. Sequences and stratigraphtc hierarchy of the Paraná basin (Ordovician to Cretaceous), southern Brazil. Bol. IG USP 29, 125–173.
Milani, E.J., Zalán, P.V., 1999. An outline of the geology and petroleum systems of the Paleozoic interior basins of South America. Episodes 22, 199–205.
Milani, E.J., Melo, J.H.G., Souza, P.A., Fernandes, L.A., França, A.B., 2007. Bacia do Paraná. Bol. Geociênc. Petrobras 15, 265–287.
Nascimento, C.A., Souza, E.S., Martins, L.L., Severiano Ribeiro, H.J.P., Santos, V.H., Rodrigues, R., 2021. Changes in depositional paleoenvironment of black shales in the Permian Irati Formation (Paraná Basin, Brazil): Geochemical evidence and aromatic biomarkers. Mar. Petrol. Geol. 126, 104917.
Oelofsen, B.W., 1981. An anatomical and systematic study of the family Mesosauridae (reptilia; proganosauria) with special reference to its associated fauna and palaeoecological environment in the whitehill sea. University of Stellenbosch, Department of Zoology. Ph.D. thesis.
Oelofsen, B., Araújo, D.C., 1983. Palaeoecological implications of the distribution of Mesosaurid reptiles in the Permian Irati Sea (Paraná Basin), South America. Rev. Bras. Geociênc. 13, 1–6.
Oelofsen, B.W., Araújo, D.C., 1987. Mesosaurus Tenuidens and Stereosternum Tumidum from the Permian Gondwana of both Southern Africa and South America. South Afr. J. Geol. 83, 370–372.
Padula, V.T., 1968. Estudos geológicos da Formação Irati, sul do Brasil. Bol. Téc. Petrobrás 11, 407–430.
Pankhurst, R.J., Rapela, C.W., Fanning, C.M., Márquez, M., 2006. Gondwanide continental collision and the origin of Patagonia. Earth Sci. Rev. 76, 235–257.
Petri, S., Coimbra, A.M., 1982. Estruturas sedimentares das Formações Irati e Estrada Nova (Permiano) e sua contribuição para elucidação dos seus paleoambientes geradores, Brasil. Proc. Congr. Latinoamericano Geol. Argentina, Actas II, 353–371.
Phelps, R.M., Kerans, C., Da-Gama, R.O.B.P., Jeremiah, J., Hull, D., Loucks, R.G., 2015. Response and recovery of the Comanche carbonate platform surrounding multiple Cretaceous oceanic anoxic events, northern Gulf of Mexico. Cretac. Res. 54, 117–144.
Rivera, T.A., Storey, M., Schmitz, M.D., Crowley, J.L., 2013. Age intercalibration of $^{40}Ar/^{39}Ar$ sanidine and chemically distinct U/Pb zircon populations from the Alder Creek Rhyolite Quaternary geochronology standard. Chem. Geol. 345, 87–98.
Rocha, H.V., Mendes, M., Pereira, Z., Rodrigues, C., Fernandes, P., Lopes, G., Sant'Anna, L.G., Tassinari, C.C.G., Lemos de Sousa, M.J., 2020. New palynostratigraphic data of the Irati (Assistência Member) and the Corumbataí formations, Paraná Basin, Brazil, and correlation with other south American basins. J. S. Am. Earth Sci. 102, 102631.
Rocha-Campos, A.C., Basei, M.A.S., Nutman, A.P., Santos, P.R., 2006. Shrimp U-Pb zircon geochronological calibration of the Late Paleozoic supersequence, Paraná Basin. Brazil. Proc. S. Am. Symp. Isot. Geol, Punta del Este, pp. 322–325.
Rocha-Campos, A.C., Basei, M.A., Nutman, A.P., Kleiman, L.E., Varela, R., Llambias, E., Canile, F.M., Rosa, O.C.R., 2011. 30 million years of Permian volcanism recorded in the Choiyoi igneous province (W Argentina) and their source for younger ash fall deposits in the Paraná Basin: SHRIMP U-Pb zircon geochronology evidence. Gondwana Res. 19, 509–523.
Rocha-Campos, A.C., Basei, M.A.S., Nutman, A.P., Santos, P.R., Passarelli, C.R., Canile, F.M., Rosa, O.C.R., Fernandes, M.T., Santa Ana, H., Veroslavsky, G., 2019. U-Pb zircon dating of ash fall deposits from the Paleozoic Paraná Basin of Brazil and Uruguay: a reevaluation of the stratigraphic correlations. J. Geol. 127, 167–182.
Rodrigues, R., Pereira, E., Bergamaschi, S., Chaves, H.A.F., Alferes, C.L.F., 2010. Organic Geochemistry of Irati Formation. Lower Permian of Paraná Basin. Proc. Congr. Latinoamericano Geoq. Org, Montevideo, pp. 42–43.
Santos, R.V., Souza, P.A., Alvarenga, C.J.S., Dantas, E.L., Pimentel, M.M., Oliveira, C.G., Araújo, L.M., 2006. Shrimp U-Pb zircon dating and palynology of bentonitic layers from the Permian Irati Formation, Paraná Basin. Brazil. Gondwana Res. 9, 456–463.
Sato, A.M., Llambías, E.J., Basei, M.A.S., Castro, C.E., 2015. Three stages in the Late Paleozoic to Triassic magmatism of southwestern Gondwana, and the relationships with the volcanogenic events in coeval basins. J. S. Am. Earth Sci. 63, 48–69.
Schmitz, M.D., Davydov, V.I., 2012. Quantitative radiometric and biostratigraphic calibration of the Pennsylvanian-Early Permian (Cisuralian) time scale and pan-Euramerican chronostratigraphic correlation. Geol. Soc. Am. Bull. 124, 549–577.
Schmitz, M.D., Schoene, B., 2007. Derivation of isotope ratios, errors, and error correlations for U-Pb geochronology using ^{205}Pb-^{235}U-(^{233}U)-spiked isotope dilution thermal ionization mass spectrometric data. Geochem. Geophys. Geosystems 8, 1–20.
Schmitz, M.D., Singer, B.S., Rooney, A.D., 2020. Radioisotope Geochronology. In: Gradstein, F.M., Ogg, J.G., Schmitz, M.D., Ogg, G.M. (Eds.), Geologic Time Scale 2020. Elsevier, Netherlands, pp. 193–2010.
Silva, A.F., 2021. Depósitos piroclásticos de queda (pfds) como ferramenta estratigráfica. Proveniência, geocronologia e reconstrução das sequências deposicionais da Formação Irati (Ph.D thesis). Universidade Federal do Rio Grande do Sul, Instituto de Geociências.
Silva, A.F., Dani, N., Remus, M.V.D., Guerra Sommer, M., Horn, B.L.D., 2017. Bentonitas da Formação Irati no setor sul da Bacia do Paraná. Geol. USP – Sér Cient. 17, 75–88.
Soares, M.B., 2003. A taphonomic model for the Mesosauridae assemblage of the Irati Formation (Paraná Basin, Brazil). Geol. Acta 1, 349–361.
Souza, P.A., Boardman, D.R., Premaor, E., Félix, C.M., Bender, R.R., Oliveira, E.J., 2021. The Vittatina costabilis Zone revisited: New characterization and implications on the Pennsylvanian-Permian icehouse-to-greenhouse turnover in the Paraná Basin, Western Gondwana. J. S. Am. Earth Sci. 106, 102968.
Strazzere, L., Gregori, D.A., Benedini, L., 2016. Early Permian arc-related volcanism and sedimentation at the western margin of Gondwana: Insight from the Choiyoi Group lower section. Geosci. Front. 7, 715–731.
Teixeira, C.A.S., Sawakuchi, A.O., Bello, R.M.S., Nomura, S.F., Bertassoli, D.J., Chamani, M.A.C., 2018. Fluid inclusions in calcite filled opening fractures of the Serra Alta Formation reveal paleotemperatures and composition of diagenetic fluids percolating Permian shales of the Paraná Basin. J. S. Am. Earth Sci. 84, 242–254.
Watson, E.B., Wark, D.A., Thomas, J.B., 2006. Crystallization thermometers for zircon and rutile. Contrib. Mineral. Petrol. 151, 413–433.
Wildner, W., Ramgrab, G.E., Lopes, R.D., Iglesias, C.D.F., 2006. Mapa Geológico do Estado do Rio Grande do Sul. Scale 1:750.000. CPRM, Serviço Geológico do Brasil. Porto Alegre, RS.
Winchester, J.A., Floyd, P.A., 1977. Geochemical discrimination of different magma series and their differentiation products using immobile elements. Chem. Geol. 20, 325–343.

Geoscience Frontiers 16 (2025) 101934

Contents lists available at ScienceDirect

Geoscience Frontiers

journal homepage: www.elsevier.com/locate/gsf

Research Paper

Paleogeographic significance of unknown hyperextended continental crust in South Atlantic conjugated margin

C.D. Teixeira [a,*], T.J. Girelli [a], H. Serratt [a,b,c], H.O.S. Oliveira [a], M.F. Cruz [a], B. Conti [d], P. Rodriguez [d], F. Chemale Jr [a]

[a] Geology and Geophysics Research Group – NGA, Universidade do Vale do Rio do Sinos, São Leopoldo, RS, Brazil
[b] Geology Graduate Program, Universidade de Brasília, Distrito Federal, Brazil
[c] UMR CNRS-IFREMER-CNRS-UBS 6538 Geo-Ocean, IUEM, Université de Bretagne Occidentale, France
[d] Exploration & Production, ANCAP, Montevideo, Uruguay

ARTICLE INFO

Article history:
Received 27 March 2024
Revised 3 July 2024
Accepted 19 September 2024
Available online 1 October 2024
Handling Editor: R. D. Nance

Keywords:
Hyperextended continental crust
Reconstruction
South Atlantic Ocean
Passive margin
Gondwana

ABSTRACT

The paleogeographic reconstruction of fragmented and dispersed continents often poses a challenge due to the lack of information regarding the nature of that extend beneath passive margin basins. To define the width of the continental crust beneath passive margin basins and its implications for paleogeographic reconstruction of conjugate continental margins, this study investigates the architecture of the stretched continental crust of the southern South Atlantic conjugate margin. The investigated region encompasses South Africa, Namibia, southern Brazil, and Uruguay, which were formed during the Mesozoic rifting of SW Gondwana. Employing a multi-tool approach combining seismic interpretation, gravity, magnetometry, and U-Pb isotopic data, the research aims to quantify the extension of stretched continental crust and its implications for plate reconstructions. The study reveals that the restored stretched crust spans at least 150 km, emphasizing the significance of considering connections between both margins for realistic paleogeographic reconstructions. Furthermore, the distinct U-Pb zircon age distribution patterns between SW Africa and SE South America reinforce the lack of direct connections despite their Gondwanan origin. The missing link estimated in this study is around 150 km, comparable in size to major mountain ranges such as the Andean or Urals. This work sheds light on critical aspects of Earth's dynamic crustal evolution and emphasizes the need for comprehensive reconstructions considering stretched and eroded crust in the South Atlantic conjugate margin.

1. Introduction

Throughout the last decades, several studies were carried out on rifted continental margins and hyperextended continental crust in the passive margin, providing knowledge on this topic in the different magma-poor, magma-rich, and sediment-rich passive margins (e.g., Peron-Pinvidic et al., 2013; Doré and Lundin, 2015; Lei et al., 2020). Many of these studies have specifically focused on the extension at rifted continental margins in association with the South Atlantic opening, offering valuable insights into the tectonic evolution of this region (e.g., Rabinowitz and LaBrecque, 1979; Moulin et al., 2010; Granot and Dyment, 2015; Chauvet et al., 2021). Although geoscientists understand this process well, accurately determining its impact on paleo-plate reconstructions remains challenging. The challenge lies mainly in precisely characterizing the amount of continental crust stretched. It occurs due to the sedimentary and volcanic package cover over the stretched continental crust (Mutter et al., 1982; Sutra et al., 2013; Nirrengarten et al., 2018). To address this, gravimetry, magnetometry, and seismic data play a crucial role in providing information essential to understanding the dynamic processes shaping the Earth's crust. This information helps create realistic paleogeographic reconstruction models and define subsurface geological structures in conjugate margins separated by the formation of oceans. Regarding this scenario, the South Atlantic Conjugate Margin (SACM), comprising South Africa, Namibia, southernmost Brazil, and Uruguay, provides an ideal opportunity to better understand the effects of stretched crust on paleo plate reconstruction (Fig. 1).

* Corresponding author.
E-mail addresses: claudiadtx@gmail.com, claudiadtx@unisinos.br (C.D. Teixeira).

https://doi.org/10.1016/j.gsf.2024.101934

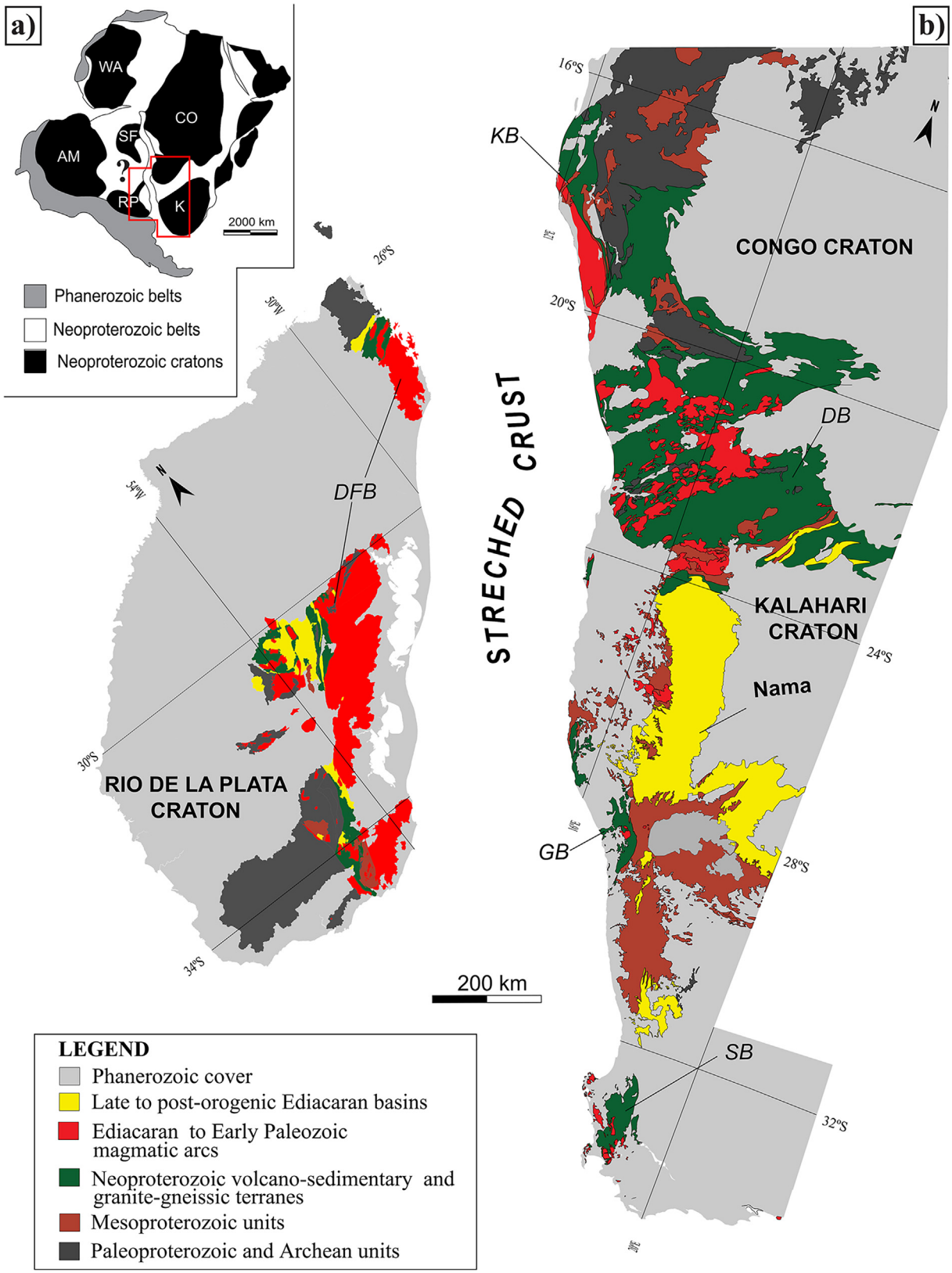

Fig. 1. (a) Distribution of main cratons in the West Gondwana context. WA–West Africa Craton; AM–Amazonian Craton, SF–São Francisco Craton; CO–Congo Craton; K–Kahalari Craton; RP–Rio de la Plata Craton; (b) detailed view of main Brasiliano/PanAfrican belts and surroundings cratonic areas. DFB–Dom Feliciano Belt; KB–Kaoko Belt; DB–Damara Belt; GB–Gariep Belt; SB–Saldanha Belt (after Becker-Kerber et al., 2020).

The South Atlantic conjugate margins exhibit significant asymmetry, with uneven extension documented in this region and observations showing significant crustal architecture asymmetry, SDR type distribution, and total volume of SDR (Chauvet et al.,

2021). This asymmetry is a crucial consideration in understanding the evolution of the margins and the distribution of stretched continental crust. Quantifying the extent of asymmetric extension is challenging, but it has significant implications for plate reconstructions and understanding the geological history of the region.

Our study aims to quantify the extension of continental crust stretched during the rifting process of SW Gondwana and better understand the impact of this in plate reconstruction models. We combined regional seismic interpretations, gravity, and magnetometry data from the South Atlantic Ocean and onshore emerged margins. Additionally, focusing on evaluating the impact of the lack of geological structures between both sides, we did a comparative analysis based on U-Pb isotopic data from zircons grains in emerged margins. Based on the results obtained by this multiple-tool approach, we could identify that the amount of stretched crust is at least 150 km. Furthermore, the U-Pb data reinforce the lack of direct correlation between these margins, which would be lost in this stretched interval. This study sheds light on three questions: (i) The absence of direct structural correlation between structures in SW Africa and SE South America; (ii) The presence of hyperextended crust on volcanic passive and sedimentary rich margins; (iii) It is critical to consider the structural ties between both margins to discuss the Precambrian tectonic evolution models.

2. Geological settings

The Gondwana history is a common point in the geological history of Africa and South America. The formation of the Gondwana paleo continent took place during the Neoproterozoic era (Veevers, 2004). Our study area (Fig. 1) was affected by the subduction of the Adamastor Ocean during the Gondwana formation (Veevers, 2004; Caxito et al., 2022). This significant event is recorded in the Pan-African/Brasiliano orogenic belts of South America and Africa (e.g., Chemale et al., 2012). This orogenic cycle profoundly influences the NE–SW structures in the southernmost regions of Brazil and Uruguay margins (Fernandes et al., 1992).

Meanwhile, consensus regarding the subduction direction remains elusive (Basei, 2000; Chemale, 2000), as does the paleogeographic reconstruction of the various orogenic belts from the Neoproterozoic to the Eopaleozoic. This uncertainty is primarily due to a lack of petrotectonic assemblages and more complete rock associations (e.g., juvenile arcs and ophiolites). One of the key areas of interest is the underlying continental crust of the passive margin basin, about which we have little information regarding the nature of these rocks. The local process of Gondwana's break-up unfolded within these structures, as observed by the margin, and aligned parallel these structures in southernmost Brazil and Uruguay. Even the emplacement of *syn*-rift magmatism during the rifting of the SW Gondwana is intricately linked to these pre-existing structures, which should be considered as the primary magmatic conduit of the SDR (Seaward Dipping Reflectors; Fig. 2; Chauvet et al., 2021; Serratt et al., 2022).

The studied sector is formed of a Precambrian basement that comprises in the eastern side the Kaoko, Damara, and Gariep belts (Begg et al., 2009; Frimmel, 2009; Haas et al., 2022) and in the western sector, the Dom Feliciano Belt (Basei, 2000; Chemale, 2000). The Damara Belt is associated with the docking between the Congo and Kalahari cratons, with an NE–SW direction and subduction towards the north under the Congo Craton (Prave, 1996; Passchier et al., 2002). The Kaoko Belt is characterized by dominantly E–NE-oriented structures and subdivided into eastern, central, western, and southern zones (Miller and Grote, 1988; Porada, 1989). The Gariep Belt is related to a part of the larger network of Pan-African/Brasiliano orogenic belts in SW-Gondwana (Frimmel, 2009). In turn, the NE–SW Dom Feliciano Belt records the docking between Rio de La Plata and Kalahari cratons with main structures-oriented NE–SW (Hartmann et al., 2007; Philipp et al., 2016; Basei et al., 2018; Will et al., 2020). These Precambrian belts were partially covered by Phanerozoic sedimentary basins, such as Paraná and Cape-Karoo (e.g., Milani and De Wit, 2008).

This supercontinent, formed during the Neoproterozoic and later incorporated in the Pangaea supercontinent, was fragmented throughout the Cretaceous, giving rise to the conjugate margin of southwestern Africa and southeastern South America. The onset of rifting was marked by extensive magmatism of the Paraná-Etendeka Large Igneous Province (LIP), approximately 134 million years ago, associated with the Tristan da Cunha plume (Gomes and Vasconcelos, 2021). This fragmentation process propagated from the south to the north, forming the Walvis Ridge at around 127–133 Ma (Macdonald et al., 2003; Torsvik et al., 2009; Heine et al., 2013), recording the movement of the African Plate over the mantle hot spot during the separation of the African and South American continents and the formation of the South Atlantic Ocean. This LIP magmatism was preceded by the SDR magmatism, recorded in both margins, and that characterizes both margins as Volcanic Passive Margins (Chauvet et al., 2021; Serratt et al., 2022). The rift and drift sedimentation in the studied sector originated in the offshore basins of Orange, Luderitz, and Walvis in Namibia and Pelotas and Punta del Este in Brazil and Uruguay.

3. Methods and materials

The accurate determination of lithospheric stretching requires a comprehensive, multi-tool approach. Our study employed seismic interpretation as a robust tool for measuring lithospheric stretching, which provided detailed insights into subsurface structures. Additionally, we complemented this approach with gravity and magnetic profiles. The integration of potential data delineated the boundaries of lithospheric stretching, offering a robust understanding of the geophysical characteristics that result from the stretching processes. Lastly, we compared the analysis of U-Pb isotopic data from zircons grains in the emerged margins.

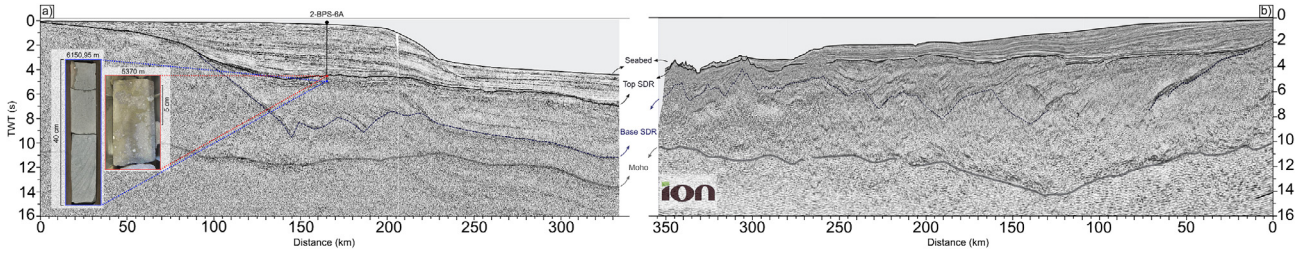

Fig. 2. Seismic profiles b–b' and well data across the conjugate margins of the northern Pelotas (a) and Lüderitz (b) basins (Fig. 3). Well 2-BPS-6A, located in the Pelotas Basin, sampled volcanic units inserted in (a). The Lüderitz Basin profile (b) was adapted from Chauvet et al. (2021).

3.1. Lithosphere stretching

The methodology employed for calculating lithosphere stretching encompasses seismic line profile interpretation previously published by Chauvet et al. (2021), crustal thickness estimation, and the calculation of stretching factors, utilizing the concept of "half-space stretching" to ascertain the lithosphere stretching factor (β; McKenzie, 1978), identifying the crust limits, followed by the determination of both non-extended and stretched crustal thicknesses. The stretched crustal thickness is measured from the base of the SDR layer to the Moho boundary. The non-extended thickness was measured as the entirety of the crustal thickness extending inland from the crustal necking. Thickness measurements are taken at various points along seismic profiles. Subsequently, the stretching factor (β) is estimated by considering the thickness ratio between the non-extended and post-extension transition crust (McKenzie, 1978).

To precisely delineate the regions of lithospheric stretching in each seismic profile, we conducted correlation analyses with magnetic and gravity responses using the Free Air anomaly grid from Sandwell et al. (2014) and the Magnetic Anomaly grid from Maus et al. (2009). This correlation allowed to match previously published magnetic anomalies by Rabinowitz and Labrecque (1979; G, M3, M0) and Moulin et al. (2010; LMA, M4, M2, M0) to delineate with more precision the regions with lithospheric stretching.

Our restoration of the stretched continental crust assumes that volcanic dykes comprise 50% of the total volume, based on observations from other volcanic passive margins (Myers, 1980) and supported by seismic, potential, drilling data from the region (Harkin et al., 2020; Serratt et al., 2022). As shown in Fig. 2, the drilling data reveals that the stretched crust consists of volcanic rocks interlayered with pyroclastic and/or sedimentary rocks. The 50% here assumed is the maximum estimation in the Myers study, so based on this, we used this number to have the less extrapolated value. The presence of extensive volcanic dykes and interlayered volcanic and sedimentary rocks can obscure the underlying continental crust, making it difficult to assess its characteristics.

3.2. Isotope record

The use of zircon databases combined with geological data is a powerful tool for estimating the cumulative growth of continental crust and discriminating the source area of different geological terranes. To compare the major source rocks for the onshore basement rocks of the studied conjugate passive margin, we use the U-Pb zircon databases of southern South America and SW Africa. For the South American margin, we compiled 16,692 individual analyses over a hundred studies conducted since 1985 in southern Brazil and Uruguay shields. Similarly, a comprehensive dataset of 16,005 individual analyses from SW Africa, encompassing Pan-African Belts and cratonic areas, was compiled by Puetz (2018) and Puetz et al. (2021). From these data, 7953 in southern Brazil and Uruguay and 2187 in Namibia correspond to zircons in igneous rocks.

3.3. Gravimetric and magnetic data

Gravity and magnetic anomalies provide constraints on the structure of the Earth's crust. It can help to detail their structural connections by integrating these data into the reconstruction. We reconstruct the pre-to-early stretching process before oceanic crust formation at 150 Ma using GPlates based on the rotational poles from Müller et al. (2019). We analyze the marine gravity and magnetic anomalies preserved on the South American and African plates using the Earth Magnetic Anomaly Model (Maus et al., 2009) and the Satellite Free-air Gravity Anomaly data (Sandwell et al., 2014).

4. Results

The connections between East South America and West African margins have been known since du Toit (1927), and hundreds of research studies improved this knowledge throughout the last century. Nevertheless, despite these efforts, certain geological gaps remain open. Since the development of GPlates Software (Müller et al., 2018), the representation of plate tectonic positions and motions has been substantially improved. In South America and Africa, the stretching process begins at 155 Ma in the southernmost portion, southward of the study area (Jokat et al., 2003). Using this as a time constraint and based on the rotational poles from Müller et al. (2019), we reconstructed the pre-to-early stretching process before oceanic crust formation at 150 Ma (Fig. 3). The reconstruction carried out incorporating the magnetic and gravimetric data to the block models allowed us to establish the lack of a clear connection between structures in both margins. The lack of a direct link raises questions about the extent of the crustal loss during the break-up.

The clues for the lack of a direct connection between these two continents begin to be clear when we interpret the seismic lines from both margins. Through the regional seismic lines in the North Pelotas Basin (Fig. 3a), it is possible to observe the SDR's below the drift sedimentary rocks, represented in detail by the basalt drill core on the right and above the stretched continental crust. A similar pattern can be observed in the Luderitz Basin (conjugate margin, Fig. 3b). So, in the southern South Atlantic Ocean, a hyperextend continental crust occurs below a thick volcanic and sedimentary package of Cretaceous to recent rocks (Fig. 3), as already described by Chauvet et al. (2021). However, determining oceanic and continental crust boundaries in volcanic passive margins is challenging, and it is key information for continental crust restoration. Knowing this, we used previously published magnetic anomalies M2 and M4 (Rabinowitz and Labrecque, 1979; Moulin et al., 2010) to help define these boundaries. The first opening stage occurred between chrons M4 and M2, and the magnetic anomaly M2 denotes early oceanic crust formation (Koopmann et al., 2014; Fig. 3). This initial stage was characterized by basement flexure, proximal SDR deposition, and high-amplitude magnetic anomalies (Serratt et al., 2022). Based on this, we could measure the continental crust that spans up to 450 km beneath the volcanic and sedimentary deposits of the passive margins.

Using this information on continental crust offshore extension, we quantified the pre-drift margin width by the calculated stretching factor. We divided the margin into two main domains: Unstretched Continental Crust (UCC) and Stretched Continental Crust (SCC) (Fig. 3 and Table 1). For the present study, we attributed the (β) as close to one for the unstretched sector, and the information about the extension of this crust is important in quantifying the total crustal gap between the onshore portions. In turn, the stretched sector (SCC) was also measured because it is important to understand the amount of stretched crust that can be restored (Table 1). The restored crust process of stretched crust considered the estimated volcanic dikes (up to 50%; see discussions) and the stretching factor (Table 1). Four sections were used for the present study: two on the South American margin (Fig. 3b and c) and two on the SW Africa margin (Fig. 3b' and c'). These sections show a stretched continental crust covered by the passive margin sedimentary rocks and SDR basalts. The section b, situated in the Pelotas Basin (PB), displays a stretched continental crust of 177.04 km, while the section of the conjugate margin (Fig. 3b') in the Walvis Basin (WB) has an estimated stretched crust

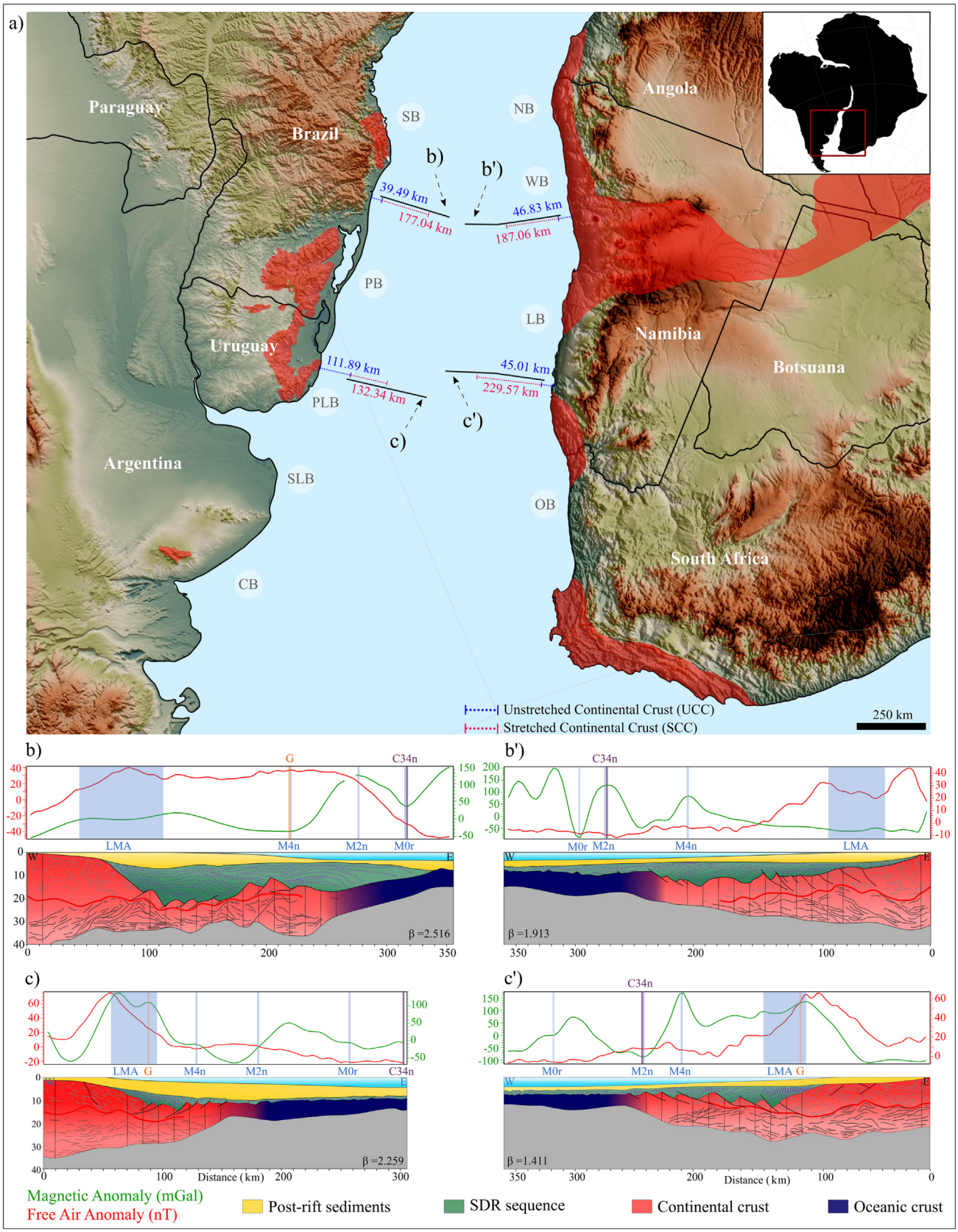

Fig. 3. (a) Sketch of SW Gondwana map reconstructed at 118 Ma according to the global plate model that includes plate deformation along major rifts and orogens of Müller et al. (2019), with the position of studies seismic profiles; background data: topography SRTM1 grid. The red areas correspond to the outcropping of Brasiliano/Pan-African terranes in the SW Gondwana. The top right inset with South America and Africa maps is 118 Ma. 2D seismic interpretation profiles are modified from Chauvet et al. (2021): (b and b') above: gravimetry and magnetic profiles; below: schematic interpretation seismic profiles b and b'; and (c and c') above: gravimetry and magnetic profiles; below: schematic interpretation seismic profiles c and c'. The gray line on the magnetic profile shows magnetic anomaly from Rabinowitz and Labrecque (1979) and Moulin et al. (2010). The darker red lines in the profiles mark the boundary of the upper and lower continental crust. The crustal stretching factor (β) is calculated along the stretched crust with regular spacing (black dashed vertical line). The boundary between the hyperextended continental crust and oceanic crust (dark blue) is unclear in seismic interpretations. Basins: NB – Namibia; SB – Santos; WB – Walvis; LB – Luderitz; PB – Pelotas; PLB – Punta del Este; OB – Orange; SLB – Salado; and CB – Colorado.

Table 1
Crustal stretching factor (β) and restored continental crust measurements for the four sections analyzed in the study. The table includes data on unstretched continental crust (UCC), stretched continental crust (SCC), and the restoration process considering volcanic dikes and the stretching factor for both the South American (Pelotas Basin) and SW Africa (Walvis Basin) margins.

Section	CCU	CCS	β	Stretched	Stretched 50%[a]	Restored[b]	Unstretched[c]	Stretched 50%[d]	Gap[e]
Northern Pelotas and Walvis basins (Section b–b')									
b	39.49	177.04	2.52	70.365	35.18	74.68	86.33	84.07	170.40
b′	46.83	187.06	1.91	97.783	48.89	95.72			
Punta del Este and Lüdertiz basins (Section c–c')									
c	111.90	132.35	2.26	58.587	29.29	141.19	156.92	110.64	267.56
c′	45.02	229.57	1.41	162.700	81.35	126.37			

UCC – Unstretched Continental Crust; SCC – Stretched Continental Crust; β – stretching factor, the magnitude of the extension; [a] – stretched restored crust considering 50% of volcanic dikes; [b] – Restored is the sum of stretched crust suppressed in 50% to incorporate the effect of magmatic dykes as proposed by Myers (1980) and the non-stretched crust of each section; [c] – Unstretched crust for sections b–b' and c–c'; [d] – stretched restored crust considering 50% of volcanic dikes for sections b–b' and c–c'; [e] – final gap: sum of unstretched and restored considering the 50% (Myers, 1980) crust for both sections.

of 187.06 km. Considering the continental crust extension, the conjugate b–b' the crustal stretching factor (β) in the South American margin is between 2.52 in the north Pelotas Basin and 1.91 in the Walvis Basin. The restored for each margin is 74.68 (PB) and 95.72 (LB; Table 1), and the final gap results from the sum of unstretched and restored crust for each side reaching in b–b' the section between northern Pelotas and Walvis basins with 170.40 km (see section b–b' in Fig. 3a).

The conjugate c–c' profiles exhibit a stretched continental crust (SCC) of 110.90 km for the Punta del Este Basin profile (PLB; Fig. 3c) and 229.57 km for the Lüderitz Basin profile (LB; Fig. 3c'). The values on the eastern Atlantic margin are from 1.91 in the Walvis Basin and 1.41 in the Luderitz Basin. The restored margins width range between 141.19 km and 123.37 km, respectively, in the Punta del Este (Fig. 3c) and Lüderitz (Fig. 3c') basins (Table 1). The final gap results from the sum of unstretched and restored crust for each side reaching in b–b' the section between Punta del Este and Lüderitz basins with 267.56 km of gap, taking into account the 50% of suppression in the stretched crust.

We compare the tectonic similarities between these regions by analyzing the distribution of zircon age patterns in the onshore rocks from the conjugate margins of southern South America and SW Africa. A compilation of 16,592 zircon grains from Southeast South America and 16,005 from southwestern Africa offers a comprehensive overview of the main crustal cycles in both areas (Fig. 4). This analysis allows us to distinguish the age pattern distribution along the continental onshore margins of southern South America and SW Africa. The age spectra in Southeast South America (in blue, Fig. 4) are distributed in three main peaks. Two of these correspond to Neoproterozoic events related to the Dom Feliciano Belt: (I) the most important one corresponds to the Ediacaran–Cryogenian interval related to the collisional stage; (II) the second one corresponds to the Tonian period, related to the arc stage; the last one (III) corresponds to the Paleoproterozoic, Rhyacian–Siderian period, related to the accretion of Rio de La Plata Craton units. These peaks are similarly identified in the igneous rocks of the region. In turn, southwestern Africa (in red, Fig. 4) presents three major peaks: (i) at the Mesoproterozoic, Stenian to Ectasian period, (ii) at the Paleoproterozoic Statherian to Orosirian period, and (iii) Meso to Paleo-Archean. Regarding the Namibian igneous rocks, the main peak is restricted to the Stenian to Ectasian period.

5. Discussion

5.1. The connections between South America–South Africa margins

The connections between East South America and West African margins have been known since du Toit (1927), and hundreds of research studies improved this knowledge throughout the last century (e.g., Seton et al., 2012; Blaich et al., 2013). Nevertheless, despite these efforts, certain geological gaps remain open. Since the development of GPlates Software (Müller et al., 2018), the representation of plate tectonic positions and motions has been substantially improved. In South America and Africa, the stretching

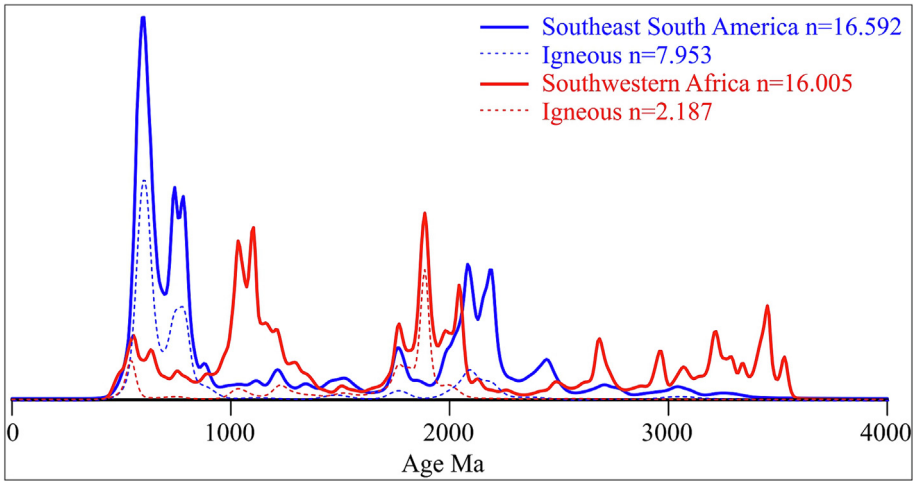

Fig. 4. U-Pb zircon data from Southeastern South America, encompassing southeast Brazil, Uruguay, and SW Africa (Pan-African Belts). The U-Pb data were plotted using IsoplotR online (Vermeesch, 2018).

process begins at 155 Ma in the southernmost portion, southward of the study area (Jokat et al., 2003). Using this as a time constraint and based on the rotational poles from Müller et al. (2019), we reconstructed the pre-to-early stretching process before oceanic crust formation at 150 Ma (Fig. 5). The reconstruction incorporating the magnetic and gravimetric data to the block models allowed us to establish the lack of a clear structure connection between the margins. The lack of direct correlation between structures on opposing margins raises significant questions about the amount of crustal loss during the continental break-up process. This discrepancy suggests that our current understanding of crustal evolution during rifting may be incomplete or oversimplified. This apparent disconnect could indicate limitations in the current reconstruction modeling approaches. They may incorrectly extrapolate features across the margins or fail to capture the full complexity of the breakup process.

The structural features of the conjugate margins of southern South America and Africa present distinct orientations that suggest these margins were not perfectly aligned prior to the opening of the South Atlantic. While the fabric of southern South America strikes NE–SW, the structural trend of the African counterpart strikes E–W (Fig. 5). This divergence in structural fabric indicates that the connection between both margins was located in a geotectonic boundary among blocks with different geological histories. A similar setting has been described for the conjugate margins of North America, where a collapse of the Caledonian orogenic belt preceded the formation of the North Atlantic Ocean (Schiffer et al., 2020). This orogenic collapse may have also occurred between southern South America and Africa during the initial stages of the rifting of SW Gondwana, which led to the development of the South Atlantic Ocean basin. This scenario is quite different from the São Francisco-Congo cratons, which were rifted inside the cratonic area where the geology of both margins reflects a more continuous structure (Heilbron et al., 2016). In the South Brazil/Namibia conjugate margin, the geology does not show an obvious geological correlation and indicates that the Atlantic margin was locally formed in an orogenic belt zone between cratons. The major Precambrian structures strongly controlled the South Atlantic opening, so it has the same structural orientation as the Pan-African/Brasiliano belt. These inherited structures might be worked as the main conduit of the SDR magmatism (Serratt et al., 2022) as well controlled the LIP volcanism and dyke orientation (Gomes and Vasconcelos, 2021). In this way, the inherited structures are a weak zone in the lithosphere and should make a quick break-up with adiabatic mantle decompression.

5.2. Recognizing the stretched crust

The clues for the lack of a direct connection between these two continents begin to be clear when we interpret the seismic lines from both margins. A hyperextended continental crust occurs below a thick volcanic and sedimentary package of Cretaceous to recent rocks (Figs. 2 and 3; Chauvet et al., 2021). However, determining oceanic and continental crust boundaries in volcanic passive margins is challenging. It involves significant uncertainties and subjectivity, leading to varying estimates of its location by 100–200 km or more across different studies focusing on the same margin (Eagles et al., 2015). These discrepancies arise from the limitations in geophysical data resolution and differences in data interpretation methodologies. For instance, features such as SDR or a high-velocity lower crust pose challenges, as they can be interpreted as either altered continental crust or igneous oceanic crust.

Additionally, the interpretation of gravity data introduces non-uniqueness, with the uncertainty in continental-oceanic boundary (COB) location often exceeding 100 km (Eagles et al., 2015). Linear gravity lows produced by oceanic fracture zones offer valuable indicators of the seaward extent of oceanic crust, but they are sporadic features, providing an intermittent COB estimate. Also, according to early models, oceanic-type accretion generates pairs of linear magnetic anomalies, indicators of oceanic crust, and can be related to isochrons formed by seafloor spreading. However, seaward-dipping reflectors at conjugate volcanic passive margins

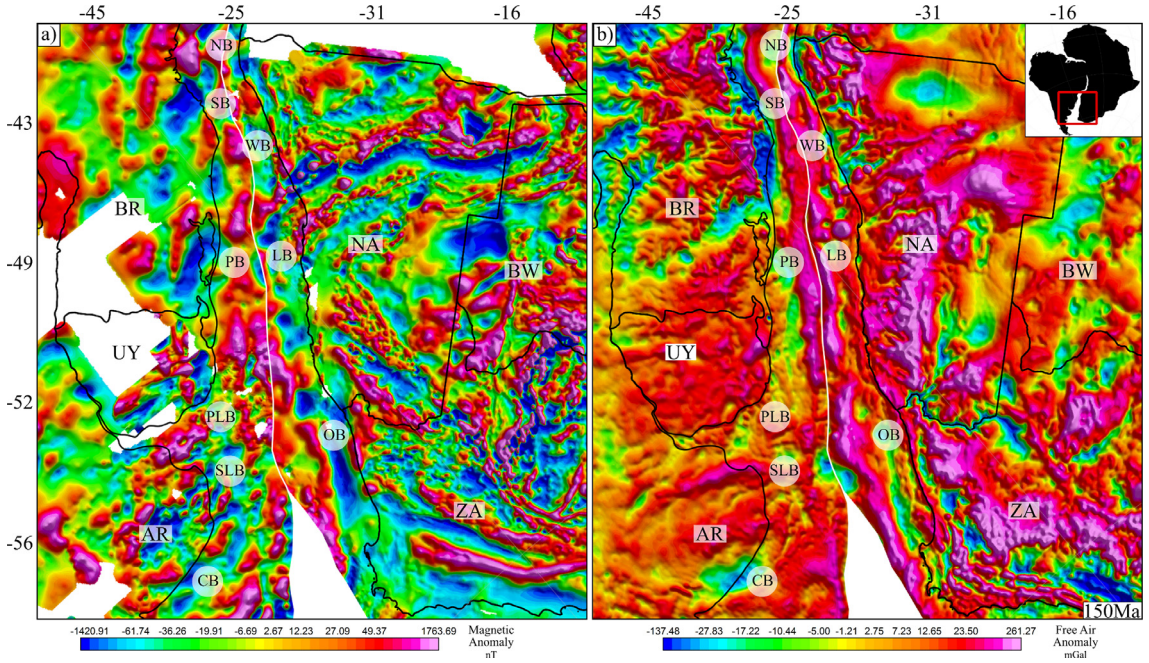

Fig. 5. Sketch of SW Gondwana map reconstructed according to the global plate model of Müller et al. (2019) showing the lack of connection between the structures of South America and African margins. White line: Large Magnetic Anomaly. Reconstructions use (a) the Earth Magnetic Anomaly Model from Maus et al. (2009) and (b) Satellite Free-air Gravity Anomaly data from Sandwell et al. (2014). Basins: NB – Namibia; SB – Santos; WB – Walvis; LB – Luderitz; PB – Pelotas; PLB – Punta del Este; OB – Orange; SLB – Salado; and CB – Colorado.

also produce linear magnetic anomalies (Geoffroy et al., 2022). Consequently, identifying an accurate COB remains challenging, underscoring the need for caution when utilizing COB estimates for reconstructions or plate kinematic modeling.

Considering this background, we utilized the previously documented magnetic anomalies M2 and M4 (Rabinowitz and Labrecque, 1979; Moulin et al., 2010) as tools to delineate these boundaries. The initial rifting phase occurred between the M4 and M2 chrons, with the magnetic anomaly M2 indicating the onset of oceanic crust formation (Koopmann et al., 2014; Fig. 3). This early stage was marked by the flexure of the basement and the extrusion of proximal Seaward Dipping Reflectors (SDRs), which caused pronounced magnetic anomalies (Serratt et al., 2022). Drawing on these findings, we were able to estimate the extent of continental crust, which spans up to 350 km beneath the volcanic and sedimentary layers of the passive margin basins along the conjugate margins in southern Brazil/Uruguay and Namibia/South Africa.

Restoring the crust involves a 125–250 km continental crust section covered by volcanic and sedimentary rocks in the Pelotas, Punta del Este, Walvis, Luderitz, and Orange basins. However, it is important to note that the methodology assumes that the bulk extension in the margin is pure shear, which is not always the case. One way to address the issue is by estimating lower-bound values of horizontal extension rates. This can be achieved by dating pairs of cross-cutting pre-flexure and post-flexure dykes, as done in eastern Greenland (Lenoir et al., 2003). Another challenge is the emplacement of dykes in the margins. In a volcanic passive margin, the volume of dykes can exceed 50% (Myers, 1980). Therefore, the restored section will be 50% smaller, with a real extension of continental crust reaching 125 to 250 km in length. This estimative is almost the most conservative scenario and does not consider the denudation that occurred in these sections; even in this more conservative scenario, the impacts of this in the geotectonic models and the understanding of the geology of this region are critical and have not been considered previously.

5.3. SW Africa, SE Brazil, and Uruguay geological correlation challenges

South America and Africa were amalgamated throughout the Pan-African/Brasiliano tectonic cycle along the Neoproteroic (Caxito et al., 2022). The comparison of U-Pb data from both margins can yield valuable insights into the crustal growth history and the main geological events that have shaped the region (Gehrels, 2014; Roberts and Spencer, 2015) and how this crustal growth history is different on both sides of South Atlantic crustal margins (Figs. 2 and 4). Although both margins shared the same Cryogenian to Ediacaran age peak, recording the continental docking during the Gondwana supercontinent amalgamation, which was less represented on the African side but still occurring, the older basement history is almost entirely different. The U-Pb zircon age distribution patterns in SW Africa show major peaks at Archean, Orosirian, and Stennian. Conversely, southern Brazil–Uruguay shows dominant peaks at Rhyacian and Tonian, revealing their distinct crustal growth history. It is clear that both margins, which were merged during the Gondwana supercontinent amalgamation, have previously undergone different crustal evolutions. This distinct crustal growth record is associated with the lack of continuity in the geological structures, and the identified stretched crust well demonstrates the geological significance of this section in correlation studies.

In trying to provide a geological model of the Neoproterozoic orogenic belts of this region, several authors proposed different models (e.g., Chemale, 2000; Basei et al., 2008; Konopásek et al., 2020). Most proposed models do not consider the unknown stretched continental crust under the passive margin basin. Here, through GPlates reconstruction and deep seismic profiles analysis presented by Chauvet et al. (2021) along both margins, we point out that the lithosphere stretching estimated the missing of at least 150–300 linear km of continental crust that is hyperextended beneath the Punta del Este (Uruguay), Pelotas (southern Brazil) and Orange, Luderitz, Namibia, and Walvis basins (southwest Africa). This result indicates that a significant portion of the Pan-African/Brasiliano orogenic belt and its underlying basement is missing. The present size of the Dom Feliciano Belt, which is the expression of Pan-African/Brasiliano orogeny in southernmost Brazil and Uruguay, is smaller than this. This missing continental crust section is comparable in size to the main sections of the Andean, Rocky, or Ural mountains.

This unknown stretched crust, comparable in size to the Earth's largest orogens and covered by Cretaceous rocks of the passive margins, must be considered in any paleogeographic and geotectonic model that intends to evaluate the connection of Pan-African/Brasiliano belts. The question is, what is the nature of this continental crust? May we speculate that the missing puzzle of the Pan-African/Brasiliano petrotectonic assemblages can be there, such as juvenile Ediacaran island and magmatic arcs, ophiolite slabs of the Adamastor Ocean, and others? Is it possible to have a more robust idea of the direction of the subduction paleo plates?.

These questions remain largely unanswered, posing significant challenges to many proposed geotectonic models without considering the existence of extended continental crust covered by thick volcanic and sedimentary layers in passive margin tectonic settings. This oversight includes the previously unrecognized stretched continental crust in the Atlantic Ocean, which is the physical extension of the Neoproterozoic to Eopaleozoic Dom Feliciano, Saldania, Gariep, and Kaoko belts (e.g., Porada, 1989; Rapela et al., 2011; Konopásek et al., 2020). The 150–300 km gap in the continental crust harbors key petrotectonic assemblages essential for understanding the processes by which these terranes were amalgamated. However, our understanding of the composition and characteristics of these assemblages remains incomplete. Even with the development of plausible tectonic models, critical puzzle pieces concerning mobile belts exposed in the emerged sections of the conjugate margins will often remain speculative.

6. Conclusion

This study enhanced our approach to understanding the conjugate margins of the South Atlantic Ocean, bringing new insights into pre-rifting geological terrain assemblage models of Pangea and SW Gondwana. The geophysical anomalies, seismic interpretations, and U-Pb isotopic data contribute to a nuanced understanding of the geological evolution in the southwestern Gondwana supercontinent, delineating the extent of the stretched crust and now concealed beneath passive margin basins. However, they are insufficient for precisely determining this extended crust's nature and composition for further geological correlation of the SW Gondwana supercontinent. The integration of paleo reconstruction models with offshore seismic interpretation profiles of hyperextended margins has revealed the inherent limitations of directly reconstructing and connecting geological terranes across different margins, such as those of southeastern South America and southwestern Africa. Consequently, current paleogeographic reconstructions and the associated geological models for the emerging continental margins of the South Atlantic lack the accuracy to account for the extensive and concealed hyperextended crust. After restoring the hyperextended crust, these previous reconstruction models fail to account for a substantial portion of the continental crust, estimated to be at least 150–300 km. This study significantly

advances our knowledge of hyperextended passive margins and contributes to a more realistic portrayal of Precambrian terrane evolution.

CRediT authorship contribution statement

C.D. Teixeira: Writing – original draft, Visualization, Software, Methodology, Investigation, Formal analysis, Data curation, Conceptualization. **T.J. Girelli:** Writing – review & editing, Visualization, Validation, Methodology, Data curation, Conceptualization. **H. Serratt:** Writing – review & editing, Validation, Methodology, Conceptualization. **H.O.S. Oliveira:** Writing – review & editing, Investigation. **M.F. Cruz:** Data curation, Validation. **B. Conti:** Validation, Resources. **P. Rodriguez:** Validation, Resources. **F. Chemale:** Formal analysis, Funding acquisition, Project administration, Supervision, Validation, Writing – review & editing.

Declaration of competing interest

The authors declare that they have no known competing financial interests or personal relationships that could have appeared to influence the work reported in this paper.

Acknowledgments

This study was supported by the UNISINOS-PETROBRAS and UNISINOS-CNODC Cooperation Agreements. We also thank the National Administration of Fuels, Alcohols, and Portland (ANCAP) and the Brazilian National Agency for Petroleum, Natural Gas, and Biofuels (ANP) for providing data access. We are grateful to Sequeent and Eliis for granting academic licenses for the Oasis Montaj and PaleoScanTM software, respectively. FCJ acknowledges the Brazilian National Council for Scientific and Technological Development (CNPq, Brazil) for grant #408194/2021-9. We are particularly grateful to Bruce Eglington, Dengliang Gao, and an anonymous reviewer for their insightful comments. Finally, we acknowledge editors M. Santosh and Richard Damian Nance for their efforts in handling the publication of this manuscript.

References

Basei, M.A.S., 2000. Geologia e modelagem geotectônica dos terrenos Pré-Cambrianos das regiões sul-oriental brasileira e uruguaia: possíveis correlações com províncias similares do sudoeste africano. Tese (Livre-Docência em Geociências). Instituto de Geociências, Universidade de São Paulo, São Paulo, p. 124. https://doi.org/10.11606/T.44.2014.tde-11022014-155501.

Basei, M.A.S., Frimmel, H.E., Campos Neto, M.D.C., Ganade de Araujo, C.E., Araujo de Castro, N., Passarelli, C.R., 2018. The tectonic history of the southern adamastor ocean based on a correlation of the Kaoko and Dom feliciano belts. In: Siegesmund (Ed.), Geology of Southwest Gondwana. Springer Nature Regional Geology.

Basei, M.A.S., Frimmel, H.E., Nutman, A.P., Preciozzi, F., 2008. West Gondwana amalgamation based on detrital zircon ages from Neoproterozoic Ribeira and Dom Feliciano belts of South America and comparison with coeval sequences from SW Africa. Geol. Soc. Lond. Spec. Publ. 294 (1), 239–256.

Becker-Kerber, B., Paim, P.S.G., Junior, F.C., et al., 2020. The oldest record of Ediacaran macrofossils in Gondwana (~ 563 Ma, Itajaí Basin, Brazil). Gondwana Res. 84, 211–228.

Begg, G.C., Griffin, W.L., Natapov, L.M., et al., 2009. The lithospheric architecture of Africa: seismic tomography, mantle petrology, and tectonic evolution. Geosphere 5 (1), 23–50.

Blaich, O.A., Faleide, J.I., Tsikalas, F., Gordon, A.C., Mohriak, W., 2013. Crustal-scale architecture and segmentation of the South Atlantic volcanic margin. Geol. Soc. Lond. Spec. Publ. 369 (1), 167–183.

Caxito, F.A., Hartmann, L.A., Heilbron, M., Bruno, H., Pedrosa-Soares, A., Basei, M.A.S., Chemale, F., 2022. Multi-proxy evidence for subduction of the Neoproterozoic Adamastor Ocean and Wilson cycle tectonics in the South Atlantic Brasiliano Orogenic System of Western Gondwana. Precambr. Res. 376, 106678.

Chauvet, F., Sapin, F., Geoffroy, L., Ringenbach, J.C., Ferry, J.N., 2021. Conjugate volcanic passive margins in the austral segment of the South Atlantic-Architecture and development. Earth-Sci. Rev. 212, 103461.

Chemale Jr, F., 2000. Evolução geológica do Escudo Sul-rio-grandense. Geologia Do Rio Grande Do Sul, 13–52.

Chemale Jr, F., Mallmann, G., de Fátima Bitencourt, M., Kawashita, K., 2012. Time constraints on magmatism along the Major Gercino Shear Zone, southern Brazil: implications for West Gondwana reconstruction. Gondwana Res. 22 (1), 184–199.

Doré, T., Lundin, E., 2015. Research focus: hyperextended continental margins—Knowns and unknowns. Geology 43 (1), 95–96.

Will, T.M., Höhn, S., Frimmel, H.E., Gaucher, C., Le Roux, Macey, P.H., 2020. Petrological, geochemical and isotopic data of Neoproterozoic rock units from Uruguay and South Africa: Correlation of basement terranes across the South Atlantic. Gondwana Res. 80, 12–32.

Du Toit, A.L. 1927. A geological comparison of South America with South Africa (No. 381). Carnegie Institution of Washington.

Eagles, G., Pérez-Díaz, L., Scarselli, N., 2015. Getting over continent ocean boundaries. Earth-Sci. Rev. 151, 244–265.

Fernandes, L.A.D., Tommasi, A., Porcher, C.C., 1992. Deformation patterns in the southern Brazilian branch of the Dom Feliciano Belt: a reappraisal. J. South Am. Earth Sci. 5 (1), 77–96. https://doi.org/10.1016/0895-9811(92)90061-3.

Frimmel, H.E., 2009. Trace element distribution in neoproterozoic carbonates as palaeoenvironmental indicator. Chem Geol. 258 (3–4), 338–353.

Gehrels, G., 2014. Detrital zircon U-Pb geochronology applied to tectonics. An. Rev. Earth Planet. Sci. 42, 127–149.

Geoffroy, L., Chauvet, F., Ringenbach, J.C., 2022. Middle-lower continental crust exhumed at the distal edges of volcanic passive margins. Commun. Earth Environ. 3 (1), 95.

Gomes, A.S., Vasconcelos, P.M., 2021. Geochronology of the Paraná-Etendeka large igneous province. Earth-Sci. Rev. 220, 103716.

Granot, R., Dyment, J., 2015. The cretaceous opening of the South Atlantic Ocean. Earth Planet. Sci. Lett. 414, 156–163.

Haas, P., Müller, R.D., Ebbing, J., Finger, N.P., Kaban, M.K., Heine, C., 2022. Modeling lithospheric thickness along the conjugate South Atlantic passive margins implies asymmetric rift initiation. Tectonics 41 (9), e2021TC006828.

Harkin, C., Kusznir, N., Roberts, A., Manatschal, G., Horn, B., 2020. Origin, composition and relative timing of seaward dipping reflectors on the Pelotas rifted margin. Mar. Petrol. Geol. 114, 104235.

Hartmann, L.A., Chemale Jr., F., Philipp, R.P., 2007. In: Iannuzzi, R., Frantz, J.C. (Eds.). Evolução geotectônica do Rio Grande do Sul no pré-cambriano 50, 97–123.

Heilbron, M., Cordani, U.G., Alkmim, F.F. (Eds.), 2016. Sao Francisco Craton. Tectonic Genealogy of a Miniature Continent. Springer, Eastern Brazil.

Heine, C., Zoethout, J., Müller, R.D., 2013. Kinematics of the South Atlantic rift. Solid Earth 4 (2), 215–253.

Jokat, W., Boebel, T., König, M., Meyer, U., 2003. Timing and geometry of early Gondwana break-up. J. Geophys. Res. Solid Earth 108 (B9). https://doi.org/10.1029/2002JB001802.

Konopásek, J., Cavalcante, C., Fossen, H., Janoušek, V., 2020. Adamastor – an ocean that never existed? Earth-Sci. Rev. 205, 103201. https://doi.org/10.1016/j.earscirev.2020.103201.

Koopmann, H., Schreckenberger, B., Franke, D., Becker, K., Schnabel, M., 2014. The late rifting phase and continental break-up of the southern South Atlantic: the mode and timing of volcanic rifting and formation of earliest oceanic crust. Geol. Soc. Lond. Spec. Publ. 420 (1), 315–340.

Lei, C., Alves, T.M., Ren, J., Tong, C., 2020. Rift structure and sediment infill of hyperextended continental crust: insights from 3D seismic and well data (Xisha Trough, South China Sea). J. Geophys. Res. Solid Earth 125 (5). https://doi.org/10.1029/2019JB018610.

Lenoir, X., Féraud, G., Geoffroy, L., 2003. High-rate flexure of the East Greenland volcanic margin: constraints from $^{40}Ar/^{39}Ar$ dating of basaltic dykes. Earth Planet. Sci. Lett. 214 (3–4), 515–528.

Macdonald, D., Gomez-Perez, I., Franzese, J., et al., 2003. Mesozoic break-up of SW Gondwana: implications for regional hydrocarbon potential of the southern South Atlantic. Mar. Petrol. Geol. 20 (3–4), 287–308.

Maus, S., Barckhausen, U., Berkenbosch, H., et al., 2009. EMAG2: a 2-arc min resolution Earth Magnetic Anomaly Grid compiled from satellite, airborne, and marine magnetic measurements. Geochem. Geophys. Geosys. 10 (8). https://doi.org/10.1029/2009GC002471.

McKenzie, D., 1978. Some remarks on the development of sedimentary basins. Earth Planet. Sci. Lett. 40 (1), 25–32. https://doi.org/10.1016/0012-821x(78)90071-7.

Milani, E.J., De Wit, M.J., 2008. Correlations between the classic Paraná and Cape-Karoo sequences of South America and southern Africa and their basin infills flanking the Gondwanides: du Toit revisited. Geol. Soc. Lond. Spec. Publ. 294 (1), 319–342.

Miller, R., Grote, W. 1988. Geological Map of the Damara Orogen, South West Africa/Namibia 1: 500 000. Geological Survey.

Moulin, M., Aslanian, D., Unternehr, P., 2010. A new starting point for the South and Equatorial Atlantic Ocean. Earth-Sci. Rev. 98 (1–2), 1–37. https://doi.org/10.1016/j.earscirev.2009.08.001.

Müller, R.D., Cannon, J., Qin, X., et al., 2018. GPlates: building a virtual Earth through deep time. Geochem. Geophys. Geosyst. 19. https://doi.org/10.1029/2018GC007584.

Müller, R.D., Zahirovic, S., Williams, S.E., et al., 2019. A global plate model including lithospheric deformation along major rifts and orogens since the Triassic. Tectonics 38 (6), 1884–1907.

Mutter, J.C., Talwani, M., Stoffa, P.L., 1982. Origin of seaward-dipping reflectors in oceanic crust off the Norwegian margin by "subaerial seafloor spreading". Geology 10 (7), 353–357.
Myers, J.S., 1980. Structure of the coastal dyke swarm and associated plutonic intrusions of East Greenland. Earth Planet. Sci Lett. 46 (3), 407–418.
Nirrengarten, M., Manatschal, G., Tugend, J., Kusznir, N., Sauter, D., 2018. Kinematic evolution of the southern North Atlantic: implications for the formation of hyperextended rift systems. Tectonics 37, 89–118. https://doi.org/10.1002/2017TC004495.
Passchier, C.W., Trouw, R.A.J., Ribeiro, A., Paciullo, F.V.P., 2002. Tectonic evolution of the southern Kaoko belt, Namibia. J. Afr. Earth Sci. 35 (1), 61–75.
Peron-Pinvidic, G., Manatschal, G., Osmundsen, P.T., 2013. Structural comparison of archetypal Atlantic rifted margins: a review of observations and concepts. Mar. Petrol. Geol. 43, 21–47.
Philipp, R.P., Pimentel, M.M., Chemale Jr., F., 2016. Tectonic evolution of the Dom Feliciano Belt in Southern Brazil: geological relationships and U-Pb geochronology. Brazilian Journal of Geology 46, 83–104.
Porada, H., 1989. Pan-African rifting and orogenesis in southern to equatorial Africa and eastern Brazil. Precambr. Res. 44 (2), 103–136.
Prave, A.R., 1996. Tale of three cratons: tectonostratigraphic anatomy of the Damara orogen in northwestern Namibia and the assembly of Gondwana. Geology 24 (12), 1115–1118.
Puetz, S.J., 2018. A relational database of global U–Pb ages. Geoscience Frontiers 9 (3), 877–891.
Puetz, S.J., Spencer, C.J., Ganade, C.E., 2021. Analyses from a validated global U-Pb detrital zircon database: enhanced methods for filtering discordant U-Pb zircon analyses and optimizing crystallization age estimates. Earth-Sci. Rev. 220, 103745.
Rabinowitz, P.D., LaBrecque, J., 1979. The Mesozoic South Atlantic Ocean and evolution of its continental margins. J. Geophys. Res. 84 (B11), 5973. https://doi.org/10.1029/jb084ib11p05973.
Rapela, C.W., Fanning, C.M., Casquet, C., Pankhurst, R.J., Spalletti, L., Poiré, D., Baldo, E.G., 2011. The Rio de la Plata craton and the adjoining Pan-African/Brasiliano terranes: Their origins and incorporation into southwest Gondwana. Gondwana Res. 20, 673–690.
Roberts, N.M.W., Spencer, C.J. 2015. The zircon archive of continent formation through time. In: Roberts, N.M.W., Van Kranendonk, M., Parman, S., Shirey, S., Clift, P.D. (Eds.), Continent Formation Through Time. Geological Society, London, Special Publications, 389, 197–225.
Sandwell, D.T., Müller, R.D., Smith, W.H.F., Garcia, E., Francis, R., 2014. New global marine gravity model from Cryo-Sat-2 and Jason-1 reveals buried tectonic structure. Science 346 (6205), 65–67. https://doi.org/10.1126/science.1258213.
Schiffer, C., Doré, A.G., Foulger, G.R., et al., 2020. Structural inheritance in the North Atlantic. Earth-Sci. Rev. 206, 102975.
Serratt, H., Teixeira, C.D., Girelli, T.J., Kehl de Souza, M., Vargas, M.R., Silva, A.M., Chemale Jr., F., 2022. Seaward-dipping reflector influence on seafloor magnetostratigraphy–A Pelotas Basin view. Geophys. Res. Lett. 49(23), e2022GL100382.
Seton, M., Müller, R.D., Zahirovic, S., et al., 2012. Global continental and ocean basin reconstructions since 200 Ma. Earth-Sci. Rev. 113 (3–4), 212–270.
Sutra, E., Manatschal, G., Mohn, G., Unternehr, P., 2013. Quantification and restoration of extensional deformation along the Western Iberia and Newfoundland rifted margins. Geochem. Geophys. Geosyst. 14, 2575–2597. https://doi.org/10.1002/ggge.20135.
Torsvik, T.H., Rousse, S., Labails, C., Smethurst, M.A., 2009. A new scheme for the opening of the South Atlantic Ocean and the dissection of an Aptian salt basin. Geophys. J. Int. 177 (3), 1315–1333.
Veevers, J.J., 2004. Gondwanaland from 650–500 Ma assembly through 320 Ma merger in Pangea to 185–100 Ma break-up: supercontinental tectonics via stratigraphy and radiometric dating. Earth-Sci. Rev. 68 (1–2), 1–132.
Vermeesch, P., 2018. IsoplotR: a free and open toolbox for geochronology. Geosci. Front. 9 (5), 1479–1493.

Earth-Science Reviews 266 (2025) 105135

Contents lists available at ScienceDirect

Earth-Science Reviews

journal homepage: www.elsevier.com/locate/earscirev

Revisiting the Dom Feliciano Belt and surrounding areas – An integrated geophysical and isotope geology approach

C.D. Teixeira [a,*], T.J. Girelli [a], H. Serratt [a,b,c], F. Chemale Jr. [a,d]

[a] Geology and Geophysics Research Group – NGA, Universidade do Vale do Rio do Sinos, São Leopoldo, RS, Brazil
[b] Geology Graduate Program, Universidade de Brasília, Distrito Federal, Brazil
[c] UMR 6538 CNRS, IUEM, Université de Bretagne Occidentale, Place Copernic, 29280 Plouzané, France
[d] Postgraduate Program in Geosciences, Universidade Estadual do Rio do Janeiro, Rio de Janeiro, RJ, Brazil

ARTICLE INFO

Keywords:
Tectonic evolution
Gondwana reconstruction
Precambrian terranes
Pan-African orogeny
Terrane compartmentalization

ABSTRACT

The reconstruction of orogenic terranes across conjugate margins separated by oceanic formation requires the integration of complementary geological records from both regions. A major challenge lies in the loss of geological evidence following orogenic events, particularly processes associated with later continental break-up, such as those in southwestern Gondwana. In southeastern Brazil, Uruguay, and southwestern Africa, these records include Archean to Mesoproterozoic terranes and Pan-African-Brasiliano mobile belts. Following the amalgamation of the Gondwana supercontinent, these terranes underwent multiple phases of uplift, subsidence, and erosion, making their paleogeographic reconstruction more complex. To overcome these complexities, various datasets, including gamma-ray spectrometry, magnetic and gravity surveys, geological mapping, and U—Pb geochronology, were integrated. Our analysis reveals distinct geophysical domains and major lineaments defined by magnetic, gravimetric, and gamma-ray anomalies, providing new insights into the western Gondwana structural framework. The study highlights the collision between the Rio de la Plata Craton and the Congo and Kalahari cratons, characterized by thrust-and-fold belts and strike-slip systems. Distinct terranes are well-constrained, including the Rio de la Plata Craton, the São Gabriel magmatic arc, the Tijucas fold-and-thrust belt, and Ediacaran to Eopaleozoic terranes (Encruzilhada, Pelotas, and Punta del Este arcs), along with late to post-orogenic basins. Our refined mapping of terrane boundaries and shear zones enhances our understanding of tectonic evolution and supports correlations between terranes now separated by the South Atlantic. These findings improve interpretations of southwestern Gondwana's tectonostratigraphic architecture and its cratonic and orogenic assembly processes.

Contents

* Corresponding author.
E-mail address: claudiadtx@gmail.com (C.D. Teixeira).

https://doi.org/10.1016/j.earscirev.2025.105135
Received 29 November 2024; Received in revised form 6 April 2025; Accepted 8 April 2025
Available online 13 April 2025

1. Introduction

The reconstruction of the tectonic process in Precambrian terranes presents significant challenges, primarily due to the lack of comprehensive data preserved on orogenic belts. The process of assembling Precambrian terranes relies on interpretations derived from extensive geological and geochemical datasets from outcrops and drill cores, complemented by geophysical data. These combined datasets provide crucial insights into crustal evolution, tectonic boundaries, and the timing of magmatic and metamorphic events, allowing for a more accurate reconstruction of past geodynamic processes. These reconstructions often contain substantial uncertainties, reflecting our limited understanding of ancient orogenic processes. Even for well-studied Phanerozoic orogens such as the Urals and Himalayas, where modern methodologies enable relatively precise plate motions supported by detailed geological, geochemical, and geophysical data (including seismic, gravity, and magnetic surveys), debate persists regarding the most accurate tectonic models. These orogenic belts retain their primary tectonic characteristics following the continental collision, albeit modified by significant erosion and variable rates of exhumation, as highlighted by numerous studies (Yin and Harrison, 2000; Brown et al., 2008; Zuza et al., 2019). This scenario underscores the complexity of understanding the formation and evolution of orogenic belts, even with the advantage of modern geological and geophysical methodologies.

The orogenic belts in southwest Gondwana (Fig. 1) are distinctively characterized by subsequent plate break-up and dispersal, alongside significant modifications from tectonic activity and erosion associated with the development of rifted passive margin basins, leading to the formation of the South Atlantic Ocean. Consequently, these basins span extensive regions of stretched crust, encompassing more than 300 km of unknown continental crust beneath the Atlantic Ocean (Fig. 1c; Teixeira et al., 2025). Southwestern Gondwana was formed by the convergence of the Kalahari, Congo-São Francisco, and Rio de la Plata cratons, incorporating fragmented orogenic belts such as the Dom Feliciano-Ribeira-Araçuaí system along eastern South America and the Gariep-Damara-Kaoko-West Africa belts along western Africa (Porada, 1979; Gresse et al., 1996; Goscombe et al., 2003; Frimmel, 2009; Basei et al., 2010, 2018; Chemale Jr et al., 2012; Siegesmund et al., 2018; Caxito et al., 2022). These belts could be analogously compared to extensive orogenic cordilleras, such as the Andes or Himalayas, which stretch more than thousands of kilometers. After their formation, these belts underwent significant intraplate deformation during the Paleozoic and extensional tectonics throughout the Mesozoic-Cenozoic during the South Atlantic rifting. Both conjugate margins preserved crustal segments of what was once a continuous orogenic system, with significantly missing crustal sections.

The Rio de La Plata Craton and the Dom Feliciano Belt have been significantly overprinted by Phanerozoic events that occurred in the western margin, particularly the Famatian, Gondwanides, and Andean orogenies. These events initially produced extensive intraplate sedimentation along the eastern margin, leading to the formation of the Paraná-Chaco Basin (Milani and de Wit, 2008). In contrast to the deposition of Paraná-Chaco Basin, which has persisted since the Jurassic, some areas underwent substantial Permo-Triassic denudation, exposing portions of the basement (de Oliveira et al., 2016a; Hueck et al., 2017). Also, during the Late Cretaceous to recent, while the western margin remained dominated by the Andean Cycle (Ramos, 2009), the eastern margin responded to both Andean tectonics and Gondwana break-up through significant fault reactivation and the development of regional structural highs, such as the Torres Arch. Thermochronological studies combining apatite and zircon fission-track and (U—Th)/He revealed that the southeastern Brazilian, Uruguay, and western African margins experienced substantial denudation ranging from 3.5 to 4.5 km (Gallagher et al., 1995; Brown et al., 2014; de Oliveira et al., 2016b; Hueck et al., 2017; Hueck et al., 2019). This

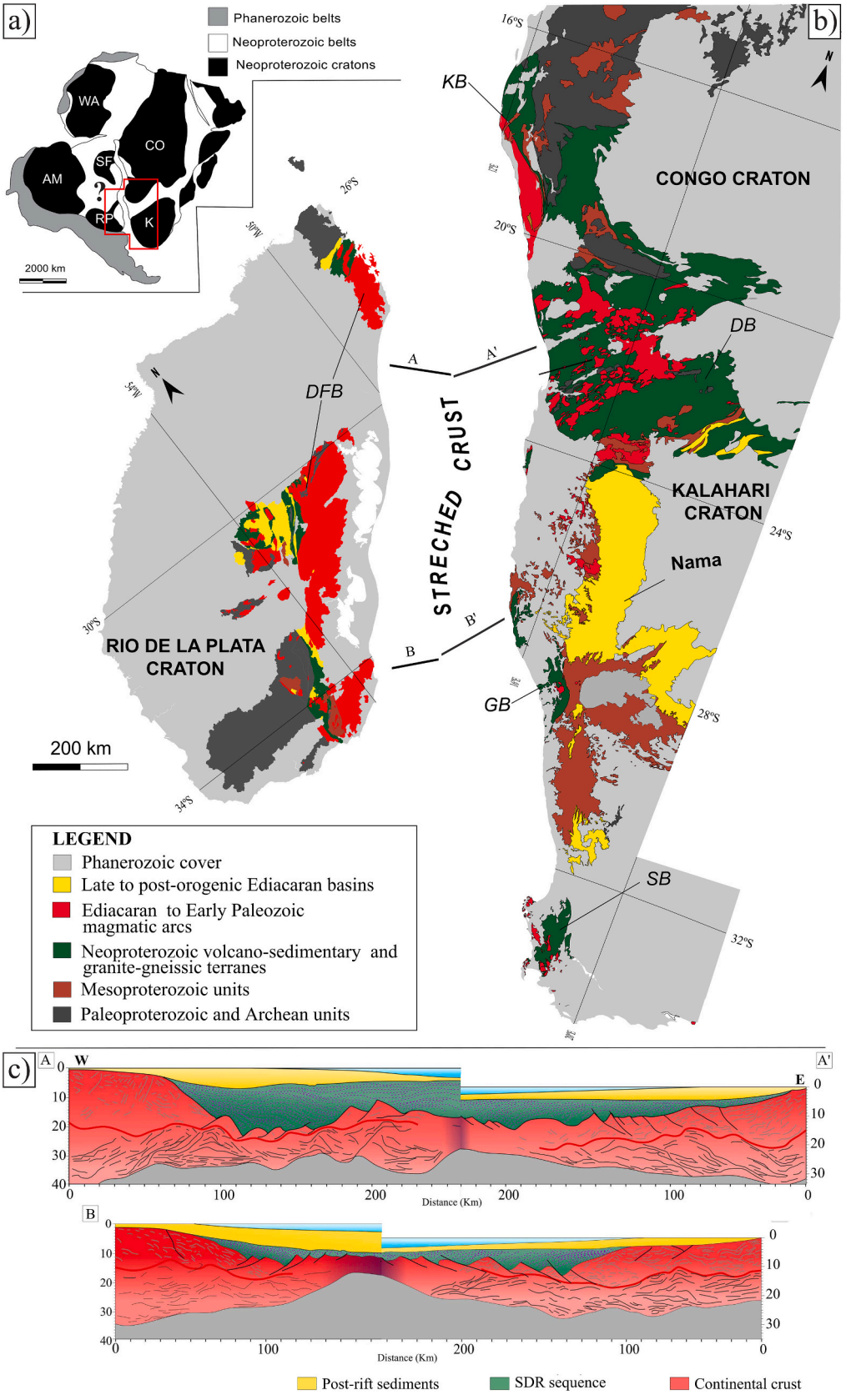

(caption on next page)

Fig. 1. a) Distribution of main cratonic areas of West Gondwana and Brasiliano/Pan-African belts, where West Africa (WA), Amazonian (AM), São Francisco (SF), Congo (CO), Kahalari (K), Rio de la Plata (RLP) cratons; b) Southwestern Gondwana reconstruction with main Brasiliano/Pan-African belts and surroundings cratonic areas DFB: Dom Feliciano (DFB), Kaoko (KB), Damara (DB), Gariep (GB), Saldanha belts (SB) (adapted from: Guadagnin et al., 2010, Chemale Jr et al., 2012, Becker-Kerber et al., 2020); c) Profiles A-A' and B-B' showing the hyperextended continental crust below the passive margin sedimentary rocks and Atlantic Ocean water. The restored crust ranges from 150 to 300 km in length for the studied area, which we do not have any information on the nature of the basement rocks and the possible petrotectonic assemblages related to the Pan-African and Brasiliano belts (simplified after Teixeira et al., 2025).

geological response for orogenic and break-up processes resulted in a differential exposition of the Rio de La Plata Craton and Dom Feliciano Belt. The western sector is mostly covered by thick sedimentary sequences, and the eastern sector is extensively denudated and faces a significant challenge in understanding regional crustal boundaries because different crustal levels are now exposed at the surface.

A critical gap in our understanding lies beneath the Atlantic Ocean, where an extensive region of stretched continental crust remains unexplored (Buiter and Torsvik, 2014; Chauvet et al., 2021). Teixeira et al. (2025) estimate that 150–300 km of restored continental crust underlies the passive margin basins of the southern South Atlantic Ocean. This unexplored domain is essential for reconstructing both the architectural framework of the orogenic system and its accretionary processes before the final collision and subsequent late to post-orogenic evolution.

The fragmented nature of these orogenic systems and the geological record have led to numerous tectonic models for the region. These models often define terranes or crustal blocks using inconsistent criteria and varying nomenclature, typically not applied to terrane classification, complicating efforts to reconstruct the geological history (Hasui et al., 1975; Costa, 1997; Chemale Jr, 2000; Basei et al., 2000). This challenge persists despite extensive datasets from southeastern Brazil, Uruguay, and southwestern Africa, including detailed geological mapping, structural analyses, petrological studies, and chronological data (e.g., Goscombe et al., 2005; Hartmann et al., 2007; Gaucher et al., 2009; Frimmel, 2009; Lehmann et al., 2016; Philipp et al., 2016; Basei et al., 2018; Oyhantçabal et al., 2018; de Toni et al., 2020b). This wealth of information underscores the complexity of accurately interpreting data to refine our understanding of the region's geological framework.

In the last decades, acquiring high-resolution geophysical data has provided new opportunities to refine our understanding of terranes formed during the Pan-African/Brasiliano Cycle and their assembly within southwestern Gondwana. Integrating geological, geochemical, and geophysical datasets – including gamma-ray spectrometry and potential field methods (magnetic and gravity) - offers a novel perspective on terrane compartmentalization and enables comparison with the established tectonostratigraphic framework.

This study presents the first integrated analysis of gamma-ray spectrometry and potential field data from Uruguay and Southern Brazil, providing new insights into the Precambrian to Eopaleozoic terrane compartmentalization of the region. By integrating geophysical data across southernmost Brazil and Uruguay, we extend known Uruguayan Shield elements into the subsurface and delineate previously unrecognized tectonic domains. This approach facilitates a constructive comparison with tectonostratigraphic geological delineation. Moreover, we synthesize published geological, geochemical, and isotopic data to define petrotectonic associations, identify major structures, and establish more precise boundaries of tectonostratigraphic terranes. These tectonostratigraphic terranes delineation followed Coney et al. (1980) proposal, which defined a terrane as a geological unit characterized by internal homogeneity and continuity of stratigraphy, tectonic style, and history, with boundaries representing fundamental discontinuities in stratigraphy that cannot be explained easily by conventional facies changes or unconformity, often juxtaposing totally distinct temporal or physical rock sequences and different lithologies. Despite the extensive array of geological and geophysical databases, questions persist regarding the complex evolutionary processes that culminated in the present tectonostratigraphic configuration. Additionally, we correlate geophysical and geochronological data from the Dom Feliciano Belt with the belts with counterparts in southwestern Africa to analyze the assembly of these conjugate margins (Fig. 1).

2. Geological background

The Southern Brazil and Uruguayan Shield represents the southernmost part of the Mantiqueira Province (de Almeida et al., 1981; Chemale Jr et al., 1995; Hartmann et al., 2007; Caxito et al., 2022), encompassing the Archean to Neoproterozoic tectonostratigraphic units (Fig. 1a). The tectonic evolution of the region is the outcome of cratonic blocks along the amalgamation of Pan-African-Brasiliano mobile belts, culminating in a collision linked to the Rio de la Plata, Kalahari, and São Francisco-Congo cratons during the Neoproterozoic to the early Paleozoic, leading to the development of the Dom Feliciano Belt (DFB) in Brazil and Uruguay, as well as the Saldanha, Gariep, Damara, and Kaoko belts in South Africa, Namibia, and Angola (Porada, 1979; Rapela et al., 2011; Philipp et al., 2016; Basei et al., 2018). The Dom Feliciano Belt accretion occurred primarily between the Tonian and Ediacaran periods (Hartmann et al., 2004; Philipp et al., 2018; Oriolo et al., 2017). Additionally, minor magmatic events during the Archean, Siderian, Statherian, and Stenian–Ectasian intervals have been recognized in adjacent areas and within the belt (Hartmann et al., 2001; Gaucher et al., 2011; Chemale et al., 2011; Camozzatto et al., 2013; Girelli et al., 2018; Monteiro et al., 2020).

The tectonic history of Southern Brazil and the Uruguayan Shield before the Neoproterozoic spans a lengthy period, from approximately 3.7 to 1.0 billion years ago, characterized by significant magmatic events and periods of quiescence. The early stages, from the Paleoarchean to Neoarchean, are marked by the Pavas Terrane in Uruguay, consisting of granite-gneissic and siliciclastic-carbonate metasedimentary rocks (Hartmann et al., 2001; Gaucher et al., 2011; Masquelin et al., 2021; Oyhantcabal et al., 2021). The subsequent Neoarchean to Rhyacian period features juvenile Rhyacian granite-greenstone terranes (Piedra Alta and Tandilla terranes), part of the Rio de La Plata Craton (Cingolani et al., 1990; Hartmann et al., 2000, 2002), and high-grade metamorphic rocks (Hartmann et al., 2008; Oriolo et al., 2016; Girelli et al., 2018), forming part of the reworked margin of the Rio de La Plata Craton, broadly defined as the Nico Perez Terrane (following the definition by Bossi and Campal, 1992). The Nico Perez Terrane and basement of the Dom Feliciano Belt include various Paleoproterozoic granite-gneissic complexes, Statherian acid magmatism and Calymmian Anorthosite, amphibolites and metamorphosed volcanosedimentary rocks, accompanied by Neoproterozoic granite-gneissic and metamorphosed volcanic rocks (Mallmann et al., 2007; Chemale et al., 2011; Camozzatto et al., 2013; Oriolo et al., 2019; Gaucher et al., 2011, 2021).

Archean to Mesoproterozoic rocks of the Uruguayan-Sul-Riograndense and Catarinense Shield are surrounded by Neoproterozoic units of the Dom Feliciano Belt, divided into four main terranes: The São Gabriel, Tijucas, and Pelotas-Aiguá-Florianópolis batholiths, and the Rocha-Punta del Este terranes (Philipp et al., 2016). The Dom Feliciano Belt records a complex Neoproterozoic tectonic evolution from 1.1 Ga ago to 500 Ma, characterized by rifting-related alkaline magmatism, passive margin sedimentation, oceanic crust formation, magmatic arc associations, fold-and-thrust belts, carbonate-bearing successions, and late- to post-orogenic volcano-sedimentary basins with granitic intrusions (Chemale Jr, 2000; Hartmann et al., 2007; Philipp et al., 2016; Basei et al., 2018; Will et al., 2020).

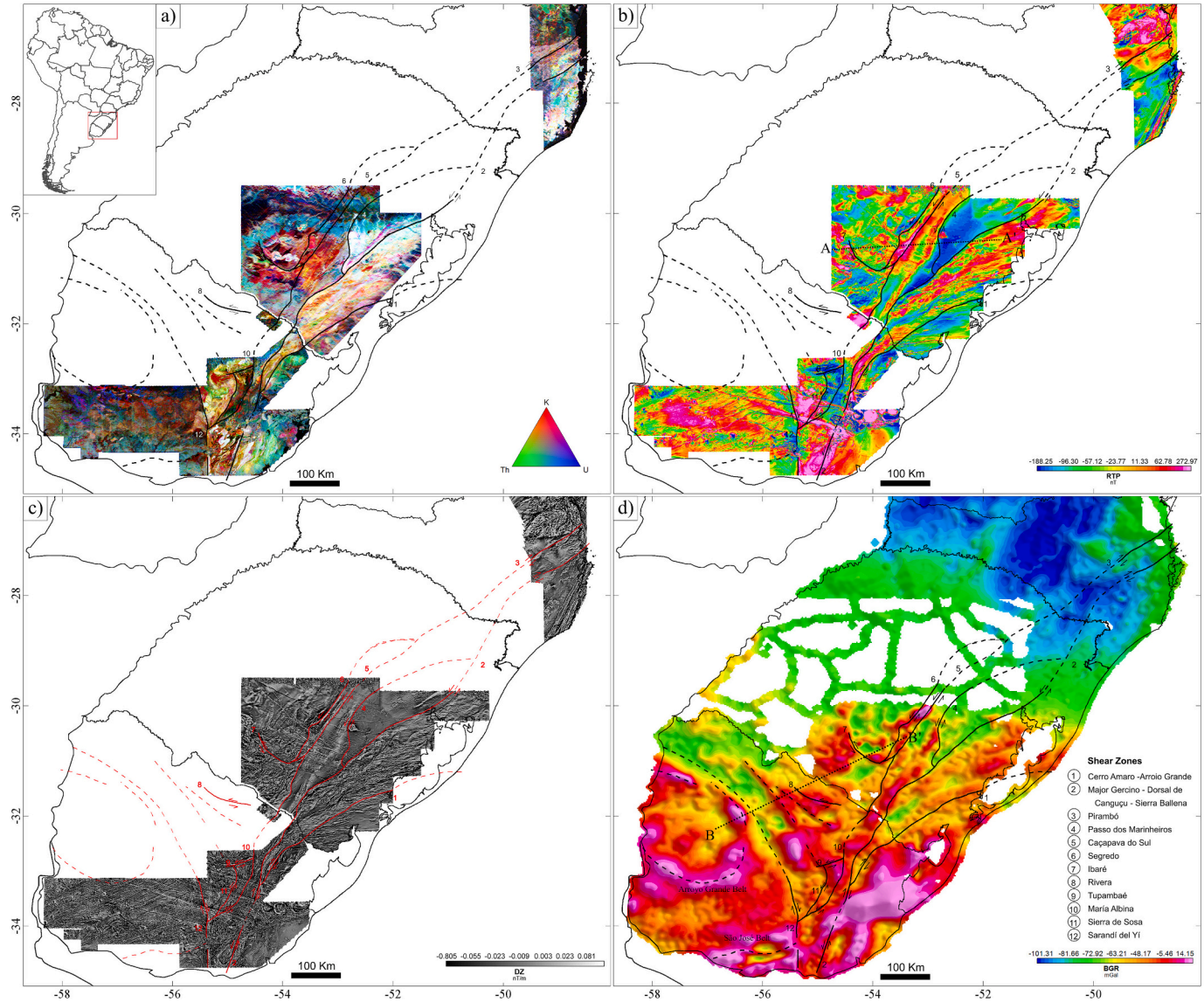

Fig. 2. Geophysical map for the USRCS and surrounding Phanerozoic covers: a) Gamma-ray spectrometry map of RGB ternary composite (K-Th-U). Black lines are interpreted lineaments based on magnetic, gravimetric, and radiometric anomalies and geologic and isotope geochemistry correlations. Inset shows the location of the study area within South America. b) Magnetic anomalies reduced to the pole. Black lines represent the main structures, and the black dashed line (A-A') indicates the location of the inversion-modeled magnetic profile. c) First vertical derivative of the magnetic field. Red lines are interpreted lineaments based on magnetic, gravimetric, and radiometric anomalies and geologic and isotope geochemistry correlations. d) Map of Bouguer anomalies. Black lines are interpreted lineaments based on magnetic, gravimetric, and radiometric anomalies and geologic and isotope geochemistry correlations. The black line (B-B′) indicates the location of the inversion-modeled gravity profiles. (For interpretation of the references to colour in this figure legend, the reader is referred to the web version of this article.)

Recent studies estimate that at least 150–300 km of restored hyperextended continental crust lies beneath the passive margin basins along the conjugate margins of southern Brazil/Uruguay and Namibia/South Africa (Teixeira et al., 2025). The nature of this continental crust as a lateral extension of the Pan-African and Brasiliano belts remains unknown, introducing uncertainties into geodynamic models of the Neoproterozoic to Early Paleozoic history. This is particularly important, as significant petrotectonic assemblages or terranes may be concealed in this region (see Fig. 1b and c). As a result, geodynamic models based on different conceptual frameworks, such as those following the Wilson Cycle (e.g., Porada, 1979; Gresse et al., 1996; Goscombe et al., 2003; Frimmel, 2009; Chemale Jr et al., 2012; Basei et al., 2018; Siegesmund et al., 2018; Caxito et al., 2022) or those favoring an intracontinental model (e.g., Konopásek et al., 2020; Percival et al., 2021), should be reassessed until more information about this 150–300 km of unknown continental crust becomes available.

3. Data and methods

Detailed airborne geophysical (gamma-ray spectrometry and magnetic) data provided by the Geological Survey of Brazil (SBG-CPRM) and the National Directorate of Mining and Geology (DINAMIGE-Uruguay) were combined for the initial delineation and interpretation of subsurface domains (Fig. 2). The gravity data used were compiled from different institutions provided by the Brazilian National Agency of Petroleum, Natural Gas and Biofuels (ANP), the Geological Survey of Brazil (SBG-CPRM), the National Administration of Fuels, Alcohols and Portland (ANCAP-Uruguay), and the International Gravimetric Bureau (BGI). The survey parameters are detailed in Supplementary Material S1. To enhance data coverage in the area, six ground gravity surveys were carried out, resulting in the establishment of 1227 new stations. This effort aimed to improve resolution and fill gaps in regions with either a lack of data or low density of gravity field data. The compiled

data and details of the new stations can be found in Tables S1 and S2 within Supplementary Material S1. For a detailed description of the processing techniques applied, refer to Talwani (1965) and Blakely (1995).

Additionally, 20,364 U-Pb individual analyses were compiled (Supplementary material - References from compiled U—Pb data). These data correspond to all published zircon, titanite, monazite, and rutile minerals aged by LA-ICP-MS, SIMS, SHRIMP, and ID-TIMS since 1985. All these published data were compiled and positioned according to their coordinate of geological map location (Fig. S1, supplementary material S1).

3.1. Gamma-ray spectrometry data

Airborne gamma-ray spectrometry was reprocessed, and the negative concentrations for each radioelements channel were treated as Erdi-Krausz et al. (2003) recommended. The minimum curvature gridding with 1/4 of the fight line spacing cell size was used to interpolate each radioelement channel. Among the treatment techniques for the interpretation are the qualitative analysis of maps and individual filtered images of K, Th, U, total count, and U/Th, U/K, and Th/K ratios; RGB or CMY ternary images (Dickson and Scott, 1997; Gunn, 1998).

3.2. Magnetometric data

The magnetic data were reduced from the International Geomagnetic Reference Field (IGRF) for the respective acquisition epochs for each survey data leading to magnetic anomaly data. The occurrence of linear features at non-perpendicular angles to the fight lines causes interpolation artifacts, often called “beading” or boudinage, making the data interpretation difficult, especially when traditional methods are used (Naprstek and Smith, 2019). Therefore, the aeromagnetic anomaly data were interpolated to a regular surface with the multi-trend gridding algorithm, which improved the result of data containing thin linear features such as dike swarms. Residual leveling errors from aeromagnetic data were removed by applying the micro-leveling technique described by Minty (1991). The merging process involved the removal of regional trends from individual surveys based on misfits in the overlapping regions. The grids were stitched into a seamless map using a suture algorithm.

The magnetic data are sensitive to the induced magnetization in rock units caused by the Earth’s current magnetic field and the remanent magnetization acquired by rock units in past geological time (Li et al., 2021). A magnetic anomaly may be bipolar at low magnetic latitudes, presenting distortions and changes in magnetic anomaly shapes, amplitude reduction, and map textures. The Reduction to Pole (RTP; Baranov, 1957) was applied to remove anomaly asymmetry caused by inclination, locating anomalies above the causative source, assuming a small remanent magnetism compared to the induced magnetism.

The relatively low inclination of the magnetic field causes the instability of data transformations, producing artifacts elongated along the direction of the magnetic declination (Li, 2008). The Total Gradient Amplitude filter (TG, also known as the 3D Analytic Signal Amplitude; Roest et al., 1992) was applied as an alternative for qualitative interpretation to approximately estimate the positions of magnetic contacts and obtain some depth estimates from data (Nabighian et al., 2005). Additional transformations were applied to balance low and high amplitudes caused by sources located at different depths and locating the source bodies more accurately. We emphasize the Vertical derivative (DZ - Blakely, 1995) and the Tilt Angle (TDR - Miller and Singh, 1994).

The Total Horizontal Gradient produces peaks in the transformed data set, which are symmetric and centered over the middle of narrow bodies and the edges of wide bodies, irrespective of the inducing field direction. The vertical derivatives enhance the high frequency/short wavelength content of the data by acting as high pass filters, and therefore, they help delimit the extent of causative bodies. The tilt-angle derivative of magnetic data enhances shallow structures, locating the zero contours of the tilt-angle of the anomaly located on the edge of the causative source body.

3.3. Gravity data

The gravity measurements focused on areas with gaps and were carried out using a Scintrex CG-5 with a repeatability accuracy of 0.005 mGal and a reading resolution of 0.001 mGal (Scintrex, 2012). The measured data were first corrected for instrumental drift by repeating the measurements at the base station (reference station) at the beginning and end of any given daily survey. Assuming that the drift was linear with time, the differences obtained from the two readings at the base station were plotted against the time to correct the drift problem. For standard gravity variation with altitude variation, the free-air correction was applied to correct the tide and drift-corrected data, and the resulting data were then corrected for latitude using the normal gravity formula (Lowrie and Fichtner, 2020) and for the Bouguer and terrain corrections, an assumed density of 2670 g/cm^3. After applying these corrections, the Bouguer anomaly is calculated at the gravity ellipsoid by adding Free-Air correction.

3.4. Depth-to-source estimation

3.4.1. Euler deconvolution

Euler’s deconvolution, defined by Thompson (1982), allows the rapid estimation of the position and depth of anomaly sources. It was later improved for three-dimensional (3D) fonts by Reid et al. (1990). The method uses the parameter, defined as the structural index, which corresponds to the decay of the anomaly with the distance between the source and the measurement point and is an estimate of the geometry of the source of geological structures (Reid et al., 2014).

The conventional approach to solving the Euler equation requires tentative values of the structural index. 3D Euler’s equation can be defined (Reid et al., 1990) and

$$(x-x_0)\frac{\partial T}{\partial x}+(y-y_0)\frac{\partial T}{\partial y}+(z-z_0)\frac{\partial T}{\partial z}=\eta T$$

where x_0, y_0, and z_0 is the position of the magnetic source whose total field T is detected at (x, y, z); T is the potential field; and η is a structural index defining the measure of the fall-off rate of the potential field (e.g., for magnetic data: $\eta = 0$ for contact, $\eta = 1$ for the top of a vertical dike or the edge of a sill, $\eta = 2$ for the center of a horizontal or vertical cylinder, and $\eta = 3$ for the center of a magnetic sphere or a dipole; for gravity data: $\eta = 0$ for dike or sill, $\eta = 1$ for cylinder and $\eta = 2$ for sphere; Thompson, 1982; Reid et al., 1990). Another important parameter to consider when applying this technique is the window size. According to Reid et al. (2014), window size should be as small as possible but greater than twice the measured data (line or grid) interval and greater than half the desired depth of investigation. The result is a cluster of points at different depths, which can be interpreted without previous knowledge of geologic data, verifying the distribution and continuity of clusters. It is important to notice that many solutions can replicate the observed geophysical field data, and the solutions are not necessarily geologically realistic (Roy et al., 2017). The 3D Euler deconvolution results, integrated with priori geological knowledge, can help the interpretation converge to a more realistic model that better reflects the background.

The application of Euler deconvolution in the magnetic data in the study region aims to obtain the solutions that condition the main structures that controlled the convergent tectonic. We applied the Standard Euler deconvolution in a specific area, with a squared window of 10 times the grid cell size and SI equal to 0 for the magnetic data, verifying its distribution and continuity, according to the source correlation suggested by Reid et al. (2014).

3.4.2. Inversion modeling

The 3D geophysical inversion techniques aim to recover physical properties for each lithology and adjust the geometry to fit the data observed, considering the contrast between these properties. The inversion estimates a three-dimensional distribution of physical parameters from observed data and models a specific physical property distribution on the subsurface, which has a geological significance. To obtain deep geological structures, magnetic and gravity inversion was carried out using VOXI Earth Modeling™ (Geosoft Oasis Montaj®, v. 2022.1). VOXI applies cloud-based inversion in potential field data, and its algorithm predicts a three-dimensional distribution of the physical property, i.e., the density and susceptibility distributions.

The inversion code applies the Tikhonov minimum gradient regularization (Zhdanov, 2002) to produce a model that conforms to a given reference Earth model and whose predicted response closely matches the input field data. The resultant model consists of a three-dimensional volume discretized into a series of cells, each containing a predicted physical property.

The generalized inversion process can be represented by

$$B = G\,m \tag{1}$$

where $\boldsymbol{B}$ is the data, represented in this gravity inversion as the **N** residual Bouguer anomaly values or the magnetic inversion as the **N** residual Magnetic anomaly, $\boldsymbol{m}$ is the model, corresponding to **M** density or magnetic values and geological model interfaces, while **G** is the $\boldsymbol{N} \times \boldsymbol{M}$ inversion matrix.

The inversion creates a theoretical physical property model that explains the measured anomalies. However, it should be noted that the obtained model is an ill-posed problem strongly affected by the non-uniqueness and instability, being one of several possible distributions of physical property that produces the observed anomalies (Cai et al., 2018).

3.4.3. Aeromagnetic 3D inversion

The Magnetization Vector Inversion (MVI; Ellis et al., 2012) method was chosen since it resolves both magnitude and direction, especially in low latitude areas or where there is a strong presence of remanence, demagnetization, or susceptibility anisotropy effects. According to Telford et al. (1990), the Earth's magnetic properties can be represented by the M (r) magnetization volume. Therefore, the Earth's magnetic field (B) related to this volume (V) at a point (r, j), comprising magnetization $M(r)$, is given by the equation (Ellis et al., 2012):

$$B\left(r_j\right) = \nabla \int_V M(r).\nabla \frac{1}{|r - r_j|}\, dr^3$$

That can be represented as the Eq. (1).

The MVI is based on the Anomalous Magnetic Field (AAMF; Shearer, 2005), producing three main vectors that must be analyzed and related to the magnetic susceptibility (k), the amplitude of the magnetization vector, the projected vector, and the perpendicular vector

$$AAMF = \overrightarrow{B_a} = \sqrt{B_x^2 + B_y^2 + B_z^2}$$

where B_x, B_Y, and B_z are the three magnetic field components in the Cartesian coordinate system. The magnetization amplitude vector is directly related to susceptibility. It has low dependence on the characteristics inherent to the Earth's magnetic field, in contrast to the projected and perpendicular vectors that align with the Earth's magnetic field (Ellis et al., 2012).

3.4.4. Gravity 3D inversion

The gravity inversion produces a density contrast model to highlight contrasting density areas and estimate their subsurface distribution. The gravity inversion model estimates parameters such as the density and geometry of a hypothesized model from a set of given gravity data (Eq. (1)). The Iterative Reweighting Inversion technique (IRI; Ingram et al., 2003; Ellis and MacLeod, 2013) was used as a constraint to increasing inversion precision. This code divides the area into voxels in an orthogonal grid and assigns a constant density value for each. Every voxel surface is cut into polyhedral sub-volumes to present geological surfaces more accurately.

The gravity data inversion was performed using the complete Bouguer anomaly as input data, considering a background density of 2300 kg/m^3. The values resulting from the gravity data inversion were obtained as density contrasts and later converted to absolute density values according to the background density.

3.5. Isotope record

A total of 20,364 U-Pb individual analyses from 684 samples were compiled for the Dom Feliciano Belt and surrounding areas. These data correspond to all published zircon, titanite, monazite, and rutile minerals with ages determined by LA-ICP-MS, SIMS, SHRIMP, and ID-TIMS since 1985 in the study area. All these published data were compiled and geographically positioned. A complete, detailed reference list with isotope information from the study area U—Pb mineral dating and Lu—Hf zircon isotope determination is found in the supplementary material S2.

We used the non-interactive model age obtained in the spreadsheet to plot the detrital data. Only the individual ages with classes 1 to 5 (sensu Puetz et al., 2021) were used to plot in Kernel Density Estimates (KDE). Class 1 represents highly concordant data, providing the most reliable and accurate age estimates; Class 2 represents medium-high concordance; Class 3 represents medium concordance, with increased uncertainty; Class 4 represents medium-low concordance, with notable deviations; and Class 5 represents marginally concordant data, close to the acceptance threshold. Classes 6 and 7 were removed from the plot due to their high discordance level.

The KDE diagrams for igneous samples were plotted using an alternative approach developed for this study, which focused on better representing the age error. We developed an approach using an Excel spreadsheet where each sample age was distributed in 100 new "pseudo-samples age" following two standard deviations of their error. Based on this approach, we could reach a more reliable error distribution and solve the miss visualization caused by the common bandwidth used in plotting software.

We found a similar challenge in providing good visualization of Neoproterozoic flare-up and quiescence periods. This is due to some geologic units being studied by several authors and showing a high concentration of ages, whereas other geologic units show a lack of studies. This causes a miss visualization when we try to represent the real scale of magmatism. Aiming to avoid this effect, we used the following approach: (I) Each Neoproterozoic magmatic unit (body scale) was individualized using GIS software, and the size in km^2 was obtained; (II) if the body had more than one age available, the size in km^2 was divided by the number of ages; (III) each central age was distributed based on two standard deviations of its error following the n km^2 related to the body area, respecting the step II criteria. This approach demonstrated the flare-up and quiescence magmatic periods more reliably. The U—Pb data were plotted using IsoplotR online (Vermeesch, 2018), and all the diagrams were plotted using adaptative KDEs based on the algorithm developed by Abramson (1984).

4. Integration of geophysical and geological data

The characterization of major tectonic structures in this study is based on integrating geological and geophysical datasets. Southeastern South America consists of distinct tectonic domains limited by major Neoproterozoic shear zones. The dominant structural grain, trending NE-SW and NNE-SSW, delineates multiple crustal domains with contrasting geophysical properties (Fig. 2). Following the terrane concept

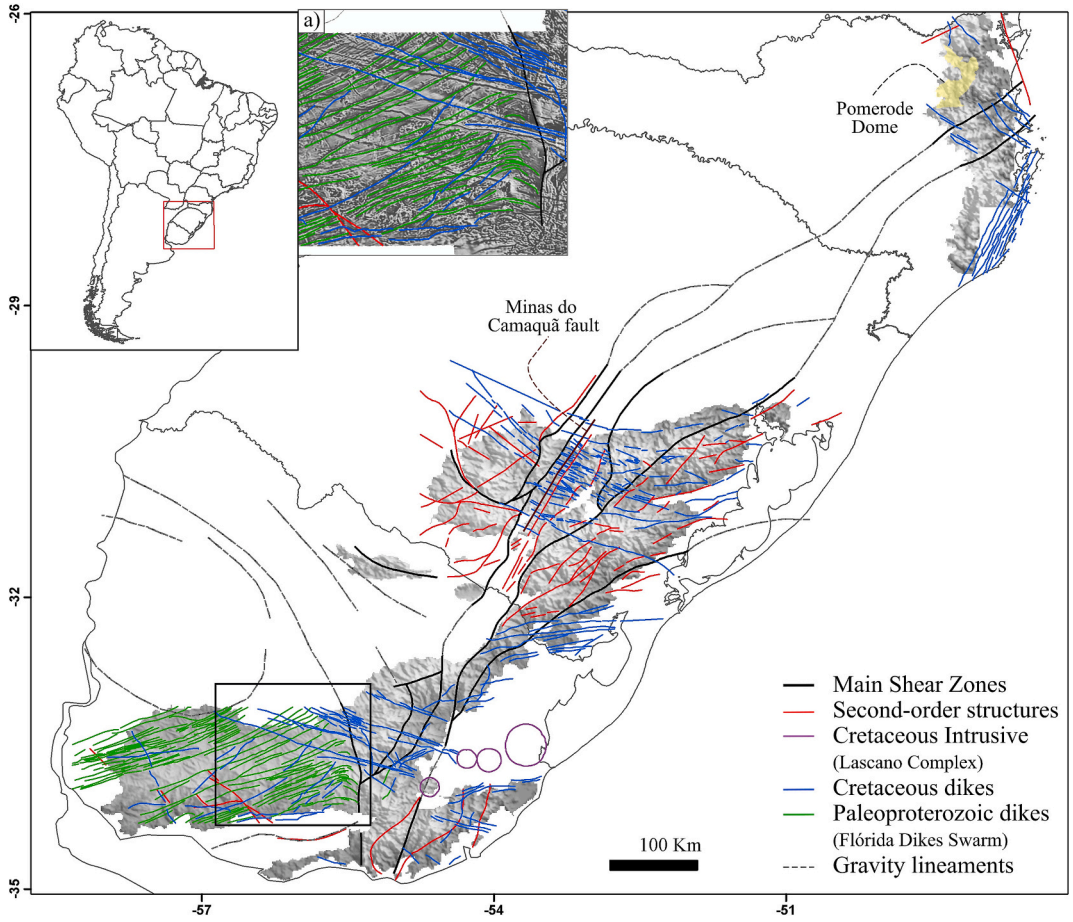

Fig. 3. Structural lineaments map based on magnetic, gravimetric, and radiometric anomalies and geologic correlations. The lineaments have been classified as first-order, second-order, dyke swarms, and gravimetric lineations. a) A detail of Piedra Alta Terrane showing on Vertical derivative map the distribution of the 1.78 Ga dyke swarm (Halls et al., 2001) that Sarandí del Yí has deformed in Meso or/and Neoproterozoic. The study area is reported on the inset map—background data: topography SRTM1 grid.

established by Coney et al. (1980), our terrane classification integrates geophysical signature and tectonostratigraphic relationships within the Uruguayan-Sul-Riograndense and Catarinense Shield (USRCS).

4.1. *Structural framework of the DFB and surrounding older terranes*

Distinct crustal domains were identified based on potential and gamma-ray spectrometry data (Fig. 3). Each geophysical unit displays internally consistent structural features and characteristic magnetic and gravimetric signatures, distinguished by their anomaly patterns, intensity, and orientation. The primary structural framework comprises deep magnetic lineaments, defined by abrupt changes in the anomaly distribution, representing major shear zones that mark terrane boundaries and outline the basement features. Secondary lineaments, typically observed within individual geophysical units, correspond to less prominent structures. Additionally, ENE-WSW- trending Late Paleoproterozoic and WNW-ESE-trending Mesozoic trending dyke swarms have been identified through their distinctive magnetic signature, exhibiting consistent anomaly patterns along strike lengths of hundreds of kilometers, despite their orientation contrasting with the regional structural grain (Fig. 3).

The ENE-WSW-trending Paleoproterozoic dikes are restricted to the Piedra Alta Terrane (PAT), where their pronounced curvature in the east indicates both the presence and predominantly dextral movement along the Sarandí del Yí Shear Zone (Fig. 3a). Gravimetric features have enabled the delineation of contrasting crustal boundaries and basement faulting, particularly in regions where gravity data provides the only subsurface constraint. Through these linear features and the gravity anomaly signature, we interpret the northwestern extension of this terrane. Well-marked NW-*SE*-oriented structure reveals the continuity of Piedra Alta Terrane and its boundary with the Nico Perez Terrane, characterized by rougher internal features indicated by high-amplitude gravimetric anomalies associated with polydeformed granulite-facies bearing gneisses of the Valentines and Santa Maria Chico Complex complexes (Girelli et al., 2018).

The Cretaceous dikes are more widely spaced and exhibit a stronger magnetic signature with a larger amplitude. They display two distinct orientations, WNW-ESE and NE-SW (Fig. 3), with the latter restricted to the Santa Catarina Shield. In the central Sul-Riograndense Shield, magnetic data indicates that dikes are not noticeably affected by any major shear zone. However, they exhibit southward deflection, with increased vergence near the NE-SW-trending Minas do Camaquã fault, as evidenced in the first vertical derivative of the magnetic field.

4.2. *Tectonic compartmentalization*

This study identifies and delineates the major structural lineaments through integrated analysis of magnetic, gravimetric, and gamma-ray spectrometry anomalies integrated with geologic correlations (Fig. 2). These datasets provide crucial evidence for distinguishing terranes of Archean to Mesoproterozoic and Neoproterozoic to Eopaleozoic ages based on their distinct geophysical, geological, and isotope signatures (Fig. 4). Terrane boundaries are established according to the criteria outlined by Coney et al. (1980).

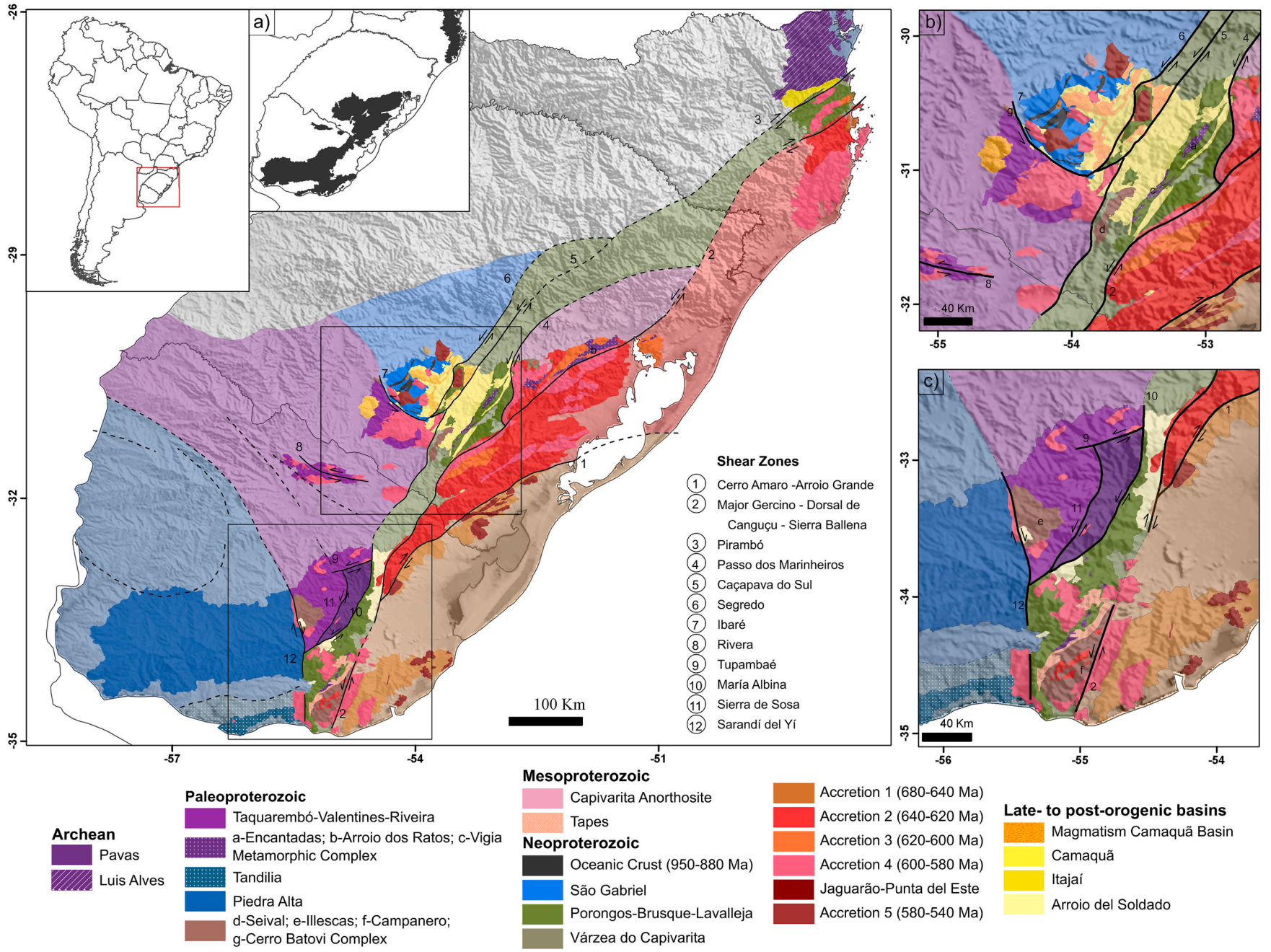

Fig. 4. Main tectonic units of the Precambrian (modified after; Mallmann et al., 2007; Philipp et al., 2016; Girelli et al., 2018; Takehara and Laux, 2019; Abre et al., 2020; Gaucher et al., 2021); a) Precambrian to Eopaleozoic outcropping rocks; b) Detailed geological map of São Gabriel Terrane and adjacent areas; c) Detailed map of the central portion of USRCS in Uruguay. The present map contains extensions of the Piedra Alta Terrane (light blue), Nico Perez Terrane (light purple), and Tijucas Supraterrane (light green) based on the geophysical data (mostly Bouguer Anomaly Map), where the basement is covered by the Phanerozoic rocks of the Paraná Basin and Paraná LIP Magmatism in Uruguay, Rio Grande do Sul and Santa Catarina (see text for further explanation). (For interpretation of the references to colour in this figure legend, the reader is referred to the web version of this article.)

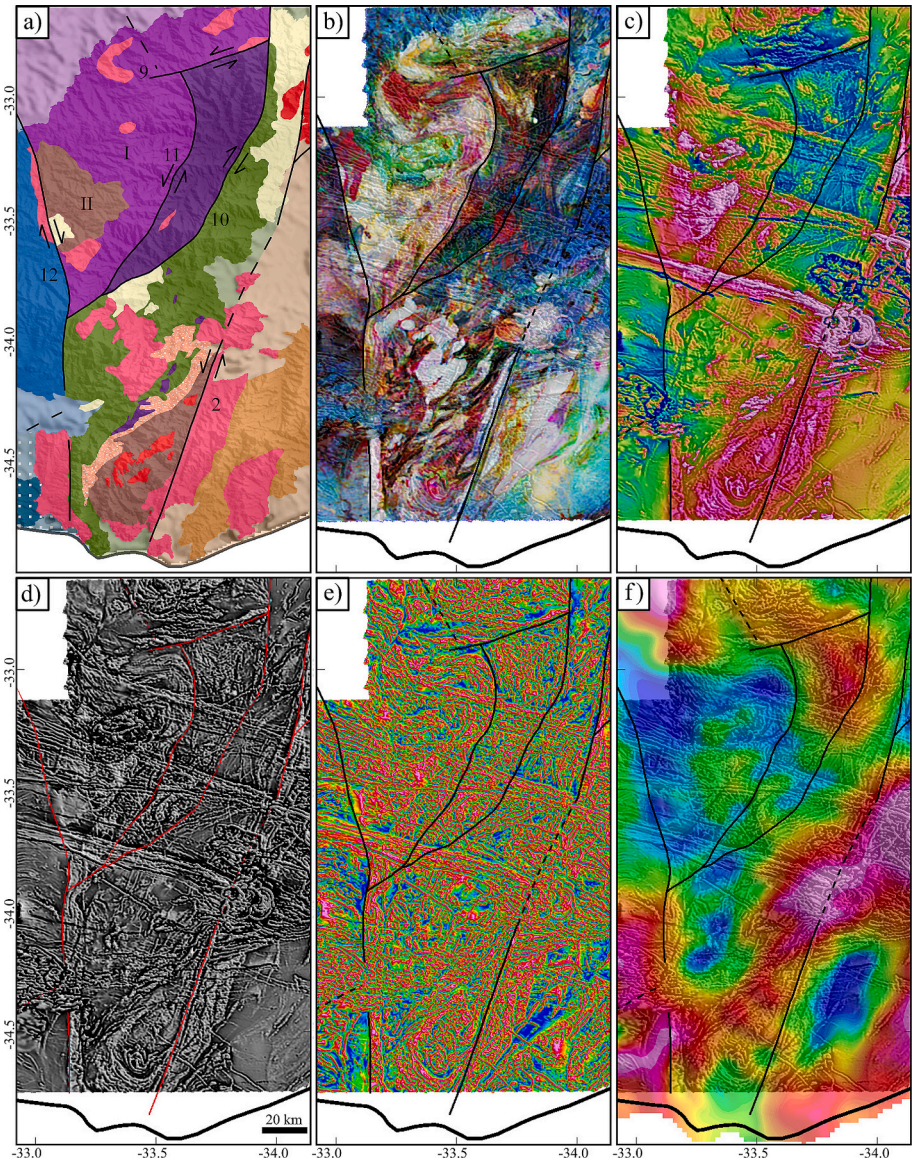

Fig. 5. Integrated geological and geophysical maps of the Nico Perez Terrane in Uruguay. a) The geological map is superimposed on topography. I = Valentines Granulite Complex and II = Illescas Batholith. For a detailed legend, refer to Figs. 2 and 4. b) Ternary composition RGB. The gamma-ray data is colour-subtitled with red indicating areas of high potassium concentration, green for high thorium, and blue for high uranium; c) Map of Magnetic anomalies reduced to the pole; d) First Vertical Derivative map; e) Tilt derivative (TDR) map; f) Bouguer Anomaly map. Geophysical maps are superimposed on the First Vertical Derivative map for enhanced interpretation. Warmer colors indicate high magnetic and gravimetric field strength, while cooler colors indicate lower strength. (For interpretation of the references to colour in this figure legend, the reader is referred to the web version of this article.)

4.2.1. Archean-Paleoproterozoic

4.2.1.1. Pavas Terrane. The Pavas Terrane (PT) is characterized by a low amplitude magnetic signature and low concentrations of all radioelements (Fig. 5). This terrane consists predominantly of TTG (Tonalite-Trondhjemite-Granodiorite) gneisses, with intercalated mafic-ultramafic bodies and a sequence of metasedimentary rocks with indistinct gamma-ray signatures. The TTG gneisses and the mafic-ultramafic formations constitute the La China Complex, while the metasedimentary sequence, comprising quartzites, metapelites, and marbles, form the Cebollati Group (Gaucher et al., 2011; Masquelin et al., 2021; Oyhantcabal et al., 2021), also known as the Las Tetas Complex by Hartmann et al. (2001). Regional Bouguer gravity data reveal prominent westward-trending anomalies in the northern sector of the terrane, contrasting with the gravity signature of its southern portion. The Tupambaé Shear Zone defines the north boundary (lineament 9, Figs. 4 and 5), which strikes approximately east-west and is characterized by low amplitude magnetic anomalies and minor radiometric variations, particularly in K and Th concentrations.

The eastern boundary coincides with the María Albina Shear Zone (lineament 10, Figs. 4 and 5), mapped smoothly in gamma-ray spectrometry data. The magnetic signatures of the Pavas Terrane highlight the WNW-ESE and *E*-W trending dyke swarms that extend from the Piedra Alta Terrane, clearly visible by reduced-to-the-pole and the vertical derivative (Figs. 8c and d, respectively).

The Pavas Terrane geological history records up to 500 Ma of magmatism, spanning from the Paleoarchean (oldest magmatic event dated at 3246.8 ± 10.09 Ma; Masquelin et al., 2021) to the Neoarchean (youngest igneous activity at 2707 ± 7 Ma; Sánchez Bettucci et al., 2021). Detrital zircon preserved in the paraderived rocks (Las Tetas Complex), supported by 88 grains (Hartmann et al., 2001), reveals a dominant provenance peak in the Neoarchean, at approximately 2.8 Ga, with the oldest detrital zircon dated at 3262 ± 14 Ma.

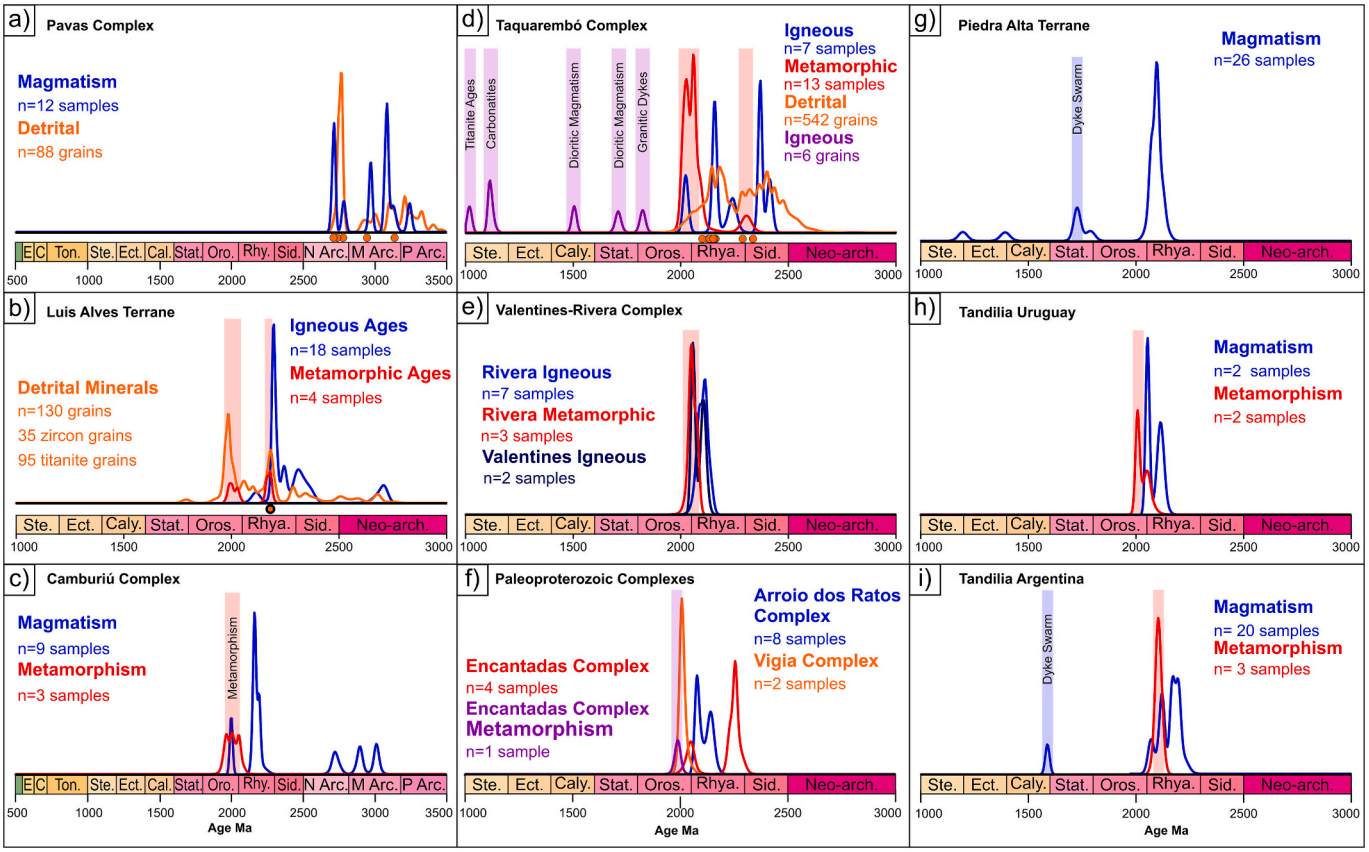

Fig. 6. Histogram showing the distribution of U—Pb zircon ages for the Archean to Paleoproterozoic terranes of the Uruguaian-Sul-Riograndense and Catarinense Shield. This data compilation is based on references found in Supplementary Material S2. a) Archean Pavas Terrane. It reveals significant Mesoarchean and Neoarchean components within the populations of the orthoderived rocks (La China Complex) and the paraderived rocks (Cebollatti Group/Las Tetas Complex) of the Pavas Terrane; b) Histogram with U—Pb zircon age distribution of the Luis Alves Terrane showing dominant Rhyacian and Siderian ages for the magmatic activity, whereas the metamorphic ages are 2183 ± 17 (Heller et al., 2021). Some detrital zircons are also Rhyacian. Subordinate Neoarchean crystallization age is also present (see text for explanation); c) Histogram with U—Pb zircon age distribution of the Camburiú Complex with dominant Rhyacian magmatism and metamorphic peak at 2050 ± 56 (Basei et al., 2013); d) Histogram with U—Pb zircon age distribution of the NPT in the Taquarembó region showing dominant Rhyacian and Siderian ages of ortho and paraderived granulitic rocks and main metamorphic peak at 2061 ± 19 (Girelli et al., 2018). It is also recorded those Mesoproterozoic intrusions that intruded after the high-grade metamorphism; e) Histogram with U—Pb zircon age distribution of the Nico Perez Terrane in Uruguay (Valentines and Isla Rivera Complexes) showing dominant Rhyacian magmatism and metamorphic peak at 2041 ± 24 (Oriolo et al., 2016b); f) Histogram with U—Pb zircon age distribution of the Tijucas basement in the Rio Grande do Sul showing dominant Rhyacian magmatic ages for the Arroio dos Ratos Complex, Encantadas Complex, and Vigia Complex. Amphibolite metamorphism is well recorded in the Vigia and Encantadas Complex units at 2.0 Ga (Orosirian ages); g) Histogram with U—Pb zircon age distribution of the Piedra Alta Terrane (Uruguay) showing dominant Rhyacian ages of orthoderived rocks and the 1.7–1.78 Ga Dyke Swarm magmatism; h) Histogram with U—Pb zircon age distribution of the Tandilia Terrane (Uruguay) showing dominant Rhyacian ages of orthoderived rocks and main metamorphic peak at 2052 ± 38 (Pamoukaghlián et al., 2017). It also recorded those Mesoproterozoic intrusions that intruded after the high-grade metamorphism; i) Histogram with U—Pb zircon age distribution of the Tandilia Terrane (Argentina) showing dominant Rhyacian magmatism and metamorphic peak at 2092 ± 12; (Angeletti et al., 2021). It is also recorded those Mesoproterozoic intrusions (1589 ± 2.7; Teixeira et al., 2013).

4.2.1.2. Luis Alves Terrane. The Luis Alves Terrane (LAT) is distinguished by its internal segmentation marked by pronounced magnetic relief, controlled by NE-SW-trending structures, and bounded by the Itajaí-Perimbó and Dorsal de Canguçu-Major Gercino Shear Zones to the north and south, respectively (Fig. 4). The region is characterized by high-amplitude and long-wavelength magnetic anomalies, revealing an elliptical structure dome trending SW-NE, known as the Pomerode Dome (Fig. 3; Betiollo et al., 2019). This dome predominantly comprises Archean-Paleoproterozoic granulite rocks belonging to the Santa Catarina Granulite Complex. Notably, the internal structures of this dome exhibit a lack of a consistent orientation pattern. The terrane exhibits low concentrations of all radioelements, with localized radiometric domains showing distinct variations in potassium and thorium concentrations. Regional gravity data reveal a positive anomaly, indicating mass excess relative to the surrounding areas (Fig. 2d).

The Luis Alves Terrane records an accretionary history spanning 500 million years, from the Neo-archean (oldest magnetic event dated at 2716 ± 17 Ma; Hartmann and Remus, 2000) to the Rhyacian (youngest magnetic event dated at 2192 ± 14 Ma; Basei et al., 2009; Heller et al., 2021). It consists of granulitic rocks (including ultramafic, mafic, and felsic ortho- and paragneisses) of the Santa Catarina Complex, intruded by Paleoproterozoic granitic bodies (Hartmann and Remus, 2000; Basei et al., 2009) with the main magmatic event occurring at 2.2 Ga (Fig. 6b). Two major metamorphic events affected the terrane at approximately 2.15 Ga and 2.0 Ga. The detrital record of 35 zircon grains and 95 titanite grains indicate extensive metamorphic overprinting, with titanite ages predominantly recording the ~2.0 Ga granulite facies metamorphic event.

Neoarchean ages dominate the detrital and magmatic zircon grains, consistent with the predominant Nd model age for the Luis Alves Terrane, along with Siderian ages (Siga Junior, 1995). To the south, the Camboriú Complex (Fig. 6c) occurs as a sept within the Ediacaran Brusque Thrust-Fold Belt (see Tijucas Supraterrane section), which was accreted during the Rhyacian period with minor Archean magmatism and subjected to granulite facies metamorphism at ~2 Ga (Basei et al., 2013).

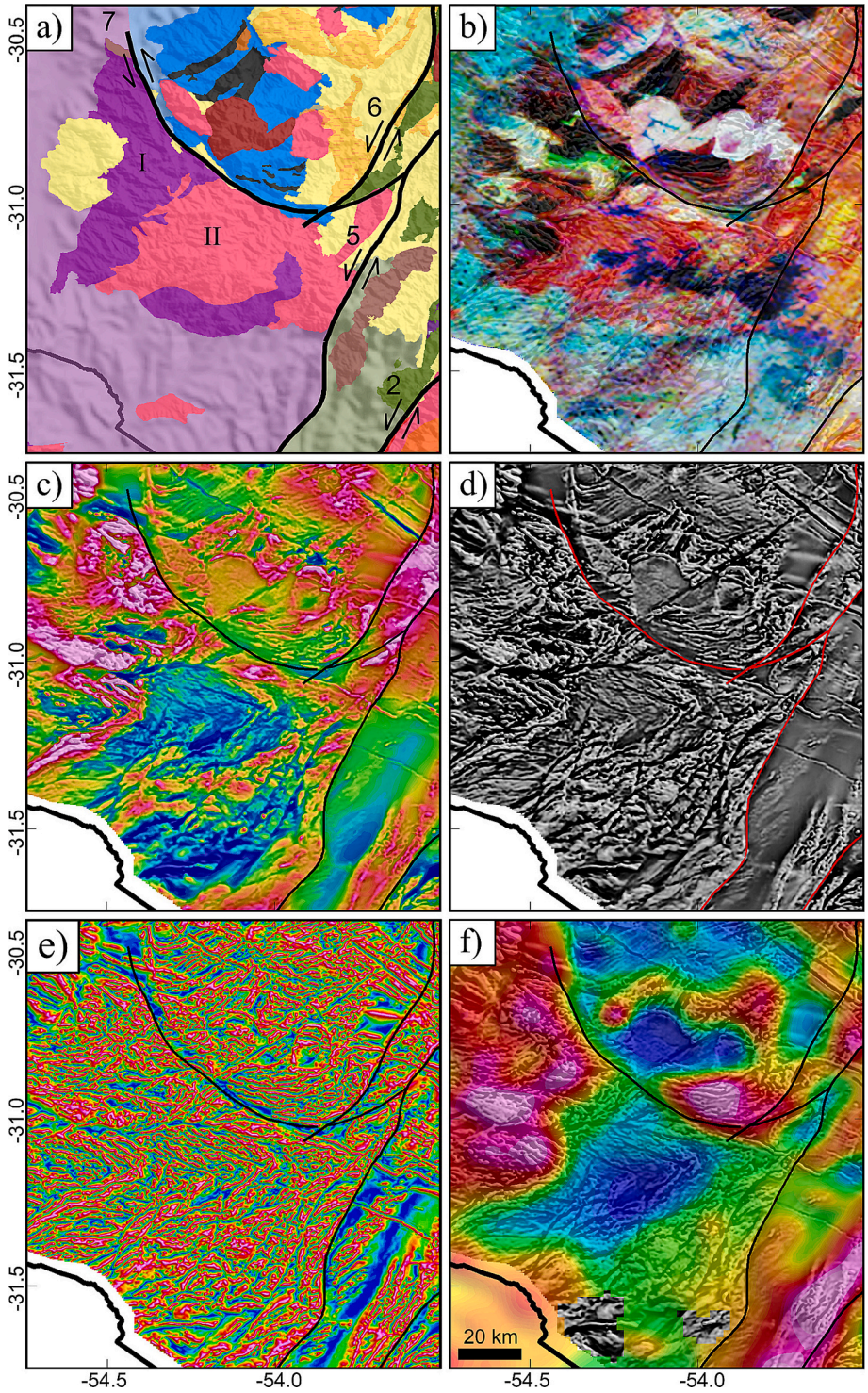

Fig. 7. Integrated geological and geophysical maps of the Nico Perez Terrane in Rio Grande Sul. a) The geological map is superimposed on topography, where: I – Santa Maria Granulitic Complex; II - Torquato Severo Batholith (for a detailed legend, see Fig. 2); b) Ternary composition RGB where red denote high potassium, green for high thorium, and blue for high uranium; c) Magnetic anomalies reduced to the pole map; d) First Vertical Derivative map; e) Tilt derivative (TDR) map; f) Bouguer Anomaly map. Geophysical maps are superimposed on the First Vertical Derivative map. Warmer colors indicate high magnetic field strength, while cooler colors indicate lower strength. (For interpretation of the references to colour in this figure legend, the reader is referred to the web version of this article.)

4.2.1.3. Nico Perez Terrane (NPT). The Nico Perez Terrane (NPT) is mainly delineated by distinctive potassium concentration patterns in the Valentines, Isla Rivera, and Taquarembó crustal blocks (Fig. 2). These regions share similar geological signatures, including granulitic rock associations and Ediacaran (Brasiliano) granitic intrusions. The internal structures of these blocks are recognized through distinctive magnetic texture *within* the Valentines Granulite Complex (Uruguay; Fig. 5) and an arcuate pattern of *E*-W-trending anomalies associated with the Santa Maria Chico Granulitic Complex (SMCGC-Brazil; Fig. 7).

In southern Brazil, the terrane is characterized by high potassium concentration and positive gravity anomaly, reflecting the presence of mafic to ultramafic granulites (Hartmann, 1998; Girelli et al., 2018;

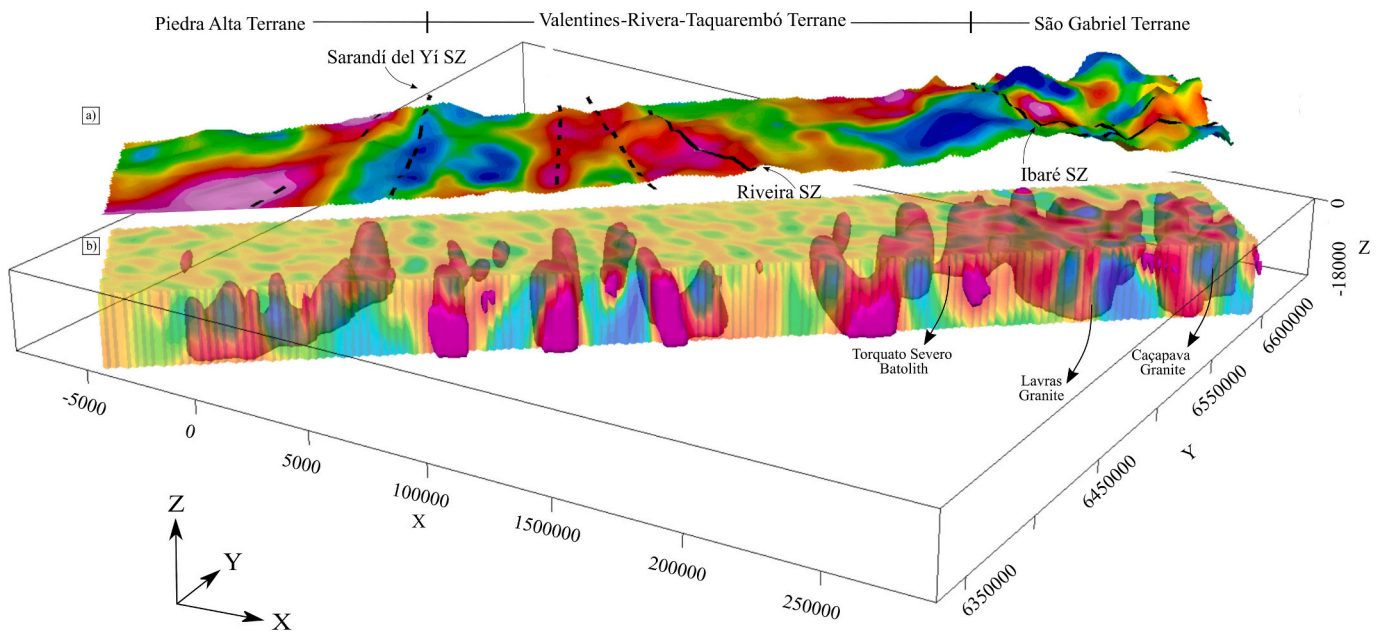

Fig. 8. 3D model derived from gravity data, revealing horst-graben structures along Profile B-B′ (refer to location in Fig. 2d). The upper part of the figure shows the residual gravity anomaly utilized in the gravity inversion process overlaid on the SRTM1 image. Beneath this, the 3D inversion of gravity data uncovers structures oriented in a northwest (NW) direction at depth within the Valentines-Rivera-Taquarembó blocks alongside the principal gravimetric bodies.

Figs. 7b and f). The Torquato Severo Batholit, which intrudes the SMCGC, is marked by low-amplitude, short-wavelength magnetic anomalies and pronounced gravity low, displaying a rugged and elongated relief (Figs. 7c and f). This batholith intruded the Paleoproterozoic granulites during the Ediacaran at 635–625 Ma (Camozzato et al., 2017). The sedimentary cover obscures the radiometric signature of this batholith. The northern boundary with São Gabriel Terrane is defined by the NW-SE trending Ibaré Shear Zone.

The eastern boundary coincides with the NE-trending Caçapava do Sul Shear Zone, separating it from the Tijucas Supraterrane, clearly visible in the vertical derivative of the magnetic field (Fig. 7d). In contrast, the Valentines Terrane in Uruguay shows high counts of the three radioelements (K, Th, and U) and negative gravity anomalies (Fig. 7b and f), comprising granulitic orthogneisses enriched in potassium feldspar (Oyhantçabal et al., 2018). The western boundary is characterized by an intermediate-amplitude magnetic signature with smooth appearance and low to medium-amplitude gravity anomalies. The geophysical framework in this region reveals significant geological features, including the Illescas Batholith, a characteristic rapakivi granite. This pluton is distinguished by high-amplitude magnetic anomalies and high total count values, with its western margin defined by the Sarandí del Yí Shear Zone. The batholith generates low-intensity anomalies in the regional gravity data (Fig. 5f). The magnetic signature displays high-amplitude, short wavelength components, creating a textured pattern that indicates a shallow causative body toward the east (Fig. 5c).

WNW-ESE and E-W trending dyke swarms, restricted to Uruguay, are particularly well-defined in the vertical derivative (Fig. 5d). The western boundary with Pavas Terrane coincides with the Sierra de Sosa Shear Zone, identifiable in both ternary radiometric images and the magnetic data (Figs. 5b and c), being also well-constrained by field data (Oriolo et al., 2016; Spoturno et al., 2019). The E-W trending Tupambaé Shear Zone in the northern sector produces a low magnetic anomaly, separating units with distinct magnetic and radiometric characteristics.

The NPT extends northwestward beneath the Paraná Basin, as indicated by gravimetric data (highlighted by the light purple area in Fig. 4a). Near Isla Rivera, prominent NW-oriented lineaments are present, including the major Rivera Shear Zone - a 1–2 km wide structure that records sinistral movement under oblique compressional conditions during the Brasiliano/Pan-African orogeny (ca. 606 Ma; Oyhantçabal et al., 2012). This shear zone significantly controlled Ediacaran orogenic gold deposits associated with brittle-ductile deformation and hydrothermal fluid flow (Oriolo et al., 2024). Gravity inversion modeling in this region reveals an extensional regime characterized by steep basement faults, indicating probable horst-graben structures (Fig. 8).

The NPT exhibits two distinct geological evolutionary histories. The Brazilian sector, represented by the Taquarembó crustal block, records an extended magmatic history with three major magmatic phases at 2.4 Ga, 2.2 Ga, and 2.05 Ga (Girelli et al., 2018; Fig. 6d). In contrast, the Rivera and Valentines blocks in the Uruguayan sector present a more constrained accretionary period from approximately 2.15 Ga to 2.05 Ga. Both sectors underwent a significant granulite facies metamorphic event at 2.05 Ga (Hartmann et al., 2008; Oriolo et al., 2016b; Fig. 6e). Detrital zircon studies, conducted exclusively in the Brazilian region, analyzed 542 zircon grains that trace a polycyclic magmatic history from 2.5 Ga to 2.1 Ga.

The Taquarembó crustal block preserves Orosirian granitic dikes and Calymanian and Statherian dioritic rocks, indicating post-tectonic magmatism (Fig. 6d). Additionally, alkaline magmatism described by Monteiro et al. (2020) includes dolomite metacarbonatite (1110 ± 4.8 Ma) and metasyenite (1123 ± 15 Ma). These units comprise isoclinal folding and greenschist to amphibolite facies metamorphism and intrude Paleoproterozoic quartz-feldspar gneisses dated at 2022.5 ± 7.9 Ma (LA-ICPMS zircon dating). The timing of deformation is constrained between 1.11 and 1.01 Ga, based on a titanite cooling age of 1018 ± 9.9 Ma obtained from Paleoproterozoic orthogneiss (Girelli et al., 2018).

4.2.1.4. Tandilia Terrane. The Tandilia Terrane (TT) has limited gamma-ray spectrometry and magnetic data coverage. The eastern sector exhibits smooth magnetic relief, with isolated high-frequency anomalies occurring within regions of low magnetic response (Fig. 2b). The vertical derivative map presents a low-amplitude distribution with a smooth texture (Fig. 2c). Regional gravity anomaly shows a prominent positive signature, marked by a mass excess compared to the surrounding regions (Fig. 2d).

The Tandilia Terrane magmatic evolution is recorded in the

southernmost regions of Uruguay and Argentina. Both domains preserve a short magmatism period spanning 2.3 to 2.1 Ga (Fig. 6h and i; Hartmann et al., 2002; Santos et al., 2003; Pamoukaghlián et al., 2017; Angeletti et al., 2021). Regional metamorphism occurred at ~2.1 Ga in Argentina (Fig. 6i) and 2.0 Ga in the Uruguay domain (Fig. 6h). The terrane was subsequently intruded by Proterozoic mafic and felsic dike swarms, contemporaneous with post-orogenic granitic plutonism, which stands out in the Tandilia region at ~1.59 Ga (Fig. 6i; Teixeira et al., 2002).

4.2.1.5. Piedra Alta Terrane. The Piedra Alta Terrane (PAT) is characterized by low gamma-ray counts and a smooth, low-amplitude magnetic signature with a few distinctive features (Figs. 2a and b). A wide and high-amplitude magnetic anomaly dominates the central-western portion of the terrane, coinciding with a gravity-low related to a

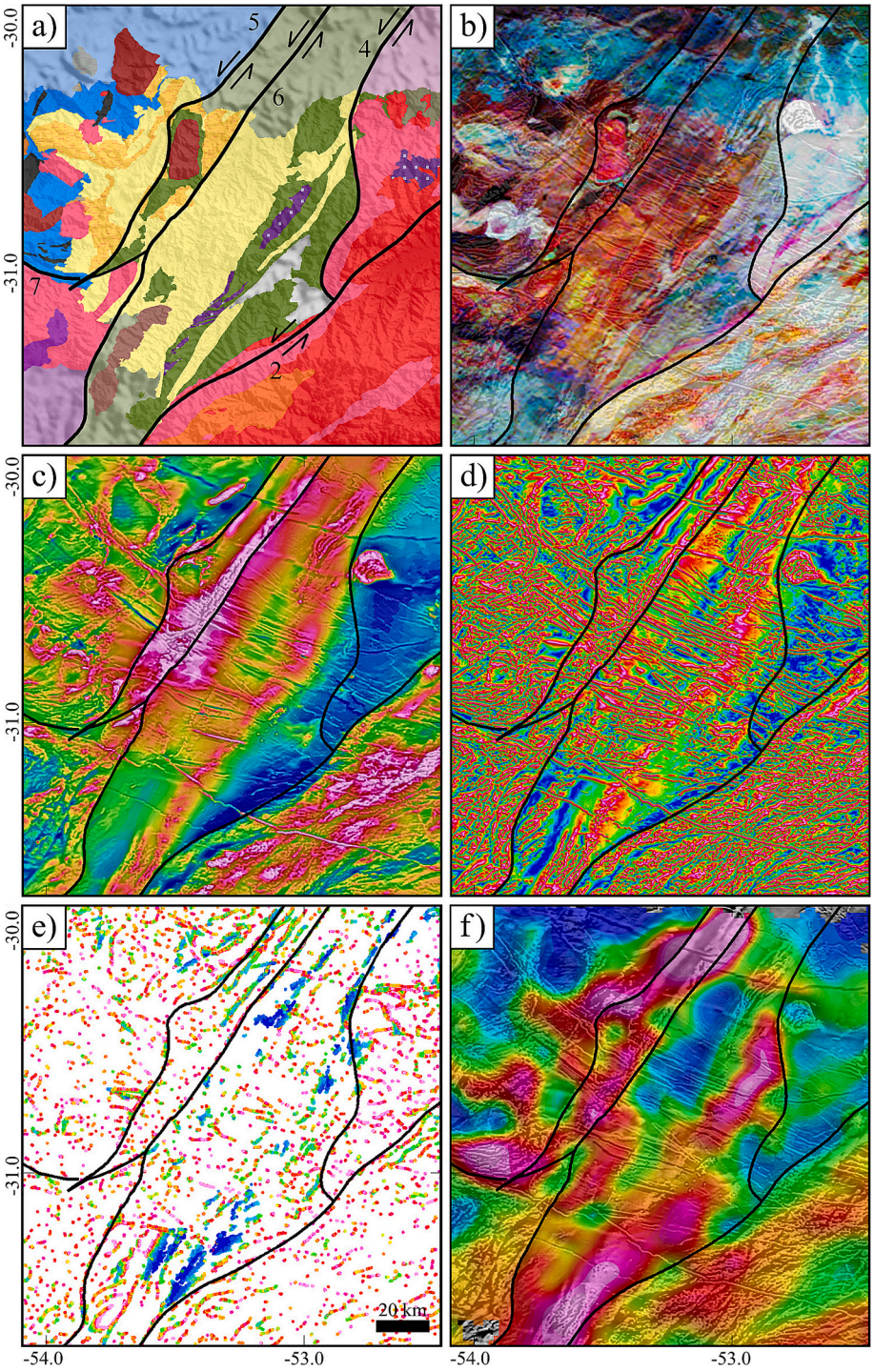

Fig. 9. a) Geological map for the basement units in the Tijucas Supraterrane superimposed on topography; b) Ternary composition RGB Gamma-ray where red denote high potassium, green for high thorium, and blue for high uranium; c) Magnetic anomalies reduced to the pole map; d) Tilt derivative (TDR) map; e) Euler solutions for magnetic data-SI equal to 0; f) Bouguer Anomaly map. Geophysical maps are superimposed on the First Vertical Derivative map. Warmer colors indicate high magnetic field strength, while cooler colors indicate lower strength. (For interpretation of the references to colour in this figure legend, the reader is referred to the web version of this article.)

granitic-gneissic domain bounded by supracrustal metamorphic belts (Sánchez Bettucci et al., 2010). Regional Bouguer gravity data show high anomalies corresponding to the Arroyo Grande Belt in the north and the San José Belt to the south (Fig. 2d).

This crustal domain comprises juvenile rocks (Nd model age of 2.28 to 1.76 Ga; Oyhantçabal et al., 2011) dominated by granite-gneisses complexes emplaced during the Rhyacian 2.05 to 2.15 Ga (Fig. 6g; Hartmann et al., 2002, Santos et al., 2003, Oriolo et al., 2016c; Santos et al., 2017; Basei et al., 2024). The eastern boundary coincides with the Sarandí del Yí Shear Zone, marked by contrasting geophysical signatures between the terrane and the adjacent Valentines Block, the latter showing low magnetic intensity and high contrast gravity anomalies (Fig. 2d) and distinctive high radiometric values in the ternary map (Fig. 2a).

The terrane is extensively dissected by two generations of dyke swarms (Fig. 3). The dominant ENE-WSW Statherian dikes constitute the Florida dikes swarm, while the second generation comprises WNW-ESE and NE-SW Cretaceous dikes that extend into adjacent terranes. The Florida dyke swarms display a gradual northward deflection from west to east, approaching the Sarandí del Yí Shear Zone, where occurs an abrupt southwards deflection, indicating dextral displacement along the shear zone (Fig. 3a).

Strong, asymmetric magnetic anomalies in the total field data, which become symmetrically centered when reduced to the pole, show low-amplitude circular signatures predominantly along the margins of the granitic-gneissic complex, interpreted as alkaline intrusions (Fig. 2b). The Piedra Alta Terrane represents the main exposed nuclei of the Rio de La Plata Craton, with its main accretionary cycle spanning 2.2 to 2.05 Ma (Fig. 6h). Later magmatic events include the Uruguayan Dyke Swarm at 1.79 Ga (Halls et al., 2001) and minor Mesoproterozoic gabbroic intrusions (Santos et al., 2017).

The Bouguer gravity map (Fig. 2d) reveals an oval-shaped basement feature beneath Paleozoic Paraná Basin rocks, interpreted as an extension of the Piedra Alta Terrane. This feature is depicted in light blue in Fig. 4, representing the subsurface continuation of the Piedra Alta Terrane.

4.2.1.6. Basement units in the Tijucas Supraterrane. The Tijucas Supraterrane (TS) extends northward to Santa Catarina State, where it comprises the metavolcanic-sedimentary sequences of the Brusque Complex and the orthogneisses of the Camboriú Complex (Basei et al., 2000). In Rio Grande do Sul State, the TS includes the Porongos Metavolcanosedimentary sequences and Paleo- and Mesoproterozoic basement rocks (Philipp et al., 2016). The supraterrane extends into Uruguay, represented by the Lavalleja Complex metavolcanosedimentary rocks and Calyminian volcano-sedimentary sequences of the Tapes Complex (Figs. 4 and 5; Mallmann et al., 2007; Gaucher et al., 2011, Gaucher et al., 2021; Oyhantcabal et al., 2021).

These regions underwent intense deformation during the Brasiliano cycle and incorporate Neoproterozoic rock assemblages (e.g., Pertille et al., 2017 and references therein) along with Paleoproterozoic Encantadas and Vigia complexes (e.g., Philipp et al., 2008), Statherian Rapakivi metagranites (Mallmann et al., 2007; Camozzato et al., 2017) and Mesoproterozoic Tapes Complex volcanosedimentary sequences (Gaucher et al., 2011, 2021; Figs. 4 and 5).

The Encantadas and Vigia Complexes (Chemale Jr, 2000) form domal structures within the Tijucas Supraterrane basement, trending N30°E-S30°W (Fig. 9e). The Encantadas Complex (sensu Chemale Jr, 2000) consists of Tonalite-Trondjemitic-Diorite gneiss (TTD), amphibolites, and metagranites. Its primary accretionary period occurred at 2.2 Ga, followed by amphibolite facies metamorphism at 2.0 Ga (Fig. 6f; Hartmann et al., 2003; Philipp et al., 2016). The Vigia Dome predominantly comprises tonalitic and granodiorite gneisses, with the subordinate occurrence of dioritic gneisses and metahornblendites of the Vigia Complex (Camozzato et al., 2017). The Vigia Complex outcropping south of the Tijucas Supraterrane records magmatism at 2.05 Ga (Fig. 6f).

The Arroio dos Ratos Complex, forming the basement of the

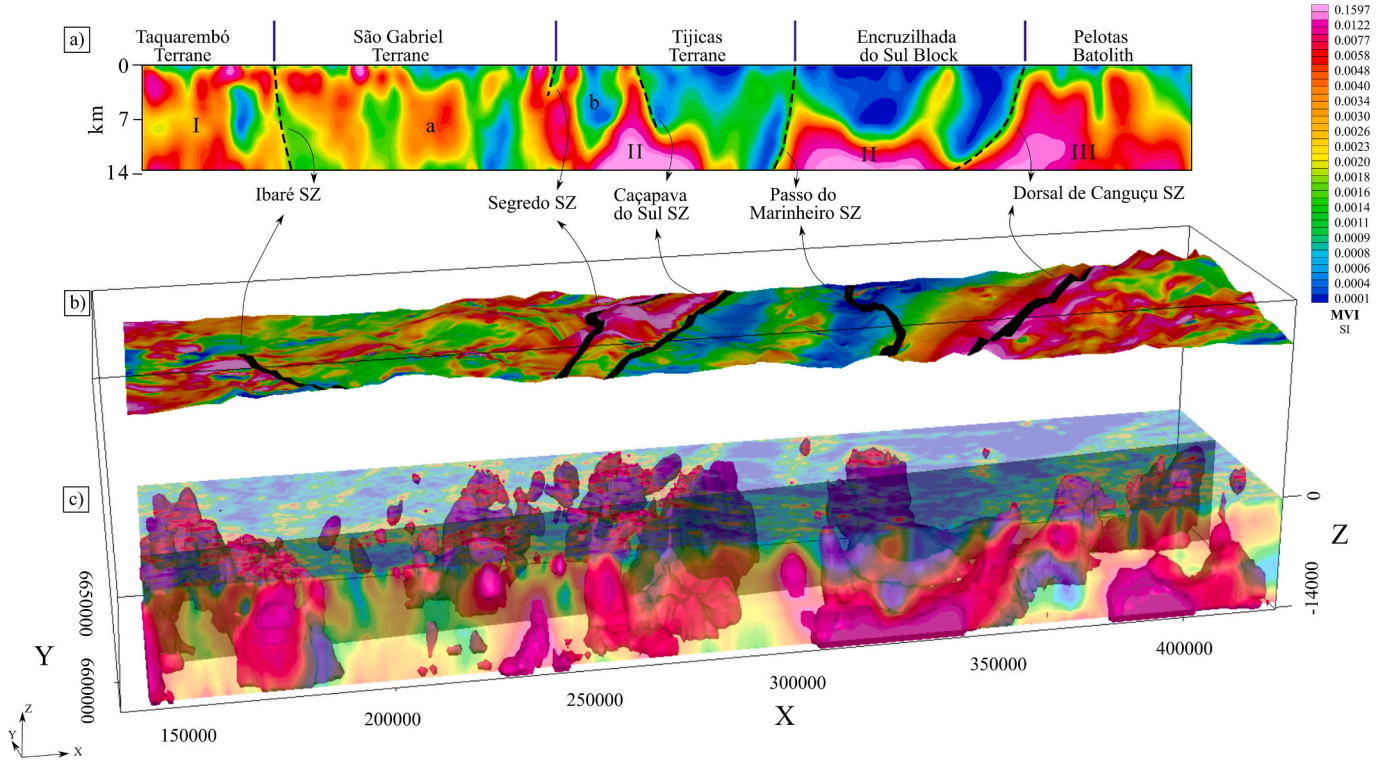

Fig. 10. The 3D model based on magnetic data showing main structures along Profile A-A' (see location in Fig. 2b). a) Residual magnetic anomaly used in the inversion and superimposed on the SRTM1 image; b) 3D inversion of magnetic data showing NE-oriented in-depth structures.

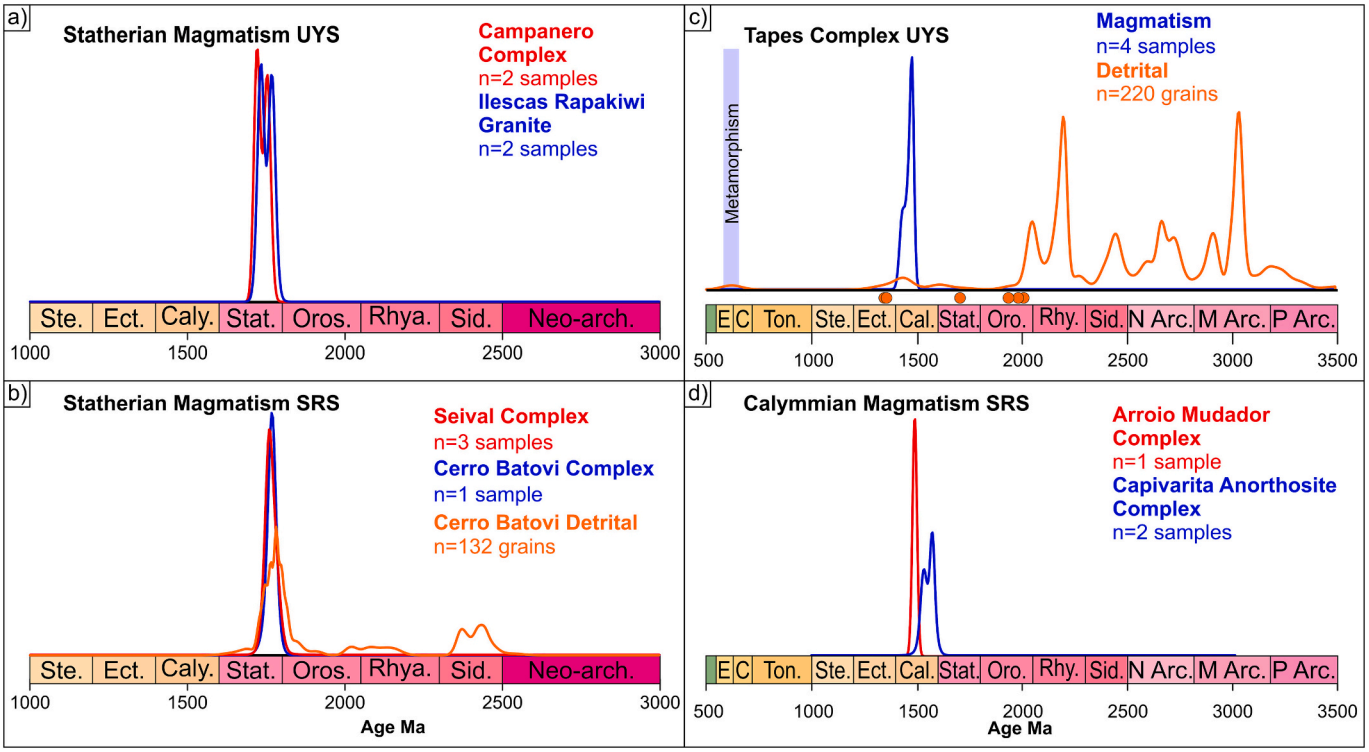

Fig. 11. a) and b) Histogram with U—Pb zircon age distribution of the Statherian magmatism in the Tijucas Supraterrane with a peak of 1.76 Ga in Uruguay and Rio Grande do Sul; c) Histogram with U—Pb zircon age distribution of the Tapes Terrane showing a Calymmian magmatic age for volcanic rocks. Metasedimentary rocks contain age peaks at 1.5 Ga, 2.1 Ga, 2.35 Ga, 2.7 Ga, and 3.0 Ga; d) Histogram of U—Pb zircon age at Sul-Riograndense Shield for the Capavirita Anorthosite (1570 ± 29 Ma; Chemale et al., 2011) and Arroio Mudador pillow lavas (1588 ± 6.2; Laux et al., 2021). n: number of samples.

Encruzilhada Block (Figura 4a and 9a) within the Tijucas Supraterrane, represents a typical TTG magmatic arc accretioned between 2.15 and 2.05 Ga (Fig. 6f). Its NE-SW structural grain was modified during the Brasiliano Orogeny (Leite et al., 2000; Gregory et al., 2015).

4.2.1.7. Statherian magmatism. Statherian magmatism events occur extensively in the USRCS and are characterized by distinctive magnetic anomalies and radioelement patterns (Figs. 5 and 11). In Uruguay, these events are represented by the Campanero Complex crystallized at 1.75 Ga (Mallmann et al., 2007a) and the Illescas Rapakivi Granite at 1.77 Ga (Fig. 11a; Oriolo et al., 2019). In Brazil, these events are present in the Cerro Batovi Complex at 1.76 Ga (Laux et al., 2010) and the Seival Complex at 1.7 Ga (Camozzato et al., 2017; Fig. 11b).

In southern Brazil, the Seival Complex displays an intermediate-to-low magnetic intensity (Fig. 9c) and forms an NE-SW trending body that was extensively reworked during the Brasiliano Orogeny. Magnetic Euler deconvolution (Fig. 9e) reveals a dominant NE-SW structural trending parallel to the main structures of the Ediacaran Magmatic Arc to the east. The western boundary coincides with the regional Caçapava lineament, which is clearly defined in magnetic inversion models (Fig. 10). This domain is defined by the predominant NE-SW trending deep-seated structures of the Brasiliano age, which contrast with poly-deformational structures of the Granulite Complex, preserved west of this lineament (Fig. 9). The Cerro Batovi Complex (Figs. 4b and 7) in the northern Taquarembó region preserves primary magmatism dated at 1.76 Ga.

Two batholiths occur in Uruguay, intruding the Valentines Granulite Complex and Tijucas Supraterrane: the Illescas Rapakivi Batholith and Campanero Batholith (Carapé), respectively (Fig. 5a). The Campanero Batholith was strongly deformed by the Brasiliano Orogeny (Mallmann et al., 2007). These bodies shows a meta- to peraluminous compositions, with a dominant shoshonitic and ferroan composition in the Ilescas Rapakivi Batholith, whereas high-K calc-alkaline and magnesian to ferroan in the Campanero Batholith (Oriolo et al., 2019). Both bodies were characterized by high-amplitude magnetic anomalies and high radioelement contents (Figs. 5b and c). The intrusions exhibit a rough magnetic relief delimited by high magnetic anomalies showing short wavelengths, suggesting a shallow causative body (Figs. 5d and e).

4.2.2. Mesoproterozoic

4.2.2.1. Tapes Terrane (UY) and Calymmian magmatism (RS).. The Tapes Terrane is characterized by distinctively low radioelement concentrations, particularly evident in the ternary images (Figs. 5a and b). The thick metabasic rocks and carbonates justify the low potassium concentration (Gaucher et al., 2021). The terrane shows a NE-trending elongated geometry defined by characteristic magnetometric and gravimetric anomalies (Figs. 5c and f). Tapes Terrane boundaries are marked by magnetic lineaments, while its internal structures are characterized by an assemblage of high-amplitude anomalies (Figs. 8d and e). A pronounced contrast marks the eastern limit, further accentuated by the high potassium concentration of the Campanero Igneous Complex (Fig. 5b). Although gravimetric anomalies lack a well-defined internal structure, significant high-amplitude signals are present. Magmatic activity in the Tapes Complex is dated at 1.47 Ga. Provenance indicates two main peaks at 3.1 Ga and 2.2 Ga, with minor peaks at 2.9, 2.7, 2.45, and 2.05 Ga (Fig. 11c).

In the Sul-Riograndense Shield, Calymmian magmatism is recorded in two small bodies: the Capivarita Anorthosite (Fig. 4; Chemale et al., 2011), which crystallized at ~1.55 Ga, and the Arroio Mudador Complex (Laux et al., 2021), which crystallized at 1.48 Ga (Fig. 11d).

4.2.3. Neoproterozoic

4.2.3.1. São Gabriel Terrane. The São Gabriel Terrane (SGT) presents distinctive geophysical signatures reflecting the diversity of rock

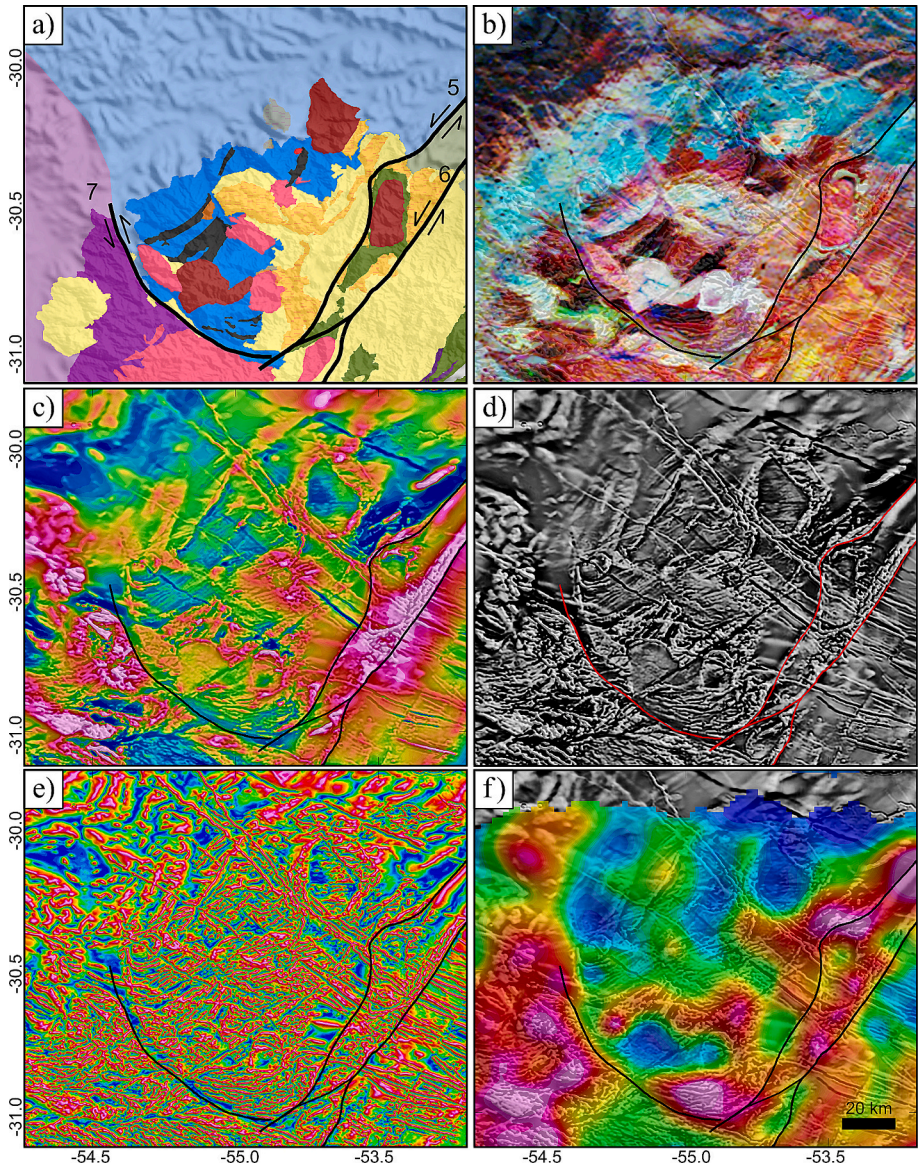

Fig. 12. a) Geological map for the São Gabriel Terrane superimposed on topography; b) Ternary composition RGB where red denote high potassium, green for high thorium, and blue for high uranium; c) Magnetic anomalies reduced to the pole map; d) First Vertical Derivative map; e) Tilt derivative (TDR) map; f) Bouguer Anomaly map. Geophysical maps are superimposed on the First Vertical Derivative map. Warmer colors indicate high magnetic field strength, while cooler colors indicate lower strength. (For interpretation of the references to colour in this figure legend, the reader is referred to the web version of this article.)

properties (Fig. 12). The terrane contains NE-oriented narrow zones characterized by low radioelement contents, especially thorium, which appear as dark bands in the ternary images and correspond to ophiolite sequences (Fig. 12b). These ophiolites show moderate to low magnetic relief, characterized by structures and features that are not well-defined (Figs. 12c and d). Maximum magnetic intensities correlate with *syn-* and post-tectonic granites and post-collisional basins, appearing as high-count circular anomalies in the ternary images and showing a low gravity signature (Figs. 12b and f). Expressive NE-trending structural lineaments characterize the southernmost granite bodies observed in the gamma-ray spectrometry and magnetic data (Figs. 12b and d).

The northern portion of SGT is characterized by thin magnetic lineaments with variable amplitudes, a signature typically associated with Cretaceous mafic dike swarms that intrude the terrane with predominant NW-trending orientation (Fig. 12c). The São Gabriel Terrane is bounded west and south by the Ibaré Shear Zone, marked by a distinctive deflection in the Vertical Derivative. Its eastern boundary follows the Segredo Shear Zone, characterized by pronounced relief and high amplitude magnetic anomalies (Figs. 12c and d).

The tectonic evolution of the São Gabriel Terrane records a prolonged history of arc accretionary processes. The main period of orogeny spans from 0.80 to 0.68 Ga (Fig. 13a; de Lena et al., 2014; Arena et al., 2016; Cerva-Alves et al., 2020; Hueck et al., 2020, 2022). Ophiolitic sequences aged at 0.94 to 0.88 represent the oldest geological units in the terrane. Zircon provenance is almost all related to terrane magmatism, with the main peak between 0.8 and 0.7 Ga.

4.2.3.2. Deformed cover (fold-and-thrust belt). The deformed cover comprises six distinct metasedimentary successions. In the Santa Catarina Shield, the Brusque Complex, with a maximum depositional age of ~800 Ma and metamorphosed at ~600 Ma, shows the main provenance population at 2.2 Ga and four minor peaks at ~2.0, 1.8, 1.55, and 1.3 Ga (Fig. 13c). In the Sul-Rio-Grandense Shield, the Porongos I Complex, with a maximum depositional age of ~790 Ma and metamorphism at ~600 Ma (Fig. 13d), exhibits a main provenance population between 2.05 and 2.3 Ga. Like the Brusque Complex, it contains Stenian and

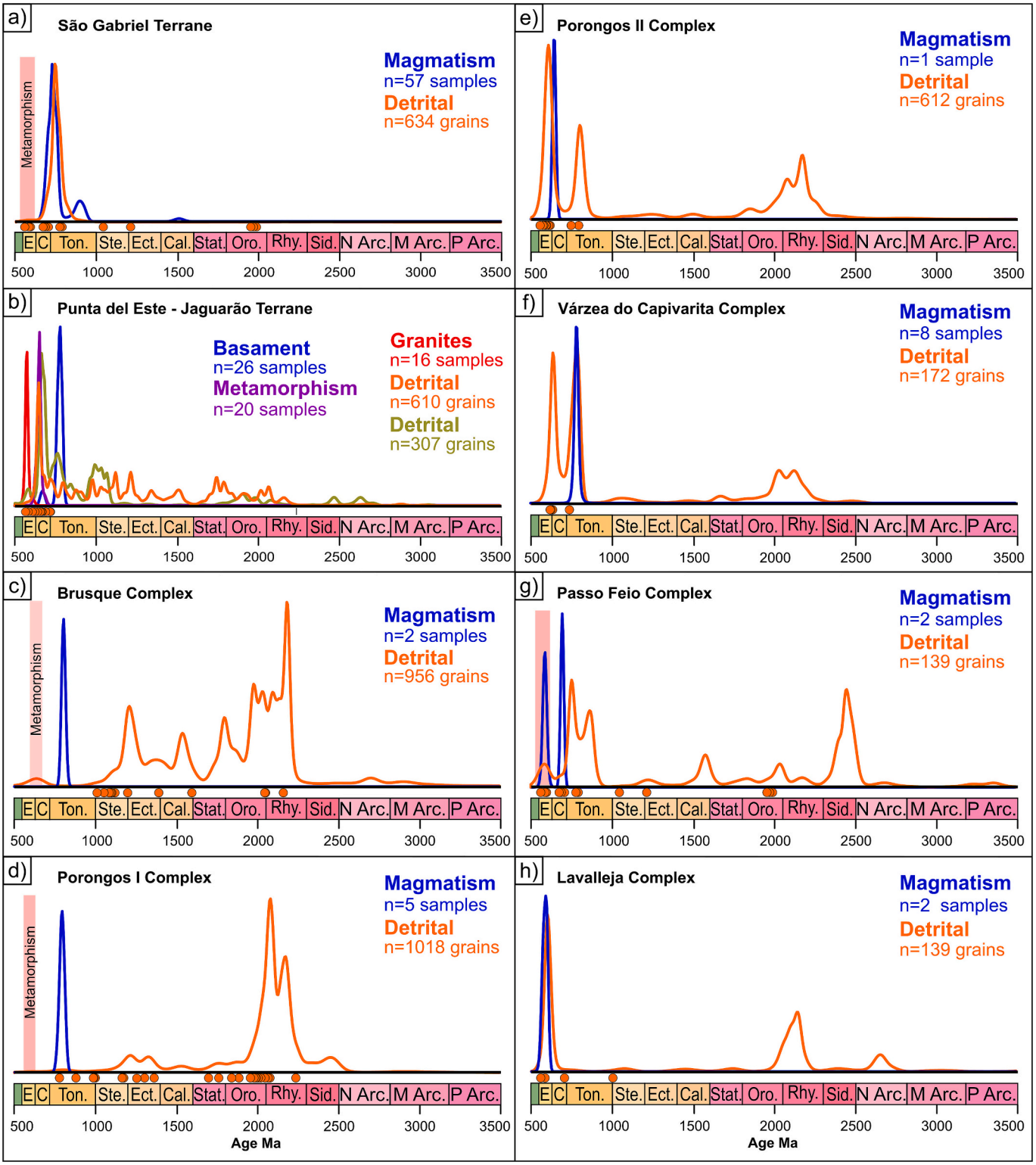

Fig. 13. U-Pb zircon age distribution for a) the juvenile São Gabriel Terrane showing the main accretionary interval ranges between 0.68 and 0.80 Ga and detrital distribution coherent with magmatism; b) the Punta del Este- Jaguarão Terrane showing two main accretionary intervals, one in the Tonian between 800 and 760 Ma and Cryogenian between 680 and 650 Ma; a high-grade metamorphic event between 660 and 640 Ma; two metasedimentary deposits, one in the Cryogenian from 0.7 to 2.2 Ga and other in Ediacaran Rocha Formation at 720–800 Ma and the other at 1000–1200 Ma; c) and d) the Neoproterozoic volcano-sedimentary sequences from the Tijucas Supraterrane. The Brusque Complex (c) and Porongos I (d) correspond to the Tonian metavolcanic and metavolcanoclastic rocks dated between 809 ± 4.1 Ma and 773 ± 3.4 Ma (Pertille et al., 2017) Detrital zircons from the older metasedimentary rocks (interpreted as passive margin deposits; Hartmann et al., 2004) show an age distribution with a dominant peak at 1.9–2.0 Ga and minor Mesoproterozoic peaks; e), f), g), and h), show the histograms of the Ediacaran volcano-sedimentary rocks with maximum depositional ages of 590 Ma and dominant magmatism around 600 Ma.

Calymmian zircon ages. Notably, it lacks significant provenance of Neoproterozoic zircon grain contribution. The Porongos II Complex has a maximum depositional age of ~580 Ma, with its main provenance population at ~600 Ma and two minor peaks at 700–800 Ma and 2.05 to 2.3 Ga (Fig. 13e). The Passo Feio Complex shares a similar detrital zircon provenance and exhibits three main peaks at ~2.4 Ga, two additional peaks at 700–800 Ma, and two minor peaks at ~1.6 and ~ 2.05 Ga (Fig. 13g). The Várzea do Capivarita Complex, covering a small portion of the Encruzilhada Block, shows three main peaks comparable to Porongos II, with the main population at 600 Ma and two additional peaks at 700–800 Ma and 2.05 to 2.3 Ga (Fig. 13f). In the Uruguayan Sheild, the Lavalleja Complex shows a similar pattern with a maximum depositional age at 570 Ma and three main provenance peaks: the most significative with ~600 Ma and two additional peaks at 2.05 to 2.3 Ga and third peaks in the Neo Archean (Fig. 13h).

4.2.3.3. Pelotas-Aiguá-Florianópolis Batholith. The Pelotas-Aiguá-Florianópolis Batholith is characterized by a short-wavelength magnetic signature, resulting in a rough magnetic texture associated with weathering, deformation, and second-order faulting (Fig. 2b and c). The Reduced-to-Pole map reveals small units consisting of magnetic lows with a smooth texture. The batholith is also distinguished by high total radioelement counts, with smaller units ranging with higher concentrations of potassium and thorium (Fig. 2a).

Due to the complex age distribution patterns within the Pelotas-Áigua-Florianópolis Batholiths, the geochronological data are presented according to the areas described in Session 2.6. (Isotope Record). The batholith records five major periods of magmatism age: 680–640 Ma, 640–620 Ma, 620–600 Ma, and 600–580 Ma, with the latter three episodes representing the most extensive magmatic activity in the area (see below in the discussion).

4.2.3.4. Jaguarão-Punta del Este Terrane. In the Uruguayan-Sul-Rio-Grandense and Catarinense Shield, the Jaguarão Complex displays low-amplitude magnetic relief underlain by high-intensity EW-oriented magnetic anomalies (Fig. 2b). This complex is bounded to the west by a pronounced contrast in potassium and thorium concentrations and an intermediate uranium concentration, corresponding to the Ayrosa Galvão Shear Zone (Fig. 2a; NE-SW, Machado et al., 1990; Cruz et al., 2023). This boundary is particularly evident in the vertical derivative of magnetic data, where structural trends shift to an NE orientation. Some narrow NE-oriented regions show high contents of radioelement minerals, resulting in distinctive white zones in the ternary images, coinciding with intermediate magnetic intensities corresponding to late intrusive granites. In the southern portion of the terrane, dike swarms are identified by high-amplitude magnetic anomalies through linear features, indicating elongated and juxtaposed magnetized bodies. These Cretaceous structures extend seaward and represent expressions of the episode of continental break-up (Figs. 2b, c, and 3).

The Punta del Este Complex is partially covered by the Cretaceous volcanic and intrusive rocks of the Laguna Merin Basin, known as the Lascano Complex (Fig. 3; Cernuschi et al., 2015). Due to the geological complexity, this terrane could be divided into two distinct geophysical domains: a high-grade basement represented by the Cerro Olivo Complex and the low-grade metasedimentary Rocha Formation (Abre et al., 2020 and references therein), distinguished by their magnetic signature and the radioelement concentration (Fig. 2a). Silva Lara et al. (2022) and references therein) suggested that this terrane does not belong to the DFB.

The Cerro Olivo Complex is characterized by high potassium and thorium concentrations and exhibits smooth magnetic relief with eastward-decreasing magnetic intensity. Its boundary with the Rocha Formation is marked by a high-gravity anomaly along the Rocha Shear Zone. Several small units, locally curvilinear units with contrasting smooth and low magnetic signatures and variable gamma-ray responses,

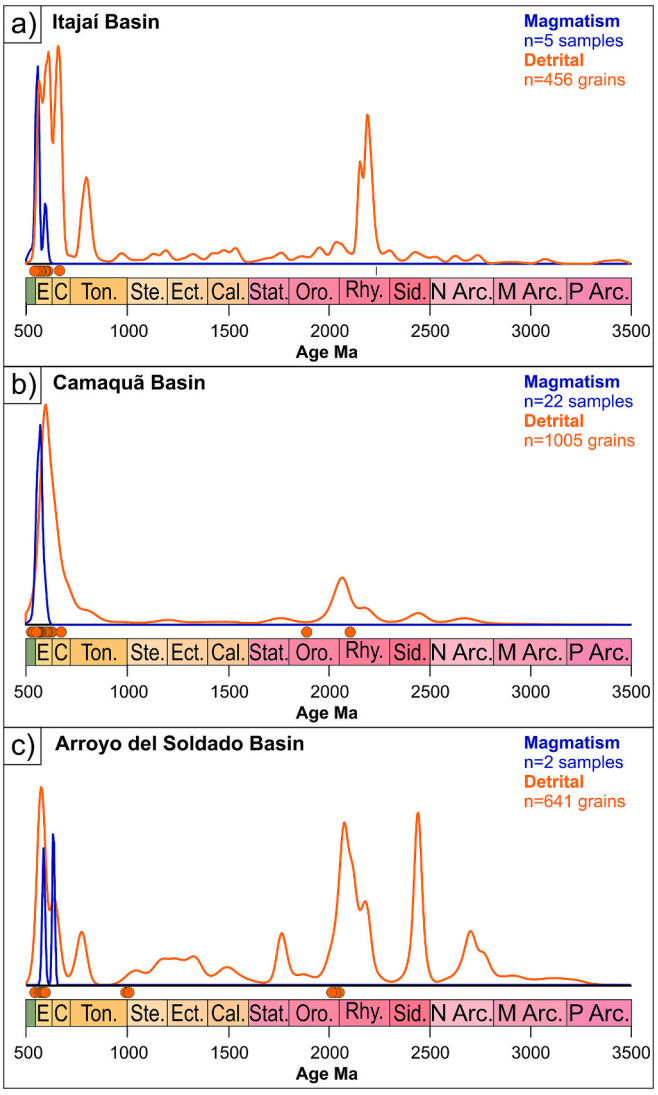

Fig. 14. Age distribution of the plutonic-volcano-sedimentary associations formed during the late to post-orogenic stages of the Dom Feliciano Belt, with deposition between 600 and 500 Ma for: a) Itajaí, b) Camaquã, and c) Arroyo del Soldado basins.

occur within the Cerro Olivo Complex, interpreted as post-tectonic intrusions previously mapped as K-granites by Masquelin (2004). The easternmost Rocha Formation is distinguished by distinctive gamma-ray signatures, notably depleted in thorium concentration and showing low gravity intensity. It exhibits moderate intensity magnetic anomalies with smooth relief and significant magnetic features enhanced in the Vertical Derivative, which enhanced the magnetic source (Fig. 2c).

The Jaguarão-Punta del Este Terrane shows two main magmatism intervals: a Tonian phase at 800 to 760 Ma (Lenz et al., 2011; Will et al., 2019; Lara et al., 2022) and a Cryogenian phase at 680 to 650 Ma (Vieira et al., 2019). A high-grade metamorphic event is registered in the terrane between 660 and 640 Ma (e.g., Lenz et al., 2011). Subsequently, these units were intruded by 580 to 550 Ma granites (Vieira et al., 2016; Will et al., 2019; Will et al., 2023). Associated metasedimentary deposits reflect different tectonic settings. The Cryogenian deposits show a dominant provenance peak at the Cryogenian, with a broad distribution of ages from 0.7 to 2.2 Ga lacking distinct peaks (Fig. 13b). In contrast, the Ediacaran Rocha Formation deposits show a main Cryogenian provenance peak and two major peaks at 720–800 Ma and 1000–1200 Ma, along with a minor Paleoproterozoic and Archean population (Fig. 13b).

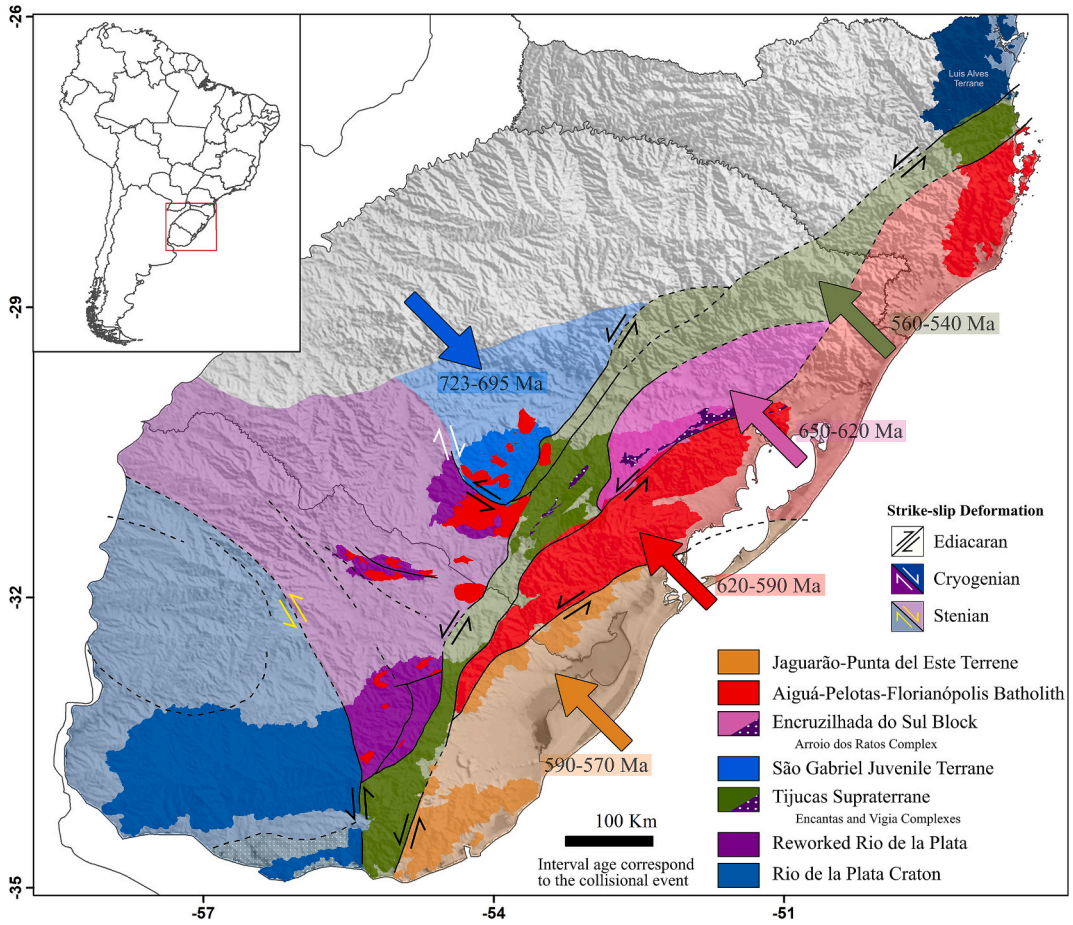

Fig. 15. Main tectonostratigraphic units of the Dom Feliciano Belt and Rio de la Plata Craton in Southern Brazil and Uruguay, showing the accretion events of the distinct terranes. The arrows suggest the main tectonic vergence from NW to SE during the Cryogenian (accretion of the São Gabriel Terrane) and ESE to WNW tectonic transport for the Tijucas supraterrane, Encruzilhada Block, Aiguá-Pelotas-Florianópolis magmatic arc, and Jaguarão-Punta del Este Terrane.

4.2.3.5. Late to post-orogenic sedimentary basins. The final stages of the Brasiliano Cycle were marked by the deposition of volcano-sedimentary sequences within the Itajaí, Camaquã, and Arroyo del Soldado basins. The zircon age provenance diagram indicates that these basins were developed between 600 and 500 Ma (Fig. 14a, b, and c). The Itajaí Basin preserves three distinct provenance peaks: an early Paleoproterozoic peak at 2.3 Ga, a Cryogenian peak at ~700 Ma, and an Ediacaran peak spanning 650–560 Ma (Fig. 14a). The Camaquã Basin has two major main provenance peaks: a Paleoproterozoic population at 2.05–2.2 Ga and a Neoproterozoic population spanning 700–550 Ma (Fig. 14b). The Arroyo del Soldado displays a more complex provenance pattern, comprising three main peaks at 2.4–2.5 Ga, 2.05–2.3 Ga, and 550–650 Ma, and three secondary peaks at ~2.7 Ga, ~1.8 Ga, and ~ 750 Ma (Fig. 14c).

5. Discussion

Numerous tectonic evolution models have been developed for the Uruguayan-Sul-Rio-Grandense and Catarinense Shield, focusing on the Neoproterozoic to Early Paleozoic interval (e.g., Fernandes et al., 1992; Chemale Jr, 2000; Basei et al., 2000; Saalmann et al., 2011; Chemale Jr et al., 2012; Philipp et al., 2016). These models particularly emphasize the correlation of belts across the Atlantic Ocean conjugate margin, attempting to reconstruct the original configuration of southwestern Gondwana around 540 Ma (e.g., Porada, 1979; de Wit et al., 2008; Rapela et al., 2011; Chemale Jr et al., 2012; Basei et al., 2018; Will et al., 2023).

Through integrating geophysical data and comprehensive geological-isotopic analysis, this study has characterized the major tectonostratigraphic units of southern Brazil and Uruguay, spanning from the Precambrian to the Eopaleozoic. These units comprise the Rio de la Plata Craton, which includes the Piedras Altas and Tadilía terranes; the reworked Rio de la Plata Craton, encompassing the Valentines-Rivera-Taquarembó crustal block or Nico Perez Terrane; the São Gabriel Terrane, the Tijucas Supraterrane; the Encruzilhada Block; the Pelotas-Aiguá-Florianópolis Batholith; and the Jaguarão-Punta del Este Terrane (Fig. 15), where it is possible to recognize the main terranes, major lineaments and age of deformation. Fig. 16 presents the major magmatic events and detrital zircon distribution patterns from the Archean to the Stenian. This figure highlights the primary magmatic contributions and orogenic events of the Rio de la Plata Craton (RLPC), its reworked margins, and the basement inliers within the Dom Feliciano Belt (DFB) during the Rhyacian. The geological record suggests a predominantly extensional tectonic environment from the late Paleoproterozoic to the end of the Mesoproterozoic.

Fig. 17 illustrates the major magmatic, sedimentary, and metamorphic events that occurred during the Neoproterozoic, emphasizing the key orogenic phases of the DFB, including the Passinho, São Gabriel, Dom Feliciano, and Jaguarão-Rocha events. Fig. 18 depicts the flare-up and steady-state magmatism of the Dom Feliciano Belt during the Neoproterozoic, considering the age and size of dated magmatic suites and complexes. A detailed overview of metamorphic ages and cooling

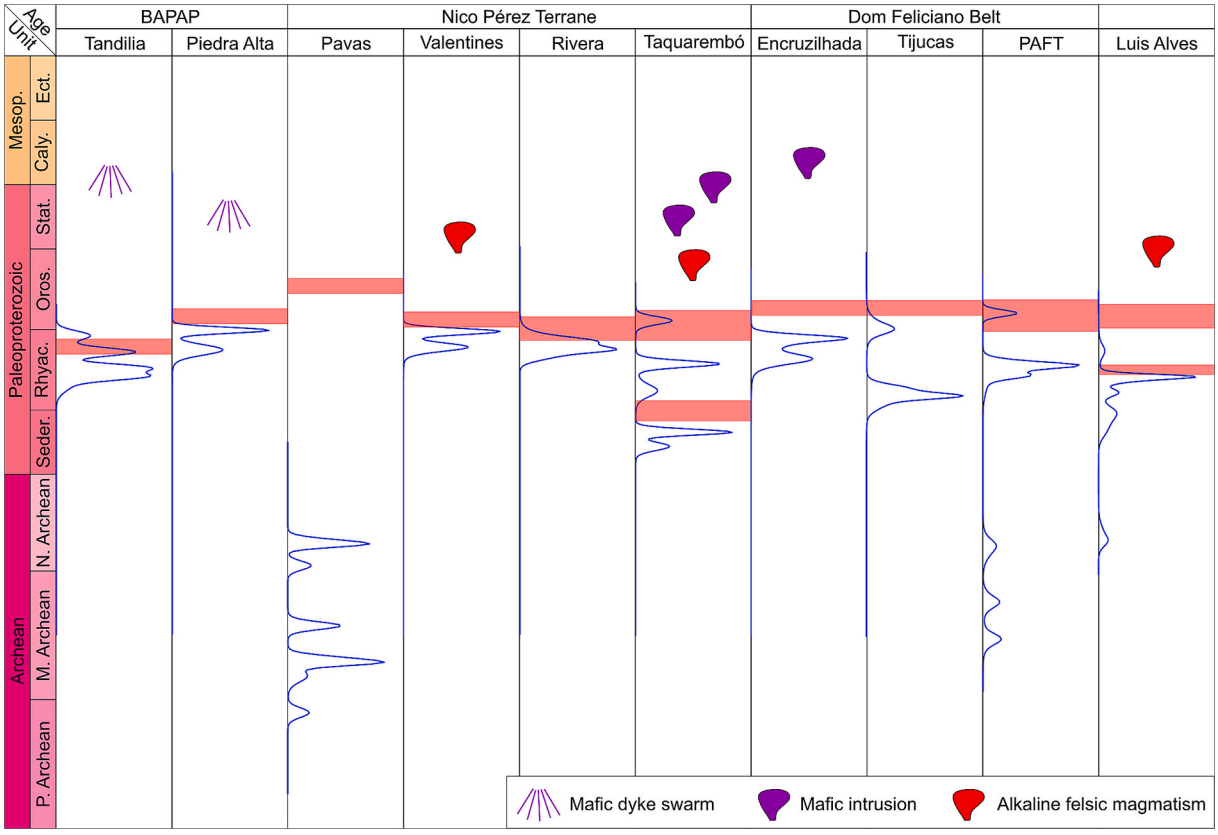

Fig. 16. Distribution of major magmatic events of Archean to Mesoproterozoic rocks in the Rio de la Plata Craton and Dom Feliciano Belt. Red bars correspond to regional metamorphism events. Blue vertical histograms show the age distribution patterns of magmatic zircon from granitic-gneisses rocks (TTGs terranes). (For interpretation of the references to colour in this figure legend, the reader is referred to the web version of this article.)

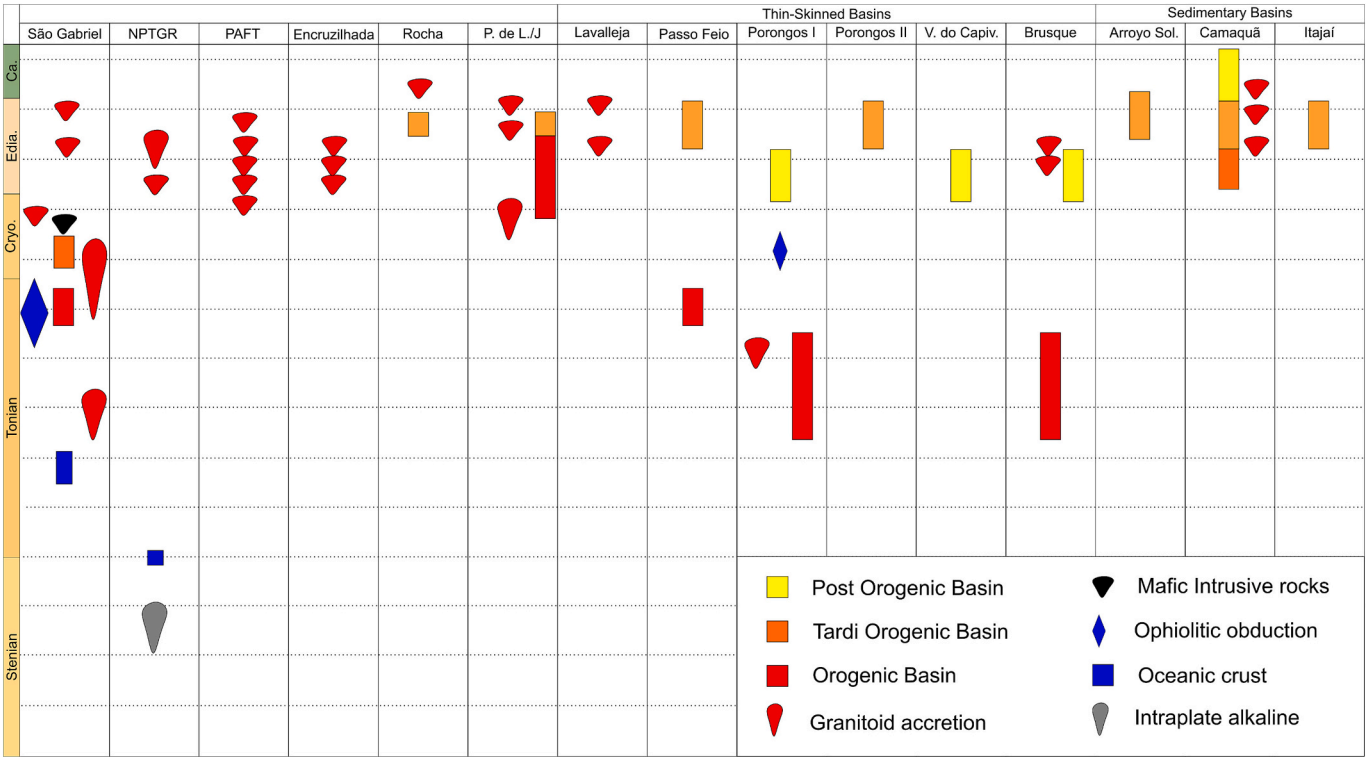

Fig. 17. Schematic chart showing the main magmatic and sedimentary events of the DFB and RLPC during the Neoproterozoic and Eopaleozoic.

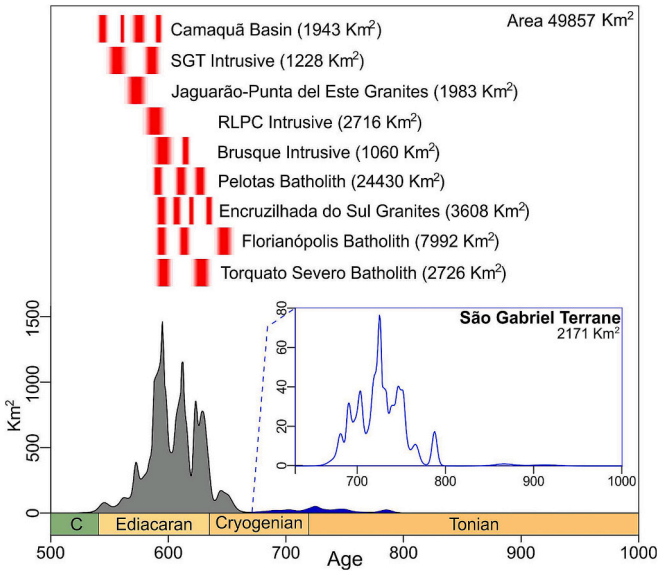

Fig. 18. The age distribution pattern for the subduction-related magmatism in the São Gabriel Terrane (Ediacaran Intrusives within the SGT) and the reworked Rio de la Plata Craton (RLPC) located in the Western Domain of the Uruguayan Sul-Riograndense and Catarinense Shield (USRCS). The granitic intrusion of the Brusque Complex falls within the Central Domain, alongside the Late Cryogenian-Ediacaran terranes, including Florianópolis, Pelotas, and Encruzilhada do Sul, which are situated in the Eastern Domain of the USRCS. Spanning from the Central to the Western domain of the USRCS, the Camaquã Basin is characterized by a volcanosedimentary association. This basin's activity culminates in a peak of flare-up magmatism at 575 Ma (see Section 2.6 for the methodology used to identify age peaks and for additional details). For further information, data, and references, please consult Supplementary Material S2.

processes in the DFB and surrounding areas is provided based on a compilation of published data. This dataset categorizes metamorphic and cooling ages according to temperature ranges: >800 °C, 600–800 °C, 450–600 °C, 350–450 °C, and < 350 °C (Supplementary material SM2).

5.1. *Basement evolution of the Dom Feliciano Belt*

Fig. 16 shows the zircon age distribution patterns for the Tandilia and Piedra terranes (Rio de la Plata Craton) compared to the Nico Pérez Terrane (reworked margin of the Rio de la Plata Craton). These patterns highlight a dominant magmatism (peak at 2.1–2.2 Ga) during the Rhyacian, followed by regional metamorphism at the Rhyacian-Orosirian transition. The Statherian magmatism is characterized by alkaline acid magmas (A-type) and mafic dyke swarms dated to 1.78 Ga and 1.57 Ga. The reworked Rio de la Plata Craton, represented by Nico Pérez Terrane (as discussed by Girelli et al., 2018; Santos et al., 2017, and references therein), exhibits a similar record of Rhyacian magmatism as the main orogenic period, along with comparable metamorphism around 2.05 Ga. The Nico Pérez Terrane also contains records of Archean and Siderian TTGs (Fig. 16). They have a common intense metamorphic event around 2.05 Ga and display a distinctive tectonic fabric compared to units west of the USRCS. The Luis Alves Terrane in the Santa Catarina Shiel exhibits geological and structural patterns like the Nico Perez Terrane (NPT). It is important to note that Oyhantçabal et al. (2011) and Oriolo et al. (2016) proposed that the Nico Pérez Terrane should not be considered part of the Rio de la Plata Craton but is instead likely a crustal fragment of the Congo Craton. They also included the Tijucas units as part of the NPT.

The Rio de La Plata Craton nucleus comprises the Piedra Alta Terrane, bounded east by the Sarandi del Yi Shear Zone. Understanding the western extension of the Piedra Alta Terrane has been challenging due to the overlying Paleozoic Paraná Basin sediments. However, recent U—Pb zircon ages by Girelli et al. (2023) and Peel et al. (2024) have provided new insights into the terrane's continuity beneath the basin, revealing basement rocks with characteristic Piedra Alta Terrane ages of 2.1 Ga. The continuation of the Piedra Alta Terrane and the Sarandi del Yi Shear Zone beneath the basin is further supported by Bouguer anomaly and gravity inversion data, which delineate these structural boundaries in the subsurface.

The eastern segments surrounding the RLPC nuclei have been interpreted as parts of the craton that underwent reworking during subsequent geological events, primarily modified during the Brasiliano Orogeny (Girelli et al., 2018). Based on integrated geological, geochronological, and geophysical data, we restrict the Nico Perez Terrane to its original definition by Bossi and Campal (1992), including the Taquarembó Block, Valentines and Rivera, Illescas, as proposed by Rapela et al. (2011). The alternative definition of the Nico Perez Terrane, which includes also the Lavelleja Complex, Campanero Batholith, and Tapes Complex units between the Sarandi del Yi and the Sierra Ballena Shear Zones (e.g., Bossi et al., 1998; Mallmann et al., 2007; Oyhantçabal et al., 2010; Oriolo et al. 2016). This is necessary as geological and geophysical data show distinctive characteristics between these domains. Our study, supported by terrane definitions (Sensu Coney et al., 1980) and geophysical mapping, demonstrates that the Tijucas Supraterrane displays characteristics distinct from the NPT, particularly in its consistent NE-SW trending structures (see geological and geophysical maps in Figs. 7 and 9). Specifically: (i) The NE-SW trending structures of the Tijucas Supraterrane, which include the Lavalleja, Campanero, and Tapes complexes, are located east of the Valentines and Pavas units in Uruguay (Fig. 7), and (ii) the NE-SW trending structures of the Tijucas units that are to east of the SGT and the Taquarembó Block in Rio Grande do Sul. (iii) Additionally, as seen in Figs. 7 and 9, it is noteworthy that the NPT units exhibit a more complex structural arrangement characterized by polyphasic deformation with distinct orientations.

A key question regarding understanding RLPC evolution remains the Sarandi del Yi Shear Zone, which represents a fundamental boundary between the Piedra Alta Terrane and the Nico Perez Terrane (NPT). This shear zone preserves evidence of two major tectonic episodes: dextral and sinistral strike-slip movements. Understanding the tectonic activity associated with this deep structure is crucial for comprehending the geological evolution. Integrated structural and geochronological studies using U—Pb dating of rutile and titanite, Ar/Ar in muscovite, and Rb—Sr whole-rock-muscovite along with Sarandi de Yi Shear Zone (Oriolo et al., 2015, 2016a) indicate that the later sinistral strike-slip movements occurred between 600 and 570 Ma (or even 623 to 566 Ma, see further discussion) under amphibolite to greenschist metamorphic facies conditions (650 to 350 °C, Oriolo et al., 2016a). This supports a progressive deformation event during the Brasiliano orogeny. The deflection of the 1.78 Ga dyke swarm in the Piedra Alta Terrane (Fig. 3) may indicate earlier movement, but the definitive timing of this initial deformation remains under discussion.

Oyhantçabal et al. (2011) and Oriolo et al. (2016a) proposed that a 623 ± 5.1 Ma *syn*- to early post-collisional granite dates the dextral displacement of the Sarandi del Yi Lineament. They also documented a structural fabric as ductile dextral shearing (450–500 °C). The structural analysis and radiometric dating provided by these authors suggest that dextral ductile shearing occurred during the Ediacaran period. Conversely, other studies, such as Bossi and Cingolani (2009) and Gaucher et al. (2011), suggested a Mesoproterozoic age for the dextral movement based on a $^{40}Ar—^{39}Ar$ age of 1240 ± 5 Ma (resulting from the thermal overprinting of deformed mafic dikes; Bossi and Navarro, 2001) and K—Ar ages of 1253 ± 32 for syn-kinematic muscovite along the Zapican Thrust in the Nico Perez Terrane (Bossi and Cingolani, 2009). The NPT also records Late Mesoproterozoic intracontinental events (Stenian) in deformed metacarbonatites (Monteiro et al., 2020) and

U—Pb sphene age (Girelli et al., 2018) from Paleoproterozoic granulites of the Taquerembó crustal block (Fig. 6d), yielding ages of 1110 ± 4.8 Ma and 1001 ± 9.9 Ga, respectively.

The present results suggest that the NPT represents a Paleoproterozoic Terrane that underwent main deformation at 2.05 Ga and was allochthonous relative to the Piedra Alta Terrane. While the terrane underwent intracratonic deformation between 1.2 and 1.0 Ga, preceding the rifting process that led to the formation of the Charrua Ocean, the timing of juxtaposition between the NPT and PAT remains debated. Subsequently, during the Neoproterozoic to Eopaleozoic, this terrane underwent multiple reactivations, primarily associated with the collision of three paleoplates: Rio de la Plata, Kahalari, and Congo-São Francisco.

5.2. Rifting-Drifting of the São Gabriel Terrane (Charrua Ocean)

Studies conducted by Girelli et al. (2018) and Monteiro et al. (2020) have documented a rifting event along the reworked margin of the Rio de La Plata Craton, constrained by 1110 ± 4.8 Ma carbonatites and 1018 ± 9.9 Ma titanite ages from the Santa Maria Chico Granulitic Complex, marking the initiation of carbonatite magmatism within the NPT in the Taquarembó region. This rifting and subsequent drift extended into the early Neoproterozoic, leading to the formation of the Charrua Ocean in the present-day São Gabriel region. The remnants of this oceanic period include the mafic-ultramafic complexes of Cerro Mantiqueira (923.2 ± 3 Ma; Arena et al., 2016); Palma (922 ± 3 Ma; Arena et al., 2017); Bossoroca (920.4 ± 9.8 Ma; Hartmann et al., 2019); Cambaizinho (923 ± 3.1, Cerva-Alves et al., 2020); and Ibaré (892.4 ± 2.8 Ma; Arena et al., 2016).

These mafic-ultramafic complexes exhibit a mid-ocean ridge basalt (MORB) geochemical signature, representing oceanic crust generation following Mesoproterozoic fragmentation between 1.1 and 1.0 Ga. The oceanic generation process (associated with the Charrua or extension of the Adamastor Ocean) occurred between 922 and 892 Ma (Leite et al., 1998; Arena et al., 2016, 2017; Hartmann et al., 2019; Cerva-Alves et al., 2020; Werle et al., 2020).

Contemporaneous, passive margin sediments were deposited in the São Gabriel and Tijucas Supraterrane, represented by the Cerro Batovi, Marmeleiro, Passo Feio I, and Porongos metamorphic sequences (Gruber et al., 2011; de Lena et al., 2014; Pertille et al., 2015; Philipp et al., 2021). These units show predominant detrital contributions from Neoarchean, Rhyacian, and Sthaterian rocks of the Rio de la Plata Craton.

5.3. Active margin record of the São Gabriel Terrane

The São Gabriel Terrane is characterized by juvenile magmatism, including mafic-ultramafic complexes (ophiolitic bodies), granite-gneissic and amphibolite assemblages associated with calc-alkaline and tholeiitic volcano-sedimentary sequences formed in a subduction zone. Mafic-ultramafic complexes dated between 923 Ma and 892 Ma were obducted onto the continental crust at 726 ± 2 Ma and 722 ± 3 Ma (Cambaizinho Ophiolite; Cerva-Alves et al., 2020), forming ophiolites within the São Gabriel Terrane during the São Gabriel Orogeny (760–680 Ma), as documented by Chemale Jr et al. (1995) and Hartmann et al. (2000). In contrast, the granite-gneissic and amphibolite assemblages, along with the volcano-sedimentary sequences, preserve geochemical and isotopic signatures characteristic of an island arc and continental magmatic arc setting within the Brazilian Precambrian framework (e.g., Babinski et al., 1996; Hartmann et al., 2011; de Lena et al., 2014; Arena et al., 2016). Chemale Jr (2000) interpreted these features as typical signatures of a juvenile accretionary prism.

Geochronological data reveal two major magmatic events: Juvenile Arc I (Passinho Event; Leite et al., 1998) and Juvenile Arc II (São Gabriel Event; Chemale Jr et al., 1995), as can be observed in Figs. 17 and 18). These events (Fig. 18) alternated between periods of magmatic quiescence (steady-state) and intense magmatic activity (flare-ups), like patterns observed in Mesozoic-Cenozoic orogenic belts (de Silva et al., 2015; Ducea et al., 2015). During the island arc stage (Juvenile Arc I), two major magmatic pulses occurred at 880 Ma and 790 Ma. In the subsequent accretionary phase (Juvenile Arc II), the São Gabriel Terrane Event, between 770 Ma and 680 Ma, with at least three flare-up periods, peaked between 760 and 750 Ma (Fig. 18, inset). The Passinho Event corresponds to the D1 deformation phase, as described by Saalmann et al. (2006), and is recorded by metasomatic zircon and rutile ages of 780 ± 5 Ma to 786 ± 13 Ma (Arena et al., 2017; Cerva-Alves et al., 2020). These ages likely represent peak island arc magmatism, associated with the TTG suites of the Passinho and Ibicuí complexes, ranging from 879 ± 14 Ma (Leite et al., 1998) to 845 ± 5 Ma and 828 ± 8 Ma (Siviero et al., 2022), extending up to 780 Ma. The structural analysis by Saalmann et al. (2006), integrated with magnetometric lineament interpretations (Fig. 3), indicates that the ductile phase associated with the primary accretion of the São Gabriel Terrane involved northwest-to-southeast-directed mass transport, controlled by the N70°W-S70°E-trending Ibaré Shear Zone. This structure, exhibiting dextral kinematics, dates to the Late Tonian (760–740 Ma), constraining the post-deformation cooling to approximately 400–425 °C (Hueck et al., 2020). Contemporaneous NE-SW-trending thrust and folding systems developed with southeastward vergence. The final collision resulted in NE-SE-oriented structures with dextral kinematics, interpreted as the collision between the São Gabriel Terrane and the Tijucas Supraterrane. Magmatic activity in the Porongos I and Brusque volcano-sedimentary complexes peaked at 780–760 Ma, coinciding with the major Juvenile Arc II magmatism period (Fig. 15).

The Ibaré Shear Zone functioned as a transfer fault during the early development of the Charrua Ocean. The Três Estradas Alkaline Complex intruded the Paleoproterozoic basement at 1.1 Ga and was subsequently deformed at 1.01 Ga during initial rifting. This structure acted as a transfer fault during peak rifting (1.0–0.92 Ga), facilitating passive margin sedimentation. These deposits are now preserved as the Cerro Batovi, Marmeleiro, Passo Feio I, and Porongos metamorphic sequences characterized by a detrital zircon age pattern of passive margin sedimentary association with peaks at Neoarchean, Rhyacian, and Statherian besides some subordinate Neoproterozoic contribution (Pertille et al., 2015; Philipp et al., 2021).

The second accretionary event, the São Gabriel Event, is represented by the two deformation phases (D2 and D3; Saalmann et al., 2006). The first deformation event (D2) is associated with ductile lineaments along the Ibaré Shear Zone, dated by K—Ar muscovite ages ranging from 757 ± 14 Ma to 743 ± 10.2 Ma (Hueck et al., 2020). This phase also includes the obduction of the Ibaré Ophiolite at 758 ± 4 Ma (Arena et al., 2017). The D2 event involved the obduction of the Bossoroca, Palma, and Ibaré ophiolites between 726 ± 2 Ma and 722 ± 3 Ma, associated with NE-SW striking thrusts and NW-SE-directed vergence, marking the closure of the Charrua Ocean and the development of orogenic basins and a continental magmatic arc TTG. These structures are evident in magnetic anomaly maps (Fig. 12d and e), which show dextral displacement of the Ibaré Shear Zone at approximately 780 Ma, 750 Ma, and 722 Ma. Thus, the NE-SW striking thrusts exhibit SE-directed vergence, acting as tear faults.

The D3 deformation phase (Saalmann et al., 2006) occurred during the transpressional collision between the São Gabriel Terrane and the Encantadas Block. NE-SW thrusting indicates plate consumption by eastward subduction beneath the Encantadas Block. This phase culminated in a continental collision, marked by the emplacement of the Sanga do Jobim Granite during dextral strike-slip motion at 690 ± 2 Ma (Remus et al., 2000). Saalmann et al. (2006) described SE-vergent oblique thrust stacks transitioning into a flower structure.

Later, post-tectonic intrusions at 682 ± 2 Ma (diorites and granodiorites; Hartmann et al., 2011) and the Mata Grande stratiform gabbro at 668 ± 3 Ma (Simões, 2014) represent the final magmatic pulses. A muscovite K—Ar age of 662.7 ± 7.1 Ma from metapelite in the Ibaré Shear Zone may record the last dextral movement associated with the

São Gabriel Event (Hueck et al., 2020).

5.4. Magmatic late Cryogenian-Ediacaran Magmatic Arc

Differing from the São Gabriel Terrane (SGT), the eastern Dom Feliciano Belt Magmatic Arc initially underwent west vergent to northwest vergent deformation (Fig. 15) that later transitioned to sinistral strike-slip tectonics (Fernandes et al., 1992). This magmatic arc includes accretion of three distinct terranes, arranged east to west: the Punta del Este Terrane, with primary magmatism between 580 and 540 Ma; the Pelotas-Aiguá-Florianópolis Batholith, with main magmatism between 640 and 600 Ma; and the Encruzilhada do Sul Block, with its main magmatic peak between 680 and 640 Ma (Fig. 15).

These terranes resulted from a collisional process during the westward subduction of the Kalahari Plate (lower plate) beneath the Rio de la Plata Craton (upper plate). Recent studies by Takehara and Laux (2019), de Toni et al. (2020b), Silva Lara et al. (2022), and Will et al. (2023) have revisited the geochemical signature of this magmatism, identifying a predominance of calc-alkaline to potassic calc-alkaline magmatism with subduction processes and significant crustal contamination (Babinski et al., 1997; Will et al., 2023).

Caxito et al. (2022) have reinterpreted the Ediacaran magmatism of the Mantiqueira Province, including the USRCS, as components of a magmatic arc associated with the Adamastor Ocean closure during the amalgamation of the Rio de la Plata, Congo-São Francisco, and Kalahari cratons. However, specific petrotectonic features of subduction zones, including accretionary prisms, juvenile arcs, ophiolitic slabs, and other elements typical of complete orogenic belts (such as the Himalayas and the Urals), remain unidentified. These features are likely situated beneath the Pelotas-Punta del Este-Orange-Lüderitz-Walvis conjugate passive margin basins, represented by a stretched continental crust forming the basement of the Atlantic Ocean continental platforms (Teixeira et al., 2025).

Each terrane records distinctive *syn*-collisional granitic magmatism: Punta del Este-Jaguarão Terrane at 570 Ma, the Pelotas Batholith at 590–600 Ma, and Encruzilhada do Sul Block at 650–640 Ma (Fig. 15). These events reflect progressive terrane accretion from west to east, driven by westward Kalahari Plate subduction. Significant magmatic flare-up episodes occurred at 650–640 Ma, 630–620 Ma, 600–590 Ma, and 580–570 Ma, potentially reflecting increased westward-moving Kalahari Plate subduction rates (Fig. 16). Similar magmatism in the western USRCS domain may indicate a Kalahari Plate slab break-off and subsequent intracontinental (retro-arc) magmatism activity. Within the more stable USRCS domain during the Ediacaran, coinciding with major magmatic flare-up or bloom episodes.

5.5. Tijucas fold-and-thrust belt

The Tijucas Supraterrane preserves extensive evidence of late-stage westward tectonic deformation, characterized by thrust-fold systems affecting Neoproterozoic volcano-sedimentary sequences (Fig. 13). This deformation has been detailed in the Lavelleja Complex by Mallmann et al. (2007), the Porongos I Complex by Battisti et al. (2018), and the Brusque Complex by de Toni et al. (2020a). The overthrusting of high-grade Várzea do Capivarita Gneiss (infrastructure, granulite to upper amphibolite facies) onto the lower-grade Porongos Complex (supra-structure, greenschist to lower amphibolite facies) is evident. Battisti et al. (2018) identified a deformational age of 578 Ma for this event due to the reworking of earlier structures in the Várzea do Capivarita Complex, previously dated by Martil et al. (2017) at 650 Ma.

The Tijucas Supraterrane also records in the Porongos Complex in the Capané region deformation and metamorphism between 550 and 540 Ma, contrasting with the rest of the USRCS (Philipp et al., 2016; Zvirtes et al., 2017; Höfig et al., 2018). The final stages of ductile deformation in the DFB are dated by fine white mica/illite fractions from mylonites of the Dorsal de Canguçu Shear Zone and of the Tijucas Supraterrane, yielding ages from 525 to 470 Ma. These ages are slightly younger than the ca. 540–530 Ma Ar/Ar ages from coarse-grained biotite (closure temperature ca. 310 °C, Harrison et al., 1985) from an internal shear zone of the Pelotas Batholith (Philipp et al., 2003), consistent with the epizone conditions (ca. 300 °C) indicated by illite crystallinity of the dated samples (K/Ar and Ar/Ar in muscovite and biotite). Three new K—Ar ages from metamorphic muscovite in mylonites and metasedimentary rocks associated with the regional foliation (SR) along the shear zone yielded Ediacaran ages between 564 ± 4.1 Ma and 553 ± 17 Ma, establishing a lower limit for post-deformation cooling (ca. 400–425 °C, Harrison, 2009; Oriolo et al., 2018) following the onset of the structure as a terrane boundary.

Following its establishment as a terrane boundary, the Ibaré Shear Zone was reactivated under lower-temperature conditions (see supplementary metamorphic chart Fig. S2, supplementary material S1). A K—Ar age of 662.7 ± 7.1 Ma (Hueck et al., 2020) sets an upper age limit for this event, likely reflecting a mixed age resulting from partial resetting of the K—Ar system during shear-assisted muscovite recrystallization throughout the Dom Feliciano Belt development, or lower limit of dextral ductile shearing of the IBSZ as can be observed in Fig. 4d (First Vertical Derivative map) those bent regional structures (NE-SW trending) of the São Gabriel Event connected to this Shear Zone. The ductile to brittle deformation of the IBS took place during the late Ediacaran and was marked by a left-handed (sinistral) displacement. This reverse movement results from the collision of those terranes located east of São Gabriel Terrane, such as the Pelotas Batholith, Jaguarão-Punta del Este Terrane, and the Tijucas Thrust and Fold Belt. The lower age limits of the sinistral displacement are constrained by fine-grained white mica/illite crystals from localized mylonitic bands, yielding ages of 581.1 ± 6.3 Ma, 567 ± 4.9, 561.6 ± 7.2, and 560 ± 7.3 (Hueck et al., 2020). The illite crystallinity index suggests formation temperatures at the epizone-anchizone transition (~ 300 °C), consistent with microstructural evidence showing temperatures close to the ductile to britle deformation, as discussed by Hueck et al. (2020).

5.6. Late Stages of the Volcano-Sedimentary Basins and Coeval Plutonism

The evolution of late to post-orogenic basins progressed from foreland retroarc through strike-slip to orogenetic collapse basins, coincident with the collision of the Kalahari, Rio de La Plata, and Congo cratons during the final tectonic stages of the Brasiliano Cycle in the Dom Feliciano Belt (e.g., Blanco et al., 2009; Guadagnin et al., 2010; de Oliveira et al., 2014; Becker-Kerber et al., 2020).

The evolution of these basins progressed through three distinct phases: (1) Retroarc Foreland Basin Phase (Late Cryogenian to Early Ediacaran) is characterized by the development of the Camaquã Basin, with its basal sequence of alluvial-fluvial-deltaic marine deposits (Paim et al., 2000), along with the Itajaí Basin (Guadagnin et al., 2010), and the Arroyo Soldado Basin (Gaucher et al., 2009; Blanco et al., 2009); (2) the Ediacaran Strike-Slip Basin Phase, marked by the development of transtensional basins along crustal-scale shear zones (Fig. 26), accompanied by extensive plutono-volcanic activity. This activity included the emplacement of several major plutonic bodies like the Lavras Batholith (600–592 Ma, Leite et al., 1998), Caçapava Batholith (560–540 Ma, Remus et al., 2000), São Sepé Granite (550–558 Ma, Remus et al., 2000), and Jaguari Batholith (572 Ma, Gastal and Lafon, 1998) - along with significant volcanic episodes, including shoshonitic volcanism represented by the Hilário andesites (592–580 (Ma; Almeida et al., 2012; Janikian et al., 2012) and alkaline acid volcanism of the Acampamento Velho Formation (574–550 Ma; Sommer et al., 2005; Chemale Jr, 2000; Janikian et al., 2012) (574–550 Ma; Sommer et al., 2005; Chemale Jr, 2000; Janikian et al., 2012); (3) The final Orogenetic Collapse Phase is represented by the continental arid deposits of the Guaritas Subbasin (540–500 Ma) within the Camaquã Basin and the terminal granitic magmatism (530–540 Ma) in the Punta del Este-Jaguarão Terrane, Aiguá Batholith, and Tijucas Supraterrane (Will et al., 2023).

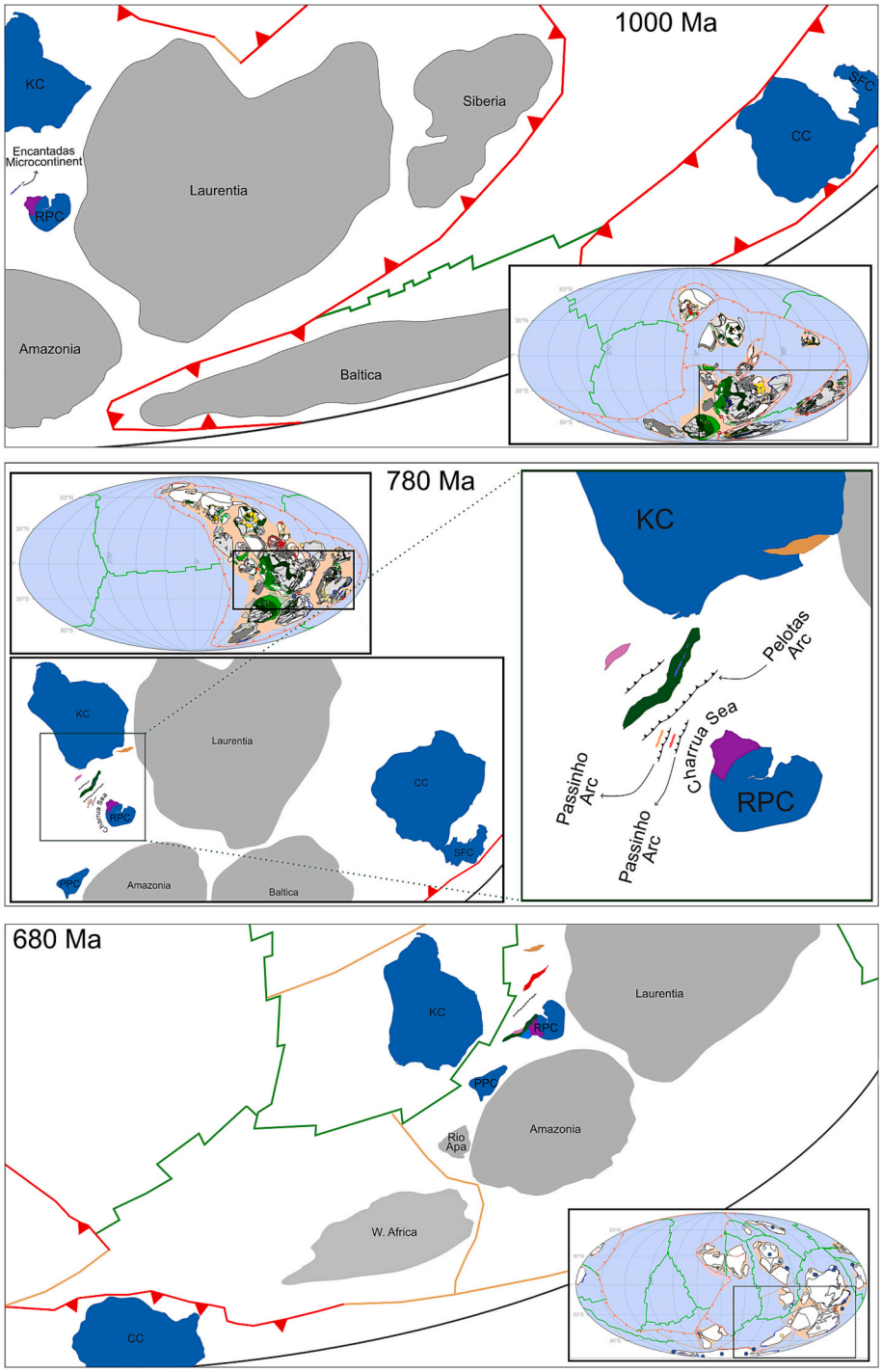

Fig. 19. Paleogeographic reconstruction of West Gondwana from 1000 to 680 Ma, based on Li et al. (2023), showing the assembly of West Gondwana during this period.

5.7. Paleogeographic reconstruction of the Rio de la Plata Craton and the Amalgamation of the Dom Feliciano Belt

Paleomagnetic constraints from the Río de la Plata craton (RLPC) are constrained to three-time intervals (Rapalini et al., 2021): (1) the Rhyacian (2.11–2.05 Ga; Rapalini et al., 2015; Franceschinis et al., 2019); (2) the Statherian (1790 Ma, Florida tholeitic dyke swarm, the Piedra Alta terrane; Teixeira et al., 2013); and (3) the Ediacaran (coeval with Gondwana assembly; Rapalini et al., 2013, 2015). This limited paleomagnetic record creates substantial uncertainty in reconstructing the Dom Feliciano Belt and the Rio de la Plata craton evolution between 1790 and 575 Ma. Recent paleomagnetic investigations by Franceschinis et al. (2022) of Neoproterozoic sedimentary cover in the Tandilia region on the Rio de la Plata granite-gneiss rock suggest that the RLPC remained independent from other Gondwana cratons until approximately 600 Ma.

The paleogeographic position of the RLPC during the Neoproterozoic remains a subject of ongoing debate. While Li et al. (2023) proposed a paleogeographic reconstruction for this period, their model presents several limitations that warrant critical examination. Notably, their reconstruction does not adequately address the compelling evidence for an active continental margin along the RLPC during the 820–690 Ma

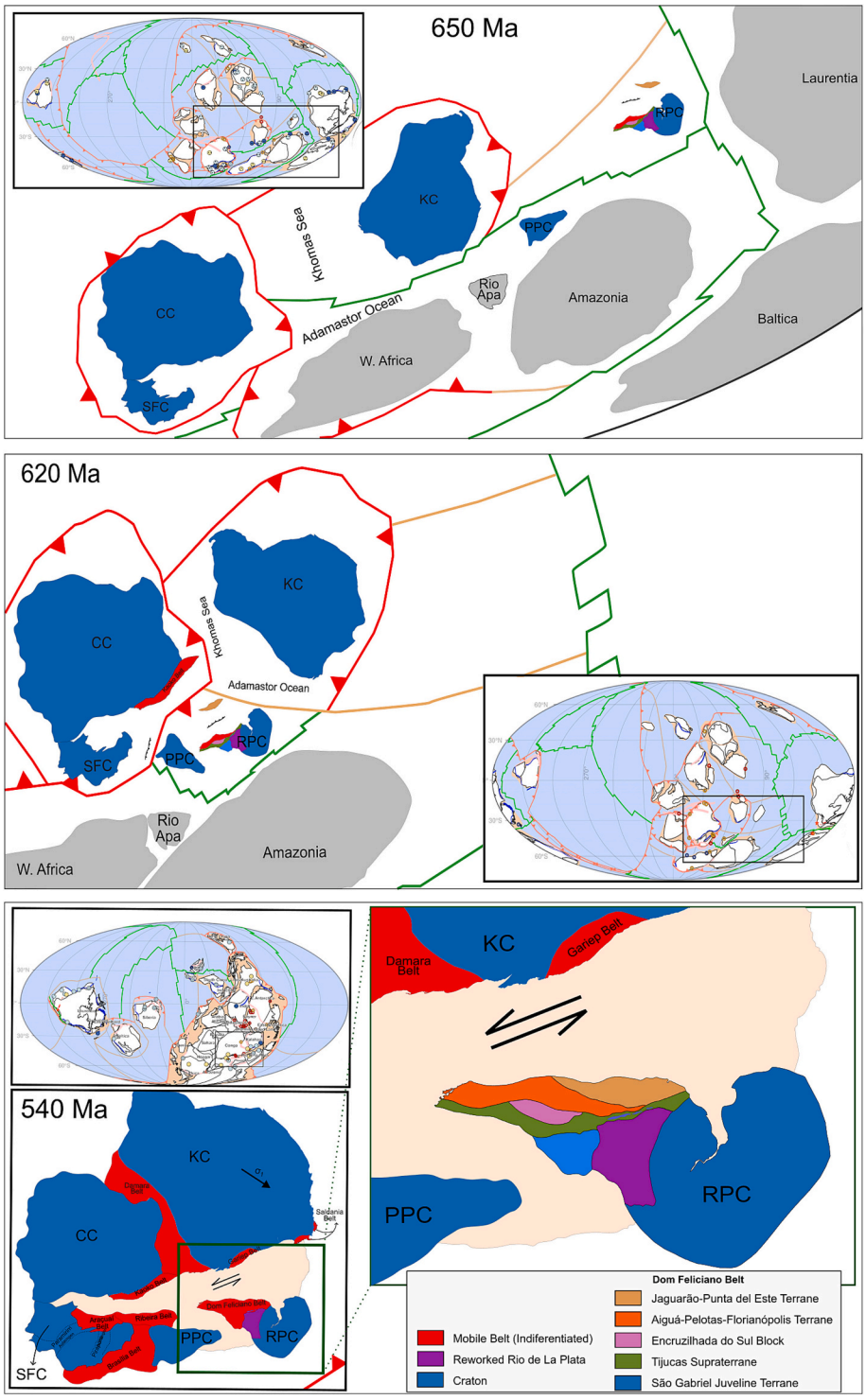

Fig. 20. Paleogeographic reconstruction of West Gondwana from 650 to 540 Ma, based on Li et al. (2023). The rose-colored region in the 540 Ma frame represents the unknown crust of the Pan African-Brasiliano Belts. Labels indicate Neoproterozoic terranes that accreted to the Rio de la Plata Craton (RLPC). (For interpretation of the references to colour in this figure legend, the reader is referred to the web version of this article.)

interval, as documented through multiple geological and geochemical indicators in this study.

An alternative reconstruction based on Li et al. (2023; Figs. 19 and 20) is here presented taking account the subduction of the RLPC that is not included in that model. So, the RLPC was positioned in proximity to Laurentia during the late Mesoproterozoic (ca. 1.1–1.0 Ga), acting as a rifted margin (Hartmann et al., 2019), followed by rifting that led to the Charrua Ocean, characterized by significant oceanic crust generation, as evidenced by ophiolitic sequences and associated marine sedimentary deposits preserved in the region. The subsequent development of an island arc (820–690 Ma) witnessed progressive evolution to a continental magmatic arc, culminating in a collision between the RLPC and Encantadas Microcontinent (basement of the Porongos Complex), as depicted in paleogeographic reconstructions at 780 Ma and 690 Ma (Fig. 19). The eastward subduction is evidenced by NW-SE vergent tectonics and contrasting isotopic signatures between the São Gabriel

Terrane (positive εNd and εHf; Babinski et al., 1997; Chemale Jr, 2000; Saalmann et al., 2005; de Lena et al., 2014; Arena et al., 2016) and the Tijucas Supraterrane Tonian volcano-sedimentary sequences, which show Paleoproterozoic crustal signatures (negative εNd; Chemale Jr, 2000; Saalmann et al., 2007). A rifting process was initiated in the Kalahari and Congo-São Francisco paleoplates during the Cryogenian, resulting in a passive margin development by 680 Ma by establishing the Adamastor Ocean. Subsequently, terrane accretion occurred between 650 and 540 Ma through westward subduction of the Kalahari plate beneath the Rio de la Plata paleoplate (Figs. 19 and 20).

6. Conclusion

Integrating geophysical and geological datasets has provided a comprehensive reassessment of the Dom Feliciano Belt and adjacent regions. Through extensive geochronological compilation and multi-method geophysical analysis, we have enhanced the resolution of individual units and refined the tectonostratigraphic framework of the Uruguayan-Sul-Rio-Grandense and Catarinense Shield.

Our analysis reveals a complex cratonic architecture where the Rio de La Plata Domain is subdivided into the Piedra Alta and Tandilia terranes, comprising Uruguayan and Argentinian domains. In its turns, the Luis Alves Terrane represents a cratonic fragment along the northern Dom Feliciano Belt. Significantly, we have redefined the Nico Perez Terrane as a reworked Rio de la Plata Craton margin, explicitly excluding Uruguayan Tijucas units from its composition.

A final Mesoproterozoic rift-drift phase led to the formation of the Charrua Ocean, which, during a convergent stage in the Tonian period, resulted in the creation of the São Gabriel Terrane's ophiolitic sequences and arc-related igneous and sedimentary rocks. Geophysical data have played a crucial role in the precise terrane boundaries along the Ibaré Shear Zone and in defining NW to SE tectonic transport of the São Gabriel Terrane with lateral juxtaposition against the Nico Perez Terrane.

Detrital zircon analysis has enabled chronostratigraphic subdivision of the schist belt domain into Tonian (Brusque and Porongos I complexes) and Cryogenian-Ediacaran (Porongos II, Várzea do Capivarita, Passo Feio, and Lavalleja complexes) sequences. Geophysical evidence supports their thin-skinned tectonic character, while structural data indicate ESE to WNW tectonic transport, correlating with Ediacaran terranes such as the Pelotas-Aiguá-Florianópolis Batholith and Punta del Este-Jaguarão Terrane.

Novel analysis of U—Pb magmatic data distribution across batholiths, stocks, volcanic bodies, and deposits has revealed distinct magmatic flare-up events punctuated by periods of quiescence throughout the Neoproterozoic. Three major Ediacaran flare-up phases mark the Brasiliano-Pan African cycle within the Dom Feliciano Belt. This integrated approach has significantly advanced our understanding of the belt's evolution, providing a robust framework for future investigations.

Declaration of competing interest

The authors declare that they have no known competing financial interests or personal relationships that could have appeared to influence the work reported in this paper.

Acknowledgments

This study was supported by the UNISINOS-PETROBRAS and UNISINOS-CNODC Cooperation Agreements. We also thank the Brazilian National Agency of Petroleum, Natural Gas and Biofuels (ANP), National Administration of Fuels, Alcohols and Portland (ANCAP), and the Geological Survey of Brazil (SBG-CPRM) for providing data access. We thank Seequent for their technical support with the OASIS Montaj and VOXI software packages. We extend our sincere gratitude to the anonymous reviewer and Dr. Sebastián Oriolo for their valuable comments and suggestions that significantly improved the manuscript. We also thank the Editor, Dr. Eugenio Aragon, for his guidance throughout the review process. FCJ acknowledges the Brazilian National Council for Scientific and Technological Development (CNPq, Brazil) for grants #301441/2019-7 and 408194/2021-9.

Appendix A. Supplementary data

Supplementary data to this article can be found online at https://doi.org/10.1016/j.earscirev.2025.105135.

Data availability

Data will be made available on request.

References

Abramson, I.S., 1984. Adaptive density flattening-a metric distortion principle for combating bias in nearest neighbor methods. Ann. Stat. 12, 880–886.
Abre, P., Blanco, G., Gaucher, C., Frei, D., Frei, R., 2020. Provenance of the late Ediacaran Rocha Formation, Cuchilla Dionisio Terrane, Uruguay: Tectonic implications on the assembly of Gondwana. Precambrian Res. 342, 105704.
Almeida, D.D.P.M.D., Chemale Jr., F., Machado, A., 2012. Late to post-orogenic Brasiliano-Pan-African volcano-sedimentary basins in the Dom Feliciano Belt, southernmost Brazil. In: Petrology–New Perspectives and Applications, 5, pp. 73–105.
Angeletti, M., Chichorro, M., Castro, A., Frisicale, M.C., Solá, R., Dimieri, L.V., 2021. New geochemical, U–Pb SIMS geochronology and Lu-Hf isotopic data in zircon from Tandilia basement rocks, Río de la Plata craton, Argentina: evidence of a sanukitoid precursor for some Paleoproterozoic granitoids. J. S. Am. Earth Sci. 108, 103199.
Arena, K.R., Hartmann, L.A., Lana, C., 2016. Evolution of Neoproterozoic ophiolites from the southern Brasiliano Orogen revealed by zircon U-Pb-Hf isotopes and geochemistry. Precambrian Res. 285, 299–314.
Arena, K.R., Hartmann, L.A., Lana, C., 2017. Tonian emplacement of ophiolites in the southern Brasiliano Orogen delimited by U-Pb-Hf isotopes of zircon from metasomatites. Gondwana Res. 49, 296–332.
Babinski, M., Chemale Jr., F., Hartmann, L.A., Van Schmus, W.R., Carlos da Silva, L., 1996. Juvenile accretion at 750–700 Ma in southern Brazil. Geology 24 (5), 439–442.
Babinski, M., Chemale Jr., F., Van Schmus, W.R., Hartmann, L.A., Da Silva, L.C., 1997. U-Pb and Sm-Nd geochronology of the Neoproterozoic granitic-gneissic Dom Feliciano Belt, southern Brazil. J. S. Am. Earth Sci. 10 (3–4), 263–274.
Baranov, V., 1957. A new method for interpretation of aeromagnetic maps: pseudo-gravimetric anomalies. Geophysics 22 (2), 359–382.
Basei, M.A.S., Siga Júnior, O., Masquelin, H., Harara, O.M.M., Reis Neto, J.M., Preciozzi, F., 2000. The Dom Feliciano belt of Brazil and Uruguay and its foreland domain, the Rio de La Plata craton: framework, tectonic evolution and correlation with similar provinces of southewestern Africa. In: Tectonic Evolution of South America. Instituto de Geociências, Universidade de São Paulo. Recuperado de, Rio de Janeiro, pp. 311–334. https://repositorio.usp.br/directbitstream/ddc7b92b-a0b3-45d0-be8f-97decb9fea63/1131022.pdf.
Basei, M.A., Nutman, A., Júnior, O.S., Passarelli, C.R., Drukas, C.O., 2009. The evolution and tectonic setting of the Luis Alves Microplate of Southeastern Brazil: an exotic terrane during the assembly of Western Gondwana. Dev. Precambr. Geol. 16, 273–291.
Basei, M.A.S., Neves, B.B.B., Junior, O.S., Babinski, M., Pimentel, M.M., Tassinari, C.C.G., Cordani, U.G., 2010. Contribution of SHRIMP U–Pb zircon geochronology to unravelling the evolution of Brazilian Neoproterozoic fold belts. Precambrian Res. 183 (1), 112–144.
Basei, M.A.S., Campos Neto, M.C., Lopes, A.P., Nutman, A.P., Liu, D., Sato, K., 2013. Polycyclic evolution of Camboriú complex migmatites, Santa Catarina, Southern Brazil: integrated Hf isotopic and U-Pb age zircon evidence of episodic reworking of a Mesoarchean juvenile crust. Braz. J. Geol. 43 (3).
Basei, M.A.S., Frimmel, H.E., Campos Neto, M.C., Araujo, C.E.G., Castro, N.A., Passarelli, C.R., 2018. The Tectonic history of the Southern Adamastor Ocean based on a Correlation of the Kaoko and Dom Feliciano Belts. In: Siegesmund, S., Oyhantçabal, P., Basei, M.A.S., Oriolo, S. (Eds.), Regional Geology Reviews: Geology of Southwest Gondwana. Springer, Berlin, pp. 63–85.
Basei, M.A.S., Bettucci, L.S., Peel, E., Franceschinis, P., Rapalini, A., Olivet, J.L., Preciozzi, F., 2024. Combined geochronological U-Pb, Hf isotopes and trace element zircon studies from Piedra Alta Terrane, Rio de la Plata Craton (West Uruguay, South America): A geodynamic model. Precambrian Res. 410, 107470.
Battisti, M.A., de Fátima Bitencourt, M., De Toni, G.B., Nardi, L.V.S., Konopásek, J., 2018. Metavolcanic rocks and orthogneisses from Porongos and Várzea do Capivarita complexes: A case for identification of tectonic interleaving at different crustal levels from structural and geochemical data in southernmost Brazil. J. S. Am. Earth Sci. 88, 253–274.
Becker-Kerber, B., Paim, P.S.G., Junior, F.C., Girelli, T.J., da Rosa, A.L.Z., El Albani, A., Pacheco, M.L.A.F., 2020. The oldest record of Ediacaran macrofossils in Gondwana (~ 563 Ma, Itajaí Basin, Brazil). Gondwana Res. 84, 211–228.

Betiollo, L.M., Hartmann, L.A., Savian, J.F., 2019. The Pomerode dome in Luis Alves Craton: Geophysics, geology, geometry and tectonic evolution. In: Simpósio Nacional De Estudos Tectônicos, 17.; International Symposium on Tectonics, 11.; Simpósio Sul-Brasileiro de Geologia, 11., 2019, Bento Gonçalves, RS. Anais[...]. SBG, Bento Gonçalves, RS. https://rigeo.cprm.gov.br/handle/doc/21528.

Blakely, R.J., 1995. Potential Theory in Gravity and Magnetic Applications. Cambridge University Press, Terra Nova. https://doi.org/10.1017/CBO9780511549816.

Blanco, G., Rajesh, H.M., Gaucher, C., Germs, G.J., Chemale Jr., F., 2009. Provenance of the Arroyo del Soldado Group (Ediacaran to Cambrian, Uruguay): implications for the paleogeographic evolution of southwestern Gondwana. Precambrian Res. 171 (1–4), 57–73.

Bossi, J., Campal, N., 1992. Magmatismo y tectónica transcurrente durante el Paleozoico inferior del Uruguay. In: Gutiérrez, J., Saavedra, J., Rábano, I. (Eds.), Paleozoico Inferior De Ibero-América. Universidad de Extremadura, Spain, pp. 343–356.

Bossi, J., Navarro, R., 2001. Grupo Carape: su reivindicacibn. Rev. Soc. Uru. Geol. 8, 2–12.

Bossi, J., Cingolani, C., 2009. Extension and general evolution of the Río de la Plata Craton. Dev. Precambr. Geol. 16, 73–85.

Brown, D., Juhlin, C., Ayala, C., Tryggvason, A., Bea, F., Alvarez-Marrón, J., Pérez-Estaún, A., 2008. Mountain building processes during continent-continent collision in the Uralides. Earth Sci. Rev. 89 (3–4), 177–195.

Brown, R., Summerfield, M.A., Gleadow, A., Gallagher, K., Carter, A., Beucher, R., Wildman, M., 2014. Intracontinental deformation in southern Africa during the late cretaceous. J. Afr. Earth Sci. 100, 20–41. https://doi.org/10.1016/j.jafrearsci.2014.05.014.

Buiter, S.J.H., Torsvik, T.H., 2014. A review of Wilson cycle plate margins: a role for mantle plumes in continental break-up along sutures? Gondwana Res. 26, 627–653.

Cai, H., Xiong, B., Zhu, Y., 2018. 3D modeling and inversion of gravity data in exploration scale. In: Gravity - Geoscience Applications, Industrial Technology and Quantum Aspect. InTech, pp. 401–406. https://doi.org/10.5772/intechopen.70961.

Camozzatto, E., Philipp, R.P., Chemale Jr., F., 2013. Idades Estaterianas no Domo da Vigia: Complexos Vigia e Porongos, Metagranito Seival e Anfibolito Tupi Silveira, Bagé, RS. In: 8 International Symposium on Tectonics (Vol. 14).

Camozzato, E., Lopes, R.D.C., Philipp, R.P., 2017. Geologia e recursos minerais da folha SH. CPRM, 22-YCI, Hulha Negra.

Caxito, F.A., Hartmann, L.A., Heilbron, M., Bruno, H., Pedrosa-Soares, A., Basei, M.A.S., Chemale, F., 2022. Multi-proxy evidence for subduction of the Neoproterozoic Adamastor Ocean and Wilson cycle tectonics in the South Atlantic Brasiliano Orogenic System of Western Gondwana. Precambrian Res. 376, 106678.

Cernuschi, F., Dilles, J.H., Kent, A.J.R., Schroer, G., Raab, A.K., Conti, B., Muzio, R., 2015. Geology, geochemistry and geochronology of the cretaceous Lascano East Intrusive complex and magmatic evolution of the Laguna Merín Basin, Uruguay. Gondwana Res. 28 (2), 837–857.

Cerva-Alves, T., Hartmann, L.A., Remus, M.V.D., Lana, C., 2020. Integrated ophiolite and arc evolution, southern Brasiliano Orogen. Precambrian Res. 341, 105648.

Chauvet, F., Sapin, F., Geoffroy, L., Ringenbach, J.C., Ferry, J.N., 2021. Conjugate volcanic passive margins in the austral segment of the South Atlantic–Architecture and development. Earth Sci. Rev. 212, 103461.

Chemale Jr., F., Hartmann, L.A., Silva, L.D., 1995. Stratigraphy and tectonism of the Brasiliano Cycle in southern Brazil. Commun. Geol. Surv. Namibia 10, 151–166.

Chemale Jr., F., 2000. Evolução geológica do Escudo Sul-rio-grandense. Geol. Rio Grande Sul 13–52.

Chemale, F., Philipp, R.P., Dussin, I.A., Formoso, M.L.L., Kawashita, K., Berttotti, A.L., 2011. Lu-Hf and U-Pb age determination of Capivarita Anorthosite in the Dom Feliciano belt, Brazil. Precambrian Res. 186 (1–4), 117–126.

Chemale Jr., F., Mallmann, G., de Fátima Bitencourt, M., Kawashita, K., 2012. Time constraints on magmatism along the Major Gercino Shear Zone, southern Brazil: implications for West Gondwana reconstruction. Gondwana Res. 22 (1), 184–199.

Cingolani, C., Bonhomme, M., Spoturno Pioppo, J.J., 1990. Resultados mineralógicos y geocronológicos preliminares sobre las unidades Piedras de Afilar, Lavalleja y Barriga Negra, RO del Uruguay. Resúmenes ampliados del Primer Congreso Uruguayo de Geología. In: Congreso Uruguayo de Geología. Montevideo, UY, pp. 25–27 abr. 1990.

Coney, P.J., Jones, D.L., Monger, J.W., 1980. Cordilleran suspect terranes. Nature 288 (5789), 329–333.

Costa, A.F.U., 1997. Teste e modelagem geofísica da estruturação das associações litotectônicas pré-cambrianas no Escudo Sul-rio-grandense. Tese de Doutorado, IG-UFRGS, Porto Alegre, p. 291.

Cruz, R.F.D., Basei, M.A.S., Philipp, R.P., Iglesias, C.M.D.F., 2023. Unveiling the stratigraphy of the northern Punta del Este Terrane (Jaguarão Domain) and its role in the Neoproterozoic tectonic evolution of the Dom Feliciano Belt (southern Brazil and Uruguay). Int. Geol. Rev. 1–23.

de Almeida, F.F.M., Hasui, Y., de Brito Neves, B.B., Fuck, R.A., 1981. Brazilian structural provinces: an introduction. Earth Sci. Rev. 17 (1–2), 1–29.

de Lena, L.O.F., Pimentel, M.M., Philipp, R.P., Armstrong, R., Sato, K., 2014. The evolution of the Neoproterozoic São Gabriel juvenile terrane, southern Brazil based on high spatial resolution U-Pb ages and δ18O data from detrital zircons. Precambrian Res. 247, 126–138.

de Oliveira, C.H.E., Junior, F.C., Jelinek, A.R., Bicca, M.M., Philipp, R.P., 2014. U–Pb and Lu-Hf isotopes applied to the evolution of the late to post-orogenic transtensional basins of the Dom Feliciano belt, Brazil. Precambrian Res. 246, 240–255.

de Oliveira, C.H.E., Jelinek, A.R., Chemale Jr., F., Bernet, M., 2016a. Evidence of post-Gondwana break-up in Southern Brazilian Shield: Insights from apatite and zircon fission track thermochronology. Tectonophysics 666, 173–187.

de Oliveira, C.H.E., Jelinek, A.R., Chemale Jr., F., Bernet, M., 2016b. Thermotectonic history of the southeastern Brazilian margin: evidence from apatite fission track data of the offshore Santos Basin and continental basement. Tectonophysics 685, 21–34.

de Silva, S.L., Riggs, N.R., Barth, A.P., 2015. Quickening the pulse: fractal tempos in continental arc magmatism. Elements 11 (2), 113–118.

de Toni, G.B., Bitencourt, M.D.F., Konopásek, J., Martini, A., Andrade, P.H.S., Florisbal, L.M., Campos, R.S.D., 2020a. Transpressive strain partitioning between the major Gercino shear zone and the Tijucas fold belt, Dom Feliciano belt, Santa Catarina, southern Brazil. J. Struct. Geol. 136, 104058.

de Toni, G., Bitencourt, M.F., Nardi, L.S.V., Florisbal, L.M., Almeida, B.S., Geraldes, M., 2020b. Dom Feliciano Belt orogenic cycle tracked by its pre-collisional magmatism: the Tonian (ca. 800 Ma) Porto Belo complex and its correlations in southern Brazil and Uruguay. Precambrian Res. 342, 105702. https://doi.org/10.1016/j.precamres.2020.105702.

de Wit, M., Stankiewicz, J., Reeves, C., 2008. Restoring Pan-African–Brasiliano connections: More Gondwana control, less Trans-Atlantic corruption. In: Pankhurst, R.J., Trouw, R.A.J., Brito Neves, B.B., De Wit, M.J. (Eds.), West Gondwana: Pre-Cenozoic Correlations across the South Atlantic Region. Geological Society, vol. 294. Special Publications, London, pp. 399–412. https://doi.org/10.1144/SP294.20.

Dickson, B.L., Scott, K.M., 1997. Interpretation of aerial gamma-ray surveys – adding the geochemical factors. AGSO J. 17 (2), 187–200.

Ducea, M.N., Saleeby, J.B., Bergantz, G., 2015. The architecture, chemistry, and evolution of continental magmatic arcs. Annu. Rev. Earth Planet. Sci. 43 (1), 299–331.

Ellis, R.G., de Wet, B., Macleod, I.N., 2012. Inversion of magnetic data from remanent and induced sources. ASEG Ext. Abstr. Region. Geol. Rev. 2012, 1–4. https://doi.org/10.1071/ASEG2012ab117.

Ellis, R., MacLeod, I., 2013. Constrained voxel inversion using the Cartesian cut cell method. ASEG Extend. Abstr. 2013 (1), 1–4.

Erdi-Krausz, G., Matolin, M., Minty, B., Nicolet, J.P., Reford, W.S., Schetselaar, E.M., 2003. Guidelines for radioelement mapping using gamma ray spectrometry data: also as open access e-book. International Atomic Energy Agency (IAEA).

Fernandes, L.A.D., Tommasi, A., Porcher, C.C., 1992. Deformation patterns in the southern Brazilian branch of the Dom Feliciano Belt: a reappraisal. J. S. Am. Earth Sci. 5 (1), 77–96.

Franceschinis, P.R., Rapalini, A.E., Sánchez Bettucci, L., Martínez Dopico, C., Milanese, F. N., 2019. Paleomagnetic confirmation of the "unorthodox" configuration of Atlantica between 2.1-2.0 Ga. Precambrian Res. 105447. https://doi.org/10.1016/j.precamres.2019.105447.

Franceschinis, P.R., Afonso, J.W., Arrouy, M.J., Gómez-Peral, L.E., Poiré, D., Trindade, R. I.F., Rapalini, A.E., 2022. Paleomagnetism of the Ediacaran Avellaneda Formation (Argentina), part I: Paleogeography of the Río de la Plata craton at the dawn of Gondwana. Precambrian Res. 383, 106909.

Frimmel, H.E., 2009. Configuration of Pan-African Orogenic Belts in Southwestern Africa. In: Gaucher, C., Sial, A.N., Frimmel, H.E., Halverson, G.P. (Eds.), Neoproterozoic-Cambrian Tectonics, Global Change and Evolution: A Focus on South Western Gondwana, Developments in Precambrian Geology, 16. Elsevier, pp. 145–151.

Gallagher, K., Hawkesworth, C.J., Mantovani, M.S.M., 1995. Denudation, fission track analysis and the long-term evolution of passive margin topography: application to the southeast Brazilian margin. J. S. Am. Earth Sci. 8 (1), 65–77.

Gastal, M.D.C.P., Lafon, J.M., 1998. Gênese e evolução dos granitóides metaluminosos de afinidade alcalina da porção oeste do escudo sul-rio-grandense: geoquímica e isótopos de Rb-Sr e Pb-Pb. Braz. J. Geol. 28 (1), 11–28.

Gaucher, C., Frimmel, H.E., Germs, G.J.B., 2009. Events and Palaeogeographic Evolution of Southwestern Gondwana in the Neoproterozoic and Cambrian. In: Gaucher, C., Sial, A.N., Frimmel, H.E., Halverson, G.P. (Eds.), Neoproterozoic-Cambrian Tectonics, Global Change and Evolution: A Focus on South Western Gondwana, Developments in Precambrian Geology, 16. Elsevier, Amsterdam, pp. 295–316.

Gaucher, C., Frei, R., Chemale, F., Frei, D., Bossi, J., Martínez, G., Cernuschi, F., 2011. Mesoproterozoic evolution of the Río de la Plata Craton in Uruguay: at the heart of Rodinia? Int. J. Earth Sci. 100 (2), 273–288.

Gaucher, C., Frei, R., Samaniego, L., Will, T.M., Chemale, F., Gargiulo, M.F., Li, Q.L., 2021. The Tapes complex (Nico Pérez Terrane, Uruguay): Constraining the Mesoproterozoic evolution of the Río de la Plata Craton. J. S. Am. Earth Sci. 105, 102906.

Girelli, T.J., Chemale Jr., F., Lavina, E.L.C., Laux, J.H., Bongiolo, E.M., Lana, C., 2018. Granulite accretion to Rio de la Plata Craton, based on zircon U-Pb-Hf isotopes: tectonic implications for Columbia Supercontinent reconstruction. Gondwana Res. 56, 105–118.

Girelli, T.J., Teixeira, D.D., Lana, C.C., Chemale Jr., F., 2023. New insights of the Rio de la Plata Craton based on geochronology and geophysics. In: Continental Crust Evolution & Early Plate Tectonics 2023 International Symposium, Beijing. 2023 CCE-EPT Beijing.

Goscombe, B., Hand, M., Gray, D., 2003. Structure of the Kaoko Belt, Namibia: progressive evolution of a classic transpressional orogen. J. Struct. Geol. 25 (7), 1049–1081.

Goscombe, B., Gray, D.R., Armstrong, R.A., Foster, D.A., Vogl, J., 2005. Event geochronology of the Pan-African Kaoko Belt, Namibia. Precambrian Res. 140 (3–4), 1–41. https://doi.org/10.1016/j.precamres.2005.07.003.

Gregory, T.F., Maria de Fatima Bitencourt, M.F., Nardi, L.V.S., Florisbal, L.M., Chemale Jr., F., 2015. Geochronological data from TTG-type rock associations of the Arroio dos Ratos complex and implications for crustal evolution of southernmost Brazil in Paleoproterozoic times. J. S. Am. Earth Sci. 57, 49–60.

Gresse, P.G., Chemale, F., Da Silva, L.C., Walraven, F., Hartmann, L.A., 1996. Late-to post-orogenic basins of the Pan-African–Brasiliano collision orogen in southern Africa and southern Brazil. Basin Res. 8 (2), 157–171.

Gruber, L., Porcher, C.C., Lenz, C., Fernandes, L.A.D., 2011. Proveniência de metassedimentos das sequências Arroio Areião, Cerro Cambará e Quartzo Milonitos no Complexo Metamórfico Porongos, Santana da Boa Vista. RS. Pesquisas Em Geociências 38 (3), 205–224. https://doi.org/10.22456/1807-9806.35157.

Guadagnin, F., Chemale Jr., F., Dussin, I.A., Jelinek, A.R., dos Santos, M.N., Borba, M.L., Alessandretti, L., 2010. Depositional age and provenance of the Itajaí Basin, Santa Catarina State, Brazil: implications for SW Gondwana correlation. Precambrian Res. 180 (3–4), 156–182.

Gunn, P.J., 1998. Interpretation of Airborne Magnetic and Radiometric Surveys. Course. AGSO, 150 p.

Halls, H.C., Campal, N., Davis, D.W., Bossi, J., 2001. Magnetic studies and U–Pb geochronology of the Uruguayan dyke swarm, Rio de la Plata craton, Uruguay: paleomagnetic and economic implications. J. S. Am. Earth Sci. 14 (4), 349–361.

Harrison, T.M., 2009. The Hadean crust: evidence from> 4 Ga zircons. Annu. Rev. Earth Planet. Sci. 37 (1), 479–505.

Harrison, T.M., Duncan, I.A.N., Mcdougall, I.A.N., 1985. Diffusion of 40Ar in biotite: temperature, pressure and compositional effects. Geochim. Cosmochim. Acta 49 (11), 2461–2468.

Hartmann, L.A., 1998. Deepest exposed crust of Brazil-geochemistry of Paleoproterozoic depleted Santa Maria Chico granulites. Gondwana Res. 1 (3–4), 331–341.

Hartmann, L.A., Remus, M.V.D., 2000. Origem e evolução das rochas ultramáficas do Rio Grande do Sul desde o Arqueano até o Cambriano. Geol. Rio Grande Sul 53–78.

Hartmann, L.A., Leite, J.A.D., Da Silva, L.C., Remus, M.V.D., McNaughton, N.J., Groves, D.I., Vasconcellos, M.A.Z., 2000. Advances in SHRIMP geochronology and their impact on understanding the tectonic and metallogenic evolution of southern Brazil. Aust. J. Earth Sci. 47 (5), 829–844.

Hartmann, L.A., Campal, N., Santos, J.O.S., McNaughton, N.J., Bossi, J., Schipilov, A., Lafon, J.M., 2001. Archean crust in the Rio de la Plata Craton, Uruguay—SHRIMP U–Pb zircon reconnaissance geochronology. J. S. Am. Earth Sci. 14 (6), 557–570.

Hartmann, L.A., Santos, J.O.S., Cingolani, C.A., McNaughton, N.J., 2002. Two Paleoproterozoic orogenies in the evolution of the Tandilia Belt, Buenos Aires, as evidenced by zircon U-Pb SHRIMP geochronology. Int. Geol. Rev. 44 (6), 528–543.

Hartmann, L.A., Santos, J.O., Leite, J.A., Porcher, C.C., Mcnaughton, N.J., 2003. Metamorphic evolution and U-Pb zircon SHRIMP geochronology of the Belizário ultramafic amphibolite, Encantadas complex, southernmost Brazil. An. Acad. Bras. Cienc. 75, 393–403.

Hartmann, L.A., Philipp, R.P., Liu, D., Wan, Y., Wang, Y., Santos, J.O.S., Vasconcellos, M. A., 2004. Paleoproterozoic magmatic provenance of detrital zircons, Porongos complex quartzites, southern Brazilian shield. Int. Geol. Rev. 46 (2), 127–157.

Hartmann, L.A., Chemale Jr., F., Philipp, R.P., 2007. In: Iannuzzi, R., Frantz, J.C. (Eds.), Evolução geotectônica do Rio Grande do Sul no pré-cambriano, 50, pp. 97–123.

Hartmann, L.A., Schneider, J.O., McNaughton, N.J., 2008. Detrital zircon U-Pb age data, and Precambrian provenance of the Paleozoic Guaritas Formation, southern Brazilian Shield. Int. Geol. Rev. 50 (4), 364–374.

Hartmann, L.A., Philipp, R.P., Santos, J.O.S., McNaughton, N.J., 2011. Time frame of 753–680 Ma juvenile accretion during the São Gabriel orogeny, southern Brazilian Shield. Gondwana Res. 19 (1), 84–99.

Hartmann, L.A., Werle, M., Michelin, C.R., Lana, C., Queiroga, G.N., Castro, M.P., Arena, K.R., 2019. Proto-Adamastor Ocean crust (920 Ma) described in Brasiliano Orogen from coetaneous zircon and tourmaline. Geosci. Front. 10 (4), 1623–1633.

Hasui, Y., Carneiro, C.D.R., Coimbra, A.M., 1975. The Ribeira folded belt. Rev. Bras. Geoci. 5 (4), 257–266.

Heller, B.M., Hueck, M., Passarelli, C.R., Basei, M.A., 2021. Zircon U-Pb geochronology and Hf isotopes of the Luís Alves Terrane: Archean to Paleoproterozoic evolution and Neoproterozoic overprint. J. S. Am. Earth Sci. 106, 103008.

Höfig, D.F., Marques, J.C., Basei, M.A.S., Giusti, R.O., Kohlrausch, C., Frantz, J.C., 2018. Detrital zircon geochronology (U-Pb LA-ICP-MS) of syn-orogenic basins in SW Gondwana: New insights into the Cryogenian-Ediacaran of Porongos complex, Dom Feliciano Belt, southern Brazil. Precambrian Res. 306, 189–208.

Hueck, M., Oriolo, S., Dunkl, I., Wemmer, K., Oyhantçabal, P., Schanofski, M., Siegesmund, S., 2017. Phanerozoic low-temperature evolution of the Uruguayan Shield along the South American passive margin. J. Geol. Soc. Lond. 174 (4), 609–626.

Hueck, M., Dunkl, I., Oriolo, S., Wemmer, K., Basei, M.A., Siegesmund, S., 2019. Comparing contiguous high-and low-elevation continental margins: New (U-Th)/He constraints from South Brazil and an integration of the thermochronological record of the southeastern passive margin of South America. Tectonophysics 770, 228222.

Hueck, M., Wemmer, K., Basei, M.A., Philipp, R.P., Oriolo, S., Heidelbach, F., Siegesmund, S., 2020. Dating recurrent shear zone activity and the transition from ductile to brittle deformation: White mica geochronology applied to the Neoproterozoic Dom Feliciano Belt in South Brazil. J. Struct. Geol. 141, 104199.

Hueck, M., Oriolo, S., Basei, M.A., Oyhantçabal, P., Heller, B.M., Wemmer, K., Siegesmund, S., 2022. Archean to early Neoproterozoic crustal growth of the southern South American Platform and its wide-reaching "African" origins. Precambrian Res. 369, 106532.

Ingram, D.M., Causon, D.M., Mingham, C.G., 2003. Developments in Cartesian cut cell methods. Math. Comput. Simul. 61 (3–6), 561–572.

Janikian, L., de Almeida, R.P., Fragoso-Cesar, A.R.S., de Souza Martins, V.T., Dantas, E. L., Tohver, E., D'Agrella-Filho, M.S., 2012. Ages (U–Pb SHRIMP and LA ICPMS) and stratigraphic evolution of the Neoproterozoic volcano-sedimentary successions from the extensional Camaquã Basin, Southern Brazil. Gondwana Res. 21 (2–3), 466–482.

Konopásek, J., Cavalcante, C., Fossen, H., Janoušek, V., 2020. Adamastor–an Ocean that never existed? Earth Sci. Rev. 205, 103201.

Laux, J.H., Bongiolo, E.M., Chemale Jr., F., Santos, T.C., 2010. U-Pb of Cerro Batovi Metamorphic Complex. First record of statherian rocks in the Rio Grande do Sul state–Brazil. In: South American Symposium on Isotope Geology, vol. 7, pp. 78–81.

Laux, J.H., Stropper, J.L., Provenzano, C.A.S., Horn, B.L.D., Klein, C., 2021. Escudo Sul-Rio-Grandense, estado do Rio Grande do Sul.

Lehmann, J., Saalmann, K., Naydenov, K.V., Milani, L., Belyanin, G.A., Zwingmann, H., Charlesworth, G., Kinnaird, J.A., 2016. Structural and geochronological constraints on the Pan-African tectonic evolution of the northern Damara Belt, Namibia. Tectonics 35, 103–135. https://doi.org/10.1002/2015TC003899.

Leite, J.A., Hartman, L.A., Mcnaughton, N.J., Chemale Jr., F., 1998. SHRIMP U/Pb zircon geochronology of Neoproterozoic juvenile and crustal-reworked terranes in southernmost Brazil. Int. Geol. Rev. 40 (8), 688–705.

Leite, J.A.D., Hartmann, L.A., Fernandes, L.A.D., McNaughton, N.J., Soliani Jr., E., Koester, E., Santos, J.O.S., Vasconcellos, M.A.Z., 2000. Zircon U-Pb SHRIMP dating of gneissic basement of the Dom Feliciano Belt, southernmost Brazil. J. S. Am. Earth Sci. 13, 739–750.

Lenz, C., Fernandes, L.A.D., McNaughton, N.J., Porcher, C.C., Masquelin, H., 2011. U–Pb SHRIMP ages for the Cerro Bori Orthogneisses, Dom Feliciano Belt in Uruguay: evidences of a ~800 Ma magmatic and ~650 Ma metamorphic event. Precambrian Res. 185 (3–4), 149–163.

Li, X., 2008. Magnetic reduction-to-the-pole at low latitudes: Observations and considerations. Lead. Edge 27 (8), 990–1002.

Li, Y., Sun, J., Li, S.L., Leão-Santos, M., 2021. A paradigm shift in magnetic data interpretation: increased value through magnetization inversions. Lead. Edge 40 (2), 89–98.

Li, Z.X., Liu, Y., Ernst, R., 2023. A dynamic 2000—540 Ma Earth history: from cratonic amalgamation to the age of supercontinent cycle. Earth Sci. Rev. 238, 104336.

Lowrie, W., Fichtner, A., 2020. Fundamentals of Geophysics. Cambridge University Press.

Machado, N., Koppe, J.C., Hartmann, L.A., 1990. A late Proterozoic U-Pb age for the Bossoroca Belt, Rio Grande do Sul, Brazil. J. S. Am. Earth Sci. 3 (2–3), 87–90.

Mallmann, G., Chemale Jr., F., Ávila, J.N., Kawashita, K., Armstrong, R.A., 2007. Isotope geochemistry and geochronology of the Nico Perez terrane, Rio de la Plata craton, Uruguay. Gondwana Res. 12 (4), 489–508.

Martil, M.M.D., de Fátima Bitencourt, M., Nardi, L.V.S., Koester, E., Pimentel, M.M., 2017. Pre-collisional, Tonian (ca. 790 Ma) continental arc magmatism in southern Mantiqueira Province, Brazil: geochemical and isotopic constraints from the Várzea do Capivarita complex. Lithos 274, 39–52.

Masquelin, H., 2004. El Complejo Cerro Olivo, Sureste de Uruguay: una revisión estratigráfica y tectónica. In: Congreso Uruguayo de Geología, vol. 4.

Masquelin, H., Aïfa, T., Scaglia, F., Basei, M.A., 2021. The Archean Pavas Block in Uruguay: Extension and tectonic evolution based on LA-ICP-MS U–Pb ages and airborne geophysics. J. S. Am. Earth Sci. 110, 103364.

Milani, E.J., de Wit, M.J., 2008. Correlations between the classic Parana´and Cape–Karoo sequences of South America and southern Africa and their basin infills flanking the Gondwanides: du Toit revisited. In: Pankhurst, R. J., Trouw, R. A. J., Brito Neves, B. B. & De Wit, M. J. (eds) West Gondwana: Pre-Cenozoic Correlations across the South Atlantic Region. Geol. Soc. Lond. Spec. Publ. 294, 319–342. https://doi.org/10.1144/SP294.17.

Miller, H.G., Singh, V., 1994. Potential field tilt—a new concept for location of potential field sources. J. Appl. Geophys. 32, 213–217. https://doi.org/10.1016/0926-9851(94)90022-1.

Minty, B.R.S., 1991. Simple micro-levelling for aeromagnetic data. Explor. Geophys. 22 (4), 591. https://doi.org/10.1071/eg991591.

Monteiro, C.F., de Oliveira, I.L., Brod, J.A., Dantas, E.L., de Araujo, C.E.G., Zacchi, É.N. P., Fuck, R.A., 2020. Nd-Sr-Hf isotopes and U-Pb ages of Mesoproterozoic Três Estradas Alkaline-Carbonatite complex, Brazil: Implications for Sul-Riograndense Shield evolution and Rodinia break-up. Precambrian Res. 351, 105963.

Nabighian, M.N., Grauch, V.J.S., Hansen, R.O., LaFehr, T.R., Li, Y., Peirce, J.W., Phillips, J.D., Ruder, M.E., 2005. The historical development of the magnetic method in exploration. Geophysics 70. https://doi.org/10.1190/1.2133784, 33ND–61ND.

Naprstek, T., Smith, R.S., 2019. A new method for interpolating linear features in aeromagnetic data. Geophysics 1–35. https://doi.org/10.1190/geo2018-0156.1.

Oriolo, S., Oyhantçabal, P., Heidelbach, F., Wemmer, K., Siegesmund, S., 2015. Structural evolution of the Sarandí del Yí Shear Zone, Uruguay: kinematics, deformation conditions and tectonic significance. Int. J. Earth Sci. 104, 1759–1777.

Oriolo, S., Oyhantçabal, P., Wemmer, K., Basei, M.A., Benowitz, J., Pfänder, J., Siegesmund, S., 2016a. Timing of deformation in the Sarandí del Yí Shear Zone, Uruguay: Implications for the amalgamation of western Gondwana during the Neoproterozoic Brasiliano-Pan-African orogeny. Tectonics 35 (3), 754–771.

Oriolo, S., Oyhantçabal, P., Wemmer, K., Heidelbach, F., Pfänder, J., Basei, M.A., Siegesmund, S., 2016b. Shear zone evolution and timing of deformation in the Neoproterozoic transpressional Dom Feliciano Belt, Uruguay. J. Struct. Geol. 92, 59–78.

Oriolo, S., Oyhantçabal, P., Basei, M.A., Wemmer, K., Siegesmund, S., 2016c. The Nico Pérez Terrane (Uruguay): from Archean crustal growth and connections with the Congo Craton to late Neoproterozoic accretion to the Río de la Plata Craton. Precambrian Res. 280, 147–160.

Oriolo, S., Oyhantçabal, P., Wemmer, K., Siegesmund, S., 2017. Contemporaneous assembly of Western Gondwana and final Rodinia break-up: implications for the supercontinent cycle. Geosci. Front. 8 (6), 1431–1445.

Oriolo, S., Wemmer, K., Oyhantçabal, P., Fossen, H., Schulz, B., Siegesmund, S., 2018. Geochronology of shear zones–A review. Earth Sci. Rev. 185, 665–683.

Oriolo, S., Oyhantçabal, P., Konopásek, J., Basei, M.A., Frei, R., Sláma, J., Siegesmund, S., 2019. Late Paleoproterozoic and Mesoproterozoic magmatism of the

Nico Pérez Terrane (Uruguay): tightening up correlations in southwestern Gondwana. Precambrian Res. 327, 296–313.
Oriolo, S., Gómez, A.L., Maffini, M.N., Oyhantçabal, P., Demarco, M.M., Perucca, M.S.V., Rubinstein, N.A., 2024. Transtension, brittle-ductile shear zones and hydrothermal ore deposits: Towards quantitative structural and kinematic models. Journal of Structural Geology 185, 105173. https://doi.org/10.1016/j.jsg.2024.105173.
Oyhantçabal, P., Siegesmund, S., Wemmer, K., Layer, P., 2010. The sierra ballena shear zone in the southernmost dom feliciano belt (Uruguay): evolution, kinematics, and deformation conditions. Int. J. Earth Sci. 99, 1227–1246.
Oyhantçabal, P., Siegesmund, S., Wemmer, K., 2011. The Río de la Plata Craton: a review of units, boundaries, ages and isotopic signature. Int. J. Earth Sci. 100 (2), 201–220.
Oyhantçabal, P., Wagner-Eimer, M., Wemmer, K., Schulz, B., Frei, R., Siegesmund, S., 2012. Paleo- and Neoproterozoic magmatic and tectonometamorphic evolution of the Isla Cristalina de Rivera (Nico Pérez Terrane, Uruguay). Int. J. Earth Sci. 101 (7), 1745–1762. https://doi.org/10.1007/s00531-012-0757-4.
Oyhantçabal, P., Oriolo, S., Philipp, R.P., Wemmer, K., Siegesmund, S., 2018. The Nico Pérez Terrane of Uruguay and Southeastern Brazil. In: Siegesmund, S., Oyhantçabal, P., Basei, M.A.S., Oriolo, S. (Eds.), Regional Geology Reviews: Geology of Southwest Gondwana. Springer, Berlin, pp. 161–188.
Oyhantcabal, P., Oriolo, S., Wemmer, K., Basei, M.A.S., Frei, D., Siegesmund, S., 2021. Provenance of metasedimentary rocks of the western Dom Feliciano Belt in Uruguay: Insights from U–Pb detrital zircon geochronology, Hf and Nd model ages, and geochemical data. J. S. Am. Earth Sci. 108, 103139.
Paim, P.S.G., Chemale Jr., F., Lopes, R.D.C., 2000. A bacia do Camaquã. Geol. Rio Grande Sul 231–274.
Pamoukaghlián, K., Gaucher, C., Frei, R., Poiré, D.G., Chemale, F., Frei, D., Will, T.M., 2017. U-Pb age constraints for the La Tuna Granite and Montevideo Formation (Paleoproterozoic, Uruguay): unravelling the structure of the Río de la Plata Craton. J. S. Am. Earth Sci. 79, 443–458.
Peel, E., Muzio, R., Fort, S., Olivera, L., 2024. Precambrian basement rocks of the southernmost tip of the Paraná basin (Northern Uruguay): Petrologic assessment from deep borehole data. Precambrian Res. 404, 107323.
Percival, J.J., Konopásek, J., Eiesland, R., Sláma, J., de Campos, R.S., Battisti, M.A., de Fátima Bitencourt, M., 2021. Pre-orogenic connection of the foreland domains of the Kaoko–Dom Feliciano–Gariep orogenic system. Precambrian Res. 354, 106060.
Pertille, J., Hartmann, L.A., Philipp, R.P., Petry, T.S., de Carvalho Lana, C., 2015. Origin of the Ediacaran Porongos Group, Dom Feliciano Belt, southern Brazilian Shield, with emphasis on whole rock and detrital zircon geochemistry and U–Pb, Lu–Hf isotopes. J. S. Am. Earth Sci. 64, 69–93.
Pertille, J., Hartmann, L.A., Santos, J.O.S., McNaughton, N.J., Armstrong, R., 2017. Reconstructing the Cryogenian–Ediacaran evolution of the Porongos fold and thrust belt, Southern Brasiliano Orogen, based on Zircon U–Pb–Hf–O isotopes. Int. Geol. Rev. 59 (12), 1532–1560.
Philipp, R.P., Machado, R., Chemale Jr., F., 2003. Reavaliação e novos dados geocronológicos (Ar/Ar, Rb/Sr e Sm/Nd) do Batólito Pelotas no Rio Grande do Sul: implicações petrogenéticas e idade de reativação das zonas de cisalhamento. Geologia USP. Sér. Científ. 3, 71–84.
Philipp, R.P., Lusa, M., Nardi, L.V., 2008. Petrology of dioritic, tonalitic and trondhjemitic gneisses from Encantadas complex, Santana da Boa Vista, southernmost Brazil: Paleoproterozoic continental-arc magmatism. An. Acad. Bras. Cienc. 80 (4), 735–748.
Philipp, R.P., Pimentel, M.M., Chemale Jr., F., 2016. Tectonic evolution of the Dom Feliciano belt in Southern Brazil based on geological relationships and U–Pb geochronology. Braz. J. Geol. 46 (1), 83–104.
Philipp, R.P., Pimentel, M.M., Basei, M.A.S., 2018. The tectonic evolution of the São Gabriel terrane, Dom Feliciano belt, southern Brazil: the closure of the Charrua Ocean. Geol. Southwest Gondwana 243–265.
Philipp, R.P., Pimentel, M.M., Basei, M.A.S., Salvi, M., De Lena, L.O.F., Vedana, L.A., Camozzato, E., 2021. U–Pb detrital zircon dating applied to metavolcano-sedimentary complexes of the São Gabriel Terrane: New constraints on the evolution of the Dom Feliciano Belt. J. S. Am. Earth Sci. 110, 103409.
Porada, H., 1979. The Damara-Ribeira orogen of the Pan-Africanbrasiliano cycle in Namibia (Southwest Africa) and Brazil as interpreted in terms of continental collision. Tectonophysics 57 (2–4), 237–265.
Puetz, S.J., Spencer, C.J., Ganade, C.E., 2021. Analyses from a validated global UPb detrital zircon database: Enhanced methods for filtering discordant UPb zircon analyses and optimizing crystallization age estimates. Earth Sci. Rev. 220, 103745.
Ramos, V.A., 2009. Anatomy and global context of the Andes: Main geologic features and the Andean orogenic cycle. Mem. Geol. Soc. Am. 204, 31–65.
Rapalini, A.E., Trindade, R.I., Poiré, D.G., 2013. The La Tinta pole revisited: paleomagnetism of the Neoproterozoic Sierras Bayas Group (Argentina) and its implications for Gondwana and Rodinia. Precambrian Res. 224, 51–70.
Rapalini, A.E., Tohver, E., Bettucci, L.S., Lossada, A.C., Barcelona, H., Pérez, C., 2015. The late Neoproterozoic Sierra de las Ánimas Magmatic complex and Playa Hermosa Formation, southern Uruguay, revisited: Paleogeographic implications of new paleomagnetic and precise geochronologic data. Precambrian Res. 259, 143–155.
Rapalini, A.E., Franceschinis, P.R., Bettucci, L.S., Arrouy, M.J., Poiré, D.G., 2021. The Precambrian drift history and paleogeography of Río de la Plata craton. In: Ancient Supercontinents and the Paleogeography of Earth. Elsevier, pp. 243–261.
Rapela, C.W., Fanning, C.M., Casquet, C., Pankhurst, R.J., Spalletti, L., Poiré, D., Baldo, E.G., 2011. The Rio de la Plata craton and the adjoining Pan-African/Brasiliano terranes: their origins and incorporation into south-West Gondwana. Gondwana Res. 20, 673–690.
Reid, A.B., Allsop, J.M., Granser, H., Millett, A.T., Somerton, I.W., 1990. Magnetic interpretation in three dimensions using Euler deconvolution. Geophysics 55 (1), 80–91.
Reid, A.B., Ebbing, J., Webb, S.J., 2014. Avoidable Euler errors–the use and abuse of Euler deconvolution applied to potential fields. Geophys. Prospect. 62 (5), 1162–1168.
Remus, M.V.D., Hartmann, L.A., McNaughton, N.J., Groves, D.I., Fletcher, I.R., 2000. The link between hydrothermal epigenetic copper mineralization and the Caçapava Granite of the Brasiliano Cycle in southern Brazil. J. S. Am. Earth Sci. 13 (3), 191–216.
Roest, W.R., Verhoef, J., Pilkington, M., 1992. Magnetic interpretation using the 3-D analytic signal. Geophysics 57 (1), 116–125.
Roy, R., Benedicto, A., Grare, A., Béhaegel, M., Richard, Y., Harrison, G., 2017. Three-dimensional gravity modelling applied to the exploration of uranium unconformity-related basement-hosted deposits: the contact prospect case study, Kiggavik, northeast Thelon region (Nunavut, Canada). Can. J. Earth Sci. 54 (8), 869–882.
Saalmann, K., Hartmann, L.A., Remus, M.V.D., Koester, E., Conceição, R.V., 2005. Sm–Nd isotope geochemistry of metamorphic volcano-sedimentary successions in the São Gabriel Block, southernmost Brazil: evidence for the existence of juvenile Neoproterozoic oceanic crust to the east of the Rio de la Plata craton. Precambrian Res. 136 (2), 159–175.
Saalmann, K., Remus, M.V.D., Hartmann, L.A., 2006. Tectonic evolution of the Neoproterozoic São Gabriel block, southern Brazil: constraints on Brasiliano orogenic evolution of the Rio de La Plata cratonic margin. J. S. Am. Earth Sci. 21 (3), 204–227.
Saalmann, K., Hartmann, L.A., Remus, M.V.D., 2007. The assembly of West Gondwana—the view from the Rio de la Plata craton. In: Special Paper 423: The Evolution of the Rheic Ocean: From Avalonian-Cadomian Active Margin to Alleghenian-Variscan Collision, pp. 1–26. https://doi.org/10.1130/2007.2423(01).
Saalmann, K., Gerdes, A., Lahaye, Y., Hartmann, L., Remus, M.V.D., Läufer, A., 2011. A Multiple accretion at the eastern margin of the Rio de la Platacraton: the prolonged Brasiliano orogeny in southernmost Brazil. Int. J. Earth Sci. (Geol. Rundsch.) 100, 355–378. https://doi.org/10.1007/s00531-010-0564-8.
Sánchez Bettucci, L., Peel, E., Oyhantçabal, P., 2010. Precambrian geotectonic units of the Río de La Plata craton. Int. Geol. Rev. 52 (1), 32–50. https://doi.org/10.1080/00206810903211104.
Sánchez Bettucci, L.S., Cordani, U.G., Loureiro, J., Peel, E., Fort, S., Sato, K., 2021. The Nico Pérez terrane (Uruguay) and its archean and paleoproterozoic inheritance. Andean Geol. 48 (3), 442–471.
Santos, J.O.S., Hartmann, L.A., Bossi, J., Campal, N., Schipilov, A., Piñeyro, D., McNaughton, N.J., 2003. Duration of the Trans-Amazonian Cycle and its correlation within South America based on U-Pb SHRIMP geochronology of the La Plata Craton, Uruguay. Int. Geol. Rev. 45 (1), 27–48.
Santos, J.O., Chernicoff, C.J., Zappettini, E.O., McNaughton, N.J., Greau, Y., 2017. U-Pb geochronology of Martín García, Sola, and dos Hermanas Islands (Argentina and Uruguay): Unveiling Rhyacian, Statherian, Ectasian, and Stenian of a forgotten area of the Río de la Plata Craton. J. S. Am. Earth Sci. 80, 207–228.
Scintrex, L., 2012. CG-5 Scintrex Autograv System Operation Manual, Part# 867700 Revision7. Scintrex Limited, Concord.
Shearer, Sarah E., 2005. Three-Dimensional Inversion of Magnetic Data in the Presence of Remanent Magnetization. MS thesis. Colorado School of Mines.
Siegesmund, S., Basei, M.A., Oyhantçabal, P., Oriolo, S. (Eds.), 2018. Geology of Southwest Gondwana. Springer.
Siga Junior, O., 1995. Domínios tectônicos do sudeste do Paraná e nordeste de Santa Catarina: geocronologia e evolução crustal. Doctoral dissertation. Universidade de São Paulo.
Silva Lara, H., Siegesmund, S., Oriolo, S., Hueck, M., Wemmer, K., Basei, M.A.S., Oyhantçabal, P., 2022. Reassessing the polyphase neoproterozoic evolution of the Punta del Este terrane, Dom Feliciano Belt, Uruguay. Int. J. Earth Sci. 111 (7), 2283–2316.
Simões, M.S., 2014. O Complexo máfico-ultramáfico Mata Grande, São Sepé, RS: petrologia e geocronologia.
Siviero, R.S., Fernandes, L.A., Koester, E., Jourdan, F., 2022. Tonian and Cryogenian 40Ar/39Ar hornblende and muscovite ages for the São Gabriel Terrane, Dom Feliciano Belt, southern Brazil. Geol. J. 57 (3), 1137–1152.
Sommer, C.A., de Lima, E.F., Nardi, L.V.S., Figueiredo, A.M.G., Pierosan, R., 2005. Potassic and low-and high-Ti mildly alkaline volcanism in the Neoproterozoic Ramada Plateau, southernmost Brazil. J. S. Am. Earth Sci. 18 (3–4), 237–254.
Spoturno, J., Oyhantçabal, P., Faraone, M., 2019. Mapa geológico del Departamento de Lavalleja a escala 1: 100.000. In: Fecha de recibido. Ministerio de Industria, Energía y Minería MIEM y Facultad de Ciencias UDELAR, Uruguay, p. 24.
Takehara, L., Laux, J.H., 2019. Área de relevante interesse mineral Batólito Pelotas - Terrenos Tijucas: estado do Rio Grande do Sul. Programa Geologia. Mineração e Transformação Mineral e Avaliação dos Recursos Minerais do Brasil, Escala 1: 500.000. CPRM, Porto Alegre, p. 186.
Talwani, M., 1965. Computation with the help of a digital computer of magnetic anomalies caused by bodies of arbitrary shape. GEOPHYSICS 30 (5), 797–817. https://doi.org/10.1190/1.1439654.
Teixeira, W., Pinese, J.P.P., Iacumin, M., Girardi, V.A.V., Piccirillo, E.M., Echeveste, H., Heaman, L.M., 2002. Calc-alkaline and tholeiitic dyke swarms of Tandilia, Rio de la Plata craton, Argentina: U–Pb, Sm-Nd, and Rb–Sr 40Ar/39Ar data provide new clues for intraplate rifting shortly after the Trans-Amazonian orogeny. Precambrian Res. 119 (1–4), 329–353.
Teixeira, W., D'Agrella-Filho, M.S., Hamilton, M.A., Ernst, R.E., Girardi, V.A., Mazzucchelli, M., Bettencourt, J.S., 2013. U–Pb (ID-TIMS) baddeleyite ages and paleomagnetism of 1.79 and 1.59 Ga tholeiitic dyke swarms, and position of the Rio de la Plata Craton within the Columbia supercontinent. Lithos 174, 157–174.
Teixeira, C.D., Girelli, T.J., Serratt, H., Oliveira, H.O.S., Cruz, M.F., Conti, B., Rodriguez, P., Chemale, F., 2025. Paleogeographic significance of unknown

hyperextended continental crust in South Atlantic conjugated margin. Geosci. Front. 16 (1), 101934. ISSN 1674-9871. https://doi.org/10.1016/j.gsf.2024.101934.
Telford, W.M., Geldart, L.P., Sheriff, R.E., 1990. Applied Geophysics, Journal of Geophysical Research, Regional Geology Reviews. Cambridge University Press, Cham. https://doi.org/10.1017/CBO9781139167932.
Thompson, D.T., 1982. EULDPH: a new technique for making computer-assisted depth estimates from magnetic data. Geophys. Region. Geol. Rev. 47, 31–37. https://doi.org/10.1190/1.1441278.
Vermeesch, P., 2018. IsoplotR: A free and open toolbox for geochronology. Geosci. Front. 9 (5), 1479–1493.
Vieira, D.T., Koester, E., Bertotti, A.L., 2016. Petrologia do granito Chasqueiro, região de Arroio grande, sudeste do Escudo sul-rio-grandense. Braz. J. Geol. 46, 79–108.
Vieira, D.T., Koester, E., Ramos, R.C., Porcher, C.C., 2019. Sr-Nd-Hf isotopic constraints and U-Pb geochronology of the Arroio Pedrado Gneisses, Dom Feliciano Belt, Brazil: a 680 Ma shoshonitic event in the final stages of the Piratini Arc evolution. J. S. Am. Earth Sci. 95, 102294.
Werle, M., Hartmann, L.A., Queiroga, G.N., Lana, C., Pertille, J., Michelin, C.R.L., Savian, J.F., 2020. Oceanic crust and mantle evidence for the evolution of Tonian-Cryogenian ophiolites, southern Brasiliano Orogen. Precambrian Res. 351, 105979.
Will, T.M., Gaucher, C., Ling, X.X., Li, X.H., Li, Q.L., Frimmel, H.E., 2019. Neoproterozoic magmatic and metamorphic events in the Cuchilla Dionisio Terrane, Uruguay, and possible correlations across the South Atlantic. Precambrian Res. 320, 303–322.
Will, T.M., Höhn, S., Frimmel, H.E., Gaucher, C., Le Roux, P.J., Macey, P.H., 2020. Petrological, geochemical and isotopic data of Neoproterozoic rock units from Uruguay and South Africa: Correlation of basement terranes across the South Atlantic. Gondwana Res. 80, 12–32.
Will, T.M., Gaucher, C., Frimmel, H.E., Ling, X.X., Shi, W., Li, X.H., Li, Q.L., 2023. Ediacaran to Cambrian tectonomagmatic events in the Southern Dom Feliciano Belt, Uruguay: from a plate margin to an intraplate setting and the assembly of SW Gondwana. Gondwana Res. 115, 155–182.
Yin, A., Harrison, T.M., 2000. Geologic Evolution of the Himalayan-Tibetan Orogen. Annu. Rev. Earth Planet. Sci. 28, 211–280. https://doi.org/10.1146/annurev.earth.28.1.211.
Zhdanov, M.S., 2002. Geophysical Inverse Theory and Regularization Problems, vol. 36. Elsevier.
Zuza, A.V., Levy, D., Wu, C., Li, B., 2019. Underthrusting and duplexing beneath the northern Tibetan Plateau and the evolution of the Himalayan-Tibetan orogen. Lithosphere 11 (2), 209–231.
Zvirtes, G., Philipp, R.P., Hartmann, L.A., Hurst, A., Palladino, G., Alessandretti, L., 2017. Spatial and genetic relationships between the fluidization and injection of eolian sand and volcanic processes, Paraná volcanic province, Brazil. In: Hurst, A., Silcock, S., Dennis, H., Huuse, M., Lovelock, C., Wild, J. (Eds.), Subsurface Sand Remobilization and Injection: Implications for Oil and Gas Exploration and Development. Geological Society of London, p. 89.
Bossi, J., Ferrando, L., Montana, J., Campal, N., Morales, H., Gancio, F., Schipilov, A., Pineyro, D., Sprechmann, P., 1998. Carta geologica del Uruguay, escala 1:500,000. GEOEDITORES, Montevideo, Uruguay.

Thermal Model

Thermal Model

A thermal model could assist in identifying H_2 generation and sink windows related to over-maturation of organic matter. In that way, Ansys MAPDL (Mechanical ANSYS Parametric Design Language) was used to perform thermal conduction analyses based on the physical principles of Fourier's Law and the energy diffusion equation. Within the software, a user can model conductive solids by defining material properties for isotropic, orthotropic, or even non-linear conductivity using either polynomial forms or tables. The simulation is built using specific conductive elements like PLANE55 to which boundary conditions, such as imposed temperatures, heat flux, and/or heat sources, are applied (Ansys, 2025). Once a steady-state or transient analysis is complete, the results can be evaluated by plotting isothermal lines, visualizing thermal gradient, and flux vectors to validate the simulation.

The original aim was to build a 3D thermal model of the basin using seismic and thermal data. The modeling strategy initially relied on the anticipated 2022 public release of the ION surveys in Brazil. This dataset, which extends to the Mohorovičić (Moho) discontinuity depth, would have enabled the construction of a full-scale crustal model. However, a national agency (in Brazil) decision extended the confidentiality period for this data until August 31, 2030. As a result, the seismic data were severely limited in depth, with only two seismic lines recording sufficient time to capture the Moho reflection (Figure 1).

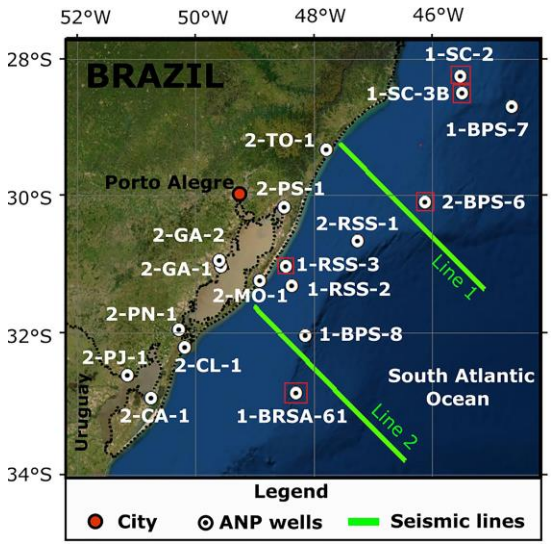

Figure 1. Location map of the deepest seismic lines available for crustal-scale study. Wells with a red rectangle around are wells with bottom hole temperatures (BHTs). Figure modified from Serratt et al. (2022).

Given the data limitations, the chosen approach was to create two 2D thermal models, each one calibrated with Bottom-Hole Temperatures (BHTs) from the closest well. The model for Line 1 (Figure 1) was calibrated using data from well 2-BPS-6, while the model for Line 2 (Figure 1) utilized data from well 1-BRSA-61. The first step involved constructing the geometry of the models from the seismic profiles. Based on previous research (Stica et al., 2014; Geoffroy et al., 2015; Gordon & Mohriak, 2015; Chauvet et al., 2021Serratt et al., 2022; Serratt et al., 2025), the crust was interpreted into five lithological units: 1) a sedimentary section, including deposits from the Pelotas and Paraná Basins; 2) a volcanic section, comprising pre-rift Paraná-LIP flood basalts, Seaward Dipping Reflectors (SDRs), and late-rift volcanic rocks (Gordon & Mohriak, 2015; Serratt et al., 2022; Serratt et al., 2025); 3) a granitic upper crust; 4) a gneissic lower crust; and 5) an unknown lower crust. The geological interpretation, initially performed in SLB PetrelTM 2020, was subsequently prepared for 2D modeling. First, the interpreted horizons were reprojected onto an arbitrary 2D plane, with its origin set at the upper-left (NE) corner of the seismic profile. Following this, the continuous linear interpretations were resampled into a series of discrete points at a constant horizontal spacing of 2 km. This process created a regularly spaced set of nodes, which will facilitate the extraction of thermal data in the following steps (Figure 2).

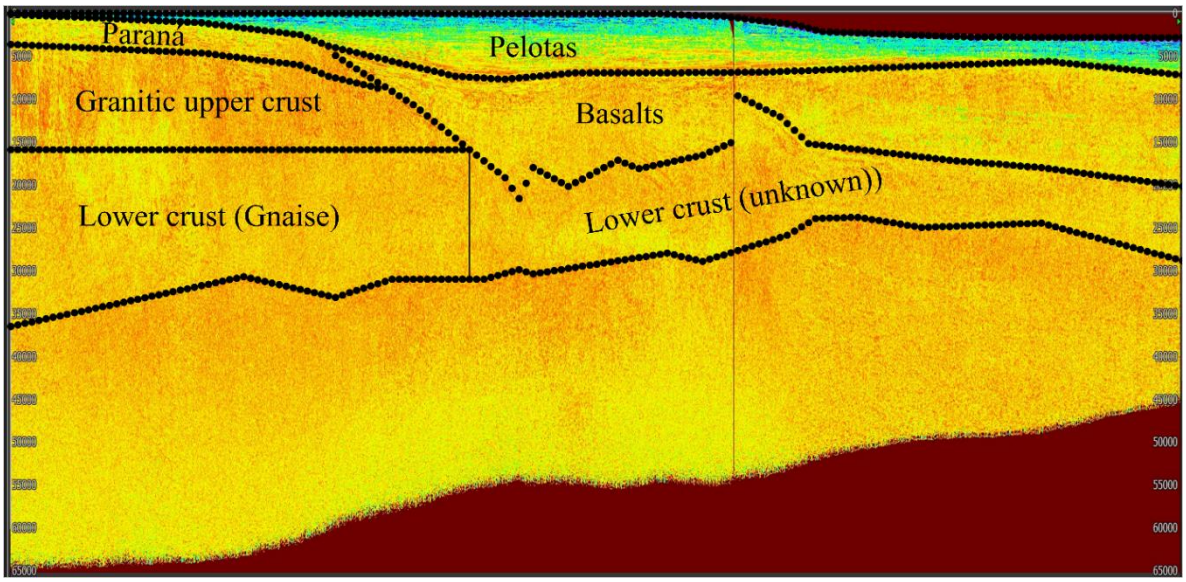

Figure 2. Interpretation of main lithological units in Line 1 (Figure 1). The instantaneous frequency attribute was used because it marked the Moho very well.

These points were converted into keypoints in Ansys by importing them into the Ansys Parametric Design Language (APDL). The APDL script was intentionally chosen for the workflow as it allows the fast testing of different thermal parameters. The thermal boundary conditions were then defined for the model by specifying temperatures at key points (Figure 3). For the lower boundary, the Moho temperature was calculated for each keypoint as a function of its depth. This calculation was based on the regional depth of the Lithosphere-Asthenosphere Boundary (LAB) at 80 km (Artemieva & Mooney, 2001). By assuming the LAB represents the 1300 °C isotherm, a linear geothermal gradient of 16.25 °C/km (1300 °C/80 km) was established and used to assign a temperature to each Moho keypoint. The vertical boundaries of the model were defined as adiabatic (by default), meaning no heat flows across them.

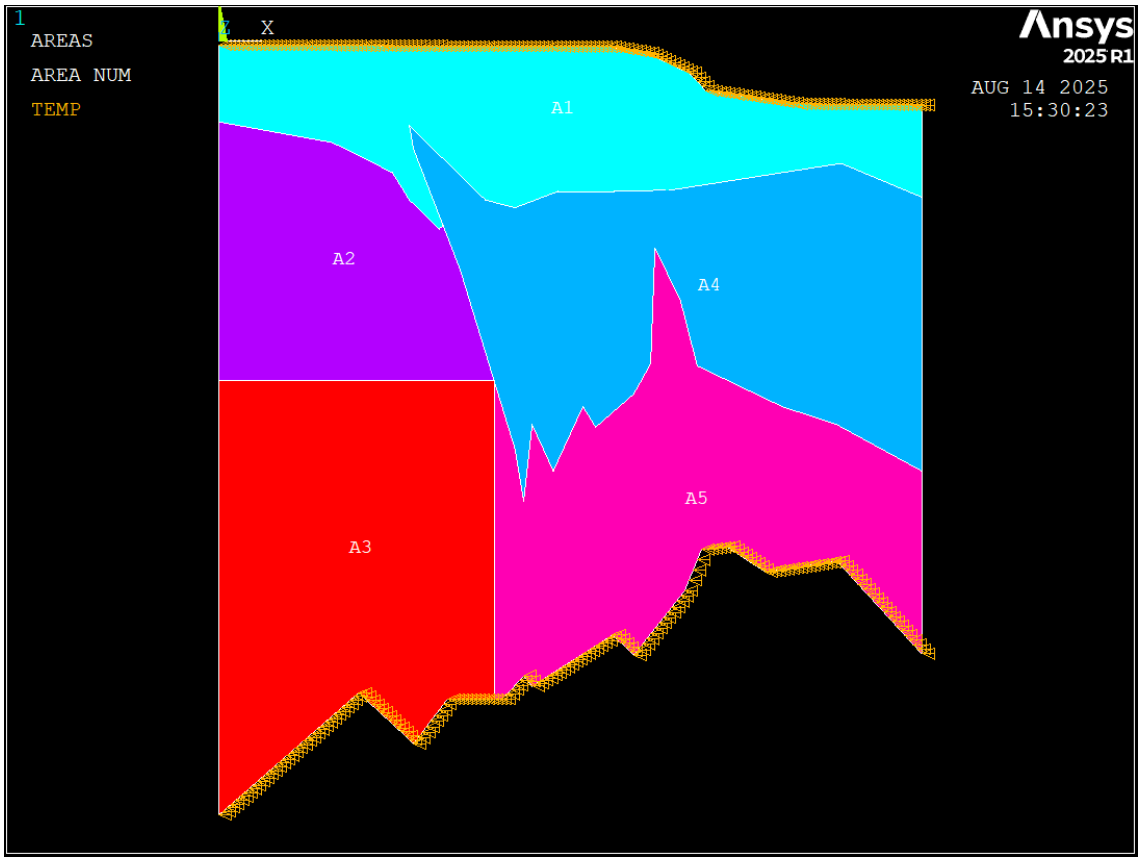

Figure 3. Geometrical modeling of Line 1 (Figure 2) on Ansys. The triangles are the imposed temperatures. A1) Sedimentary section, including deposits from the Pelotas and Paraná Basins; A2) A granitic upper crust; A3) a gneissic lower crust; A4) a volcanic section; A5) an unknown lower crust; different types of lithology were tested.

The model upper boundary condition, that is, the seafloor temperature, was calculated as a function of depth using the following empirical equation.

$$T = -4.071 \cdot \ln(D) + 34.556$$

Where T is the temperature in Celsius and D is the depth in meters.

This equation was derived from a logarithmic regression of deepest water temperatures measured against depth, using data from the World Ocean Atlas 2018 (WOA18). The regression analysis, which was constrained to the study area (26.5°S–37.5°S, 43.5°W–52.5°W), yielded a high coefficient of determination (R2=0.9263). A detailed description of this procedure is provided in Article 2 (Section 4).

The thermal model is based on two physical properties, heat generation (due to radiation) and thermal conductivity. For the basalts, we assume the heat generation as 0.15μW/m³ (Hasterok & Webb, 2017). For all lower crust divisions, it was assumed that the heat generation was 0.18μW/m³ (Rudnick & Gao, 2014). For the upper crust, excluding the sedimentary and the basalt section, the value of 1.6 μW/m³ was used (Rudnick & Gao, 2014). For the sedimentary section, ten different values (from 0.21μW/m³ to 2.1μW/m³ - (Finlay et al., 2023) were tried to determine which value best fit the data from well 2-BPS-6A-BP-RS.it. Non-linear models of thermal conductivity (λ in W/mK) as a function of temperature (T in K). For the basalts, experimental values from Hartlieb et al. (2016) were used. From granites of the upper crust and gneiss from the lower crust, the following Seipold (2001) equations were used:

$$\lambda_{granite} = \frac{1}{0.156 + 5.45 \cdot 10^{-4}T} + 0.763 \cdot 10^{-9} \cdot T^3$$

$$\lambda_{gnaise} = \frac{1}{0.191 + 5.25 \cdot 10^{-4}T} + 0.670 \cdot 10^{-9} \cdot T^3$$

For the unknown lower crust, different lithologies, mafic granulite, amphibolite, and peridotite, were tried, based on the functions given by Seipold (2001):

$$\lambda_{Amphibolite} = \frac{1}{0.315 + 3.04 \cdot 10^{-4} \cdot T} + 0.326 \cdot 10^{-9} \cdot T^3$$

$$\lambda_{Mafic\ Granulite} = \frac{1}{0.344 + 3.27 \cdot 10^{-4} \cdot T} + 0.445 \cdot 10^{-9} \cdot T^3$$

$$\lambda_{Peridotite} = \frac{1}{-42.9 + 0.389 \cdot T} + 7.2 \cdot 10^{-11} \cdot T^3$$

Pressure corrections also were made for all crystalline rocks using the Kukkonen et al. (1999) corrections :

$\lambda = \lambda_0(1 + 0.0001P)$

Where λ is the corrected value of λ_0 (original thermal conductivity in W/mK) and P, pressure values in MPa, the pressure in (MPa) was defined as the mean value of depth (in meters) multiplied by the Earth's crust pressure gradient 0,0333 Mpa/m (Hastie et al., 2016).

For the sedimentary pile, the Vosteen and Schellschmidt (2003) function was used, given by:

$$\lambda_{Sedimentary\ rock} = \frac{\lambda_{273k}}{0.99 + (T - 273) \cdot (0.0034 - (\frac{0.0039}{\lambda_{273k}})}$$

Where λ_{273k} is given by:

$$\lambda_{273k} = 0.54 \cdot \lambda_{298k} + 0.5\sqrt{1.16 \cdot {\lambda_{298k}}^2 - 0.39} \cdot \lambda_{298k}$$

It was tested with twelve different values of sedimentary thermal conductivity at 298 K (λ298k K), ranging from 0.5 to 3.25 W/m°C (Eppelbaum, 1996). Pressure corrections were made using Fuchs and Forster (2014)

$$\lambda = \lambda_0(1.095 \cdot \lambda_0 + 0.172 \cdot P)^{(0.0088\ \lambda_0 \cdot -0.006)}$$

Where λ is the corrected value of λ_0 (original thermal conductivity in W/mK) and P, pressure values in MPa.

To calibrate the model parameters, a Python script (digital Annex) was developed to systematically test all combinations of thermal parameters, focusing first on seismic Line 1 (Figure 1). Three parameters were re-combined: the radiogenic heat production within the sedimentary basin, the thermal conductivity of the unknown lower crust, and the thermal

conductivity of the sediments. This process generated a suite of 360 model configurations. For each configuration, an Ansys thermal simulation was run, and the two modeled temperatures at locations corresponding to the BHTs from well 2-BPS-6 were extracted and saved as a text file. A second Python script (Digital Annex) then compared the modeled temperatures from all 360 runs against the measured BHTs, ranking the models by their cumulative misfit. The best-fit model for Line 1 exhibited a total absolute temperature difference of 5.76 K across the two BHT points, corresponding to an average misfit of 2.88 K per measurement.

To validate the model, an additional analysis of the BHTs was performed. Firstly, temperature (°C) was plotted against depth (m, with sea level as the datum), as shown in Figure 4. This plot revealed a strong linear correlation between the two variables.

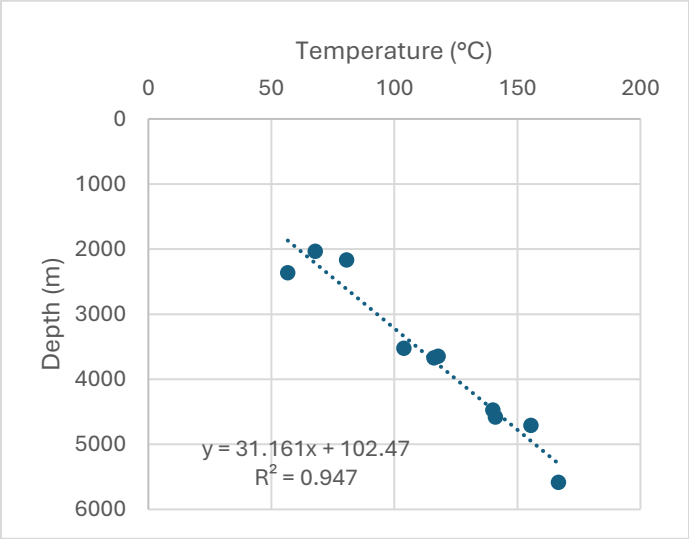

Figure 4: BHTs data plotted depth vs temperature.

The data were then plotted well-by-well to ensure the observed correlation was not a statistical artifact resulting from the Simpson Paradox. After confirming that the trend was genuine, several adjustments were made to refine the correlation model. These adjustments included: (I) changing the depth datum from sea level to the seafloor; (II) incorporating the aforementioned seafloor temperature model; and (III) adding supplementary BHT data from the Punta del Este Basin (Table 1). The final, refined model demonstrates a strong

dependence of temperature on depth (relative to the seafloor), yielding a coefficient of determination (R^2) of 0.9755.

Table 1. Thermal data used in the final model

Well	Depth(sea level datum)	Depth(sea bottom datum)	Temperature C	Temperature K	Temperature F	Method
1-BRSA-61-RSS	654	0	8.163269972	281.31327	46.69388595	SeaBottom model
1-BRSA-61-RSS	2365	1711	56.66666667	329.8166667	134	BULLARD
1-SCS-2-SC	157	0	13.97202333	287.1220233	57.14964199	SeaBottom model
1-SCS-2-SC	2164	2007	80.55555556	353.7055556	177	LACHENBRUCH & BREWER
1-SCS-2-SC	3669	3512	116.1111111	389.2611111	241	LACHENBRUCH & BREWER
1-SCS-2-SC	4580	4423	141.1111111	414.2611111	286	LACHENBRUCH & BREWER
2-BPS-6-A	337	0	10.86244239	284.0124424	51.5523963	SeaBottom model
2-BPS-6-A	4471	4134	140	413.15	284	LACHENBRUCH & BREWER
2-BPS-6-A	5586	5249	166.6666667	439.8166667	332	LACHENBRUCH & BREWER
1-SCS-3B	187	0	13.26015682	286.4101568	55.86828228	SeaBottom model
1-SCS-3B	2032	1845	67.77777778	340.9277778	154	LACHENBRUCH & BREWER
1-SCS-3B	3644	3457	117.7777778	390.9277778	244	LACHENBRUCH & BREWER
1-SCS-3B	4706	4519	155.5555556	428.7055556	312	LACHENBRUCH & BREWER
1-RSS-3-RS	50	0	18.63015434	291.7801543	65.53427782	SeaBottom model
1-RSS-3-RS	3522	3472	103.8888889	377.0388889	219	LACHENBRUCH & BREWER
Gaviotín X1	81	0	16.66619749	289.8161975		SeaBottom model
Gaviotín X1	1035.5	954.5	52.5	325.65		Novo et al., 2024
Gaviotín X1	2554.4	2473.4	84.7	357.85		Novo et al., 2024
Gaviotín X1	3047.1	2966.1	98.6	371.75		Novo et al., 2024
Gaviotín X1	3629.3	3548.3	132	405.15		Novo et al., 2024
Raya	3407	0	-1.8	271.35		Novo et al., 2024
Raya	5630	2223	103.3	376.45		Novo et al., 2024

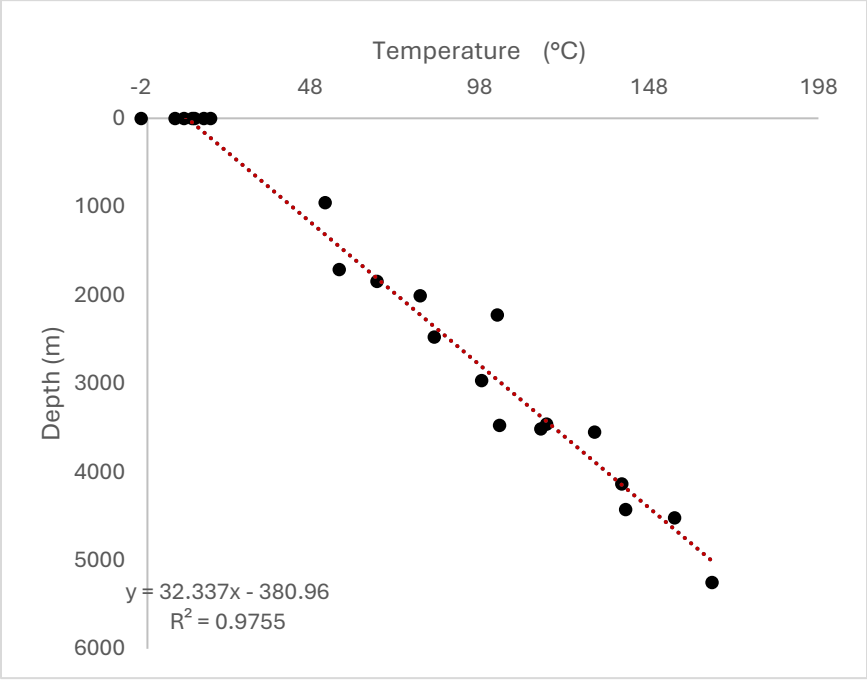

Figure 5. Bottom-Hole Temperatures (BHTs) and the seafloor temperature model are plotted against depth.

A direct comparison between the linear regression model and the vertical temperature profile from the 2D Ansys simulation model for Line 1, restricted to the basin depths, reveals a significant divergence (Figure 6). The two models only converge near the BHTs used for calibration of the Ansys model; Once the algorithm 2 selects just models that converge for these two values only. Elsewhere along the profile, their predictions differ widely (Figure 6). This difference suggests that the 2D simulation model, while honoring the BHTs, fails to capture the thermal behavior of the basin. The dominance of large-scale heat transfer processes can explain this apparent failure of the 2D simulation model. The BHT dataset, derived from wells across proximal, distal, northern, and southern regions with varied crustal and basalt thicknesses, remarkably conforms to a single, strong linear trend (as previously shown in Figure 5). This uniformity across geologically distinct areas strongly suggests that lateral (horizontal) heat flow is homogenizing the basin's thermal field. A dip direction 2D model cannot account for these 3D effects and is therefore only accurate where locally calibrated. Consequently, despite its simplicity, the linear regression model is a more robust and representative tool for predicting the regional thermal state of the basin, implying that local geological variations have a subordinate impact on basin-wide temperatures. In that way, the simulations were not utilized. The regression model was used for the analysis of the H_2 system in Article 2 (Section 4).

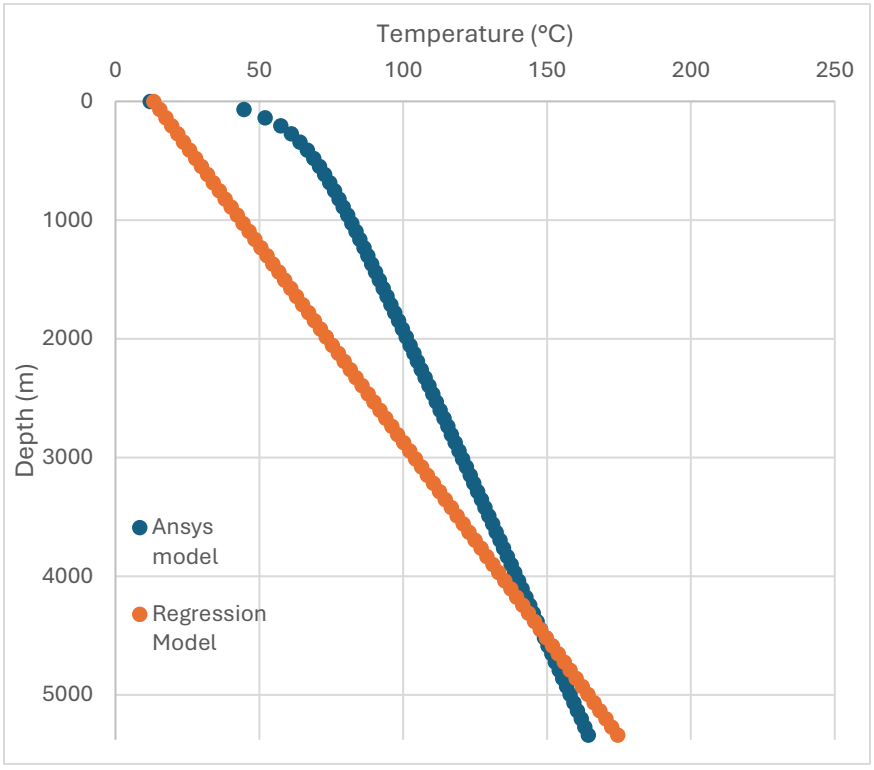

Figure 6 Comparison between the regression of wells data and the best Ansys simulation in the sedimentary section (5368m depth from the sea bottom), the Ansys data was extracted as close as possible to well 2-BPS-6 to simulate a profile at this well location. This plot extends to the SDRs, although the linear model should not be representative at this point.

References

Ansys, Inc. (2024). *Command reference*. Ansys Help. https://ansyshelp.ansys.com/public/account/secured?returnurl=/Views/Secured/corp/v242/en/ans_cmd/Hlp_C_CmdTOC.html

Artemieva, I. M., & Mooney, W. D. (2001). Thermal thickness and evolution of Precambrian lithosphere: A global study. *Journal of Geophysical Research: Solid Earth*, *106*(B8), 16387-16414.

Chauvet et al., 2021. F. Chauvet, F. Sapin, L. Geoffroy, J.C. Ringenbach, J.N. Ferry. Conjugate volcanic passive margins in the austral segment of the South Atlantic–architecture and development.Earth Sci. Rev., 212 (2021), Article 103461,

Eppelbaum, L., Modelevsky Jr, M., & Pilchin, A. (1996). Geothermal investigations in the Dead Sea Rift zone, Israel: implications for petroleum geology. Journal of Petroleum Geology, 19(4), 425-444.

Finlay, A. J., Wray, D. S., Comfort, G., & Moore, J. K. (2023). Radioactive heat production variations in the Faroe–Shetland Basin: key new heat production, geological and geochronological data for regional and local basin modelling. Petroleum Geoscience, 29(4), petgeo2022-039.

Geoffroy, E.B. Burov, P. Werner. Volcanic passive margins: another way to break up continents. Sci. Rep., 5 (1) (2015), pp. 1-12,

Gordon, W.U. Mohriak. Seismic Volcano-Stratigraphy in the Basaltic Complexes on the Rifted Margin of Pelotas Basin, Southeast Brazil (2015).

Hartlieb, P., Toifl, M., Kuchar, F., Meisels, R., & Antretter, T. (2016). Thermo-physical properties of selected hard rocks and their relation to microwave-assisted comminution. Minerals Engineering, 91, 34-41.

Hasterok, D., & Webb, J. (2017). On the radiogenic heat production of igneous rocks. Geoscience Frontiers, 8(5), 919-940. https://www.sciencedirect.com/science/article/pii/S1674987117300579

Rudnick, R. L., & Gao, S. 3.01—Composition of the Continental Crust A2—Holland, Heinrich D. Treatise on Geochemistry, 1-64.

Seipold, U. (2001). Der Wärmetransport in kristallinen Gesteinen unter den Bedingungen der kontinentalen Erdkruste.

Serratt, C. Domingues Teixeira, T.J. Girelli, M.K. de Souza, M. Rodrigues Vargas, A. Moreira Silva, F. Chemale Jr. Seaward-dipping reflector influence on seafloor magnetostratigraphy—a Pelotas Basin view. Geophys. Res. Lett., 49 (23) (2022), Article e2022GL100382

Serratt, H., Girelli, T. J., Da Cruz, M. F., Teixeira, C. D., Lehn, I., Rizzi, M., ... & Junior, F. C. (2025). Unraveling the geological history of the South Atlantic margin: Records of West Gondwana Breakup from South Brazil and Uruguay margin. *Tectonophysics*, 230790.

Stica et al., 2014. J.M. Stica, P.V. Zalán, A.L. Ferrari. The evolution of rifting on the volcanic margin of the Pelotas Basin and the contextualization of the Paraná–Etendeka LIP in the separation of Gondwana in the South Atlantic Mar. Pet. Geol., 50 (2014), pp. 1-21,

Vosteen, H. D., & Schellschmidt, R. (2003). Influence of temperature on thermal conductivity, thermal capacity and thermal diffusivity for different types of rock. Physics and Chemistry of the Earth, Parts a/b/c, 28(9-11), 499-509.